

**DRAFT**  
EIC PDR  
August 4, 2025

# Electron Ion Collider Preliminary Design Report





**Contributors:**

E-C. Aschenauer<sup>1</sup>, R. Ent<sup>2</sup>, S. Joosten<sup>3</sup>, M. Żurek<sup>3</sup>, ADD NAMES AND INSTITUTIONS

---

<sup>1</sup>Brookhaven National Laboratory, USA

<sup>2</sup>Thomas Jefferson National Accelerator Facility, USA

<sup>3</sup>Argonne National Laboratory, USA



# Contents

<b>0</b>	<b>Style Guide</b>	<b>2</b>
0.1	Chapter Abstract	2
0.2	Wordsmithing	3
0.2.1	Passive voice	3
0.2.2	Verb tenses	3
0.2.3	Apostrophes	3
0.2.4	Capitalization and names	3
0.2.4.1	Pieces of EIC	3
0.2.4.2	Internal phrases	3
0.2.4.3	Discipline-specific approaches or “guiding principles” or buzz phrases	4
0.2.4.4	Formal group names	4
0.2.4.5	Headings	4
0.2.5	Captions	4
0.2.6	Spelling	4
0.2.6.1	Exceptions to U.S. spelling	4
0.2.6.2	Capitalization	4
0.2.7	Commas	5
0.2.7.1	Commas in numbers	5
0.2.8	Plurals and possessives	5
0.2.9	Abbreviations	5
0.2.9.1	Textual treatment of Figures and Tables	5
0.2.9.2	Radio frequency	5
0.2.9.3	etc., et cetera	6
0.2.10	Hyphenation of multi-word adjectival phrases	6
0.2.11	Double letters	10
0.2.12	Mathematical symbols, subscripts and superscripts	10
0.2.13	Quotation marks	10
0.2.14	Citations, references and the bibliography	10
0.2.15	Miscellaneous	11
0.2.15.1	“Calculations show that . . .”	11
0.2.15.2	“Should”, “must”, and reference to future studies	11
0.2.15.3	“Enable”	11
0.2.15.4	Reporting technical results without a clear statement of their import	11
0.2.15.5	Excessive and inconsistent use of lists	11
0.2.15.6	Cross-references	12
0.2.15.7	Isotopes	12
0.2.15.8	*** asterisks in comments	12
0.3	Dimensions and units	12
0.4	Numbering – chapters, sections, and subsections	13

0.4.1	This is the heading of a subsection . . . . .	13
0.4.1.1	A subsubsection heading like this has no period at the end . . . . .	13
	This paragraph heading ends with a period. . . . .	13
0.4.2	More formatting rules and standards . . . . .	14
0.4.2.1	Clearpages and Pagebreaks . . . . .	14
0.5	Equations, Tables, Figures, and plots . . . . .	14
0.5.1	Equations . . . . .	14
0.5.2	Tables . . . . .	14
0.5.3	Converting between LaTeX and Excel table formats . . . . .	14
0.5.4	Figures . . . . .	17
0.5.5	Plots . . . . .	17
0.6	Italics and bold face type . . . . .	17
0.7	Issues that this Style Guide does not yet address . . . . .	18
<b>2</b>	<b>Physics Goals and Requirements</b> . . . . .	<b>19</b>
2.1	EIC Context and History . . . . .	19
2.2	The Science Goals of the EIC and the Machine Parameters. . . . .	21
2.3	Reconstruction Tools and Special Probes . . . . .	21
2.3.1	Reconstruction of DIS kinematics . . . . .	21
2.3.2	Semi-inclusive kinematics and hadron identification . . . . .	24
2.3.3	Reconstruction of kinematics for exclusive and diffractive processes . . . . .	25
2.3.4	Electron identification . . . . .	27
2.3.5	Muon identification . . . . .	28
2.3.6	Jets: a versatile probe . . . . .	29
2.4	The EIC Science - ePIC performance for key observables . . . . .	30
2.4.1	Origin of Nucleon Mass . . . . .	30
2.4.1.1	Inclusive neutral current cross sections . . . . .	31
2.4.2	Origin of Nucleon Spin . . . . .	33
2.4.3	Multi-Dimensional Imaging of the Nucleon . . . . .	34
2.4.3.1	Imaging in Momentum Space . . . . .	34
2.4.3.2	Imaging in Transverse Position Space . . . . .	37
2.4.3.3	Upsilon production . . . . .	40
2.4.4	Properties of Nuclear Matter . . . . .	42
2.4.4.1	Gluon Saturation . . . . .	42
2.4.4.2	Nuclear Modifications of Parton Distribution Functions . . . . .	43
2.4.4.3	Passage of Color Charge Through Cold QCD Matter . . . . .	43
2.4.5	Additional physics opportunities . . . . .	46
<b>8</b>	<b>Experimental Systems</b> . . . . .	<b>48</b>
8.1	Experimental Equipment Requirements Summary . . . . .	48
8.2	General Detector Considerations and Operations Challenges . . . . .	49
8.2.1	General Design Considerations . . . . .	49
8.2.2	Backgrounds and Rates . . . . .	49
8.2.3	Radiation Level . . . . .	50
8.2.3.1	Doses and fluences from e+p minimum-bias events . . . . .	50
8.2.3.2	Doses and fluences from hadron beam+gas events . . . . .	51
8.2.3.3	Doses and fluences from electron beam+gas events . . . . .	52
8.3	The ePIC Detector . . . . .	55
8.3.1	Introduction . . . . .	55
	The Context . . . . .	55
	The Detector . . . . .	56

	Technological Synergistic Aspects of the Detector Design . . . . .	62
8.3.2	Magnet . . . . .	63
	Introduction . . . . .	63
	Requirements . . . . .	63
	Geometry and Materials of the Yoke . . . . .	66
	Description of the magnet . . . . .	66
	Magnet Design . . . . .	71
	Conductor Design . . . . .	77
	Mechanical Design . . . . .	78
	Transient Analysis and Quench Protection . . . . .	82
	Quench Analysis . . . . .	82
	Cryogenic Design . . . . .	88
	Instrumentation and Controls . . . . .	93
	Summary . . . . .	95
8.3.3	Tracking . . . . .	95
8.3.3.1	The silicon trackers . . . . .	98
	Requirements . . . . .	98
	Justification . . . . .	101
	Implementation . . . . .	105
8.3.3.2	The MPGD trackers . . . . .	119
	Requirements . . . . .	119
	Justification . . . . .	121
	Performance . . . . .	126
	Implementation: . . . . .	126
	Additional Material: . . . . .	131
8.3.4	Particle Identification . . . . .	135
8.3.4.1	The time-of-flight layers . . . . .	139
	Requirements and Justifications . . . . .	139
	Implementation . . . . .	148
	Additional Material . . . . .	159
8.3.4.2	The proximity focusing RICH . . . . .	160
	Requirements . . . . .	160
	Justification . . . . .	161
	Implementation . . . . .	168
8.3.4.3	The high performance DIRC . . . . .	176
	Requirements . . . . .	176
	Justification . . . . .	176
	Performance . . . . .	179
	Performance Systematic Studies . . . . .	180
	Simulation tools and validation . . . . .	180
	Reconstruction methods . . . . .	181
	Implementation . . . . .	182
	Additional Material . . . . .	188
8.3.4.4	The dual radiator RICH . . . . .	189
	Requirements . . . . .	189
	Justification . . . . .	189
	Performance . . . . .	194
	Implementation . . . . .	196
8.3.5	Electromagnetic Calorimetry . . . . .	207
8.3.5.1	The backward endcap electromagnetic calorimeter . . . . .	208
	Requirements . . . . .	208

	Justification . . . . .	208
	Implementation . . . . .	214
	Additional Material: prototype and beam tests . . . . .	220
8.3.5.2	The barrel electromagnetic calorimeter . . . . .	222
	Requirements . . . . .	222
	Justification . . . . .	222
	Implementation . . . . .	232
	Additional Material . . . . .	239
8.3.5.3	The forward endcap electromagnetic calorimeter . . . . .	245
	Introduction . . . . .	245
8.3.6	Hadronic Calorimetry . . . . .	258
8.3.6.1	The backward endcap hadronic calorimeter . . . . .	258
	Requirements . . . . .	258
	Justification . . . . .	259
	Implementation . . . . .	265
	Additional Material . . . . .	273
8.3.6.2	The barrel hadronic calorimeter . . . . .	276
	Requirements . . . . .	276
	Justification . . . . .	277
	Performance . . . . .	281
	Implementation . . . . .	285
8.3.6.3	The forward endcap hadronic calorimeter . . . . .	295
	Requirements . . . . .	295
	Justification . . . . .	295
	Implementation . . . . .	300
	Additional Material . . . . .	308
8.3.7	Far-forward detectors . . . . .	310
8.3.7.1	The detectors in the B0 bending magnet . . . . .	310
	Requirements . . . . .	310
	Justification . . . . .	311
	Implementation . . . . .	313
8.3.7.2	The roman pots and the off-momentum detectors . . . . .	316
	Requirements . . . . .	316
	Justification . . . . .	318
	Implementation . . . . .	320
	Additional Material . . . . .	325
8.3.7.3	The Zero Degree Calorimeter . . . . .	325
	Requirements . . . . .	325
	Justification . . . . .	328
	Implementation . . . . .	329
	Additional Material . . . . .	338
8.3.8	Far backward detectors . . . . .	338
8.3.8.1	The luminosity system . . . . .	340
	Introduction . . . . .	340
	Requirements . . . . .	343
	Systematic Uncertainties - . . . . .	344
	Justification . . . . .	344
	Implementation . . . . .	348
	Additional Material . . . . .	350
8.3.8.2	The low $Q^2$ taggers . . . . .	350
	Requirements . . . . .	350

	Justification . . . . .	354
	Performance . . . . .	357
	Implementation . . . . .	357
	Additional Material . . . . .	360
8.3.9	Polarimeters . . . . .	361
8.3.9.1	The electron polarimeters . . . . .	361
	Requirements . . . . .	361
	Justification . . . . .	361
	Implementation . . . . .	362
8.3.9.2	The proton polarimeters . . . . .	362
	Requirements . . . . .	362
	Justification . . . . .	363
	Implementation . . . . .	363
8.3.10	Readout Electronics and Data Acquisition . . . . .	364
8.3.10.1	Requirements . . . . .	364
8.3.10.1.1	Requirements from Physics . . . . .	364
8.3.10.1.2	Requirements from Radiation Hardness . . . . .	364
8.3.10.1.3	Requirements from Data Rates . . . . .	367
8.3.10.2	Device Concept and Technological choice: Streaming Readout . . . . .	368
8.3.10.3	Subsystem Description (components) . . . . .	369
8.3.10.3.1	ASICs and digitization PCBs . . . . .	369
8.3.10.3.2	FEB . . . . .	376
8.3.10.3.3	RDO . . . . .	377
8.3.10.3.4	DAM - Data Aggregation and Manipulation Hardware . . . . .	379
8.3.10.3.5	GTU - Global Timing Unit . . . . .	380
8.3.10.3.6	Protocols . . . . .	382
8.3.10.3.7	DAQ/Online Computing - Echelon 0 . . . . .	384
8.3.10.3.8	Slow Controls . . . . .	387
8.3.10.4	Implementation . . . . .	388
8.3.10.5	Calibration, alignment and monitoring: . . . . .	388
8.3.10.6	Status and remaining design effort: . . . . .	388
8.3.10.7	Environmental, Safety and Health (ES&H) aspects and Quality Assessment (QA planning: . . . . .	389
8.3.10.8	Construction and assembly planning: . . . . .	389
8.3.10.9	Collaborators and their role, resources and workforce . . . . .	389
8.3.11	Software and Computing . . . . .	389
	Computing Use Cases . . . . .	390
	Computing Resources . . . . .	393
	Distributed Computing . . . . .	399
	Project Organization and Collaboration . . . . .	402
	Long Term Software and Computing Plan . . . . .	403
8.4	Detector Integration . . . . .	404
8.4.1	Installation and Maintenance . . . . .	404
8.5	Detector Commissioning and Pre-Operations . . . . .	404



# List of Figures

1	Example of a non-graphical figure. . . . .	17
2.1	Neutral-Current Deep Inelastic Scattering of an electron by a proton. . . . .	22
2.2	Resolution of the inelasticity $y$ , as a function of $x_B$ and $Q^2$ , when reconstructed using the electron method (blue), $\Sigma$ method (green), or Double-angle method (orange). The color of each point indicates the best performing reconstruction method. . . . .	24
2.3	Resolution of the hadron fractional momentum $z$ as a function of the true $z$ for pions, in three $x$ and $Q^2$ bins when the reconstructed kinematics for the DIS lepton, hadron, or both are considered. . . . .	25
2.4	PID efficiencies (top) and purities (bottom) of kaons as a function of the true hadron momentum are shown in three rapidity ranges relevant for the different detector choices of ePIC. . . . .	26
2.5	Resolution of $t$ as a function of the true $t$ for both B0 and RP for $ep$ 10 on 100 GeV. .	28
2.6	Figure of merit for muon identification as a function of momentum in the ePIC central barrel. . . . .	29
2.7	Jet energy scale (Left) and jet energy resolution (Right) as a function of particle-level jet energy for backward (blue squares), mid (red triangles), and forward (green diamonds) rapidities. . . . .	30
2.8	Projected $ep$ neutral current reduced cross sections at 5x41 GeV. Statistical uncertainties assume an integrated luminosity of $10 \text{ fb}^{-1}$ . . . . .	31
2.9	Projected $ep$ neutral current reduced cross sections at 10x100 GeV. Statistical uncertainties assume an integrated luminosity of $10 \text{ fb}^{-1}$ . . . . .	32
2.10	Projected $ep$ neutral current reduced cross sections at 18x275 GeV. Statistical uncertainties assume an integrated luminosity of $10 \text{ fb}^{-1}$ . . . . .	32
2.11	Statistical and total uncertainty for selected bins in $x_B$ as a function of $Q^2$ for pessimistic and optimistic estimates of systematic uncertainty. . . . .	33
2.12	Projected measurements of $A_1^p$ (right) and $A_1^n$ (left). . . . .	34
2.13	Statistical (error bars) and total (error bands) uncertainty for each selected bins in $x_B$ and $Q^2$ and for selected ranges in $z$ , for positive-pion $A_1$ asymmetries at $5 \times 41 \text{ GeV}^2$ (top two rows) and $18 \times 275 \text{ GeV}^2$ (bottom two rows). An additional global scale uncertainty of 2% accounts for the uncertainty in the beam polarizations, as indicated in the figure. The central value on the vertical axis of the data points has no meaning. . . . .	35

2.14	Left: Expected statistical and total uncertainty of un-polarized TMD PDFs for $\pi^+$ in the $Q^2 - x_B$ plane. The inner (colored) circle shows the statistical uncertainty, while the outer circle provides the total uncertainty for each $Q^2 - x_B$ bin. The color shows the beam energy configuration which provides the highest statistics in a specific bin. Right panel: Expected uncertainties of valence down (green) and sea quark (orange) TMD PDFs at $x = 0.1$ (left) and $x = 0.001$ (right) as obtained based on the MAP24 [1] global TMD fit. The lighter shaded regions show the uncertainties based on existing data while the darker shaded regions show the expected uncertainties after including ePIC data. . . . .	37
2.15	Top: Expected uncertainties in three example $x$ - $Q^2$ bins for the Collins asymmetries for positive pions as a function of the momentum fraction $z$ and in three bins of hadron transverse momentum relative to the virtual photon direction assuming a luminosity of $10 \text{ fb}^{-1}$ . Bottom, the same but as a function of the hadron transverse momentum in bins of $z$ . . . . .	38
2.16	Collins asymmetries for hadrons in jets . . . . .	39
2.17	Generated and reconstructed $t$ -distributions for fully-exclusive DVCS events. . . . .	40
2.18	Reconstructed minus generated track $\theta$ for all reconstructed DVCS photons (left), as well as as a function of the generated photon $\theta$ (right). Note that the left plot is on a logarithmic scale. . . . .	40
2.19	The reconstructed mass distribution of the $Y$ three states in the electron channel from the electron-proton collisions at $18 \times 275 \text{ GeV}$ , utilizing the tracker with realistic seeding. The top left plot shows the invariant mass distribution of the $Y$ three states in the rapidity range from -3 to 4. The other plots display invariant mass distribution for specific rapidity intervals: (top middle) $-3 < y < -1$ , (top right) $-1 < y < 0$ , (bottom left) $0 < y < 1$ , (bottom middle) $1 < y < 2$ , and (bottom right) $2 < y < 4$ . The resolution of the $Y$ three states is indicated on each plot as $\sigma$ . . . . .	41
2.20	Left: differential distribution of the momentum transfer $ t $ of coherent $\phi$ meson electroproduction in electron-gold collisions with $18 \times 110 \text{ GeV}$ . The Monte Carlo model is provided by Sartre and the reconstructed distribution is obtained from full ePIC simulation with the official August 2024 simulation campaign. Right: the momentum transfer $t$ reconstruction resolution as a function of the true $t$ . . . . .	43
2.21	Left: Differential cross-section of momentum transfer $t$ distribution for coherent (blue) and incoherent (black) exclusive $J/\psi$ production in $ePb$ collisions. Right: Differential measurement of $t$ and the residue distributions after each veto based on the far-forward detector system. . . . .	44
2.22	Invariant mass distributions of $\pi + K$ pairs with (red circles) and without (black squares) topological selections in $10 \times 100 \text{ GeV}$ $e+p$ (top) and $e+Au$ (bottom) collisions with a minimum $Q^2$ of $1 \text{ GeV}^2$ . Different panels from left to right correspond to different $D^0$ rapidity intervals: $-3 < y < -1$ (left), $-1 < y < 1$ (middle) and $1 < y < 3$ (right). . . . .	45
2.23	Projection of relative statistical errors on $D^0$ yield ratios between $10 \times 100 \text{ GeV}$ $e+Au$ and $e+p$ collisions as a function of $D^0$ $p_T$ for three different $D^0$ rapidity intervals. . . . .	45
8.1	Table presenting the Experimental Equipment Requirements Summary in the YR. At present, the table is not updated and it is here as a mere space holder. . . . .	48
8.2	Vacuum level at IP6 for three different integrated electron current assumed for the backout. . . . .	50

8.3	This figure shows the total energy deposited in 2cm x 2cm x 1cm bins spanning the full size of the ePIC central detector from minimum-bias e+p events generated in PYTHIA6 for 10 GeV electrons colliding with 275 GeV protons. This energy combination represents the highest potential luminosity for the EIC. The results are shown as energy deposits per $\text{fb}^{-1}$ .	51
8.4	Total ionizing dose per $\text{fb}^{-1}$ for the central region of ePIC detector from minimum-bias e+p events.	52
8.5	1 MeV neutron equivalent fluences for the central ePIC detector from minimum-bias e+p events. Peak regions of MEQ fluence are seen near the beam pipe, and within the hadronic calorimeters, where the inclusion of dense absorber materials (e.g. iron) provides ample scattering centers to produce hadronic showers which can include high numbers of low-energy neutrons to provide peak MEQ fluences.	53
8.6	Fluxes of protons (left) and neutrons (right) with kinetic energy $> 20$ MeV from minimum-bias e+p events. These fluxes are important to understand areas where detector electronics could often experience SEUs, and require intervention (e.g. re-setting).	53
8.7	This figure shows the total energy deposited in 2cm x 2cm x 1cm bins spanning the full size of the ePIC central detector from hadron beam+gas events with 275 GeV protons. The results are shown as energy deposits per $\text{fb}^{-1}$ .	54
8.8	Total ionizing dose from hadron beam+gas events per $\text{fb}^{-1}$ for the central region of ePIC detector.	55
8.9	1 MeV neutron equivalent fluences for the central ePIC detector from hadron beam+gas events. Peak regions of MEQ fluence are seen near the beam pipe, and especially near the radial interior of the calorimeters, similar to what is seen in the minimum-bias events.	56
8.10	Fluxes of protons (left) and neutrons (right) with kinetic energy $> 20$ MeV from hadron beam+gas events.	56
8.11	This figure shows the total energy deposited in 2cm x 2cm x 1cm bins spanning the full size of the ePIC central detector from electron beam+gas events with 10 GeV electrons. The results are shown as energy deposits per $\text{fb}^{-1}$ .	57
8.12	Total ionizing dose from electron beam+gas events per $\text{fb}^{-1}$ for the central region of ePIC detector.	58
8.13	A schematic showing how hadrons and the scattered electron for different $x - Q^2$ are distributed over the detector rapidity coverage. THIS FIGURES IS A PLACE HOLDER: IT IS FROM YR AND REQUIRES REVISION.	59
8.14	A schematic showing the ePIC central detector subsystems. THIS FIGURES IS A PLACE HOLDER	60
8.15	Cumulative material budget in radiation lengths (top row) and interaction lengths (bottom row) for the whole CD (left column) and zooming at the CD tracking region (right column). THIS FIGURES IS A PLACE HOLDER BECAUSE IT HAS TO BE COMPLETED WITH SUBSYSTEM CONTOURS AND REQUIRES GRAPHICAL IMPROVEMENTS.	60
8.16	A schematic showing the ePIC far detector subsystems. THIS FIGURES IS A PLACE HOLDER	61
8.17	MARCO Magnet inside the iron yoke.	64
8.18	IR Layout showing all the other magnets	65
8.19	BH curve of 1020 steel	67
8.20	MARCO cold mass layout inside the cryostat.	67
8.21	Schematic cross section of coil pack and conductor	67
8.22	Electric schematic of MARCO Solenoid	68
8.23	Conductor entrance and exit schematic for each module	69

8.24	Design of the Splices exits from the mandrel . . . . .	69
8.25	Schematic cross-section of the splice to be place inside the groove . . . . .	70
8.26	Schematics of the geometry at the interface between each coil . . . . .	70
8.27	Schematics of the tie-rods geometry . . . . .	71
8.28	Magnet assembly inside the cryostat . . . . .	71
8.29	Schematics of the cryostat with the magnet inside . . . . .	71
8.30	The 2D finite element model . . . . .	72
8.31	Magnetic field on the coil and yoke from 3D OPERA model for the 2.0 T field . . . . .	73
8.32	Field uniformity in the required area . . . . .	74
8.33	Projectivity in the required area . . . . .	74
8.34	5G line around the ePIC yoke. Thanks to the high level of symmetry, the field is the same in both Y and X direction . . . . .	74
8.35	5G line around the ePIC yoke. Thanks to the high level of symmetry, the field is the same in both Y and X direction . . . . .	75
8.36	Cross-section of the RICC conductor . . . . .	78
8.37	Jc curve @4.7 K, load line and load line margin . . . . .	79
8.38	2D axisymmetric mechanical model including the coils and the mechanical structure . . . . .	79
8.39	3D model geometry . . . . .	80
8.40	Scheme of the electric circuit of the MARCO magnet . . . . .	83
8.41	Current flowing in the magnet and in the mandrel during a fast discharge . . . . .	83
8.42	Logic structure of the COMSOL quench model . . . . .	84
8.43	Model used in COMSOL . . . . .	84
8.44	Current decay in the coils and in the mandrel . . . . .	85
8.45	Number of quenched turns as a function of time in the three different modules . . . . .	86
8.46	Resistive coil voltage as a function of time for the three modules . . . . .	86
8.47	Power dissipated in the primary and secondary circuit . . . . .	87
8.48	Hotspot temperature in the three modules of the magnet . . . . .	87
8.49	Temperature distribution on the coils and mandrel after 65s from quench . . . . .	88
8.50	Cryogenics flowchart of the MARCO solenoid . . . . .	89
8.51	Schematics of the thermosiphon system . . . . .	90
8.52	Primary and spare tubes of the thermosiphon heat exchanger . . . . .	91
8.53	Primary and spare piping on top of the mandrel . . . . .	92
8.54	Helium phase separator and cryogenic chimney overview. . . . .	92
8.55	Relative momentum resolution versus total momentum for charged pions (points) together with physics requirements (curves) in different pseudorapidity ranges as indicated. The results are based on full GEANT simulations of the central tracking system (SVT+MPGD+AC-LGAD) using the ePIC software stack and ACTS-based track finding and reconstruction using suitably tuned ACTS parameter settings. The error bars indicate the size of the statistical uncertainties in the simulation. . . . .	97
8.56	Distance of closest approach in the radial direction between reconstructed charged pion trajectories and the event origin versus transverse pion momentum (points) together with physics requirements (curves) in different pseudorapidity ranges as indicated. The results are based on full GEANT simulations of the central tracking system (SVT+MPGD+AC-LGAD) using the ePIC software stack and ACTS-based track finding and reconstruction. The error bars indicate the size of the statistical uncertainties in the simulation. . . . .	97
8.57	Tracking efficiency versus pseudorapidity $\eta$ for charged pions with initial momenta of 1 GeV to 20 GeV. . . . .	98

8.58	The number of generated charged particles vs. the generated pseudorapidity of those particles (filled black). The number of reconstructed tracks vs. the reconstructed pseudorapidity of those tracks (red crosses). The y axis shows the number of particles (tracks) per pseudorapidity bin per event. The events were generated with a $Q^2$ minimum of 1 $GeV^2$ ; the scattered electron peak can be seen at negative pseudorapidity. The particles (tracks) shown all have a generated (reconstructed) transverse momentum greater than 500 MeV/c. . . . .	99
8.59	The distribution of the track hit purity for NC DIS events with a $Q^2$ minimum of 1 $GeV^2$ . The track hit purity is defined as the fraction of measurements in a track which are associated with a given generated charged particle. The peak at 1 indicates that most of the tracks ( 99%) are associated only with a single particle. . . . .	100
8.60	Maps of simulated 1 MeV neutron equivalent fluence (left) and total ionising dose (right) over the ePIC tracking envelope. This is a conservative estimate assuming 10 years of running at top luminosity with 100% efficient accelerator and detector. The black lines indicate the approximate location of the ePIC SVT detector layers. . . . .	100
8.61	Schematic layout of the ePIC SVT showing the central region consisting of the inner and outer barrel made of three and two cylindrical layers, respectively, together with the endcap regions made of five annuli each. The figure also shows the surrounding Micro Pattern Gas Detector (MPGD) layers and the envelope of the Time of Flight PID detector. . . . .	101
8.62	Sketch of the MOSAIX sensor on a 300 mm wafer showing the size of the RSU, LEC, REC and of the full sensor for the three different widths. All positions are in mm. . . . .	104
8.63	Left: A close-up of a beam telescope constructed using 6 single-RSU sensors from the ITS3 Engineering Run 1, with a seventh sensor, the Device Under Test (DUT), placed in the middle. Right: Comparison of results from beamtests at FNAL and from simulations for the cluster extent as a function of the beam incident angle onto the DUT. . . . .	105
8.64	Schematic overview of data and slow control lines to groups of up to four EIC-LAS in the OB and disks. . . . .	107
8.65	SVT global support structure, consisting of a surrounding carbon composite support tube and a projective arrangement of spokes that form cones connecting the IB, OB, and innermost disks. Also shown are several outer disks and the beampipe. . . . .	109
8.66	Left: CAD representation of the IB global support (top) and IB half-barrel CAD view with sensors and cable routing (bottom). Right: Exploded CAD view of IB. The orange element is the kapton shield. In blue the air conveyors are shown. . . . .	110
8.67	Left: OB staves for L3 and L4. Two staves per layer are shown. Right: Exploded view of an OB stave. . . . .	110
8.68	CAD model of the preliminary (half-) disk design. Modules are shown in alternatingly inward (dark gray) and outward (white) facing orientations. Common bus FPCs are shown in orange. RDOs (green) are arranged on the outside of the disk ring, inside of the interface to the SVT global support structure. . . . .	111
8.69	Co-cured support structure of first L4 quarter length stave prototype (without silicon sensors). The co-cure comprises carbon fibre skins, K9 cross ribs, central carbon fibre I beam spar and Kapton side closeouts (compare to fig. 8.67). . . . .	113
8.70	(Left) First test piece of the carbon composite corrugated disk core made in the LBNL composite shop. Heaters with two different heating zones that can mimic the sensor power density are placed on the carbon composite facesheet and are used for thermal measurements. (Right) Observed $\Delta T$ on the LEC section of the test heater versus coolant air velocity using corrugated carbon fiber veil prototype test piece. Measurements taken with various sizes of PGS placed underneath heater. . . . .	114

8.71	An example of a low technology readiness level prototype for the FPC of the OB L4. Prototype made by RPE LTU. The figure shows the main FPC with four bridge FPCs.	115
8.72	ePIC Tracking Subsystems	119
8.73	Nhits	120
8.74	Radiation dose	120
8.75	[CyMBaL CAD model](a) CyMBaL CAD model showing the assembly of the 32 modules. (b)CAD model of a CyMBaL module. The light blue represents examples of readout strips measuring the $r \cdot \varphi$ coordinate (called Z-strips as they run along the z axis). The light yellow represents examples of readout strips measuring the z coordinate (called C-strips as they are arcs of a cylinder). The light red lines represent examples of trail lines to bring the C-strip signals to the FEBs. For the explanation of the services see the text.	122
8.76	(a) $\mu$ RWELL-BOT in ePIC central detector; (b) Arrangement of 24 $\mu$ RWELL-BOT modules in dodecagon shape.	123
8.77	Hadron and lepton beam pipes and $\mu$ RWELL-ECT disks layout.	124
8.78	Integration of the MPGD-ECT disks in the ePIC detector.	128
8.79	Design details of MPGD-ECT disks	129
8.80	MPGD General Timeline	130
8.81	Lorentz angle for different gas mixtures	132
8.82	$\mu$ RWELL-BOT $\varphi$ -module design view	133
8.83	Thin-gap GEM- $\mu$ RWELL hybrid vs. std $\mu$ RWELL detector	133
8.84	The histogram shows the relative yield of charged hadrons from Pythia simulations for $18 \times 275$ GeV $ep$ collisions as a function of momenta and pseudorapidity, $\eta$ . The contours indicate the $3\sigma$ separation region of the different ePIC PID subsystems for $\pi/K$ (a), $K/p$ (b), and $e/\pi$ (c), respectively.	137
8.85	EPIC magnetic field map with the PID detector envelopes overlaid. Shown is the 1.7 T setup.	138
8.86	(a) Estimates of the 1-MeV neutron equivalent fluence in $\text{cm}^{-2}/\text{fb}^{-1}$ and (b) the sum of electromagnetic and charged-hadron doses in $\text{rads}/\text{fb}^{-1}$ integrated in $1 \text{ fb}^{-1}$ equivalent Pythia events for $10 \times 275$ GeV $ep$ collisions. The values shown are averaged over the azimuthal angle.	139
8.87	Geometries of BTOF with strip sensors and FTOF with pixel sensors.	140
8.88	BTOF $1/\beta$ as a function of momentum (p) in the simulation performance with PYTHIA DIS events (left). Upper limits on the $3\sigma$ particle separation from BTOF and FTOF as a function of pseudorapidity (right).	141
8.89	Fluence accumulated for 6 months at 100% time, corresponding to one year of data taking, the fluence has to be multiplied by the assumed 10 years of lifetime of the ePIC detector. Red squares highlight the barrel, endcap, and B0 tracker detectors. Simulation from Fluka.	142
8.90	A schematic design of service hybrids for FTOF, which serves 3 modules or 12 sensors/ASICs.	146
8.91	A schematic design of the module for FTOF, which consists of $2 \times 2$ AC-LGAD sensors and ASICs.	147
8.92	Schematic of the AC-LGAD subsystem readout chain. Each component is undergoing design, (pre-)prototyping, testing under various environments, and customization to meet the specific requirements of individual subsystems.	147
8.93	schematic drawings of the cooling pipes in one BTOF stave (left) and half of the whole FTOF (right). Each BTOF stave has one input line and a return line, while the FTOF has a total of 4 input lines and 4 return lines.	148

8.94	BTOF supporting mechanical structure with engagement rings situated and supported by the EPIC global support tube structure (GST). The width of each of the three engagement rings is 5 mm. . . . .	150
8.95	Left: Picture and beam test results for HPK strip sensor, 1 cm long, 500 $\mu\text{m}$ pitch, and 50 $\mu\text{m}$ metal electrode width. Right: Picture and beam test results for HPK pixel sensor, 4x4, 500 $\mu\text{m}$ pitch, and 150 $\mu\text{m}$ metal electrode width. Sensors were read out by an FNAL 16ch board, plots from Ref. [2]. . . . .	152
8.96	Left: Degradation of the gain layer for AC-LGADs of several wafers (with different n+, oxide, and active thickness) from HPK latest sensor production, showing no change in gain layer doping up to $10^{13}$ Neq, which is an order of magnitude over the ePIC TOF radiation requirement. Sensors were irradiated at the TRIGA reactor (Lubjiana) with 1 MeV neutrons. Right: Normalized comparison of response profile of two nearby strips for two HPK 0.5 cm length, 500 $\mu\text{m}$ pitch, 50 $\mu\text{m}$ strip width: one before irradiation and one after $1 \times 10^{14}$ Neq. Even if the total signal is degraded, the charge-sharing profile will remain unchanged. Bottom: Current over voltage measurement for irradiated HPK sensors. . . . .	153
8.97	Left: FCFD Jitter measurements with 3.5 pF input capacitance and charge injection. Right: EICROC Discriminator jitter versus the injected charge, determined from data on an oscilloscope. Plots from the eRD112 and eRD109 2024 reports. . . . .	154
8.98	Picture of ppRDO connected with CMS ETL module board v0 for testing. . . . .	154
8.99	Assembled BTOF stave prototype at Purdue. . . . .	155
8.100	Assembly process of BTOF stave. The drawing is not to scale. . . . .	156
8.101	Assembly process of FTOF modules. RB3 type is shown as an example. The drawing is not to scale. . . . .	157
8.102	Collaboration institutions and their potential responsibilities. . . . .	158
8.103	simulation of $1/\beta$ as a function of particle momentum for BTOF and FTOF performance. . . . .	160
8.104	The proposed pFRICH detector. See the text for more details. (Figure documentation)	163
8.105	HRPPD photosensor CAD model with a passive interface board. Compression interposers between anode base plate and this PCB are not shown. (Figure documentation) . . . . .	163
8.106	Left: EIC HRPPD QE as a function of wavelength. Center: QE map in the full active area at a wavelength of 365 nm. Right: Single photon timing resolution measured using Elmo 780 femtosecond laser with a wavelength of 390 nm. (Figure documentation) . . . . .	164
8.107	(Left) The reconstructed Cherenkov angle for electrons, pions, kaons, and protons as a function of momentum. (Middle) $N_\sigma$ separation between the electron and pion hypotheses as a function of momentum. (Right) Same as the middle panel, for pion and kaon hypotheses. (Figure documentation) . . . . .	166
8.108	(left) Yield ratio of $\pi^-/e_{\text{scat}}$ before (open black squares) and after (black full squares) pFRICH veto on $\pi^-$ in PYTHIA 6 $e+p$ collisions at $18 \times 275$ GeV for $-3.0 < \eta < -2.5$ . (right) Kaon candidates identified using the pFRICH (full markers) in MC DIS $e+p$ collisions at $18 \times 275$ GeV in PYTHIA 8. The open markers show contributions from correctly identified kaons and other hadrons misidentified as kaons. (Figure documentation) . . . . .	166
8.109	Left: Aerogel transmittance as a function of wavelength for factory, BNL, and Temple University measurements. Right: Mirror sample reflectivities as measured at BNL as a function of wavelength. (Figure documentation) . . . . .	168
8.110	Left: optical setup of an existing HRPPD QA station at BNL. Right: optical table of the future full size mirror QA station at BNL. See text for more details. (Figure documentation) . . . . .	173



8.111 ePIC hpDIRC geometry in the Geant4 standalone simulation. . . . .	177
8.112 a) Schematic of the side view of one hpDIRC section and an exploded view of the 3-layer lens. b) Photo of prototypes of the 3-layer spherical lenses. c) Photec AuraTek MAPMT253 MCP-PMT. . . . .	178
8.113 The expected performance of the hpDIRC as a function of the particle polar angle in terms of photon yield (a) for pions and $\pi/K$ separation power (b). These results are based on a standalone Geant4 simulation of 6 GeV/c particles. . . . .	179
8.114 Photographs of the PANDA Barrel DIRC prototype (a), including a close-up of the readout section (b) taken during the CERN test beam. Performance plots illustrating the comparison between simulated and experimental data for photon yield (c) and single photon Cherenkov angle resolution (SPR) (d). . . . .	181
8.115 Technical drawings of the ePIC hpDIRC detector, showing the XY cross-section of the bar box (a) and the YZ cross-section of the connection between the bar box and the readout box (b). . . . .	182
8.116 ePIC hpDIRC schedule chart alignment with EIC Project schedule . . . . .	185
8.117 Photos of available setups developed during the hpDIRC R&D program that will be used for future QA of 3-layer lenses with laser setup at ODU (a), bars and other optics at Jefferson Lab (b) and readout chain including sensors and electronics and other hpDIRC components in hpDIRC prototype at CRT at SBU (c). . . . .	186
8.118 (Left) dRICH detector model with highlighted the major components. (Center) Model of the dRICH photodetector unit (PDU) module with its major components highlighted. (Right) dRICH detector box model with 208 PDUs forming a curved active surface. . . . .	190
8.119 (Left) Dark current measurements on sample SiPM sensors for the studies of repeated irradiation-annealing . (Right) Projected increase of the DCR of SiPM as a function of the integrated luminosity (delivered fluence) for the PDU closer to the beam pipe (worst case scenario). The "no annealing" and the "annealing limit" curves show the limits of possible operations. The dashed line indicate the desired maximum DCR threshold. . . . .	191
8.120 (Left) Transverse map of the expected 1-MeV equivalent neutron fluence per $1 \text{ fb}^{-1}$ of integrated luminosity in e+p interactions at the maximum EIC center-of-mass energy at the location of the dRICH photodetector ( $210 < z < 260 \text{ cm}$ ). The average, maximum and minimum values within the region of the dRICH photodetector ( $100 < R < 180 \text{ cm}$ , indicated by the dashed lines) are reported. (right) Block diagram of the dRICH gas system. . . . .	194
8.121 (Left) Contributions to the single-photon angular resolution for aerogel. (Right) Contributions to the single-photon angular resolution for radiator gas. . . . .	195
8.122 (Left) Reconstructed mass vs momentum for pions, kaons and protons. (Right) Reconstructed mass vs momentum for pions and electrons. Distinct values derived from aerogel and gas are shown, to highlight the complementary coverage and effective interplay of the two radiators. The study is performed at the large rapidity endpoint $3.2 < \eta < 3.5$ . . . . .	196
8.123 (Left) dRICH mechanical model. (Center) Service routing around the dRICH. (Right) Installation and extraction tool. . . . .	197
8.124 (Left) Test stand for SiPM characterization. (Center) Performance comparison between different SiPM models. (Right) Prototype version of the SiPM carrier board (top) and FEB (bottom). . . . .	198



8.125 (Left) Fraction of residual irradiation damage measured on multiple SiPM candidate samples after “forward-bias annealing” cycles at increasing temperature and integrated annealing time. The measurements are shown for individual sensors (gray points) and as averages (coloured points, uncertainty of the average and RMS are indicated on the plot). (Right) Temperature increase of the SiPM sensor with respect to the temperature of the SiPM carrier board as a function of the “forward-bias annealing” power at different temperature values of the circulating thermostat system. . . . .	199
8.126 (Left) $C_2F_6$ measured transmittance in the near UV-region. (Center) Aerogel tile real-size demonstrator. (Right) Mirror demonstrator with an optimized dRICH core structure. . . . .	200
8.127 (Left) Baseline prototype with reference multi-anode PMT sensors at the SPS-H8 beam line of CERN. (Center) First ePIC-drive SiPM detector box under test at the PS-T10 beam line of CERN. (Right) Real-scale prototype model mimicking the basic dRICH construction unit (sector). . . . .	201
8.128 (Left) Cherenkov angular resolution obtained for $C_2F_6$ as a function of the recorded number of photons. The SPE values is consistent with expectations. (Center) SPE angular resolution measured on aerogel as a function of the refractive index. The expected resolution is obtained for an index greater than $n=1.025$ . (Right) Comparison in photon yield of sensor with different SPAD size. All the measurements has been obtained with the dRICH prototype. . . . .	202
8.129 (Left) Prototype PDU and assembled detector plane. (Center) Cumulated ring imaging for a mixed hadron beam at 10 GeV/c. (Right) Dual-radiator interplay at 10 GeV/c: After the gas information is used to tag pions (clear histogram), an effective separation between kaon and proton is provided by the aerogel (shaded histogram). . . . .	202
8.130 dRICH construction timeline . . . . .	205
8.131 CAD drawing of the backward ECal attached to the Global Support Tube (GST) by means of rails. The outer structure shows the external cooling using Friction Stir Welding (FSW) technology. The shape of the inner support structure is optimized to maximize the pseudo-rapidity coverage around the beam pipes. . . . .	211
8.132 Conceptual design of the ePIC electron endcap electromagnetic calorimeter support. . . . .	212
8.133 Left: waveform (top) and integrated signal (bottom) showing single photo-electron signals in Hamamatsu 15 $\mu$ m pixel SiPMs. Signals are produced with a low-intensity LED. Right: Linearity measurement, showing 2% linearity up to 3500 photo-electrons. . . . .	212
8.134 PCB holding the 16 SiPMs of a PWO-II crystal. An SMC LED is mounted on each PCB (the white component centered at the bottom of the board in this figure). . . . .	213
8.135 EEEMCal performance estimated from single particle simulations using the full ePIC detector geometry. Left: energy resolution as a function of the incident particle energy. Right: pion rejection factor as a function of energy and different values of electron efficiency. (Performance plots were produced by the backwards_ecal benchmark) . . . . .	214
8.136 Left: Layout of the EEEMCal subsystem showing the external and internal cooling plates (yellow), a front copper plate, and some insulating barrier (blue) between the crystals and the heat source (FEBs, inside cooled boxes). Right: Simulated temperature distribution of crystals in stationary mode with plates at 19° C and room temperature of 26° C. A uniform heat source of 1 kW is assumed behind the crystals. . . . .	216
8.137 Steady-state simulation at 2 different room temperatures. Data show the temperature difference across the detector for different configurations of the cooling system. The nominal configuration (dark green) shows the best performance and yields a maximum temperature variation of 0.4° C in the central crystals. . . . .	216

8.138	Left: Transient-state simulation showing the temperature variation of crystals as a function of time for a room temperature variation from 26° C to 23° in 6 hours. The thermal inertia of crystals is sufficiently high that the temperature variation of all of them is below 0.1° C. Right: typical temperature variations in IP6 as measured by the STAR experiment. Temperature is constant within $\pm 1.5^\circ$ C within a few hours.	217
8.139	Temperature variation of PWO crystals measured in the NPS calorimeter, consisting of 1080 PWO crystals and 500 W FEBs. The cooling concept used for this detector is similar to the one planned for the ePIC backward ECal, and shows that the required crystal temperature stability is achieved.	217
8.140	EEEMCal installation fixtures that allow for installing the detector safely into the ePIC detector barrel.	218
8.141	Backward ECal 5×5 crystal prototype and full readout 400-channel electronic chain based on the HGCROC chip.	220
8.142	Waveforms for a 5-GeV electron in the 16 SiPM of a PWO crystal	221
8.143	Structure of Barrel Imaging Calorimeter and its sectors.	223
8.144	Components of Barrel Imaging Calorimeter imaging AstroPix layers.	224
8.145	Sketch of the mechanical envelopes for the BIC ESB.	224
8.146	Simulated energy resolution and sampling fraction for photons in different rapidity ranges of BIC.	228
8.147	Simulated angular resolutions for photons at BIC.	229
8.148	Simulated performance on particle identification from BIC	230
8.149	Simulated performance on MIP response in BIC	231
8.150	Example performance of AstroPix.v3 chip	233
8.151	Barrel Imaging Calorimeter high-level schedule for design and production phases.	240
8.152	Simulated energy response of photons and electrons in Pb/ScFi and energy response tail in different rapidity range of BIC.	241
8.153	Simulated energy resolution and sampling fraction for electrons in different rapidity ranges of BIC.	242
8.154	Low-energy photon response in BIC at $\eta = +1$ .	242
8.155	Measured energy responses in Baby BCAL to positrons and pions	243
8.156	Barrel Imaging Calorimeter org chart.	244
8.157	The front face of the ePIC hadron end-cap.	247
8.158	Matrix of scintillating fibers prepared to build production FEMC blocks and SEM image of tungsten powder.	248
8.159	Front and back views of LG plates with installed SiPMs.	250
8.160	Structural and installation tests at BNL.	251
8.161	Response of calorimeter vs position in hodoscope (left panel). Energy resolution for different impact angles (right panel).	252
8.162	Signal (single photon) efficiency and background (merged di-photons) contamination for different cut value of the NN output for 60 GeV (left panel). Probability of misidentifying $\pi^0$ as a single photon vs energy (right panel)	253
8.163	FEMC front end electronics.	254
8.164	Neutron detection efficiency vs. $E$ and thresholds	260
8.165	Position resolution $R_{xy}$ and cluster efficiency vs. $E$ for different tile sizes	261
8.166	Ratio of $e/\pi$ response vs. $E$	261
8.167	<b>Top:</b> Primary, generated particle $E$ distributions in nHCal acceptance $-4.0 < \eta < -1.0$ . <b>Bottom:</b> Primary, generated particle $p$ distributions in nHCal acceptance $-4.0 < \eta < -1.0$ . Repository: <a href="https://github.com/OSUNuclearPhysics/ePIC_preTDR_nHCal_DIS_MCPart">https://github.com/OSUNuclearPhysics/ePIC_preTDR_nHCal_DIS_MCPart</a>	262

8.168	<b>Top:</b> Primary, generated particle $E$ distributions in $-2.0 < \eta < -1.0$ range. <b>Bottom:</b> Primary, generated particle $p$ distributions in $-2.0 < \eta < -1.0$ range. Repository: <a href="https://github.com/OSUNuclearPhysics/ePIC_preTDR_nHCal_DIS_MCPart">https://github.com/OSUNuclearPhysics/ePIC_preTDR_nHCal_DIS_MCPart</a> . . .	263
8.169	<b>Top:</b> Primary, generated particle $E$ distributions in $-3.0 < \eta < -2.0$ range. <b>Bottom:</b> Primary, generated particle $p$ distributions in $-3.0 < \eta < -2.0$ range. Repository: <a href="https://github.com/OSUNuclearPhysics/ePIC_preTDR_nHCal_DIS_MCPart">https://github.com/OSUNuclearPhysics/ePIC_preTDR_nHCal_DIS_MCPart</a> . . .	264
8.170	<b>Top:</b> Primary, generated particle $E$ distributions in $-4.0 < \eta < -3.0$ range. <b>Bottom:</b> Primary, generated particle $p$ distributions in $-4.0 < \eta < -3.0$ range. Repository: <a href="https://github.com/OSUNuclearPhysics/ePIC_preTDR_nHCal_DIS_MCPart">https://github.com/OSUNuclearPhysics/ePIC_preTDR_nHCal_DIS_MCPart</a> . . .	265
8.171	Acceptance of photoproduced $J/\psi \rightarrow \mu^+\mu^-$ in $e + p$ collisions at $18 + 275$ GeV. <b>Top left:</b> Acceptance vs. $\mu_1$ and $\mu_2$ hitting different HCals. <b>Top Right:</b> Acceptance vs. $-t$ for different number of $\mu$ in nHCal. <b>Bottom Left:</b> Acceptance vs. Bjorken $x_{bj}$ for different number of $\mu$ in nHCal. <b>Top Right:</b> Acceptance vs. Pomeron $x_p$ for different number of $\mu$ in nHCal. Repository: <a href="https://github.com/OSUNuclearPhysics/ePIC_preTDR_nHCal_VM_Sartre_kine">https://github.com/OSUNuclearPhysics/ePIC_preTDR_nHCal_VM_Sartre_kine</a> . . .	266
8.172	Acceptance of photoproduced $J/\psi \rightarrow \mu^+\mu^-$ in $e + p$ collisions at $20 + 100$ GeV. <b>Top left:</b> Acceptance vs. $\mu_1$ and $\mu_2$ hitting different HCals. <b>Top Right:</b> Acceptance vs. $-t$ for different number of $\mu$ in nHCal. <b>Bottom Left:</b> Acceptance vs. Bjorken $x_{bj}$ for different number of $\mu$ in nHCal. <b>Top Right:</b> Acceptance vs. Pomeron $x_p$ for different number of $\mu$ in nHCal. Repository: <a href="https://github.com/OSUNuclearPhysics/ePIC_preTDR_nHCal_VM_Sartre_kine">https://github.com/OSUNuclearPhysics/ePIC_preTDR_nHCal_VM_Sartre_kine</a> . . .	267
8.173	Acceptance of photoproduced $\Phi \rightarrow K^+K^-$ in $e + p$ collisions at $18 + 275$ GeV. <b>Top left:</b> Acceptance vs. $K_1$ and $K_2$ hitting different HCals. <b>Top Right:</b> Acceptance vs. $-t$ for different number of $K$ in nHCal. <b>Bottom Left:</b> Acceptance vs. Bjorken $x_{bj}$ for different number of $K$ in nHCal. <b>Top Right:</b> Acceptance vs. Pomeron $x_p$ for different number of $K$ in nHCal. Repository: <a href="https://github.com/OSUNuclearPhysics/ePIC_preTDR_nHCal_VM_Sartre_kine">https://github.com/OSUNuclearPhysics/ePIC_preTDR_nHCal_VM_Sartre_kine</a> . . .	268
8.174	Acceptance of photoproduced $\Phi \rightarrow K^+K^-$ in $e + p$ collisions at $20 + 100$ GeV. <b>Top left:</b> Acceptance vs. $\mu_1$ and $\mu_2$ hitting different HCals. <b>Top Right:</b> Acceptance vs. $-t$ for different number of $K$ in nHCal. <b>Bottom Left:</b> Acceptance vs. Bjorken $x_{bj}$ for different number of $K$ in nHCal. <b>Top Right:</b> Acceptance vs. Pomeron $x_p$ for different number of $K$ in nHCal. Repository: <a href="https://github.com/OSUNuclearPhysics/ePIC_preTDR_nHCal_VM_Sartre_kine">https://github.com/OSUNuclearPhysics/ePIC_preTDR_nHCal_VM_Sartre_kine</a> . . .	269
8.175	Energy resolution of jets vs. jet energy $E$ compared for inclusive jets(squares) and jets with neutral veto(triangles). Track only jets(blue) are also compared to track and nHCal cluster jets(red). Repository: <a href="https://github.com/OSUNuclearPhysics/ePIC_preTDR_nHCal_neutralJetRes">https://github.com/OSUNuclearPhysics/ePIC_preTDR_nHCal_neutralJetRes</a> . . .	270
8.176	<b>Left:</b> Acceptance vs. $x$ for 2, 1 and no diffractively produced jets with thrust axis in nHCal acceptance. <b>Right:</b> Acceptance vs. inelasticity $y$ for 2, 1 and no diffractively produced jets with thrust axis in nHCal acceptance. Repository: <a href="https://github.com/OSUNuclearPhysics/ePIC_preTDR_nHCal_Diff2Jet_Pythia">https://github.com/OSUNuclearPhysics/ePIC_preTDR_nHCal_Diff2Jet_Pythia</a> . . .	271
8.177	<b>Left:</b> Fraction of MC particle pairs per cm as a function of distance between straight line projections of particle pairs onto nHCal surface. <b>Right:</b> Fraction of MC particle pairs per cm as a function of distance between straight line projections of neutron paired with X(any particle) onto nHCal surface. Repository: <a href="https://github.com/OSUNuclearPhysics/ePIC_preTDR_nHCal_Diff2Jet_Reco">https://github.com/OSUNuclearPhysics/ePIC_preTDR_nHCal_Diff2Jet_Reco</a> . . .	271
8.178	<b>Left:</b> Fraction of MC truth cluster pairs per cm as a function of distance between clusters created by neutron paired with X(any particle). <b>Right:</b> Fraction of reconstructed cluster pairs per cm as a function of distance between clusters created by neutron paired with X(any particle). Repository: <a href="https://github.com/OSUNuclearPhysics/ePIC_preTDR_nHCal_Diff2Jet_Reco">https://github.com/OSUNuclearPhysics/ePIC_preTDR_nHCal_Diff2Jet_Reco</a> . . .	272

8.179 Position of the reconstructed clusters in $x, y$ for 2-particle position resolution study. Repository: <a href="https://github.com/OSUNuclearPhysics/ePIC_preTDR_nHCal_PosRes">https://github.com/OSUNuclearPhysics/ePIC_preTDR_nHCal_PosRes</a> . . . . .	272
8.180 Ratio of reconstructed, charged hadron corrected cluster energy to the sum of neutron MC energy deposits for different values of the distance between neutron and pion impact points on the nHCal surface. Repository: <a href="https://github.com/OSUNuclearPhysics/ePIC_preTDR_nHCal_PosRes">https://github.com/OSUNuclearPhysics/ePIC_preTDR_nHCal_PosRes</a> . . . . .	273
8.181 Ratio of reconstructed, charged hadron corrected cluster energy to the sum of neutron MC energy deposits vs. neutron MC energy deposits in scintillator tiles only. Comparison for different values of the distance between neutron and pion impact points on the nHCal surface. Repository: <a href="https://github.com/OSUNuclearPhysics/ePIC_preTDR_nHCal_PosRes">https://github.com/OSUNuclearPhysics/ePIC_preTDR_nHCal_PosRes</a> . . . . .	274
8.182 Work organization structure of nHCal project within ePIC. . . . .	275
8.183 The charged (black lines), neutral EM (blue lines), and neutral hadron (red lines) fractions of jets at the truth level in $\eta \in (-3.5, 1.0)$ (upper left panel), $ \eta  < 1$ (upper right panel), and $\eta \in (1.0, 3.5)$ (lower left panel). Received from John Lajoie in private communication. <b>THIS IS A PLACEHOLDER</b> . . . . .	276
8.184 Transverse cutaway view of an sPHENIX Outer HCal module, showing the tilted tapered absorber plates. Light collection and cabling is on the outer radius at the top of the drawing. . . . .	278
8.185 Scintillator tiles in a layer of the Outer HCal. . . . .	278
8.186 Leakage current in HCal measured once per fill as a function of total number of ZDC coincidence hits . . . . .	281
8.187 Energy deposited on BHCAL tiles (left panels) and reconstructed tile energies (right panels) by single $\mu^-$ (top row) and $\mu^+$ (bottom row) as a function of tile pseudorapidity. Muons were simulated using the 2024.11.1 simulation geometry with energies between 2 and 20 GeV. Repository: <a href="https://github.com/ruse-traveler/EpicBHCALPTDRStudies">https://github.com/ruse-traveler/EpicBHCALPTDRStudies</a> . . . . .	282
8.188 Energy deposited on BHCAL tiles (left panels) and reconstructed tile energies (right panels) by all particles in $10 \times 100$ (top row) and $18 \times 275$ (bottom row) NC DIS events as a function of particle pseudorapidity. Distributions were simulated using the 2024.11.1 simulation geometry with $Q^2 > 1000 \text{ GeV}^2$ . Repository: <a href="https://github.com/ruse-traveler/EpicBHCALPTDRStudies">https://github.com/ruse-traveler/EpicBHCALPTDRStudies</a> . . . . .	283
8.189 Reconstructed energy of leading BHCAL cluster for 1 (green) - 20 GeV (purple) single $\pi^-$ (left) and $\pi^+$ (right) in BHCAL-only simulations. Pions were simulated using the 2024.10.1 simulation geometry. Solid lines are Gaussian fits. Repository: <a href="https://github.com/ruse-traveler/EpicBHCALPTDRStudies">https://github.com/ruse-traveler/EpicBHCALPTDRStudies</a> . . . . .	284
8.190 Uncalibrated (top row) vs. LD-calibrated energy (middle row) and MLP-calibrated (bottom row) of lead BHCAL clusters for 2 (orange), 5 (pink), 10 (blue), and 20 GeV (purple) $\pi^-$ (left column) and $\pi^+$ (right column). Distributions were simulated using the 2024.10.1 simulation geometry. Repository: <a href="https://github.com/ruse-traveler/EpicBHCALPTDRStudies">https://github.com/ruse-traveler/EpicBHCALPTDRStudies</a> . . . . .	288
8.191 Linearity (top row) and energy resolution (bottom row) of calibrated single $\pi^-$ (left column) and $\pi^+$ (right column). Red lines indicate LD-calibrated energies, purple lines indicate MLP-calibrated energies, black lines indicate the linearity, resolution of summing BHCAL clusters without calibration. Distributions were simulated using the 2024.10.1 simulation geometry. Repository: <a href="https://github.com/ruse-traveler/EpicBHCALPTDRStudies">https://github.com/ruse-traveler/EpicBHCALPTDRStudies</a> . . . . .	289

8.192	Uncalibrated (to left) vs. LD-calibrated energy (top right) and MLP-calibrated (bottom) of lead BHCAL clusters for 2 (orange), 5 (pink), 10 (blue), and 20 GeV (purple) neutrons. Distributions were simulated using the 2024.10.1 simulation geometry. Repository: <a href="https://github.com/ruse-traveler/EpicBHCALPTDRStudies">https://github.com/ruse-traveler/EpicBHCALPTDRStudies</a> . . . . .	290
8.193	Linearity (left) and energy resolution (right) of calibrated single neutrons. Red lines indicate LD-calibrated energies, purple lines indicate MLP-calibrated energies, black lines indicate the linearity, resolution of summing BHCAL clusters without calibration. Distributions were simulated using the 2024.10.1 simulation geometry. Repository: <a href="https://github.com/ruse-traveler/EpicBHCALPTDRStudies">https://github.com/ruse-traveler/EpicBHCALPTDRStudies</a> . . . . .	291
8.194	ratio of uncalibrated lead BHCAL cluster to the sum of all BHCAL clusters for 2 (grey) - 10 GeV (blue) single neutrons. Distributions were simulated using the 2023.06.1 simulation geometry. Repository: <a href="https://github.com/ruse-traveler/EpicBHCALPTDRStudies">https://github.com/ruse-traveler/EpicBHCALPTDRStudies</a> . . . . .	292
8.195	<b>JES/R for full (tracks + ECal + HCal):</b> The $JES - 1 = \langle \Delta p/p \rangle$ (open markers) and JER (closed markers) plotted as a function of $p_{jet}$ in the lab frame for jets in $\eta \in (-3.5, 1.0)$ (red points), $ \eta  < 1$ (black points), and $\eta \in (1.0, 3.5)$ (blue points). In the barrel region, jets are constructed from reconstructed tracks and ECal clusters <i>without</i> a nearby track. Neutral hadrons are included in the jets by smearing the particle energy by the measured energy resolution of the sPHENIX OHCAL. Jets are reconstructed via the Centauro algorithm ( $R = 0.8$ ) and transformed back into the lab frame. Jets are required to have at least 2 particles, and exclusively charged or neutral jets are rejected. From ECCE responses to the EIC DPAP Panel; received from John Lajoie in private communication. <b>THIS IS A PLACEHOLDER</b> . . . . .	293
8.196	JB variables at truth ("vertex", black) and reconstructed level for particle $ \eta  < 3.5$ (blue) and $ \eta  < 4$ (red) in $18 \times 275$ CC DIS events. Detector simulation and reconstruction was carried out using a fast simulation using Delphes. Figure 8.21 from the EIC Yellow Report. <b>THIS IS A PLACEHOLDER</b> . . . . .	293
8.197	<b>Truth vs. reconstructed <math>E_T^{miss}</math>:</b> the truth (x-axis) vs. reconstructed (y-axis) $E_T^{miss}$ for $10 \times 275$ CC DIS events. Detector simulation and reconstruction was carried out using a fast simulation using Delphes. Figure 4 from arXiv:2006.12520. <b>THIS IS A PLACEHOLDER</b> . . . . .	294
8.198	Renderings of the forward calorimeter assembly (top left), tile assembly of 8 scintillator tiles of the LFHCAL with the SiPMs sitting in a dimple on each tile, detailed stacking example (middle right) and 8-tower module design (bottom). . . . .	297
8.199	Renderings of the absorber structure for the insert modules surrounding the beam pipe (top) and their individual layer composition (bottom). . . . .	298
8.200	Left: Visualization of 8M-scintillator assembly with its individual components. Right: Samples of the individual components used for the 2024 test beam campaign. . . . .	298
8.201	Combined energy resolution of the forward calorimeter system as a function of pseudo rapidity $\eta$ for single pions, evaluated within the primary LFHCAL acceptance. These results are obtained using the graph-neural network approach described in Ref. [3]. . . . .	300
8.202	Combined position resolution of the forward calorimeter system as a function of pseudo rapidity $\eta$ for single pions, evaluated within the primary LFHCAL acceptance. These results are obtained using the graph-neural network approach described in Ref. [3]. . . . .	301
8.203	Visualization of the individual components of an 8M module. . . . .	301
8.204	Visualization of the full LFHCAL in its cradle (top) and details of its moving mechanism (bottom). . . . .	303
8.205	General timeline of the LFHCAL design, construction and assembly. . . . .	306

8.206	Organizational chart of the LFHCal & insert consortium, indicated by the numbers are the associated WBS structures. . . . .	309
8.207	All four far-forward subsystems in the outgoing hadron beam direction. The green cylinders are accelerator dipole and quadrupole magnets. . . . .	310
8.208	Left: A cutaway view of the detectors in the B0 magnet. The beampipes are shown in blue and gray, the four tracking detectors are dark brown and the calorimeter is gray (the figure orientation is such that IP is to the left of the magnet). Right: The transverse profile of the calorimeter in the B0 magnet. Both figures are from the DD4HEP implementation of the detectors. . . . .	311
8.209	A simulation of the expected number of pixel hits for a $6 \times 6 \text{ mm}^2$ SiPM coupled to a $\text{PbWO}_4$ crystal as function of the energy of a photon impinging on the crystal. An ideal SiPM response is shown as well as the response of a $10 \text{ }\mu\text{m}$ pitch SiPM with 18% photo-detection efficiency and a $15 \text{ }\mu\text{m}$ pitch SiPM with 32% photo-detection efficiency (matching the specs of S14160-6010PS and S14160-6015PS). The realistic SiPM responses are shown with and without occupancy effects. . . . .	312
8.210	Left: The B0 tracker's acceptance of protons ( $E=110 \text{ GeV}$ ), as a function of $\theta_x$ and $\theta_y$ . Right: The top panel shows the reconstructed vs generated proton $p_T$ . Each slice of this distribution is fit to a Gaussian function and from this fit a resolution (middle panel) and bias (bottom panel) are extracted. . . . .	313
8.211	Proton acceptance as a function of $\eta$ spanning the central tracker, B0 tracker, and Roman Pots. . . . .	314
8.212	The B0 EM calorimeter's acceptance of photons shown for soft (less than $5 \text{ GeV}$ ) and hard (greater than $60 \text{ GeV}$ ) photons. Acceptance is defined as more than $100 \text{ MeV}$ deposited in the calorimeter. The position of the calorimeter crystals is indicated as a grid. The un-instrumented regions which nevertheless high nominal acceptance, correspond to upstream interactions whose shower products are visible in the B0 calorimeter. . . . .	314
8.213	The energy reconstructed and associated resolution for the B0 EM calorimeter of photons with $\theta < 13 \text{ mrad}$ in the soft (left) and hard (right) energy reconstruction regimes. The top panels show the reconstructed photon energy vs the generated energy. Each slice of this distribution is fit to a Gaussian function and from this fit a resolution (middle panels) and energy scale shift (bottom panels) are extracted. . .	315
8.214	Depiction of the envelopes from protons with $x_L \sim 1.0$ (left) and with $x_L \sim 0.5$ (right). The RP and OMD systems are placed to obtain an almost-continuous acceptance of protons across a broad range of proton rigidities. . . . .	317
8.215	Summary of transverse momentum resolutions for the Roman pots and off-momentum detectors using stand-alone detector simulations. Contributions are separated by those induced by intrinsic detector choices (e.g. pixel sizes) and those from beam effects (e.g. angular divergence), which have an outsized impact on momentum measurements at very-forward rapidity. . . . .	320
8.216	Transverse momentum resolution for Roman pots using the full ePIC simulation framework. This plot is from the ePIC framework, where Fig. 8.215 shows performance from standalone simulations which include beam effects and optimized matrix reconstruction, shows both the nominal performance with the current reconstruction algorithm (in blue), and (in red) the expected improvement from the machine learning model which has been developed and tested in standalone simulations. This ML algorithm (based on deep neural networks) is currently being implemented in ePIC. A presentation on this work and the resulting performance of the model was presented at the Deep-Inelastic Scattering conference in 2023 [4]. Work is underway to integrate this model into the ePIC framework for RP and OMD reconstruction. . . . .	321



8.217 Strawman concept for the layout of the RP and OMD sensor staves. Work is on-going to get the necessary electronics engineering support to design the final PCB. The connector on the end of the PCB is presently assumed to be a TE connectivity Erni 354096-E 32 pin serial connector. Work is still needed to understand how to apply thermal cooling to the staves without using compressed gases or liquids (not allowed in the primary machine vacuum). Presently, cooling plates/heat sinks which are thermally coupled to outside the vacuum and cooled with an LN2 chiller are assumed, but only preliminary thermal analysis has been carried out. . . . .	322
8.218 Strawman concept a readout board concept to communicate with and readout RP and OMD sensor staves. Work needs to be done to solve the issue of power distribution, and to ensure the EICROC ASIC can indeed be readout by the lpGBT. . . . .	322
8.219 Current layout of a single RP layer using a 1x3 stave configuration, with the staves following the concept shown in Fig. 8.217. This configuration leads to a full detector layer with dimensions $\sim 26\text{cm} \times 10\text{cm}$ , with some work to be done to finalize the exact amount of overlap between individual staves to provide uniform acceptance in the transverse plane. . . . .	323
8.220 Depiction of the location of the RP sensor packages for the three different “main” EIC hadron beam energies, all in the optics configuration with the maximal low- $p_T$ acceptance. Optimization of the stave layout and movement stages is still underway to ensure best fiducial acceptance. . . . .	323
8.221 SiPM-on-tile ZDC. . . . .	330
8.222 SiPM-on-tile ZDC modular design is composed of quadrants. . . . .	331
8.223 ZDC mechanical . . . . .	331
8.224 Left: ZDC neutron-shower position resolution for neutrons as a function of the generated energy. Results are shown with an unstaggered layout (blue) and staggered layout with the positions reconstructed with the baseline (orange), HEXPLIT (green), and GNN (red) reconstruction algorithms. Right: Energy resolution (top row) and scale (bottom row) obtained with the strawman (open symbols) and GNN (filled symbols) for simulated single neutrons. The resolutions are compared to those of the CALICE beamtest [?] (orange squares) with (filled) and without (open) software compensation, as well as the CALICE GNN reconstruction (orange diamond) [5]. . . . .	332
8.225 Energy resolution (top row) and scale (bottom row) obtained with the strawman (left) and GNN (right), at various ranges in $\theta$ . The positions on the face of the detector corresponding to each color are visualized in the inset. . . . .	332
8.226 Examples of 4 reconstructed 3D shower shapes in the ZDC for events with 1 neutron ( $N_n = 1$ ), 2 neutrons ( $N_n = 2$ ), 4 neutrons ( $N_n = 4$ ), and 9 neutrons ( $N_n = 9$ ). The color code represents hit energy in terms of $E_{\text{MIP}}$ . The marker size is displayed proportionally to hit energy for display purposes. . . . .	333
8.227 Energy measured for each integer number of neutrons with energy equal to 100 GeV, reconstructed with GNN (orange) and strawman (blue). The events are weighted by a factor of $e^{-N_n}$ . The black, vertical lines are drawn at the total true energies of events with different numbers of neutrons. Here we show events containing up to nine neutrons. This performance illustrates just instrumental effects, excluding nuclear effects like smearing caused by Fermi motion and fission. In the laboratory frame, these nuclear effects would contribute in quadrature about 5 GeV per 100 GeV neutron, according to BEAGLE [?], which happens to be similar to the widths of the strawman reconstruction shown here. . . . .	334
8.228 Topology of $\Lambda^0$ decay in neutral-channel decay. Not shown to scale. Figure reproduced from Ref. [6]. . . . .	334

8.229	Left: Decay position distribution, for different $\Lambda^0$ energies. Middle: acceptance as a function of energy and decay position. Right: Acceptance as a function of energy, integrated over decay position, for $\Lambda^0$ s along the proton axis (black solid curve) and with varying amounts of transverse momentum (colored dashed curves). Figure reproduced from Ref. [6]. . . . .	335
8.230	Top row: event display for example events, with the hits color coded by energy deposited, in units of MIPs. Bottom row: the same events, with subcell hits from HEX-PLIT algorithm color-coded by which cluster the subcell hits have been assigned to by the 3D topological clustering algorithm. The olive (cyan) line(s) represent the truth-level trajectories of the incident photons (neutron). Figure reproduced from Ref. [6]. . . . .	335
8.231	Distribution of the cluster shape parameters, at three different $\Lambda^0$ energies. The red lines show the cuts used to identify the photon clusters. . . . .	336
8.232	Left: truth decay position of $\Lambda^0$ ( $x$ axis), compared to the reconstructed values ( $y$ axis). A thin red dashed line is shown at $y = x$ . Middle: the decay position resolution as a function of the $\Lambda^0$ energy. Right: distribution for the decay positions of reconstructed events for different $\Lambda^0$ energies. Figure reproduced from Ref. [6]. . . . .	336
8.233	Left: distribution for the reconstructed $\Lambda^0$ mass before (red) and after (blue) fitting the vertex position with the IDOLA algorithm. Middle: Same for the reconstructed $\Sigma^0$ mass. Right: the $\Lambda^0$ ( $\Sigma^0$ ) mass resolution as a function of the $\Lambda^0$ ( $\Sigma^0$ ) energy. Figure reproduced from Ref. [6]. . . . .	337
8.234	Energy resolution as a function of the $\Lambda^0$ energy. For comparison, the values obtained in Ref. [7] for single neutrons are shown in gray. Figure reproduced from Ref. [6]. . . . .	337
8.235	Left: Polar angle resolution for $\Lambda^0$ (filled symbols) and neutrons (open symbols) with baseline reconstruction and GNN reconstruction. Right: The resolution for reconstructing the transverse momentum for $\Lambda^0$ (filled symbols) and neutrons (open symbols) using a GNN at 150 GeV (blue) and 250 GeV (orange). These values reflect the resolution without beam effects. The beam effects terms for $\sigma_{\text{beam}}=150 \mu\text{rad}$ are shown as dashed curves. Figures reproduced from Ref. [6]. . . . .	338
8.236	Assembly of a ZDC prototype representing approximately 10% of the full ZDC size.	339
8.237	The layout of the luminosity monitor in the ZEUS experiment [?]. . . . .	340
8.238	Relative suppression due to the beam-size effects $(d\sigma_{\text{corr}}/dy)/(d\sigma_{\text{BH}}/dy)$ is shown as a function of $y = E_\gamma/E_e$ for three cases of collider parameters, HERA, EIC 1 & EIC 2. The corresponding beam energies and Gaussian lateral beam sizes at the interaction point are listed. Figure from Ref. [?]. . . . .	342
8.239	Unpolarised Bethe-Heitler cross-Section (left panel) and the polarised component (right panel), calculated in Ref. [?]. . . . .	343
8.240	Luminosity system layout showing the Direct Photon Detector and Pair Spectrometer, as well as the sweeper and analyzing magnets. . . . .	345
8.241	Pair Spectrometer calorimeters and their components: (1) The two Pair spectrometer calorimeters; (2) one layer, made out of three modules, with the fibers oriented perpendicular to the beam direction (the orientation of the fibers alternate from horizontal to vertical); (3) one module; (4) zoomed-in view of a set of 16 fibers which are read out by a SiPM. . . . .	346
8.242	PSCal sampling fraction as a function of incident electron energy. Events incident on the top or bottom 2cm of the front face of the calorimeter have been excluded in this sample. This selection cut removes events where the full shower is not contained within the calorimeter. . . . .	347



8.243 PSCal energy resolution as a function of generated electron energy. In this study, monoenergetic electrons (at the discrete values shown) were generated at the front face of the calorimeter. . . . .	347
8.244 Rate of single and coincidence events for the PS detectors. . . . .	348
8.245 Multiple fibers threaded through a pair of brass meshes. . . . .	349
8.246 (a) Tungsten powder and epoxy-only test module. (b) A section of another test module showing the interior. . . . .	349
8.247 Left: Low- $Q^2$ taggers in relation to beamlines and central detector. Right: Tagger module with calorimeter and tracker from recent CAD model. . . . .	351
8.248 Acceptance ranges of the Central Detector and Low- $Q^2$ Trackers as function of $Q^2$ and $x$ . . . . .	351
8.249 Low- $Q^2$ tagger coverage. . . . .	352
8.250 Hit rates on tracker layers for Quasi Real (Top) and bremsstrahlung (bottom) electrons, incident on Tagger 1 (left) and Tagger 2 (right), This design is based on layers with three carrier boards, each containing twelve Timepix4 hybrid sensors. The dashed lines indicated the centre lines of the Timepix4 ASICs, where the vertical columns terminate. . . . .	354
8.251 Maximum and integrated rates for Low- $Q^2$ trackers. . . . .	355
8.252 Layout of SciFi calorimeter. . . . .	356
8.253 Energy resolution for Cherenkov fiber calorimeter. . . . .	357
8.254 Top - Reconstruction of the initial electron energy, $\theta$ and $\phi$ angles from fitted tracks. Bottom - Integrated reconstruction difference. . . . .	358
8.255 Reconstruction of the initial electron as a function of $Q^2$ . . . . .	359
8.256 Acceptance as a function of $Q^2$ and $E_{e'}$ . . . . .	359
8.257 ePIC DAQ component counts . . . . .	365
8.258 ePIC DAQ component count summary . . . . .	366
8.259 Maximum data volume per RDO with noise estimates by detector. (Data Rate evaluation: <a href="https://github.com/jml1985/epicJTools">https://github.com/jml1985/epicJTools</a> ) . . . . .	366
8.260 Schematic of the ePIC Streaming DAQ . . . . .	368
8.261 ePIC Electronics and ASICs summary . . . . .	369
8.262 Scope of the electronics and ASICs developments . . . . .	370
8.263 Discrete block diagram . . . . .	370
8.264 Discrete Adapter (left) and digitizer FEB PCBs . . . . .	371
8.265 Discrete key specifications . . . . .	371
8.266 CALOROC block diagram . . . . .	371
8.267 CALOROC Key Specifications . . . . .	372
8.268 EICROC block diagram . . . . .	372
8.269 EICROC timing performance . . . . .	373
8.270 EICROC Key Specifications . . . . .	373
8.271 FCFD block diagram of the frontend . . . . .	374
8.272 FCFD timing performance . . . . .	374
8.273 FCFD Key Specifications . . . . .	375
8.274 ALCOR Si Die (left) and block diagram . . . . .	375
8.275 ALCOR Key Specifications . . . . .	375
8.276 TOF pre-prototype RDO . . . . .	378
8.277 3D model of dRICH RDO . . . . .	379
8.278 The FLX-155 board identified for use as a DAM board . . . . .	380
8.279 Schematic layout based for the GTU . . . . .	381
8.280 Physical concept for the fiber distribution for the GTU . . . . .	382
8.281 Operation of firmware trigger under assumption that the trigger decision for the dRICH depends upon data from fHCAL . . . . .	384

8.282 Proposed ePIC slow controls network topology . . . . .	387
8.283 DAQ/Computing schedule . . . . .	388
8.284 Electronics and DAQ Resources . . . . .	390
8.285 Butterfly Computing Model <i>see text for details</i> ). . . . .	394
8.286 Storage resource estimates aggregated over Echelon 1 and Echelon 2 sites, for a nominal Phase 1 datataking year. . . . .	396
8.287 Processing resource estimates aggregated over Echelon 1 and Echelon 2 sites, for a nominal Phase 1 datataking year. . . . .	397
8.288 Organizational chart of the Software and Computing Effort in ePIC. The Streaming Computing Working Group is joint with Electronics and DAQ Working Group in the Technical Effort to ensure that DAQ and Computing are developed together. . .	402

# List of Tables

1	Table illustrating “rules” . . . . .	15
2	Short top-level parameters caption. . . . .	15
3	A parameter table made available for export, using the /Tables subdirectory . . . .	15
4	A table with fixed third column width, enabling text filling. . . . .	15
5	Two ways to squeeze tables. . . . .	16
6	A third way to squeeze tables. . . . .	16
2.1	The 8 twist-2 and the 16 twist-3 TMDs and their dependence on the nucleon $N$ and the quarks $q$ polarisation (unpolarized: U, longitudinally polarized: L, transversely polarized: T). . . . .	36
2.2	Event composition in incoherent $J/\psi$ production before and after full event selection	43
8.1	MARCO Magnet Requirements . . . . .	65
8.2	MARCO geometric Specifications . . . . .	68
8.3	MARCO Materials . . . . .	72
8.4	Design parameter for various fields . . . . .	72
8.5	Caption . . . . .	73
8.6	Impact of axial misalignment and tolerances . . . . .	76
8.7	Impact of radial misalignment- Cold Mass . . . . .	76
8.8	Impact of radial misalignment- Module 1 . . . . .	76
8.9	Impact of radial misalignment- Module 2 . . . . .	77
8.10	Impact of radial misalignment- Module 3 . . . . .	77
8.11	Impact of missing one layer . . . . .	77
8.12	Caption . . . . .	78
8.13	Caption . . . . .	79
8.14	Materials acceptance criteria . . . . .	81
8.15	Materials acceptance criteria . . . . .	81
8.16	Ramp up/down results . . . . .	82
8.17	List of cryogenic valves . . . . .	90
8.18	Thermosiphon load cases . . . . .	93
8.19	Heat load summary . . . . .	94
8.20	Heat Load budget . . . . .	94
8.21	Physics requirements on the relative momentum measurement, $dp/p$ , at the event vertex, $\eta$ , and on the determination of the radial distance of closest approach, $DCA_r$ , of the particle trajectory to the event vertex. The requirements are given for different ranges in pseudorapidity as parametrizations in the total momentum, $p$ , in GeV and transverse momentum, $p_T$ , in GeV, respectively. . . . .	96
8.22	Radius, length and material budget of the SVT IB and OB layers. . . . .	102

8.23	Position along the beam pipe, outer radius and material budget for the SVT layers in the EE and HE regions. Disks in the electron direction are labeled ED0 to ED4. Disks in the hadron direction are labeled HD0 to HD4. Disks ED0/1/2 and disks HD0/1 have the same inner opening. Each of the other five disks has a different inner opening. . . . .	103
8.24	Summary of power and readout services for the different regions of the sPIC SVT (slow control and data links are differential pairs of wires). A services group is one MOSAIX segment in the IB, and up to four EIC-LAS sensors (i.e four segments) in the OB and endcaps. . . . .	106
8.25	Different sources of radiation dose . . . . .	121
8.26	Hit rate per unit area in the MPGD trackers for different beam gas . . . . .	121
8.27	Maximum rate per readout channel for different beam gas . . . . .	122
8.28	The ECT disks geometrical envelope and active areas dimensions. . . . .	124
8.29	The ECT disks angular and pseudorapidity acceptance. . . . .	125
8.30	Services requirements for the three MPGD tracking subsystems. . . . .	127
8.31	Main equipment required in the production site and availability at sites. . . . .	134
8.32	Main equipment required in the production site and availability at sites . . . . .	135
8.33	UVa Personnel Effort (%FTE) . . . . .	135
8.34	FIT Personnel Effort (%FTE) . . . . .	135
8.35	JLab Personnel Effort (%FTE) . . . . .	136
8.36	Required performance for physics and proposed configurations for the TOF detector system. The Barrel TOF consists of strip sensors with a pitch of 0.5 mm in the azimuthal direction and a length of 1 cm along the beam direction, while the Forward TOF consists of pixel sensors with a pitch of 0.5 mm. . . . .	140
8.37	RAW and NEQ fluence per system for the lifetime of the ePIC experiment, assuming 10 years of data taking at 50% time. . . . .	142
8.38	Baseline BTOF, FTOF and B0 AC-LGAD geometries. . . . .	144
8.39	Readout chips BTOF, FTOF and B0 AC-LGAD geometries. . . . .	145
8.40	Summary of BTOF and FTOF low voltage and high voltage power supply cables to distribution panels and then to the detector FEE (the exact numbers are being checked at the time of writing). . . . .	149
8.41	The BTOF is designed with a barrel geometry surrounding the beam pipe and interaction point, while the FTOF is a disk geometry perpendicular to the beam direction on the hadron side (positive z). . . . .	150
8.42	Expected pFRICH time of flight based particle identification performance. Highest momenta at which $3\sigma$ separation for a respective pair of mass hypotheses can be achieved is quoted, for aerogel and HRPPD window radiators separately. . . . .	167
8.43	Institutions contributing to the pFRICH effort and their roles and resources. Starred entries indicate no institutional commitment. . . . .	175
8.44	List of the voltage services to the dRICH electronics, indicating the number of primary power-supply channels and boards as well as the cross-section of the cables (AWG). The number of power-supply boards is defined assuming to use commercial 8-channel low-voltage boards. . . . .	196
8.45	Planned quality assurance (QA) stations, organized in order to provide redundancy and support specific characterization studies. . . . .	204
8.46	Overview of Institutes and roles in the dRICH activity. . . . .	206
8.47	Table of crystal properties. . . . .	209
8.48	PWO specifications. . . . .	210
8.49	EEEMCAL WBS Structure . . . . .	215
8.50	Selected BIC Parameters. . . . .	225
8.51	AstroPix and Pb/ScFi layer parameters. . . . .	226

8.52	AstroPix chip parameters for BIC. . . . .	226
8.53	SiPM specifications for BIC. . . . .	227
8.54	Scintillating fiber specifications for BIC. . . . .	227
8.55	Energy resolution parameters for photons in BIC for different $\eta$ ranges. . . . .	228
8.56	Expected data rates for ScFi/Pb and Imaging layers of the BIC. . . . .	233
8.57	Some requirements on performance of FEMC and its parameters . . . . .	246
8.58	Requirements and Technical specifications for FEMC scintillating fibers. . . . .	249
8.59	Requirements and Technical specifications for FEMC SiPMs. . . . .	251
8.60	Requirements for the FEB . . . . .	253
8.61	Control and status registers on the FEB . . . . .	255
8.62	Maximum expected background rates for backward HCal. The assumed threshold is 170 keV. . . . .	259
8.63	Properties of HCal scintillating tiles. . . . .	279
8.64	Properties of Kuraray Y-11 (200) wavelength shifting fibers. . . . .	279
8.65	Design parameters for the Barrel Hadronic Calorimeter w/o additional absorber, based on the sPHENIX Outer Hadronic Calorimeter. . . . .	280
8.66	Overview of the calorimeter design properties for the LFHCal. . . . .	296
8.67	Examples of reactions that yield high-energy neutral particles within the ZDC acceptance. In each case, the leading particle's energy and polar scattering angle are used to constrain the Mandelstam variables $t$ or $u$ . The azimuthal angle can also be exploited for spin-dependent modulation measurements and for studying $\Lambda^0$ polarization and deuteron structure. While these reactions are labeled as having an electron in the final state, it should be understood that they can correspond to either the electroproduction (large $Q^2$ ) or photoproduction ( $Q^2 \approx 0$ ) regime. The references provided are representative of the literature discussing the corresponding channel, although they do not constitute an exhaustive list. . . . .	326
8.68	Bethe-Heitler $ep$ bremsstrahlung cross section in mb (and the corresponding event rates in GHz, for the nominal EIC luminosities), for various beam energies in GeV and three selection criteria. Table from Ref. [?]. . . . .	343
8.69	Summary of systematic uncertainties at ZEUS DPD and PS detector. [?] . . . . .	344
8.70	Noise Estimates . . . . .	367
8.71	Expected worse case data rate contributions for the ePIC detector. ( <a href="https://github.com/jml1985/epicJTools">https://github.com/jml1985/epicJTools</a> ) . . . . .	367
8.72	SALSA specifications. . . . .	376
8.73	Types of RDO . . . . .	377
8.74	RDO downlink words . . . . .	382
8.75	DAM/RDO Decoded Synchronous Command Structure. This structure is defined to allow continuous availability of the critical beam related bits and more rare commands. The data in the 40 bits worth of flexible command data encoding remains flexible but must contain enough control bits to select what structure it has. The "type", "type specific" division is an potential holding this flexibility . . . . .	382
8.76	DAQ Computing Resources . . . . .	384
8.77	Slow Controls data volume and network traffic . . . . .	387
8.78	Echelon 0 networking and storage requirements. . . . .	394
8.79	Echelon 1 networking requirements. Values shown are for a single E1 site. . . . .	395
8.80	Fractions of production workflows performed outside of Echelon 1 sites (i.e. at Echelon 2 and opportunistic sites) . . . . .	396

multi-chapters

# Chapter 0

## Style Guide

The following is the Style guide as developed for the full design report. This is the guide the accelerator team is following and it will make merging the documents together much easier if everyone uses this guide.

### 0.1 Chapter Abstract

**Summary:** Each chapter begins with a stand-alone single “punch line” page that serves as a chapter abstract. Rather than simply duplicating the Table of Contents outline of the subject matter of the chapter, a well-constructed abstract will lay out the key ideas and conclusions that chapter editors wish to convey to readers. The Executive Summary will also describe these key ideas, in a modestly longer form (perhaps  $\sim 250 - 1000$  words per chapter). This sample **non-EIC** chapter abstract emphasizes key ideas such as the separation of pre-existing and new subsystems, and the level of technical risk.

**The Cryogenic System** consists of the cryoplant that provides cooling for cryomodules; the test and instruments cryoplant that provides cooling for test stands and liquid helium for instruments; cryoplant that provides 16 K helium cooling for the target hydrogen moderators, and the distribution system that connects the linac cryoplant to cryomodules. The linac cryoplant and test/instrument cryoplant share common gas management and storage systems. The target cryoplant system is completely separate due to potential for tritium contamination.

**The Vacuum System** provides vacuum for the linac beam line, target system and instrument lines. It uses well established technology and procedures based on experience at similar facilities, including RHIC, Tevatron, and LHC. It has low technical risk.

**Test Stands** provide testing and validation of both RF equipment (klystrons and modulators) and cryomodules. Cryogenic connection to cryomodules in the test stands will prototype similar connections in the linac tunnel. The test stand program accommodates the unavoidable uncertainty in EIC construction schedule by allowing for RF equipment testing in a temporary location if necessary. Cryomodule testing will be carried out at the EIC site. All cryomodules will be tested at nominal temperatures and RF power levels before tunnel installation.

## 0.2 Wordsmithing

### 0.2.1 Passive voice

Authors should avoid the passive voice as much as possible – as in this sentence. This rule is sometimes made to be broken – as in this sentence :). The crucial point is that authors should not use passive voice to avoid identifying the specific individual or group of individuals within the EIC organization which is/are (or will be) responsible for fulfilling some specific function. It's not good enough to say, "Quality management will be implemented". The purpose of the Design Report is to explain for EIC itself, and for readers outside of EIC, who will implement quality management, and how they will do it. Excessive use of passive voice is not just bad writing. It communicates confusion or uncertainty about the path from aspiration to reality.

### 0.2.2 Verb tenses

The simplest way to make everything consistent is to apply a general rule:

Use past tense for things that happened in the past, present tense for things that are happening now, and future tense for things that will happen in the future.

If the designs call for something to happen, they call for it in the present tense. But it will happen in the future tense. Avoid inconsistent usage across chapters, across authors, and even within the same paragraph by a single author.

### 0.2.3 Apostrophes

Decades are written as in the 1960s and 1970s, NOT as in the 1980's or 1990's.

### 0.2.4 Capitalization and names

#### 0.2.4.1 Pieces of EIC

For example, linac, accelerator, target station, test stand. For the sake of consistency these terms will not be capitalized.

#### 0.2.4.2 Internal phrases

Correct capitalization for specific "internal" EIC phrases and names will be accumulated here. For example:

Pre-construction Phase NOT Pre-Construction phase  
Decommissioning Phase NOT De-commissioning phase  
Work Packages NOT Work-packages



### 59 **0.2.4.3 Discipline-specific approaches or “guiding principles” or buzz phrases**

60 Such as design integration, systems engineering, defense in depth. Recommend capitalizing none  
61 of them, but the important thing is to be consistent.

### 62 **0.2.4.4 Formal group names**

63 When authors identify the parts of the EIC organization who will be responsible for doing some-  
64 thing, then capitalize the formal names of that groups from the org chart. Recommend avoiding  
65 informal terms such as “test stand personnel”, where possible.

### 66 **0.2.4.5 Headings**

67 The titles of sections and subsections should have only the first letter capitalized.

## 68 **0.2.5 Captions**

69 Write Figure and Table captions in a self-contained way, to carry a complete self-contained descrip-  
70 tion of the figure. Define symbology in all figures, either in the text or (preferably) in the caption.  
71 Captions always end with a period. Use the format:

```
72 \caption[Short caption for List of Tables or Figures.]{Long caption to carry a complete
73 self-contained description of the figure or table, in the chapter text.}
```

## 74 **0.2.6 Spelling**

75 The Design Report follows American spelling rules. For example, with “z” not “s”, and “program”  
76 not “programme”:

```
77     emphasize not emphasise
78     meter not metre
79
```

### 80 **0.2.6.1 Exceptions to U.S. spelling**

81 1. (None so far).

### 82 **0.2.6.2 Capitalization**

83 The words “Figure”, “Table”, “Chapter” and “Section” should always be capitalized in the text if  
84 they occur with a number. For example, Figure 3.8 occurs in Chapter 3 and Table 5.5 is in Section  
85 5.1.3, but there are many other figures and tables in other section, subsections and chapters.

## 0.2.7 Commas

The incorrect placement of a comma can change the meaning of a sentence. For example, compare “Let’s eat Mom” and “Let’s eat, Mom”. And compare “Scientists, who conduct important research, are well respected in the community” with “Scientists who conduct important research are well respected in the community”.

Commas go where there is a natural pause in a long sentence, where additional information has been added to a sentence and where, if removed, the sentence would still make sense. They are used when listing items – between each item on the list. They are used where two shorter sentences are made into one (usually with the addition of “and”), but still consist of two separate parts. And they are used after “lead” words [however, therefore, consequently, in fact].

### 0.2.7.1 Commas in numbers

Write 2.4 million and not 2,4 million (as in some parts of Europe).

No commas in numbers below 10,000 – thus, write 1240 and 9999, but 12,400 and 99,999.

## 0.2.8 Plurals and possessives

For example, use

WPs not WP’s (plural)  
EIC’s not EIC’ (possessive)

## 0.2.9 Abbreviations

### 0.2.9.1 Textual treatment of Figures and Tables

The words “Figure” and “Table” should always be capitalized in the text. Include a reference or discussion of all Tables and Figures in the main text of the chapter. For example, “Figure 3.8 shows thus-and-such”. The abbreviations Fig. and Tab. should not be used.

### 0.2.9.2 Radio frequency

The phrase “radio frequency” is always two words and is never hyphenated or capitalized, whether used as an adjective or as a noun. Thus, the two radio frequencies used in the radio frequency system are 352.21 MHz and 704.42 MHz. The upper case abbreviation “RF” is acceptable in many circumstances.

### 0.2.9.3 etc., et cetera

It is acceptable to use “e.g.” within parentheses, but not outside. For example, Jack and Jill met many animals (e.g. Reynard the Fox) when going down the hill. It is also correct to say that Jack and Jill met many animals, for example Reynard the Fox, but no tortoise. Similar rules apply for “i.e.”.

The periods (i.e. the full stops) should not be dropped, for example “ie” or “eg”.

It is incorrect to use ok, o.k., or okay.

The following are acceptable:

e.g.

etc.

i.e.

RF (in many circumstances)

### 0.2.10 Hyphenation of multi-word adjectival phrases

In general, hyphenate an adjectival phrase where the second part is a past (-ed) or present (-ing) participle of a verb. Consider the following illustrative (nonsensical) paragraph:

This chapter describes the *beam physics design* of the *neutron-generating* spallation target. Following a brief overview, the chapter presents a detailed description of the *beam physics* of EIC, which drive the accelerator design. The accelerator consists of several sections: the ion source, *normal-conducting* linac, *superconducting* linac and *beam transport* sections. The chapter also describes the *radio frequency* system.

Simplified advice available online includes: “*When two or more words are combined to form a modifier immediately preceding a noun, join the words by hyphens if doing so will significantly aid the reader in recognizing the compound adjective.*” Not so simple are phrases like “high-power proton beam” where “proton beam” itself is a single idea. Some judgement is involved ....

For the sake of consistency, the editors have created and are expanding a spreadsheet of words and phrases specifying hyphenation policy for the Design Repoprt. Here are somewhat-arbitrary rules for whether or not to hyphenate some common multi-word phrases, *when they are used as an adjective, a noun, or as a verb*. Alphabetically:

1D, 2D, 3D, 4D

accelerator-driven

back up (verb)

back-flow (noun adj)

backscattering

backup (adj noun)

baseline (adj or noun)

beam dynamics

beam guide

beam instrumentation

153	beam physics
154	beampipe
155	beam port
156	beam time
157	beam transport
158	beamline
159	bispectral
160	bottom-up approach
161	broadband
162	by-product
163	clamshell clamshell-style
164	clean room
165	cold box
166	co-chair (noun)
167	contact-less
168	cool-down (noun or adj)
169	coordinate
170	cost-saving
171	cross reference (noun)
172	cross-reference (verb)
173	cross section
174	cryo-building
175	cryo-pump
176	cryo-system
177	cryomodule
178	cryoplant
179	debunched
180	decision making (noun)
181	decommissioning
182	de-excitation
183	deionised
184	down-mix
185	downtime
186	eigenmode (noun adj)
187	equipartitioning
188	failover
189	failsafe
190	feed box
191	feedthrough
192	follow up (verb)
193	follow-up (adj and noun)
194	hands-on (adj)
195	high level
196	high- $\beta$
197	high-current (adj)
198	high-power
199	high-resolution
200	hot cell
201	<i>in situ</i> (italicize)
202	innermost
203	inrush

204	interdependency
205	interlayer
206	intra-layer
207	intra-nuclear
208	Joule-Thomson valve
209	layout (noun)
210	life-cycle (noun)
211	line-of-sight
212	long-pulse
213	lookup
214	Lorentz detuning (noun)
215	Lorentz-detuning (adj)
216	low-resolution
217	magnetoresistance
218	medium- $\beta$
219	metadata
220	micropattern
221	microphonics
222	midpoint
223	middleware
224	multi-component
225	multi-layer
226	multi-pacting
227	multi-particle
228	multi-resistant
229	nanoparticle
230	nano-sized
231	nanostucture
232	neutron-generating
233	noninvasive (seen both ways in different dictionaries)
234	normal-conducting
235	on-board
236	ongoing
237	on-site (adj)
238	outermost
239	outgassing
240	overarching
241	phase space (noun)
242	phase-space (adj)
243	pinpoint
244	plug-in
245	post mortem (noun or adj)
246	pre-cools
247	premoderator
248	prequalification
249	radio frequency
250	radionuclide
251	radiotoxic
252	ramp up (verb)
253	ramp-up (noun)
254	read-back

255	ready-made
256	requalification
257	roadmap
258	safety-critical
259	short-pulse
260	short-term
261	shut off (noun verb)
262	shut-off (adj)
263	space charge (noun)
264	space-charge (adj)
265	staff-based
266	start-up
267	state-of-the-art
268	storm water
269	stripline
270	sub-atmospheric
271	subcomponent
272	sub-cool
273	sub-millimeter
274	sub-second
275	superconducting
276	switchyard
277	systemwide
278	thermo-mechanical
279	thermo-plastic
280	thermo-responsive
281	thermosyphon
282	time-frame
283	time scale
284	time-saving
285	time-stamp (noun and verb)
286	timeline
287	timesaving (adj and noun)
288	tool-set
289	top level
290	trade-off
291	tunable
292	tune up (verb)
293	tune-up (adj and noun)
294	twofold
295	uniaxial
296	uninterruptible
297	un-irradiated
298	up-mix
299	uptime
300	von Mises
301	waste water (noun)
302	waveguide
303	work flow (noun)
304	work-flow (adj)
305	workspace

world-leading  
 X-ray (upper case X)  
 zigzag (noun or adj)

### 0.2.11 Double letters

In UK spelling, both “focussing” and “focusing” are considered to be correct. In the Design Report we use single “s” spelling in all cases.

Note the ‘double “l” rule for UK English – label becomes labelled, travel becomes travelled, et cetera. Not so with U.S. English in the Design Report.

### 0.2.12 Mathematical symbols, subscripts and superscripts

Mathematical symbols are written in math-mode, even when they are embedded in text. For example, a longitudinal dimension  $L$  is often called a length. Descriptive subscripts and superscripts, as in  $L_{acc}$  or  $L^{overhead}$ , are not written in Roman font. They appear to be italics, no matter how long or short they are.

### 0.2.13 Quotation marks

L<sup>A</sup>T<sub>E</sub>X is fussy about some things, like quotation marks. Sooner or later an author, a chapter editor, or a general editor must pay attention. This the correct way to put “a certain piece of text” inside quotation marks. The following “certain piece of text” is incorrect.

### 0.2.14 Citations, references and the bibliography

**Please use inspire hep bibtex entries and notation whenever possible.**

Don’t use a “pointer” (for example [4]) in place of naming a reference [8]. That is, use “Joe Blow [4] describes thus and such,” NOT, “[4] describes thus and such”. There should be a space in the text before the citation, so “Joe Blow[4]” is wrong. Multiple citations should be placed with the same square brackets. In the L<sup>A</sup>T<sub>E</sub>X vernacular, use Joe Blow~\cite{Blow2011} or Joe Blow~\cite{Blow2011,Smith2012}.

We are using bibtex to handle the references, which are gathered into one bib file per chapter, although all references appear in a single bibliography at the end of the Design Report.

During the editing process we are (currently by default) using the L<sup>A</sup>T<sub>E</sub>X package showkeys, which flags references (to Tables, Figures, sections and subsections) and citations (to references) above the text, or in the margin. This should aid in generating cross-references, for example, even though it is rather ugly. It will be turned off in the final stages of editing, before printing. (Comments and feedback, please!)

### 0.2.15 Miscellaneous

#### 0.2.15.1 “Calculations show that ...”

This usage, with no indication who carried out the calculations, provides no way for a reader to check the work, or to build upon it in the future. Citations of internal documents, or of individuals to contact to get more information would be helpful for readers, and would also convey a greater sense of credibility. For example, “Relativistic Heavy Ion Collider (2021), unpublished calculations by members of the XYZ working group. Contact Sven Larsson (sven.larsson@bnl.gov) for details.”

#### 0.2.15.2 “Should”, “must”, and reference to future studies

In general, authors should convey the conviction that EIC will do what it should do. In those cases where there is an ongoing internal debate, the Design Report should convey the sense that such debates will be resolved on the basis of a reasoned and careful assessment of the evidence. Only write about future studies in those limited cases where it is needed to show “that we know what we are doing”.

#### 0.2.15.3 “Enable”

Incorrect usage:

“Neutrons pass easily through most materials, enabling the study of large or bulk samples and buried interfaces.”

Correct usage:

“In addition, as the BLM system will be a major tool for beam tune-up, it should also be designed in a way that enables it to pin-point the loss location as precisely as possible.”

The point is that the direct object of enable is made capable of doing something – roughly a synonym for empower. You enable the direct object to do something (enable it to pin-point ...). You could rewrite the first sentence to say, “enabling the study of large or bulk samples ... to take place.” Then it would be correct – although more unwieldy than just saying “making possible the study of ...”

#### 0.2.15.4 Reporting technical results without a clear statement of their import

In general, it is a mistake to assume that “the numbers speak for themselves”. Using words to summarize the meaning of results helps readers to understand them; it also signals that the authors understand the implications of the results they report.

#### 0.2.15.5 Excessive and inconsistent use of lists

Sometimes the use of lists is appropriate, but often there are too many in a draft. Authors should rework most lists into narrative form. For the remaining lists, authors should follow editorial guide-



lines to ensure consistent style across the entire Design Report.

After minimizing the number of lists, Design Report editors will convert most of the remaining lists to enumerated lists. The first letter of each item will be upper case, even when the items in the list are not formulated as complete sentences. Items will generally end with a semi-colon unless the phrases are very short, in which case a comma will be used. The last item in the list will be followed by a period. In those cases in which each item in a list consists of multiple sentences, items will be ended with a period.

### 0.2.15.6 Cross-references

Should be added throughout the whole Design Report, but only down to \subsection level, so that cross-references can be found and numbered in the Table of Contents. This implies that subsections should be reasonably balanced in length – not too many pages long.

### 0.2.15.7 Isotopes

Write  $^3\text{He}$ , for example, not 3He or He-3.

### 0.2.15.8 \*\*\* asterisks in comments

Sometimes a comment is inserted in a sentence, perhaps indicating that something needs to happen later, such as add a value, a citation, or more text. In this case please include (at least) 3 asterisks in a row \*\*\* so that text searches (for example `grep *** *.f`) are made easier. ALSO CONSIDER WRITING IN UPPER CASE\*\*\*.

## 0.3 Dimensions and units

Systeme Internationale (SI) units will be used wherever possible. For example, use MPa instead of bar. Some exceptions are inevitable, for example Kilpatrick units. Unusual units should be briefly explained, on their first introduction.

When in doubt, the siunitx package does the Right Thing, for example using:

- `\si{\units}`                      lower case si
- `\SI{numbers}{\units}`        upper case SI

A longitudinal dimension – or length –  $L$  should be written in one of these ways:

- $L = 100 \text{ m}$                        $\$L = 100\$~\text{m}$
- $L = 100 \text{ }\mu\text{m}$                        $\$L = 100\$~\text{\si{\micro\metre}}$
- $L = 100 \text{ km}$                        $\$L = \$ \text{\SI{100}{km}}$
- $L = 10^2 \text{ km}$                        $\$L = \$ \text{\SI{e2}{km}}$

so that the dimension (“m” or “μm” or “km”) is not in italics, and is separated from the numerical value by a non-breakable space – for example “~” in L<sup>A</sup>T<sub>E</sub>X vernacular. Do not write  $L = 100\text{m}$ ,  $100m$  or  $100\ m$ . Note that text and mathematical equals signs are different in length (= and =): always use the latter.

Powers of ten are written in one of these ways:

- $3.14 \times 10^{39}$                       `$3.14 \times 10^{39}$`
- $3.14 \times 10^{39}$                       `\SI{3.14e39}{}`

Complex dimensions may be written in one of these ways:

- $F = 42\text{ J cm}^{-2}\text{ s}^{-1}$                       `$F = 42$~J cm$^{-2}$ s$^{-1}$`
- $F = 42\text{ J cm}^{-2}\text{ s}^{-1}$                       `$F=$ \SI{42}{J.cm^{-2}.s^{-1}}`

Exceptionally, percentages are written without a space – 42% is correct but 42 % is not. In L<sup>A</sup>T<sub>E</sub>X vernacular a % sign is the beginning of a comment, so it is necessary to say \% ... sentence is invisible in the pdf file.

Temperatures are written as 273 K or 100°C or 101°C, without a space between the number and the °C unit symbol.

Angles are preferably written  $\theta = 7.5$  degrees, although 7.5° is acceptable.

## 0.4 Numbering – chapters, sections, and subsections

In the `\documentclass{report}` style, a “section” (such as this, with the numeric label 0.4) has two numbers associated with it.

### 0.4.1 This is the heading of a subsection

A “subsection” (like this, 0.4.1) is labelled by 3 numbers, namely “chapter\_number.section\_number.subsection\_number”. Sections and subsections begin with a bold face font.

#### 0.4.1.1 A subsubsection heading like this has no period at the end

In bold font, it has no numerical label, and sits separately from the text that immediately follows, even if there is no white space between `\subsubsection{}` and the first word of the text. It does not appear in the Table of Contents.

**This paragraph heading ends with a period.** Subsequent text remains in the same paragraph. The editors will use their judgement to prevent the excessive use of paragraph headings and boldface text.

## 0.4.2 More formatting rules and standards

### 0.4.2.1 Clearpages and Pagebreaks

As a rule there is NO `\clearpage` or `\pagebreak` before a new section (or subsection), and hence no white space.

## 0.5 Equations, Tables, Figures, and plots

### 0.5.1 Equations

Start with a simple equation, like Equation 1:

$$H = \frac{\sqrt{3 \langle x^4 \rangle \langle x'^4 \rangle + 9 \langle x^2 x'^2 \rangle^2 - 12 \langle x x'^3 \rangle \langle x^3 x' \rangle}}{2 \langle x^2 \rangle \langle x'^2 \rangle - 2 \langle x x' \rangle^2} \quad (1)$$

Avoid ending a sentence with an equation, in order to avoid deciding whether or not to put a period after the equation.

Here is a simple equation array:

$$\begin{aligned} M_{virg}(\sigma) &= M_{virg0} + k_{virg} \cdot \sigma \\ M_{rel}(\sigma) &= M_{rel0} + k_{rel} \cdot \sigma \end{aligned} \quad (2)$$

### 0.5.2 Tables

- Table 1 is a relatively complicated multi-column table, while Table 2 is a standard 3-column parameter table.
- Table 3 shows how to make a table exportable, for example to the Parameter Tables appendix.
- The source text for Table 4 shows how to enable text filling in columns.
- Table 5 shows 2 ways to squeeze tables, with the `\scalebox{}` and `\phantom{}` commands.
- Table 6 shows a third way, using `\tabcolsep{}`.

The vertical spacing of Table rows is set in “preamble.tex” by the line `\renewcommand{\arraystretch}{1.0}`.

### 0.5.3 Converting between LaTeX and Excel table formats

More than one free utility enables table conversion with a drag-and-drop interface. E.g.:

**Excel to LaTeX** try <https://tableconvert.com/excel-to-latex>

**LaTeX to Excel** try <https://tableconvert.com/latex-to-excel>

Facility	Location	Status	First oper.	Power [MW]	Instruments	Integrated flux [ $10^{14}\text{cm}^{-2}$ ]	Peak flux [ $10^{15}\text{cm}^{-2}\text{s}^{-1}$ ]
ESS	Lund	Pre-constr.	2019	5	22	–	40
J-PARC	Tokai	Re-furbish	2009			–	

**Table 1:** A standard Table looks like this, using “toprule”, “midrule” and “bottomrule” separation lines.

Parameter	Unit	Value
Energy	GeV	2.5
Current	mA	50
Pulse length	ms	2.86
Pulse repetition frequency	Hz	14
Average power	MW	5
Peak power	MW	125

**Table 2:** Long version of caption for top-level parameters.

Parameter	Unit	Value
Energy	GeV	2.5

**Table 3:** A parameter table made available for export, for example to Appendix E “Parameter Tables”, using input from a /Tables subdirectory file.

System	Subsystem	Test
Target	Shaft and drive	Run at up to 25 Hz.
	Target segments	Leak test at pressure.
	Target Safety System	Demonstrate trip signals generated for all defined cases.
Primary helium loop	Pump, heat exchanger, filter	Pressure and flow tests without target.
	Full loop with target	Full operational test without heat.

**Table 4:** A table with fixed third column width, enabling text filling.

Nuclide	Decay time [years]						
	0	6	40	100	1000	10 <sup>4</sup>	10 <sup>5</sup>
<sup>3</sup> H	0.9	83.4	96.4	72	0	0	0
<sup>14</sup> C	0	0	0	0	0.3	0.6	0
<sup>36</sup> Cl	0	0	0	0	0	0	0.7
<sup>39</sup> Ar	0	0	0	0.1	0.7	0	0
<sup>154</sup> Dy	0	0	0	0	0	0.2	4.3
<sup>163</sup> Ho	0	0	0	0.7	29.7	53.4	0

**Table 5:** Two ways to squeeze tables, with the “scalebox” and “phantom” commands.

Nuclide	Decay time [years]						
	0	6	40	100	1000	10 <sup>4</sup>	10 <sup>5</sup>
<sup>137</sup> La	0	0	0	0	1.4	8.7	57.6
<sup>148</sup> Gd	0	0.2	0.9	11.6	0.1	0	0
<sup>150</sup> Gd	0	0	0	0	0	0.3	5.6
<sup>154</sup> Dy	0	0	0	0	0	0.2	4.3
<sup>157</sup> Tb	0	0.1	0.6	9.3	7.2	0	0
<sup>154</sup> Dy	0	0	0	0	0	0.2	4.3
<sup>163</sup> Ho	0	0	0	0.7	29.7	53.4	0

**Table 6:** A third way to squeeze tables, with the “tabcolsep”.

#### 0.5.4 Figures

Many figures, like Figure 1, are non-graphical images – perhaps a photograph, drawing or sketch.



**Figure 1:** This is an example of a non-graphical figure. We need to address the means by which we can give “all” graphs the same look and feel.

#### 0.5.5 Plots

It is clear that for the ePIC detector sections we will mostly be using ROOT and Python, while the accelerator team most likely will be using a different package; so as soon as a figure style is agreed on, we will need to make style packages for ROOT and Python so all figures in the manuscript look stylistically the same.

As teams develop initial plots, please be sure to each the codes available so that they can be remade in a common style.

### 0.6 Italics and bold face type

In general, restrain the use of *italics* and **bold face**.

Long quotations will be set in italics. Italics will also be used (sparingly) for traditional purposes of emphasis (e.g. “when she was good, she was *very* good.”)

Occasionally, authors wish to draw attention to the subject matter being addressed in a block of text. Usually, this should be done by headings and subheadings. In those limited instances in which use of altered type face is appropriate within the body text, the editors will use bold face, rather than italics. One such situation is for short introductory phrases at the beginning of paragraph-long items in an enumerated list.

## 0.7 Issues that this Style Guide does not yet address

This Style Guide addresses “consistency of style” issues. Here is a numerical list of issues that could or should be significantly expanded:

1. the use of pronouns
2. specialized terminology
3. acronyms
4. the use of italics
5. the use of digits (e.g. 1) where written numbers are more appropriate
6. the overuse of capital letters (Boron vs. boron, User vs. user, etc.).
7. balancing the length of sections and subsections
8. global glossary
9. Lists
10. Plots (see placeholder [0.5.5](#))

## Chapter 2

# Physics Goals and Requirements

### 2.1 EIC Context and History

The Electron-Ion Collider is a major new research facility to advance the long term vision for Nuclear Physics to discover and understand the emergent phenomena of Quantum Chromo-Dynamics (QCD). The developing of the physics case for the EIC has been a tremendous community effort over the last few decades.

A joint report on the EIC Science case was put together at the Institute for Nuclear Theory (INT) in 2010 [9]. This set the base for the following release in 2014 of a White Paper (WP) [10] outlining the fundamental questions that would have been addressed at the EIC. In the following year, the US 2015 Long Range Plan for Nuclear Science recommended a high-energy high-luminosity polarized EIC as the highest priority for new facility construction.

In 2016, the worldwide fast growing community of scientists interested in the EIC organized itself under the EIC Users Group (EICUG) [www.eicug.org].

In 2017, the National Academy of Sciences, Engineering, and Medicine (NAS) assessed the science case of the EIC as “compelling, fundamental, and timely”. Quoting from the NAS report [11] released in 2018, the EIC can uniquely address three profound questions about nucleons—neutrons and protons—and how they are assembled to form the nuclei of atoms:

- How does the mass of the nucleon arise?
- How does the spin of the nucleon arise?
- What are the emergent properties of dense systems of gluons?

In December 2019, following the extremely positive assessment by the NAS, the US Department of Energy (DoE) established EIC Critical Design 0 (CD0), a “mission need” declaration, formally starting the EIC Project.

At about the same time, in late 2019, the EICUG launched an intensive, year-long consideration of the EIC physics measurements and scientific equipment. This initiative yielded the EICUG Yellow Report (YR) [8], defining the detector requirements needed to deliver the science case endorsed by NAS and highlighted in the WP and all the subsequent studies and publications. The YR provided the basis for further development of concepts for experimental equipment best suited for



$\eta$	Nomenclature		Tracking				Electrons and Photons				$\pi/K/p$		HCAL		Muons
			Resolution $\sigma_p/p[\text{GeV}/c]$	max $X/X_0$	min $p_T$	transverse pointing $dca(xy),$ $p_T[\text{GeV}/c]$	longitudinal pointing $dca(z),$ $p_T[\text{GeV}/c]$	Resolution $\sigma_E/E[\text{GeV}]$	PID	$E_{\text{min}}$	Momentum range	Separation	Resolution $\sigma_E/E[\text{GeV}]$	$E_{\text{min}}$	
$\downarrow p/A$	Far Backward Detectors	low- $Q^2$ tagger	Not Accessible												
		Reduced Performance													
$<-4.6$ $-4.6$ to $-4.0$ $-4.0$ to $-3.5$ $-3.5$ to $-3.0$ $-3.0$ to $-2.5$ $-2.5$ to $-2.0$ $-2.0$ to $-1.5$ $-1.5$ to $-1.0$ $-1.0$ to $-0.5$	Backward Detector	$0.2\% * p$ $\oplus 5\%$	70 MeV/c to 150 MeV/c	8	9	$1\%/E$ $\oplus 2.5\%/\sqrt{E}$ $\oplus 1\%$	$\pi$ supp. up to $10^4$	20 MeV	$<10 \text{ GeV}/c$	$50\%/\sqrt{E}$ $\oplus 10\%$	500 MeV	18			
		$0.04\% * p$ $\oplus 2\%$		$40 \mu\text{m}/p_T$ $\oplus 10 \mu\text{m}$	$100 \mu\text{m}/p_T$ $\oplus 20 \mu\text{m}$	$2\%/E$ $\oplus (4 - 8)\%/\sqrt{E}$ $\oplus 2\%$	$\pi$ supp. up to $10^3 - 10^2$	50 MeV				18			
$-0.5$ to $0.0$ $0.0$ to $0.5$ $0.5$ to $1.0$ $1.0$ to $1.5$ $1.5$ to $2.0$ $2.0$ to $2.5$ $2.5$ to $3.0$ $3.0$ to $3.5$ $3.5$ to $4.0$ $4.0$ to $4.6$	Central Detector	Barrel	$0.04\% * p$ $\oplus 1\%$	$< 5\%$	$30 \mu\text{m}/p_T$ $\oplus 5 \mu\text{m}$	$30 \mu\text{m}/p_T$ $\oplus 5 \mu\text{m}$	$2\%/E$ $\oplus (12 - 14)\%/\sqrt{E}$ $\oplus 2 - 3\%$	$\pi$ supp. up to $10^2$	100 MeV	$<6 \text{ GeV}/c$	$> 3\sigma$	500 MeV	18		
		Forward Detector	$0.04\% * p$ $\oplus 2\%$	$70 \text{ MeV}/c$ to $150 \text{ MeV}/c$	$40 \mu\text{m}/p_T$ $\oplus 10 \mu\text{m}$	$100 \mu\text{m}/p_T$ $\oplus 20 \mu\text{m}$	$2\%/E$ $\oplus (4 - 12)\%/\sqrt{E}$ $\oplus 2\%$	$3\sigma \text{ } e/\pi$ up to $15 \text{ GeV}/c$	100 MeV	$<50 \text{ GeV}/c$			$50\%/\sqrt{E}$ $\oplus 10\%$	18	
			$0.2\% * p$ $\oplus 5\%$		8	9							18		
	Far Forward Detectors	Proton Spec- trometer	Reduced Performance												
		Zero Degree Neutral Detection	Not Accessible												
1	2	3	4	5	6	7	8	9	10	11	12	13	14	15	18

Table 1: Detector matrix showing various ranges of  $\eta$  and their performance characteristics.

EIC science needs.

The ePIC Collaboration has been established in July 2022 at the EICUG Meeting at Stony Brook University. ePIC was born as a merger of two pre-conceptual designs, ECCE [12] and ATHENA [13] and is a general purpose detector designed to deliver the whole EIC core science program.

The purpose of this chapter is to study key measurements in order to demonstrate that ePIC is capable of delivering on its mission.

Processes taken into consideration are chosen for both their relevance to the core science and the specific challenges that they pose to the detector.

All the studies contained in this chapter are based on a full GEANT4 simulation of the ePIC detector and on reconstruction tools available in the October 2024 simulation campaign. As the development of both simulation and tools progresses, we will update our studies for the next versions of this document.

In some instances, our ability to demonstrate the detector performance for a relevant measurement might be hampered by the absence of a needed tool that was yet to be developed/finalized. When this occurs, it must not be taken as that the detector cannot accomplish a certain measurement or that we are overlooking certain physics. Our goal is to be able to show those results by the final version of the TDR (90% design completion).

There are many studies performed by the ePIC's Physics Working Groups that will not enter this selection but that are absolutely relevant for the EIC core science and beyond. Furthermore, many details that went into the physics studies, both on the analysis and the impact on the current knowledge, will be omitted for the purpose of this TDR. The ePIC collaboration plans to separately publish a "science paper" containing all the missing information that cannot be given within the present document.

## 2.2 The Science Goals of the EIC and the Machine Parameters.

This Section will be filled by Elke Aschenauer and Rolf Ent for the EIC Project.

## 2.3 Reconstruction Tools and Special Probes

This section will discuss the reconstruction methods for the different event topologies encountered in deep inelastic scattering (DIS), semi-inclusive DIS, and exclusive processes. Then, we will detail some of the particle and jet reconstructions that will be most important for the analyses presented later.

### 2.3.1 Reconstruction of DIS kinematics

The inclusive DIS process can be written as

$$e(k) + P(p) \rightarrow e(k') + X(p'), \quad (2.1)$$

where  $e$  ( $e'$ ) indicates the initial (scattered) electron,  $P$  the proton target, and  $X$  the inclusive hadronic final state system. This process is shown diagrammatically in Figure 2.1. The event kinematics are described using three Lorentz invariant quantities, related by the center-of-mass energy

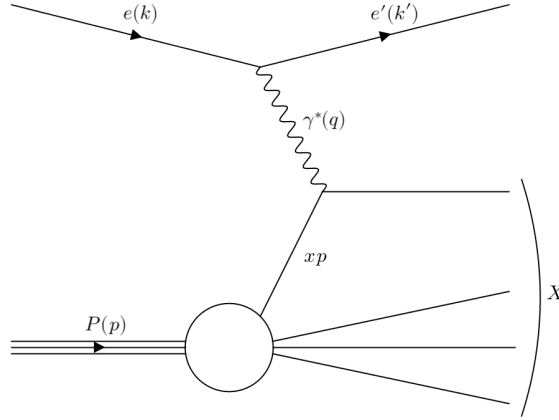


**Figure 2.1:** Neutral-Current Deep Inelastic Scattering of an electron by a proton.

547 S, as

$$Q^2 = xy(s - m_p^2) \simeq sxy. \quad (2.2)$$

548 For a virtual photon with four-momentum  $q$ , the virtuality  $Q^2$  is

$$Q^2 \equiv -q^2 = -(k - k')^2, \quad (2.3)$$

549 while the Bjorken variable  $x$ , and the inelasticity  $y$  are given by

$$x \equiv \frac{Q^2}{2p \cdot q}, \quad y \equiv \frac{p \cdot q}{p \cdot k}. \quad (2.4)$$

550 In a reference frame where the proton target has infinite momentum,  $x$  is the momentum fraction  
 551 carried by the struck parton (neglecting quark masses). If the rest frame of the target proton is cho-  
 552 sen instead, the inelasticity  $y$  simply describes the fractional energy loss of the scattering electron,  
 553  $y = 1 - \frac{E'_e}{E_e}$ . The center-of-mass energy  $W$  of the photon-proton system may also be considered, and  
 554 is given by

$$W^2 \equiv (p + q)^2 = m_p^2 - Q^2 + 2p \cdot q. \quad (2.5)$$

555 In the laboratory frame, the ingoing (outgoing) electron and proton four-momenta are given by  $k$   
 556 ( $k'$ ) and  $p$  ( $p'$ ) respectively, which can be written as

$$k = (E_0, 0, 0, -E_0)$$

$$k' = (E_e, E_e \sin \theta_e, 0, E_e \cos \theta_e)$$

$$p = (E_p, 0, 0, E_p)$$

$$p' = (E_h, p_{t,h}, 0, p_{z,h})$$

557 for scattering in the  $x - z$  plane. By convention, the electron beam is aligned with the  $-z$ -axis,  
 558 and the proton beam with the  $+z$ -axis. The center-of-mass energy is therefore given by  $s = 4E_e E_p$ ,  
 559 neglecting mass. The virtual photon four-momentum is  $q = k - k'$ , so the kinematic variables may  
 560 be reconstructed using electron information alone by evaluating the four-momenta

$$y_e = 1 - \frac{E_e(1 - \cos \theta_e)}{2E_0}, \quad Q_e^2 = 2E_0 E_e(1 + \cos \theta_e). \quad (2.6)$$

561 The resolutions on kinematic variables reconstructed using this method are

$$\frac{\delta y}{y} = \frac{1-y}{y} \left( \frac{\delta E_e}{E_e} \oplus \frac{\delta \theta_e}{\tan \frac{\theta_e}{2}} \right), \quad \frac{\delta Q^2}{Q^2} = \frac{\delta E_e}{E_e} \oplus \tan \frac{\theta_e}{2} \cdot \delta \theta_e \quad (2.7)$$

562 and it can be seen that the  $y$  resolution diverges at low  $y$ , while the  $Q^2$  resolution diverges as  
 563  $\theta_e \rightarrow 180^\circ$ . To counteract this divergence, methods that utilize the hadronic final state (HFS) mea-  
 564 surement, which do not degrade in resolution at low  $y$  values, are often used. The inclusive HFS is  
 565 defined as the sum over all final state particles other than the scattered electron, and is described  
 566 using the quantities

$$\delta_h = \sum_h E_h - p_{z,h} \quad \text{and} \quad p_{t,h}^2 = \left( \sum_h p_{x,h} \right)^2 + \left( \sum_h p_{y,h} \right)^2. \quad (2.8)$$

567 The Double-angle method enables the kinematics to be reconstructed using the electron scattering  
 568 angle  $\theta_e$  and the inclusive HFS angle  $\gamma_h$  as

$$y_{DA} = \frac{\alpha_h}{\alpha_e + \alpha_h}, \quad Q_{DA}^2 = \frac{4E_0^2}{\alpha_e(\alpha_e + \alpha_h)} \quad (2.9)$$

569 where  $\alpha_e \equiv \tan \frac{\theta_e}{2}$  and  $\alpha_h \equiv \tan \frac{\gamma_h}{2} = \frac{\delta_h}{p_{t,h}}$ . In the Jacquet-Blondel, or “hadron-only” method, the  
 570 kinematics are reconstructed as

$$y_{JB} = \frac{\delta_h}{2E_0}, \quad Q_{JB}^2 = \frac{p_{t,h}^2}{1 - y_h} \quad (2.10)$$

571 while the  $\Sigma$  method is calculated as

$$y_\Sigma = \frac{\delta_h}{\delta_h + E_e(1 - \cos \theta_e)}, \quad Q_\Sigma^2 = \frac{E_e'^2 \sin^2 \theta_e}{1 - y_\Sigma}. \quad (2.11)$$

572 For each of the methods described above,  $x$  is calculated as  $x = \frac{Q^2}{s y}$ . In addition to the methods  
 573 described in this appendix, there are methods that emerge when the input variables are permuted,  
 574 which are summarized elsewhere [14].

575 In summary, for our studies only four reconstruction methods are considered:

- 576 • **Electron method:** uses only scattered electron.
- 577 •  **$\Sigma$  method:** uses both scattered electron and HFS.
- 578 • **Double-angle method (DA):** uses both scattered electron and HFS.
- 579 • **Jacquet-Blondel method (JB):** uses only HFS.

580 The JB method relies solely on the HFS, which is less well measured compared to the scattered  
 581 electron. While the JB method does not usually give the best resolution, it is the only reconstruction  
 582 method possible for charged-current interactions (where the outgoing DIS lepton is a neutrino).

583 Figure 2.2 shows the  $y$  resolution at ePIC as a function of  $x_B$  and  $Q^2$  for 18 GeV on 275 GeV  $ep$   
 584 collisions. The scattered electron reconstruction that informs these resolutions uses the momentum  
 585 and polar angle measured by the tracking system. The resolution could be further improved by  
 586 using electromagnetic calorimeter clusters for the electron energy measurement. This is particularly

important for small scattering angles, as the tracking performance is degraded, but a high quality energy measurement may be obtained using the backward endcap electromagnetic calorimeter.

The optimal reconstruction method changes with the kinematics, with the electron method providing the best reconstruction at large  $y$  values. The resolution of the electron method degrades as  $1/y$ , so the  $\Sigma$  and DA methods are employed for  $y \lesssim 0.2$ , ensuring that a  $y$  resolution of 30% or lower can be obtained for the full kinematic range.

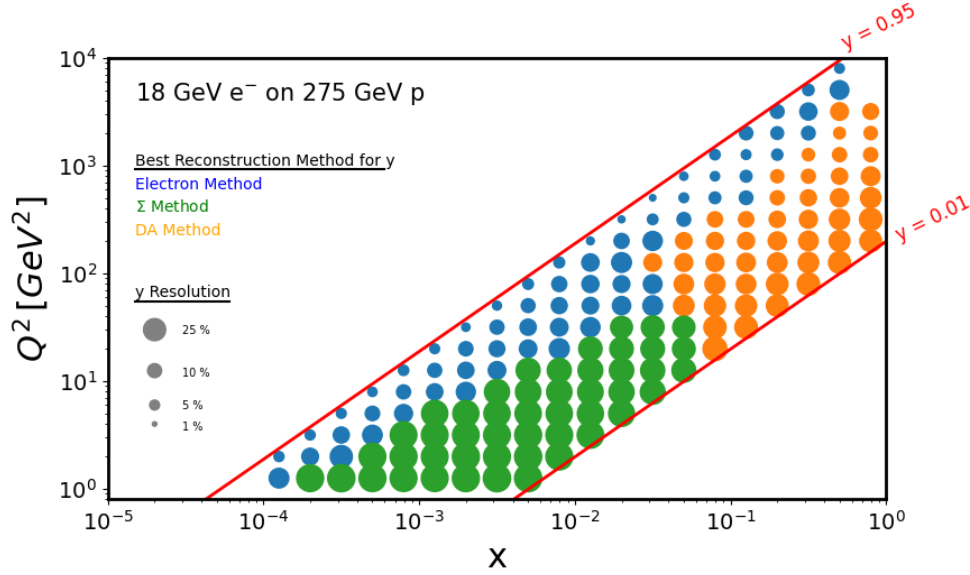


**Figure 2.2:** Resolution of the inelasticity  $y$ , as a function of  $x_B$  and  $Q^2$ , when reconstructed using the electron method (blue),  $\Sigma$  method (green), or Double-angle method (orange). The color of each point indicates the best performing reconstruction method.

### 2.3.2 Semi-inclusive kinematics and hadron identification

In semi-inclusive DIS (SIDIS) the detection of final-state hadrons provides additional sensitivity to the flavor of the struck parton in the nucleon. This is obtained via fragmentation functions (FF), for example  $D_{1,q}^h(z, Q^2)$ , which describe the formation of final-state hadrons  $h$  from initial partons  $q$  at a certain fractional momentum relative to the parton  $z$ , and additionally also depending on its transverse momentum and spin. Fragmentation functions are also universal objects like the PDFs and can therefore be extracted in other processes such as in  $e^+e^-$  annihilation and hadronic collisions and be used in semi-inclusive DIS. The flavor sensitivity originates from the fact that a hadron at high  $z$ , such as a positive pion originating from an up quark or a positive kaon from an anti-strange quark, is more likely to contain the initially struck parton.

The corresponding SIDIS cross sections are then products or convolutions of the corresponding PDFs and FFs, i.e.:

$$\frac{d\sigma^2}{dx dz} \propto \sum_q e_q^2 f_q(x, Q^2) D_{1,q}^h(z, Q^2). \quad (2.12)$$

When transverse momenta and spin are also involved the resulting transverse momentum of the hadron relative to the virtual photon/ $Z$  direction  $\mathbf{P}_{hT}$  needs to be also considered and typically con-

tains a convolution of the intrinsic transverse momenta of distributions and fragmentation. Experimentally, these transverse momenta are typically expressed by its magnitude  $P_{hT}$  and azimuthal angle  $\phi_h$  while a transverse spin of the incoming nucleon results in another azimuthal angle  $\phi_S$ .

The reconstruction of these kinematic variables initially relies on the DIS kinematics, as the virtual photon direction and its boost are necessary to calculate them. Additionally, excellent tracking is required to not further smear the SIDIS variables.

An example for the momentum fraction  $z$  is shown in Fig. 2.3, where the  $z$  resolution is plotted as a function of true  $z$ . The resolutions for transverse hadron momenta are generally similar while the azimuthal angles appear to be more robust.

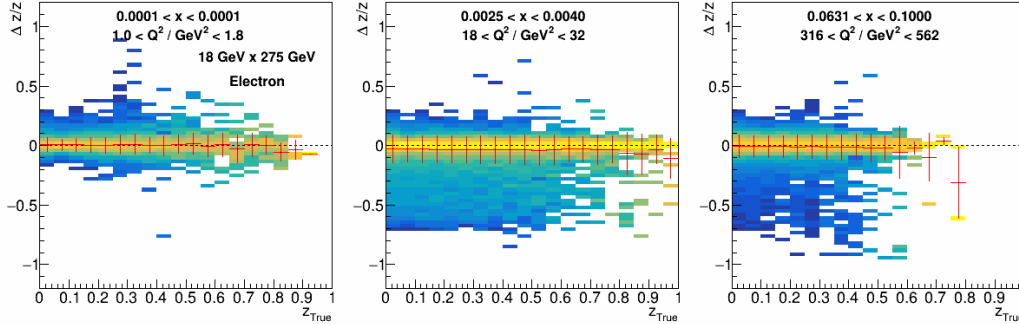


**Figure 2.3:** Resolution of the hadron fractional momentum  $z$  as a function of the true  $z$ , in three  $x$  and  $Q^2$  bins when the reconstructed kinematics for the DIS lepton and hadron are considered (red). The uncertainties describe the RMS of the resolutions while the central value represents the mean resolution.

As the flavor of the struck parton is obtained via the hadron type (and its fractional momentum), the correct reconstruction of the hadron is most important. Fig. 2.4 displays the efficiencies, mis-identification rates and purities for kaons in three regions of the ePIC detector that correspond to where the backward TOF and pFRICH, the central TOF and DIRC and the dRHIC provide the main particle identification, respectively. One sees that overall the efficiencies are reasonably high, while the boundaries between low momenta (dominated by the TOF information) and the higher momenta (dominated by the RHICes) are clearly visible. Given the large amount of pions in comparison to kaons, even a good PID efficiency results in a sizeable contamination with pions.

### 2.3.3 Reconstruction of kinematics for exclusive and diffractive processes

Among the diverse scientific objectives at the EIC, exclusive reactions and diffractive processes play a pivotal role in uncovering the structure of nucleons and nuclei in transverse coordinates, as well as in studying their emergent dynamics.

In experimental terms, diffractive processes are identified by the presence of a rapidity gap — a region in the detector with no particle activity. These processes were extensively studied at HERA, where they were interpreted using the concept of *Pomeron exchange*. The Pomeron is modeled as a color-singlet object composed of two gluons with zero spin, mediating the interaction between the virtual photon (emitted by the electron) and the hadron.

The key kinematic variables used to describe diffraction are:

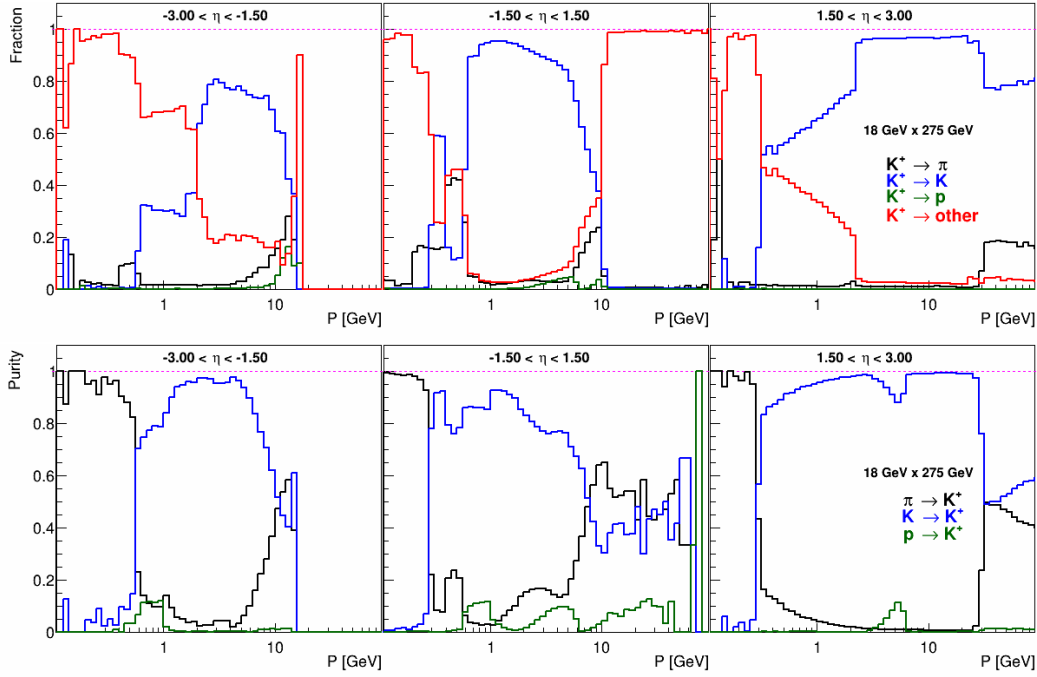


**Figure 2.4:** PID efficiencies (top) and purities (bottom) of kaons as a function of the true hadron momentum are shown in three rapidity ranges relevant for the different detector choices of ePIC. The efficiencies and purities are shown in blue, while the corresponding misidentification rates are displayed in red (kaons) and dark green (protons).

- $x_P = \frac{x}{\beta}$ : the fraction of the hadron's momentum carried by the Pomeron;
- $t = -(p' - p)^2$ : the squared four-momentum transfer between the initial ( $p$ ) and final ( $p'$ ) hadron states;
- $\beta = \frac{Q^2}{Q^2 + M_X^2 - t}$ : where  $Q^2$  is the virtuality of the photon and  $M_X^2$  is the invariant mass squared of the diffractive hadronic system.

To analyze diffractive events, one needs the standard DIS kinematic variables ( $x$  and  $Q^2$ ), along with measurements of the momentum transfer  $t$  and the properties of the final-state hadronic system. A crucial experimental signature is the presence of a rapidity gap and/or the direct detection of the scattered hadron. In cases where the diffractive final state  $M_X$  consists of a single particle or a well-defined state, the process is referred to as an *exclusive reaction*, reflecting the constrained and clean event topology.

Specifically, exclusive reactions refer to processes in which the entire final state of particles is detected, enabling precise reconstruction of the reaction dynamics. The "exclusivity" of such reactions imposes stringent requirements on detector acceptance. In these events, the scattered proton or nucleus typically loses only a small fraction of its momentum and often escapes undetected through the beam pipe. Ensuring exclusivity therefore relies on dedicated forward detection systems, including the far forward proton spectrometer, which consists of components such as the B0 detector, Roman pots, off-momentum detectors, and the zero-degree calorimeter (used for detecting neutral particles). Once exclusivity is established, it becomes essential to measure the relevant kinematic

variables with high precision and broad acceptance. Of particular importance is the distribution of the momentum transfer  $t$ , which plays a key role in the imaging program.

There are several methods to reconstruct the momentum transfer variable  $t$ , each offering distinct advantages depending on the specific reaction under study. Broadly, these methods can be categorized into three types:

- (i) *Hadron-only* method,
- (ii) *Lepton + observable* method,
- (iii) *A hybrid approach* that combines elements of both with imposed exclusivity.

For instance, in the case of deeply virtual Compton scattering (DVCS) on a proton, method (i) corresponds directly to Eq. 1. The reconstruction of  $p'$  can be based on B0 and/or the roman pots, where  $p$  is the nominal incoming proton beam momentum. Alternatively,  $t$  can be reconstructed using the four-momenta of the incoming electron, the scattered electron, and the produced real photon—this constitutes method (ii).

In practice, it is often beneficial to combine these approaches or use partial information from each to enhance the accuracy of  $t$ -reconstruction. This flexibility becomes especially important in regions of phase space where certain methods are limited or inapplicable—for example, when the outgoing heavy nucleus is not detectable.

Beyond the three primary reconstruction methods, further improvements can be made by exploiting the differences among them to suppress events with poor resolution—though this comes at the cost of reduced statistics. Another recent proposal suggests reconstructing the momentum transfer  $t$  along a specific projected direction to mitigate the impact of detector smearing [?]. This approach can be used in conjunction with, and as an enhancement to, the traditional methods outlined above. Such developments are particularly crucial for the imaging program of heavy nuclei at the highest collision energies at the EIC.

In Section 2.4, three measurements related to nucleon and nucleus imaging will be highlighted: DVCS in  $ep$ , exclusive three Upsilon states production in  $ep$ , and exclusive Vector Meson production in  $eA$  collisions.

Based on the YR [8], the requirement for the DVCS in  $ep$  is to have a good acceptance of forward proton detection to cover a wide range of  $t$  for different  $x_B$  and  $Q^2$  phase spaces above  $Q^2 > 1 \text{ GeV}^2$ . For Upsilon productions, the requirement is to have a tracking system in the main detector to separate the  $\Upsilon(1s)$ ,  $\Upsilon(2s)$ , and  $\Upsilon(3s)$  state. The relative cross section of the different states is the key to this measurement. For the exclusive Vector Meson production, e.g.,  $J/\psi$  and/or  $\phi$ , the requirement is to have a good momentum resolution to see the diffractive minima and a large acceptance in the far-forward detector to veto the incoherent background contributions.

### 2.3.4 Electron identification

Regardless of kinematics reconstruction method used, it is crucial to identify the scattered electron in the event final state. Indeed, it can be challenging to separate the electron signal from the large  $\pi^-$  background present in DIS collisions. Therefore, a rudimentary electron identification algorithm has been already developed in ePIC.

The first step is to separate final state electrons from pions. This is done by applying a cut on  $E/p$ , where  $p$  is the track momentum and  $E$  is the ECAL cluster energy matched to that track. Electrons



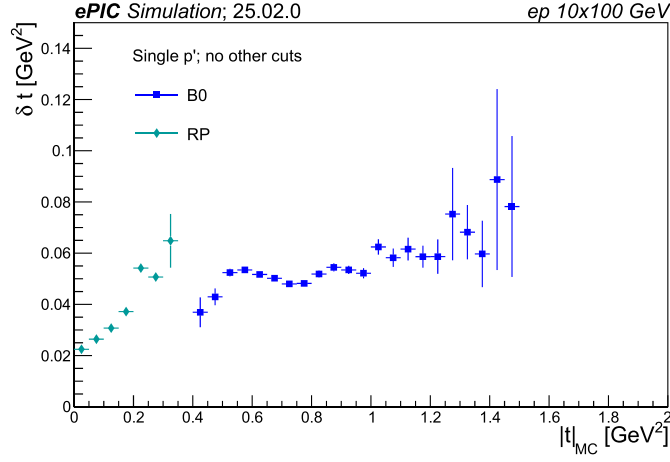


**Figure 2.5:** Resolution of  $t$  as a function of the true  $t$  for both B0 and RP for  $ep$  10 on 100 GeV.

will typically deposit all of their energy in the ECAL and have  $E/p \approx 1$ , while pions will pass through the ECAL and peak at  $E/p < 1$ . Currently, two sets of cuts are used:  $0.9 \leq E/p \leq 1.2$  to cleanly select electrons, as well as a looser  $0.7 \leq E/p \leq 1.3$  selection as the input to the following algorithm for identifying the scattered DIS electron.

The next step is to identify the scattered DIS electron, as other electrons may be present in the final state. In many cases the electron with the greatest momentum can be accurately identified as the scattered electron. To improve upon this, the current analysis utilizes the so called  $E - p_z$  algorithm. This algorithm selects the electron which maximizes the difference between the sum of the energy of the electron and hadronic final state and the sum of the  $z$  component of their momentum, with the ideal case approaching  $2E_e$ , twice the energy of the electron beam.

Future iterations of the DIS electron identification algorithm will incorporate information from the PID detectors (hpDIRC, pfRICH, TOF), applying cuts on shower shape parameters of the calorimeter clusters, as well as refinement of the selection criteria.

### 2.3.5 Muon identification

The ability to identify muons in the final state would significantly increase the reach of EIC physics. To evaluate the feasibility of muon identification, single particle simulations studies were performed with the ePIC simulation and reconstruction frameworks. Muons and pions have been generated and reconstructed in the central barrel region for momenta between 0.1 and 15 GeV. The

analysis of the reconstructed events rely on two variables: the  $E/p$ , and shower radius. The momentum  $p$  is obtained from the reconstructed track, while the energy and shower radius can be obtained from either the electromagnetic or hadronic calorimeters.

The separation between muons and pions has been evaluated using a log likelihood analysis. The figure of merit (FOM) has been set as the ratio between the accepted muons and the accepted muons and pions selecting for the likelihood larger than 0 for the different subsystems involved. Figure 2.6 shows the FOM variable as a function of momentum of the thrown muon for different use of cuts and detector systems. As can be seen the highest discrimination power is obtained from the  $E/p$  information, while the shower shape provides some additional discrimination at low momentum.

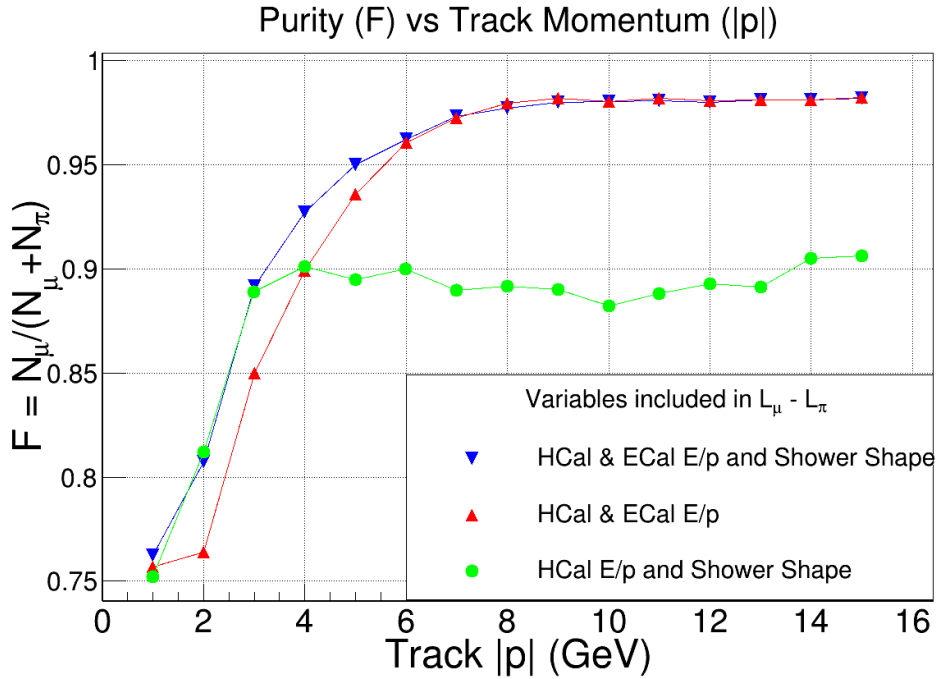


**Figure 2.6:** Figure of merit for muon identification as a function of momentum in the ePIC central barrel.

### 2.3.6 Jets: a versatile probe

As demonstrated in the YR [8], jets are an important observable, bringing both complementary and unique insight to many of the EIC science goals. In order to comprehensively evaluate the impact that they can have, jet reconstruction has been integrated into the ePIC reconstruction framework, EICrecon. It utilizes the FastJet package to implement various jet definitions. The default settings, which are used for jets saved to the shared output trees and included in the analyses below, include the Anti- $k_T$  algorithm, E-scheme recombination, a resolution of 1.0, and a minimum jet transverse momentum of 1 GeV/c. In addition, constituents were required to have transverse momenta greater than 200 MeV/c to be included in the clustering.

Due to the lack of mature algorithms for integrating information from tracking, calorimetry, and particle identification subsystems, the reconstructed jets used to benchmark the ePIC detector per-

formance and evaluate physics impact are clustered exclusively from charged particle tracks.

The primary metrics for evaluating the quality of jet reconstruction at ePIC are the jet energy scale (JES) and jet energy resolution (JER). These quantities were calculated by comparing the energies of matched particle-level and reconstructed jets. Because the reconstruction currently uses track-only jets and we are primarily interested in quantifying the effects of the detector, only stable charged particles were used when clustering the particle-level jets. For each particle-level jet, the closest reconstructed jet in  $\eta - \phi$  space was considered the matching jet as long as  $\Delta R = \sqrt{\Delta\eta^2 + \Delta\phi^2}$  was less than 0.1. The quantity: [(reco - particle)/particle] jet energy was found for each set of matching jets and fit with a triple Gaussian function. A triple Gaussian was used to try to take into account the tails of the distribution. The mean of fit is taken as the JES while the sigma is taken as the JER. To get a more differential picture of the jet performance, this procedure was performed as a function of particle-level jet energy for three pseudorapidity ranges as shown in Fig. 2.7.

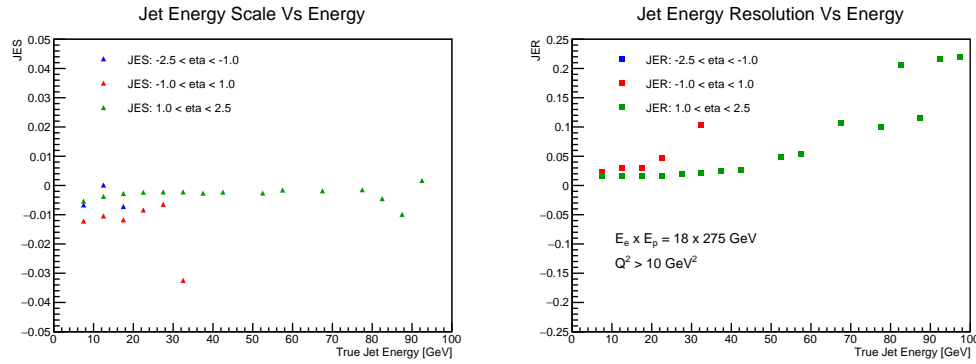


**Figure 2.7:** Jet energy scale (Left) and jet energy resolution (Right) as a function of particle-level jet energy for backward (blue squares), mid (red triangles), and forward (green diamonds) rapidities.

## 2.4 The EIC Science - ePIC performance for key observables

The ePIC Collaboration has been established with the goal of realizing a general purpose detector capable of delivering on the whole EIC science program. In the following, we will investigate the detector performance to measure key processes for each of the EIC science milestones, as highlighted by the NAS report [11].

### 2.4.1 Origin of Nucleon Mass

Nucleons are made of quarks bound together by massless gluons. The Higgs mechanism can only explain the source of the quark masses. Nevertheless, the masses of valence quarks account only for  $\sim 1\%$  of a nucleon's mass and thus cannot explain the mass of all the visible matter in the universe. The reminder of the proton mass must originate from the field energy of quarks and gluons in the sea.

The most accessible description of hadrons in terms of their constituent partons is by parton distribution functions (PDFs), representing the fractional (longitudinal) momentum carried by each

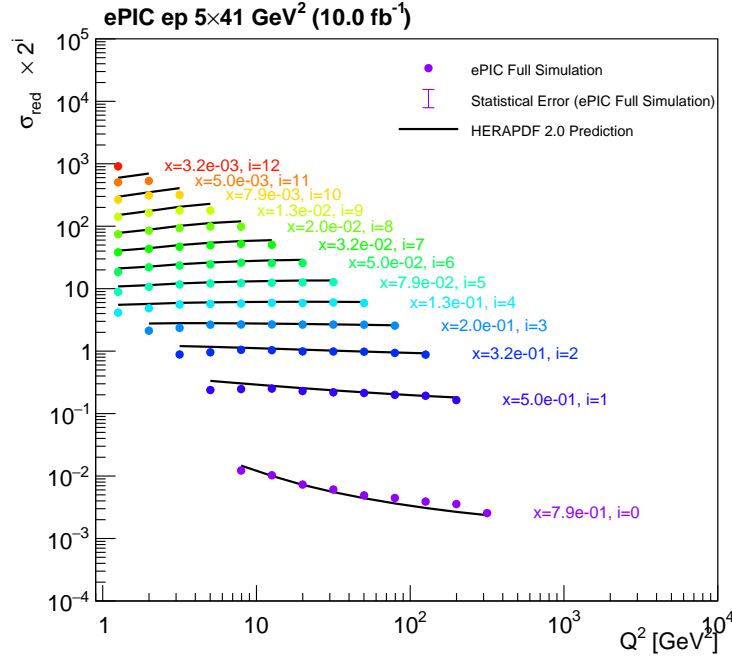


**Figure 2.8:** Projected  $ep$  neutral current reduced cross sections at 5x41 GeV. Statistical uncertainties assume an integrated luminosity of  $10 \text{ fb}^{-1}$ .

parton flavor. The inclusive DIS cross section is sensitive to PDFs through the structure functions  $F_1$  and  $F_2$ , which are linear combinations of the PDFs.

Tomographic images of quarks and gluons, also achievable at ePIC, are discussed in Sec.2.4.3.

The performance in identifying the DIS scattered electron and the resolution measuring its energy and momentum are key for inclusive measurements. The performance parameters for tracking and calorimetry as devised by the dedicated studies in the YR [8] are needed for high quality measurements of inclusive cross sections.

#### 2.4.1.1 Inclusive neutral current cross sections

To extract neutral-current cross sections, corrections for acceptance and bin migration are defined by comparing reconstructed events to generated events. These corrections are then applied to the reconstructed events. Note that since the same reconstructed events are used for both the corrections and cross section extraction, this by definition yields the cross sections of the underlying event generator.

The projected neutral-current reduced cross sections for three center of mass energies are shown in Figures 2.8-2.10. These use the electron identification and event selection criteria as described in Sec: 2.3.4. However, at this stage the kinematics have been reconstructed using the electron method only. The statistical uncertainties are estimated assuming an integrated luminosity of  $10 \text{ fb}^{-1}$  for each center of mass energy.

As a consequence of the high luminosity provided by the EIC, the statistical uncertainty for neutral-

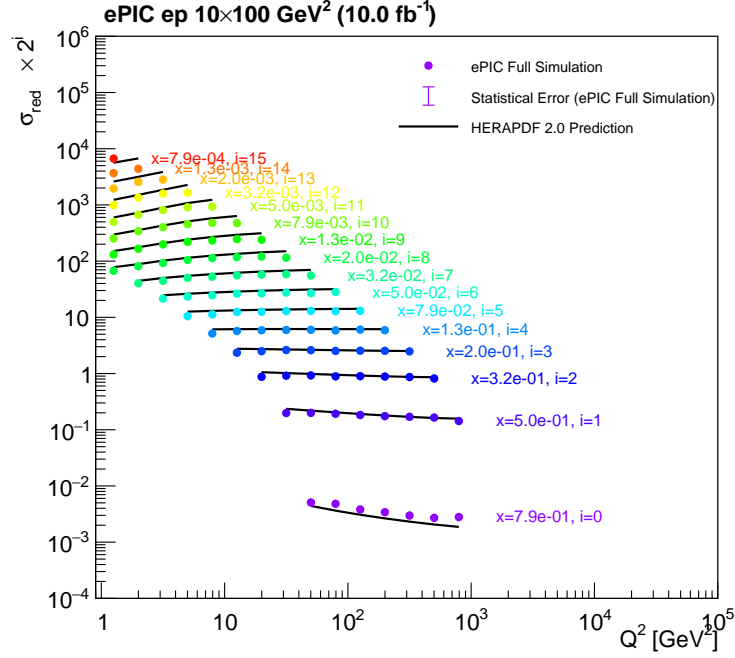


**Figure 2.9:** Projected  $ep$  neutral current reduced cross sections at 10x100 GeV. Statistical uncertainties assume an integrated luminosity of  $10 \text{ fb}^{-1}$ .

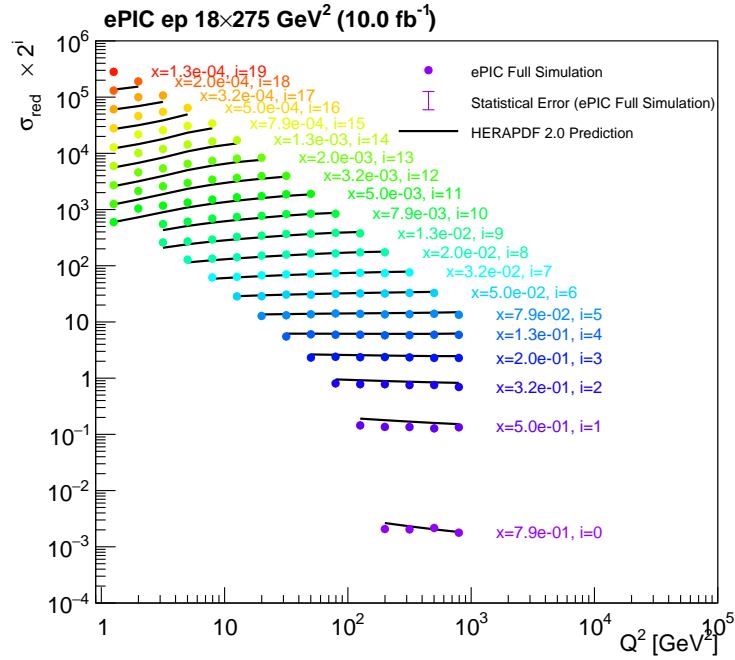


**Figure 2.10:** Projected  $ep$  neutral current reduced cross sections at 18x275 GeV. Statistical uncertainties assume an integrated luminosity of  $10 \text{ fb}^{-1}$ .

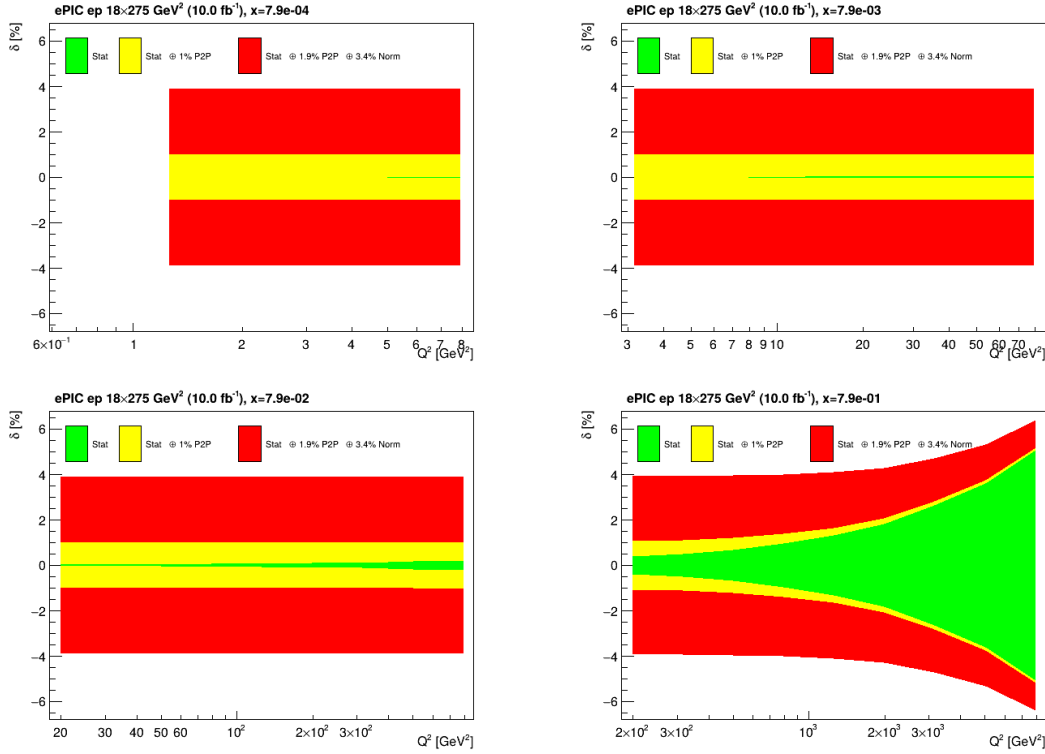


**Figure 2.11:** Statistical and total uncertainty for selected bins in  $x_B$  as a function of  $Q^2$  for pessimistic and optimistic estimates of systematic uncertainty.

current cross section measurements is minimal, with the cross section uncertainties instead being dominated by systematics. It is difficult to achieve precise estimates of systematic uncertainties for an accelerator and detector that are yet to be constructed. Detailed studies of systematic uncertainties were carried out at HERA, with no single source dominating. The instrumentation solutions for ePIC and the EIC were chosen such that a significant improvement in systematic uncertainty relative to HERA may be achieved. Estimates for the statistical and total uncertainties on the neutral-current reduced cross section, using the highest center-of-mass energy beam setting, are indicated in Figure 2.11, for bins in  $x$  across four orders of magnitude, as a function of  $Q^2$ . The total uncertainty is considered for two scenarios, with HERA inspired values of 1.9 % point-to-point uncorrelated uncertainty and 3.4 % normalization uncertainty providing a conservative scenario. A 1 % totally uncorrelated uncertainty is chosen as an optimistic scenario, with the understanding that the actual systematic precision achieved at ePIC will likely fall between these two estimates. From Figure 2.11 it can be understood that, even in the optimistic scenario for systematics, the statistical uncertainty only dominates at the largest values of  $x$  and  $Q^2$ .

## 2.4.2 Origin of Nucleon Spin

Thanks to the availability of polarized electron and hadron beams at the EIC, inclusive DIS can be used to probe the contribution of nucleon spin from quark helicity. Double-spin asymmetries between different relative electron/hadron polarization states are sensitive to polarized PDFs through the spin structure function  $A_1 \propto g_1 = \sum_q e_q^2 (\Delta q - \Delta \bar{q})$ . The gluon contribution to nucleon spin is

inferred by the  $Q^2$  dependence of the spin structure functions, therefore it is critical for the measurements to cover a wide range of kinematics. For the proton,  $A_1^p$  is measured directly in polarized proton collisions. For the neutron,  $A_1^n$  must be inferred from measurements of polarized helium-3, with model-dependent corrections for the proton contribution.

The projected nucleon double-spin asymmetries  $A_1^p$  and  $A_1^n$  are shown in Figure 2.12. The statistical uncertainties are estimated assuming an integrated luminosity of  $10 \text{ fb}^{-1}$  for each target and center of mass energy, equally split between the the beam polarization configurations required for the asymmetry measurement. The reconstruction, event selection, and kinematic cuts are described in Sec. 2.3.4.

**Figure 2.12:** Projected measurements of  $A_1^p$  (right) and  $A_1^n$  (left).

When extracting the double spin asymmetries for semi-inclusive measurements,  $A_1^{p,h}$ , the selection of final state hadrons,  $h$ , provides further sensitivity to the flavor of the struck parton. Given that DIS is generally  $u$ -quark dominated, the detection of a negative pion or a kaon with high momentum fraction relative to the initial parton momentum increases the sensitivity to down quarks, and strange quarks. The role of sea quarks and, particularly, strange quarks in the decomposition of the proton spin is still only poorly understood and is in most global fits only constrained using hyperon decays and the assumption of  $SU(3)_F$  symmetry. Using this assumption, the strange quark contribution to the nucleon spin is pushed toward negative values in the so far inaccessible region. The ePIC measurements will be able to access its contribution over a wide range in  $x$  and determine whether these symmetry assumptions are really valid. Similarly, the contributions by sea quarks can be determined using semi-inclusive DIS.

Figure 2.13 shows, for selected bins in  $x_B$ ,  $Q^2$  and  $z$ , the expected kinematic coverage for semi-inclusive production of positively charged pions for beam energies of  $5 \times 41$  and  $18 \times 275 \text{ GeV}^2$  together with the expected measurement uncertainties. The vertical error bars represent the statistical uncertainty relative to a luminosity of  $10 \text{ fb}^{-1}$ , while the error bands represent the total uncertainty. As can be seen from the figures, the low and high beam-energy configurations cover complementary kinematic regions, allowing for a coverage in  $x_B$  from high  $x_B$  values down to  $x_B = 10^{-4}$ .

### 2.4.3 Multi-Dimensional Imaging of the Nucleon

One-dimensional PDFs reveal the distribution of longitudinal parton momenta in the direction of the nucleon momentum. Nevertheless, a fast moving nucleon has still sizable transverse spatial dimensions.

The 3D parton structure of hadrons in momentum space is encoded in transverse momentum dependent parton distributions (TMDs). The non-perturbative quantities that encode the spatial distributions in the transverse plane are called generalized parton distributions (GPDs).

#### 2.4.3.1 Imaging in Momentum Space

Using semi-inclusive DIS, it is possible to extract information on the three-dimensional momentum structure of the nucleon by making use of transverse momentum dependent parton distribution functions (TMDs-PDFs or shortly TMDs). Depending on the polarization of the nucleon and the parton within the nucleon, there are in total 8 twist-2 TMDs, while the 16 TMDs, which exist at the

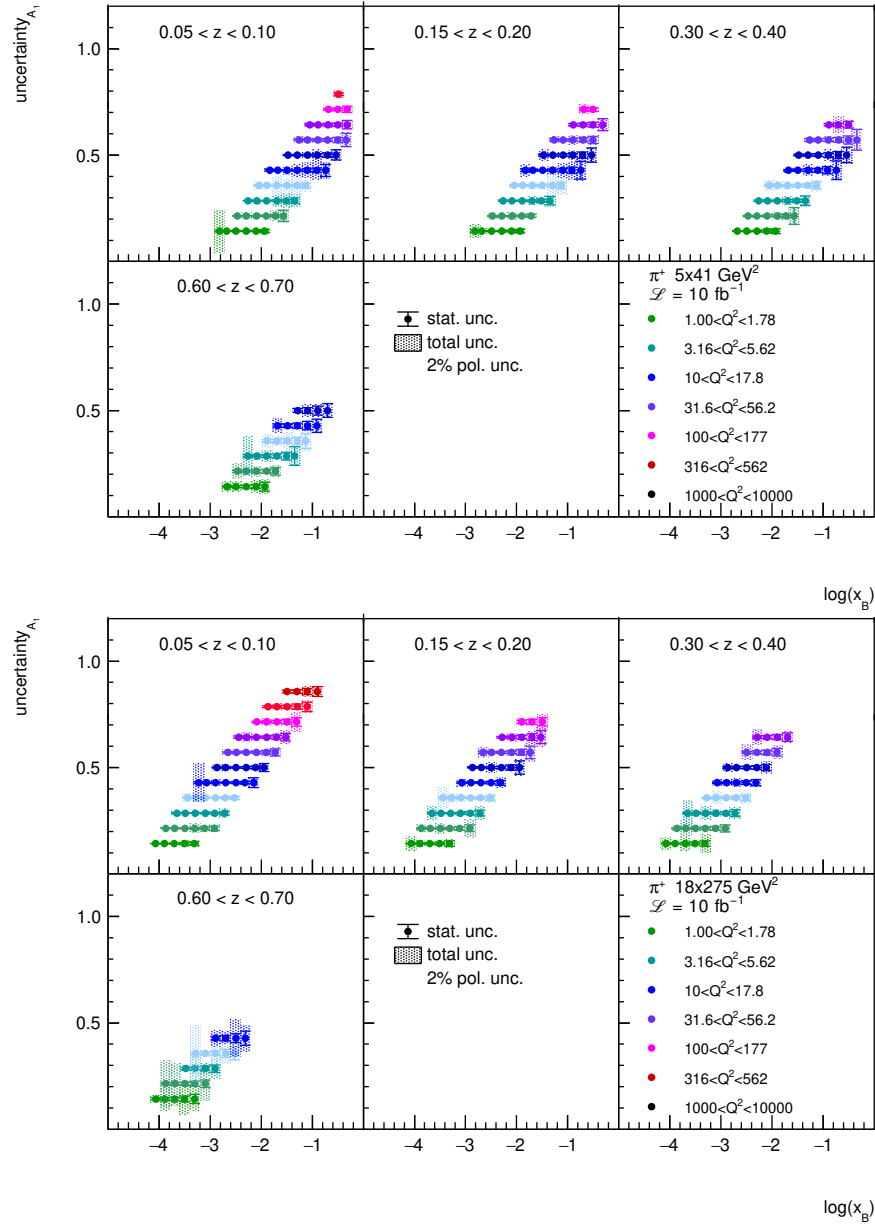


**Figure 2.13:** Statistical (error bars) and total (error bands) uncertainty for each selected bins in  $x_B$  and  $Q^2$  and for selected ranges in  $z$ , for positive-pion  $A_1$  asymmetries at  $5 \times 41 \text{ GeV}^2$  (top two rows) and  $18 \times 275 \text{ GeV}^2$  (bottom two rows). An additional global scale uncertainty of 2% accounts for the uncertainty in the beam polarizations, as indicated in the figure. The central value on the vertical axis of the data points has no meaning.

twist-3 level, also take quark-gluon correlations into account. Table 2.1 provides an overview on the TMDs up to twist-3.

Since the semi-inclusive DIS process also involves the hadronization of the parton which is kicked out of the nucleon during the scattering process, the observables are typically sensitive to a convo-



N \ q	U	L	T	twist 3
U	$f_1$		$h_1^\perp$	$f^\perp, g^\perp, h, e$
L		$g_{1L}$	$h_{1L}^\perp$	$f_L^\perp, g_L^\perp, h_L, e_L$
T	$f_{1T}^\perp$	$g_{1T}$	$h_1, h_{1T}^\perp$	$f_T, f_T^\perp, g_T, g_T^\perp, h^\perp, e_T, h_T^\perp, e_T^\perp$

**Table 2.1:** The 8 twist-2 and the 16 twist-3 TMDs and their dependence on the nucleon  $N$  and the quarks  $q$  polarisation (unpolarized: U, longitudinally polarized: L, transversely polarized: T).

lution of a TMD and a fragmentation function (FF), which describes this hadronization. These fragmentation functions are typically studied in hadron production in  $e^+e^-$  collisions, like at BELLE or BESIII, where they can be accessed in a clean way [15].

The measurement of cross sections and their angular modulations as well as beam, target and double spin asymmetries in semi-inclusive DIS, allows us to access a series of model independent structure functions, which can be directly related to a convolution of different TMDs and FFs [16, 17]. The measurement of different hadrons in the final state allows a flavor separation of the TMDs. Besides the classical DIS variables  $Q^2$  and  $x_B$ , semi-inclusive DIS observables are typically studied in terms of the energy fraction of the virtual photon carried by the outgoing hadron  $z$  and the transverse momentum of the outgoing hadron relative to the virtual photon direction  $P_T$  to access the full kinematic dependence of the TMDs.

For all SIDIS measurements, a few key requirements have to be fulfilled by the ePIC detector. First of all, an excellent particle identification over an as large as possible fraction of the kinematic and angular range of the scattered electrons and hadrons is required, since no exclusivity variables are available to further constrain the final state. Here, especially, a good pion to Kaon and proton separation up to high momenta is desirable. Furthermore, a differential binning of the observables in terms of the relevant kinematic variables requires a good momentum resolution to reduce distortions from bin migration effects. Both aspects will directly affect the achievable systematic uncertainties and therefore the total precision of the measurement.

Already with an un-polarized nucleon the ePIC experiment can provide flavor-separated TMDs over a large range in  $x_B$  and  $Q^2$ , and for transverse momenta that reach from the low, TMD-dominated, region into the perturbative region. The wide range of scales, as shown in Fig. 2.14 (left) will also solve the existing uncertainties in the TMD evolution where non-perturbative contributions require experimental input. As shown in Fig. 2.14 (right), the data expected from ePIC will significantly reduce the uncertainties of the extraction of unpolarized TMDs over most of the kinematic range.

The unpolarized TMD PDFs also serve as a baseline for any polarized TMD observable which are obtained as single or double spin asymmetries. The most relevant are the Sivers function  $f_{1T}^\perp$  [18, 19] and the quark transversity  $h_1^\perp$  which is obtained together with either the Collins fragmentation function or a di-hadron fragmentation function. Examples of the expected uncertainties on these asymmetries are displayed in Fig. 2.15 where one can see that over a larger range of phase space very precise uncertainties can be obtained. Those will in turn enable the extraction of flavor-separated transversity and their first moments, the tensor charges. These tensor charges are of particular interest as they can relate to interactions outside the standard model. Lattice-QCD can model the tensor charges very well and any differences with the measurements would provide a hint for BSM physics.

Collins asymmetries can also be obtained from identified hadrons within jets, in which case the Collins fragmentation function is described as a function of the fractional hadron momentum  $z$

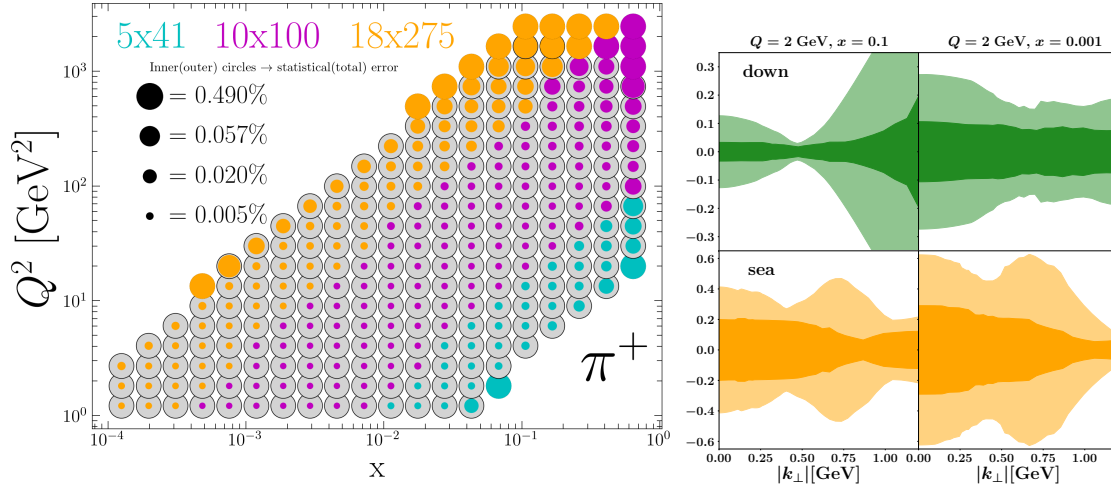


**Figure 2.14:** Left: Expected statistical and total uncertainty of un-polarized TMD PDFs for  $\pi^+$  in the  $Q^2 - x_B$  plane. The inner (colored) circle shows the statistical uncertainty, while the outer circle provides the total uncertainty for each  $Q^2 - x_B$  bin. The color shows the beam energy configuration which provides the highest statistics in a specific bin. Right panel: Expected uncertainties of valence down (green) and sea quark (orange) TMD PDFs at  $x = 0.1$  (left) and  $x = 0.001$  (right) as obtained based on the MAP24 [1] global TMD fit. The lighter shaded regions show the uncertainties based on existing data while the darker shaded regions show the expected uncertainties after including ePIC data.

and transverse momentum  $j_t$  relative to the jet momentum and its axis. Such measurements rely on excellent calorimetry and tracking resolution and the ability to accurately identify particles. Figure 2.10 illustrates projected statistical precision for Collins asymmetry measurements of charged  $\pi$ ,  $K$  and  $p$  in jets as a function of  $z$  integrated over  $5.0 < p_{T,jet} < 51.9$  GeV/c. In the actual measurements the hadron-in-jet Collins asymmetries will also be binned in  $x$  and  $Q^2$  since their main goal is the access to the quark transversity distributions and tensor charges. One advantage of jet related measurements over the pure SIDIS measurements is that the transverse momenta from distribution and fragmentation are not convoluted. They therefore provide additional information on transversity and can further help pinning it down together with the SIDIS Collins measurements and similar measurements using di-hadron fragmentation functions.

### 2.4.3.2 Imaging in Transverse Position Space

The correlations between parton momentum and spatial position, enabling a tomographic image of the nucleon, are encoded into the Generalized Parton Distributions (GPDs). As briefly introduced earlier in Section 2.4.3, GPDs can be extracted via measurements of exclusive reactions, e.g. the exclusive production of a real photon or of a meson, while the proton remains intact. Exclusivity requires all the final-state particles to be detected. The EIC's high luminosity and wide kinematic coverage make it an ideal venue for studying exclusive channels.

The exclusive production of a real photon, a process known as Deeply Virtual Compton Scattering (DVCS), is a benchmark process for probing GPDs. In this reaction, an electron scatters off a proton (or nucleus), emitting a high-energy photon while leaving the proton intact. The EIC will provide access to DVCS across a wide range of momentum transfer ( $t$ ), allowing for detailed stud-

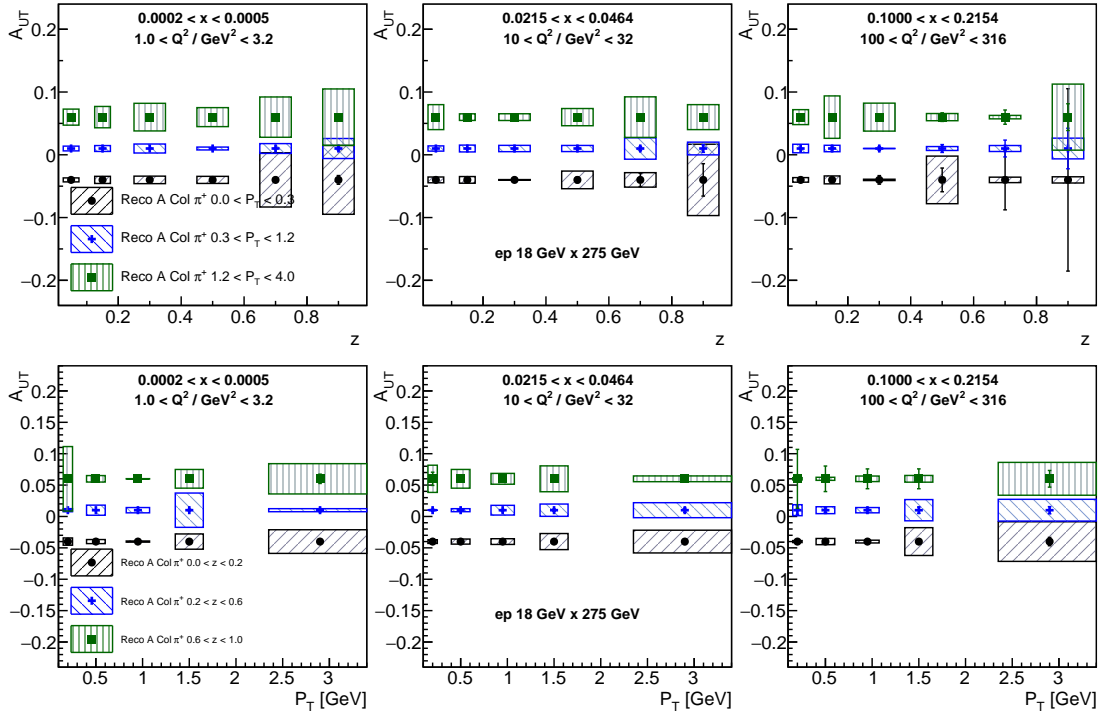


**Figure 2.15:** Top: Expected uncertainties in three example  $x$ - $Q^2$  bins for the Collins asymmetries for positive pions as a function of the momentum fraction  $z$  and in three bins of hadron transverse momentum relative to the virtual photon direction assuming a luminosity of  $10 \text{ fb}^{-1}$ . Bottom, the same but as a function of the hadron transverse momentum in bins of  $z$ .

ies of the spatial distribution of partons and their evolution with varying energy scales. Precision measurements at ePIC will also test QCD factorization and constrain theoretical models of GPDs, improving our understanding of the spin and angular momentum contributions of quarks and gluons to nucleon spin.

Exclusive Vector Meson Production involves the coherent production of mesons such as  $\rho$ ,  $\phi$ ,  $J/\psi$ , and  $Y$  in electron-proton or electron-nucleus collisions. At ePIC, measurements of vector meson production will probe gluon distributions at small Bjorken- $x$ , providing insight into gluon saturation effects and the emergence of collective phenomena in QCD. Heavy vector mesons like  $J/\psi$  are particularly sensitive to the gluon content of the nucleon, offering a window into the high-density regime of QCD.

DVCS events have been simulated using the EpIC Monte Carlo generator [20] with a minimum  $Q^2$  of  $1 \text{ GeV}^2$ . The analysis of such events provides a good test of a large number of subsystems within the ePIC detector, namely the scattered electron and final state photon are detected in either the central barrel or endcaps, and the scattered proton is detected in the far forward region within the B0 spectrometer or the Roman Pot detectors.

DVCS candidate events were identified by applying a series of cuts on the individual final state particles, as well as on the properties of the full reaction. The cuts applied were as follows:

- exactly 1 photon, scattered electron and scattered proton were reconstructed in the final state.
- the reconstructed electron and photon have momenta no more than 10% higher than the

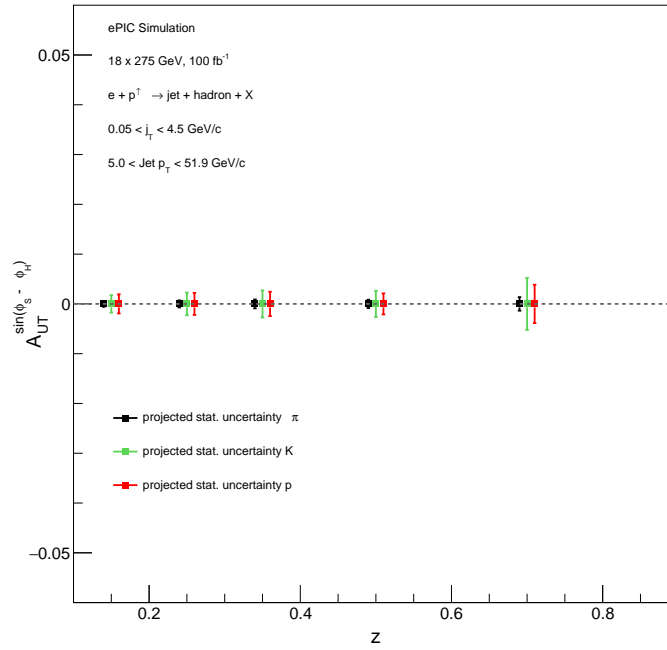


**Figure 2.16:** Projected statistical precision, indicated by vertical bars around data points, for measurements of Collins asymmetries of identified hadrons in jets as a function of hadron  $z$ . In case the vertical bars are invisible, they are smaller than the marker size.

corresponding beam momentum; for this study, that corresponds to a maximum of 11 GeV for scattered electrons and 110 GeV for scattered protons.

- track  $\theta$  cuts for the reconstructed proton (where  $\theta$  is defined as the angle from the positive  $z$ -axis to the track of interest) to ensure the track matches the acceptance of the detector expected. Tracks reconstructed in the Roman Pots are required to have  $\theta < 5.5$  mrad; tracks in the B0 spectrometer are required to have  $5.5 < \theta < 20$  mrad.
- a minimum  $Q^2$  of 1 GeV<sup>2</sup>, to match the conditions of the initially generated events.
- a maximum  $t$  for events with the proton detected in the Roman Pots of 0.3 GeV<sup>2</sup>.
- a maximum missing mass of the full final state,  $M_{\text{miss}}^2$  of 1 GeV<sup>2</sup>.

As mentioned, a key parameter on which the DVCS process depends is the Mandelstam variable  $t$  of the reaction. The generated and reconstructed distributions of  $t$ , calculated for events with full exclusivity (exactly one reconstructed electron, proton and photon), are shown in figure 2.17. As well as studying the underlying physics process, DVCS can be used to test the performance of the ePIC subdetectors. Figure 2.18 shows the angular resolution of the barrel calorimeters, calculated using the detected DVCS photon. Of particular note from figure 2.18 are the following points:

- the angular reconstruction of the barrel is, on the whole, very good. No more than 0.5% of all photons are reconstructed more than 5° from their generated track, and more than 75% are reconstructed to within 1°.
- the significant majority of the generated photons are detected in the electron endcap calorimeter, in the range  $2.8 < \theta < 3.1$  rad.

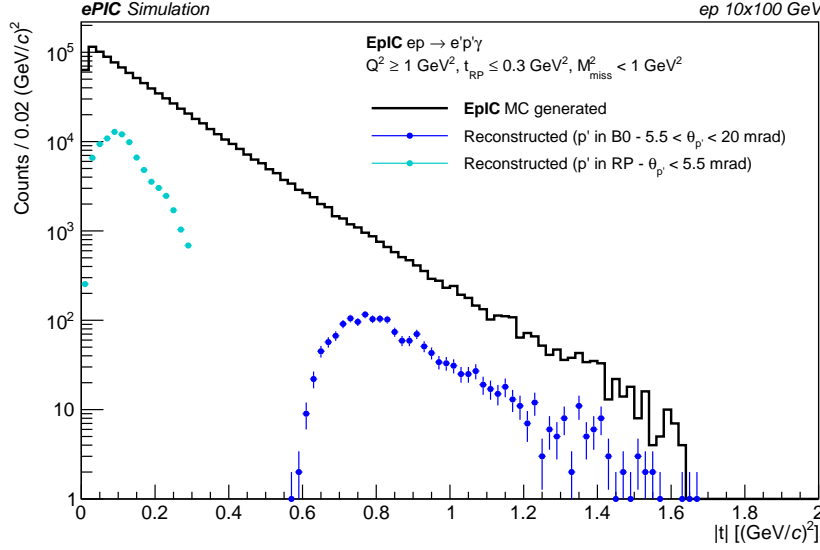


**Figure 2.17:** Generated and reconstructed  $t$ -distributions for fully-exclusive DVCS events.

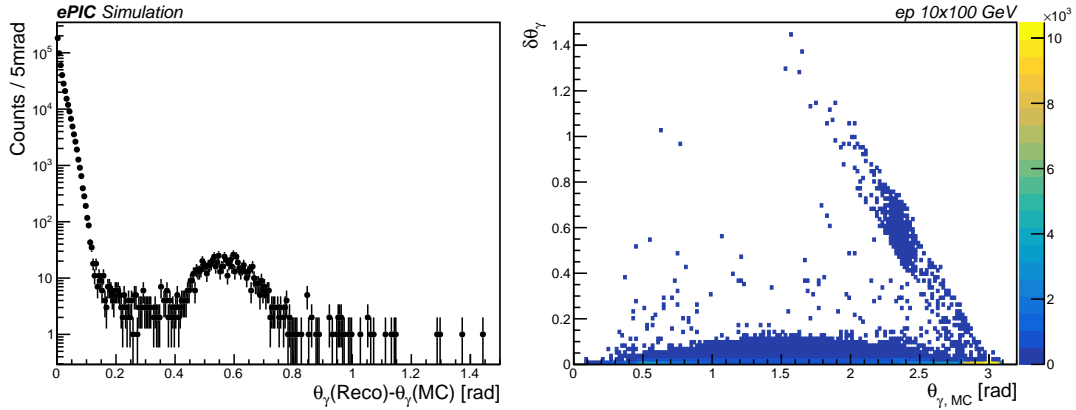


**Figure 2.18:** Reconstructed minus generated track  $\theta$  for all reconstructed DVCS photons (left), as well as as a function of the generated photon  $\theta$  (right). Note that the left plot is on a logarithmic scale.

Overall, based on the feasibility study, this measurement can be fully carried out by the ePIC detector. In particular, the study on DVCS is sensitive to the performances of both the far-forward detector system, especially the B0 and Roman Pot, as well as the Barrel Imaging Calorimeter, which are both discussed in more details in Chapter 8.

### 2.4.3.3 Upsilon production

The study of exclusive heavy quarkonia production is an excellent tool for investigating quantum chromodynamics (QCD) at the Electron-Ion Collider (EIC). Due to the heavy masses of both charm

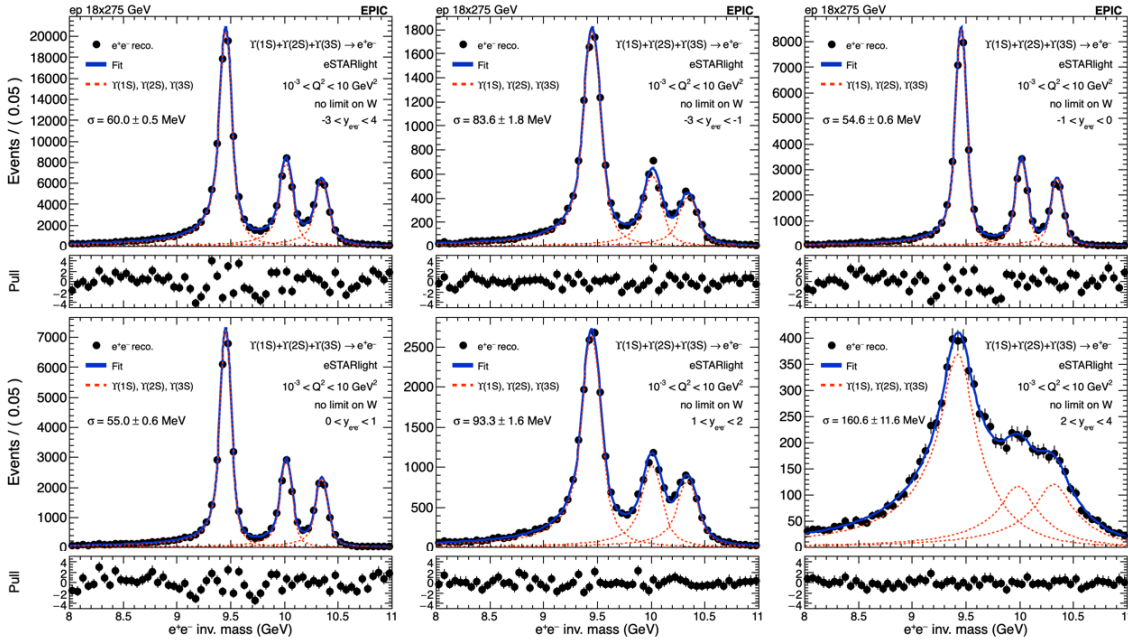


**Figure 2.19:** The reconstructed mass distribution of the  $Y$  three states in the electron channel from the electron-proton collisions at  $18 \times 275$  GeV, utilizing the tracker with realistic seeding. The top left plot shows the invariant mass distribution of the  $Y$  three states in the rapidity range from  $-3$  to  $4$ . The other plots display invariant mass distribution for specific rapidity intervals: (top middle)  $-3 < y < -1$ , (top right)  $-1 < y < 0$ , (bottom left)  $0 < y < 1$ , (bottom middle)  $1 < y < 2$ , and (bottom right)  $2 < y < 4$ . The resolution of the  $Y$  three states is indicated on each plot as  $\sigma$ .

and bottom quarks, which are significantly greater than  $\Lambda_{QCD}$ , studying heavy quarkonia enables QCD research in the perturbative regime, facilitating the exploration of gluon PDFs [21]. Numerous studies have employed ultraperipheral collisions (UPCs) to examine the properties of heavy quarkonia and their implications for QCD [22–25].

In lowest order perturbative QCD, the cross-section for exclusive heavy meson production is proportional to the square of the gluon density, at a  $Q^2 = (M_V/2)^2 + Q_{\gamma'}^2$ , while the Bjorken- $x$  depends on the photon energy; at low  $Q^2$ ,  $x = M_V/\gamma m_p \exp(y)$ , where  $\gamma$  is the Lorentz boost of the ion, and  $y$  is the final state rapidity. So, it serves as an important probe of gluons at low- $x$ , with the lowest  $x$  gluons being probed at large  $y$ . Wide  $y$  coverage is important to probe the lowest  $x$  values. The interest goes beyond just the cross-section;  $d\sigma/dt$  for coherent production is sensitive to the transverse distribution of gluons in the target, while incoherent production may be sensitive to nuclear fluctuations, including gluonic hotspots [26].

Among vector mesons, the  $Y$  is particularly attractive. At next-to-leading order, quarks also contribute to vector meson production, but the quark contribution to  $Y$  production is much smaller than for the  $J/\psi$  [27]. And, the theoretical uncertainties due to scale and other factors are much smaller for the  $Y$  than for the  $J/\psi$  [27, 28].

The  $Y$  states are notable as the heaviest vector mesons accessible at the EIC, allowing to probe a high intrinsic  $Q^2$ . The three different  $Y$  states are all composed mainly of  $b\bar{b}$ , but have three different wave functions; thus, by comparing production of the three states, it will be possible to



reduce the systematic uncertainties on the gluon distribution extraction.

The production of the three  $\Upsilon$  states in the electron channel was simulated in electron-proton collisions at a center-of-mass energy of  $18 \times 275$  GeV. The Monte Carlo samples were generated using eSTARlight, covering a range of  $10^{-3} < Q^2 < 10$  GeV<sup>2</sup>, with no restrictions on  $W$ . The  $\Upsilon$  states were produced according to their relative ratio based on [29] and then combined. The reconstruction of these Monte Carlo samples was simulated using EICRECON version 1.15.0. The figure showcases the momentum resolution of the ePIC tracking system in terms of separating the three  $\Upsilon$  states, which is presented across various rapidity regions for the reconstructed  $\Upsilon$  states. The top left plot in Figure 2.19 represents the resolution for all rapidity regions combined, while the other plots present results for specific intervals:  $-3 < y < -1$ ,  $-1 < y < 0$ ,  $0 < y < 1$ ,  $1 < y < 2$ , and  $2 < y < 4$ . In the forward region, corresponding to  $2 < y < 4$ , a degradation in resolution was observed. However, in a similar study done by the muon channel (not shown), it is found to have an improvement on the resolution of approximately 1 to 8 % due to reduced final state radiation. Additionally, these studies help assess detector performance, particularly the momentum resolution of the tracking system.

## 2.4.4 Properties of Nuclear Matter

### 2.4.4.1 Gluon Saturation

One of the three central questions highlighted in the National Academy of Science report on Electron-Ion Collider (EIC) science is to understand the properties of high parton density matter and the onset of gluon saturation. A critical observable for understanding the dynamics of gluonic matter is the spatial distribution of gluons within nuclei, particularly in systems likely to be in the saturation regime at high energy.

To achieve gluon imaging of nuclei, exclusive and diffractive vector meson electroproduction involving electron-heavy nuclei collisions has been proposed [10]. In Fig. 2.20 (left), the differential cross section for  $\phi$  meson production is shown for electron-gold collisions at an energy configuration of  $18 \times 110$  GeV. The input is derived from the Monte Carlo model Sartre, and the reconstructed distribution is obtained after a full ePIC simulation based on the version from August 2024. The reconstruction is achieved by detecting a scattered electron in the backward calorimeter and reconstructing the two kaons from  $\phi$  decay using tracking data.

As shown, the diffractive structure is barely visible in the reconstructed data due to insufficient momentum transfer ( $t$ ) resolution. The main limitation stems from the electron reconstruction, where the momentum resolution is hampered by the small scattering angle relative to the electron beamline. The magnetic field in this region is insufficient to provide the necessary lever arm for achieving the required momentum resolution. More specifically, Fig. 2.20 (right) presents the momentum transfer  $t$  reconstruction resolution as a function of true  $t$ . Efforts to improve the resolution are ongoing.

On the other hand, the incoherent vector meson production needs to be vetoed in the event in order to suppress its contamination to the coherent process. This is enabled by the far-forward detector system (B0, Roman Pot, Off-Momentum Detector, zero-degree calorimeter). By vetoing signals in the forward detectors one can reject up to two orders of magnitude of the incoherent background. Table 2.2 summarizes the fraction of signal and background events after each veto.

The  $t$  spectra of coherent and incoherent (before veto) are shown in Fig. 2.21 left, and the residue distribution of incoherent production events (that pass event selection) are shown in Fig. 2.21 right.

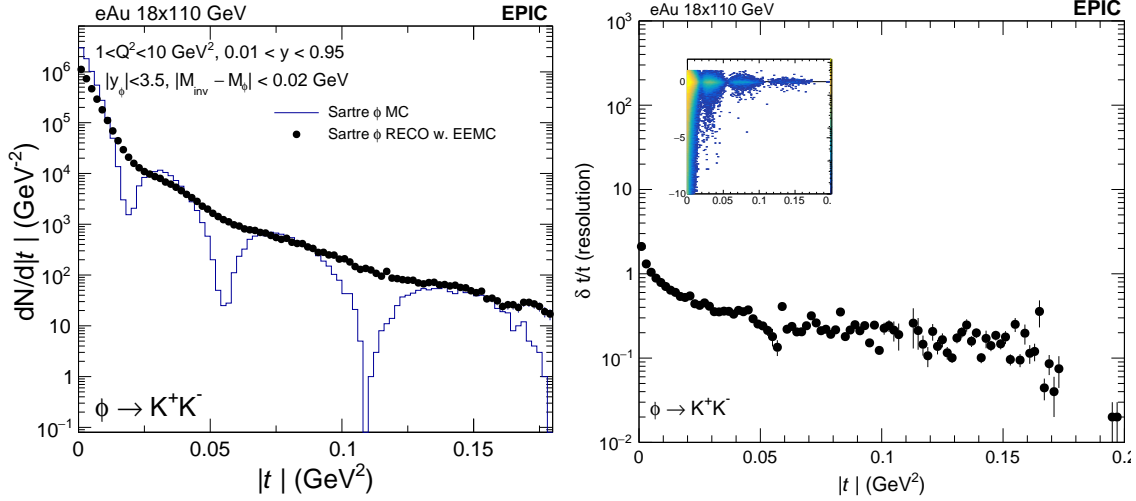


**Figure 2.20:** Left: differential distribution of the momentum transfer  $|t|$  of coherent  $\phi$  meson electroproduction in electron-gold collisions with 18x110 GeV. The Monte Carlo model is provided by Sartre and the reconstructed distribution is obtained from full ePIC simulation with the official August 2024 simulation campaign. Right: the momentum transfer  $t$  reconstruction resolution as a function of the true  $t$ .

	Signal efficiency	Background efficiency
3 tracks	0.97383	0.914885
$J/\psi$ mass window	0.898815	0.827045
Veto signals in B0	0.898805	0.429656
Veto signals in OMD	0.898805	0.29286
Veto signals in ZDC	0.898795	0.013776

**Table 2.2:** Event composition in incoherent  $J/\psi$  production before and after full event selection

Therefore, the vetoing power is sufficient to suppress the incoherent production down to a level below the first diffractive minimum but not quite for the second and third minima.

#### 2.4.4.2 Nuclear Modifications of Parton Distribution Functions

[A study will be performed later and added before the final version of the TDR.]

#### 2.4.4.3 Passage of Color Charge Through Cold QCD Matter

The  $e+A$  collisions at the EIC also provide a unique opportunity to study how the presence of a nuclear environment affects the evolution of colored objects, from which nuclear properties can be extracted.



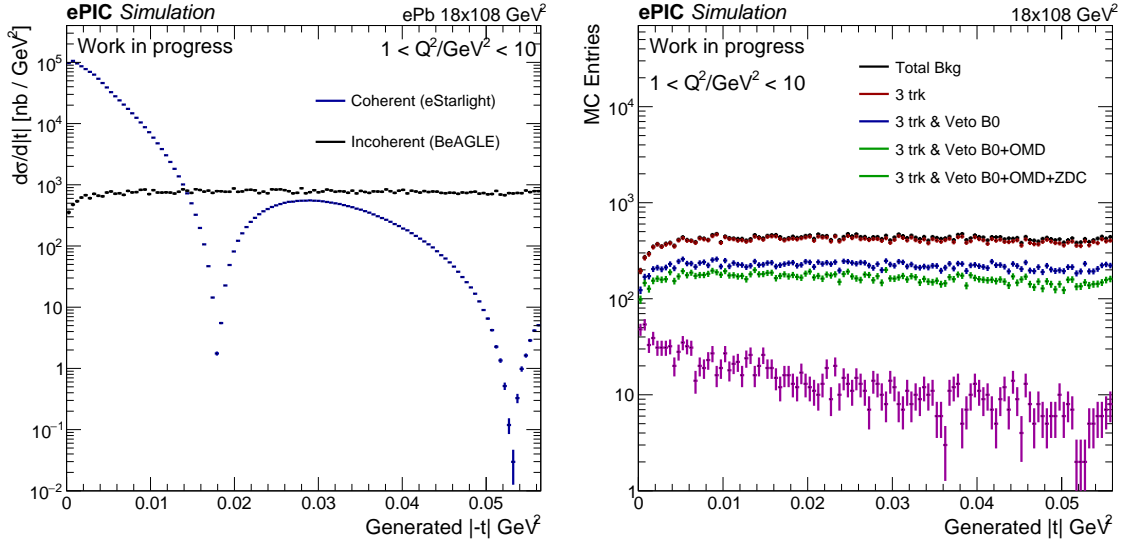


**Figure 2.21:** Left: Differential cross-section of momentum transfer  $t$  distribution for coherent (blue) and incoherent (black) exclusive  $J/\psi$  production in  $ePb$  collisions. Right: Differential measurement of  $t$  and the residue distributions after each veto based on the far-forward detector system.

Previous measurements of charged hadron multiplicities in semi-inclusive DIS off nuclei by the HERMES collaboration have revealed a clear suppression compared to those off the deuteron target [?]. However, the underlying physics mechanism causing such a suppression is still under debate with two primary candidates: parton energy loss before hadronization vs. hadron absorption after hadronization in cold QCD matter, as both of them can describe the HERMES measurements. At the EIC, charm quarks will be copiously produced, making it possible to measure  $D^0$  mesons with high precision. Thanks to its large mass, the parton energy loss picture will lead to a suppression of  $D^0$  mesons at high  $z$  and an enhancement at low  $z$  in  $e+A$  collisions with respect to that in  $e+p$  collisions, while the hadron absorption scenario should result in a suppression at all  $z$  [?]. These two distinct behaviors make  $D^0$  meson measurements at the EIC a powerful tool for identifying the underlying mechanism and studying properties of cold QCD matter. Due to its short proper decay length of  $\sim 123 \mu\text{m}$ , a high-precision tracking device with great pointing resolution is needed to separate the  $D^0$  decay vertex from the collision vertex. To reconstruct the  $D^0$  meson through its exclusive hadronic decay channel of  $D^0 \rightarrow \pi^+ + K^-$ , particle identification with high purity and efficiency is also required. As detailed in Table ??, the ePIC detector is well suited to make such measurements thanks to its excellent pointing resolution, powerful particle identification capability and large acceptance. Performance studies of topological reconstruction of  $D^0$  mesons are carried out in  $10 \times 100$  GeV  $e+p$  and  $e+Au$  collisions with a minimum  $Q^2$  of 1 GeV<sup>2</sup>. Identified  $\pi$  and  $K$  tracks with opposite electric charges are paired, and topological variables are calculated using the helix swimming method [?] and used to suppress combinatorial background pairs. Resulting invariant mass distributions of opposite-sign  $\pi + K$  pairs in different pair rapidity intervals are shown in Fig. 2.22. The black squares denote distributions for all pairs, where the  $D^0$  signal is overwhelmed by background, while red circles correspond to the case after applying topological selections and the signal-to-background ratios are greatly enhanced. As expected, the best signal significance is achieved at mid-rapidity ( $-1 < y < 1$ ), where the track pointing resolution and particle identification are the best. Based on these studies, the projected statistical errors on the yield ratios of  $D^0$  mesons, also referred to as  $R_{eA}$ , are shown in Fig. 2.23 as a function of  $D^0$   $p_T$ . At

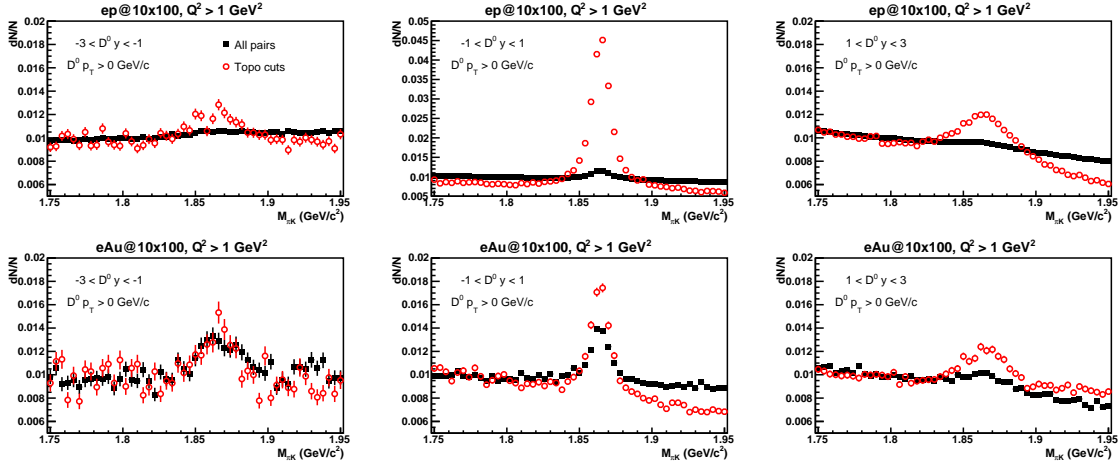


**Figure 2.22:** Invariant mass distributions of  $\pi + K$  pairs with (red circles) and without (black squares) topological selections in  $10 \times 100$  GeV  $e+p$  (top) and  $e+Au$  (bottom) collisions with a minimum  $Q^2$  of  $1 \text{ GeV}^2$ . Different panels from left to right correspond to different  $D^0$  rapidity intervals:  $-3 < y < -1$  (left),  $-1 < y < 1$  (middle) and  $1 < y < 3$  (right).

1039 mid and forward rapidities, a precision of a few percent can be achieved, while in the backward  
 1040 rapidity, the error bars are substantially larger. These results demonstrate that the high precision

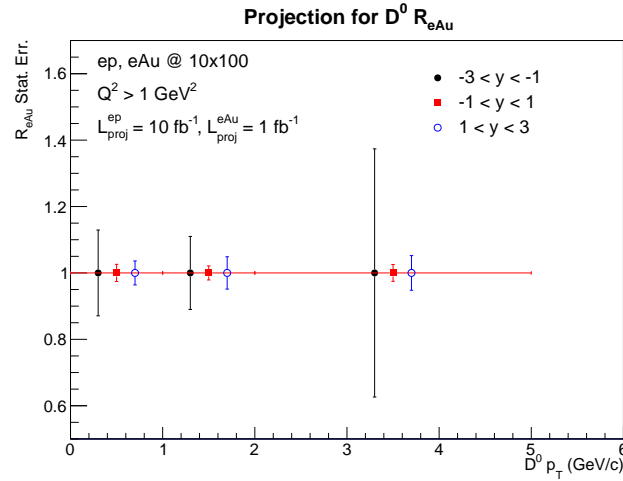


**Figure 2.23:** Projection of relative statistical errors on  $D^0$  yield ratios between  $10 \times 100$  GeV  $e+Au$  and  $e+p$  collisions as a function of  $D^0 p_T$  for three different  $D^0$  rapidity intervals.

1040 measurements of  $D^0$  mesons in both  $e+p$  and  $e+Au$  collisions at EIC will provide quantitatively  
 1041 new insights to the propagation of colored objects in cold QCD matter.  
 1042

### 1043 2.4.5 Additional physics opportunities

1044 The combination of the high versatility of the EIC (polarized beams, high luminosity, and variable  
 1045 center of mass energy) with the detector capabilities of ePIC allow for measurements beyond the  
 1046 highlighted by the NAS report. In particular two types of measurements show great promise:  
 1047 determination of new  $\gamma - Z$  interference structure functions, and a probe of charged lepton flavor  
 1048 violation. Both of these measurements will require at least  $100 \text{ fb}^{-1}$  of data in order to reach a  
 1049 meaningful result.

1050 As initially reported by Zhao and collaborators [30] single spin parity violating asymmetries can be  
 1051 used to determine  $F_1^{\gamma Z}$  and  $F_3^{\gamma Z}$  when considering the polarization of the electron beam, and  $g_1^{\gamma Z}$   
 1052 and  $g_5^{\gamma Z}$  when considering the polarization of the proton beam. Depending on the available po-  
 1053 larized beams these structure functions can be extracted from electron-proton or electron-deuteron  
 1054 collisions. These measurements rely on inclusive DIS data that will be collected for the core physics  
 1055 of the EIC and can be obtained without additional requirements on the accelerator or detector. The  
 1056 same data can be included in global analysis frameworks to extract the weak mixing angle in a  
 1057 region right under the Z-pole, albeit with large statistical uncertainties.

1058 Charged lepton flavor violation can be probed at the EIC through measurements of tau leptons  
 1059 in the final state. First reported in the EIC White paper [10] a measurement  $ep \rightarrow \tau + X$  has the  
 1060 potential to reach sensitivities beyond what is expected to be measured at other facilities in the  
 1061 next decade. This can be achieved using only the three-pion decay channel of the tau, due to its  
 1062 unique detector signature in spite of the fact that it represents only 10% of the tau decay branching  
 1063 ratio. Recent analyses have shown that the single muon decay channel (with a branching ratio of  
 1064 17%) can provide additional constraining power due the significantly suppressed standard model  
 1065 background for transverse momenta larger than 10 GeV. Improvements beyond what has been  
 1066 currently studied with ePIC (see 2.3.5) will be needed in order to fully take advantage of this decay  
 1067 channel.

1068 Additional measurements are being proposed, but most would require upgrades to the base ePIC  
 1069 detector and will not be discussed here.



Chapter 8

Experimental Systems

8.1 Experimental Equipment Requirements Summary

The YR table (Fig. 8.1) is being reviewed and an updated table with accompanying text will be included in the draft Version1.

Table 10.6: This matrix summarizes the high level requirements for the detector performance. The interactive version of this matrix can be obtained through the Yellow Report Physics Working Group WIKI page ([https://wiki.bnl.gov/eicug/index.php/Yellow\\_Report\\_Physics\\_Common](https://wiki.bnl.gov/eicug/index.php/Yellow_Report_Physics_Common)).

Pseudo- $\eta$	Nomenclature		Tracking			Electrons and Photons				n/p/p		HCAL		Muons
			Resolution	Allowed	minimum pT	SI Vertex	Resolution $\sigma_E$	PID	min E	p-range	Separat	Resolution $\sigma_E$	Energy	
6.9 to 3.8		low-Q2 tagger	$\sigma_{\text{E}} < 1.5\%$ ; 10-6											
5.0 to 4.5			$< Q^2 < 10\text{-}2\text{ GeV}^2$		300 MeV pions									
4.5 to 4.0			Instrumentation to separate charged particles from photons		300 MeV pions		25% $\sqrt{E}$ (+1-3%)		50 MeV					
4.0 to 3.5			$\downarrow$ p/A	Auxiliary Det					50 MeV			-50% $\sqrt{E} \pm 6\%$		
3.5 to 3.0	Central Detector	Backward Detector	$\sigma_{\text{pT}} \text{pT} = 0.1\%$ 0.5%	$< 100\text{ MeV pions, } 135\text{ MeV kaons}$	$\sigma_{\text{xy}} = 30\text{ }\mu\text{m} + 40\text{ }\mu\text{m}$	TI suppression up to 1:1E-4	50 MeV	$\leq 7\text{ GeV/c}$	$\geq 3\sigma$	-45% $\sqrt{E} \pm 6\%$	$\sim 600\text{ MeV}$	muons useful for bkg. improve resolution		
$\sigma_{\text{pT}} \text{pT} = 0.05\%$ 0.6%			$\sigma_{\text{xy}} = 20\text{ }\mu\text{m}, \sigma_{\text{pT}} = 30\text{ }\mu\text{m} + 20\text{ }\mu\text{m}$		50 MeV									
$\sigma_{\text{pT}} \text{pT} = 0.05\%$ 0.6%			$\sigma_{\text{xy}} = 20\text{ }\mu\text{m}, \sigma_{\text{pT}} = 30\text{ }\mu\text{m} + 20\text{ }\mu\text{m}$		50 MeV									
			$\sigma_{\text{xy}} = 20\text{ }\mu\text{m}, \sigma_{\text{pT}} = 30\text{ }\mu\text{m} + 20\text{ }\mu\text{m}$		50 MeV									
			$\sigma_{\text{xy}} = 20\text{ }\mu\text{m}, \sigma_{\text{pT}} = 30\text{ }\mu\text{m} + 20\text{ }\mu\text{m}$		50 MeV									
			$\sigma_{\text{xy}} = 20\text{ }\mu\text{m}, \sigma_{\text{pT}} = 30\text{ }\mu\text{m} + 20\text{ }\mu\text{m}$		50 MeV									
			$\sigma_{\text{xy}} = 20\text{ }\mu\text{m}, \sigma_{\text{pT}} = 30\text{ }\mu\text{m} + 20\text{ }\mu\text{m}$		50 MeV									
			$\sigma_{\text{xy}} = 20\text{ }\mu\text{m}, \sigma_{\text{pT}} = 30\text{ }\mu\text{m} + 20\text{ }\mu\text{m}$		50 MeV									
			$\sigma_{\text{xy}} = 20\text{ }\mu\text{m}, \sigma_{\text{pT}} = 30\text{ }\mu\text{m} + 20\text{ }\mu\text{m}$		50 MeV									
			$\sigma_{\text{xy}} = 20\text{ }\mu\text{m}, \sigma_{\text{pT}} = 30\text{ }\mu\text{m} + 20\text{ }\mu\text{m}$		50 MeV									
		$\sigma_{\text{xy}} = 20\text{ }\mu\text{m}, \sigma_{\text{pT}} = 30\text{ }\mu\text{m} + 20\text{ }\mu\text{m}$	50 MeV											
3.0 to 2.5		Forward Detectors	$\sigma_{\text{pT}} \text{pT} = 0.05\%$ 1.0%		$\sigma_{\text{xy}} = 30\text{ }\mu\text{m} + 40\text{ }\mu\text{m}$		50 MeV	$\sim 10\text{ GeV/c}$	50 MeV					
2.5 to 2.0			$\sigma_{\text{pT}} \text{pT} = 0.1\%$ 2.0%		$\sigma_{\text{xy}} = 30\text{ }\mu\text{m} + 40\text{ }\mu\text{m}$		50 MeV		50 MeV					
2.0 to 1.5			$\sigma_{\text{pT}} \text{pT} = 0.1\%$ 2.0%		$\sigma_{\text{xy}} = 30\text{ }\mu\text{m} + 40\text{ }\mu\text{m}$		50 MeV		50 MeV					
1.5 to 1.0			$\sigma_{\text{pT}} \text{pT} = 0.1\%$ 2.0%		$\sigma_{\text{xy}} = 30\text{ }\mu\text{m} + 40\text{ }\mu\text{m}$		50 MeV		50 MeV					
1.0 to 0.5	$\sigma_{\text{pT}} \text{pT} = 0.1\%$ 2.0%		$\sigma_{\text{xy}} = 30\text{ }\mu\text{m} + 40\text{ }\mu\text{m}$	50 MeV	50 MeV									
0.5 to 0.0	Auxiliary Detectors	Instrumentation to separate charged particles from photons	Tracking capabilities are desirable for forward tagging	300 MeV pions	$\sigma_{\text{xy}} = 30\text{ }\mu\text{m} + 40\text{ }\mu\text{m}$	$\sigma_{\text{xy}} = 30\text{ }\mu\text{m} + 40\text{ }\mu\text{m}$	(10-12)% $\sqrt{E}$ (+1-3%)	$< 3\text{ cm granularly}$	50 MeV	$\sim 5\text{ GeV/c}$	$\sim 35\% \sqrt{E}$			
3.5 to 4.0														
4.0 to 4.5														
4.5 to 5.0														
$> 6.2$														

## 8.2 General Detector Considerations and Operations Challenges

### 8.2.1 General Design Considerations

This section will discuss the detector challenges with cross-reference to the appropriate sections. The Sec.s to refer to are related to machine parameters (not in chapter 8), 8.1 “Experimental Equipment requirement Summary”, 8.2.2 “Background and Rates” and 8.2.3 “Radiation Level”. At present, all these sections are not available. Therefore, for Version0, a mere list of topics that will be covered is provided.

Discussion of challenges related to:

- Physics requirements (ref. to Sec. 8.1);
- Beams rates, polarization, luminosities (ref. to Sec.s in the machine chapters);
- Integration with the machine and hermeticity (ref. to Sec.s in the machine chapters, ref. to Sec. 8.1);
- Rates and multiplicity (ref. to Sec.c in the machine chapters, to Sec. 8.2.2);
- Radiation hardness (Ref. to Sec. 8.2.3).

### 8.2.2 Backgrounds and Rates

Different to hadron-hadron colliders the The combination of the relatively low signal rate of the electron - hadron collisions and the requirement for stringent systematic control in deep inelastic scattering measurements calls for low beam backgrounds and detector noise. There are several backgrounds sources from the two beams:

- Hadron beam
  - Background from losses during injection: This background does not impact the data taking, but adds to the overall radiation loss in the detector..
  - Hadron beam scattering with the residual gas molecules : The particles are produced like in a fixed target scattering in a forward cone in the hadron beam direction.
- Electron beam:
  - Beam-gas scattering through Coulomb and Bremsstrahlung (Bethe-Heitler) processes: Elastic and inelastic beam particle scatterings on residual gas molecules and the hadron beam
  - Touschek effect: Incoherent scattering of the particles in the same beam bunch.
  - Beam bunch replacement: The electron bunches get replaced at full energy with a frequency of 1 Hz to keep the average polarization at 0.7. This can lead to background due to the beam de-excitation, if the bunches are replaced.

All these backgrounds can be mitigated through the electron and hadron beam collimation system, but not if the scattering occurs directly at IR-6. For the scattering with the residual gas molecules the vacuum level in the extended interaction region is absolutely critical.

Figure 8.2 shows the vacuum level at IR-6 for different integrated electron current. The different integrated electron currents result in higher or lower vacuum levels as result of the vacuum bake-out, which is linear dependent to the integrated electron current.

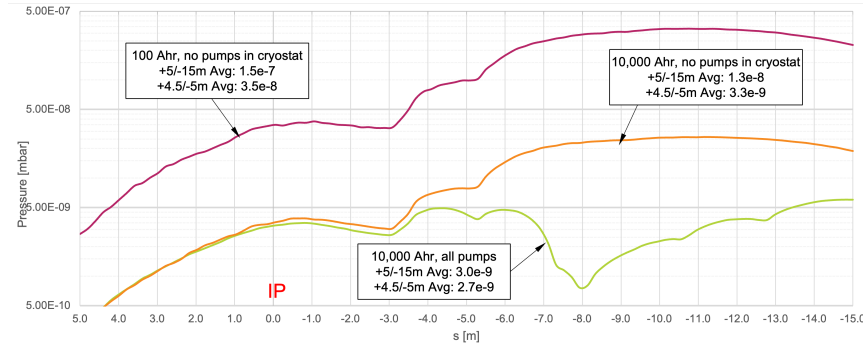


**Figure 8.2:** Vacuum level at IP6 for three different integrated electron current assumed for the backout.

### 8.2.3 Radiation Level

Radiation levels for ePIC are detailed on the ePIC Wiki page for radiation doses [31], but relevant details will be discussed here.

#### 8.2.3.1 Doses and fluences from e+p minimum-bias events

For all plots shown below, 1M minimum-bias PYTHIA6 e+p events (10 GeV electrons colliding with 275 GeV protons) were used, since that represents the largest potential luminosity (event rate) that the EIC will produce.

The radiation doses for ePIC are presently calculated using the Starsim framework for the STAR experiment, which uses a combination of GEANT3 [32] for particle transport and simulation of secondary particle production, and connects to both GCALOR and FLUKA for hadronic transport, especially important for calculation of fluences from non-ionizing energy loss (NIEL). NIEL fluences are cumulative in their impacts to silicon devices, and must be understood early in an experimental design.

Figure 8.3 shows the total energy deposit per  $\text{fb}^{-1}$  throughout the main ePIC detector. This is to verify the correct inclusion of the ePIC geometry into the Starsim framework, and enables rapid inspection of areas of ePIC where significant amounts of energy are deposited. It is clear that areas nearest to the outgoing hadron beam have the highest amounts of deposited energy from minimum-bias events.

Figure 8.4 shows the total ionizing dose per  $\text{fb}^{-1}$ , and per  $2\text{cm} \times 2\text{cm} \times 1\text{cm}$  bin (or voxel) throughout the main ePIC detector. The radiation dose has been calculated such that the dose per voxel is scaled by the GEANT step length and normalized to make the doses in a particular (x, y, z) location invariant to changing bin sizes. In general, the doses around the ePIC main detector from minimum-bias events are modest, and only peak at  $1\text{ kRad per fb}^{-1}$  in the regions at the outgoing hadron beam pipe, and on the inner portion of the forward MPGD disks. There is also a significant peak of radiation dose ( $\sim 1\text{ kRad per fb}^{-1}$ ) in the PbWO4 calorimeter inside the B0 magnet.

For most of ePIC, total ionizing dose will not be the primary concern for radiation damage to detector components. In addition to total ionizing dose, 1 MeV neutron equivalent (MEQ) fluences are a concern for potential cumulative damage to silicon detectors, especially silicon photo multipliers, given that dark currents can notably increase with accumulation of neutron fluences, especially as

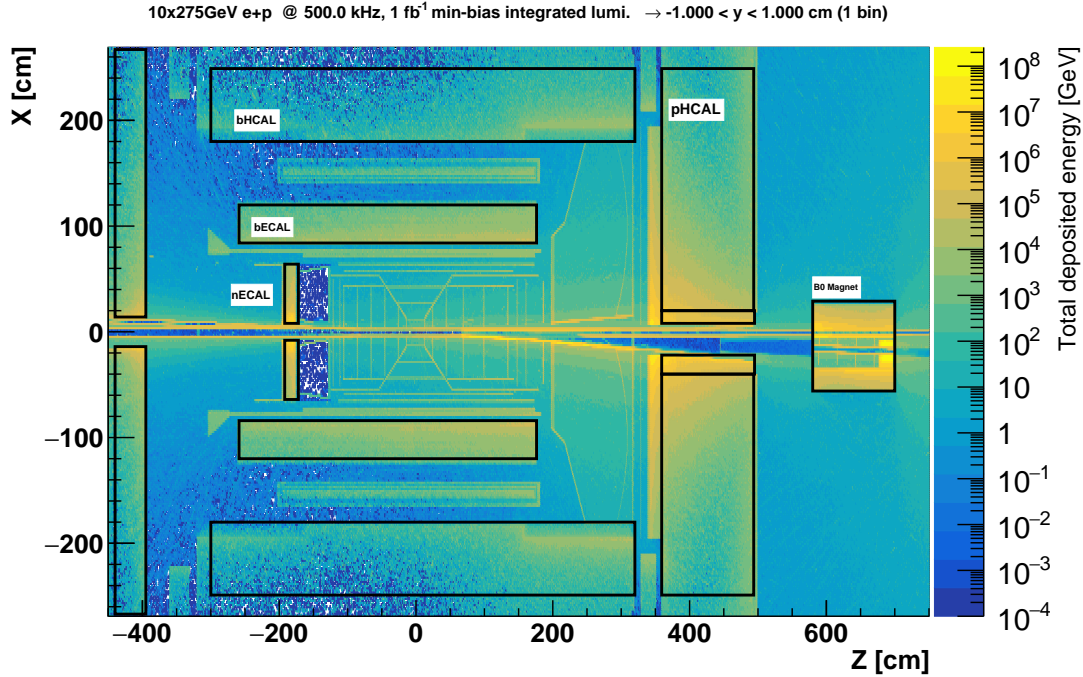


**Figure 8.3:** This figure shows the total energy deposited in 2cm x 2cm x 1cm bins spanning the full size of the ePIC central detector from minimum-bias e+p events generated in PYTHIA6 for 10 GeV electrons colliding with 275 GeV protons. This energy combination represents the highest potential luminosity for the EIC. The results are shown as energy deposits per fb<sup>-1</sup>.

they begin to exceed 10<sup>11</sup>cm<sup>-2</sup> 1 MEQ fluence. The 1 MEQ fluences are summarized for the central detector in Fig. 8.5.

The last important radiation type to consider is high energy proton and neutron ( $E > 20$  MeV) fluxes which can lead to acute issues with detector electronics in the form of single event upsets (SEU). These fluxes are shown for the ePIC central detector in Fig. 8.6.

In general, minimum-bias e+p events do not pose a major threat to most ePIC subsystems in terms of radiation damage, but there are areas of concern, especially for neutron fluences in the hadron-going calorimetry, and near the beam pipe.

### 8.2.3.2 Doses and fluences from hadron beam+gas events

For all plots shown below, 100k hadron beam+gas events with a 275 GeV proton beam energy (impinging on H<sub>2</sub> molecules at rest) are used.

Figure 8.7 shows the total energy deposit per fb<sup>-1</sup> throughout the main ePIC detector from hadron beam+gas events. The energy deposits from hadron beam+gas events look different from what we see in minimum-bias events because the hadron beam+gas are hadronic collisions, and also because the events are distributed along the entire beamline, up- and down-stream of the ePIC detector. This allows secondaries from many meters away from ePIC in the incoming hadron direction to



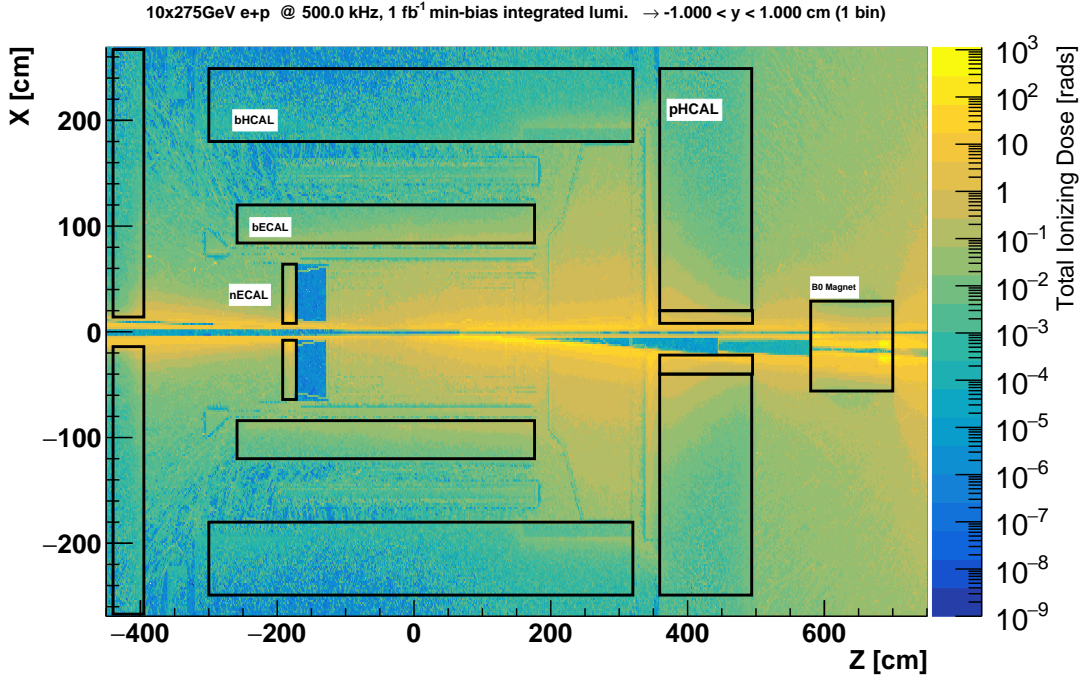


**Figure 8.4:** Total ionizing dose per fb<sup>-1</sup> for the central region of ePIC detector from minimum-bias e+p events.

impinge upon the ePIC detector, where minimum-bias collisions would not produce secondaries from those locations.

Figure 8.8 shows the total ionizing dose per fb<sup>-1</sup>, and per 2cm x 2cm x 1cm bin (or voxel) throughout the main ePIC detector. In general, the ionizing doses around the ePIC main detector from hadron beam+gas events are even more modest than those from minimum-boas events, and only peak at <100 Rad per fb<sup>-1</sup> in the regions nearest the beamline.

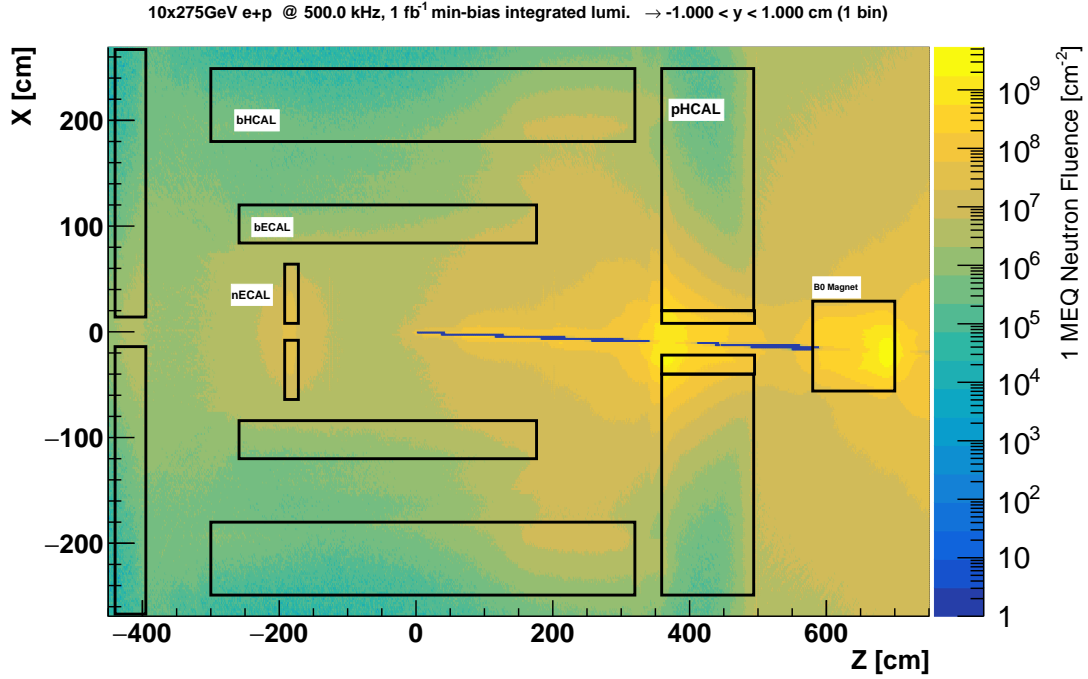
For most of ePIC, total ionizing dose will not be the primary concern for radiation damage to detector components. In addition to total ionizing dose, 1 MeV neutron equivalent (MEQ) fluences are a concern for potential cumulative damage to silicon detectors, especially silicon photo multipliers, given that dark currents can notably increase with accumulation of neutron fluences, especially as they begin to exceed 10<sup>11</sup>cm<sup>-2</sup> 1 MEQ fluence. The 1 MEQ fluences are summarized for the central detector in Fig. 8.9.

High energy proton and neutron ( $E > 20$  MeV) fluxes are also considered, as before. These fluxes from hadron beam+gas events are shown for the ePIC central detector in Fig. 8.10.

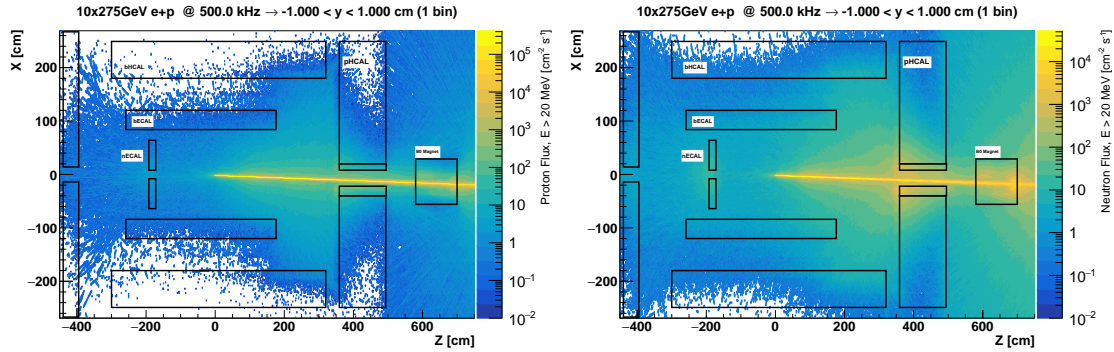
### 8.2.3.3 Doses and fluences from electron beam+gas events

For all plots shown below, 300k electron beam+gas events with a 10 GeV electron beam energy (impinging on H2 molecules at rest) are used.

Figure 8.11 shows the total energy deposit per fb<sup>-1</sup> throughout the main ePIC detector for electron

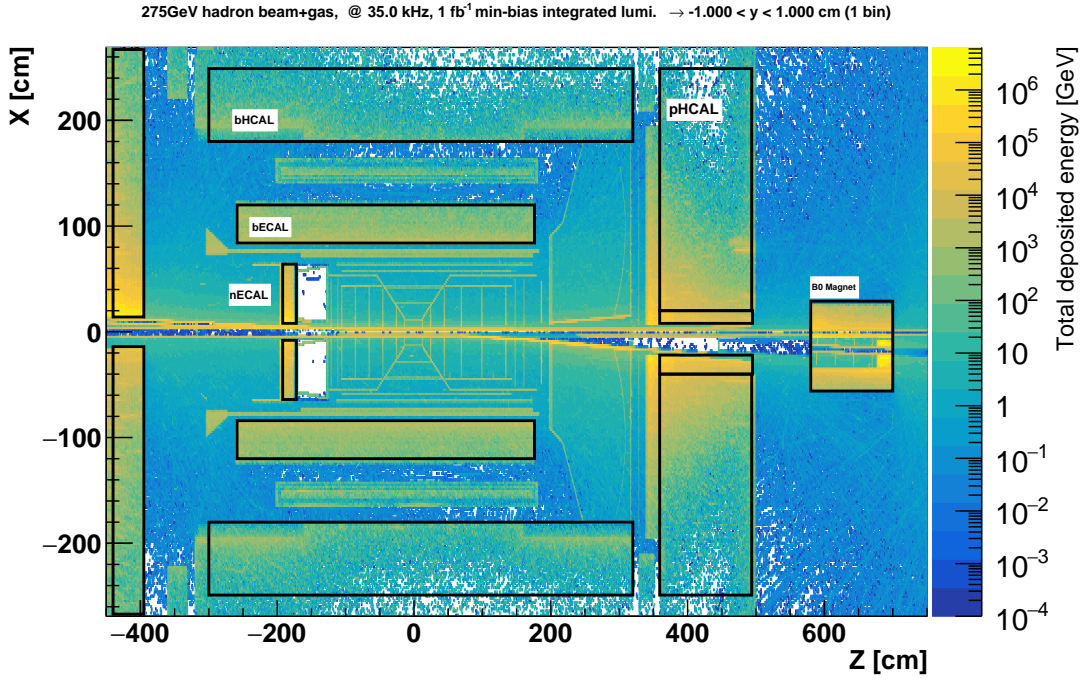


**Figure 8.5:** 1 MeV neutron equivalent fluences for the central ePIC detector from minimum-bias e+p events. Peak regions of MEQ fluence are seen near the beam pipe, and within the hadronic calorimeters, where the inclusion of dense absorber materials (e.g. iron) provides ample scattering centers to produce hadronic showers which can include high numbers of low-energy neutrons to provide peak MEQ fluences.



**Figure 8.6:** Fluxes of protons (left) and neutrons (right) with kinetic energy  $> 20$  MeV from minimum-bias e+p events. These fluxes are important to understand areas where detector electronics could often experience SEUs, and require intervention (e.g. resetting).

1177 beam+gas events. The energy is deposited asymmetrically in the ePIC detector due to the fact that  
 1178 beam+gas events produced upstream of ePIC (before the B0 magnet) can produce an off-energy  
 1179 electron which will then enter the B0 magnet and be bent off-axis into one side of the ePIC detector.  
 1180 This, combined with a very high rate for the electron beam+gas creates a narrow collimated beam  
 1181 of electrons with go through ePIC at angle, producing a high ionizing dose along the way.



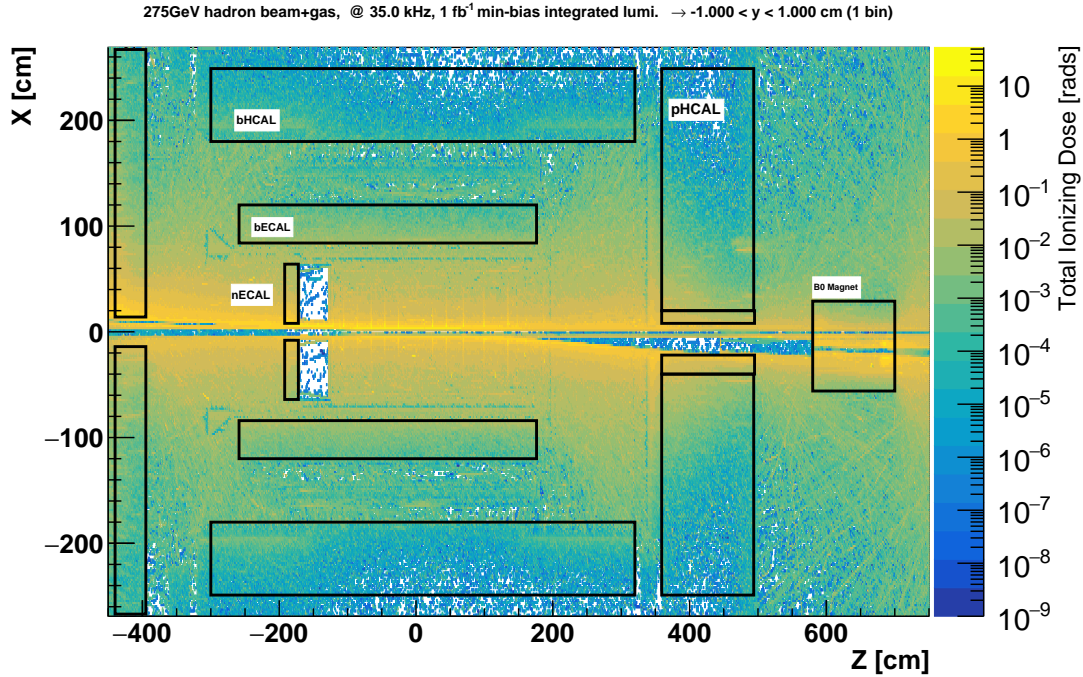
**Figure 8.7:** This figure shows the total energy deposited in 2cm x 2cm x 1cm bins spanning the full size of the ePIC central detector from hadron beam+gas events with 275 GeV protons. The results are shown as energy deposits per fb<sup>-1</sup>.

Figure 8.12 shows the total ionizing dose per fb<sup>-1</sup>, and per 2cm x 2cm x 1cm bin (or voxel) throughout the main ePIC detector from electron beam+gas events. As seen with the energy deposits, the ionizing doses are not deposited symmetrically in ePIC, and some hot spots are seen, ranging between 1 and 10 kRad per fb<sup>-1</sup> in the tracking system, and in a small portion of the backward EMCAL.

Different from the other radiation sources, the total ionizing dose from the electron beam+gas events have the potential to provide a very significant amount of ionizing dose to a broader region of ePIC. In the hottest regions of the detector, doses from 1 to 10 kRad per fb<sup>-1</sup> are possible.

These results are only a subset of what has been studied, and many more details are available on the Wiki page [31]. These radiation studies need to be repeated as the machine develops, and when the ePIC geometry changed. Even minor changes to the geometry of the detector can potentially have a large impact on the doses and fluences in sensitive areas of ePIC. Work is underway to import these calculations into the ePIC simulation framework to make it easier to track changes with the ePIC geometry.





**Figure 8.8:** Total ionizing dose from hadron beam+gas events per fb<sup>-1</sup> for the central region of ePIC detector.

## 8.3 The ePIC Detector

### 8.3.1 Introduction

**The Context** The development of the EIC science and the experimental equipment required to successfully implement the science as documented in the NSAC and NAS reports has been driven by an international EIC community, formalized in 2016 in the EIC User Group [33], at present (September 2024) formed by more than 1500 members from almost 300 institutions and 40 countries. Several conceptual general-purpose detectors had been elaborated. A next step effort was required by the EIC project approval with the signature of CD0 in December 2019. The User Group engaged in advancing the state of documented physics studies, which dictate the detector requirements, and consolidate the general-purpose detector concept matching these requirements. This effort resulted in the EIC Yellow Report completed in early 2021 and then published in Nuclear Physics A [34]. This document guided the two proposals for a general-purpose detector elaborated in 2021, which resulted in further progress in the conceptual detector design. In 2022, a merging process of the communities presenting the two proposals and of the two conceptual approaches resulted in the formation of the ePIC Collaboration [35] (July 2022) and in baselining of the ePIC detector as EIC project detector. At present (September 2024), ePIC has more than 850 members from 177 Institutions and 25 countries, confirming the international vocation of the community pursuing the EIC science and detector.

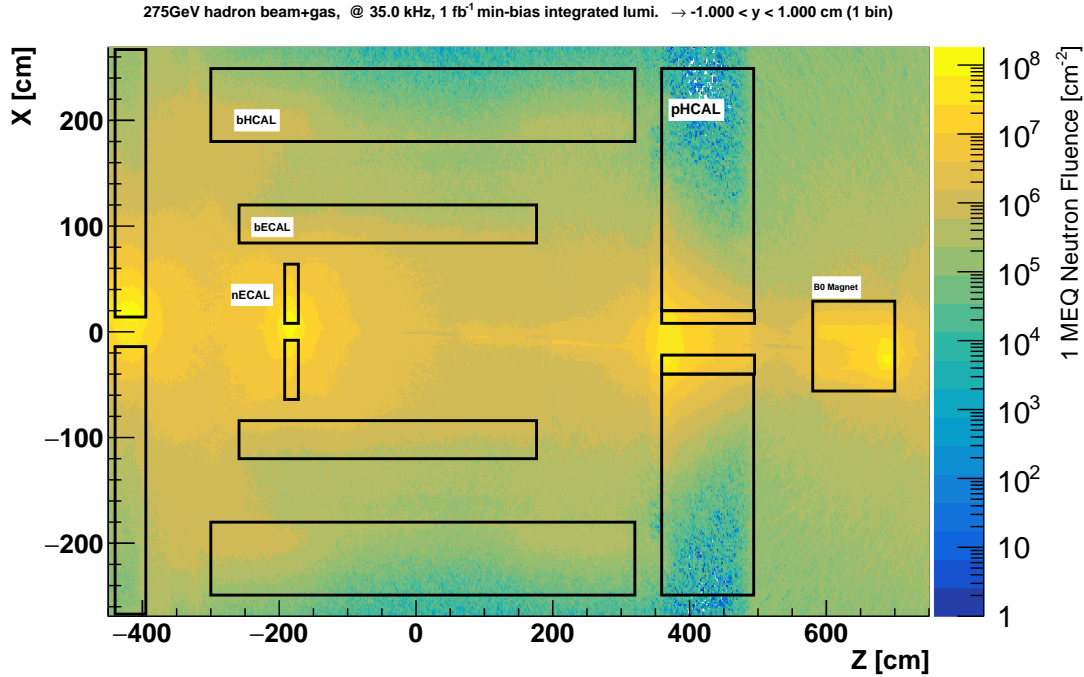


**Figure 8.9:** 1 MeV neutron equivalent fluences for the central ePIC detector from hadron beam+gas events. Peak regions of MEQ fluence are seen near the beam pipe, and especially near the radial interior of the calorimeters, similar to what is seen in the minimum-bias events.

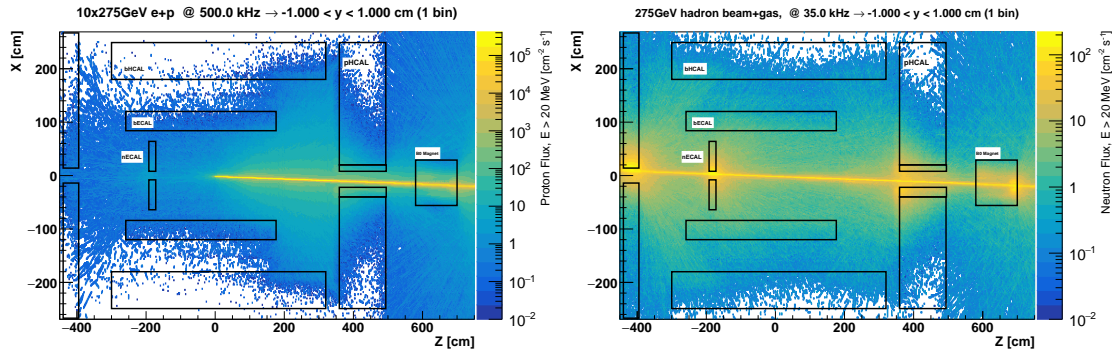


**Figure 8.10:** Fluxes of protons (left) and neutrons (right) with kinetic energy > 20 MeV from hadron beam+gas events.

1214 **The Detector** THIS DETECTOR DESCRIPTION IS AN INTRODUCTION TO THE WHOLE  
 1215 SECTION 8.3. IT WILL BE REVISED WHEN THE SUBSYSTEM MATERIAL IS UPLOADED TO  
 1216 ENSURE A BETTER CONSISTENCY OF THE SECTION 8.3.

1217 The detector challenges and the technologies matching these challenges are discussed in Sec. 8.2.1.  
 1218 The resulting design of the ePIC detector consists in a Central Detector (CD) surrounding the Inter-  
 1219 action Point 6 (IP6) making optimal use of the space available at the Interaction Region (IR) com-

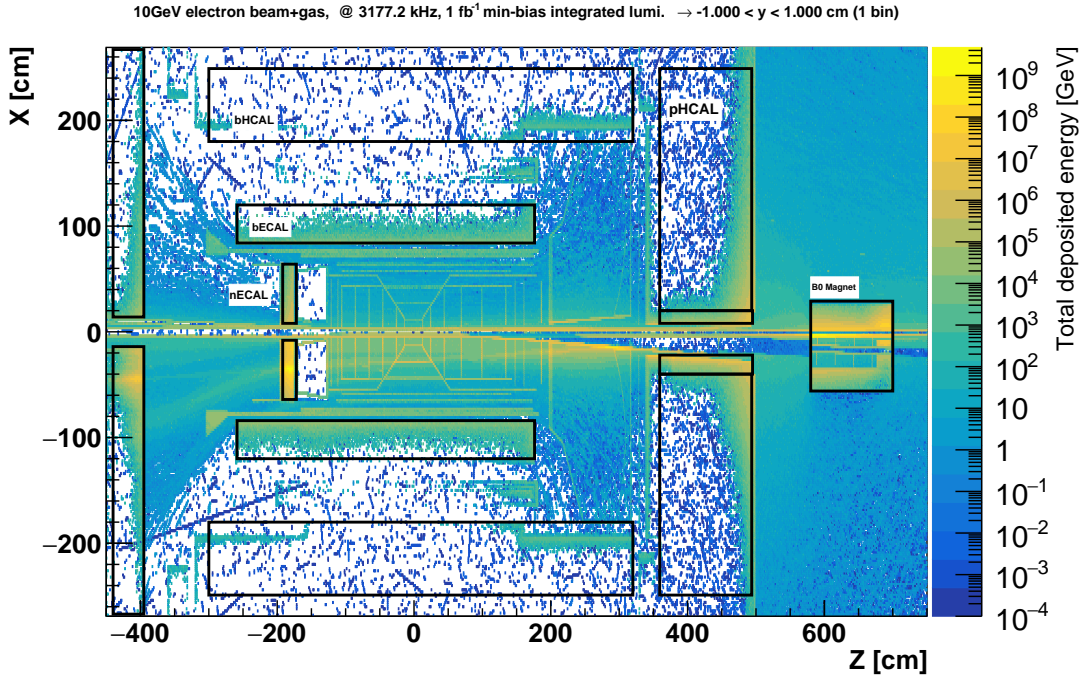


**Figure 8.11:** This figure shows the total energy deposited in 2cm x 2cm x 1cm bins spanning the full size of the ePIC central detector from electron beam+gas events with 10 GeV electrons. The results are shown as energy deposits per fb<sup>-1</sup>.

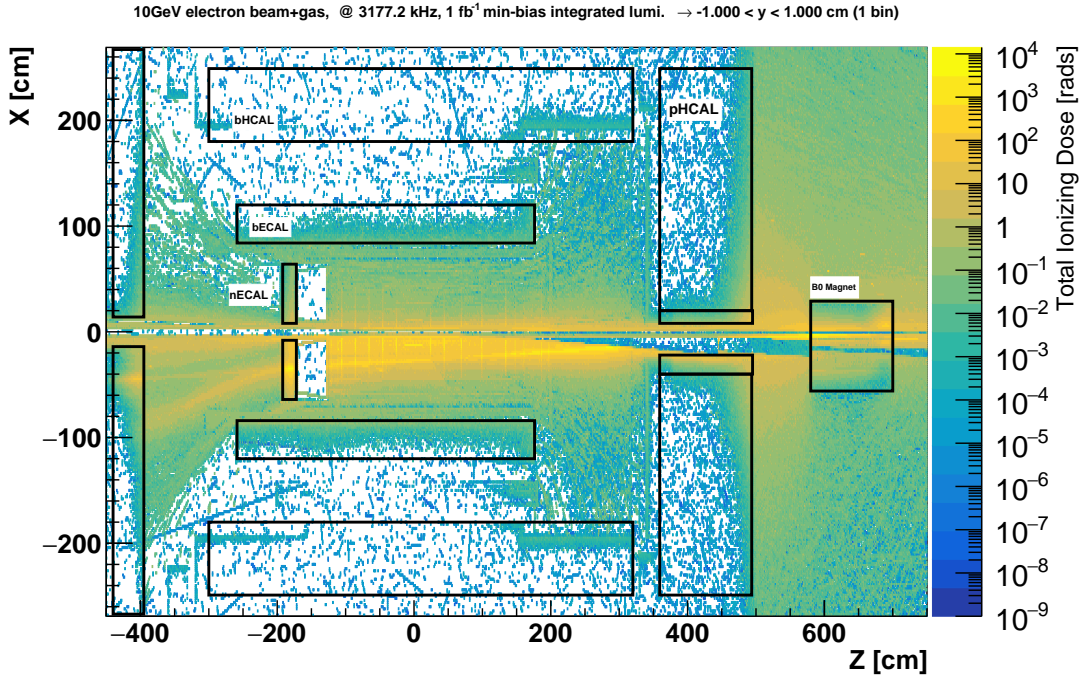
plemented by equipment situated along the outgoing beam lines, the Far Detectors (FD), which complete the phase-space coverage.

Figure 8.13 illustrates the CD kinematic coverage; Fig. 8.14 presents a schematic overview of the CD structure. The overall CD length is imposed by the constrain of the IR design. The asymmetric beam energies reflect in an asymmetric design of the detector and, together with the requirements from physics, imposes the choice of the different detector technologies that have been adopted. The setup is designed around the solenoid providing the magnetic field for the momentum analysis. The adoption of a solenoid shapes the CD in a barrel region where the subsystem have pseudo-cylindrical layouts and two endcap regions, the forward one equipping the region around the outgoing ion beam and the backward endcap around the outgoing electron beam. The barrel subsystems cover, approximately, the pseudorapidity  $\eta$  region (-1.5, 1.5), while the endcaps equip the regions up to pseudorapidity  $|3.5 - 4.0|$ , the upper bound being dictated by the beampipe layout. The separation in barrel and endcap region is not rigid with exceptions where the optimization of the detector design suggests it. For instance, the most inner layers of the tracking system have acceptance well beyond  $\eta < |1.5|$ , the barrel Cherenkov PID counter and the barrel electromagnetic calorimeter extends in the backward endcap.

The CD subsystems have a layered structure, from inside to outside: tracking subsystems, particle identification devices, electromagnetic calorimeters, solenoid coils in the barrel, and hadronic calorimeters.

The reference operation condition of the new **MARCO magnet** (Sec. 8.3.2), specifically designed for ePIC, is with 1.7 T field intensity and it can provide up to 2 T. It has good homogeneity in the





**Figure 8.12:** Total ionizing dose from electron beam+gas events per fb<sup>-1</sup> for the central region of ePIC detector.

central region and provides projective field lines in the forward endcap to match the requirements posed by the usage of a gaseous radiator in the forward RICH. The solenoid axis coincides with the electron beam line in the IR to limit the synchrotron radiation from the beam electrons. This results in helicoidal trajectories of the beam ions, due to the crossing angle of the two beams.

The **tracking system** (Sec. 8.3.3) is the most inner subsystem in order to ensure the minimum distortion of the trajectories by the material crossed by the particles. It consists of pseudo cylindrical layers completed by discs in the endcaps. The low material budget (Fig. 8.15) is guaranteed by the selected tracker technologies, with the thin ITS3 MAPS, even in support-less arrangement in the most inner layers, and MPGDs for the most external layers. The two tracker technologies support each other thanks to key complementary characteristics. MAPS sensors offer extremely fine space resolution, but poor timing information in the order of a few microsecond range. In-time hits can be selected combining MAPS information with the measurements in the MPGDs, which have time resolution of 10-20 ns. Further space and time information will be provided by the time-of-flight layers in the barrel and the forward endcap and by the first layer of the barrel imaging electromagnetic calorimeter equipped with AstroPix MAPS sensors. The minimization of the material budget is one of the ingredients allowing fine resolution for momentum determination and vertex reconstruction. To this end, fine intrinsic resolution is requested for the trackers and it is provided by the ITS3 MAPS. The momentum resolution is affected by the available lever arm and the solenoidal configuration of the magnetic field, the latter having its largest impact on the very forward and backward trajectories.

The tracking information is also a key ingredient for the performance of the Cherenkov imaging devices; in particular, very fine resolution of the particle direction is needed for the barrel DIRC. The most external tracker layers in the barrel, positioned in front of the DIRC, further support this

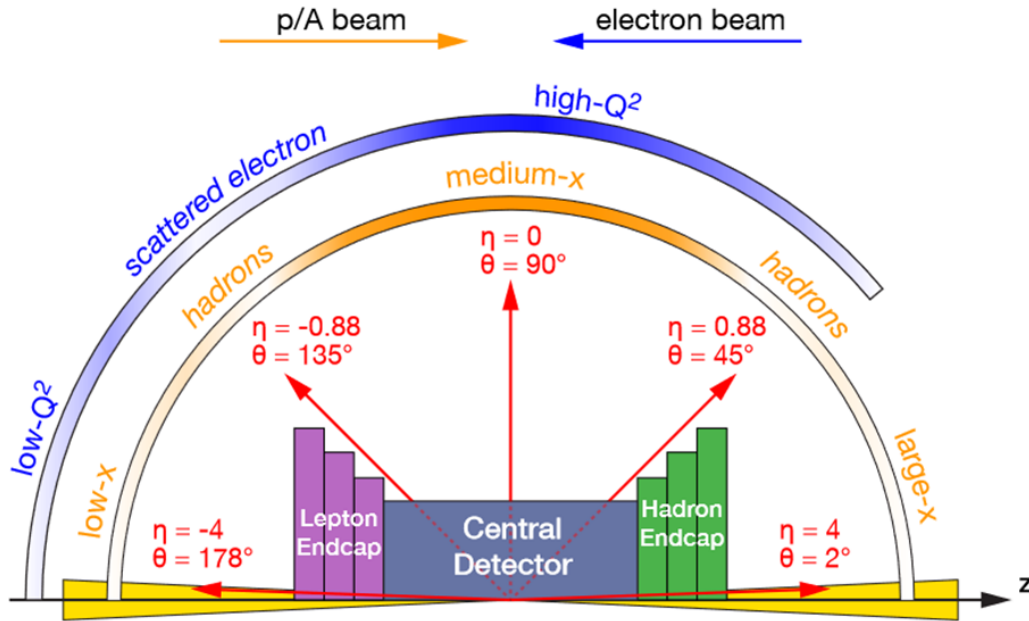


**Figure 8.13:** A schematic showing how hadrons and the scattered electron for different  $x - Q^2$  are distributed over the detector rapidity coverage. THIS FIGURES IS A PLACE HOLDER: IT IS FROM YR AND REQUIRES REVISION.

1264 requirement.

1265 The **particle identification subsystems** (Sec. 8.3.4) surround the tracking systems. Their mission  
 1266 is twofold: (i) supporting the electromagnetic calorimeters by complementing the pion/electron  
 1267 separation to ensure the high purity of the electron sample; (ii) identifying hadrons, as needed by  
 1268 a large fraction of the physics program. The coverage of the wide kinematic domain imposes the  
 1269 adoption of a variety of technologies with time-of-flight measurements complementing Cherenkov  
 1270 imaging devices. Time-of-flight dedicated layers by AC-LGADs are present in the barrel and in  
 1271 the forward endcap, the barrel layer being by strip sensor elements to reduce the material budget,  
 1272 while the forward endcap layer is by pixelized AC-LGADs. In the backward endcap, the fine  
 1273 time-resolution provided by the photosensors of the Cherenov counter, which are sitting in the  
 1274 endcap acceptance, provide timing information via the Cherenkov light generated in the sensor  
 1275 window. The Cherenkov imaging counter in the backward endcap is a proximity focusing RICH  
 1276 with aerogel radiator and extended proximity gap to increase the resolution and, correspondingly,  
 1277 enlarging the momentum range for particle identification. As already underlined, the use of fine-  
 1278 time resolution HRPPDs by MCP technology as photosensors also provides timing information.  
 1279 The whole detector components are positioned in the acceptance, in front of the electromagnetic  
 1280 calorimeter. This layout is compatible with the overall detector design; in fact, the bulky elements,  
 1281 namely the sensors with readout electronics and services are just in front of the calorimeter acting as  
 1282 a pre-shower element. In the barrel, a high performance DIRC is used, this choice being dictated by  
 1283 the reduced space. The DIRC fused silica bars, acting as radiator and as photon lightguides, make  
 1284 possible positioning the image expansion elements and the read-out electronics with its services  
 1285 in the backward region, outside the acceptance cone. The dual radiator RICH (Sec) in the forward  
 1286 endcap is equipped with two radiators, aerogel and gas, therefore acting as a couple of Cherenkov  
 1287 imaging counters dedicated to particle identification in two different momentum ranges, while



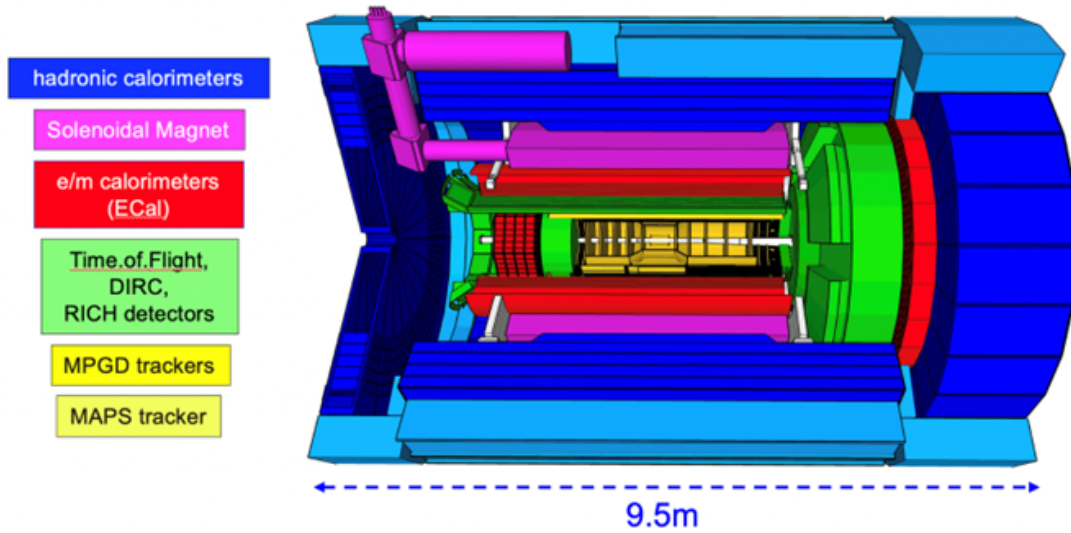


**Figure 8.14:** A schematic showing the ePIC central detector subsystems. THIS FIGURES IS A PLACE HOLDER

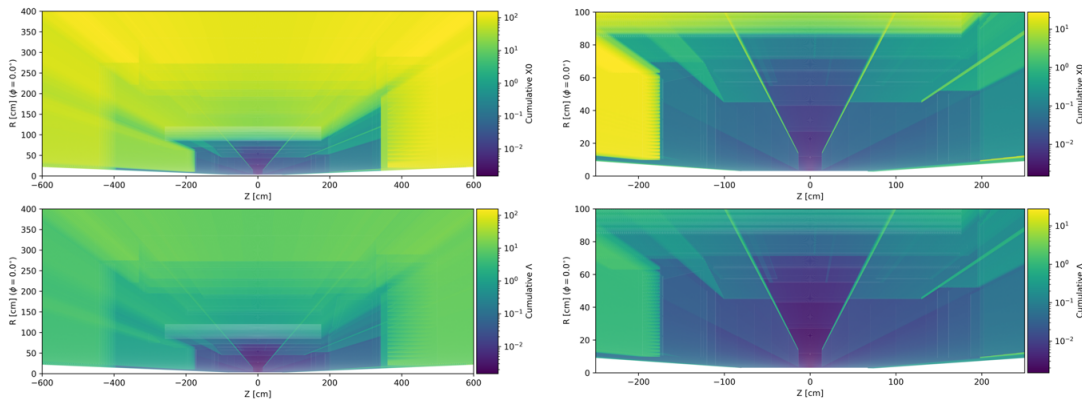


**Figure 8.15:** Cumulative material budget in radiation lengths (top row) and interaction lengths (bottom row) for the whole CD (left column) and zooming at the CD tracking region (right column). THIS FIGURES IS A PLACE HOLDER BECAUSE IT HAS TO BE COMPLETED WITH SUBSYSTEM CONTOURS AND REQUIRES GRAPHICAL IMPROVEMENTS.

1288 economizing in space and single photon sensors. It is a focusing RICH with spherical mirrors as  
 1289 focusing elements. The photosensors and related services are placed outside the acceptance thank  
 1290 to appropriate mirror orientation.

1291 The electromagnetic calorimeters (Sec. 8.3.5) are external to the particle identification devices and,  
 1292 once more, the different technologies are imposed by the physics requirements, the kinematic  
 1293 ranges and the overall constrains. The budget of the material in front of the calorimeters is low  
 1294 and mainly concentrated near to the calorimeter front face. The backward endcap electromag-  
 1295 netic calorimeter is by fine granularity lead tungstate crystal offering very fine energy resolution.  
 1296 In the barrel, the electromagnetic calorimeter has a hybrid architecture combining imaging layers  
 1297 by AstroPix MAPS and sampling calorimetry by lead and scintillating fibers with sampling layer

between the imaging layers and in the most external calorimeter portion. The layout is pseudo cylindrical with the read-out equipment at the cylinder edges minimizing the space requirement in the crowded barrel area. The electromagnetic calorimetry in the forward region is by sampling calorimetry with scintillating fibers inserted in matrices of tungsten powder embedded in epoxy. This calorimeter offer a near to 1 ratio of the signal amplitude response for electrons and hadrons and, therefore, it is design to operate in duet with the hadronic calorimeter place immediately behind.

All the **hadron calorimeters** (Sec. 8.3.6) are by iron as converter and scintillating active elements, even if with very different implementations. The forward endcap calorimeter is by SiPM-on-tile technology, with finer granularity in the central zone, near to the beam pipe, to cope with the higher rates. The barrel calorimeter, placed behind the solenoid coils, acts as a tail catcher. The backward endcap calorimeter ... (to be completed: layout in evolution).

All the calorimeter subsystem in the ePIC detector make use of SiPMs as photosensors, even if of different size and pixelization, with common approach for the readout chain.

The global layout of the FDs (Sec.s 8.3.7 and 8.3.8) is illustrated in a artistic view in Fig. 8.16.

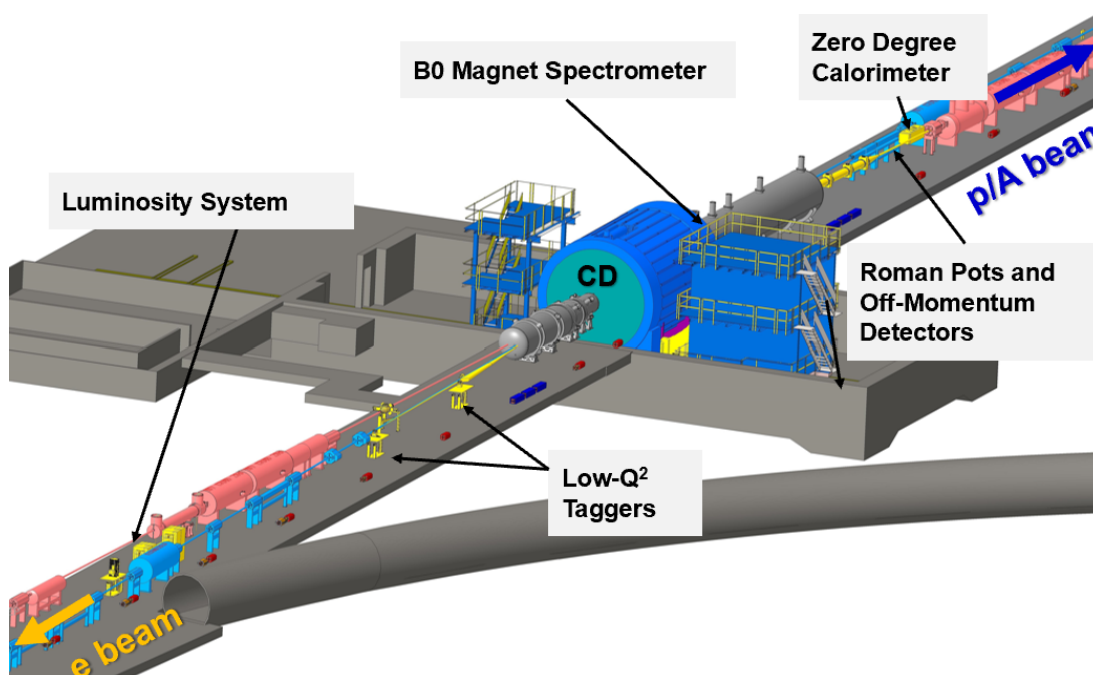


**Figure 8.16:** A schematic showing the ePIC far detector subsystems. THIS FIGURES IS A PLACE HOLDER

The **forward FDs** include tracking and electromagnetic calorimetry inserted in the first dipole of the ion beam line B0, off-momentum detector trackers and roman-pot trackers and a zero-degree-calorimeter. The technology for the trackers is by AC-LGADs, which have good radiation hardness. The B0 electromagnetic calorimeter is by lead tungstate crystals. The zero-degree-calorimeter is formed by a long SiPM-on-tile module with fine granularity adequate for photon and neutron detection. A crystal layer can be inserted in front of it for those studies that require the detection of low energy photons.

The **luminosity system** is part of the backward FD. Based on the measurement of the photons from the Betha-Heitler process at IP, it consists of a high-rate calorimeter for direct photon detection and a couple of pair spectrometers to detect the electrons and positrons generated by the Betha-Heitler photons in the exit window. The high-rate calorimeter and the calorimeters in the pair spectrometers are by tungstate and scintillating fibers. Tracking in the pair spectrometer is by AC-LGADs. The **low- $Q^2$**  taggers consist in tracking stations followed by an electromagnetic calorimeter. The selected technologies must cope with extremely high rate in this kinematic region. Therefore, tracking is by TimePix4 and calorimetry by tungstate and scintillating fibers.

Integral elements of the detector are the **electronic read-out chain**, the data acquisition system (Sec. 8.3.10) and the **software implementation and computing model** (Sec. 8.3.11). The overall underlining model that has guided the selection of the components and the design of the readout/DAQ/software/computing architecture is the streaming readout concept. Streaming readout has been selected to simplify the readout scheme as no triggers are required and to increase the information selection flexibility, to improve the event building from the holistic detector information, to improve, via continuous dataflow, the knowledge of backgrounds and, therefore, enhances the control over systematics. In this approach, already at the front-end level, the ASICs, which are intimate related to the sensors and their performance, have been selected with architectures compatible with their usage in streaming readout mode.

Independent setups are designed to measure and monitor the **beam polarization** (Sec. 8.3.9). Rapid, precise beam polarization measurements will be crucial for meeting the goals of the EIC physics program as the uncertainty in the polarization propagates directly into the uncertainty for relevant observables as asymmetries. The basic requirements for beam polarimetry are non-destructive with minimal impact on the beam lifetime, uncertainty at the 1% level, the capacity of measuring the beam polarization for each bunch in the ring with rapid, quasi-online analysis in order to provide timely feedback for accelerator setting up. The electron beam polarimetry will be based on the well established Compton polarimeter techniques, where the polarized electrons scatter from 100% circularly polarized laser photons. This approach offers the advantage that both longitudinal and transversal polarizations are measured. Hadron polarimetry has been successfully performed on RHIC polarized proton beams for nearly two decades. Through continual development a relative systematic uncertainty  $\pm 1.5\%$  was achieved for the most recent RHIC polarized proton run. As the only hadron polarimeter system at a high energy collider it is the natural starting point for hadron polarimetry at the EIC. Hadron polarization will be measured via a transverse single spin left right asymmetry in the pp interaction on targets by plastic material (H-C composition), where the experimental challenge is the control of the background events.

**Technological Synergistic Aspects of the Detector Design** The synergistic aspects of the ePIC detector have been carefully maximized in view of the optimal usage of the workforce and the financial resources. This is illustrated by the following examples.

SiPM sensors, recently introduced in calorimetry applications, are adopted for all the electromagnetic and hadronic calorimeters in ePIC. They offer a cost-effective technology that can operate in magnetic field, can provide wide dynamic range when the sensor type is properly chosen to tune the response parameters, and present low noise level by applying appropriate thresholding. The use of a common technology makes possible to access the effect of the radiation by a single effort and the use of the same front-end ASIC CALOROC.

Also the calorimetry reconstruction software is synergistic for the overall set of subsystems.

In electromagnetic calorimetry, the sampling approach with tungsten and scintillating fiber is adopted for the forward endcap calorimeter and in FDs: calorimetry in B0, luminosity system and

1366 low- $Q^2$  taggers.

1367 In hadron calorimetry, the SiPM-on-tile technology is used for the forward endcap calorimeter and  
1368 its insert in the central area, as well as for the zero-degree calorimeter.

1369 In particle identification by Cherenkov imaging counters, MCP-based photosensors are used for  
1370 the backward endcap RICH and the barrel DIRC, that can be read by the same read-out ASIC  
1371 HGCROC (information to be crosschecked). The backward endcap RICH and the forward endcap  
1372 RICH use aerogel as radiator and the quality assessment station will be used for both batches.  
1373 The reconstruction software in both RICHes has large communalities and it is based on the same  
1374 ray-tracing algorithm.

1375 AC-LGADs form the time-of-flight layers and are used for tracking in the forward FD in B0, off  
1376 momentum detectors and roman pots, and selected for the pair spectrometers of the luminosity  
1377 system.

1378 In tracking by MAPS, the different sensors of the inner layers, the outer layers and the forward  
1379 and backward disks are all evolutions of the ITS3 sensor, therefore all based on stitching the same  
1380 readout chip element.

1381 The same hybrid MPGD architecture with a preamplifying GEM layer followed by a  $\mu$ RWELL is  
1382 used in the most outer tracker in the barrel and the most external discs in the endcaps. All MPGDs,  
1383 namely the hybrid MPGDs and the cylindrical Micromegas in the barrel are coupled to the same  
1384 front-end ASIC: SALSA.

1385 A single integrated effort is at the basis of the tracking reconstruction with the use of the software  
1386 package AC.

### 1387 8.3.2 Magnet

1388 **Introduction** A high-performance solenoid is required for the ePIC detector. The needed mag-  
1389 netic rigidity for secondary particles in the ePIC detector will be assured by a one-of-a-kind 2 T  
1390 superconducting solenoid. The magnet design work is a collaborative work between JLab Magnet  
1391 group, CEA, Saclay and BNL. MARCO (Magnet with Renewed Coils) presents some unusual de-  
1392 sign characteristics respect to other detector magnets: the most important is its conductor, a NbTi  
1393 Rutherford cable in Copper Channel (RICC), especially optimized to stand the forces during the  
1394 cool-down and energization while providing a high enthalpy stability and a fast quench propaga-  
1395 tion. The coils of the magnet are wound internally on a thin brass mandrel, which provides both  
1396 a similar thermal retrain than the coil pack and, the needed rigidity without compromising the  
1397 transparency of the magnet. The magnet will be cool-down by a thermosiphon, the cooling circuit  
1398 is closed by a helium phase separator vessel placed outside the iron yoke and cryogenically con-  
1399 nected to the main LHe circuit of the accelerator. The magnet is shifted of 10 cm towards the lepton  
1400 side respect to the interaction point to better accommodate the sub-detectors. Such asymmetry has  
1401 been considered while designing the iron yoke around, in order to minimize the magnetic forces  
1402 acting on the magnet. In the following sections, the design of the overall magnet will be presented.  
1403 Figure 8.17 shows the magnet assembly overview in its iron yoke. The iron yoke is divided in three  
1404 sections, respectively Lepton, Barrel and Hadron, made of several components, including some  
1405 hadronic calorimeters. Their names indicate the sides from which the particles beams come.

1406 **Requirements** The magnet is located in the interaction region of the EIC, therefore, some of the  
1407 requirements are driven by the other magnets in the IR and nearby beam lines in the tunnel. Table

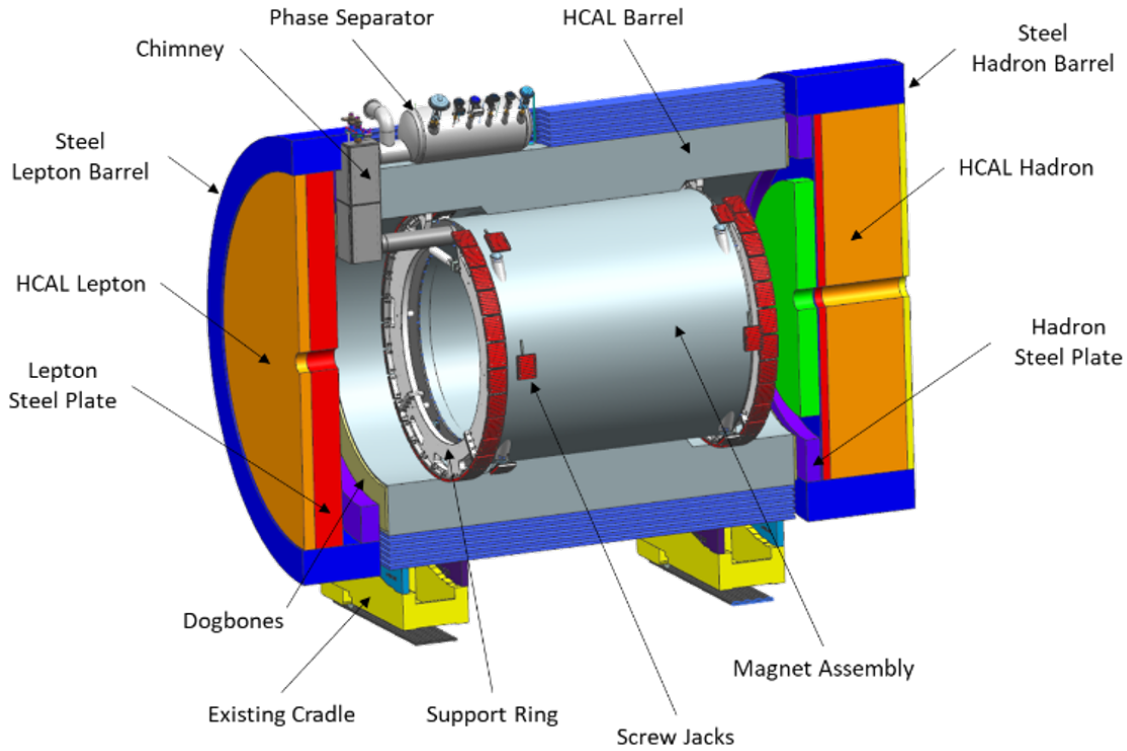


**Figure 8.17:** MARCO Magnet inside the iron yoke.

1408 8.1 shows the MARCO magnet requirements.

1409 Regarding the magnetic performances demanded, there are three zones of main interest:

1410 **The Flat Field area** Described as cylinder of radius 80 cm for a total length of 200 cm, centered  
 1411 on the interaction point IP. The For this area, the requirement is to have a field uniformity defined  
 1412 as:

$$\text{Field uniformity} = 100 \frac{dB}{B_{\text{center}}}$$

1413 Where: TO BE COMPLETED

1414 **The RICH Area** In order to maximize the RICH performances based on the gas radiator, it is  
 1415 critical to minimize the bending of the tracks in the volume of the gas radiator, for this one need to  
 1416 shape the field such that it is parallel to the different scattering angles of particles covered by the  
 1417 RICH. The RICH area extends from  $z=+180$  cm to  $+280$  cm with the shape of a truncated cone. The  
 1418 projectivity in this region should be less than 10 T/Amm<sup>2</sup> or less than 0.1 mrad @30GeV/c for a  
 1419 proton. The projectivity can be calculated as:

1420 INSERT FORMULA





**Geometry and Materials of the Yoke** The magnetic flux generated by the superconducting coils is returned via three distinct sections of yoke: the Barrel Yoke, the Lepton Yoke and the Hadron Yoke (as shown in 8.17). Their geometry has been defined through an optimization process which includes both the experimental constraints and the requirements for the fringe field.

- **Barrel Yoke:** the Barrel Yoke consists of the HCal Barrel Calorimeter and the Steel Barrel Yoke. The HCal Barrel Calorimeter is made with 32 assembled sectors composed by 10 rows of 8 mm scintillators tiles (24 tiles per row), tilted with an angle of  $12^\circ$ . In each sector, 26.1 mm x 42.4 mm x 6300 mm tapered 1020 steel plates are piled up and used to separate each scintillator tile. The total fraction of steel in the volume is 70%. Dogbones made by the same steel enclose the calorimeter. Their fraction of steel in the volume is 66%. The Steel Barrel Yoke is made by 6 concentric rings of steel 1020, 50 mm thick, 6300 mm long, surrounding the HCal Barrel Calorimeter. Each ring is separated from the other by 40 mm. A specific volume is dedicated to the installation of the He phase separator, from which all the cryogenics circuits inside the cold mass are supplied. The Steel Barrel Yoke main purpose is to reduce the stray field.
- **Hadron Yoke:** The Hadron Yoke consists of the HCal Hadron Calorimeter, the Steel Barrel Hadron Yoke and the HCal Hadron Oculus. Its name is given by the convention on the direction of the beams. In this case, the hadron beam is the one exiting the detector. The HCal Hadron Calorimeter is made by 70 pieces of 4 mm thick scintillator tiles, 10 pieces of 16 mm thick tungsten plates and 60 pieces of 16 mm thick steel 1020 plates. The average fraction of steel 1020 in the total volume is 75%. The Steel Barrel Hadron Yoke as well as the HCal Hadron Oculus are two structures in steel 1020 surrounding the calorimeter and returning the magnetic flux.
- **Lepton Yoke:** The Lepton Yoke is composed by the HCal Lepton Calorimeter, the Steel Barrel Lepton Yoke and the HCal Lepton Oculus. Its name is given by the convention on the direction of the beams. In this case, the electrons beam is the one exiting the detector. The HCal Lepton Calorimeter is made by 50 pieces of 4 mm thick scintillator tiles, 10 pieces of 16 mm thick tungsten plates and 60 pieces of 16 mm thick steel 1020 plates. The average fraction of steel 1020 in the total volume is 75%. The Steel Barrel Lepton Yoke as well as the HCal Lepton Oculus are two structures in steel 1020 surrounding the calorimeter and returning the magnetic flux.

For all the electro-magnetic simulations, the envelope of each component of the yoke has been considered, and for each volume a dilution percentage corresponding to the average fraction of steel present has been taken into account. The BH curve for 1020 steel is shown in Figure 8.19

**Description of the magnet** The solenoid is made of three modules with three identical superconducting coils wound internally on a mandrel in brass 70-30. The coils are indirectly cooled using a thermosiphon (as shown in Figure 8.20). All the cryogenics circuits are connected to a LHe phase separator, connected itself to the main cryogenics circuit of the accelerator. The connection is made through a chimney, where the current leads are also placed.

For each module, 6 single layers of RICC conductor are wound internally to a mandrel, for a total number of turns per layer varying between 92 and 93, according to the conductor exits. The total number of turns per module is 556. Layers are named L1, L2, L3, L4, L5, L6 with L1 being the innermost and L6 the outermost. Each layer is separated by an inter-layer fiber glass insulation of 2 layers of 0.2 mm to achieve a good electrical insulation after winding and to prevent the conductor

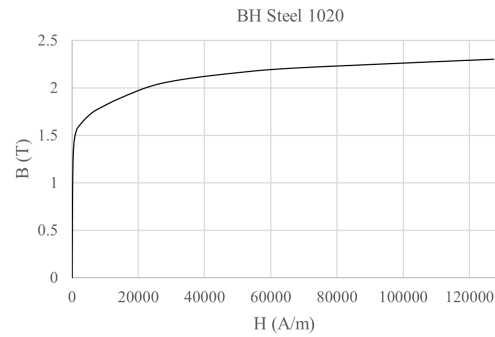


**Figure 8.19:** BH curve of 1020 steel

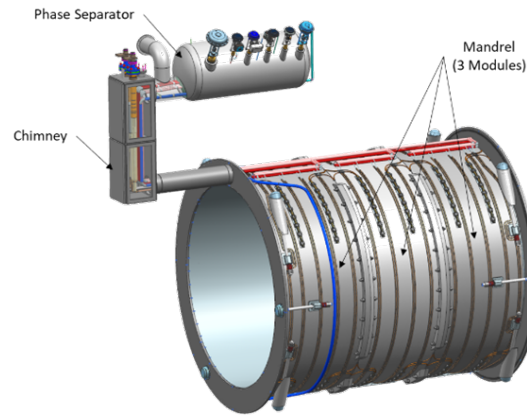


**Figure 8.20:** MARCO cold mass layout inside the cryostat.

1471 damages. The coil pack is separated from the mandrel by 1 mm of ground insulation, the same  
 1472 value as CMS solenoid, to prevent electrical short-circuits, to protect the conductor insulation dur-  
 1473 ing winding, and to facilitate the impregnation keeping a good thermal coupling for cool-down and  
 1474 quench-back. A schematic cross-section of the coil pack with the thickness of each item is shown in  
 1475 Figure 8.21. Figure 8.21 also shows the schematic cross-section of the RICC NbTi conductor chosen,  
 1476 with the dimensions of each element. On the inner side of the coil pack, the impregnation should  
 1477 provide an average thickness of G10 of 2 mm.

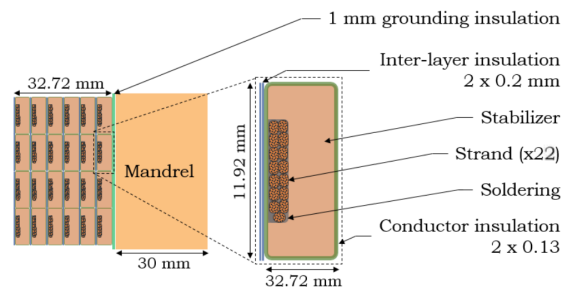


**Figure 8.21:** Schematic cross section of coil pack and conductor



Parameter	Value	Unit
Bore radius	1420	mm
Cryostat outer radius	1770	mm
Cryostat axial length	3850	mm
Mandrel Length (300K)	3620	mm
Mandrel Length (4K)	3608	mm
Number of Modules	3	
Z- (MOD1) / Z+ (MOD3) Modules Length (300K)	1228	mm
Central Module (MOD 2) Length (300K)	1164	mm
Coils Inner Radius (300K)	1509.5	mm
Coil Inner Radius (4K)	1502.5	mm
Coils Thickness	32.7	mm
Coils Outer Radius (300K)	1542.2	mm
Ground Insulation Thickness	1	mm
Mandrel Inner Radius	1543.2	mm
Mandrel Thickness	30	mm
Mandrel Outer Radius (300K) without Flanges	1573.2	mm
Number of Layers per Module	6	
Number of Turns per Module	556	

**Table 8.2:** MARCO geometric Specifications

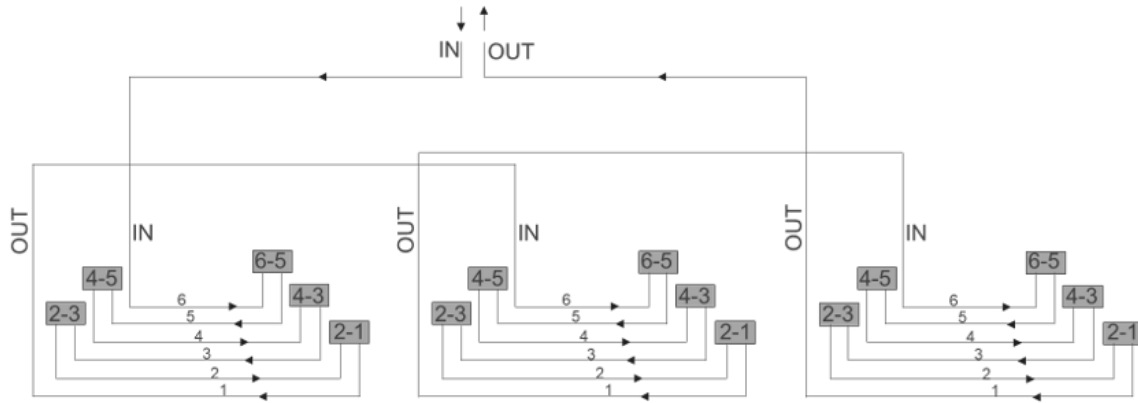


**Figure 8.22:** Electric schematic of MARCO Solenoid

1478 The geometric specifications and dimensions of MARCO solenoid are reported in Table 8.2. The  
 1479 electric scheme for the solenoid is shown in Figure 8.22. Each layer is made by winding one conduc-  
 1480 tor unit length (1 km long), and all the layers are connected in series with conductor splices outside  
 1481 the mandrel. Conductor exits are positioned at approximately 120° on the mandrel as shown in  
 1482 Figure 8.23.

1483 Such arrangement preserves the number of turns. The extremities (front/rear) of each coil pack  
 1484 have in total 5 turns over 6. The exits will be made with grooves cut in the mandrel. Each groove  
 1485 will be:

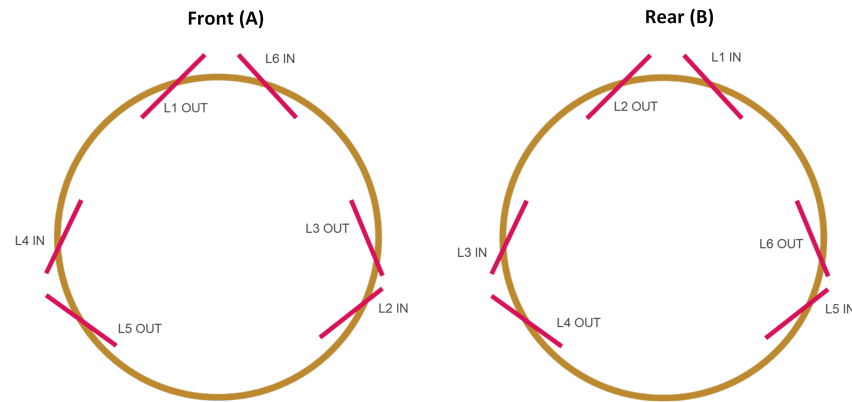


**Figure 8.23:** Conductor entrance and exit schematic for each module

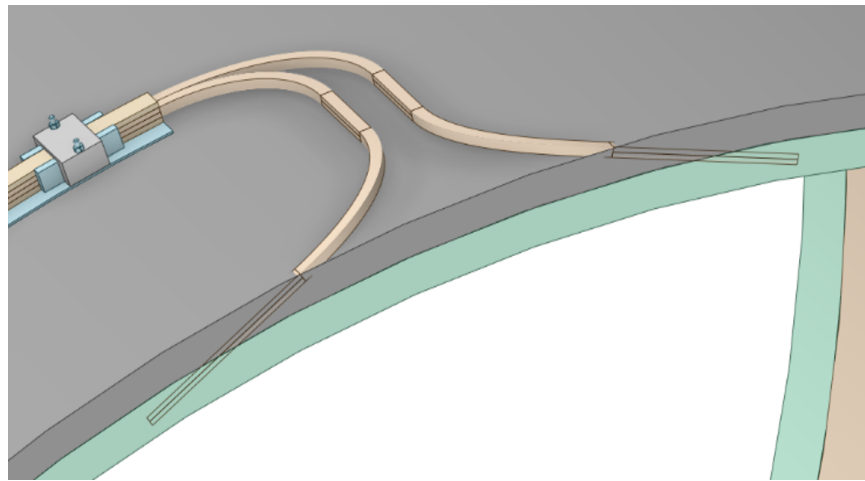


**Figure 8.24:** Design of the Splices exits from the mandrel

- 1486 • Thick enough to double the conductor in order to increase the stability and to insulate it with  
1487 G10 fillers and fiberglass insulation Figure E;
- 1488 • Tangent to the outer diameter of each terminal with a 1 mm G10 plate between the splice and  
1489 the mandrel;
- 1490 • Separated with a distance larger than two times of the hard-way radius of the conductor (2 x  
1491 120 mm).

1492 A schematic of the grooves' arrangement is shown in Figure 8.24 and Figure 8.25. Splices between  
1493 doubled conductors are thermalized thanks to a series of copper plates connected to the mandrel  
1494 itself cooled down by the thermosiphon.

1495 In order to fulfill the requirements in Table 8.2, the mandrel is longer than the coil for each module.  
1496 The extra length is equal to 24.84 mm (2x11.92 mm [2 turns] plus 1 mm for tolerances), which gives  
1497 a separation of 55.5 mm between each coil. This gap will be filled with G10 wedges, which will be

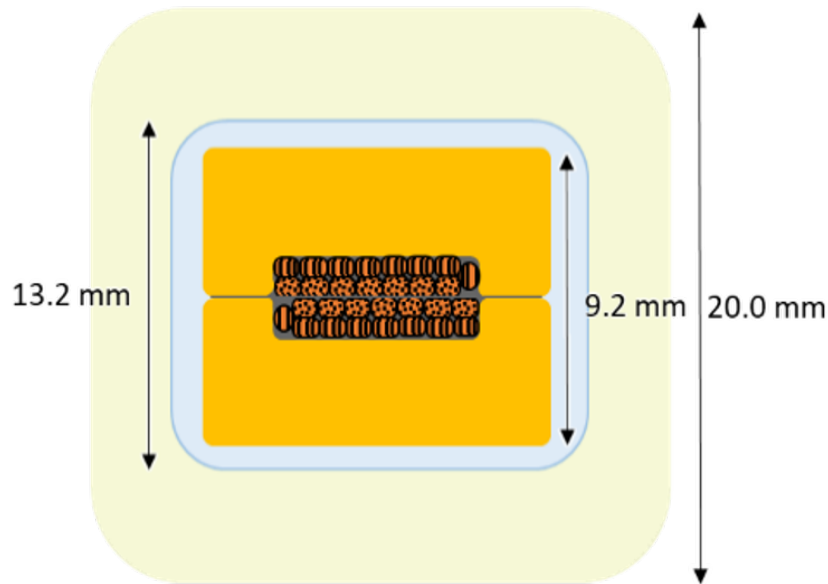


**Figure 8.25:** Schematic cross-section of the splice to be place inside the groove

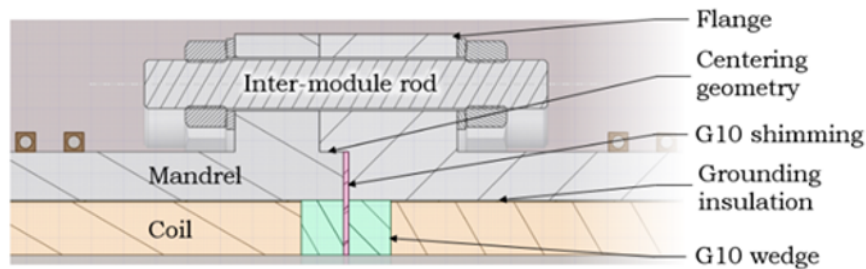


**Figure 8.26:** Schematics of the geometry at the interface between each coil

1498 glue to the mandrel, plus a 3 mm insulation between each module to take care of the tolerances of  
1499 manufacturing, positioning and tolerance stack up Figure 8.26.

1500 Each module is impregnated independently and bolted together through flanges. Flanges are not  
1501 continuous on the entire circumference of the mandrel in order to let the thermosiphon pipes, the  
1502 conductor splices and wire sensors all the space required. On the two outer modules, 4 radial and  
1503 3 axial tie-rods in  $\text{Ti}_6\text{Al}_4\text{V}$  are present to sustain the mass of the magnet and the efforts during the  
1504 cool-down and the energization. A schematic description of the tie-rods is shown in Figure 8.27.  
1505 A general scheme of the magnet assembly inside the cryostat is shown in Figure 8.28. In the same  
1506 figure, the two thermosiphon manifolds (the main and the spare) with the respective supply lines  
1507 and heat exchangers are showed. The cold mass is placed inside a cylindrical vacuum vessel made  
1508 in Al6061-T6 Figure 8.29, with a thickness on the inner and outer shell of respectively 14 mm and  
1509 25 mm. The two shells joint together through flanges 40 mm thick. Inside the cryostat, a thermal  
1510 shield made in Al3003 with 3 4 internal panels and 3 4 outer panels is located. The thermal shield  
1511 is cooled by 3 circuits in parallel, cooling the internal panels first. Between the vacuum vessel and  
1512 the outer shield, there are 30 layers of MLI; while between the coil and the internal shield, there are  
1513 10 layers of MLI to guarantee the superinsulation.

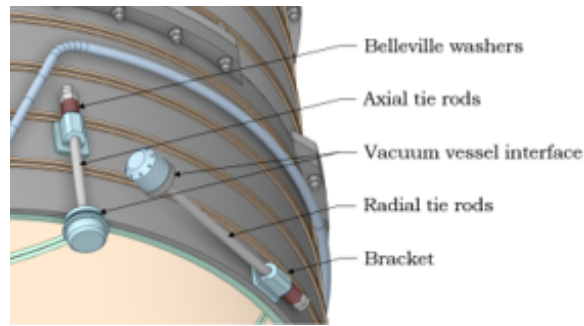


**Figure 8.27:** Schematics of the tie-rods geometry

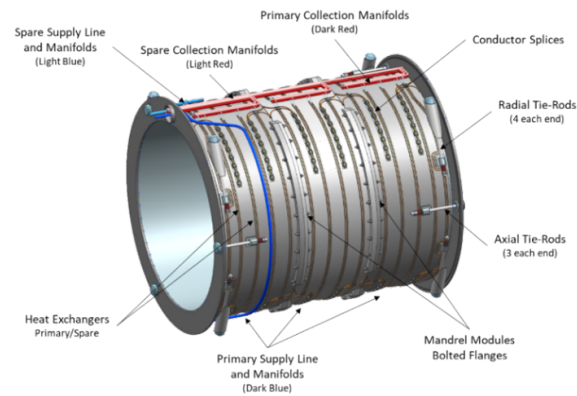


**Figure 8.28:** Magnet assembly inside the cryostat

1514 The full list of the main materials is reported in Table 8.3, The Thickness/Nuclear interaction length  
 1515 weighted according to the material densities for MARCO is 0.495.

1516 **Magnet Design** The magnetic design has been performed using OPERA, with 2D and 3D finite  
 1517 element models. Given the high level of symmetry in the magnet, both models give the same  
 1518 results in terms of magnetic field and magnetic performances. The 2D axisymmetric model is used  
 1519 to compute the magnetic field turn-by-turn and to determine the magnetic field peak on the cable

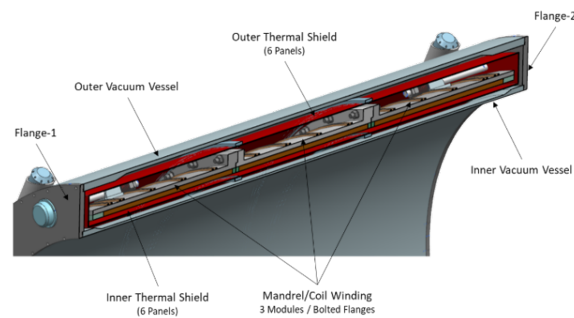


**Figure 8.29:** Schematics of the cryostat with the magnet inside

Component	Radial thickness (mm)	Material	Nuclear interaction l
Inner vacuum vessel	14	Al6061	107.2
Inner thermal shield	5	Al3003	107.2
Inner G10	2	G10	78.4
Coil	33.7	14 % Insulation 80 % Cu 6 % NbTi	Insulation: 78.4 Cu: 13
Mandrel	30	Brass 7030	137.7
Outer thermal shield	5	Al3003	107.2
Outer vacuum vessel	25	Al6061	107.2

Table 8.3: MARCO Materials

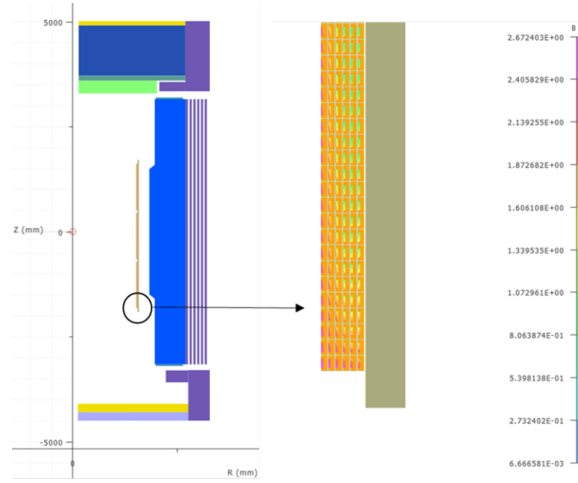


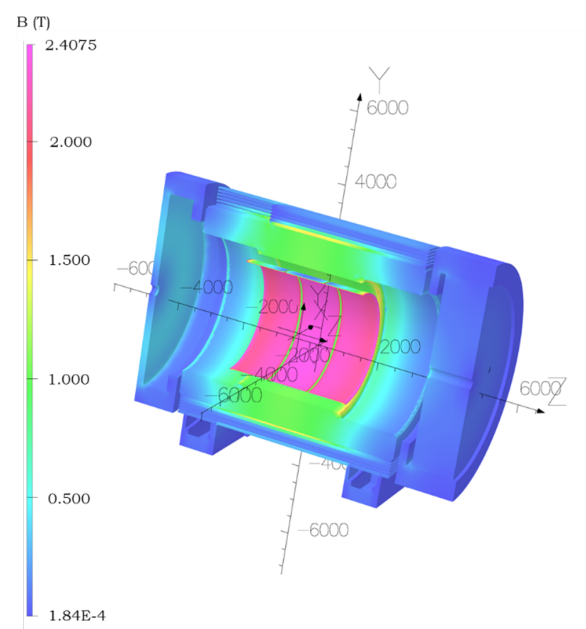
Figure 8.30: The 2D finite element model

Figure 8.30 (On the left, the geometry considered, on the right the results for the magnetic field peak on the cable, located at the extremity of module 1), while the 3D model (Figure 8.31) is to take into account the role of the mandrel during the ramp-up/ramp-down and the quench, as well as the effect of the cradles and the phase separator.

Three are the magnetic fields at the interaction point IP that are relevant for physics: 1.5T, 1.7T and 2.0T. The nominal magnet performances for each case are reported in Table 8.4:

Parameter	BIP = 1.5 T	BIP = 1.7 T	BIP = 2.0 T	Units
Current	2942	3335	3924	A
BIP	1.505	1.706	2.000	T
Bpeak	2.003	2.271	2.672	T
Energy	25.440	32.689	45.008	MJ
Lcoils	5.847	5.847	5.846	H
Lmandrel	2.347x10-6	2.347x10-6	2.347x10-6	H
Mcoils-mandrel	3.570x10-3	3.570x10-3	3.570x10-3	H
Fz	-23.8	-29.2	-32.2	kN

Table 8.4: Design parameter for various fields



**Figure 8.31:** Magnetic field on the coil and yoke from 3D OPERA model for the 2.0 T field

Parameter	Value	Requirements	Unit
Field uniformity	12.5 %	12.5 %	
Projectivity	3.28	$\leq 10$	T/Amm <sup>2</sup>
BRCS	0.035	$\leq 0.007$	Tm
BB0ApF	15.4	$\leq 10$	G
BQ1ApR	10.9	$\leq 10$	G

**Table 8.5:** Caption

1526 It is important to notice that the primary inductance of the magnet  $L_{\text{coils}}$  is essentially constant. The  
1527 iron yoke plays a negligible role on the performances of the magnet since it does not saturate Figure  
1528 L. The same trend is observed on the secondary inductance  $L_{\text{mandrel}}$ . The total axial force acting on  
1529 the magnet due to its interaction with the yoke is monotone respect to the current (it increases as the  
1530 current increases) and it points always in the lepton direction ( $-z$ ). The maximum value of the force  
1531 is 32.2 kN, and it is negligible respect to the forces the magnet can stand during transportation. The  
1532 magnet is well balanced respect to the yoke.

1533 The difference on the magnetic field peak in 2D and 3D is because in 3D the contribution of the  
1534 self-field of the cable cannot be taken into account.

1535 The magnetic performances for the 2T central field are given in table 8.5. The simulated field uni-  
1536 formity and projectivity are shown in Figure 8.32 and 8.33 respectively.

1537 The design meets the requirements for the field uniformity and the projectivity, however the fringe  
1538 field is slightly high. Since the values for the fringe field are in the order of 1 mT, a series of local  
1539 shields around the magnets and the RCS are investigated. The fringe field for 5 G and 15G are  
1540 shown in Figure 8.34 and 8.35.

1541 In order to assess the robustness of the design, different fault scenarios have been considered, these

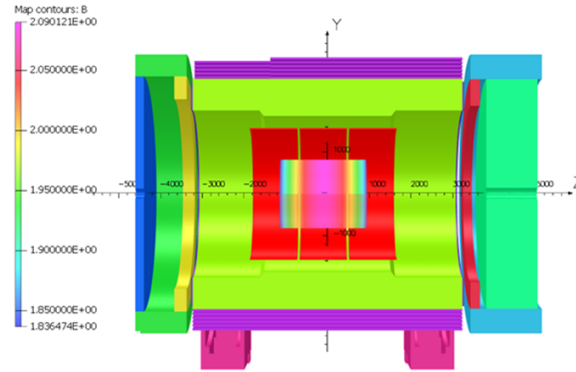


**Figure 8.32:** Field uniformity in the required area

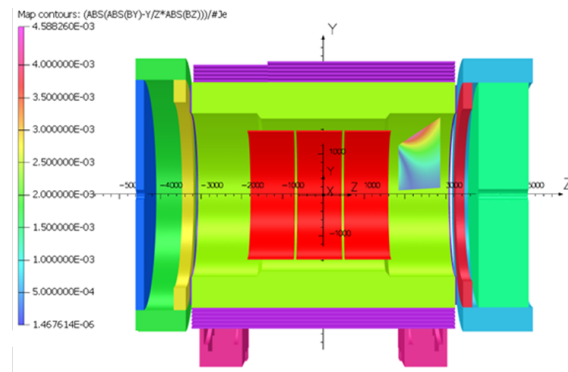


**Figure 8.33:** Projectivity in the required area

1542 are

1543 Table E summarizes the impact of axial misalignment and tolerance, Table F to table I summarizes  
 1544 the results of the radial misalignment, and table J summarizes the results of missing layer in any  
 1545 one module. It is important to notice that the total axial force  $F_z$  can change of direction respect to  
 1546 the nominal design, the tie-rods have been designed accordingly to stand these changes. The axial  
 1547 misalignment, the radial displacements of the modules or the cold mass have a negligible impact

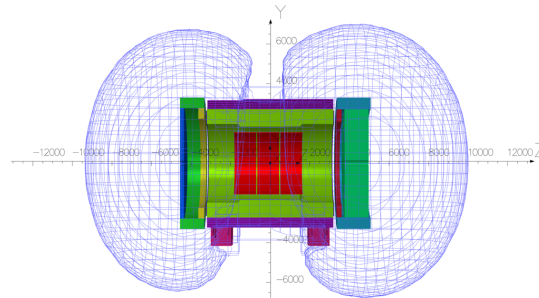


**Figure 8.34:** 5G line around the ePIC yoke. Thanks to the high level of symmetry, the field is the same in both Y and X direction

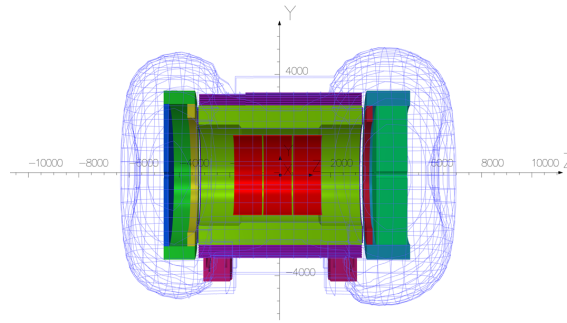


**Figure 8.35:** 5G line around the ePIC yoke. Thanks to the high level of symmetry, the field is the same in both Y and X direction

on the field quality and central field. The main concern is the forces acting on the magnet, they are of the order of the weight of the magnet itself and lower than the transportation loads. Therefore, a tolerance in the position of the coils of 5 mm is acceptable.

In order to assess the robustness of the design, different fault scenarios have been considered:

#### A) Tolerances

- Every module can be displaced along Z with a gaussian distribution  $G(\mu, \sigma) = G(0.0, 5.0 \text{ mm})$ ;
- Every module can have a different inner radius modeled with a gaussian distribution  $G(\mu, \sigma) = G(1502.5 \text{ mm}, 5.0 \text{ mm})$ ;
- Every module can have a different angle (as if the mandrel has a conical shape and not cylindrical) modeled with a gaussian distribution  $G(\mu, \sigma) = G(0.0, 0.03 \text{ deg})$ ;
- The cold mass can be displaced along Z with a gaussian distribution  $G(\mu, \sigma) = G(0.0, 10.0 \text{ mm})$ ;
- 1000 simulations are considered for this study.

#### B) Radial Misalignment

- Every module can be displaced along Y with a maximum displacement of 5.0 mm.
- The cold mass can be displaced along Y with a maximum displacement of 5.0 mm.

#### C) Impact of a missing layer

#### D) Impact of variation in permeability

#### E) Impact of misaligned yoke

- Every yoke element can be displaced along Z with a gaussian distribution  $G(\mu, \sigma) = G(0.0, 5.0 \text{ mm})$  with respect to the nominal position.
- Every yoke can have a different inner/outer radius modeled with a gaussian distribution  $G(\mu, \sigma) = G(0.0, 5.0 \text{ mm})$  with respect to the nominal position.
- 1000 simulations are considered for this study.



Parameter	Value	Unit
$\Delta$ BIP	$\pm 10$	mT
$\Delta$ Energy	$\pm 0.231$	MJ
$\Delta$ Fz	+14.4/-50.4	kN
$\Delta$ Field uniformity	$\pm 1\%$	
$\Delta$ BRCS	1.9E-4	Tm
$\Delta$ BB0ApF	$\pm 0.2$	G
$\Delta$ BQ1ApR	$\pm 0.15$	G

**Table 8.6:** Impact of axial misalignment and tolerances

Parameter	MOD1	MOD2	MOD3	MAGNET	Unit
$\Delta$ y				$\pm 5$	mm
$\Delta$ Fy	$\pm 12.3$	$\pm 14.5$	$\pm 15.3$	$\pm 42.2$	kN
$\Delta$ Fz				-32.5	kN

**Table 8.7:** Impact of radial misalignment- Cold Mass

Table 8.6 summarizes the impact of axial misalignment and tolerance, Table 8.7 to table 8.10 summarizes the results of the radial misalignment, and table 8.11 summarizes the results of missing layer in any one module. It is important to notice that the total axial force  $F_z$  can change of direction respect to the nominal design, the tie-rods have been designed accordingly to stand these changes. The axial misalignment, the radial displacements of the modules or the cold mass have a negligible impact on the field quality and central field. The main concern is the forces acting on the magnet, they are of the order of the weight of the magnet itself and lower than the transportation loads. Therefore, a tolerance in the position of the coils of 5 mm is acceptable.

In case that one layer is missing in MOD1 or MOD3, the operation of the magnet is compromised due to the high non-homogeneity of the magnetic field. Otherwise, the magnet can still respect the requirements if only MOD2 has one missing layer. The detail operating margins need to be calculated in the event of a missing layer and based on which the operating limits must be set accordingly for all materials. A variation of  $\pm 10\%$  of the BH curve in Figure 8.19 shows that the variation of the main parameters is negligible (less than 1 part per  $10^4$  for each).

The impact of axial misalignment, fabrication tolerances with respect to the nominal position, and dimensions of the yoke has been studied in the 2D model using Monte Carlo simulations. Only the fringe field was analyzed for this study. The impact of yoke misalignment is negligible with respect to the fringe field. Even with misalignment / tolerances of 15 mm, the maximum variation of the fringe field is:

- $\Delta B_{B0ApF} = \pm 1.5$  G

Parameter	MOD1	MOD2	MOD3	MAGNET	Unit
$\Delta$ y	$\pm 5$				mm
$\Delta$ Fy	-0.5	$\pm 14.5$	$\pm 15.3$	$\pm 42.2$	kN
$\Delta$ Fz	+0.7	-39.2		-32.5	kN

**Table 8.8:** Impact of radial misalignment- Module 1

Parameter	MOD1	MOD2	MOD3	MAGNET	Unit
$\Delta y$		$\pm 5$			mm
$\Delta F_y$	64.4	$\pm 14.5$	$\pm 15.3$	$\pm 42.2$	kN
$\Delta F_z$	-64.3	-39.7		-32.5	kN

**Table 8.9:** Impact of radial misalignment- Module 2

Parameter	MOD1	MOD2	MOD3	MAGNET	Unit
$\Delta y$			$\pm 5$		mm
$\Delta F_y$	27.8	$\pm 14.5$	$\pm 15.3$	$\pm 42.2$	kN
$\Delta F_z$	-27.6	-39.4		-32.5	kN

**Table 8.10:** Impact of radial misalignment- Module 3

1592 •  $\Delta B_{Q1ApR} = \pm 1.2 \text{ G}$

1593 •  $\Delta B_{RCS} = \pm 3 \times 10^{-5} \text{ Tm}$

1594 **Conductor Design** The conductor chosen for MARCO is a NbTi “Rutherford In Copper Chan-  
 1595 nel (RICC)”. A schematic cross-section of the conductor is shown in figure 8.36. The insulation  
 1596 thickness is made in fiberglass and consists of  $2 \times 0.13 \text{ mm}$  50% overlap tape. The Rutherford cable  
 1597 is soldered into the copper channel. In the analysis performed in the mechanical design, the sol-  
 1598 dered has been considered as AgSn 3.5/96.5, however, for fabrication, the solder will be defined in  
 1599 accordance with the manufacturer. An alternative could be SbSn. The solder section is expected to  
 1600 be less than 2% respect to the overall section of the conductor.

1601 The main specifications of the conductor are listed in table 8.12. Each layer will have its own  
 1602 conductor length.

1603 The worst condition the conductor can experiment are in the first turn of the L1 layer, MOD1,  
 1604 where are located the magnetic field peak  $B_{\text{peak}} = 2.672 \text{ T}$  and an expected temperature of 4.7K.  
 1605 At the nominal current, according to the Bottura scaling law and a critical current degradation of  
 1606 15% (cabling plus soldering), the expected current sharing temperature is  $T_{\text{cs}} = 7.15\text{K}$ , giving a  
 1607 temperature margin of 2.45K and a load-line margin of 46.1%. In terms of stability, the conductor  
 1608 has an enthalpy margin of  $6.7 \text{ kJxm}^{-3}$ , providing a quite large margin respect to other detector  
 1609 magnets. The conductor performances are reported in Table 8.13 and the load line plot for the

Parameter	MOD1	MOD2	MOD3	MAGNET	Unit
$\Delta \text{BIP}$	1.923	1.838	1.906	2.000	mm
$\Delta \text{Energy}$	40.610	39.679	40.590		kN
$\Delta F_z$	-90.8	-39.4	+42.3	-23.3	kN
$\Delta \text{Uniformity}$	19.3 %	8.5 %	19.3 %	12.5 %	
$\Delta \text{BRCS}$	0.040	0.035	0.030	0.035	
$\Delta \text{BB0ApF}$	13.7	14.6	14.6	15.3	
$\Delta \text{BQ1ApR}$	10.5	10.5	9.7	10.9	

**Table 8.11:** Impact of missing one layer

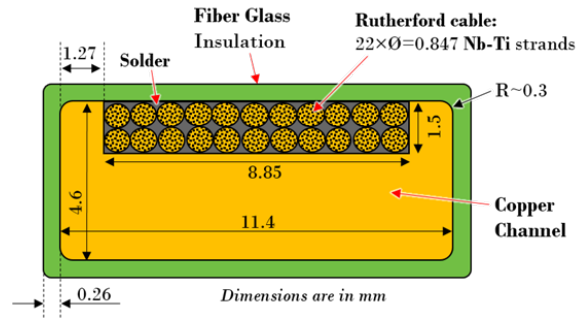


Figure 8.36: Cross-section of the RICC conductor

Parameter	Value	Unit
Strand diameter	0.847	mm
Cu/NbTi	1.3	
$I_c$ @ 3T and 4.2K	$\approx 630$	A
Filament diameter	$\approx 30$	$\mu\text{m}$
Filament twist pitch	30	mm
NbTi strands	22	
Transposition pitch	50	mm
Width	6.8	mm
Thickness	1.26	mm
Copper channel section	39.1	$\text{mm}^2$
Insulated conductor section	61.1	$\text{mm}^2$
Nominal current	3924	A
RRR conductor	$\approx 100$	
$\sigma_{0.2\%}$ @ 293 K	$\approx 165$	MPa
Unit length	1.05	km
Total length	18.9	km

Table 8.12: Caption

reference case study  $B_0=2\text{T}$  is shown in Figure 8.37, The working point (green rectangle) is shown, corresponding to a current sharing temperature of 7.15 K.

**Mechanical Design** The mechanical design has been performed using 2D and 3D finite element models, respectively in Cast3m and ANSYS. Material properties and coil pack homogenization. For both models, a certain level of homogenization of the material properties for the coil pack has been assumed. For the 2D model the cable has been homogenized, while for the 3D all the coil pack has been. The homogenization has been calculated using ANSYS Workbench 2023 R2 with the “Material Designer” module.

The 2D mechanical analysis was conducted in Cast3m using its magneto-static solver to calculate the Lorentz forces and its mechanical solver to analyze their impact on the magnet structure. The magnetic model includes the iron yoke, the mechanical one does not. A schematic of the mechanical model geometry is shown in Figure 8.38. A zoom of one of the two areas where the 3 modules are assembled is shown. The iron yoke is not shown in this model. Each turn is modeled, with its own

Parameter	BIP = 1.5 T	BIP = 1.7 T	BIP = 2.0 T	Units
Current In	2942	3335	3924	A
Top	4.7	4.7	4.7	K
Bpeak	2.003	2.271	2.672	T
T margin	3.06	2.82	2.45	K
LL margin	59.6%	54.2%	46.1%	
In/Ic	17.9%	22.1%	29.3%	

Table 8.13: Caption

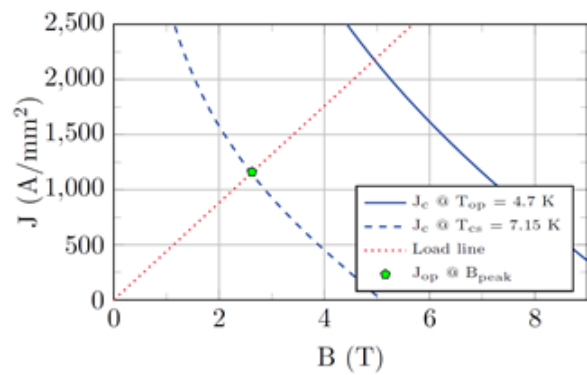


Figure 8.37: Jc curve @4.7 K, load line and load line margin

1623 cable, copper channel and insulation. As contact conditions, for each module, the coil, the ground  
1624 insulation and the mechanical structure are bonded together to simulate the impregnation. The  
1625 coil wedges are bonded to mechanical structure and have a sliding contact with possible separation  
1626 with the coils and with the inter-module wedges.

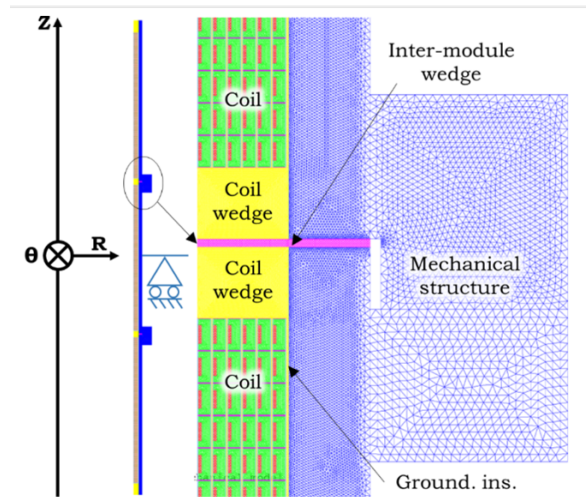


Figure 8.38: 2D axisymmetric mechanical model including the coils and the mechanical structure

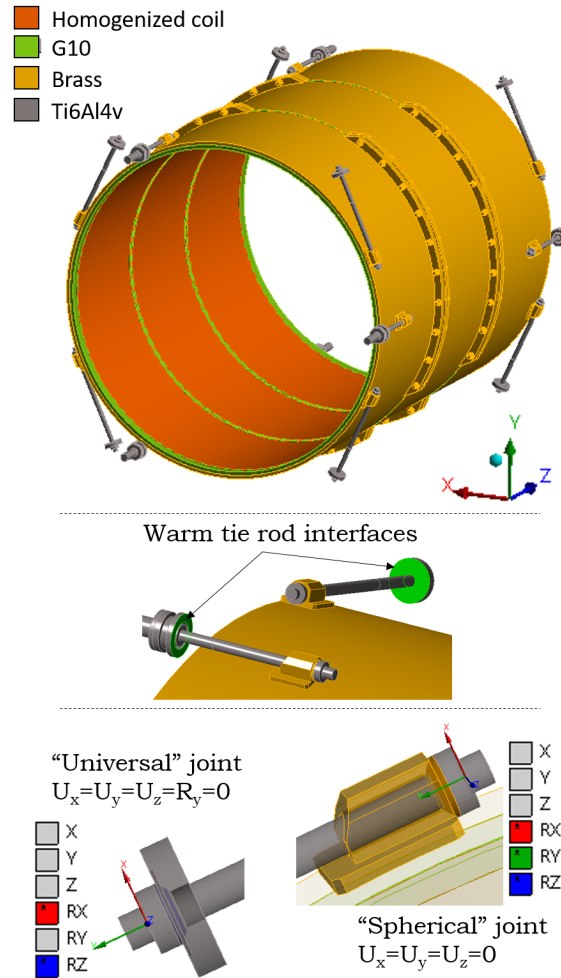


Figure 8.39: 3D model geometry

1627 The 3D mechanical analysis was conducted in ANSYS Workbench, importing the magnetic force  
 1628 density from the OPERA 3D model. Figure 8.39 (a) 3D model geometry and materials, b) zoom on  
 1629 the tie-rods and their warm interfaces and c) the tie-rods ball joints with their boundary conditions)  
 1630 shows the geometry of the model, the tie-rods warm interfaces and the ball joints definition with  
 1631 their boundary conditions.

1632 The acceptance criteria for the design are given in Table 8.14. The main principle behind is to  
 1633 have an equivalent Von Mises stress and a shear stress in each component below the 2/3 of the  
 1634 corresponding elastic limits for each material. For what concerns the conductor, a minimum elastic  
 1635 limit of 165MPa is imposed to the manufacturer. This can be easily achieved through cold-work  
 1636 on the copper channel. For the shear limit on G10, a factor of 0.4 has been assumed as acceptance  
 1637 criteria in order to be more conservative.

1638 Each component of the cold-mass fulfills the acceptance criteria. The results related to the Von  
 1639 Mises peak stress and shear peak stress between the 2D and 3D models are remarkably close es-  
 1640 pecially for the coils. The effect of tie-rods is notable in 3D for the mandrel, which has a VM peak  
 1641 stress of 280 MPa (106 MPa for the 2D). The reason is the local stress induced by the tie-rods on

295 K			
Material	Properties	Reference Value (MPa)	Acceptance criteria (MPa)
Coil	Yield strength	165	110
	Shear strength	15	10
G10	Yield strength	257	103
	Shear strength	42	17
Brass7030	Yield strength	413	275
	Shear strength	220	88
Ti6Al4V	Yield strength	1030	687
4.5 K			
Coil	Yield strength	200	133
	Shear strength	72	24
G10	Yield strength	496	198
	Shear strength	73	29
Brass7030	Yield strength	517	345
	Shear strength	264	106
Ti6Al4V	Yield strength	1693	1129

**Table 8.14:** Materials acceptance criteria

COOL-DOWN				
Material	Properties	Reference Value (MPa)	Acceptance criteria	
Coil	Von Mises Peak Stress	55	70	
	Shear Peak Stress RZ	14	11	
G10	Von Mises Peak Stress	54	94	
	Shear Peak Stress RZ	23	21	
Brass7030	Von Mises Peak Stress	105	300	
	Shear Peak Stress RZ		16	
Ti6Al4V	Von Mises Peak Stress	NA	761	
COOL DOWN + ENERGIZATION				
Coil	Von Mises Peak Stress	81	78	
	Shear Peak Stress RZ	17	12	
G10	Von Mises Peak Stress	84	77	
	Shear Peak Stress RZ	23	18	
Brass7030	Von Mises Peak Stress	106	280	
	Shear Peak Stress RZ	NA	20	
Ti6Al4V	Von Mises Peak Stress	NA	839	

**Table 8.15:** Materials acceptance criteria

1642 their pads. Due to the lack of space caused by the Barrel Yoke, the tie-rods cannot be made to com-  
 1643 pensate totally the thermal shrinkage during the cool-down, inducing a higher stress than what  
 1644 could be forecast. However, thanks to the fact that the mandrel is in brass, this is not an issue. A  
 1645 summary of the results for cool-down and energization is shown in Table 8.15.

Parameter	Value	Unit
Ramping rate	1	A/s
Power dissipated at $t = +\infty$	3.642	W
Eddy current at $t = +\infty$	-1015.3	A
Resistance ( $P/I^2$ )	3.516	$\mu\Omega$
Mutual inductance	3.570	mH
Inductance of the mandrel	2.346	$\mu\text{H}$
Coupling coefficient btw mandrel and coils	0.964	

Table 8.16: Ramp up/down results

**Transient Analysis and Quench Protection** The transient analysis was performed for the magnet during different ramp-up and ramp-down scenarios. Since the mandrel is made from Brass 70/30, it plays a noticeable role during the transients of the magnet, in particular during ramp-up / ramp-down, fast discharge, and quench. Its magnetic behavior has been simulated using OPERA. The ramping rate (up and down) of the magnet is 1.0 A/s, which is a compromise found between ramping the magnet in approximately one hour and not overheating it at the same time due to the mandrel dissipated power. This case has been used to define the main magnetic specifications of the mandrel, the results are given in Table ??.

The impact of the flanges is significant, showing that the current tends to pass through them between the adjacent modules.

Fast discharge is the worst case for induced eddy currents in the mandrel due to the dump resistor of the circuit, the  $dI/dt$  being the highest at the beginning of the discharge. As for the quench protection, for the fast discharge case the following circuit (Figure 8.40) has been considered:

The dump resistance  $R_d$  has been determined limiting the maximum voltage across the magnet to 1000 V. In case of fast discharge, the mandrel behaves as shown in figure 8.41. The current in the mandrel can increase up to 165 kA in 0.3 s; a vertical force of  $F_y = -22$  kN acts on the mandrel, due to the asymmetric distribution of the eddy currents around the flanges. Such force is well below the loads that the magnet can encounter during transportation, and it is well compensated by the tie-rods. The total time needed to fast discharge the magnet is 120 s.

**Quench Analysis** Both a single coil analytical quench analysis (more conservative) and a detailed FE quench analysis in COMSOL have been performed to design the quench protection. In this section only the detailed FE quench analysis is described. The quench analysis has been conducted using COMSOL, with a coupled 2D axisymmetric FE model and 1D model to consider the heat propagation—the first for the transverse propagation and the second for the azimuthal propagation. The logic structure of the model is shown in Figure 8.42. Once the geometry, material properties and operational conditions are defined, the magnetic model is solved to determine the resistivity ( $\rho$ ) of each element (with respect to the magnetic field and temperature) and thermal conductivity ( $k$ ). Once the magnetic field, the temperatures and materials properties are defined over the domain, the model calculates the critical current density  $J_c$  and solves the coupled thermal and electric model associated to the geometry. The model considers the full geometry of the magnet, and it defines every turn with details of the conductor. The conductor is represented by a homogenized material (homogenized cable and copper stabilizer). The insulation is modelled separately to consider its own material properties. A representation of the geometry is shown in Figure 8.43.

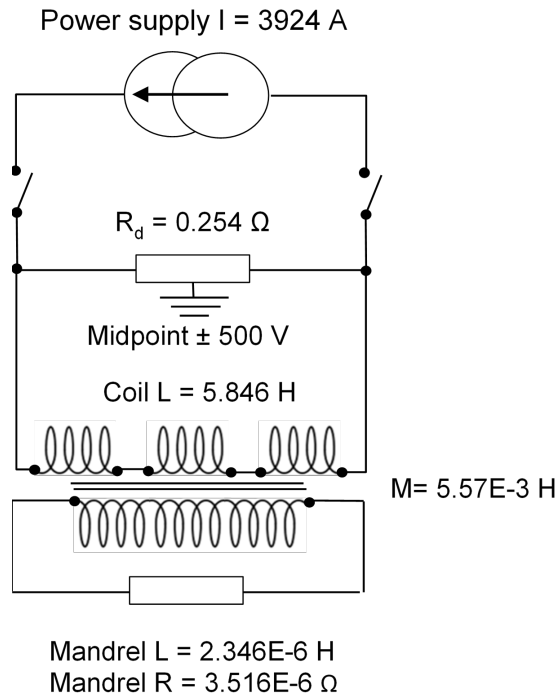


**Figure 8.40:** Scheme of the electric circuit of the MARCO magnet

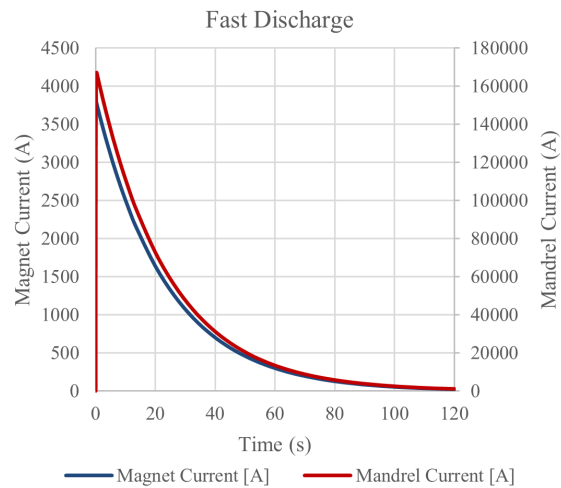


**Figure 8.41:** Current flowing in the magnet and in the mandrel during a fast discharge



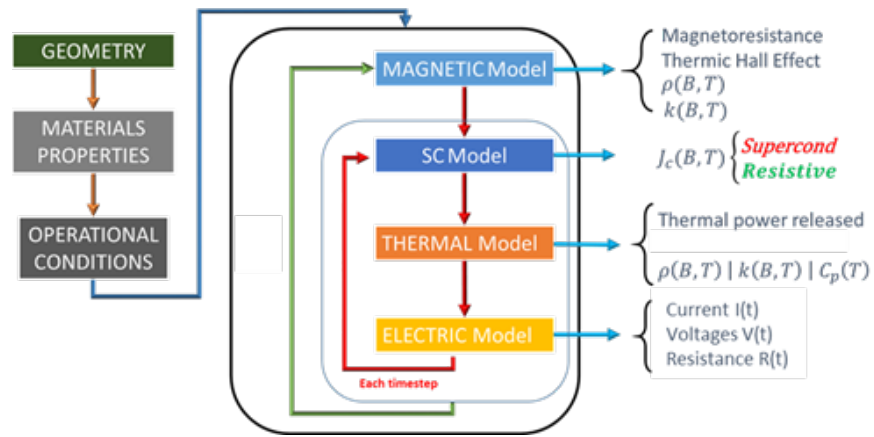


Figure 8.42: Logic structure of the COMSOL quench model

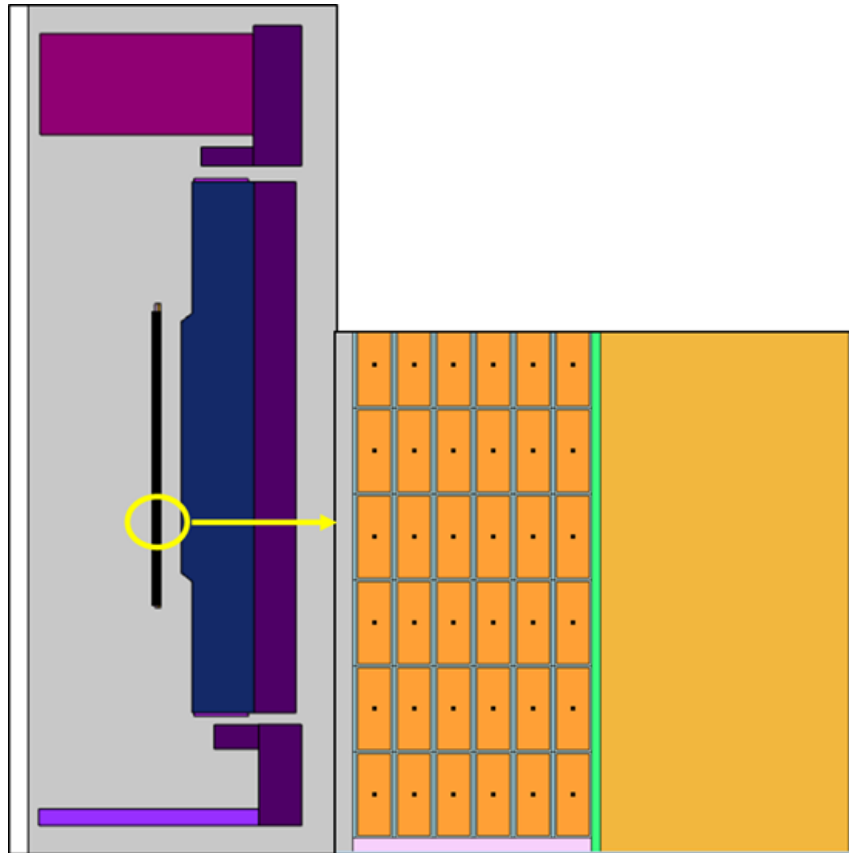
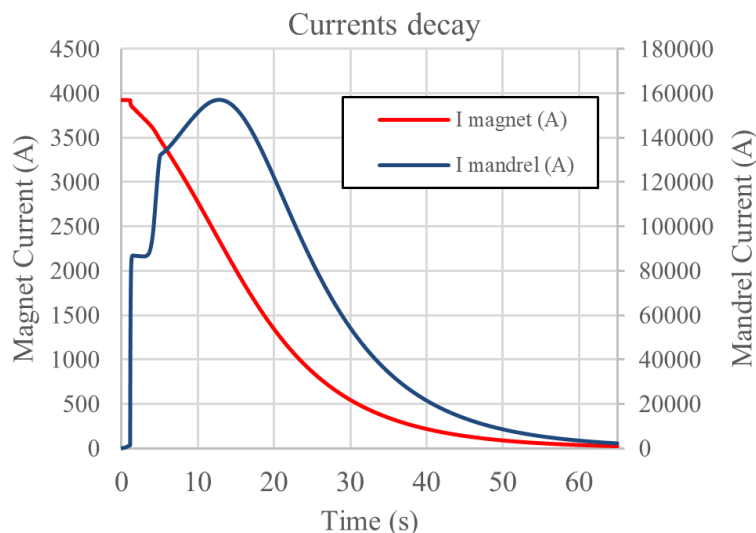


Figure 8.43: Model used in COMSOL



**Figure 8.44:** Current decay in the coils and in the mandrel

1680 The material properties are from Cryocomp. The thermal hall effect and magnetoresistivity in cop-  
 1681 per are considered. The quench starts at the bottom angle of MOD1, where the peak magnetic field  
 1682 is located. The case studied is the one at the nominal current (3924 A) and maximum nominal tem-  
 1683 perature (4.7 K). Once the quench starts and after that the resistive tension reaches 1 V, a validation  
 1684 time of 1 s is needed to validate the quench and open the breakers to activate the dump resis-  
 1685 tance. A dump resistance of  $0.254 \Omega$  is used to limit the maximum voltage to 1000 V. The magnetic  
 1686 model is solved by COMSOL with the same geometry and material properties used in the OPERA  
 1687 model. The superconducting model calculates at every turn to determine if the conductor is in the  
 1688 superconductive state, in the resistive state, or in the current sharing state. It uses the Bottura fit  
 1689 parameters used to design the MARCO conductor to calculate the critical current density in the  
 1690 cable. A simple model of current redistribution is considered: if the critical current  $I_c \geq 0$  and  $I_c \leq$   
 1691  $I(t)$ , where  $I(t)$  is the current flowing through the cable, the ohmic power dissipated is smoothed by  
 1692 an inverse sigmoid.

1693 The thermal model solves the heat transfer equations in 2D associated with every node of the model  
 1694 and the 1D propagation along the length of the conductor according to the computed azimuthal  
 1695 quench velocity. The ohmic power releases at every turn when quenched is considered starting  
 1696 at the node in the center of the conductor geometry. The electrical model calculates the resistivity  
 1697 and voltage associated with every turn and the eddy currents induced in the mandrel during the  
 1698 quench current decay.

1699 In the nominal case scenario, the magnet is protected by the dump resistance  $R_d$ . Due to the high  
 1700 inductance, the current decay is very slow and it takes 65 s to reach less than 1% of the original  
 1701 current in the magnet. The time constant of the quench circuit is 20.31 s.

1702 Figure 8.44 shows the current decay in the coils and the eddy current in the mandrel. Thanks to the  
 1703 good magnetic coupling between the coils and the mandrel, the mandrel is subjected to the high  
 1704 eddy current, which generates the quench-back in the coils as shown in Figure 8.45.

1705 The resistive coils voltage profile during quench shows no issue; the maximum voltages inside the  
 1706 coils are around 1000 V, the acceptable criterion defined for the magnet as shown in Figure 8.46.

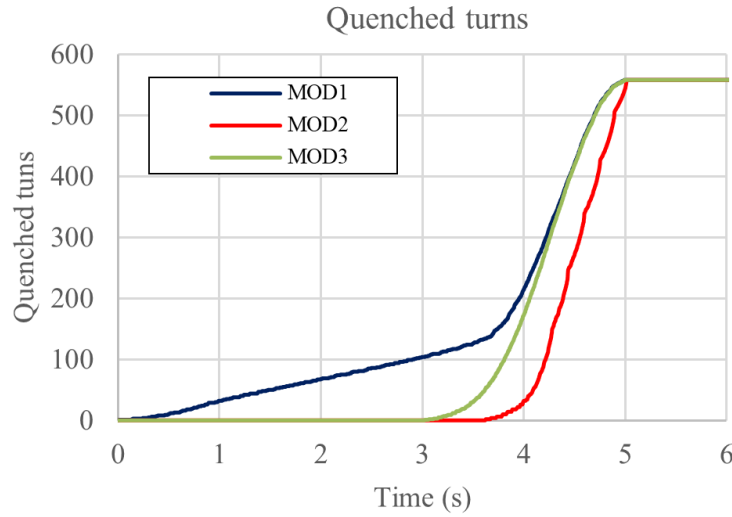


**Figure 8.45:** Number of quenched turns as a function of time in the three different modules

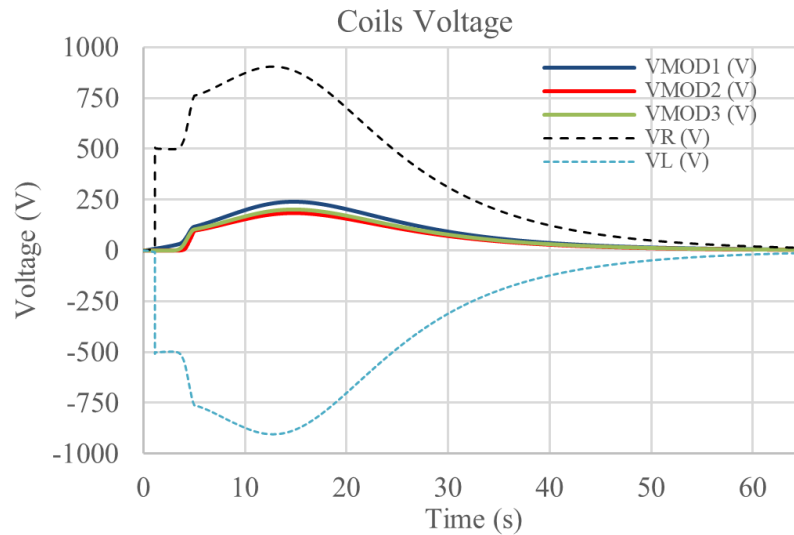


**Figure 8.46:** Resistive coil voltage as a function of time for the three modules

1707 The total power dissipated in the circuit is shown in Figure 8.47. The dump resistance has a peak  
 1708 power of 3.8 MW; the coils, 1.5 MW; the mandrel, 86 kW. The maximum temperature (hotspot)  
 1709 reaches during quench is 96 K shown in Figure 8.48, showing no issue for the structural integrity of  
 1710 the magnet. The hotspot is located at the quench starting point as shown in Figure 8.49. Since the  
 1711 quench starts in MOD1 (blue line), the corresponding hotspot temperature is higher than the ones  
 1712 in the other two modules. The difference between MOD2 and MOD3 (both quench thanks to the  
 1713 quench-back by the mandrel) in maximum temperature is due to the different magneto-resistance  
 1714 the two modules have.

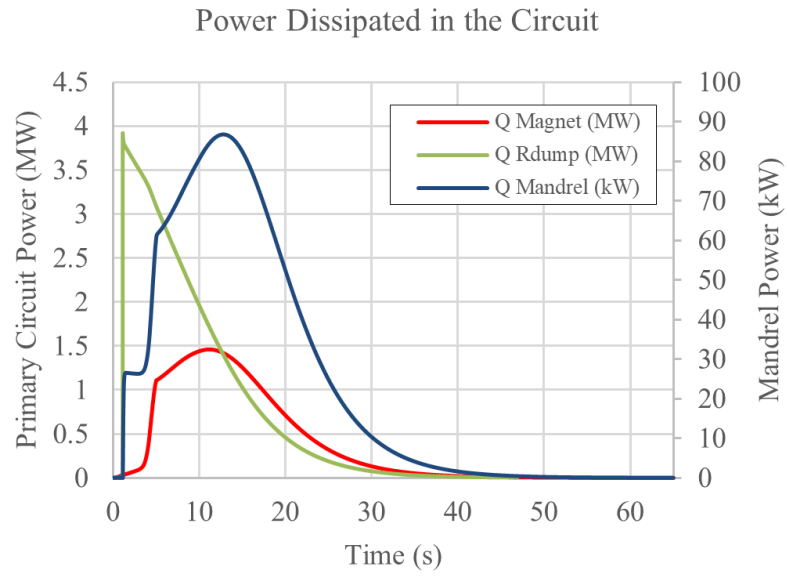


**Figure 8.47:** Power dissipated in the primary and secondary circuit

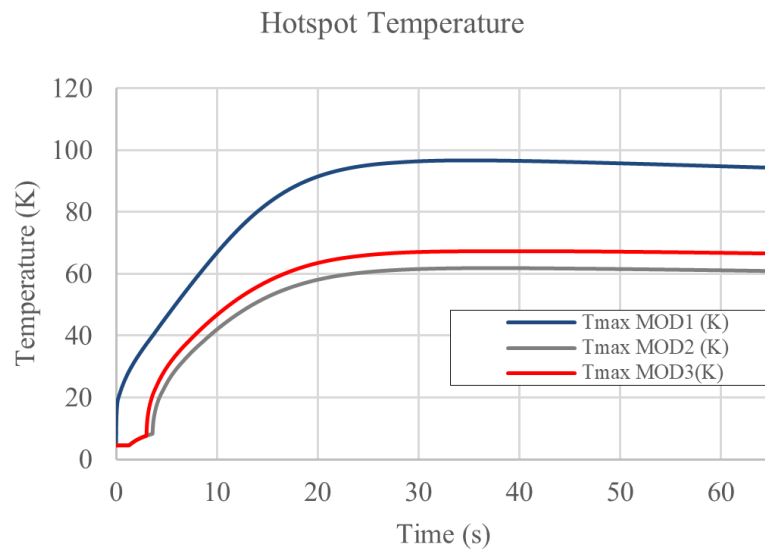


**Figure 8.48:** Hotspot temperature in the three modules of the magnet

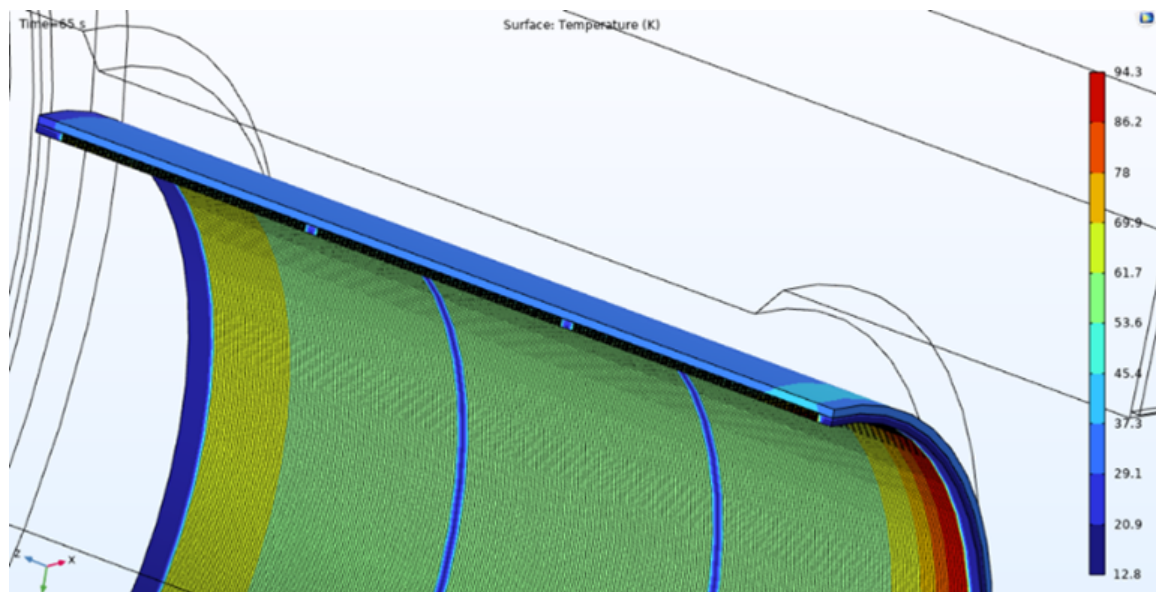


**Figure 8.49:** Temperature distribution on the coils and mandrel after 65s from quench

**Cryogenic Design** The MARCO magnet is a conduction-cooled magnet and it is indirectly cooled using the cooling tubes on the outside of the brass mandrel. The internal cryogenic system involves a cold mass, which consists of a mandrel and coils with two 28-tube exchangers of the thermosiphon soldered on the mandrel, a phase separator on top used also as a storage tank of liquid helium at 4.55 K, and one cryogenic chimney that holds the helium vapor cooled current leads and connect the phase separator to the cold mass. The solenoid is equipped with 5 cold valves with warm actuators and 3 warm valves (given in Table 8.17). It also has a thermal shield to insulate the parts at 4.5 K; the thermal shield is cooled by helium gas between 45 K and 65 K. The internal cryogenic system is connected to the BNL refrigeration supply through flexible lines. The cryogenics flow chart is shown in Figure 8.50.

The solenoid is cooled by a two-phase flow helium thermosiphon. Twenty-eight exchanger tubes (2x5 tubes for module 1, 2x4 tubes for module 2, 2x5 tubes for module 3) are soldered on the brass mandrel. Liquid helium is stored in the phase separator tank and flows through valve FV2 down in the downward branch to supply 6 distributors (bottom manifolds). This flow of helium is heated up in the exchanger tubes, collected by 6 collectors (top manifolds), and goes back to the tank through 3 return lines. Three heaters (10 W maximum each) are placed on the return lines in case that there is not sufficient heat load on the cold mass. Figure 8.51 shows the piping schematics of thermosiphon. The return lines go back in the phase separator tank at a higher level than the feeding line which is connected directly to the bottom of the tank, the difference of height is the riser. The risers make the return two phase flows pour out the return tubes above the liquid surface area in the phase separator tank. When the level of liquid is zero the tank is empty, when it is nominal it is equal to 0.3 m whereas the risers are 0.4 m high.

There are two thermosiphon piping systems. One is primary and one is spare. If the primary has a leak, it is possible to use the spare one by disconnecting the primary piping in the vacuum vessel of the phase separator tank and connecting the spare piping. The heat exchanger tubes are made of copper. They have an outer form of a square (14 mm x 14 mm) and an inner diameter of 8 mm. They are soft soldered onto the brass mandrel. At their extremities, stainless steel junction tubes (jumpers) are brazed inside the copper tubes, and these junctions is welded to the stainless-steel

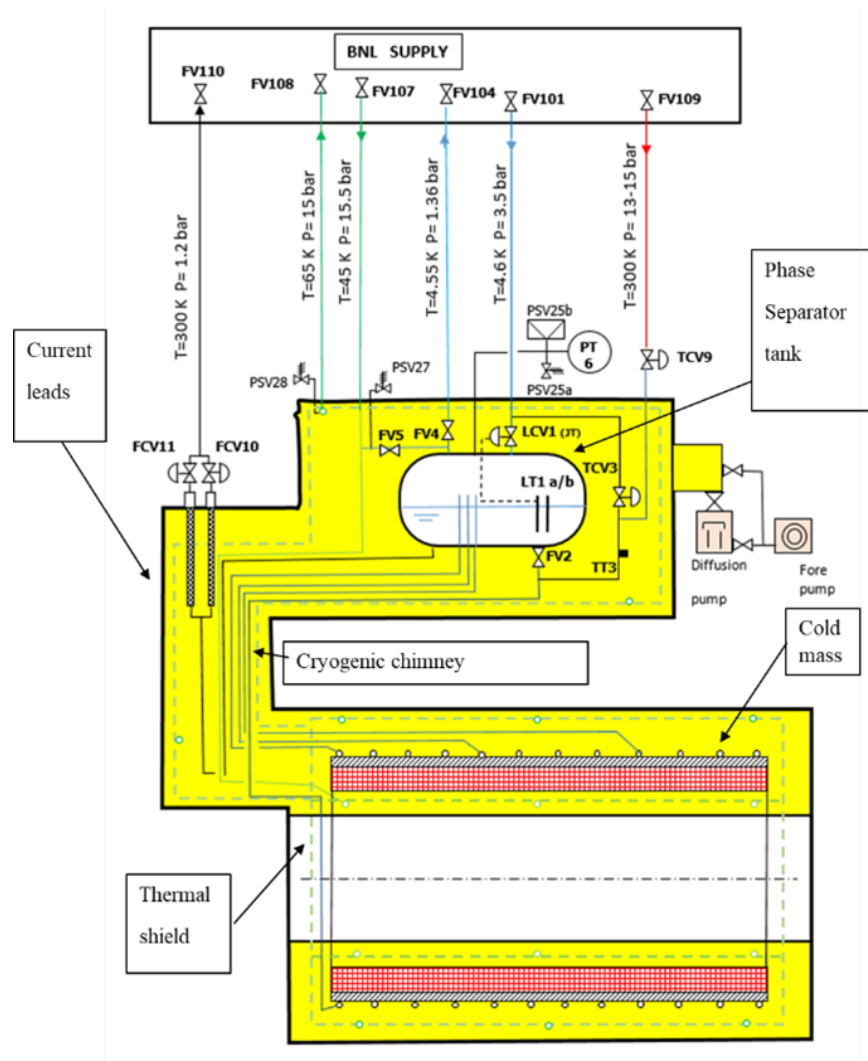


**Figure 8.50:** Cryogenics flowchart of the MARCO solenoid

manifolds. Figure 8.52 and 8.53 show in details how the thermosiphon is designed.

The outlet pressure of the return lines in the phase separator tank must be the same as the pressure inside the tank, defining thus the mass-flow rate and then the vapor quality. The case under consideration is the shut-down of the refrigerator when the liquid helium level is dropping in the phase separator tank. The limit is where the level is equal to zero and thus the tank is empty. This is the limiting case for the thermosiphon because the differential height between the downward branch and the return lines (upward branch) is maximum and equal to the riser (0.4 m). The riser is needed to ensure that the two-phase flow goes back to the phase separator tank above the liquid helium surface in any case. The diameters ( $\varnothing 8$  mm) of the exchanger tubes of the supply and return lines, and the diameter ( $\varnothing 30$  mm of manifolds) have been chosen to lower the frictional pressure drop. The main pressure drop is in the riser due to the gravity. In addition, the manifolds are almost isobaric as their pressure drop is less than 1 Pa. Several heat loads scenario has been considered for the thermosiphon, according to the possible heat loads (given in Table 8.18) present inside the

Name	Description
FV101	BNL supercritical helium shut-off valve
FV104	BNL vapor helium shut-off valve
FV107	BNL inlet helium for thermal shield shut-off valve
FV108	BNL outlet helium for thermal shield shut-off valve
FV109	BNL inlet warm helium for cool-down shut-off valve
FCV110	BNL outlet helium for current leads shut-off valve
PSV27	Inlet helium for thermal shield safety valve
PSV28	Outlet helium for thermal shield safety valve
PSV25a	Relief valve for the phase separator tank at 4.5 bar abs. (quench)
PSV25b	Burst disc for the phase separator tank at 6 bar abs. (vacuum loss)
PT6	Pressure measurement of the phase separator tank
FCV10	Flow control valve for current lead a
FCV11	Flow control valve for current lead b
TCV9	Warm temperature control valve for cool-down
TCV3	Cold temperature control valve for cool-down
TT3	Temperature of the mixed gas coming from TCV3 and TCV9 for the cool-down
FV2	Feeding shut-off valve of the thermosiphon
FV4	Vapor helium shut-off valve
FV5	Bypass shut-off valve for vapor helium into the shield in case of refrigerator shut-off
LCV1	Level control valve for the liquid helium in the tank (Joule Thomson valve)
LT1a/b	Liquid helium measurement in the tank with spare

Table 8.17: List of cryogenic valves

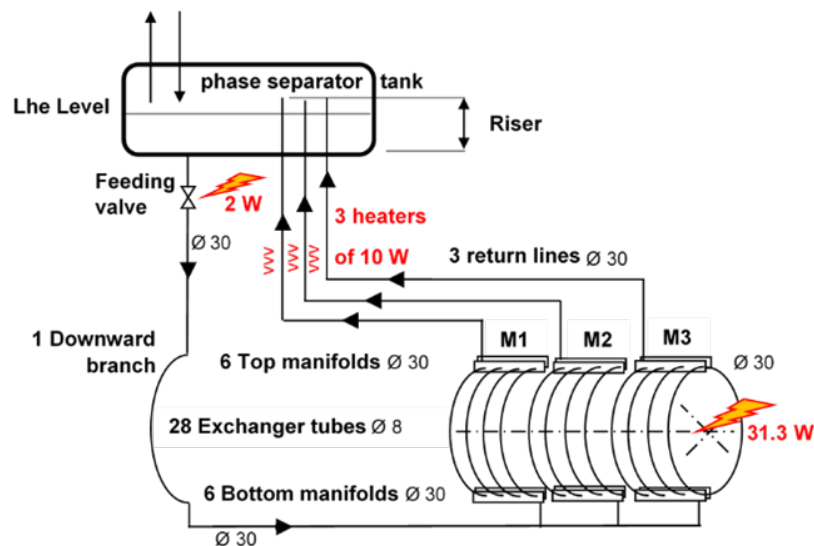
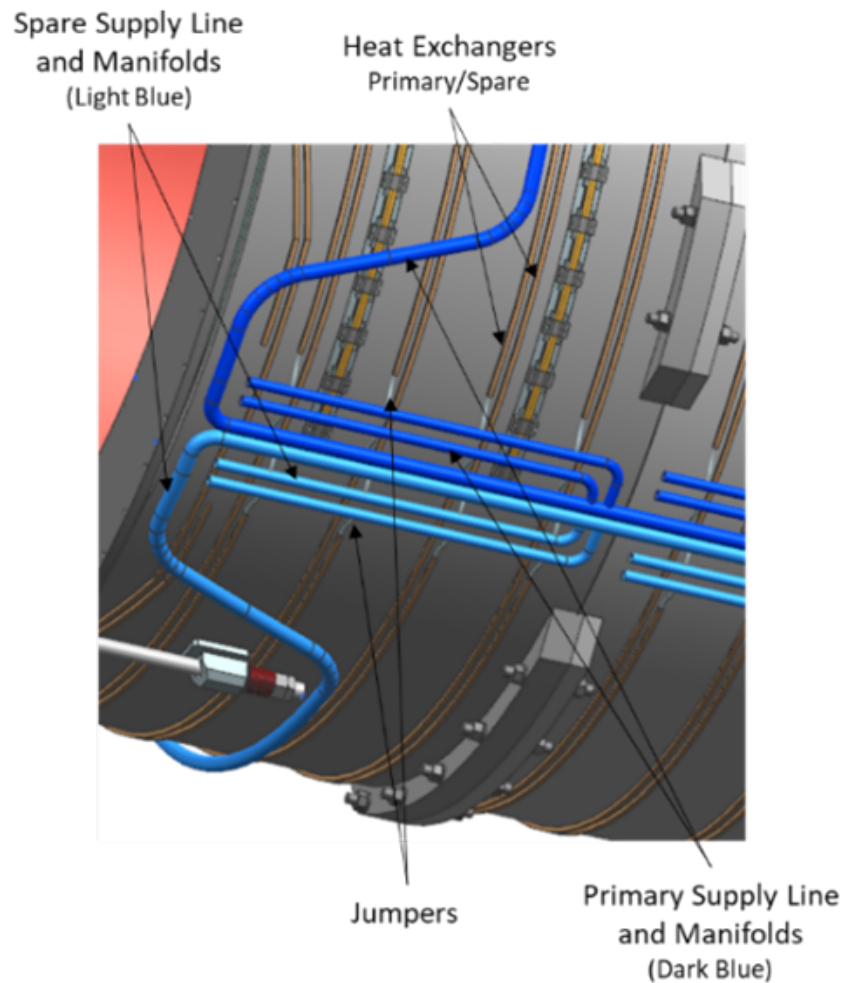


Figure 8.51: Schematics of the thermosiphon system



**Figure 8.52:** Primary and spare tubes of the thermosiphon heat exchanger

1756 cryostat. For any of these cases, the vapor quality is below 10% and the speed of the He in the  
 1757 return line is always greater than 0.1 m/s, assuring the proper operation of the thermosiphon.

1758 The thermal shield of the cold mass is made of 3 x 4 internal panels, 3 x 4 external panels, and  
 1759 end plates. It is made of Al 3003 with a thickness of 5 mm. The tube, which connects the BNL  
 1760 flexible supply line and the thermal shield piping, has an inner diameter of 10 mm and an outer  
 1761 square form of 14 mm x 14 mm. This tube passes through the phase separator vacuum vessel and  
 1762 the cryogenic chimney without cooling any surface; it goes directly to the inner part of the cold  
 1763 mass thermal shield and supplies, in parallel, the left circuit and the right circuit. The left and right  
 1764 external shields are then cooled afterwards. The end plates are indirectly cooled by connecting with  
 1765 them. The two half flows are joined together at the inlet of the cryogenic chimney and then cools  
 1766 the thermal shield in the cryogenic chimney. Like the thermosiphon system, there are two cooling  
 1767 circuits for the thermal shield. One is the primary and the other is the spare.

1768 The helium phase separator is on top of the detector, embedded in the iron and connected to the  
 1769 magnet assembly through the cryogenic chimney shown in Figure 8.54. In addition to the cryo-



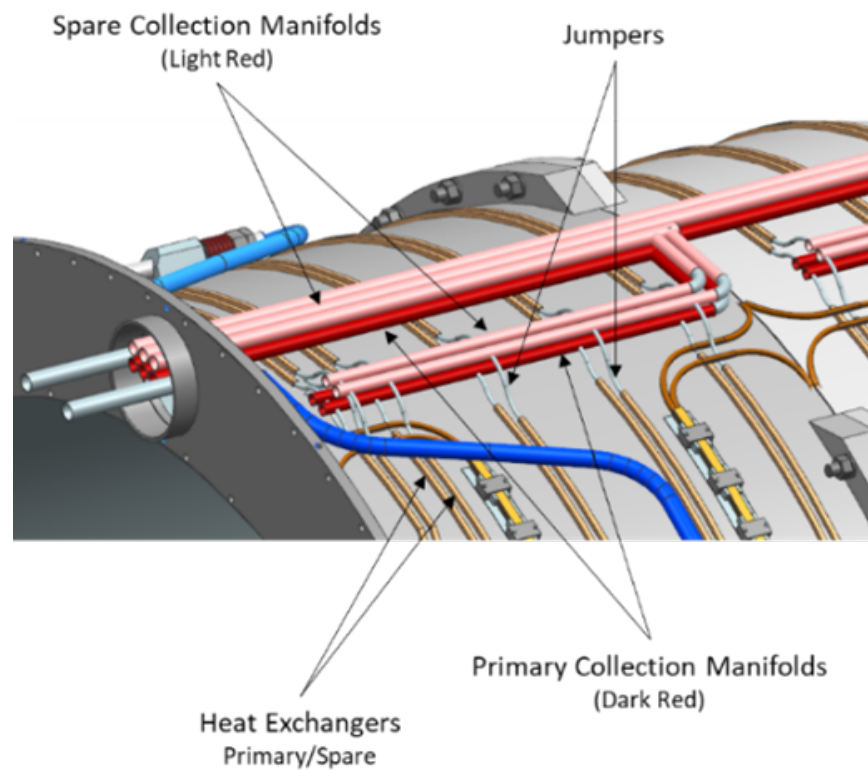


**Figure 8.53:** Primary and spare piping on top of the mandrel

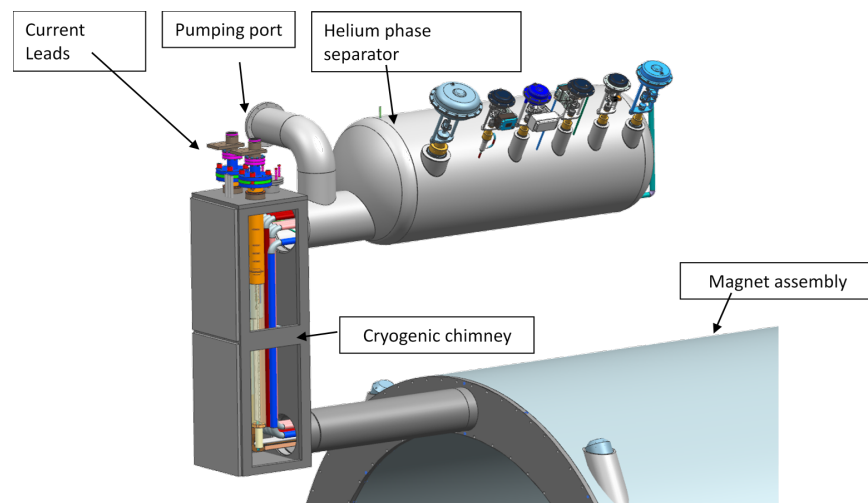


**Figure 8.54:** Helium phase separator and cryogenic chimney overview.

Cold mass heat load at zero current	25	W
Heaters (off)	0	W
Total mass flow rate	25.4	g/s
Vapor quality	6 %	
Flow speed in the return lines	0.13	m/s
Cold mass heat load during ramp-up/down	30	W
Heaters (off)	0	W
Total mass flow rate	29.1	g/s
Vapor quality	6.2	
Flow speed in the return lines	0.14	m/s
Cold mass low level heat load	10	W
Heaters (on)	20	W
Total mass flow rate	18.3	g/s
Vapor quality	9.8	
Flow speed in the return lines	0.10	m/s
Cold mass high level heat load	60	W
Heaters (off)	0	W
Total mass flow rate	45.6	g/s
Vapor quality	9.8	
Flow speed in the return lines	0.24	m/s

Table 8.18: Thermosiphon load cases

genic lines, the cryogenic chimney also houses the helium vapor cooled current leads. A vacuum pumping port is located between the cryogenic chimney and the phase separator vacuum vessel. The total volume of the inner helium vessel is 284 L; the liquid helium buffer used in normal operation is 110 L which is the volume of liquid needed to ramp down the current at 1 A/s in case of a refrigerator shut-down the liquid helium level in the tank is then 0.3 m. The set pressure of the burst disc is 6 bar. The protection against overpressure is studied according to European regulations, for the helium circuits including the phase separator (inner vessel): EN21013-3 and for the vacuum vessel (outer vessel): EN 13458-2.

The cryogenic heat loads are calculated for all the components of the cryogenic system and they are listed in Table 8.19 and the heat load budgets at 4.5 K and 65 K are given in Table 8.20.

The maximum heat load (when ramping up the current) at 4.5 K is 57 W. The total heat load budget on the thermal shield is 600 W.

**Instrumentation and Controls** In order to operate and monitor the MARCO solenoid an extensive instrumentation plan have been conceived. The instrumentation covers the electrical measurements, the cryogenics data measurements as well as the mechanical ones. The electrical measurements gather the voltage measurements and the current measurements. The cryogenics ones collect the temperature data, the pressure, the liquid helium level, the He mass flows and the vacuum level. Finally, the mechanical measurements concern especially the tie-rods whose stress is

Heat load source	Value	Unit
Tie-rods for the cold mass @4.5K	3.68	W
Tie-rods for the cold mass @65K	79.2	W
Tie-rods for the phase separator tank @4.5K	0.48	W
Tie-rods for the phase separator tank @65K	12.8	W
Cold valve LCV1 @ 4.5K	0.31	W
Cold valve FV2 @ 65K (@4.5K)	10 / (3)	W
Cold valve TCV3 @ 4.5K	0.36	W
Cold valve FV4 @ 65K (@4.5K)	5 / (1.4)	W
Cold valve FV5 @4.5K	0.31	W
Bellows for valve PSV25a / burn disc PSV25b @4.5K	0.19	W
Flexible lines @ 4.5K	2	W
Thermal shield supports @ 55K	32	W
Heat radiation (radiation flux = 0.3W/m <sup>2</sup> ) @4.5K	23.1	W
Heat radiation (radiation flux = 5 W/m <sup>2</sup> ) @65K	420	W
Conductor junctions (1.0n $\Omega$ each)	0.32	W
Hysteresis from NbTi filaments	0.8	W
Eddy current in strand copper (ramp-up/down)	0.2	W
Eddy current in the mandrel (ramp-up/down)	3.7	W
Helium vapor cooled current leads	12	W

**Table 8.19:** Heat load summary

4.5 K		
Element	Value	Unit
Cold mass at zero current	25	W
Cold mass at ramping up/down (1 A/s)	30	W
Phase separator tank	10.2	W
Current leads	12	W
Margin	5	W
45 K - 65 K (loads on thermal shields)		
Thermal radiation	420	W
Support conduction	32	W
Thermal intercept	107	W
Margin	61	W

**Table 8.20:** Heat Load budget

1788 monitored during all the magnet life.

1789 Voltage Taps: The electrical instrumentation scheme has been done based on the magnet protection  
 1790 analysis and choices. As the magnet will be protected by a Main Safety System (MSS) the voltage  
 1791 will be monitored for each coil segment with a redundancy. The quench detector will be made by  
 1792 making the difference between two segments of the coil having the same inductance, allowing to  
 1793 remove the inductive voltage and read only the resistive voltage. This will permit the MSS to detect  
 1794 the transition time and protect the magnet by opening the contactor to discharge the magnet on the  
 1795 dump resistor. With the redundancy, 50 voltage taps shall be positioned in the magnet giving 25

differences of potential to measure and send to the MSS and acquisition system. These measured values can be combined in 16 quench detectors with 12 for the coils, 2 for the current leads and 2 for the busbars (one per current lead and one per busbar). For the coils the voltage threshold has been set to 0.1 V to 1 V in the simulation with at least one second of validation time. For the busbars, the voltage threshold is smaller and have been set to 10 mV with a validation time of 10 ms. Finally, the voltage threshold of the current leads shall be smaller than the maximum operating voltage in the current leads. Two DCCTs shall be position to monitor and regulate the current. The first one between the power supply and the contactor shall be used for the power supply regulation while the second one be-tween the coil and the dump resistor will be used to monitor the current in case of quench or contactor opening.

**Cryogenic Instrumentation:** For the cryogenic instrumentation plan, different type of sensors will be used. The first ones are the temperature sensors whose are divided in two types, the PT100 for all the temperature above 50 K i.e., for the thermal screen and the CERNOX® sensors used for all the 4.5 K measurements. For the PT100, 10 will be placed on the thermal screen while 6 will be placed on the current leads. Concerning the CERNOX, 12 will be distributed all over the magnet and shell and 6 distributed between the bus-bars, the phase separator, the thermosiphon inlet and outlet. Completing the thermal sensors flow meters (2 for the current leads, 2 to 4 for the thermosiphons inlet and outlet and 2 for the 50 K shield inlet and outlet) will be used to monitor the cryogenic operation as well as 2 liquid helium level gauges, 2 manometers and 2 vacuum gages.

**Mechanical sensors:** To monitor the tie-rods preload during the magnet assembly in its cryostat, the transport, the mag-net cool down and energization, it is planned to use load cells placed at the end of each tie-rods. These load cells shall be dimensioned adequately pending the stress analyses made during the manufacturing design phase.

**Summary** MARCO will be a unique solenoid for detector magnets, it will use a Rutherford in Copper Channel Conductor (RICC) and a mandrel in brass 70/30, it will meet the stringent criterion on the transparency typical of every detector magnet.

### 8.3.3 Tracking

The tracking system occupies a volume at the center of the ePIC detector with a radius of  $R = 75\text{cm}$  and a length of  $-165\text{ cm} < z < 200\text{ cm}$  along the beam axis. It consists of a combination of the Silicon Vertex Tracker (SVT) based on thinned Monolithic Active Pixel Sensors (MAPS), at its core that are surrounded by outer Micro-Pattern Gas Detectors (MPGD) along with Time-of-Flight layers based on AC-LGAD technology in the barrel and forward acceptance regions which also provide hit points with good resolution. The system provides tracking for charged particles over a wide pseudo-rapidity of  $-3.5 < \eta < 3.5$  and momenta larger than 0.5 GeV. The SVT consists of five barrel layers and two arrays of five disks on either side of the beam collision region. The SVT has low mass and high-granularity, thereby ensuring high spatial resolution. The outer MPGD and AC-LGAD layers provide additional space points. They are configured such that their hits can be used to form tracklets and their comparatively fast timing improves noise and background rejection. Detailed descriptions of these subsystems are provided in subsequent sections.

Table 8.21 summarizes the resolution requirements on the particle momentum measurement at the event vertex and the determination of the radial distance of closest approach of the particle trajectory to the event vertex for different ranges in pseudorapidity and with the dependencies on momentum and transverse momentum, respectively. The momentum threshold is lower than 0.5 GeV for most of the tracking acceptance.

$\eta$ range	$dp/p$ [%]	$DCA_r$ [ $\mu\text{m}$ ]
$(-3.5, -2.5)$	$0.10 \times p \oplus 2.0$	$30/p_T \oplus 40$
$(-2.5, -1.0)$	$0.05 \times p \oplus 1.0$	$30/p_T \oplus 20$
$(-1.0, 1.0)$	$0.05 \times p \oplus 0.5$	$20/p_T \oplus 5$
$(1.0, 2.5)$	$0.05 \times p \oplus 1.0$	$30/p_T \oplus 20$
$(2.5, 3.5)$	$0.10 \times p \oplus 2.0$	$30/p_T \oplus 40$

**Table 8.21:** Physics requirements on the relative momentum measurement,  $dp/p$ , at the event vertex,  $\eta$ , and on the determination of the radial distance of closest approach,  $DCA_r$ , of the particle trajectory to the event vertex. The requirements are given for different ranges in pseudorapidity as parametrizations in the total momentum,  $p$ , in GeV and transverse momentum,  $p_T$ , in GeV, respectively.

To study the tracking performance, we have implemented the preliminary design – its geometry, material, and point resolutions – in the ePIC software stack (version 24.10.1). In the initial studies, we have generated single pions at the nominal collision vertex of (0,0,0) in the momentum range from 500 MeV to 20 GeV. These pions were then propagated through the detector volume in the GEANT4-based DD4hep simulation package. We then processed the recorded detector hits with the reconstruction framework called “EICrecon” for digitization, and track finding and fitting via the ACTS combinatorial Kalman Filter.

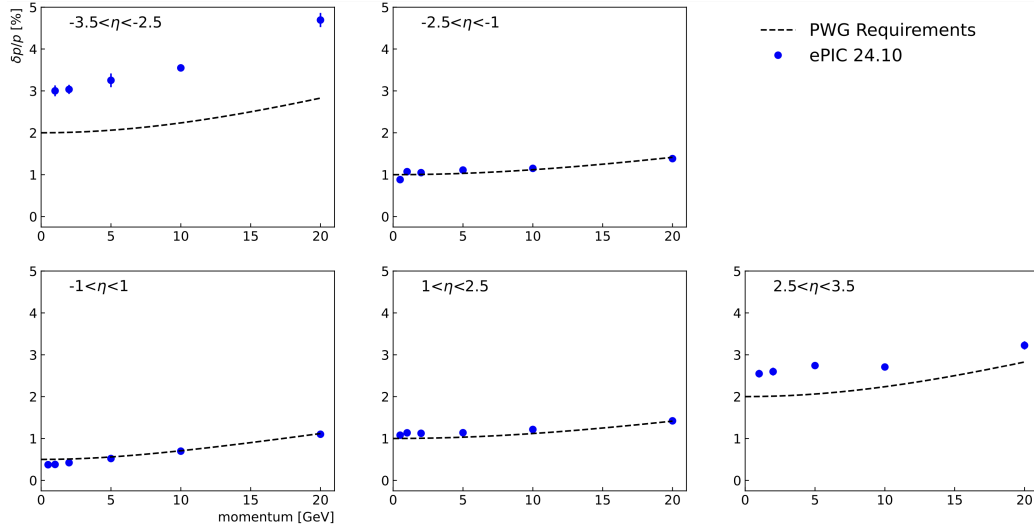
Figure 8.55 shows the simulated relative momentum resolution for single charged pions versus their total momentum for different pseudorapidity regions, together with the requirements. The simulations show that the momentum resolutions are substantially met over most of the SVT acceptance. The performance in the range of smallest pseudorapidity,  $-3.5 < \eta < -2.5$ , is limited by constraints on the SVT lever arm from ePIC’s outer subsystems in this region and overall detector size. In this range, the momentum measurement of the scattered electron in coherent diffraction poses the most stringent resolution requirement and achieving the physics objectives will rely on the combination with calorimetric energy measurement. The requirements in the range of largest pseudorapidity,  $2.5 < \eta < 3.5$  can be met for the ultimate solenoidal field strength of 2 T.

Figure 8.56 shows the simulated radial distance of closest approach,  $DCA_r$ , for the reconstructed trajectories of simulated charged pions to the event origin versus pion transverse momentum in different pseudorapidity regions, together with the requirements. The simulations show that the requirements on  $DCA_r$  are substantially met over the SVT acceptance.

Figure 8.57 shows the track reconstruction efficiency versus pseudorapidity for representative momenta. The track finding and reconstruction efficiencies are above 95% for  $-3.5 < \eta < 3.5$  over a wide kinematic range. The detector acceptance drives the drop-off in efficiency near extreme  $\eta$  for all momenta, whereas current algorithmic limitations are responsible for the somewhat stronger drop-off for the lowest momenta.

In addition to single-track simulations, we have also performed multi-track simulations in the form of simulated Neutral Current (NC) DIS events and studied the tracking performance. These events were generated using Pythia8, and they incorporate a realistic beam spot distribution as well as beam angular and energy divergence effects at the event generation level. Their reconstruction used the same framework and settings as used for the single-track simulations.

Figure 8.58 shows the pseudorapidity distribution for both the generated charged particles and for



**Figure 8.55:** Relative momentum resolution versus total momentum for charged pions (points) together with physics requirements (curves) in different pseudorapidity ranges as indicated. The results are based on full GEANT simulations of the central tracking system (SVT+MPGD+AC-LGAD) using the ePIC software stack and ACTS-based track finding and reconstruction using suitably tuned ACTS parameter settings. The error bars indicate the size of the statistical uncertainties in the simulation.

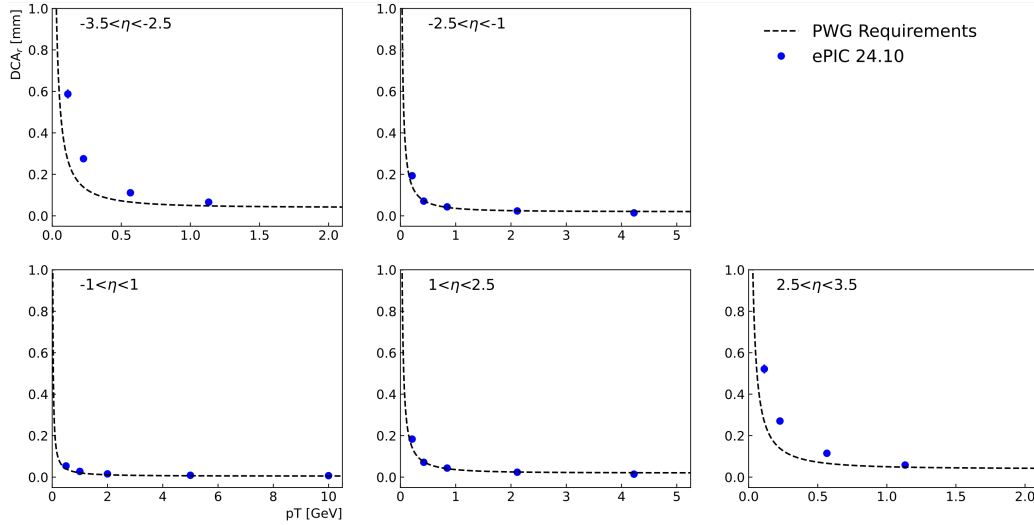


**Figure 8.56:** Distance of closest approach in the radial direction between reconstructed charged pion trajectories and the event origin versus transverse pion momentum (points) together with physics requirements (curves) in different pseudorapidity ranges as indicated. The results are based on full GEANT simulations of the central tracking system (SVT+MPGD+AC-LGAD) using the ePIC software stack and ACTS-based track finding and reconstruction. The error bars indicate the size of the statistical uncertainties in the simulation.

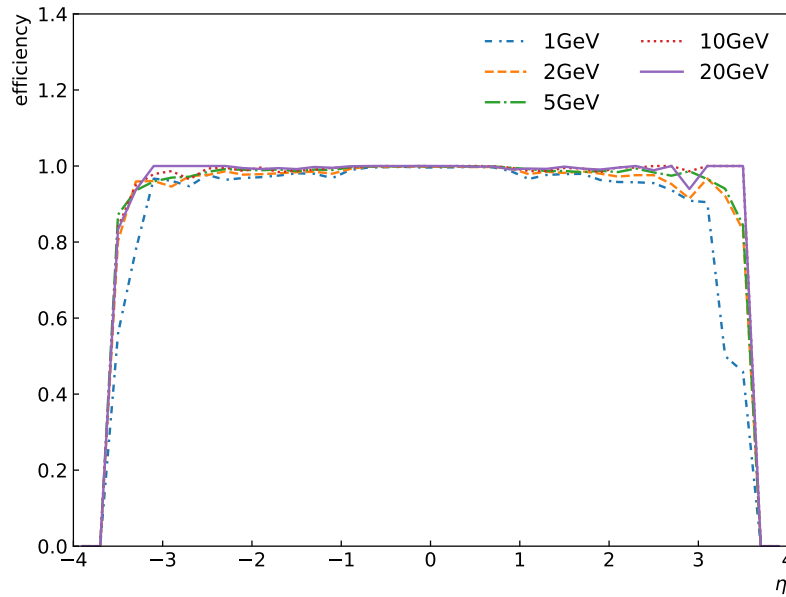


**Figure 8.57:** Tracking efficiency versus pseudorapidity  $\eta$  for charged pions with initial momenta of 1 GeV to 20 GeV.

1871 the reconstructed tracks. The reconstructed track pseudorapidity distribution qualitatively agrees  
 1872 with the truth spectrum above the transverse momentum of 500 MeV/c shown. This result demon-  
 1873 strates the ability of the ePIC tracking detector system and track finding and fitting software to  
 1874 efficiently and accurately reconstruct tracks in DIS events where multiple tracks are present.

1875 Figure 8.59 shows how often the tracks in these DIS events are matched to a single or multiple  
 1876 generated charged particles. For the set of track measurements (hits) used in each track fit, each  
 1877 of those measurements is associated with a single generated charged particle in the simulation.  
 1878 The track hit purity is then calculated as the fraction of those measurements in the track which are  
 1879 associated with one generated charged particle. As can be seen, almost 99% of the tracks in the DIS  
 1880 sample used are associated with only a single particle.

1881 We are in the process of incorporating beam backgrounds and detector noise to further advance  
 1882 these performance studies.

### 1883 8.3.3.1 The silicon trackers

#### 1884 Requirements

1885 **Requirements from physics:** The Silicon Vertex Tracker (SVT) needs to meet stringent perfor-  
 1886 mance requirements, set by the EIC science program, on acceptance and resolutions for charged-  
 1887 particle trajectories. At a high level, the SVT needs to precisely measure the trajectories of the  
 1888 scattered electron and charged hadrons produced in electron-ion beam collisions over a wide kine-

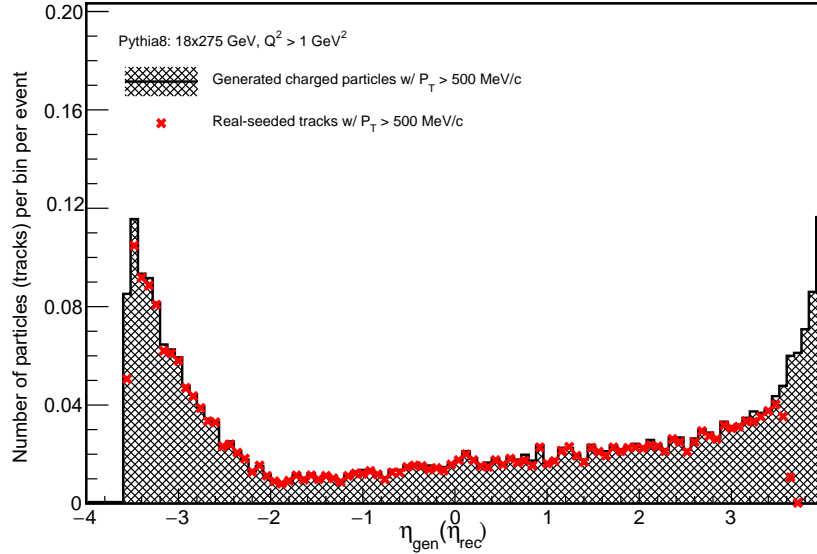


**Figure 8.58:** The number of generated charged particles vs. the generated pseudorapidity of those particles (filled black). The number of reconstructed tracks vs. the reconstructed pseudorapidity of those tracks (red crosses). The y axis shows the number of particles (tracks) per pseudorapidity bin per event. The events were generated with a  $Q^2$  minimum of  $1 \text{ GeV}^2$ ; the scattered electron peak can be seen at negative pseudorapidity. The particles (tracks) shown all have a generated (reconstructed) transverse momentum greater than  $500 \text{ MeV}/c$ .

1889 matic range. The scattered ion, if it remains intact, is outside of the SVT acceptance. The SVT also  
 1890 needs to measure charged decay-particles from hadrons containing heavy quarks and from vector  
 1891 mesons. It is to aid in particle-identification a) through determination of the displacement of the  
 1892 geometrical origin of the decay particles (secondary vertex) from the collision point (event vertex)  
 1893 via precision reconstruction of both vertices and b) by providing direction and position information  
 1894 on charged-particle trajectories through the outer gaseous tracking subsystems and into the outer  
 1895 particle-identification subsystems.

1896 The SVT is the innermost subsystem of the ePIC central detector. Constraints from the overall  
 1897 detector size and the outer subsystems limit the active volume of the SVT to  $-105 < z < 135 \text{ cm}$   
 1898 and a radius of approximately  $42 \text{ cm}$ . In combination with the  $1.7 \text{ T}$  solenoidal field, this leads to a  
 1899 requirement on the point resolution of better than  $10 \mu\text{m}$  as well as the need to minimize traversed  
 1900 material by limiting the number of detection surfaces and minimizing their radiation lengths.

1901 **Requirements from Radiation Hardness:** We have evaluated the radiation levels in the SVT  
 1902 using the current knowledge of the beam configuration and beam backgrounds from beam gas  
 1903 interactions and synchrotron radiation. Figure 8.60 shows the current estimates for neutron equiv-  
 1904 alent fluence, and dose. The black lines indicate the approximate locations of the SVT detection  
 1905 surfaces. These radiation maps have been estimated for the beam configuration with the highest  
 1906 luminosity ( $10 \text{ GeV}$  electron beam and  $275 \text{ GeV}$  proton beam at  $10^{34} \text{ cm}^{-2} \text{ s}^{-1}$ ), and include contri-  
 1907 butions from hadron and electron beam gas interactions. The results assume that the machine and  
 1908 detector run at 100% efficiency for 6 months per year over a period of 10 years. Even under these



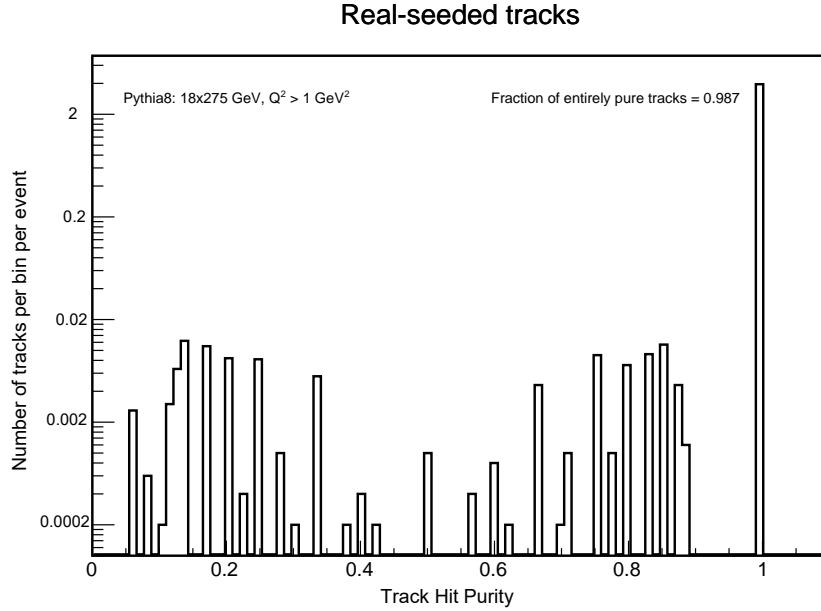


**Figure 8.59:** The distribution of the track hit purity for NC DIS events with a  $Q^2$  minimum of  $1 \text{ GeV}^2$ . The track hit purity is defined as the fraction of measurements in a track which are associated with a given generated charged particle. The peak at 1 indicates that most of the tracks (99%) are associated only with a single particle.

conservative assumptions, the radiation doses in the SVT will be low to moderate, and are expected to be acceptable. The majority of the SVT will see fluence levels well below  $10^{11} \text{ n}_{eq} \text{ cm}^{-2}$ . The innermost central layers and layers in the hadron going direction will experience slightly higher fluence between  $10^{11}$  and  $10^{12} \text{ n}_{eq} \text{ cm}^{-2}$ , with some small regions reaching above  $10^{12} \text{ n}_{eq} \text{ cm}^{-2}$ . The dose rate map indicates that areas close to the beam pipe will experience a total ionising dose between ten and a few hundred krad, while the rest of the SVT remains below 10 krad.

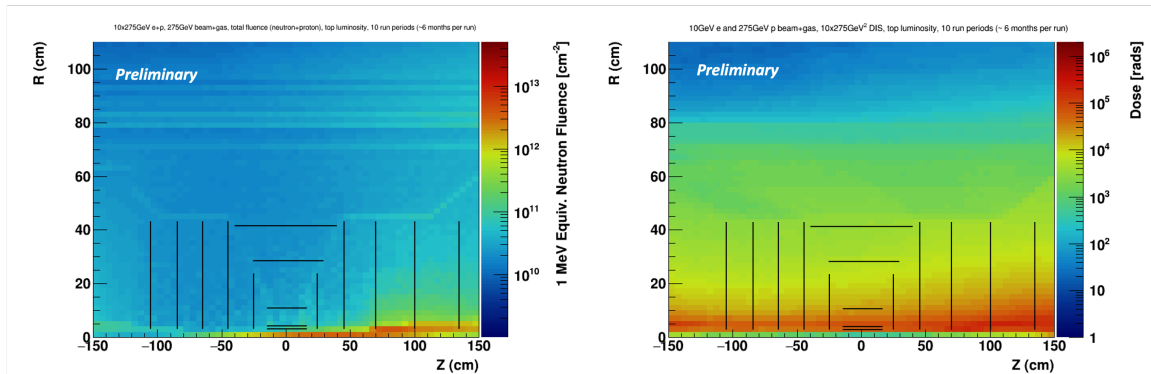


**Figure 8.60:** Maps of simulated 1 MeV neutron equivalent fluence (left) and total ionising dose (right) over the ePIC tracking envelope. This is a conservative estimate assuming 10 years of running at top luminosity with 100% efficient accelerator and detector. The black lines indicate the approximate location of the ePIC SVT detector layers.

**Requirements from Data Rates:** EIC physics rates are expected to be below 0.5 MHz. That is, only a small fraction of the EIC beam crossings produces a physics event and physics event pileup from within a single beam crossing is negligible. The dominant fraction of these events originate from a region,  $|z| < 80 - 100$  mm, surrounding the nominal interaction point. We thus estimate that event pileup within the SVT is determined by its readout frame or integration window of  $2 \mu\text{s}$  or a small multiple thereof. Within this window, SVT will also accumulate hits from noise and beam backgrounds. We estimate that the associated hit load and data volume will exceed that from physics events. Hit occupancies will be low in view of the high SVT granularity. We estimate a hit probability per pixel per readout frame of  $\mathcal{O}(10^{-7})$  and a typical total data rate at the level of 15 Gbps. The sensor and readout chain need to be efficient under these conditions.

### Justification

**Device concept and technological choice:** To meet the stringent requirements on charged-particle tracking and vertexing, we have designed the SVT to provide a well-integrated, large acceptance, high granularity, and low-mass tracking and vertexing subsystem. The SVT has four regions covering a total active area of approximately  $8.5 \text{ m}^2$ . An Inner Barrel (IB) and Outer Barrel (OB), made of three and two active layers, respectively, cover the mid-central pseudorapidity range and have an active volume that extends radially to approximately 42 cm. Endcaps, each with five active annuli surrounding the beampipe, are placed on either side of the nominal interaction point with their active area constrained to  $-105 < z < 135$  cm and an outer radius equal to that of the OB. The Electron Endcap (EE) is positioned in the direction of the electron beam and has acceptance for a large fraction of the scattered electrons, while the Hadron Endcap (HE) provides acceptance for many of the hadrons produced in physics collisions. Figure 8.61 shows the SVT regions and geometrical layout.

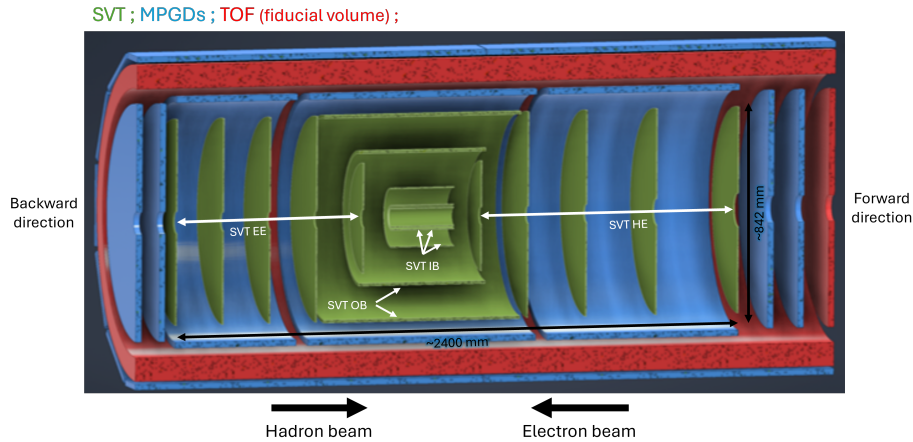


**Figure 8.61:** Schematic layout of the ePIC SVT showing the central region consisting of the inner and outer barrel made of three and two cylindrical layers, respectively, together with the endcap regions made of five annuli each. The figure also shows the surrounding Micro Pattern Gas Detector (MPGD) layers and the envelope of the Time of Flight PID detector.

We designed the SVT to cover the required pseudorapidity range and to reach spatial resolutions as low as  $\leq 6 \mu\text{m}$  through a combination of high granularity ( $\sim 20 \mu\text{m}$  pixel pitch), lightweight support structures, cooling, and electrical services enabled by a low power sensor design ( $\leq 40 \text{ mW}$ )

$\text{cm}^{-2}$ ). Our development aims at achieving 0.05%  $X/X_0$  in the IB, 0.25%  $X/X_0$  in the innermost OB layer and in the disks, and 0.55%  $X/X_0$  in the outermost OB layer. We selected a sensor technology based on the ALICE-ITS3 development [36] to meet our requirements. This is a new generation, large area Monolithic Active Pixel Sensor (MAPS) in a commercial 65 nm CMOS imaging process.

### Subsystem description:

General device description: Tables 8.22 and 8.23 show the positioning and size of the SVT active layers, together with their material budget target. We designed the IB to provide precise vertex reconstruction, while also contributing to momentum measurement. This is achieved with a combination of very thin layers at optimised radii. The IB will use the ALICE ITS3 wafer scale sensor [36] with a suitable adaptation of the ITS3 ultra-thin detector concept to the large EIC beam pipe diameter. The IB design has three layers of silicon sensors thinned below  $50\ \mu\text{m}$  and bent around the beam pipe, with minimal mechanical support, air cooling, and no electrical services in the active area, to reach the very low material budget target of  $X/X_0 = 0.05\%$ . The innermost layer is positioned as close as possible to the beam pipe, taking into account the constraints coming from the large beam pipe radius and the requirements from beam pipe bake-out, which will be performed with the IB installed. The position of the second layer is chosen to maximize vertex resolution. The outermost layer of the IB aims at maintaining the very low material budget at a radius of 120 mm and serves both vertexing and sagitta measurements. The OB, EE and HE will be equipped with the EIC Large Area Sensor (LAS), a modified version of the ITS3 sensor, optimized for high yield, low cost, and large area coverage. These sensors will be thinned to  $50\ \mu\text{m}$  and mounted on lightweight support structures, in the form of staves for the OB and disks for the endcaps, with integrated cooling and electrical interfaces for power, data and slow control. The OB layers and the endcap disks are positioned to provide high precision measurements over a large lever arm to improve momentum resolution and optimize acceptance at large pseudorapidity. The inner openings of the disks will accommodate beam pipe bake-out constraints as well as beam pipe divergence. These translate into six different inner opening geometries over ten disks.

Region	Layer	radius [mm]	length [mm]	$X/X_0$
IB	L0	36	270	0.05%
	L1	48	270	0.05%
	L2	120	270	0.05%
OB	L3	270	540	0.25%
	L4	420	840	0.55%

**Table 8.22:** Radius, length and material budget of the SVT IB and OB layers.

Sensors: The SVT will be constructed with MAPS sensors, that integrate sensing and front-end electronics functionalities in one device. The ePIC SVT will use MAPS sensors developed in a 65 nm CMOS imaging process based-off the ALICE ITS3 development [36]. This technology enables a high granularity and low power consumption design, and offers stitching on 300 mm wafers for the development of large area sensors. These characteristics are key to delivering a high precision detector through high spatial resolution and minimized material budget.

Region	Disk	$z$ [mm]	$r_{out}$ [mm]	$X/X_0$	Region	Disk	$z$ [mm]	$r_{out}$ [mm]	$X/X_0$
EE	ED0	-250	240	0.25%	HE	HD0	250	240	0.25%
	ED1	-450	415	0.25%		HD1	450	415	0.25%
	ED2	-650	421	0.25%		HD1	700	421	0.25%
	ED3	-850	421	0.25%		HD3	1000	421	0.25%
	ED4	-1050	421	0.25%		HD4	1350	421	0.25%

**Table 8.23:** Position along the beam pipe, outer radius and material budget for the SVT layers in the EE and HE regions. Disks in the electron direction are labeled ED0 to ED4. Disks in the hadron direction are labeled HD0 to HD4. Disks ED0/1/2 and disks HD0/1 have the same inner opening. Each of the other five disks has a different inner opening.

The SVT IB will use the ALICE ITS3 sensor, called MOSAIX. A sketch of MOSAIX on a wafer is shown in figure 8.62. MOSAIX is composed of an active matrix of Repeated Sensor Units (RSUs). Twelve RSUs are stitched along the length of the sensor, giving a total length of  $\approx 27$  cm. The sensor will be three, four, and five RSUs wide ( $\approx 6, 8$ , and  $10$  cm) for L0, L1 and L2, respectively. Each RSU is further divided into 12 tiles that can be switch off independently in case of faults to improve yield over such large area device. A row of 12 RSUs, together with the left and right endcap (LEC, REC) is called a segment. The LEC contains circuits for power, slow control and data. The REC hosts another set of power connections to ensure a uniform power distribution over the full sensor length. Data links for each segment can be configured with three links, plus one spare, at 10.24 Gb/s or six links, plus two spares, at 5.12 Gbps. For each segment, seven electrical links provide clock, synchronisation and control signals, referred to here as slow control signals. The clock runs at 160 MHz, while the control signals will run at 5 Mbps. MOSAIX has different power domains for analogue and digital circuitry at 1.2 V, plus two more domains for specific blocks, one at 1.2 V and one at 1.8 V [36]. The sensor's bias voltage will be in a range between -1.2 and -4.8 V.

The SVT OB and endcaps cover an area of approximately  $8 \text{ m}^2$ . Considerations based on yield, cost, integration, and coverage require the use of a sensor with a smaller size than the wafer-scale sensor used in the IB. These regions will use the MOSAIX sensor with modifications to reduce the size. This sensor would still be large in traditional terms and is therefore referred to as the EIC Large Area Sensor (EIC-LAS). The EIC-LAS will be one RSU wide and either 5 or 6 RSUs long. Power will need to be fed into the EIC-LAS only from the LEC given the reduced length. In addition to reducing the size of the sensor, the EIC-LAS will see a reduction of the number of data links to match the lower SVT data rate, reduce material and ease integration aspects. To further ease the integration of the EIC-LAS in the OB and endcaps, EIC-LAS sensors will be powered in series by a constant current and a dedicated communication protocol will be used to reduce the number of slow control links from the counting room to the sensor. These features will be provided by a supporting ASIC, referred to as the Ancillary ASIC (AncASIC).

FEE: One AncASIC will be used per EIC-LAS. This chip includes three main features. It integrates the shunt low-dropout (SLDO) regulator for serial powering. This regulator will generate the voltages needed by the EIC-LAS from the input current. This design is adapted from the original SLDO design for the upgrades of the ATLAS and CMS pixel detectors at the HL-LHC [37]. One AncASIC will integrate five SLDO regulators. The AncASIC will also contain a Negative Voltage Generator (NVG) block. The NVG is a diode-based charge-pump circuit (Dickson-type charge pump voltage multiplier). It will generate the sensor's negative

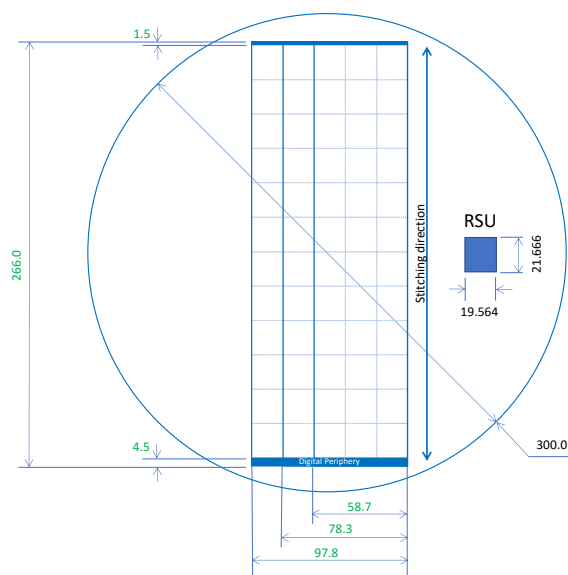


**Figure 8.62:** Sketch of the MOSAIX sensor on a 300 mm wafer showing the size of the RSU, LEC, REC and of the full sensor for the three different widths. All positions are in mm.

2011 bias voltage from one of the regulated power supplies at 1.2 V generated by the SLDOs. The  
2012 third block is the Slow Control (SC). Slow control signals from the counting room will be  
2013 transmitted over I2C for multiple EIC-LAS sensors over one link. The SC block will decode  
2014 them into the MOSAIX format (i.e. into seven links). The AncASIC will be produced in a 110  
2015 nm SOI process offering multiple Multi-Project Wafer (MPW) runs per year and the required  
2016 transistors' ratings for the SLDO and NVG.

Other components: All components of the SVT detector are designed with the goal of achieving the low material budget target, while providing a robust, high precision system. Traditionally the bulk of the material in silicon detectors is contributed by the powering system. While the IB will be powered using a traditional voltage based powering scheme, a current based power distribution scheme, so called serial powering, is adopted for the OB and disks to reduce the mass associated to the SVT power distribution. Groups of up to four EIC-LAS sensors are powered in series by a constant current, with the electronics low voltage generated close to the sensors by the SLDO regulators in the AncASIC. This scheme reduces cabling material and provides the only viable powering solution to fit within the available space for services in the ePIC detector. For the smaller IB system, a traditional voltage based, direct powering scheme is foreseen. Data, slow control signals and power are routed over aluminium-based flexible printed circuits (FPC) between the SVT active elements (MOSAIX, EIC-LAS, AncASIC) and the readout (RDO) boards. Four different RDO boards are used in the SVT: the interface board, the control board, the fiber aggregator board, and the power board. The interface board receives data from the sensors for transmission to the counting room. The control board receives slow control signals from the counting room to be transmitted to the MOSAIX and EIC-LAS (through the AncASIC), and to the VTRX+ devices. Lightweight communication between these RDO boards and the counting room is achieved by use of optical fibers. A fiber aggregator board achieves a reduction of the optical fiber lines through multiplexing via FPGA to match the number of fibers to the available channels of the data acquisition board in the counting room. The data acquisition board is common to all ePIC sub-detectors and it is the FELIX board developed for CERN experiments [38].

The electro-optical interface components used on the interface and control boards are the lpGBT [39] and VTRx+ [40] devices developed by CERN. The power board provides interface for power distribution for sensors and AncASIC as well as devices on the RDO boards. Whilst the functionality of the RDO boards and FPC remains the same, different designs will be needed for IB, OB and disks to accommodate the different powering schemes, number of data links, and sensors grouping. The preferred cooling solution for the SVT detector is air cooling, baselined for the two innermost layers of the IB and under study elsewhere. The OB, EE and HE are designed to allow air flow through the low mass staves and disks, made of carbon composite material, that support the sensors.

**Performance** As discussed in the preceding section, we have simulated track finding and reconstruction within the ePIC software framework to quantify momentum and vertexing resolutions in the nominal 1.7 T solenoidal field strength of the MARCO magnet. The sensor response in these simulations requires cross-validation with actual measurements.

We have performed beamtests at FNAL with a single-RSU sensor, called babyMOSS, from the ITS3 Engineering Run 1 (ER1) submission. In these tests, a particle telescope was constructed using six sensors, with a seventh sensor, the Device Under Test (DUT), placed in the middle. The angle of the DUT with respect to the incident beam was varied in the horizontal plane of the telescope. Figure 8.63 shows a close-up of the telescope and results for the cluster extent as a function of the incident beam angle onto the DUT from data and simulations. The results show that the cluster size increases with the particle incident angle, consistent with a geometrically driven expectation. The analysis of the point resolution as a function of the particle incident angle is in progress. Initial results are consistent with the expectation from the pixel pitch.

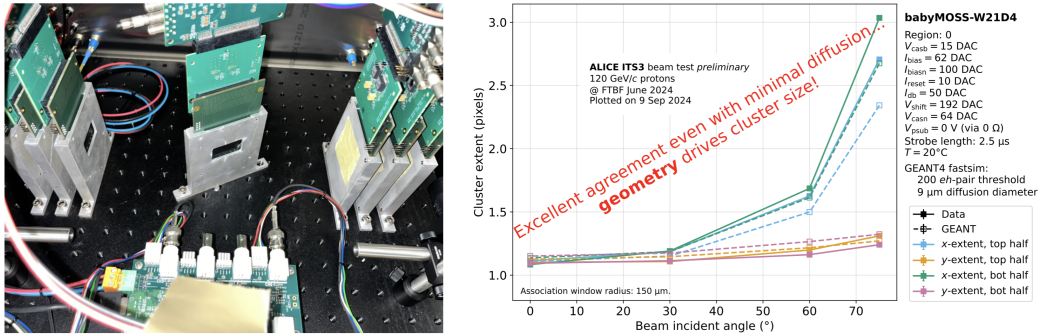


**Figure 8.63:** Left: A close-up of a beam telescope constructed using 6 single-RSU sensors from the ITS3 Engineering Run 1, with a seventh sensor, the Device Under Test (DUT), placed in the middle. Right: Comparison of results from beamtests at FNAL and from simulations for the cluster extent as a function of the beam incident angle onto the DUT.

## Implementation

**Services:** Services to the SVT are of two types: electrical/fiber-optical services and cooling. Electrical/fiber-optical services to the SVT comprise power, data and slow control. Services are routed to/from the IB from the hadron going direction. Services for OB are routed to/from the electron and hadron going directions. For the IB (MOSAIX sensor and direct powering), electrical



services will be by MOSAIX segment. For the OB and endcaps (EIC-LAS and serial powering), they will be by group of up to four EIC-LAS. A summary of the data, slow control and power lines needed in the different regions of the SVT is given in Table 8.24.

Region	Sensor	Electrical services group	# power lines/group	# slow control links/group	# data links/group
IB	MOSAIX	MOSAIX segment	10	7	8
OB	EIC-LAS	Up to 4 EIC-LAS	2	3	4
EE/HE	EIC-LAS	Up to 4 EIC-LAS	2	3	4

**Table 8.24:** Summary of power and readout services for the different regions of the sPIC SVT (slow control and data links are differential pairs of wires). A services group is one MOSAIX segment in the IB, and up to four EIC-LAS sensors (i.e four segments) in the OB and endcaps.

2068

2069 The table illustrates the reduction in power lines using serial powering versus direct powering. In  
 2070 the IB, each MOSAIX segment will need ten lines (including the return line) to serve the four power  
 2071 domains of the electronics plus the sensor bias. For each segment, the full MOSAIX current will be  
 2072 transmitted. In the OB and endcaps two lines (including the return line) will be needed to deliver  
 2073 the same power to up to four EIC-LAS (i.e. four segments). The current flowing on these lines will  
 2074 be the current needed by one EIC-LAS only, reducing the current being transmitted to the detector  
 2075 by up to a factor four, and correspondingly reducing cables cross section and material budget.

2076 Figure 8.64 shows the data and slow control distribution for a group of four EIC-LAS in the OB  
 2077 and disks. Each data line connects to one input of a VTRx+ on the interface board. Given the high  
 2078 speed of the data transmission, this board will be placed at the end of each stave and disk for signal  
 2079 integrity. The VTRx+ transmits the data of a group of up to four EIC-LAS over a bundle of optical  
 2080 fibers to the counting room (each VTRx+ has a pigtail bundling up to 5 optical fibers). Slow control  
 2081 signals are transmitted over optical fibers to the control board, placed along the SVT support struc-  
 2082 ture. Once converted into electrical signals, one lpGBT elink provides the slow control signals to  
 2083 up to four AncASICs. Each lpGBT has 16 elinks, meaning that each control board will serve mul-  
 2084 tiple groups of up to four EIC-LAS. The slow control signals are transmitted between the control  
 2085 board and the AncASIC either in a daisy-chain architecture (as shown in the figure) or via multi-  
 2086 drop. The exact configuration is still being evaluated. The AncASIC converts the incoming I2C  
 2087 protocol to the MOSAIX protocol expected by the EIC-LAS. As the OB and endcaps are powered in  
 2088 series, each EIC-LAS is on a different ground potential. A dedicated communication scheme is thus  
 2089 needed. Data lines will be AC-coupled. For the slow control, a standard DC transmission is also  
 2090 being investigated with the ground difference between EIC-LAS sensors being accommodated.

2091 Flexible printed circuits (FPCs) are required to electrically connect MOSAIX sensors, EIC-LAS sen-  
 2092 sors and AncASIC chips to the interface and control boards. In the IB the FPC will connect to the  
 2093 LEC of the MOSAIX sensor. In the OB and disks, a main FPC will run along staves and disks, serv-  
 2094 ing groups of up to four EIC-LAS sensors. It will connect to the AncASICs through bridge FPCs  
 2095 (see prototype in fig. 8.71). The maximum length of the main FPC is constrained to a maximum  
 2096 of 40 cm based on signal integrity and power drop considerations. Two and four main FPCs will

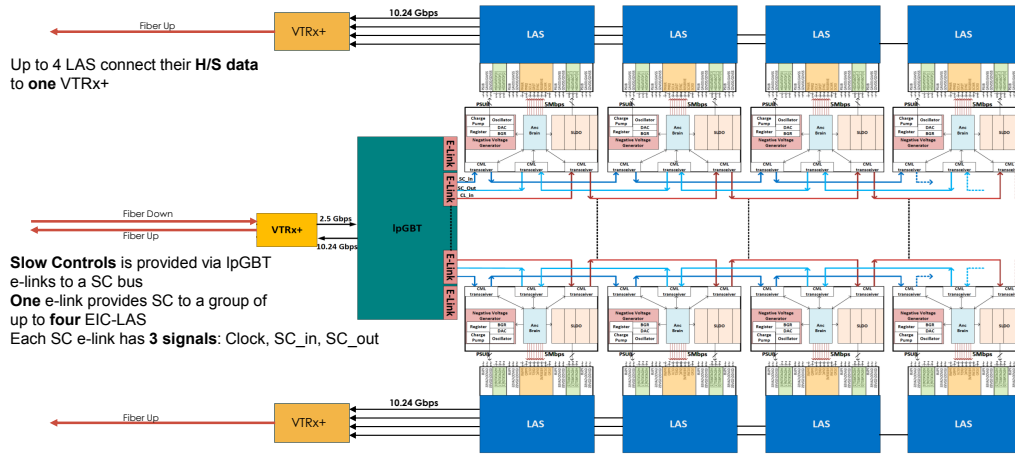


**Figure 8.64:** Schematic overview of data and slow control lines to groups of up to four EIC-LAS in the OB and disks.

be needed on L3 and L4, respectively, to cover the full length of the stave. The FPCs must have a low mass in order to maintain the low material budget of the SVT. It is therefore advantageous to select conductive tracks made of aluminium ( $X_0 = 8.9$  cm) instead of traditional copper ( $X_0 = 1.4$  cm). Dielectrics like polyimide ( $X_0 = 28.57$  cm) are the default solution for the manufacturing technologies of aluminium-based FPCs deployed in scientific experiments. The selection of the dielectric material is dependent on its loss-tangent properties versus the frequency of the signals to be transmitted. Typically the most stringent requirements for signal attenuation are set by the high-speed data transmission lines. In case of the ePIC SVT, it is envisaged that data links can transmit signals as fast as 10.24 Gb/s for a length of  $\sim 50$  cm. The baseline configuration for the FPCs assumes a stack-up made of two aluminium conductive layers (each  $\sim 15$   $\mu\text{m}$  thick) separated by a polyimide dielectric substrate ( $\sim 35$   $\mu\text{m}$ ), and then additional polyimide cover layers ( $\sim 35$   $\mu\text{m}$  combined thickness) to insulate the conductive tracks from external electrical shorts. This cross section ( $\sim 100$   $\mu\text{m}$  in total) would equate to a combined material budget of  $\sim 0.06\%$   $X_0$ . The combination of serial powering, slow control daisy-chained/multi-drop configuration and impedance matching at  $100\ \Omega$  for clock, control lines and data, enables a reduction of the number of signals to be propagated. This is particularly important for staves and disks where the FPCs overlap the sensitive area of the MAPS. By combining these power and signal distribution techniques, it is estimated that the minimum width for the FPC can be as narrow as 6 mm. This is  $\sim 1/3$  of the width of the LAS ( $\sim 19$  mm).

The transmission of the signals to the counting room will see a further stage of processing. The data fiber-optic lines will be aggregated in the aggregator board, common to all SVT regions, which has multiple fiber inputs, an FPGA for extracting the payload from these fibers, and one fiber output towards the FELIX board, thus reducing the number of fiber inputs at the data acquisition boards. For the FPGA, we are considering both a radiation tolerant PolarFire FPGA and an SRAM based FPGA, with the choice to be made depending on the location of this board and radiation levels present. For the optical interface, we are considering both a FireFly optical transceiver and a standard SFP (Small Form Factor Pluggable) transceiver. It is estimated that approximately 5000 data fiber links run from the sensors to the aggregator board. Assuming an aggregation factor of 10, there will be approximately 500 fibers towards the DAQ FELIX boards, which can be accommodated by 11 FELIX boards (assuming each FELIX board will have 48 fiber inputs).



2127 Cooling adds to the service load, including the target radiation lengths in the SVT active areas.  
 2128 The preferred cooling solution for the SVT detector is air cooling (using dry air), baselined for the  
 2129 two innermost layers of the IB and under study elsewhere, with liquid cooling in strategic places  
 2130 as necessary. We will operate the sensors at or near room temperature ( $\sim 25^\circ\text{C}$ ), which requires a  
 2131 lower coolant temperature. Thermal performance of the cooling is measured was the temperature  
 2132 difference between the sensor and the coolant, i.e.  $\Delta T = T_{\text{sensor}} - T_{\text{inlet air or coolant}}$ . Our target for  
 2133 thermal tests and simulations is  $\Delta T$  of  $10^\circ\text{C}$ . FEA analysis is underway based on current power  
 2134 dissipation estimates.

2135 For the inner layers of the IB, the baseline is air cooling with thermally conductive foam near the  
 2136 LEC. Measurements from ALICE ITS3 show this is reasonable to cool the MOSAIX sensor [36]. Air  
 2137 will be forced between L0 and L1. To cool L2, the possibility for natural convection with liquid  
 2138 cooling near the LEC if necessary is under study. The air inlet and outlet are under design, with the  
 2139 bulk of the material to be placed on the hadron-going side of the detector.

2140 In addition to cooling during operation, the IB will need to be kept cool during beam-pipe bake-out.  
 2141 The aim is for no additions to the operational cooling, i.e. no additional material (e.g. insulators)  
 2142 or changes (i.e. liquid instead of air). Ongoing ANSYS studies at Jlab and LBNL, discussed further  
 2143 down, have shown that there are options to keep the detector cool under these constraints. Tests  
 2144 of sensor prototypes by ePIC (flat sensor prototypes) and ITS3 (wafer-scale, curved mechanical  
 2145 prototypes) institutes, at temperatures up to  $50^\circ\text{C}$  in a climate chamber have shown no electrical  
 2146 and no mechanical failures.

2147 The target for both the OB staves and the EE and HE disks is air cooling. We are targeting a maxi-  
 2148 mum air velocity of  $12\text{ m/s}$  within the structures of the staves and disks. Current estimates are ap-  
 2149 proximately  $1700\text{ m}^3\text{h}^{-1}$  total air split between the staves and disks. This will require compressed  
 2150 air to mitigate the otherwise excessive size and number of air tubes coming into the detector and  
 2151 pressure regulation inside the detector. Studies are ongoing to reduce these numbers, including the  
 2152 use of thermally conductive materials (e.g. carbon foam) to help with heat dissipation. The SVT  
 2153 will be interlocked to turn off in the case of failure of its cooling system, including conditions so as  
 2154 to prevent pressurizing the system beyond its design values.

2155 **Subsystem mechanics and integration:** The SVT IB, OB, and disks are supported by their  
 2156 own support structure. The outermost components of this structure are carbon composite half-  
 2157 cylinders, which jointly form the experiment's so-called inner support tube. The inner support tube  
 2158 surrounds the entire SVT and spans its entire length. Cones inside the inner support tube connect  
 2159 the OB to the IB and to the innermost disks. These cones are supported from the inner support tube  
 2160 and are projective to the nominal collision point. They are currently designed to consist of spokes.  
 2161 The outermost disks connect to the inner support tube. This entire SVT support structure, shown  
 2162 schematically in fig. 8.65, is integrated in and supported off the experiment's global support tube.

2163 The IB layers will be made of two symmetric half-layers, which will be the basic assembly elements  
 2164 of the detector. The two innermost layers (L0 and L1) will be based on four MOSAIX sensors (two  
 2165 for each half-layer), while the outermost layer (L2) will contain eight MOSAIX sensors (four for  
 2166 each half-layer). The MOSAIX sensors for L0, L1, L2 will be three, four and five segments wide,  
 2167 respectively. All the sensors equipping a given half-layer will be placed one next to the other to  
 2168 fully cover the half-layer surface and bent on a cylindrical shape at the corresponding radius (c.f.  
 2169 table 8.22).

2170 Each IB half-layer will consist of the following components: the MOSAIX sensors, a local support  
 2171 structure mainly made in carbon foam shaped as a frame along the edges of the sensors, two sets  
 2172 of FPCs wire-bonded to the sensor peripheries for powering and data/control transmission. The

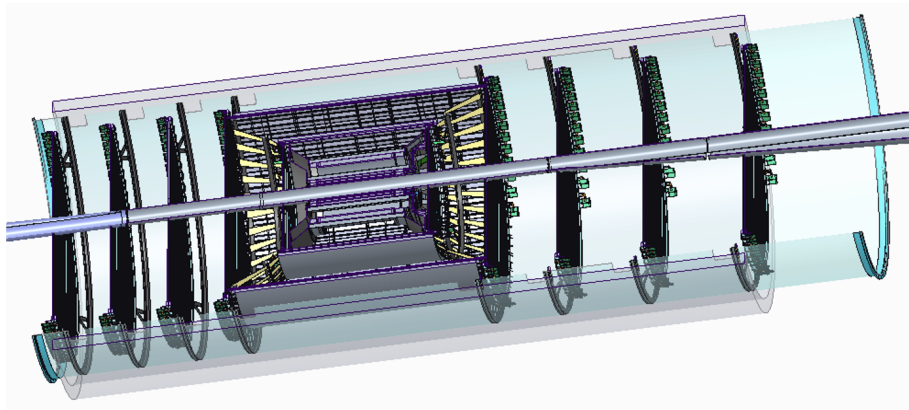


**Figure 8.65:** SVT global support structure, consisting of a surrounding carbon composite support tube and a projective arrangement of spokes that form cones connecting the IB, OB, and innermost disks. Also shown are several outer disks and the beampipe.

2173 sensor cooling will be air-flow based and delivered through appropriate ducts that will be part of  
2174 the local support structure and matched to the global mechanics described below.

2175 The IB global support will be the main structure supporting the MOSAIX sensors already assem-  
2176 bled in half-barrels. The current design foresees a cylindrical frame structure for each layer, sup-  
2177 ported by two conical endcaps, one for L0-L1 and a second for L2, the last including a flange  
2178 for connection to the L0-L1 half-cone and to the OB. The material is currently fixed in a carbon  
2179 fiber composite, whose thickness will be approximately 0.5 mm. A half-cylindrical shell made of  
2180 polyamide is placed outside and close to L2 for mechanical stability in the current design. Electrical  
2181 services for the IB are brought in/out from the hadron going side and are routed along the inner  
2182 surface of the conical support. In the current design the routing of the power cables to the REC  
2183 needs that the longerons of the local mechanics have also the role of cable trays. The requirement  
2184 of rigidity and the U-shape for cables routing suggests carbon fiber composite as a preferred mate-  
2185 rial choice, while alternatives are being considered. Figure 8.66 shows CAD representations of the  
2186 IB support.

2187 For the OB, EE, and HE, we introduced a modular approach in the SVT design to simplify the  
2188 assembly process of these complex detector elements, reduce risks and increase the predictability  
2189 of the production rate. EIC-LAS sensors and AncASICs will be assembled into modules, that will  
2190 pre-assemble and pre-test and then mount/interlink in the final staves or disks. The EIC-LAS  
2191 sensors and AncASICs will be connected via flexible printed circuits boards and micro-electronics  
2192 interconnection techniques to form an electrically coherent unit, and supported by a mechanical  
2193 frame to be interfaced with cooling systems and to meet handling requirements.

2194 The design of a module for the outer barrel envisions two EIC-LAS with their respective two An-  
2195 cASIC (see Fig. 8.67). The mechanical frame is made of a thin film of polyimide that holds together  
2196 all the module components. The design of a module for the disks envisages one LAS and one An-  
2197 cASIC and a mechanical frame made of a carbon fibre plate. We will test modules standalone after  
2198 their assembly and before their assembly into staves or disks.

2199 The outer barrel layers will be segmented in staves. The staves are composite structures using  
2200 carbon fibre (CF) skins, a central CF I-beam spar and cross-ribs made of K9 foam. The side walls will  
2201 be formed by the FPCs. The structure has openings where modules will be placed. During module  
2202 mounting the modules are glued on top of these openings, forming a closed hollow structure with

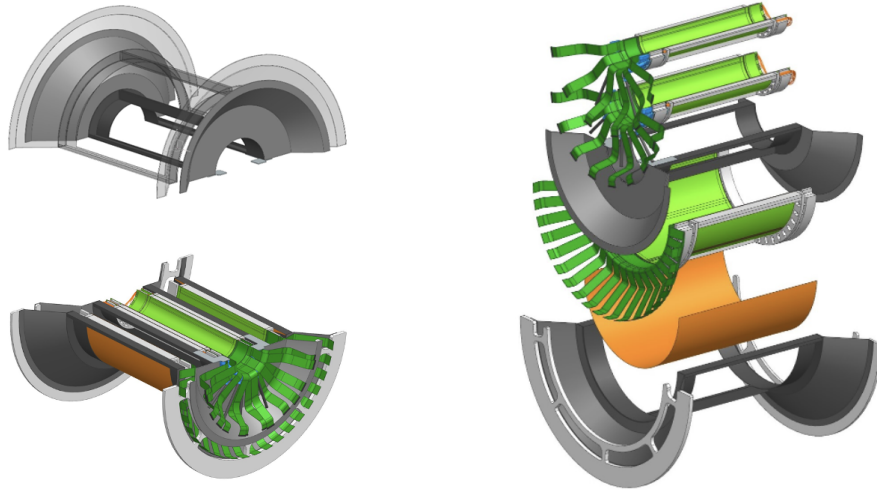


**Figure 8.66:** Left: CAD representation of the IB global support (top) and IB half-barrel CAD view with sensors and cable routing (bottom). Right: Exploded CAD view of IB. The orange element is the kapton shield. In blue the air conveyors are shown.

large second moment of area, and thus high stiffness. The closed structure provides a contained channel for the forced flow of air through the stave, that will remove the heat from the sensors and ancillary ASICs. In addition to their structural function, the cross-ribs made of highly thermally-conductive K9 foam are placed underneath high-power density components (the left endcap of the EIC-LAS and the AncASIC) to improve the transfer of the heat into the air coolant flow. Drawings of the stave design with all its components are shown in Fig. 8.67.

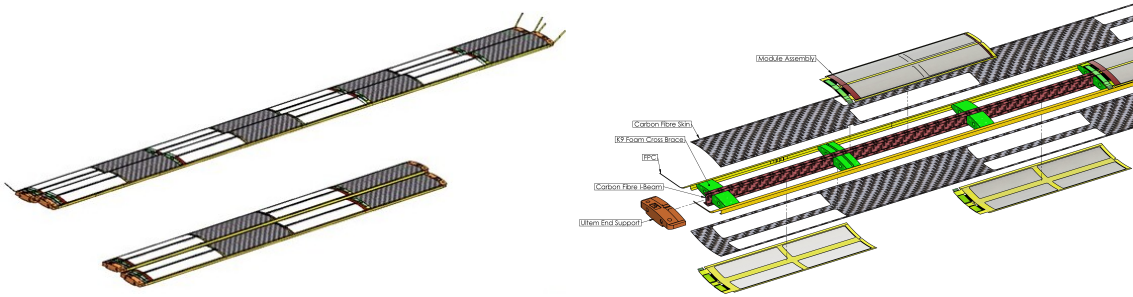


**Figure 8.67:** Left: OB staves for L3 and L4. Two staves per layer are shown. Right: Exploded view of an OB stave.

Each stave is one OB module (i.e. two EIC-LAS) wide, and has modules on both facings, staggered in  $z$  so that the active areas of the modules provide overlap for tracks from the vertex. L4 staves will hold 4 modules on each facing, or 8 modules in total, while L3 staves will have half that number. The dimensions of the staves are dictated by the layout of the SVT and we achieve the required coverage with LAS made up of 6 RSUs in L3 and 5 RSUs in L4, respectively. L3 will consist of two halves with 44 staves in total in a castellated layout to cover the full azimuth. L4 will consist of two halves and have 70 staves. Our initial FEA analysis of the modal frequencies finds  $f_1 = 91.6$  Hz.

The staves will connect mechanically at their ends to segmented half-cones that are part of the SVT support structure. This interface still needs to be detailed, but will constrain stave rotations at the

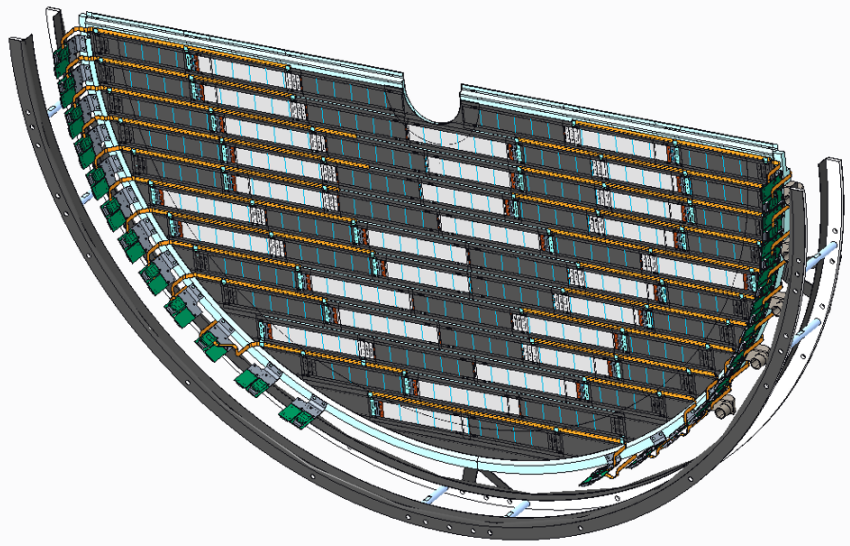


**Figure 8.68:** CAD model of the preliminary (half-) disk design. Modules are shown in alternatingly inward (dark gray) and outward (white) facing orientations. Common bus FPCs are shown in orange. RDOs (green) are arranged on the outside of the disk ring, inside of the interface to the SVT global support structure.

2218 support, while allowing for limited misalignment of the support cones and thermal expansion of  
 2219 components. The interface will also contain the couplings of the air channel inputs to the supply  
 2220 distribution. The cones interface at their outer radius with a support tube surrounding the entire  
 2221 SVT, including its services, and also connect to the the global support structure of the IB and the  
 2222 innermost disks.

2223 The EE and HE disks are a two-sided design with a corrugated carbon composite core. A CAD  
 2224 model of the disk design is shown in Figure 8.68. The purpose of the corrugation is to add strength  
 2225 without adding too much mass. The corrugated channels can be used for air flow to cool the disks.  
 2226 It also gives options for sensor layout to maximize overlaps of inactive area. Modules with one  
 2227 EIC-LAS will be tiled over the valleys of the corrugation on either side of the disk, creating overlap  
 2228 along the long axis of the sensor. Modules will be placed in an alternating inward and outward  
 2229 facing orientation along the corrugation which ensures that an active area of the neighboring sensor  
 2230 covers the insensitive LEC.

2231 Each disk will have a ring at the outer radius that will sandwich the corrugated core to provide  
 2232 mechanical support, a mounting point for the RDOs, and an inlet for air cooling. Those rings  
 2233 will then connect mechanically to either the SVT support cone (ED0-1, HD0-1) or support cylinder  
 2234 (ED2-4, HD2-4). This design is currently being optimized in conjunction with the global mechanics.

2235 **Calibration, alignment and monitoring:** Calibration procedures are needed to optimize the  
 2236 settings for the pixels in the MOSAIX and EIC-LAS sensors. We anticipate these to be similar to  
 2237 those used for the existing ITS2 sensor (i.e ALPIDE), and ITS3 sensor prototypes, and consist in  
 2238 data-taking scans where one injects a charge into groups of pixels and varies their settings. We  
 2239 have made initial estimates of the time required to perform such scans and anticipate that they can  
 2240 be done in a parallel fashion in approximately half an hour with the final readout system.

Alignment procedures are needed to achieve the required resolutions. We will survey the IB (half-) layers, the OB staves, and the EE and HE disks with precision coordinate measuring machines during their construction and will pursue a global survey during installation. Final alignment will be track-based.

Monitoring will include sensor settings and other slow-control data, including temperatures, as well as analysis in near-realtime of residuals in alignment and other observables.

#### **Status and remaining design effort:**

R&D effort: The development of the MOSAIX sensor is well underway. Two submissions have already taken place in 2020 and 2022. The former, so called MLR1, included numerous test structures for technology exploration and to develop prototype circuit blocks for future sensors. The latter, ER1, contained exploratory designs to study stitching principles, methodology and yield. The submission of the MOSAIX sensors (ER2) aiming to satisfy ITS3 requirements is planned for beginning of 2025. ePIC designers are integrated in the MOSAIX design team and contributing to the development of logic libraries, and circuitry for data transmission over the full sensor length between RSUs. The final submission (ER3) will be the MOSAIX production version for the ITS3 detector and the ePIC SVT IB.

Work on the EIC-LAS has started in terms of defining the required modifications (reduction of size and data links). Design work will start once the design database is available upon signature of the necessary CERN-EIC agreement.

The AncASIC is in development with good progress on all functional blocks. The design of the first NVG prototype is completed both at schematics and layout level. The SLDO prototype schematic is ready and simulated, and work on the layout is ongoing. Parts of the slow control block relating to the communication with the lpGBT are begin designed, with the interface to the EIC-LAS to be defined once the MOSAIX slow control interface is completed. MPW runs are foreseen to prototype and verify each block, before submitting the full chip, ready for production in early 2027.

E&D status and outlook – IB: We have developed a preliminary design for the two innermost (L0 and L1) half-layers of the IB and its global support mechanics. Different solutions have been explored for bending and assembly of each half-layer: connecting two sensors in a single object and following a “half-layer” based procedure has been considered largely preferable mainly due to advantages from overlaps with the ITS3 building concept. Once the two half-layers have been individually built, they are assembled in a L0-L1 half-barrel. Blank silicon pieces with dimensions corresponding to the final MOSAIX sensors have been used to advance the design of the L0-L1 assembly and will serve to build the first half-barrel prototypes. In parallel, a preliminary design of the whole SVT IB mechanics, including an external shell to L2, has been also developed and a first mock-up is being built.

We will evolve the designs for the half-barrel assembly and for the global mechanics, towards properly engineered realistic ones. The next half-barrel assembly to be built will integrate prototypes of most of the components of the final detector and allow for thermo-mechanical studies to finalize the cooling design. Test campaigns in a climate chamber and in a wind tunnel facility for ageing and cooling studies are planned. Building of a first L2 half-layer prototype, based on the guidance from the L0-L1 assembly experience, is also scheduled to happen in parallel.

For the SVT IB global mechanics, we will use carbon fiber composites as the main material for the support, given the low mass and excellent mechanical properties. In the coming months



an engineered version is planned, with the goal of both verifying possible space conflicts within the global mechanics and matching with the SVT IB assembly procedures.

E&D status and outlook – OB: We are currently prototyping (fig. 8.69) the curved surface stave design for L4 to evaluate the performance of the design, as well as tooling and assembly procedures. In the first phase we are prototyping the stave design with the curved facings, as this is the more challenging to construct. Interfaces to the support cones will be designed in parallel with the design work on these structures.

These prototypes will be equipped with mechanical dummy sensors ( $40\ \mu\text{m}$  unpatterned silicon) for mechanical studies, and thermo-mechanical dummy sensors ( $40\ \mu\text{m}$  silicon encapsulated in  $25\ \mu\text{m}$  and  $50\ \mu\text{m}$  thick Kapton layers with a  $5\ \mu\text{m}$  thick Cu trace layer). In particular, we will verify/measure: Manufacturability (co-cure), mechanical integrity and good compaction of carbon fibre; Mechanical response spectrum up to 500 Hz and associated  $Q$  values; Deformations with air flow up to 20 m/s; Surface temperatures with thermo-mechanical dummy sensors powered up to 40 W per stave; Thermo-mechanical deformations with thermo-mechanical dummy sensors powered up to 40 W per stave. The results from these studies will guide us in finalizing the stave design. In the first phase we are pro-

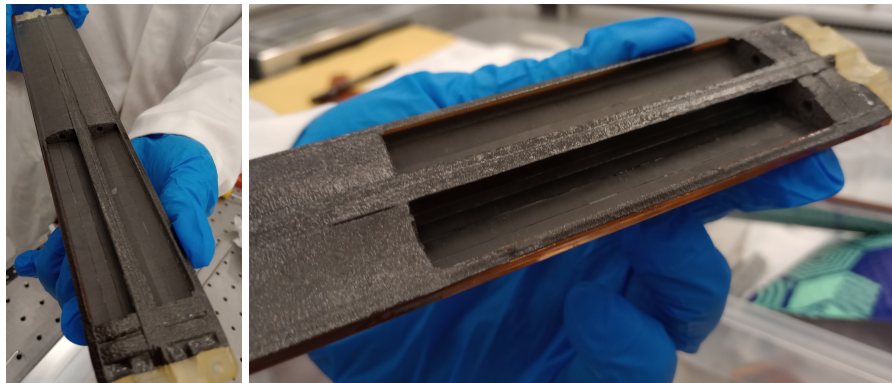


**Figure 8.69:** Co-cured support structure of first L4 quarter length stave prototype (without silicon sensors). The co-cure comprises carbon fibre skins, K9 cross ribs, central carbon fibre I beam spar and Kapton side closeouts (compare to fig. 8.67).

totyping the stave design with the curved facings, as this is the more challenging to construct. Interfaces to the support cones will be designed in parallel with the design work on these structures.

E&D status and outlook – Disks: Work continues on the design and layout of the disks. We are finalizing the carbon fiber layouts for both the corrugated core and the flat module sheets. The first prototype was made using a non-woven, randomly oriented mat of thin carbon fiber called carbon fiber veil for both the face sheets and corrugation and had a density of 500 gsm. However, the veil is not ideal for thermal performance and can be challenging to layup on the corrugated tooling. New prototypes are being made with K13CU unidirectional carbon fiber, which has a much improved thermal conductivity.

The initial test piece has been tested for thermal performance using copper trace heaters. The prototype is shown on the left side of Figure 8.70 and the thermal test results with the heaters are shown on the right. The measured  $\Delta T$  is well within  $10\ ^\circ\text{C}$  for the expected EIC-LAS RSU power density, but is high for the expected ELC power density, though trending in the right direction with increased air flow, and is dependent on the planned design dissipation. The thus far high values of  $\Delta T$  for the LEC region can be due to many factors, including the low

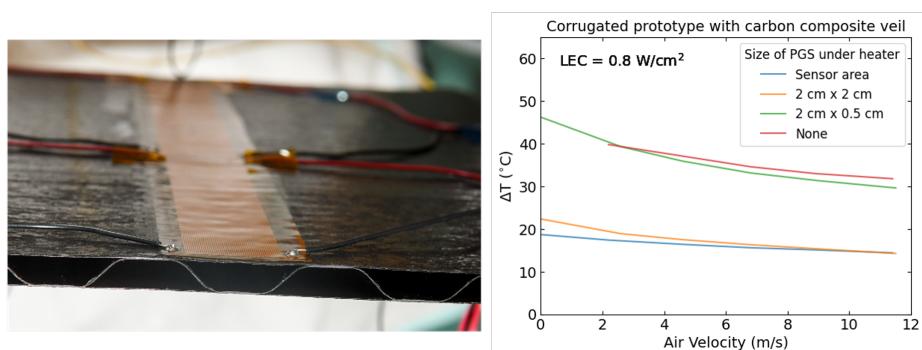


**Figure 8.70:** (Left) First test piece of the carbon composite corrugated disk core made in the LBNL composite shop. Heaters with two different heating zones that can mimic the sensor power density are placed on the carbon composite facesheet and are used for thermal measurements. (Right) Observed  $\Delta T$  on the LEC section of the test heater versus coolant air velocity using corrugated carbon fiber veil prototype test piece. Measurements taken with various sizes of PGS placed underneath heater.

thermal conductivity of the carbon fiber veil and the overall thinness of the contact surface. We are studying mitigation possibilities using pyrolytic graphite sheets (PGS), which have a large in-plane thermal conductivity (upwards of 800 W/m·K) and significantly improve the thermal performance of the prototype. The new face sheets made with K13CU have similar thermal conductivity to the PGS and initial tests are promising. A new, full prototype is being assembled with the K13CU carbon fiber.

We are currently working on prototypes focused on the development of assembly tooling, module handling, and thermal and mechanical tests. Prototypes will undergo vibration tests to understand mechanical stability. Mechanical dummy silicon (40  $\mu\text{m}$  unpatterned silicon) is in hand to construct a quarter disk mechanical prototype. We expect thermo-mechanical dummies (as described above for the OB staves) at the end of 2024 to create a thermo-mechanical prototype.

The bench tests will be paired with ANSYS structural and fluent simulations to understand the performance under air flow and the structural integrity of the disk. This will also need to be accompanied by bench tests and simulations that include the disk support ring and the outer ring.

**E&D status and outlook – FPCs:** The first iteration of FPC prototypes is underway targeting an initial design for OB L4. A definition stage captured the current design requirements for powering, data transmission and geometrical factors. This was followed by a design stage and then by an order submission to RPE LTU (Ukraine). The first set of prototypes (Figure 8.71) are currently being manufactured. The prototypes from RPE LTU will be distributed for testing to SVT institutes. In parallel, prototypes from Omni Circuit Board (Canada) are being evaluated and a third supplier, Q-Flex Inc. (USA), has been approached to procure low level prototypes. The aim is to evaluate the capabilities of three different suppliers to manufacture FPCs with aluminium conductors. Signal and power integrity of the FPCs will be tested and the performance over samples of different suppliers compared. A key requirement is signal attenuation for the high speed differential transmission lines (10 Gb/s). Wire bonding and single point Tape Automated Bonding (spTAB) are being evaluated as potential interconnection techniques in ongoing and future prototypes.

**E&D status and outlook – Powering:** The need to regulate voltages for the MOSAIX sensors

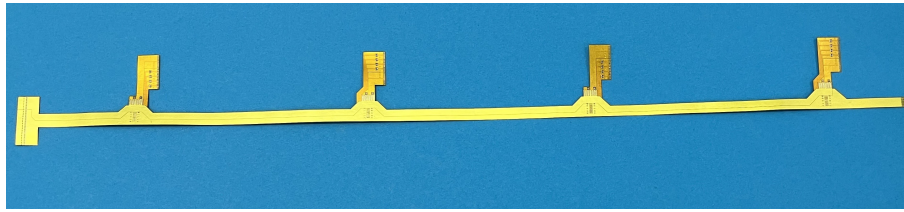


**Figure 8.71:** An example of a low technology readiness level prototype for the FPC of the OB L4. Prototype made by RPE LTU. The figure shows the main FPC with four bridge FPCs.

as close to the IB (to minimise losses) dictates the need for a(t least one) powering board. Considerations for the design and development of these boards are ongoing; this includes deciding how many regulation stages give the best balance between power losses (fewer stages is likely to mean longer lengths of the most lossy cables, when delivering low voltage and high current), versus additional material in the detector volume (more stages equals more high material powering board, and the final voltage regulation is likely closer to the active area of the IB).

Conceptual powering schemes were developed and used to define specifications for the AncASIC and FPC designs for the OB and Disks. Requirements are being iterated based on limitations introduced by these designs so that they can be iteratively improved. Testing and confirmation of requirements will occur as prototypes become available; this includes:

- Verifying output voltages and current capacity of the individual SLDOs.
- Verifying output voltages of NVGs.
- Daisy-chaining AncASICs to verify serial powering chain performance.
- Quantifying performance of the FPCs in terms of current carrying capacity and voltage-drop along the conductor lengths.
- Combining the above elements to test full serial powering chain prototypes (1 FPC feeding current to 4 AncASICs, each loaded with an EIC-LAS-like structure).

E&D status and outlook – Powering: The need to regulate voltages for the MOSAIX sensors as close to the IB (to minimise losses) dictates the need for one or more types of powering board. Considerations for the design and development of these boards are ongoing; this includes deciding how many regulation stages give the best balance between power losses (fewer stages is likely to mean longer lengths of the most lossy cables, when delivering low voltage and high current), versus additional material in the detector volume (more stages equals more high material powering board, and the final voltage regulation is likely closer to the active area of the IB).

The design of the serial powering scheme is evolving alongside the AncASIC and FPC designs for the staves and disks, to define length of serial powering chain, the data and slow control transmission schemes. Testing and confirmation of requirements will occur as prototypes become available. This includes:

- Verifying output voltages and current capacity of the individual SLDO regulators.
- Verifying output voltages of the NVG.
- Daisy-chaining AncASICs to verify current flow in the powering chain.
- Quantifying performance of the FPCs in terms of current carrying capacity and voltage-drop along the conductor lengths.



- Combining the above elements to test full serial powering chain prototypes (one FPC feeding current to four AncASICs, each connected to a load mimicking the EIC-LAS current consumption ).

E&D status and outlook – Readout: Work on readout electronics has mainly concentrated on testing evaluation boards of the various components being considered for SVT readout: lpGBT, VTRx+, radiation tolerant FPGA PolarFire, optical FireFly. An initial prototype for the fiber aggregator board was discussed and is now under development using a commercial FPGA board (ZCU102) mated with the optical FireFly FMC card to provide up to 8 fiber inputs and multiple fiber outputs. The VLDB+ board from CERN (containing both lpGBT and VTRx+) was used to setup a full chain starting from a Skyworks clock generator board as a stand-in for the Global Timing Unit (GTU), a Xilinx ZCU102 board running lpGBT-FPGA firmware as a stand-in for the FELIX board, and the VLDB+ board as the RDO. A measurement of the jitter of the clock recovered by the lpGBT demonstrated adequate performance of this chain to provide a low-jitter clock to the sensors.

We are currently developing a test system for the serializer chiplet of the ER1 prototype submission in collaboration with ITS3 colleagues. This serializer is a prototype for the 10Gbps serializer to be deployed in the LEC the MOSAIX. The test system consists of an FMC card which contains the bonding pads for the serializer chiplet, as well as various drivers and connectors including the possibility to drive the high-speed signal onto a Flex-PCB to test the signal integrity over those traces. The FMC card itself will connect to a commercial Xilinx FPGA board for pattern generation and checking.

Another prototype development is the "MOSAIX Mock-up" board, consisting of an FMC daughter card which contains the various readout components (2 data VTRx+ and an lpGBT / VTRx+ combination for the slow control interfaces). It will interface to a ZCU102 board where firmware will simulate the responses to slow controls commands, while also allowing to simulate data packets to be sent over the up to 8 fiber optic lines of the 2 VTRx+ interfaces in order to develop both data acquisition protocols and slow controls interfaces of the readout electronics to the MOSAIX sensor without the need of an actual MOSAIX sensor.

E&D status and outlook – Cooling: Our prior work has shown that foam can be an important factor in the cooling and thermal performance of staves and disks. This is an integral part of the OB stave design and is being pursued as an option for under the LEC and AncASIC in the disk design. Both will be tested using thermal and thermo-mechanical dummies with upcoming prototypes.

The final air cooling system will be designed based on the overall air volume of the SVT. Current estimates put the total air volume around 1000 cfm total, which would require a pressurized system. The air will be pressurized before entering the ePIC detector volume and then regulated down to various pressures as required by the different parts of the SVT (e.g. OB design requires air above 1 atm).

Simulations from LBNL and JLab have shown that during beam-pipe bake-out a 5 mm distance from the beam-pipe can keep the silicon below 30 °C with air flow below 10 m/s. However, air flow between the beam-pipe and L0 brings down the temperature of the beam-pipe and can affect ability to reach the 100 °C required inside. Studies are ongoing to determine what hot gas temperature is needed to bring the beam-pipe to temperature and what effect that has on the silicon. We also plan to study if airflow only between L0 and L1 is sufficient to keep the detector below the current 30 °C requirement as this will help mitigate the effect of the air cooling on the beam-pipe itself. Simulations will be paired with thermo-elastic studies in a climate chamber that will study cycling, longevity, and assess the point of failure.

Other activity needed for the design completion: We are continuing our testing characterization of the products from the ITS3 sensor development sequence. We are currently preparing

for the first tests on MOSAIX at CERN, in collaboration with ITS3, using a high-frequency wafer probe setup that we are jointly developing. Laboratory tests of thinned and diced wafers are also being planned, as well as beamtests and irradiation efforts.

The AncASIC will be manufactured in a different process than the MOSAIX and EIC-LAS sensors. We are readying an initial MPW submission in this 110 nm process and are planning for its testing and validation. Test structures and the main functional modules of AncASIC, the SLDO, NVG and Slow Control, will undergo irradiation to verify their correct functioning in the expected radiation environment.

Status of maturity of the subsystem: The SVT underwent an incremental Preliminary Design Review (PDR1) in March, 2024. The maturity of the SVT is currently estimated to be at the 45% level overall, with considerable variation for different elements. The development of the EIC-LAS requires access to the MOSAIX design database, which is subject to a BNL-CERN agreement that has not been signed to date. The project identified the need for early procurement of the VTRx+ optical link module for data transmission and the lpGBT low power gigabit transceiver in the SVT readout and slow-control chain as part of potential CD-3B scope. The Final Design Review (FDR) for these elements was successfully passed in June 2024. The remaining effort, while substantial, is progressing and is anticipated to be more than 60% ready by the EIC CD-2 project phase at the end of 2025.

**Environmental, Safety and Health (ES&H) aspects and Quality Assessment (QA planning):** We will follow and adhere to all applicable ES&H standards during the development, construction, installation, and ultimately commissioning and operation of the SVT. Hazards include those associated with adhesives, carbon composites, flammables, wafer-probing and wire-bonding, use of radioactive sources, testbeams, and irradiation facilities, and electrical safety. Where possible, we will work across institutions to implement standardized controls and mitigations, as well as documented safety procedures.

System tests in the development phase of the SVT are integral to our quality assessment. Quality Control forms an integral part of the work breakdown structure (WBS) and schedule during construction and assembly.

**Construction and assembly planning:** The L0-L1 half-barrels will be manufactured in Italy by INFN: the current plan is to have a main assembly site in Bari and a second one in Padova currently being equipped. The L2 production half-layers will be built in the US. Both construction activities will rely on a first step for QC of the sensors through wafer probing. They will also include a final QC step of the corresponding complete assembly: this will include operation with air-cooling to verify thermal performance and testing of readout and control lines. After a successful pass of the QC step, L0-L1 half-barrels and L2 half-layer will be shipped to BNL. The global IB mechanics will be produced by INFN in Padova, undergo a QC step based on a metrological survey and finally shipped to BNL. At BNL the L0-L1 half-barrels and L2 half-layers will be assembled to the global mechanics to form complete IB half-barrels. All the connections to services (powering, cooling and readout) will be put in place to allow a final QC step.

Modules and staves for the OB layers will be manufactured in the UK. Currently we plan to manufacture modules at two sites, Birmingham and Daresbury Lab. This production includes electrical bonding of the sensors and ancillary ASICs to the bridge FPC. Module construction concludes with a QC on the completed module before shipping to the stave loading sites. Stave production, which comprises manufacture of the stave composite structures, and gluing of modules onto the structures and electrical bonding of the bridge FPCs to the main FPCs, will be performed at Oxford

and RAL. Again, the final step of the stave construction will be a QC of the completed stave. This will comprise operation with internal air cooling to verify thermal performance, operation of control lines and readout of modules. After successful pass of these QC steps, staves will be shipped individually to BNL. At BNL staves will be mounted on the support half-cones from the inside, starting with the outermost layer L4. This involves mechanical connection, connection of the air supply, and connection of the FPCs to the RDO boards on the support cones, and mounting of the RDOs on the outside of the support cones. After the mounting of the L4 staves they will be tested, and after that the same procedures will be repeated for the inner OB layer, L3.

Disks and their modules will be produced and assembled in the US. LBNL, Purdue, and LANL are expected to be disk assembly sites, with LBNL and Purdue also serving as module assembly sites. Assembly of modules includes gluing of sensors to carbon composite structures, as well as electrical connection (wire or tab bonding) to a bridge FPC and the AncASIC. Modules will undergo QC before being assembled onto disk structures. The corrugated carbon composite disk structures and module flat sheets will be produced at LBNL and shipped to LANL and Purdue. Disk support rings will be produced by an outside vendor, validated at LBNL, then shipped to disk assembly sites. Disks will be assembled in halves, first on one side and then the other. Disk assembly includes gluing modules and common bus FPCs onto the front and rear sides of the discs and making electrical connections. QC is planned for each corrugated row assembly and then again after completion of the front and rear sides of each disk. Disks will be shipped in halves to BNL, where they will be installed into the larger SVT assembly. Disks are the last piece to be installed, after the IB and OB. Installation will occur from the inner disks outward. ED0 and HD0 will be mounted to the SVT support cones. ED2–4 and HD2–4 will be mounted to the support cylinder. ED1 and HD1 could be mounted to either and will be iterated with global mechanics. Installation must include the connection of the services, connecting of the air supply, and mounting of the RDOs. Each half disk will be tested after installation.

The IB, OB, and disks can thus be constructed concurrently. We plan to produce the outer global support structures at Purdue and/or LBNL. Readout will be led by ORNL with testing at multiple sites. The construction of the SVT can be completed in three to four years in a technically driven schedule.

**Collaborators and their role, resources and workforce:** The SVT currently has collaborators at 20 institutions with the main institutional roles and resources outlined above.

**Risks and mitigation strategy:** The SVT depends crucially on its sensors, the ITS3 sensor used in the IB and the ITS3-based EIC-LAS used in the OB, EE, and HE, since they form the only known way to meet the full performance requirements within ePIC. Their development is ongoing and thus presents a risk. The project and institutions involved in the SVT have identified one main branchpoint, related to the possibility that the EIC-LAS development is delayed and becomes incompatible with the overall EIC project schedule. If this branchpoint were triggered, the SVT OB will be replaced with two MPGD barrel layers derived from the outer MPGD tracker, specifically its innermost (micromegas) layer. The SVT EE and HE will in this case each be replaced with in total up to seven near-identical MPGD disks, specifically based on the existing uRWELL disks. The SVT IB remains based on the wafer-scale sensor of the ALICE-ITS3 upgrade in this case. The ALICE-ITS3 project is about to submit the second engineering run of its wafer-scale sensor and its timelines are compatible with those of the EIC project. In case of unforeseen future (sensor) delay, we will need to reprioritize ePIC efforts towards the ALICE-ITS3 sensor.

### 8.3.3.2 The MPGD trackers

#### Requirements

**Requirements from physics:** Micro-Pattern Gas Detector (MPGD) technologies have been chosen to complement the Si based tracking layers. MPGDs are relatively fast detectors able to provide precision space point measurements with good timing resolution, while also maintaining the overall conservative material budget that is required of the ePIC detector [41]. MPGDs will play a role in pattern recognition for central tracking system in the required pseudorapidity range of  $-3.5 \leq \eta \leq 3.5$ , and aid in PID reconstruction.

The EIC collider is expected to deliver collisions with bunches crossing every  $\sim 10$  ns [42], which will require the MPGD detectors to provide timing resolution of 10-20 ns to separate events from adjacent bunches. For ep collisions of  $10 \times 275$  GeV, the DIS physics rate is expected to be around 500 kHz, while hadron and electron beam gas backgrounds rates are estimated to be 32.6 kHz and 3.17 MHz, respectively [43]. These rates are well within the rate capabilities of MPGDs. Combining the timing information from the MPGDs with information from the Si detectors will allow pattern recognition algorithms to discriminate between physics and background signals. In addition to providing hit information with good timing resolutions, the MPGDs will provide

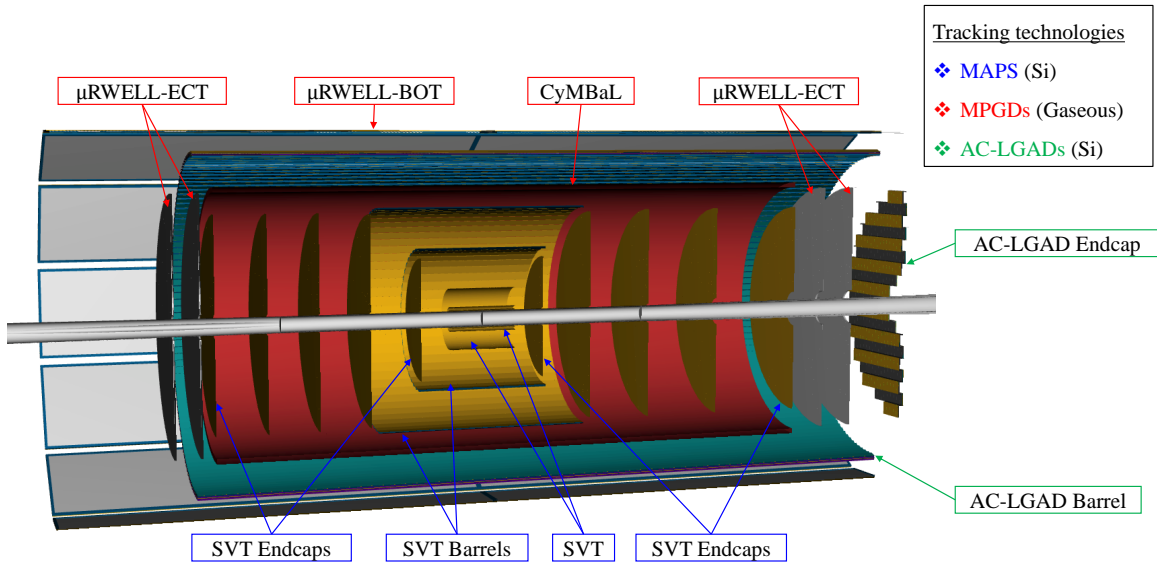
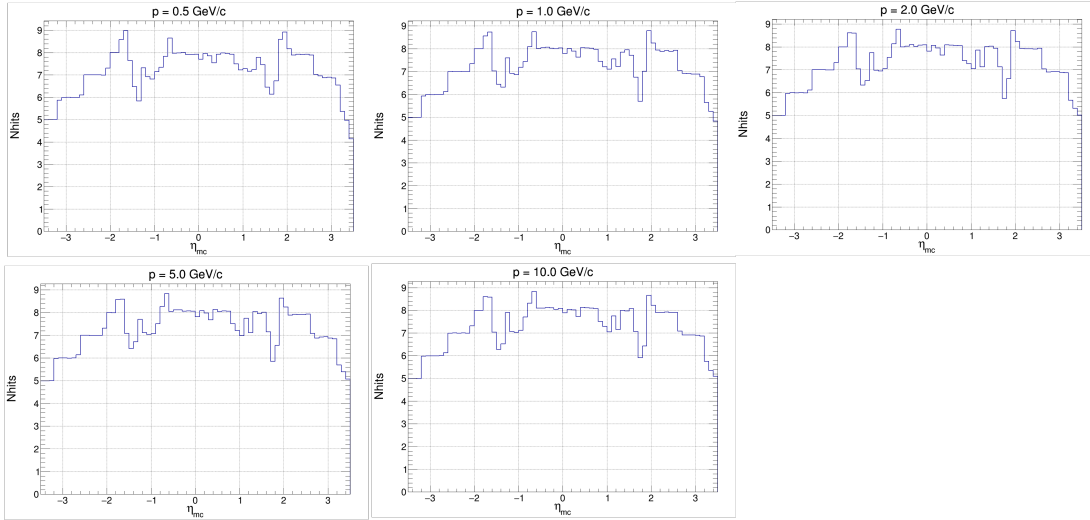


Figure 8.72: ePIC tracking subsystems.

additional hit points needed for robust track reconstruction. Early simulations showed that the number of hit points used in the track reconstruction reduced from around 6 hits near  $\eta = 0$ , to only 3 hits at  $|\eta| > 3$ , due to tracks moving out of the acceptance of some of the Si layers. The ePIC endcap gaseous trackers, ( $\mu$ RWELL-ECT) were implemented to recover additional hits at larger  $\eta$  values. Figure 8.73 shows the average number of hits per event in the current ePIC tracking detector as a function of  $\eta$  for different momentum ranges. In this configuration the ePIC tracker measures at least 5 hits per event in the region ( $|\eta| < 3.5$ ).

Finally, as detailed in the Yellow Report [41], the hpDIRC requires the track entering the PID

2546 volume to have good angular resolution (0.5 mrad at  $p = 6$  GeV) in order to meet its performance  
 2547 requirements. This will be accomplished by providing the hpDIRC with precision hit points just  
 2548 before a particle enters its volume via the ePIC barrel outer tracker ( $\mu$ RWELL-BOT), and after it  
 exits the hpDIRC volume via the first tracking layer of the barrel imaging calorimeter.



**Figure 8.73:** Total tracker hits vs.  $\eta$  for various momentum ranges ([gitHub Repo](#)).

2549

2550 **Requirements from Radiation Hardness:** Detailed simulation on radiation dose in ePIC has  
 2551 been performed. Figure 8.74 shows the estimate of hadron and EM radiation doses in ePIC simula-  
 2552 tion along with location of MPGD layers [43]. Table 8.25 shows the maximum estimated radiation  
 2553 dose from various sources for MPGD trackers at various locations with 10 years of running at top  
 2554 machine luminosity and 100% detector and accelerator efficiency based on e+p PYTHIA simula-  
 tion. The MPGD trackers in ePIC will experience low radiation dose and based on past experience

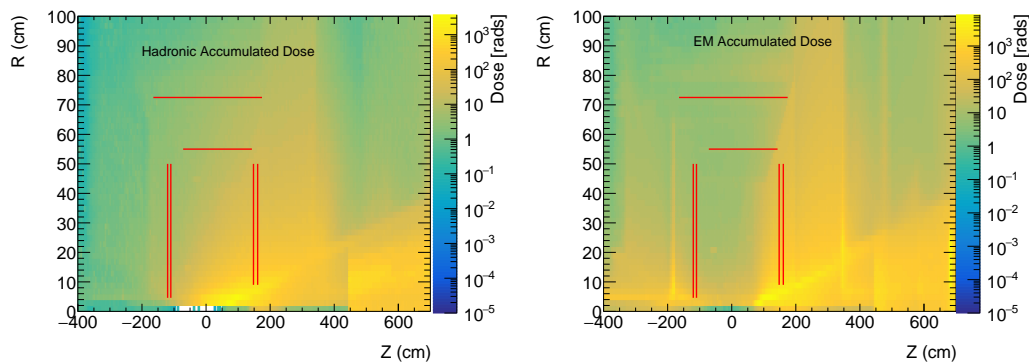


**Figure 8.74:** (left) EM radiation and (right) Hadron radiation dose estimate for minimum bias PYTHIA e+p events at 10x275 GeV at top machine luminosity for 6 months of running at 100% machine and detector efficiency [43]. The locations of MPGD trackers are shown by red lines [44]. ([gitHub Repo](#)).

2555

MPGD tracker	EM Radiation dose [krad]	Hadron Radiation dose [krad]	1 MeV neutrons equivalent fluence [ $\text{cm}^{-2}$ ]	1 MeV protons equivalent fluence [ $\text{cm}^{-2}$ ]
CyMBaL	0.22	0.15	$2.7 \times 10^{10}$	$2.0 \times 10^{10}$
$\mu$ RWELL-BOT	0.3	0.1	$2.8 \times 10^{10}$	$4.2 \times 10^9$
electron ECT	0.064	0.03	$1.1 \times 10^{10}$	$1.7 \times 10^9$
hadron ECT	0.87	0.23	$3.0 \times 10^{10}$	$8.5 \times 10^9$

**Table 8.25:** Maximum dose of radiation by different sources at MPGD tracker layers for e+p minimum-bias event at 500 kHz event rate for 10 years EIC running with 6 months run time per year and 100% efficiency [43].

with MPGD trackers in various experiments [45–47] there will be negligible aging issues. The electronics will be mounted close to the MPGD trackers, and will be based on SALSA readout ASICs. It will also require specific DC-DC converter components able to stand the ePIC radiation and magnetic field levels. Both components are described in section 8.3.10 of this document.

**Requirements from Data Rates:** Table 8.26 shows hit rate per unit area for each MPGD subsystem in ePIC which is far lower than rate capability of MPGD detectors [48,49]. Table 8.27 shows the maximum hit rate experienced by a channel for various MPGD trackers in ePIC [43]. The rates are low enough for ASIC developed for MPGDs which can handle rate of 100 kHz/channel.

MPGD tracker	DIS e+p rate [Hz/ $\text{cm}^2$ ]	Hadron beam gas rate [Hz/ $\text{cm}^2$ ]	Electron beam gas rate [Hz/ $\text{cm}^2$ ]
CyMBaL	26.37	14.33	5.5
$\mu$ RWELL-BOT	9.82	5.33	1.7
electron ECT	144.68	78.63	437
hadron ECT	1326.36	720	201

**Table 8.26:** Hit rate per unit area of various MPGD trackers for e+p DIS events at  $10 \times 275$  GeV with  $1.54 \times 10^{34} \text{cm}^2 \text{s}^{-1}$  luminosity scaled from e+p DIS events at  $18 \times 275$  GeV and  $1.54 \times 10^{33} \text{cm}^2 \text{s}^{-1}$  luminosity, 10 GeV electron beam gas and 275 GeV hadron beam gas

2563

**Justification** The requirements cited above drives the necessity of using MPGD trackers at various locations of ePIC. MPGDs can be built over large area and their ability to handle high rates and good spatial resolution makes them excellent candidate for large trackers.

**Device concept and technological choice:** The MPGD trackers are based on two different technologies and are described [below](#)

**CyMBaL:** The role of the Cylindrical Micromegas Barrel Layer (CyMBaL) is to wrap around

MPGD tracker	DIS e+p events [Hz]	Hadron beam gas [Hz]	Electron beam gas [Hz]
CyMBaL	3.68	0.05	4.78
$\mu$ RWELL-BOT	2.76	0.04	4.78
electron ECT	9.2	3.56	102
hadron ECT	101.2	4.39	39.88

**Table 8.27:** Maximum hit rate by a single channel of various MPGD trackers for e+p DIS events at  $10 \times 275$  GeV with  $1.54 \times 10^{34} \text{cm}^2 \text{s}^{-1}$  luminosity scaled from e+p DIS events at  $18 \times 275$  GeV and  $1.54 \times 10^{33} \text{cm}^2 \text{s}^{-1}$  luminosity, 10 GeV electron beam gas and 275 GeV hadron beam gas.

the SVT in its entire length to provide an additional hit point. Consequently, the main requirement is to have as little as possible acceptance gaps. In order to limit the impact on particle reconstruction in the outer detectors, CyMBaL has to be light in material budget, possibly less than  $X/X_0 \sim 1\%$ . CyMBaL (Figure 8.75a) is composed as a set of 32 Micromegas tiles arranged in a way to ensure full coverage in  $\varphi$  (8 modules) and in  $z$  (4 modules). The space envelope assigned to CyMBaL spans the range between 55 cm and 60 cm in radius and it is asymmetric in the longitudinal direction, covering the range  $-105 \text{ cm} < z < 143 \text{ cm}$ . CyMBaL is designed in two symmetric halves that meet at  $z = 19 \text{ cm}$  (due to the asymmetric keeping zone). In each half, the 16 modules are arranged in two cylinders, the inner one (in  $|z|$ ) sitting at a radius of 55 cm and the outer one at 57.5 cm. In order to limit the complexity of the detector production, the design is aiming at limiting the differences among the modules, possibly having only a single design for the module PCBs that will be assembled with different bending radii. The preliminary design of a CyMBaL module is

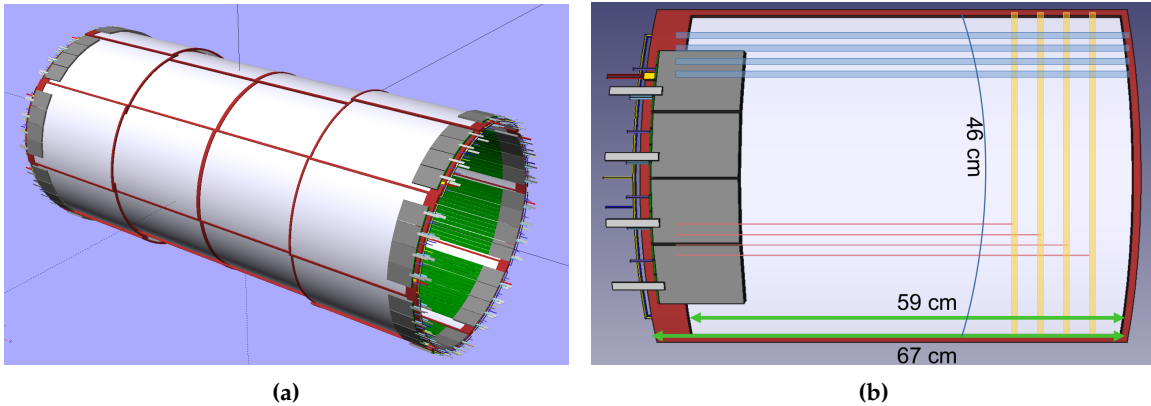


**Figure 8.75:** [CyMBaL CAD model](a) CyMBaL CAD model showing the assembly of the 32 modules. (b) CAD model of a CyMBaL module. The light blue represents examples of readout strips measuring the  $r \cdot \varphi$  coordinate (called Z-strips as they run along the  $z$  axis). The light yellow represents examples of readout strips measuring the  $z$  coordinate (called C-strips as they are arcs of a cylinder). The light red lines represent examples of trail lines to bring the C-strip signals to the FEBS. For the explanation of the services see the text.

shown in Figure 8.75b. A module is a cylindrical tile 48 cm wide (equivalent to about 50 degrees in the azimuthal direction) and 67 cm long, and the active region is about  $46 \times 59 \text{ cm}^2$ . In the current



design, the module dimensions allow for an overlap of 2.8 cm in the  $r \cdot \phi$  direction and about 2 cm in  $z$ . The sensor is based on the bulk resistive Micromegas technology [50] with a 3 mm conversion gap.

The main purpose of the resistive layer (surface resistivity  $1 - 10 \text{ M}\Omega/\square$ ) is to share the charge, induced by the amplification, to neighboring strips in order to improve the spatial resolution. The resistive layer will also prevent sparks in the amplification region, although the expected particle rates are low and spark limitation would not be a major concern. The signal will be readout by orthogonal strips to provide a two dimensional information of the position of the charged particle crossing the sensitive area. The strips running along the longitudinal direction (therefore called Z-strips) will provide the  $r \cdot \phi$  measurement of the hit and they will be directly routed to the connector area. The strips running along the azimuthal direction (C-strips, C for cylindrical) will provide the  $z$  information of the hit and they will need to be connected with vias to routing trails to bring the signals to the connectors. The pitch of the readout strips will be  $\sim 1 \text{ mm}$  and the resistive layer will allow the charges to be shared among neighboring strips for a better centroid reconstruction. The total number of strips per module will be 1024 and they will be readout by four FEBs, each one equipped with  $4 \times 64$ -channel SALSA chips. The module's frame will consists of carbon fiber hollow square beams and arcs of about 3 mm in size. Being hollow, these beams not only will provide the mechanical rigidity and support for the detector, but will be also used to distribute the gas inside the detector. As shown in Figure 8.75, the FEBs will be mounted at the two ends of CyMBaL to concentrate the material budget in just few areas. Low-mass micro-coaxial cables will be used to bring the signals from the modules to the FEBs: the inner modules will need cables of about 50 cm in length, while short ( $\lesssim 10 \text{ cm}$ ) cables are sufficient for the outer modules. It is expected that the detector gain will be sufficiently high to overcome any noise induced by the additional capacitance of the cables.

**$\mu$ RWELL-BOT:** ePIC MPGD Barrel Outer Tracker ( $\mu$ RWELL-BOT layer) is the outermost gaseous tracking layer installed in the barrel region of ePIC central tracker. The detector sits right

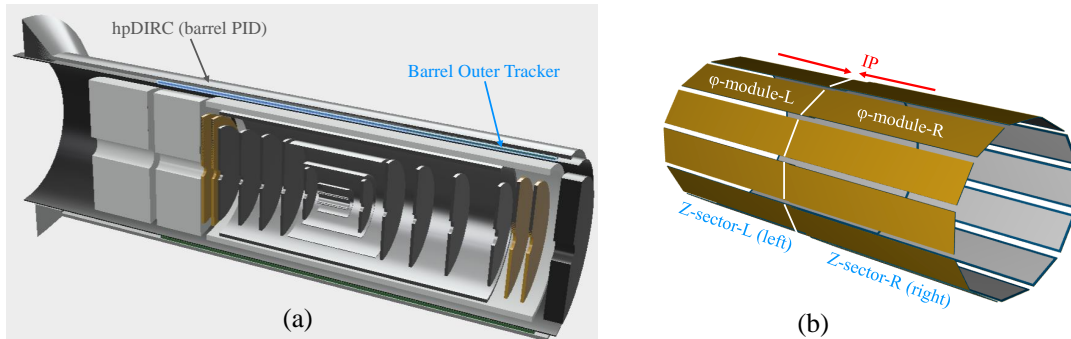


**Figure 8.76:** (a)  $\mu$ RWELL-BOT in ePIC central detector; (b) Arrangement of 24  $\mu$ RWELL-BOT modules in dodecagon shape.

at a radius of 72.5 cm right in front of the high performance DIRC (hpDIRC) as shown in the layout at the top left of Figure 8.76. The tracker is split in two sectors (Z-sector) along the beam axis  $z$ . Each Z-sector consists of 12  $\mu$ RWELL-BOT rectangular modules ( $\phi$ -modules) arranged in dodecagon shape to cover  $2\pi$  acceptance in the azimuthal direction ( $\phi$ ) as shown in the top right of Figure 8.76. The  $\mu$ RWELL-BOT  $\phi$ -modules are designed to match the hpDIRC acceptance in both  $z$  and  $\phi$  as shown on the bottom right of Figure 8.76. Mechanical constraints associated to the detector support frames as well as the very limited space available for integration in the ePIC detector support frames result in an acceptance gap of  $\sim 13\%$  in  $\phi$  and  $\sim 1\%$  in  $z$ . The material budget  $X/X_0$  of the detector is  $\sim 1.5\%$  in the active area but will become significantly higher at



the edges of the detector where the front end electronics cards, cables and services are be located. The design of the full size  $\mu$ RWELL-BOT module engineering test article shown in Figure 8.82 developed as part of the Project Engineering Design (PED) effort based on thin-gap GEM- $\mu$ RWELL technology (see paragraph section 8.3.3.2 and Figure 8.83) is complete and the fabrication of the chamber is scheduled for the first half of 2025.

**$\mu$ RWELL-ECT:** Monte Carlo simulations show that the endcap regions of the ePIC detector experience the highest backgrounds in the experiment and charged particle tracking requires several hit points in the  $|\eta| > 2$  region for good pattern recognition. To optimize the ePIC baseline tracker design, two planar Micro-Pattern Gaseous Detectors (MPGD) disks, with a central hole for the beam pipe are located both in the hadronic and the leptonic sectors (see the right drawing of Figure 8.77). The ECT disks geometrical envelope is reported in Table 8.28. It takes into account the integration constraints within the ePIC detector and the beam pipes dimensions. As shown in the left drawing of Figure 8.77, the hadron and lepton beam pipes slightly diverge from the interaction point. Therefore the ECT inner radii are calculated taking into account the envelope radii and their center offset. For simplicity the inner radius is fixed by the largest of the two values calculated for the disk located at the larger  $z$  position at each endcap region. As a result the two lepton disks located closer to the interaction point, will have a smaller inner radius than the two hadron disks (4.65 cm vs 9 cm) as they are located closer to the interaction point, while the outer radii of 50 cm are equal for all the four disks and are fixed by the available volume inside the ePIC detector. The ECT disks envelope also includes the MPDG gas frames of 1.5 cm thickness, and a

MPGD Disk	Longitudinal location $z$ (cm)	Outer Radius (cm)	Inner Radius (cm)	Outer Active Area Radius (cm)	Inner Active Area Radius (cm)
HD MPGD 2	161	50	9	45	10.5
HD MPGD 1	148	50	9	45	10.5
LD MPGD 1	-110	50	4.65	45	6
LD MPGD 2	-120	50	4.65	45	6

**Table 8.28:** The ECT disks geometrical envelope and active areas dimensions.

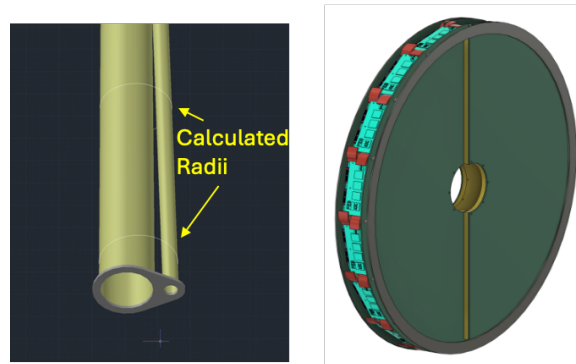


**Figure 8.77:** Left: Hadron and lepton beam pipes slightly diverge from the interaction point. The ECT inner radii are calculated taking into account the envelope radii and their center offset, the hadron beam pipe forming a larger angle with the  $z$  axis. Right: layout of a couple of  $\mu$ RWELL-ECT disks.

3.5 cm outer service ring, to locate services and electronics front-end boards. The resulting active area dimensions of the disks are also reported in Table 8.28 and the corresponding angular and pseudorapidity acceptances are reported in Table 8.29. The final active ranges in pseudorapidity are  $2.0 < \eta < 3.3$  for the hadron sector and  $-3.6 < \eta < -1.7$  for the lepton sector, constrained by the available space.

MPGD Disk	$ \theta $	$ \theta $	$ \eta $	$ \eta $
	min (deg)	max (deg)	min	max
HD MPGD 2	3.7	15.5	2.0	3.4
HD MPGD 1	4.0	16.9	1.9	3.3
LD MPGD 1	3.1	22.1	1.6	3.6
LD MPGD 2	2.8	20.4	1.7	3.7

**Table 8.29:** The ECT disks angular and pseudorapidity acceptance.

A GEM- $\mu$ RWELL hybrid technology [51] with XY 2D readout, similar to the one described for the  $\mu$ RWELL-BOT and shown in Figure 8.83(b), has been chosen to match all the performance requirements. The main difference is related to the drift region gap, which is 3-6 mm wide to ensure an intrinsic efficiency higher than 97-98%. A 2D strip read-out COMPASS-like scheme, where the charge is collected by XY orthogonal strips located on two different printed circuit board (PCB) layers, has been chosen. The strip widths of the two coordinates must be optimized (in a ratio of about 1:3) to balance the signal amplitude in the two dimensions, since the upper layer strips screen the charge collected on the lower ones.

The XY Cartesian readout scheme was preferred over the  $R\phi$  geometry for two reasons: i) the high radial strip density at the center hole and ii) the possibility offered by the XY geometry to route all the strips to connectors located on the outer service ring. The cathode and the 2D readout PCB are supported by a 3 mm thick honeycomb structure to minimize the detector material budget, which amounts to  $0.85\%X/X_0$  in the active region.

**Front End Electronics (FEE):** To meet the requirement of streaming readout new front-end chips for MPGD trackers in ePIC are being developed by Sao Paulo Universities and CEA Saclay IRFU. The SALSA chip, which associates an analog front-end adapted to MPGD detectors, an ADC per channel with a 50MS/s digitization rate on 12 bits, and a data processing unit, has the following characteristics:

- 64 channels with large input capacitance range (up to 1 nF), optimized for 50-200 pF.
- Large range of peaking times: 50-500 ns.
- Large gain ranges: 0-50 to 0-5000 fC.
- Large range of input rates, up to 100 kHz/ch.
- Reversible polarity.

**Other components.** The **gas mixing unit** will be a critical component of the MPGD trackers. The mixing unit preferably will use Mass Flow Controllers based on Proportional-Integral-Derivative (PID) control systems. Furthermore, the mixing unit should be able to mix either two or three different inert gases depending on the final composition of the operating gas. The preferred mixture for

CyMBaL is Ar-isobutane (95:5) see Figure 8.81, however if concern is raised for flammability of this gas mixture then a three gas mixing unit will provide the possibility of adding a third gas (preferably  $\text{CO}_2$ ) at the expense of isobutane. This will help in maintaining stability by operating the detector at lower voltage (due to the isobutane component), make the gas faster and non-flammable (due to the  $\text{CO}_2$ ) component. Additionally **sensors** will be installed to monitor the temperature, pressure and humidity close to MPGD modules and if possible also to monitor temperature of incoming and outgoing gas to give an idea of heating of gas volume inside detector itself. The High Voltage Power Supplies (HVPS) are another important component for MPGD trackers to bias the detector. The preferred way of biasing each module of MPGD tracker is by using voltage divider. The HVPS will have low ripple ( $< 5 \text{ mVpp}$ ) to reduce noise from HVPS along with the capability of monitoring current drawn by the detector.

**Performance** The MPGD tracking detectors share 2D spatial resolutions performances better  $\simeq 150 \mu\text{m}$ , timing resolutions of the order of  $10 - 20 \text{ ns}$ , rate capability better than  $10 \text{ kHz}/\text{cm}^2$ , and detectors response not impacted by temperature instabilities, which may be compensated in the calibration procedures. The radiation hardness of the components material will sustain the doses reported in Table 8.25. The specific performances of each MPGD subsystem are reported in the following.

**CyMBaL:** The CyMBaL design aims at providing complete azimuth ( $\phi$ ) coverage. Along the longitudinal direction where the two halves of the system meet, only  $\sim 3 \text{ cm}$  will not be covered. CyMBaL modules are expected to provide a hit spatial resolution around  $150 \mu\text{m}$  with a time resolution of  $10 - 20 \text{ ns}$ . The modules are expected to operate with efficiencies above 95%. The magnetic field, being orthogonal to the drift field, will cause the primary electrons to drift away from the electric field lines, the so called Lorentz angle. This effect could degrade the  $r \cdot \phi$  resolution. To limit the Lorentz angle, the module's drift fields will be set at about  $3 \text{ kV}/\text{cm}$  and adjusted among modules to account for possible longitudinal variation of the magnetic field.

**$\mu\text{RWELL-BOT}$ :** The barrel outer tracker will provide hit space point resolution better than  $150 \mu\text{m}$  on average in the eta range of  $-1 \leq \eta \leq 1$  and  $100 \mu\text{m}$  in the azimuthal direction and a timing resolution of  $\sim 10 \text{ ns}$ . The tracker has an acceptance gap of 13% along  $\phi$  because of space constraints imposed by the limited space in the ePIC detector. The tracker will operate at a nominal efficiency of  $\sim 95\%$ . As shown in Figures 8.26 and 8.27, the particle rate per unit area and per readout channel is very low and will not pose any challenge in term of tracking performance, safety operation and long term stability of the  $\mu\text{RWELL-BOT}$  trackers for the lifetime of the ePIC detector.

**$\mu\text{RWELL-ECT}$ :** The MPGD-ECT disks are designed to provide intrinsic spatial resolution for perpendicular tracks less than  $150 \mu\text{m}$ . Technological solutions and data analysis procedures exist to guarantee similar performances also for inclined or curved tracks. The active area of the detector has a material budget less than 1% in units of radiation length ( $X_0$ ) and will cover all azimuthal angles in the polar region specified in Table 8.29. A time resolution in the  $10 - 20 \text{ ns}$  range is achievable using the gas mixtures described above. A single disk efficiency of  $\simeq 96-97\%$  is required to provide 92-94% combined efficiency for two disks in the same region.

## Implementation:

**Services:** The MPGD tracking detectors subsystem are divided in different modules, each one requiring: gas supply lines and outlet, front end boards (FEB) connected to 5-line optical fibers (VTRX+) for data transfer to the RDO, low voltage lines (four lines for each FEB: one pair for the 1.8 V and one for the 3.3 V.), high voltage cables, temperature and humidity sensors and cooling in and out lines. Studies on the type of cooling and possible implementation in a serialize distribution will be done in synergy with the other subsystem of ePIC.

The service requirements for each MPGD tracking subsystem is summarized in Table 8.30.

Subsystem	CyMBaL	$\mu$ RWELL-BOT	$\mu$ RWELL-ECT
Number of Modules	32 Micromegas tiles	24 GEM- $\mu$ RWELL $\varphi$ -modules	4 GEM- $\mu$ RWELL disks
Gas supply lines per module	1 in / 1 out	1 in / 1 out	8 in / 8 out
Number of FEB per module	4	14	32
Low voltage lines per module	16	56	128
High voltage lines per module	2	1 (or 4)	16
Cooling lines per module	1 in / 1 out	1 in / 1 out	4 in / 4 out
VTRX+ lines per module	4	14	32

**Table 8.30:** Services requirements for the three MPGD tracking subsystems.

2726

**Subsystem mechanics and integration:** CyMBaL integration and mechanics rely on the central tracker global support structures. CyMBaL modules will be connected to the support structure. For  $\mu$ RWELL-BOT, the support structure connecting the carbon fiber tube and EM-Cal will serve as  $\mu$ RWELL-BOT and HP-DIRC support structure whereas for  $\mu$ RWELL-ECT, the outer ring of each disk hosts all the services listed in Table 8.30. The FEB are mounted perpendicularly to the disks.

Because of the divergence of the beam pipes, the disks cannot longitudinally slide along them but need to be shaped in sectors to be mounted around the pipes. Moreover, as the width of the Cu-kapton foil base material for the MPGD detectors restricts one dimension to about 550 mm, an implementation of the endcap trackers would consist of two half-circular disks with “D-shaped” cut-outs for the beam pipe, eventually sub segmented in four quadrants. As sketched in Figure 8.78, the disks integration and mechanics rely on the central tracker global support structures, using the same layout of the Silicon trackers. The MPGD-ECT disk are the most outer elements in the endcap region and the last to be installed in the mounting scheme of the tracking system.

**Calibration, alignment and monitoring:** The three MPGD subsystems will generally follow similar calibration, alignment and monitoring procedures. There are two main calibration tasks that have been identified. The first is to determine the optimal HV settings for the MPGDs, which will be determined through efficiency scans. These scans will be performed prior to data taking campaigns and after changes in running conditions (e.g. changes in gas composition). The second calibration task is to determine pedestal values and the common noise to be subtracted from the ADC samples, which will be determined through dedicated calibration runs. To meet the overall ePIC tracking performance precise knowledge of the tracking detector positions will need to be known. The alignment of the MPGD modules will be surveyed and entered into a database before integration. This information will be used to establish a starting point for the software alignment, which will be based on track reconstruction with and without magnetic field applied and

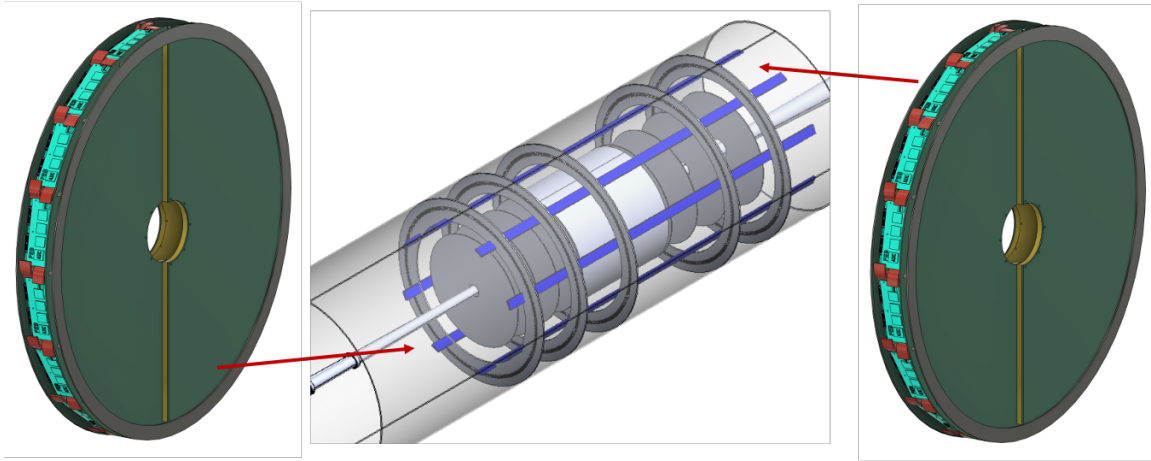


**Figure 8.78:** Integration of the MPGD-ECT disks in the ePIC detector.

will involve all of the ePIC tracking detectors. To assure that the MPGD detectors are performing optimally there are several criteria that will be monitored, which include the gas composition, the environmental conditions near the MPGDs (e.g. temperature, humidity and pressure), currents drawn by the MPGD layers from the power supply and general detector performance. Changes in the environmental conditions can be addressed by adjusting the detector gain via a feedback loop. The currents drawn by each high voltage channel will be read out and logged with a frequency of about 1 Hz. Additionally, we will need to monitor and log the low voltage currents and FEB temperatures. Not only will this allow us to monitor for abnormal values, but also implement automatic safety measures should a particular value fall outside of an acceptable range. Finally, during data taking we will monitor basic detector performance parameters such as hit occupancy maps, 2D efficiency, signal amplitude and timing distributions will be constantly monitored.

**Status and remaining design effort:** R&D and PED

**CyMBaL:** The resistive Micromegas technology has been extensively used in nuclear and particle physics experiments. In particular, 1D-readout cylindrical Micromegas tiles are in use at JLab in the Barrel Micromegas Tracker (BMT) of the CLAS12 experiment since 2017 [52], in experimental conditions which are more challenging than those expected at the EIC. The main focus of the ongoing R&D is to upgrade the BMT technology to 2D readout. In order to limit the number of readout channels, the R&D also focus on exploiting the charge sharing through the resistive layer and using  $\sim 1$  mm pitch readout strips. Several combinations of strip readout patterns together with layers of different resistivity have been tested in a beam test in MAMI in 2023. Further studies are ongoing with the cosmic rays test bench in Saclay and an additional beam test at CERN is planned for 2025. The design of a CyMBaL module prototype has begun and its production and tests are expected to be completed in 2026.

**$\mu$ RWELL-BOT:** The R&D phase for the development of the  $\mu$ RWELL-based trackers for EIC detector was completed in summer 2023 and transitioned into project engineering design (PED) effort. The goal for PED effort is to develop a full size thin-gap GEM- $\mu$ RWELL engineering test article as a beta version of pre-production  $\phi$ -module of  $\mu$ RWELL-BOT tracker in ePIC detector. The design effort including the CAD drawings of all mechanical parts that is frames and support structures as well as the sensitive devices such as the GEM foil, the  $\mu$ RWELL and the U-V strip



readout PCB is in advanced stage and expected to be completed by the end of 2024. The fabrication of the full size engineering test article will take place during the first half of 2025. The second half of the year 2025 will be dedicated to a full characterization of the prototype on a cosmic test bench setup and in beam at the CERN NA H4 beam test area including test in its 1.5 T GOLIATH magnet to study the performance of the detector in a magnetic field strength similar to the one expected from the ePIC magnet. The PED effort to develop the  $\mu$ RWELL-BOT module including a detailed review of the design choices and options, the timeline and outlook for the completion of the engineering test article effort.

**$\mu$ RWELL-ECT:** Disk design and modules segmentation is undergoing. The choice of the connectors will have in impact on the final strip pitch and the total number of read-out channels for each disk: usage of Hirose connectors (140 pins for 126 channels) would limit the maximum number of connectors and read-out channels if compared with obsolete Panasonic ones. Segmentation of the disks in four quadrants may avoid the use of a support structure for the GEM foil. A final decision on the final layout will be based on the results of prototype testing. Figure 8.79 shows some design details under investigation.

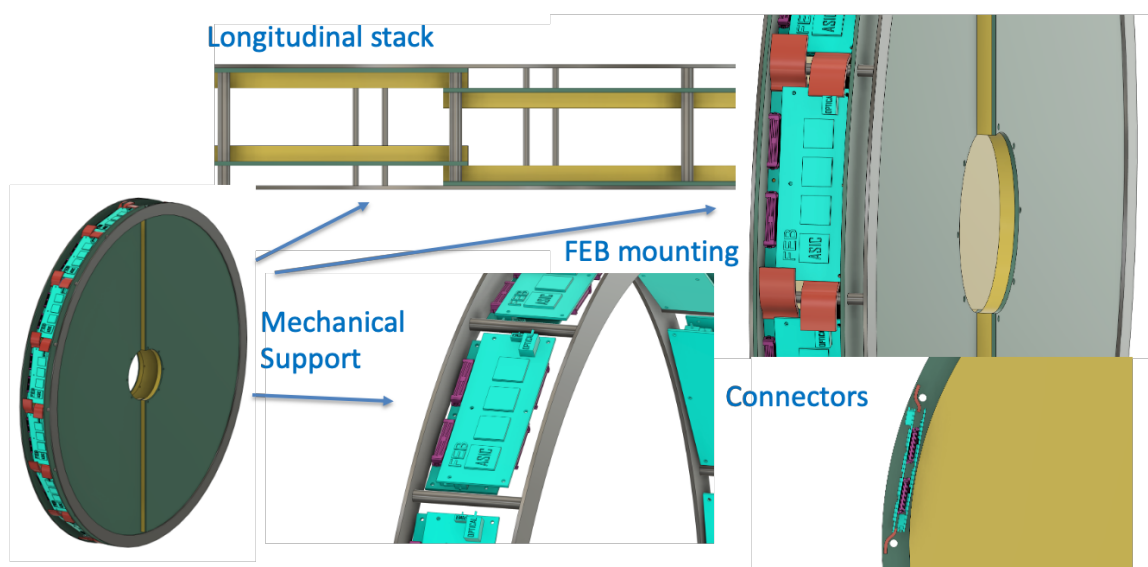


**Figure 8.79:** Design details of MPGD-ECT disks

**Environmental, Safety and Health (ES&H) aspects and Quality Assessment:** Considering MPGD consortium is composed of international collaboration so each production site for module assembly will follow guidelines of their local government to be in compliance with ES&H requirements. This include minimizing wastes during assembly procedure and disposal of harmful wastes in safe manner as directed by local government along with general electric and mechanical safety. During final integration of the detector subsystem at BNL, scientists and technicians will follow DOE guidelines as directed by BNL ES&H department.

The Quality Assessment protocol will cover the entire production lane of MPGD detectors. The readout PCBs will be assessed for mechanical precision and electrical continuity. The resistive layers will be checked for uniformity. During each step of the assembling, electrical continuity and high voltage capability of the different electrodes will be tested. Once the assembly of the module is finished, the module is checked for gas leakage and HV stability before bringing it outside of the

clean rooms. Each finished detector will be then tested with cosmic rays in dedicated test benches. In these tests, the main parameters that will be studied for each module are the noise levels and the number of dead channels, efficiency and effective gain uniformity over the detector active area . A database will be used to log all the information and results for each produced module.

**Construction and assembly planning.** Each of the MPGD detectors share a similar construction, assembly and QA timeline for having the detectors arrive at BNL in late 2029. This general timeline is shown in Figure 8.80.

The construction and assembly of the MPGD subsystems will take place at various places. CEA-Saclay will be the main production site for CyMBaL modules, while the readout PCBs will be produced by industry partners. At Saclay, all the remaining parts of the production process will be realized. The resistive layer will be added using serigraphy and the low-tension micromesh will be added using the bulk process [53], which will be performed in the Saclay MPGD Lab. The curving and mechanical integration of the final detector will be done in a dedicated clean room. CERN will serve as the primary source for  $\mu$ RWELL and GEM foils, as well as the readout PCBs for the  $\mu$ RWELL-BOT and  $\mu$ RWELL-ECT detectors. Other components, such as the frames, will be produced by industry partners. The production sites of the  $\mu$ RWELL-BOT subsystem are Jefferson Lab, Florida Institute of Technology and University of Virginia whereas INFN and Temple University will be in charge of the  $\mu$ RWELL-ECT subsystem.

A set of technical documents will be developed for each MPGD sub-detector, ensuring that all modules are produced under consistent conditions, using appropriate infrastructure, and following standardized procedures for construction and quality control testing. Each production site will procure and inspect the components separately. It is crucial that all production sites are equipped with suitable clean room infrastructure for the construction and assembly of their respective  $\mu$ RWELL modules, as well as identical instrumentation for a standardized component inspection and module characterization. Each of the institutes will be responsible for the construction and characterization of their respective  $\mu$ RWELL modules (+ spares). [The equipment needed for each subsystem will listed in in appendix before the next draft.](#) Each institution will leverage its existing MPGD infrastructure (clean room and detector lab and existing equipment) to minimize instrumentation costs but will upgrade where needed to meet the more demanding requirement of  $\mu$ RWELL technology assembly.

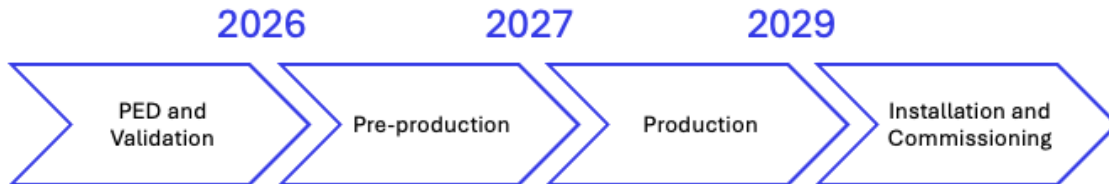


**Figure 8.80:** General overview ePIC MPGD tracker construction and assembly timeline.

#### Collaborators and their role, resources and workforce :

**CyMBaL:** Design, production and tests will be lead by CEA Saclay. [The details of the workforce, role and resources for each subsystem will be added in appendix before the next draft.](#)

**$\mu$ RWELL-BOT:** Jefferson Lab, Florida Institute of Technology, and the University of Virginia will participate in the construction, assembly, and characterization of  $\mu$ RWELL-BOT  $\varphi$ -modules to ensure timely mass production. Each of the three institutes will be responsible for the construction and characterization of eight  $\mu$ RWELL-BOT  $\varphi$ -modules (+). The essential equipment needed for each institute are listed in Tab. 8.32. Wherever possible, existing equipment from the collaborating groups will be utilized to minimize instrumentation costs. They will collaborate to develop a set of technical documents, ensuring that all modules are produced under consistent conditions, using appropriate infrastructure, and following standardized procedures for construction and quality control testing. All components of a  $\mu$ RWELL-BOT  $\varphi$ -module will be designed by Jefferson Lab, however, each production site will procure and inspect the components separately. It is crucial that all three production sites are equipped with suitable clean room infrastructure for the construction and assembly of  $\mu$ RWELL-BOT  $\varphi$ -modules, as well as identical instrumentation for a standardized component inspection and module characterization. Each of the three institutes will be responsible for the construction and characterization of eight  $\mu$ RWELL-BOT  $\varphi$ -modules (+ spares). The essential equipment needed for each institute are listed in Table 8.32. Each institution will leverage on its existing MPGD infrastructure (clean room and detector lab and existing equipment) to minimize instrumentation costs but will upgrade wherever possible to meet the more demanding requirement of  $\mu$ RWELL technology assembly. The personnel effort, expressed as a percentage of research time over the duration of the project, at each institute is provided in Tables 8.33, 8.34, 8.35.

**$\mu$ RWELL-ECT:** Temple University and INFN Roma Tor Vergata — will participate in the design, production, assembly, and characterization of  $\mu$ RWELL-ECT disks, with the engineering support from Jefferson Lab and the collaboration of INFN LNF MPGD group lead by Gianni Bencivenni, inventor of the  $\mu$ -RWELL technology. INFN Roma Tor Vergata will focus on the two hadron disks while Temple University will be in charge of the lepton disks. Each of the two institutes will be responsible for the construction and characterization of 4-8  $\mu$ RWELL-ECT modules, depending on final design. The essential equipment needed for each institute are listed in Table 8.31. Wherever possible, existing equipment from the collaborating groups will be utilized to minimize instrumentation costs.

**Risks and mitigation strategy:** Based on past experiences with MPGD technology following risks and mitigation strategies are identified.

- Delay in production of MPGD foils at CERN is the biggest risk. Considering this it has been decided to place procurement request well in advance to provide enough time to procure the MPGD foils. Additionally there is possibility of using additional person power and also prepare additional set up for assembling each module in each assembly sites so that at least 2 modules are assembled at the same time.
- Minor risk of higher humidity content within the MPGD modules is possible however it can be mitigated by flowing gas at higher rate.
- It is possible that the gain provided by any of the MPGD module after installation in experimental hall is lower than what has been estimated during QA. This can be mitigated either by increasing the content of primary ionized gas in gas mixture or increasing the high voltage on MPGD electrodes without affecting detector stability.

**Additional Material:**



**Gas choice:** MPGDs will preferably operate with a mixture of argon-isobutane 95:5. This choice is being driven by two factors. On the one hand, MPGDs will operate in a solenoidal magnetic field of up to 2 T, while the drift electric field will be in the radial direction. This induces a Lorentz force on the primary electrons moving them in the azimuthal direction. In order to limit the effective angle of the resulting drift velocity with respect the electric field, one should aim at using a gas mixture that has a low electron drift velocity. A comparison of the Lorentz angle versus the drift

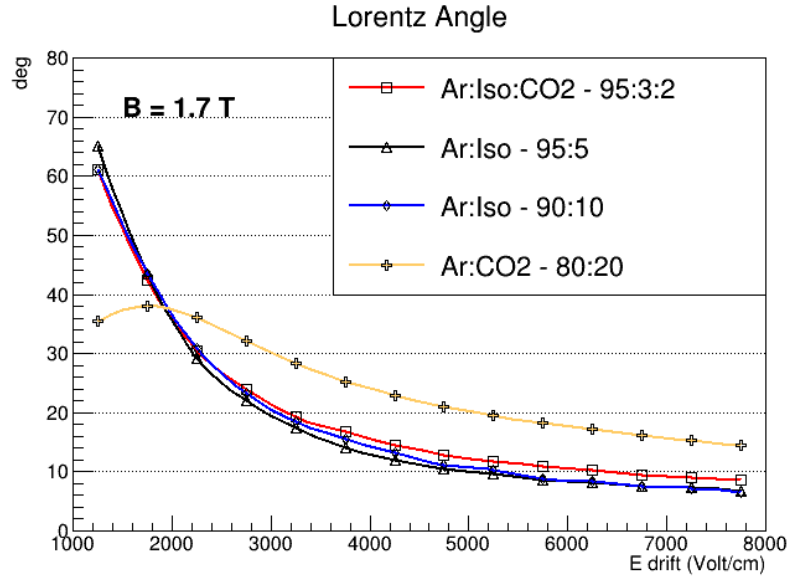


**Figure 8.81:** Comparison of the Lorentz angle as a function of the drift field for several gas mixtures. This study was done using Magboltz in Garfield++ [54].

filed among several argon based gas mixtures, commonly used in MPGD applications, is shown in Figure 8.81. One can see that in a 1.7 T magnetic field, an with drift voltages higher than 3 kV / cm, the Lorentz angle for Ar:Isobutane 95:5 mixture is lower than 20 degrees. On the other hand, the gas mixture must provide enough gain to ensure a good signal-over-noise ratio. Gases with a high fraction of argon ensure enough primary electrons and achieve high gains.

**$\mu$ RWELL-BOT  $\varphi$ -module design:** is a large rectangular MPGD detector based on the thin-gap GEM- $\mu$ RWELL hybrid detector concept described in detail in 8.83. The detector has an active area of 1700 mm  $\times$  330 mm and an overall dimension of 1815 mm  $\times$  360 mm and a thickness of 2 cm including the on-detector front end electronic boards (FEB cards) and cables and services. The thin-gap concept, defined by smaller drift gap of  $\sim 1$  mm in the drift region of the detector, combined with the double amplification with GEM and  $\mu$ RWELL structures and the proper choice of gas mixture guarantees a high performance the detector in all aspects satisfying the main requirement of the ePIC tracker such as a detector efficiency above 95%, a timing resolution better than 10 ns and space point resolution better than 150  $\mu$ m on average in the pseudorapidity range of  $-1 \leq \eta \leq 1$ .

**Thin-gap GEM- $\mu$ RWELL hybrid detectors:** Thin-gap GEM- $\mu$ RWELL hybrid technology [55] was developed to satisfy the requirements of MPGD in term of space point and timing resolutions as well as detection efficiency above 95% and stable operation condition in the full angular

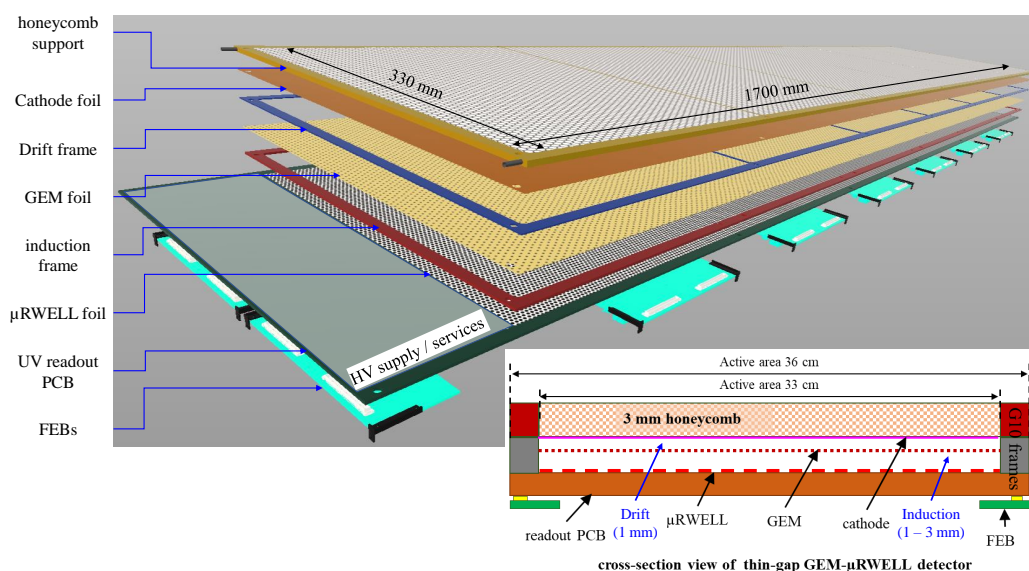


**Figure 8.82:** Exploded 3D view of the CAD design of the  $\mu$ RWELL-BOT  $\phi$ -module with a breakdown of its essential sensitive items. *Bottom right:* Cross section view of the detector.

2912 acceptance of the ePIC detector. Three distinctive features are implemented in a thin-gap MPGD detector:

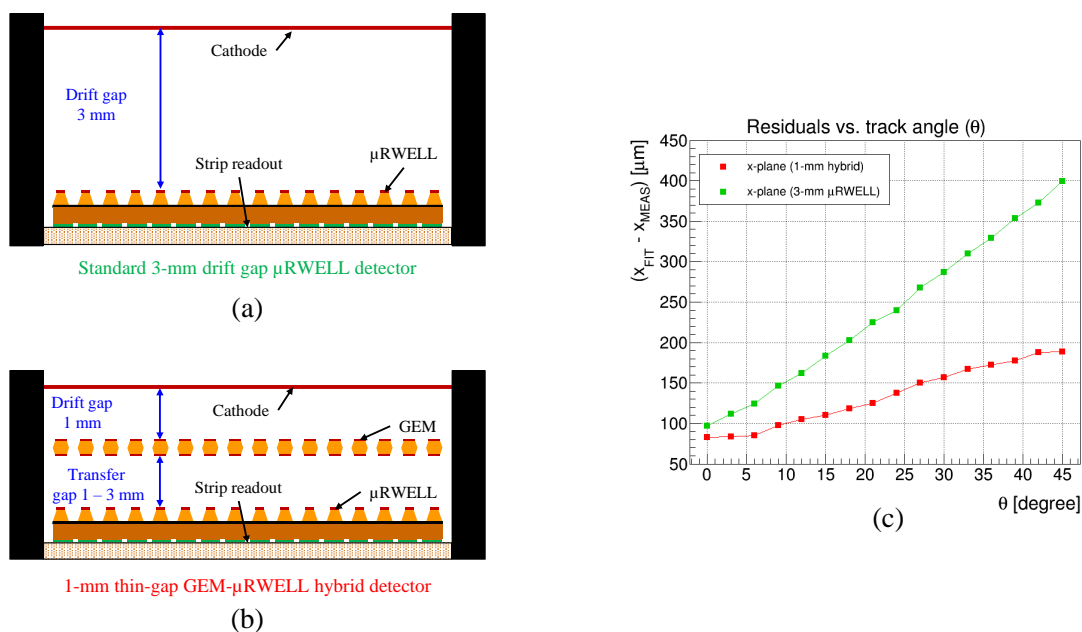


**Figure 8.83:** (a) Cross sectional view of a standard 3-mm gap  $\mu$ RWELL detector; (b) Cross sectional view of a 1-mm gap thin-gap GEM- $\mu$ RWELL hybrid detector; (c) Spatial resolution as a function of the angle of impinging particle for standard gap  $\mu$ RWELL prototype (green) and for thin-gap GEM- $\mu$ RWELL detector (red).

1. **Thin gap drift:** The basic idea of a thin-gap MPGD is to minimize the thickness of gas volume in the ionization region between the cathode and the first amplification stage of detector from the 3 mm typically used in a standard MPGD to  $\sim 1$  mm gap as shown on the two cartoons (a) and (b) of Figure 8.83). A smaller gas volume reduce the length of the ionization trail left by the particles traversing the detector at large angle. This, subsequently minimize the impact on the degradation of the spatial resolution.
2. **Hybrid amplification:** To recover from the smaller total charge produced in the ionization region due to the smaller gap, a higher gain from the amplification layer is needed. An optimal way to achieve large gain is to use a two-stage amplification with hybrid MPGD structures composed of a GEM foil used as pre-amplification and the  $\mu$ RWELL layer for the second amplification. A second advantage with the hybrid amplification is the flexibility to safely operate the detector at large gain.
3. **2D capacitive-sharing strip readout:** Capacitive-sharing readout structure is critical for thin-gap MPGDs to achieve required spatial resolution performance. Performance of  $\mu$ RWELL detector implementing capacitive-sharing 2D-strip readout is described in detail in [56]. For thin-gap  $\mu$ RWELL-GEM hybrid detector, without capacitive-sharing structure, smaller strip segmentation (with pitch  $\leq 200$   $\mu$ m) would be required to achieve the the required spatial resolution. One can achieve same level of spatial resolution with larger pitch  $\geq 1$  mm) capacitive-sharing strip readout and therefore reducing the number of electronics channel by more than a factor 5. This represents a significant cost saving and reduction of the volume of cabling, services regarding the complexity of integration and maintenance for experiment.

The plot (c) of Figure 8.83) shows some preliminary results from beam test studies of the improvement of the spatial resolution as a function of the angle of incoming particles with the thin-gap (red curve)  $\mu$ RWELL-GEM hybrid prototype compared to the standard gap  $\mu$ RWELL prototype. Detailed description of the beam test setup and additional performance results will be provided in Appendix in future version.

**Table 8.31:** Main equipment required in the production site and availability at sites.

Equipment	Purpose	INFN Roma Tor Vergata	Temple University
ISO7 cleanroom	Inspection & Assembly	y	y
Stretcher system	Construction process	y	n
Ultrasonic Cleaner	GEM frame prep	n	y
Fume hood	GEM frame prep	y	y
Microscope	GEM visual inspection	y	y
Giga-Ohm insulation meter	GEM electrical inspection	y	n
HV box	GEM electrical cleaning	y	n
Oven	Construction process	y	n
Electronic instrumentation	Module characterization	y	n
Gas supplies	Module characterization	y	n
Shipping containers	Transport b/w sites	y	n

**Table 8.32:** Main equipment required in the production site and availability at sites

Equipment	Purpose	JLab	UVA	FIT
ISO7 cleanroom	Inspection & Assembly	y (need upgrade)	y	y
Stretcher system	Construction process	n	y	n
Assembly system	Assembly process	n	n	n
Isonic Ultrasonic Cleaner	GEM frame prep	n	y	n
Fume hood	GEM frame prep	n	y	n
Microscope	GEM visual inspection	n	y	y
Giga-Ohm insulation meter	GEM electrical inspection	n	y	y
HV box	GEM electrical cleaning	n	n	n
Oven	Construction process	n	n	n
Electronic instrumentation	Module characterization	y (partial)	n	y
Gas supplies	Module characterization	y	n	y
Shipping containers	Transport b/w sites	n	n	n

**Table 8.33:** UVa Personnel Effort (%FTE)

Personel	Effort
Faculty	25%
Research Scientist	50%
Graduate Student	50%
Graduate Student	50%
Undergraduate Student	25%
Technician	50%

**Table 8.34:** FIT Personnel Effort (%FTE)

Personel	Effort
Faculty	20%
Graduate Student	50%
3 Undergraduates	10%
2 Technicians	100%

### 2939 8.3.4 Particle Identification

2940 In addition to tracking and calorimetry, Particle IDentification (PID) is a crucial component of the  
 2941 ePIC experiment's physics program. The identification of stable particles is achieved either by ana-  
 2942 lyzing the way they interact, or by determining their mass measuring their velocity and momentum  
 2943 simultaneously. The difference in interaction is primarily used for identifying leptons, photons and  
 2944 neutral hadrons, which leave very different signatures in the electromagnetic calorimeters. Charge  
 2945 hadrons cannot be distinguished by their interaction in the calorimeter, but their velocity can be  
 2946 measured using dedicated time-of-flight and Cherenkov detectors. All dedicated ePIC PID detec-

**Table 8.35:** JLab Personnel Effort (%FTE)

Personel	Effort
Staff scientist	50%
Staff scientist	50%
Post doc	50%
1 Technicians	100%

tors discussed in this section measure the velocity,  $\beta$ , of the particle and thus allow to determine its mass. In short, they tie together  $\vec{p}$ ,  $\beta$ , and  $m$ . In a second step this PID information can of course also be used in a refit of the particle's trajectory. The knowledge of the particle type and its mass does improve the multiple scattering evaluation and serve as a further constraints.

ePIC has stringent requirements on its PID capabilities as detailed in the Yellow Report [8]. The two-dimensional histogram in Fig. 8.84 illustrates the simulated yield of charged hadrons as a function of momentum and pseudorapidity,  $\eta$ , over the range  $-5 < \eta < 5$  at the highest EIC energy of  $\sqrt{s} = 141$  GeV. Studies of the key semi-inclusive and exclusive processes define the upper limit requirements for  $3\sigma$  separation of  $\pi/K/p$  for different pseudorapidity regions [8]:

- $p \leq 7$  GeV/c for  $-3.5 < \eta < -1.0$
- $p \leq 6$  GeV/c for midrapidity  $-1.0 < \eta < 1.0$
- $p \leq 50$  GeV/c for the forward region or  $1.0 < \eta < 3.5$

Pure and efficient kaon identification is particularly relevant to semi-inclusive DIS studies, where quark flavor tagging provides critical insights into the transverse momentum distribution and potentially the orbital angular momentum of the strange sea quarks. Kaon identification is also needed to reconstruct charmed hadrons, which are sensitive probes of gluon distributions in protons and nuclei.

Achieving the PID goals of the ePIC experiment requires multiple detection technologies tailored to specific momentum and pseudorapidity ranges. Cherenkov radiation detection is the primary method at higher momenta but is limited in its low-momentum reach. After the Yellow Report, it was realized that improving low-momentum PID is critical for light vector meson and charm meson/baryon reconstruction. To address this, Time-of-Flight (ToF) detectors based on finely pixelated AC-LGAD sensors were added in the barrel ( $0.5 \times 10$  mm pixels) and forward region ( $0.5 \times 0.5$  mm pixels). In addition to PID they will additional hits for tracking. The  $\eta$ -dependence of the momentum spectrum along with space constraints necessitate different technologies in the forward, backward, and barrel regions. The solution chosen by ePIC involves:

- A dual radiator RICH (dRICH) in the forward region utilizing aerogel and gas radiators, a set of focusing mirrors, and instrumented by SiPMs.
- Additional low-momentum PID in the forward region is achieved by an AC-LGAD based ToF that also provides an additional layer of tracking points.
- A large radius high-performance DIRC (hpDIRC) in the barrel, which adds focusing to the original DIRC design.

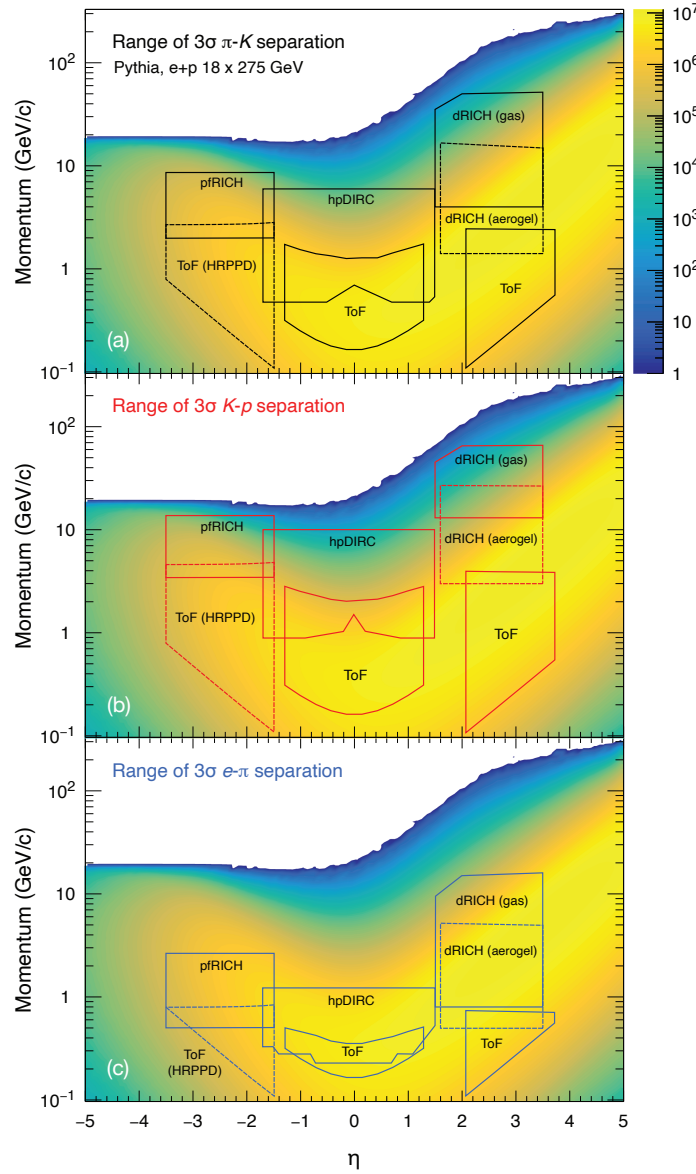


**Figure 8.84:** The histogram shows the relative yield of charged hadrons from Pythia simulations for  $18 \times 275$  GeV  $ep$  collisions as a function of momenta and pseudorapidity,  $\eta$ . The contours indicate the  $3\sigma$  separation region of the different ePIC PID subsystems for  $\pi/K$  (a),  $K/p$  (b), and  $e/\pi$  (c), respectively.

- The hpDIRC is complemented by an AC-LGAD ToF detector at smaller radius. The AC-LGAD layer provides PID information for low momentum particles that do not reach the hpDIRC or are too slow to leave Cherenkov signal in it.
- A proximity-focusing aerogel RICH (pFRICH) to cover the electron endcap region. This design features minimal material budget and provides additionally excellent ToF through its novel HRPPD photosensors.

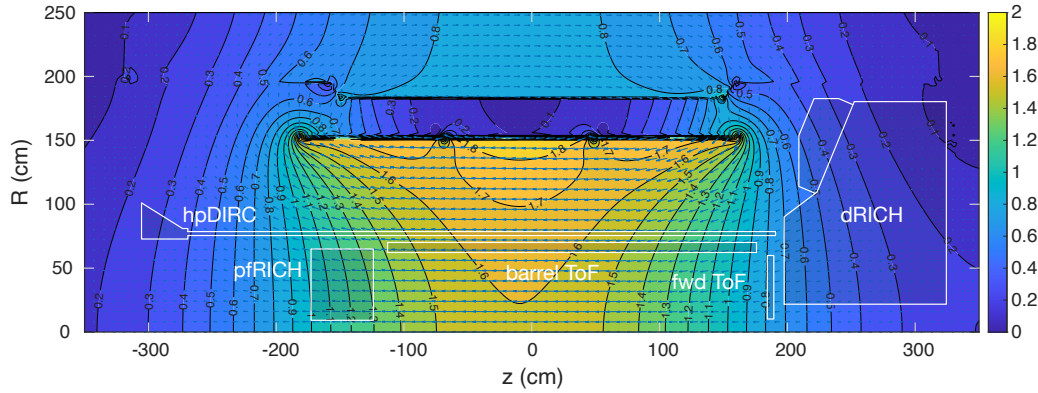


**Figure 8.85:** EPIC magnetic field map with the PID detector envelopes overlaid. Shown is the 1.7 T setup.

Figures 8.84 illustrates the achieved coverage in the  $\eta$  vs.  $p$  plane of the various PID subsystems. The contours indicate the  $3\sigma$  range for  $e/\pi$ ,  $\pi/K$ , and  $K/p$ -separation, respectively. This unprecedented wide coverage of PID in momentum and over a wide range of  $\eta$  makes ePIC a truly unique collider detector. As shown, the PID systems provide, in addition to hadron PID, a significant contribution to the  $e$ -identification and its purity ( $e/h$ ). When combined with the EM calorimeters, these subsystems will provide excellent suppression of the low-momentum charged-pion backgrounds, which otherwise limit the ability of the EMCal to measure the scattered electron in kinematic region where it does not provide sufficient  $e/h$  separation.

ePIC's Cherenkov detectors, dRICH, pFRICH, and hpDIRC, must overcome various challenges related to their respective photosensors. One is the strong magnetic field that rules out the use of conventional photomultipliers. Figure 8.85 shows the realistic ePIC magnetic field for the 1.7 T setup with highlighted Cherenkov PID detectors envelopes. In the region of the hpDIRC detector plane, where the MCP-PMTs will be located, the magnetic field is at a level of 0.2-0.3 T. The field at position of the pFRICH HRPPD sensors is about 1.2 T and the field at the dRICH is 0.3-0.6 T.

Another significant challenge is the sensors' sensitivity to radiation, particularly in the forward region where the dRICH is located. Figure 8.86 depicts the radiation map for ePIC with the PID subsystem contours. Shown are the estimates of the 1-MeV neutron equivalent fluence and (b) the sum of electromagnetic and charged-hadron dose simulated with  $10 \times 275$  GeV  $ep$  Pythia events. SiPMs, while ideal in terms of quantum efficiency and wavelength sensitivity, do suffer from increased dark currents due to radiation exposure. However, cooling during operation and thermal annealing have been demonstrated to mitigate this issue [?, 57]. Other photosensors used, show enough radiation hardness (HRPPD) or are situated in less radiation-intensive areas (MCP-PMT).

In the following subsection the different PID subsystems in ePIC are discussed in detail. Subsection 8.3.4.1 discusses the ToF systems, followed by 8.3.4.2 on the pFRICH, ?? describes the hpDIRC and we end with details on the dRICH system in 8.3.4.4.



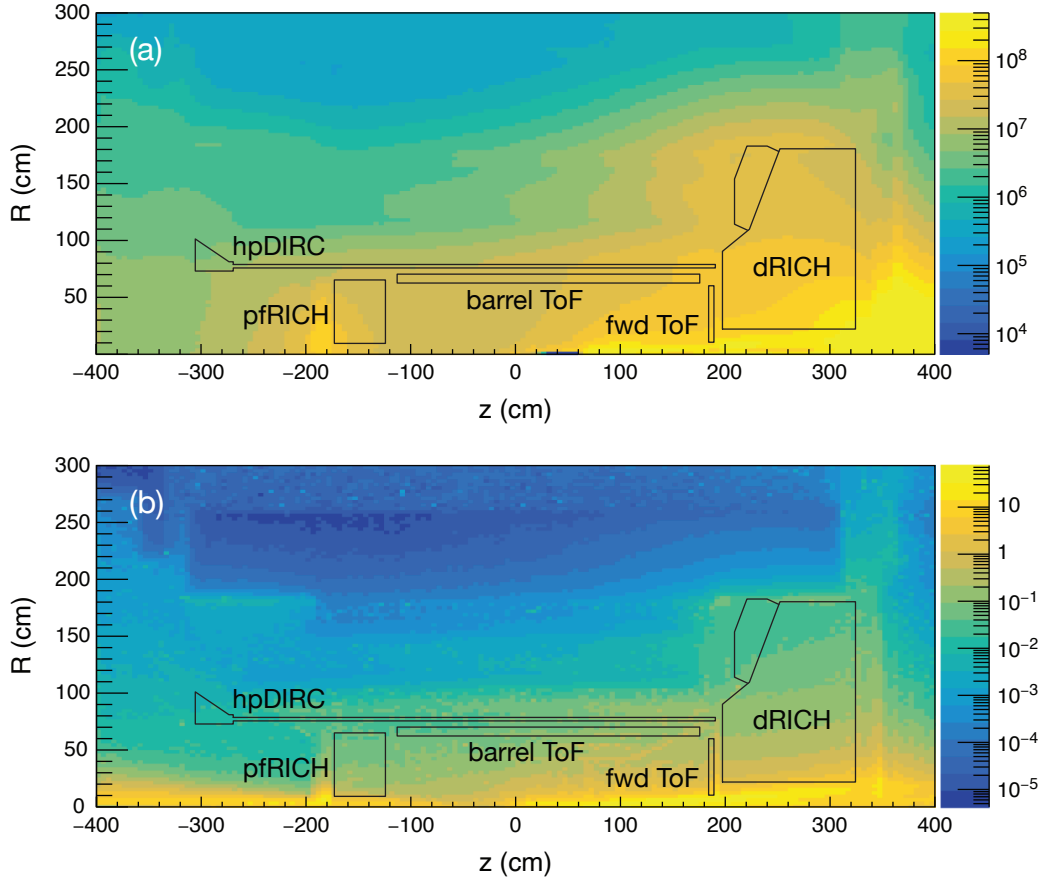


**Figure 8.86:** (a) Estimates of the 1-MeV neutron equivalent fluence in  $\text{cm}^{-2}/\text{fb}^{-1}$  and (b) the sum of electromagnetic and charged-hadron doses in  $\text{rads}/\text{fb}^{-1}$  integrated in  $1 \text{ fb}^{-1}$  equivalent Pythia events for  $10 \times 275 \text{ GeV}$   $ep$  collisions. The values shown are averaged over the azimuthal angle.

#### 8.3.4.1 The time-of-flight layers

##### Requirements and Justifications

**Requirements from physics:** The ePIC detector is designed to provide charged particle identification for  $e^\pm$ ,  $\pi^\pm$ ,  $K^\pm$  and  $p(\bar{p})$  over a wide range of three-dimension momentum space ( $\eta$  and  $p_T$ ). For specific physics justification, readers are referred to the physics sections; instead, specific PID requirements can be found in the overview of the particle identification preceding the present section. With a single-hit timing resolution of 35 ps from the Barrel TOF (BTOF) and 25 ps from the Forward TOF (FTOF), the AC-LGAD TOF detector system can provide particle identification for charged particles up to a few GeV. E.g.,  $\pi$ - $K$  separation at the  $3\sigma$  level for  $p_T < 1.2 \text{ GeV}/c$  for  $-1.2 < \eta < 1.6$ , and  $p < 2.5 \text{ GeV}/c$  for  $1.9 < \eta < 3.6$ , respectively. By combining the PID information for low-momentum particles from the TOF detectors and high-momentum particles from the Cherenkov detectors, ePIC will have excellent PID capability over a wide momentum

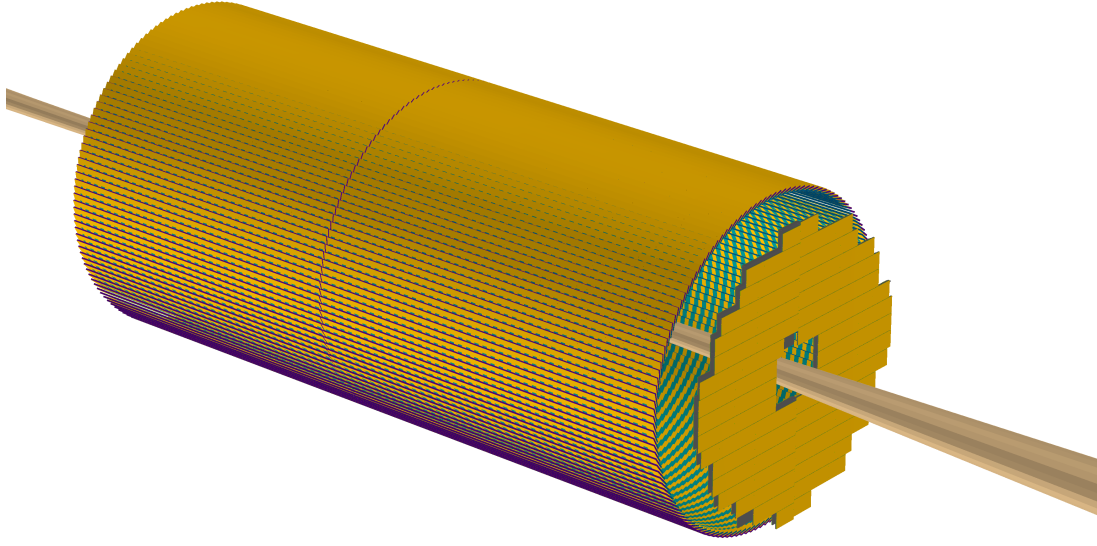


**Figure 8.87:** Geometries of BTOF with strip sensors and FTOF with pixel sensors.

range in a nearly  $4\pi$  acceptance, which is crucial to achieving the goals of the EIC physics program. Besides precise timing resolution, AC-LGAD sensors can also provide precise spatial resolution, thus aiding track reconstruction and momentum determination. The timing and spatial resolution requirements and the material budget requirements are evaluated in the ePIC MC simulation framework to find the optimal configuration. The BTOF and FTOF layouts are shown in Fig. 8.87. Table 8.36 summarizes the current specifications of the timing and spatial resolutions, material budgets, spatial coverage, channel counts, and dimensions. Figure 8.88 shows the performance of the TOF detector in the form of  $1/\beta$  as a function of particle momentum  $p$  for  $ep$  DIS events from PYTHIA+GEANT4 simulation. The TOF detector, combined with the other ePIC PID detectors, is crucial to demonstrate that ePIC's PID performance can meet the requirements.

Subsystem	Area ( $m^2$ )	dimension ( $mm^2$ )	channel count	timing $\sigma_t$ (ps)	spatial $\sigma_x$ ( $\mu m$ )	material budget ( $X/X_0$ )
Barrel TOF	12	0.5*10	2.4M	35	30 ( $r \cdot \phi$ )	3%
Forward TOF	1.1	0.5*0.5	3.2M	25	30 ( $x, y$ )	5%

**Table 8.36:** Required performance for physics and proposed configurations for the TOF detector system. The Barrel TOF consists of strip sensors with a pitch of 0.5 mm in the azimuthal direction and a length of 1 cm along the beam direction, while the Forward TOF consists of pixel sensors with a pitch of 0.5 mm.

**Requirements from Radiation Hardness:** The radiation fluence and dose at ePIC are significantly less than in the LHC experiments. The maximum fluence foreseen for the lifetime of the TOF detectors will be  $< 5 \times 10^{12} n_{eq}/cm^2$ , as seen in Fig. 8.89 and Tab. 8.37. Here, the highest fluence between raw and 1 MeV  $n_{eq}/cm^2$  fluence was considered, as the standard NIEL correction is not

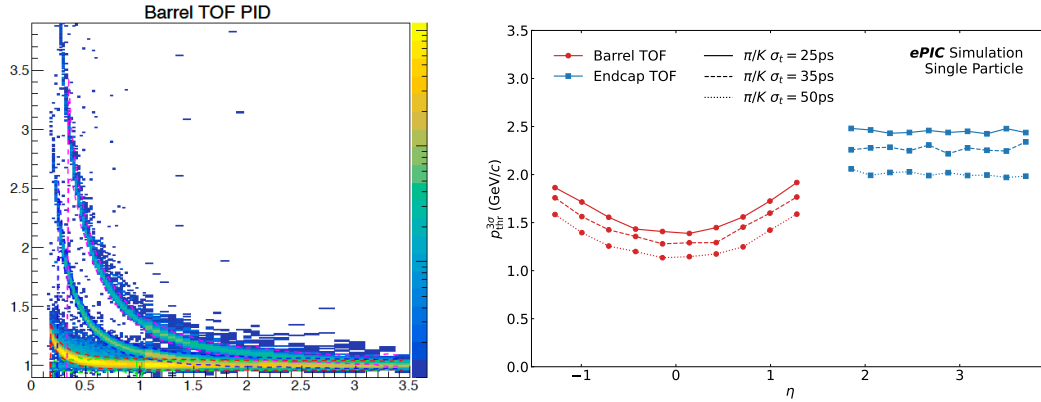


**Figure 8.88:** BTOF  $1/\beta$  as a function of momentum ( $p$ ) in the simulation performance with PYTHIA DIS events (left). Upper limits on the  $3\sigma$  particle separation from BTOF and FTOF as a function of pseudorapidity (right).

3036 applicable for some effects in AC-LGAD radiation damage.

3037 Much work has been done to characterize and improve the radiation resistance of AC-LGAD gain  
 3038 layers to meet the requirements at the LHC [58] (up to  $2.5 \times 10^{15}$  1MeV  $n_{eq}/\text{cm}^2$ ). Because of the  
 3039 sensitivity of the sensor performance to the value of the N+ sheet resistance (a feature absent from  
 3040 the conventional AC-LGADs used for the LHC), AC-LGADs may be significantly less radiation tol-  
 3041 erant than their conventional cousins. Indeed, N-type doping is known to be particularly sensitive  
 3042 to hadronic irradiation, with N-bulk sensors inverting to P-bulk even before an exposure of  $1 \times 10^{14}$   
 3043 is accumulated. Furthermore, LHC AC-LGAD detectors are designed to run at  $-30^\circ\text{C}$  to reduce the  
 3044 post-radiation leakage current, while in the ePIC, the sensors will be operated at room or slightly  
 3045 lower temperatures throughout the experiment's lifetime. The leakage current increase due to ra-  
 3046 diation damage has to be low enough to avoid thermal runaway in the system; that is, temperature  
 3047 increase triggers additional dark current in positive feedback. That is related to the cooling system  
 3048 extracting the heat of the sensor combined with the power dissipation from the readout chip. This  
 3049 is especially important for the far forward and endcap regions where the chips are bump-bonded  
 3050 on top of the sensors, and the thermal connection with the cooling system is sub-optimal.

3051 Therefore, a radiation exposure run was performed before the ePIC AC-LGAD design was final-  
 3052 ized. To probe the radiation effect from ionizing and non-ionizing particles, several sensors from  
 3053 HPK and BNL were irradiated at the FNAL ITA facility (400 MeV protons) and the TRIGA reactor  
 3054 in Ljubljana (MeV-scale neutrons). The radiation exposure was done in steps, allowing potential  
 3055 charge-collection pathologies, should they exist, to be mapped out to develop models and correc-  
 3056 tions. By studying the sensor performance before and after irradiation, the change in N+ resistivity  
 3057 can be characterized, and this particular risk can be addressed. Sensors irradiated with 1 MeV neu-  
 3058 trons were received in the Summer of 2024 and subsequently tested. The results are encouraging,  
 3059 as seen in the following sections. Sensors irradiated at the FNAL ITA facility are still cooling down  
 3060 from the activation. They will likely be available for testing in early 2025.

3061 **Requirements from Data Rates:** As the sensors and ASICs differ between the BTOF and FTOF,  
 3062 the rate requirements are presented separately for both sub-components. On top of that, the phase  
 3063 space coverage is different (mid-rapidity vs forward rapidity), which mandates different particle

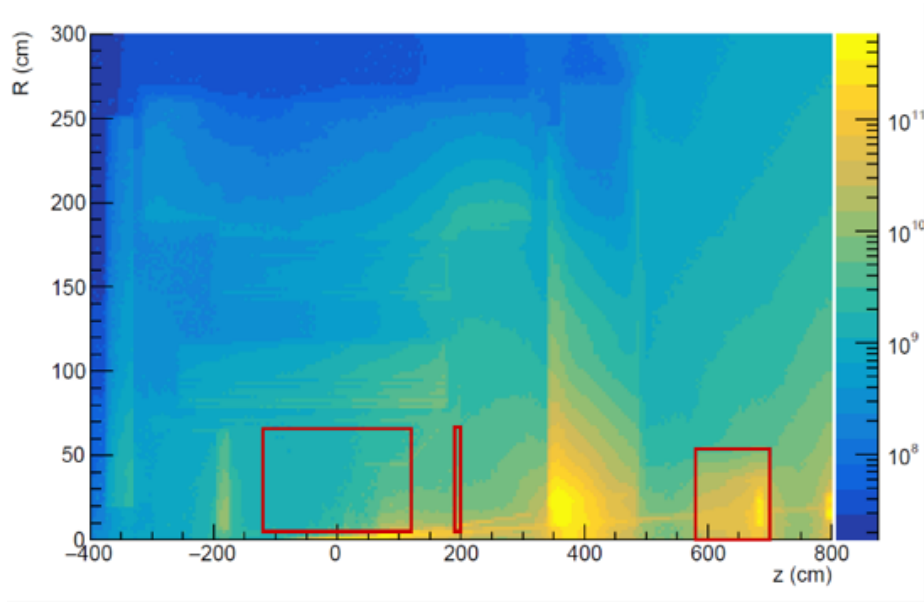


**Figure 8.89:** Fluence accumulated for 6 months at 100% time, corresponding to one year of data taking, the fluence has to be multiplied by the assumed 10 years of lifetime of the ePIC detector. Red squares highlight the barrel, endcap, and B0 tracker detectors. Simulation from Fluka.

RAW fluence			
System	Average	Min	Max
Barrel	$5.4 \times 10^{10}$	$3.4 \times 10^{10}$	$5.9 \times 10^{11}$
End-cap	$1.3 \times 10^{11}$	$5.1 \times 10^{10}$	$1.6 \times 10^{12}$
B0 trackers	$3.9 \times 10^{11}$	$3.3 \times 10^{10}$	$1.8 \times 10^{12}$
NEQ fluence			
System	Average	Min	Max
Barrel	$3.6 \times 10^{10}$	$1.1 \times 10^{10}$	$1.3 \times 10^{12}$
End-cap	$1.2 \times 10^{11}$	$3.2 \times 10^{10}$	$8.4 \times 10^{11}$
B0 trackers	$4.5 \times 10^{11}$	$2.7 \times 10^{10}$	$4.2 \times 10^{12}$

**Table 8.37:** RAW and NEQ fluence per system for the lifetime of the ePIC experiment, assuming 10 years of data taking at 50% time.

3064 rates and background calculations.

3065 **BTOF:** The BTOF simulations show an average of 5 charged particles per  $ep$  collision at the highest  
 3066 center of mass energy. At a 500 kHz collision rate, this amounts to a 2.5 MHz particle rate on  
 3067 the surface of the BTOF barrel. BTOF contains 2.4 million channels, which give an average hit  
 3068 frequency per channel of 1 Hz. Due to charge sharing of the AC-LGAD strips, a particle is expected  
 3069 to generate signals on a maximum of 3 strips/channels of the readout ASIC.

3070 **FTOF:** The FTOF simulation shows an average of 2 charged particles per  $ep$  collision at the highest  
 3071 center of mass energy. At a 500 kHz collision rate, this amounts to a 1 MHz particle rate on the  
 3072 surface of the FTOF disk. Since FTOF is expected to contain 5.8 million channels, the average hit

frequency per channel is 0.2 Hz. Due to charge sharing of the AC-LGAD pixels, a particle hit is expected to generate signals on a maximum of  $3 \times 3$  pixels/channels of the readout ASIC.

**Electronics Noise:** Noise measurements have consistently shown a rate of 30 Hz per channel. Such a noise rate is achieved with a  $5\sigma$  cut and is deemed to be even somewhat pessimistic but is the number that is planned to be used during these calculations.

**Data Rates:** A typical CERN-developed ASIC's zero-suppressed data format will be assumed, which is: 32 bits header,  $N \times 32$  bits of channel data (ADC, TDC, ch Id), and 32 bits trailer. Such data formats are used in, e.g., HGCROC, which is a precursor to our expected ASICs.

For BTOF, the expected signal rate of bits per second per ASIC is  $1 \text{ Hz (particle rate)} \times 5 \times 32 \text{ (bits for 3 hits)} \times 64 \text{ (channels)} = 10 \text{ kbps}$ , while the noise rate is  $30 \text{ Hz (noise)} \times 3 \times 32 \text{ (bits for a single hit)} \times 64 \text{ (channels)} = 185 \text{ kbps}$ . Summing up these two contributions, the total data rate reaches 195 kbs per ASIC. Since an RDO reads out 128 ASICs per half stave, a rate per RDO (or fiber) of 24 Mbps is expected. For the entire BTOF, which contains 288 half staves, a total rate requirement of 7 Gbps is expected.

For FTOF, the expected signal rate of bits per second per ASIC is  $0.2 \text{ Hz (particle rate)} \times 11 \times 32 \text{ (bits for 9 hits)} \times 1024 \text{ (channels)} = 72 \text{ kbps}$ , while the noise rate is  $30 \text{ Hz (noise rate)} \times 3 \times 32 \text{ (bits for a single hit)} \times 1024 \text{ (channels)} = 3000 \text{ kbps}$ . The per-ASIC data rate arrives at 3.1 Mbps by summing up these two contributions. In the worst case of 28 ASICs per RDO (or fiber), it reaches 87 Mbs per fiber link to DAQ. In the total FTOF sub-detector of 212 RDOs, 18 Gbps is reached.

These rates are very small and well within the reach of the ASIC and interconnects, as well as the electronics and DAQ fiber interfaces. The data rates are dominated by the electronics noise, which can be controlled by raising or lowering the ASIC's various ADC or TDC thresholds, thus adjusting the system performance even ASIC-to-ASIC if required.

### Subsystem description:

**General device description:** The BTOF consists of 144 tilted staves, each of which is made of two half staves with a total length of around 270 cm sitting at a radial position of around 65 cm. Strip sensors are mounted on low-mass Kapton flexible printed circuit boards (FPCs) and are wire-bonded with frontend ASICs. The FPCs are glued onto mechanical structures made from low-density carbon fiber (CF) materials, bringing power and input/output signals to the sensors and ASICs. The heat generated by the frontend ASICs is removed by an embedded aluminum cooling tube in the CF structure. The FTOF consists of detector modules made from pixel sensors bump-bonded with frontend ASICs. These detector modules are mounted from both sides onto a thermally conductive supporting disk with embedded liquid cooling lines located around 190 cm away from the center of the experiment. Since the irradiation flux at the EIC is much smaller than that at the LHC, it is assumed that the radiation damage will not be a concern; therefore, the sensors can be operated at room temperature.

**Sensors:** The sensors identified for the TOF timing layers are AC-coupled Low-Gain Avalanche Diode (AC-LGAD), a relatively new sensor technology that can provide both exceptional position resolution and timing resolution [2,59–61] while maintaining low channel density. In AC-LGADs, the signal produced by charged particles in the sensor active volume is amplified via an internal p+ gain layer near the sensor surface. The signal is induced on a continuous resistive n+ layer on top of the p+ gain layer, which is AC coupled to patterned metal readout electrodes, which are on the sensor surface and separated by a dielectric layer from the n+ layer. The internal signal amplification and thin active volume enable precise

timing measurement, while charge sharing among neighboring electrodes can provide precise position measurement. AC-LGADs will be used for TOF PID and tracking in the BTOF, FTOF, and far forward detectors.

The BTOF will employ strip sensors 1 cm long with a pitch of 500  $\mu\text{m}$  and a metal electrode width of 50  $\mu\text{m}$  (a larger pitch up to 1000  $\mu\text{m}$  is also under investigation). The sensor thickness will likely be 50  $\mu\text{m}$  to reduce the input capacitance to the preamplifiers, but 30  $\mu\text{m}$  thick strip sensors are also under investigation. The full sensor size will be  $3.2 \times 2 \text{ cm}^2$  with 1 cm segments. The FTOF will use pixel AC-LGADs with a pitch of 500  $\mu\text{m}$  and metal electrode size of 50  $\mu\text{m}$  (a large pitch up to 1000  $\mu\text{m}$  and electrode size of 150  $\mu\text{m}$  are also under investigation). The thickness of the pixel sensors will likely be 20  $\mu\text{m}$  to maximize the time resolution reach, as the input capacitance is not a concern for small pixels. Nevertheless, 30  $\mu\text{m}$  thick pixel sensors are also under investigation. The full-size sensor will be  $1.6 \times 1.6 \text{ cm}^2$  with  $0.5 \times 0.5 \text{ mm}^2$  pixels. A summary of the geometry is in Tab. 8.38. Studies on smaller-scale devices are presented in [2, 59] and in the following sections. Different thicknesses and geometry were investigated in the scope of the eRD112 effort, and the best results obtained are shown in Sec 8.3.4.1. Full-size strip sensor prototypes have been produced for the first time in the most recent HPK fabrication and are received at the time of writing. Procurement of the full-size pixel sensor prototypes is still in progress. A complete evaluation of the full-size prototype sensors is expected by mid-2025.

System	Size	Type	Pitch	Ch/sensor	Thickness
Barrel	$3.2 \times 2 \text{ cm}$	Strips	$500 \mu\text{m} \times 1 \text{ cm}$	128	50 $\mu\text{m}$
End-cap	$1.6 \times 1.6 \text{ cm}$	Pixels	$500 \mu\text{m} \times 500 \mu\text{m}$	1024	20 $\mu\text{m}$
B0 trackers	$1.6 \times 1.6 \text{ cm}$	Pixels	$500 \mu\text{m} \times 500 \mu\text{m}$	1024	20 $\mu\text{m}$

**Table 8.38:** Baseline BTOF, FTOF and B0 AC-LGAD geometries.

**Frontend Electronics (FEE):** The FEE for AC-LGAD-based detectors is focused on the development of two different ASICs and service hybrids with performance and requirements aimed at the barrel (strips) and endcap (pixels), respectively. Different ASICs for the two subsystems are necessary since the geometry, integration method, and requirements differ between BTOF and FTOF. An ASIC featuring a Constant Fraction Discriminator (CFD) chip is being developed at Fermilab for the BTOF, focused on optimizing the analog frontend design to read out AC-LGAD strip sensors with large input capacitance. Two versions of the ASICs, FCFDv0, and FCFDv1, featuring single- and multi-channel preamplifier and CFD, respectively, have been fabricated and tested. The new versions, FCFDv1.1, with further improvement to the frontend design tailored to 1 cm AC-LGAD strip sensors, and FCFDv2, with digital readout, are under development with an expected delivery date in early 2025 and 2026, respectively.

The EICROC project by the French group is instead focused on designing an ASIC for reading finely-pixelated AC-LGAD sensors, optimized for the pixel-based AC-LGADs detectors at ePIC such as B0, OMD, Roman Pots, and FTOF. The first version, EICROC0, is a  $4 \times 4$  channel ASIC with  $0.5 \times 0.5 \text{ mm}^2$  pixel size, featuring components like a trans-impedance preamplifier, 10-bit TDC for timing, 8-bit ADC for amplitude measurement, and an I2C slow control interface. It is designed for low capacitance and sensitivity to low charges (2 fC), operating with 1 mW per channel and targeting 30 ps timing and 30  $\mu\text{m}$  spatial resolution. The prototype is currently under testing. The next version, EICROC1, expected in early 2025, will feature a  $32 \times 32$  channel configuration to study power distribution; it will be followed by the final  $32 \times 32$  channel version for full-scale implementation. This will be followed by EICROC2, the final  $32 \times 32$  channel version, projected for full-scale implementation by the



end of 2026. EICROC2 will have a digital backend compatible with the ePIC DAQ system. Tab. 8.39 summarizes the current baseline ASICs for the different timing layers.

System	ASIC	Time Res.	Input C.	Hybridization
Barrel	FCFD	35 ps	10s pF	wire bonds
End-cap	EICROC	20 ps	100s fF	bump bonds
B0 trackers	EICROC	20 ps	100s fF	bump bonds

**Table 8.39:** Readout chips BTOF, FTOF and B0 AC-LGAD geometries.

The service hybrids (SH) consist of a readout board (RB) and a power board (PB). A schematic design of a service hybrid is shown in Fig. 8.90 for FTOF and serves 3 modules or 12 sensors/ASICs. The readout board aggregates data from multiple ASICs to an lpGBT (from CERN) transceiver chip via e-links. Then, it converts to optical signals via a VTRx+ chip (from CERN) to be transmitted to the backend data acquisition system. The lpGBT and VTRx+ are designed for HL-LHC and have proven to be sufficiently radiation-hard for the EIC environment. The VTRx+ has one uplink up to 10 Gbs (for receiving clock and control signals), and four downlinks (for data transmission), each up to 2.56 Gbs, and it can transmit data up to four lpGBTs. The readout board also hosts interface connectors for the module board (as described later) and the power board, as well as for input LV and HV cables. The power board provides low voltages for ASICs (1.2 V), lpGBT (1.2 V), and VTRx+ (2.5 V and 1.2 V) on the readout board from the DC-DC converters. The CERN bPOL48V module is chosen as the main converter, which takes an input of 15 V and converts it into 1.2 V and 2.5 V. As illustrated in Fig. 8.90, the RB is on top of the PB and sensor module. The PB directly contacts the cooling structure, facilitating efficient cooling of heat dissipating from the DC-DC converters. The SH has three different types with different lengths, serving 3 (12), 6 (24), and 7 (28) modules (sensor/ASICs). This will provide the most efficient coverage of a circular-shaped disk while minimizing the number of cables and fibers. The example shown in Fig. 8.90 is the shortest version (about 100 mm long) which serves 3 modules. The latest layout design for the FTOF disk is shown in Fig. 8.87 (right), where different colored boxes indicate different types of SHs. Prototyping of the SH is in an advanced stage. A pre-prototype readout board (ppRDO), based on an Xilinx FPGA chip and a commercial SFP+ optical transceiver, has been developed and is under testing. The first prototype RB and PB using the CERN chips will be under development soon and will be based on a similar existing CMS endcap timing layer (ETL) detector design.

**Flexible Printed Circuit boards:** A Flexible Printed Circuit (FPC) will read data and distribute power to the sensors and ASICs. A material budget of 3%  $X/X_0$  is required in the acceptance region, meaning the FPC material should be as lightweight as possible. Additionally, the FPC must be up to 135 cm in length. To meet these stringent requirements, careful consideration of the FPC material is necessary, as signal loss is expected with such a long FPC, especially if using polyimide, a standard material in FPCs. The sPHENIX experiment encountered a similar challenge with their Inner Tracker (INTT, also a silicon sensor tracker). It successfully addressed the issue using Liquid Crystal Polymer (LCP) instead of polyimide as the dielectric material. This technology will be adopted for the TOF sub-detector as well.

**BTOF stave design:** Barrel staves are divided into two half-staves, with services and connections coming from the outer side. The half-staves are composed of several modules. The half-staves comprise a support structure with an integrated cooling pipe, flexible printed circuit (FPC), sensors, and ASICs. Sensors and ASICs will be mounted on both the top and bottom sides of the half-stave, making it double-sided, with enough overlap to achieve 100% coverage in the stave direction. The lateral overlap and tilting ensure 100% coverage in the



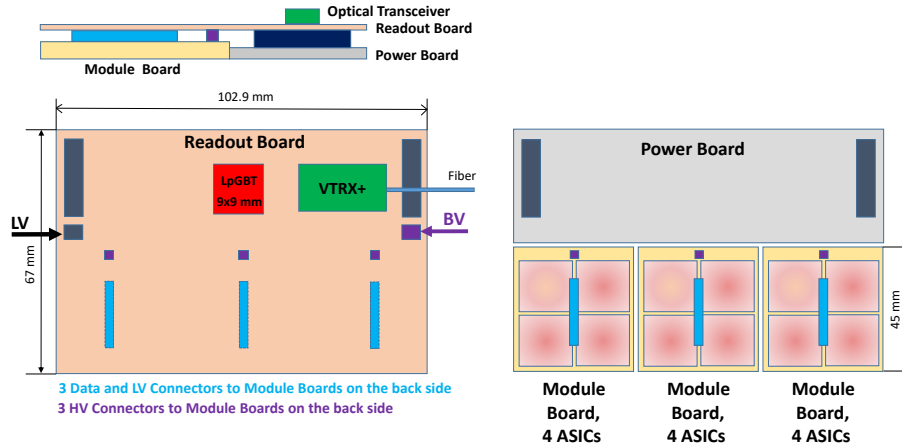


**Figure 8.90:** A schematic design of service hybrids for FTOF, which serves 3 modules or 12 sensors/ASICs.

direction parallel to the staves. There are 64 sensors and 64-128 ASICs on each side of the half-stave in total. The number of ASICs depends on the final design; each ASIC will serve either one sector for one sensor or one sector for two sensors.

**FTOF module design:** A schematic design of the module for FTOF is shown in Fig. 8.91. Each module consists of  $2 \times 2$  AC-LGADs sensors and ASICs glued together. The unit is covered by a module PCB board (MB), which provides LV power (1.2 V) and transmits the data of ASICs via a board-to-board connector to the RB. In addition, the MB also has an HV connector for the RB to provide the HV to the AC-LGAD sensors. The ASIC readout will be wire-bonded to a metal pad near the edge of the module on the side facing the baseplate and cooling structure, as illustrated in Fig. 8.91 (right). The AC-LGAD sensors and ASICs will be connected via bump bonding. The dimensions shown are preliminary and will be adjusted as the prototyping progresses. In the current design, the AC-LGAD sensors are placed underneath the ASIC. The motivation is to have the sensor as close as possible to the cooling structure to ensure a lower and stable temperature, which has been proven essential for achieving optimal time resolution with a narrow range of temperature gradients. An alternative option would be to swap the ASIC and sensor layers, which has the advantage of more efficiently dissipating the heat primarily generated by the ASIC. A final choice will be made as the prototype progresses, especially after realistic thermal performance studies have been carried out.

**Performance** The AC-LGAD systems, including the BTOF, FTOF, and far-forward systems (Roman Pots, OMD, and B0 tracker), share a common readout chain that is currently under development. Performance evaluations are conducted in various laboratory environments as part of ongoing R&D efforts. A schematic of the full readout chain is shown in Fig. 8.92. The effort can be divided into two parts: 1) integrating the sensors with ASIC and 2) developing the readout and power boards.

The Fermilab team has been developing an ASIC targeting the AC-LGAD strip sensors for BTOF. Studies have shown that a Constant Fraction Discriminator (CFD) could provide a better timing resolution for small signal amplitudes from AC-LGAD than a leading-edge discriminator [62].

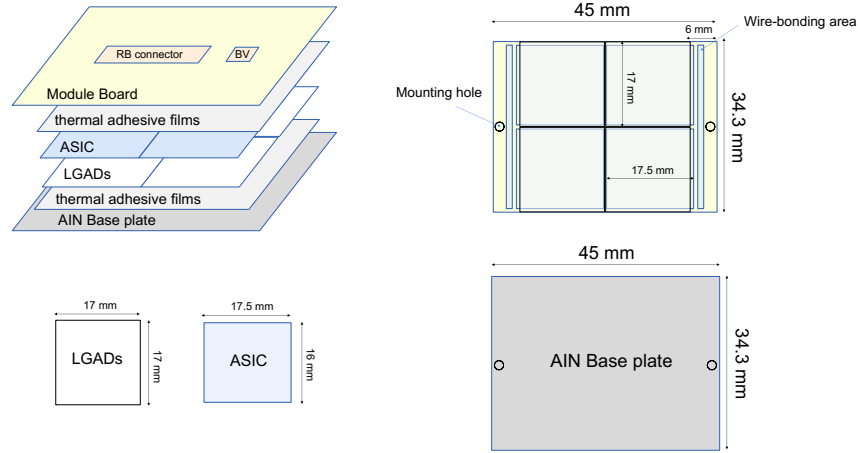


**Figure 8.91:** A schematic design of the module for FTOF, which consists of  $2 \times 2$  AC-LGAD sensors and ASICs.

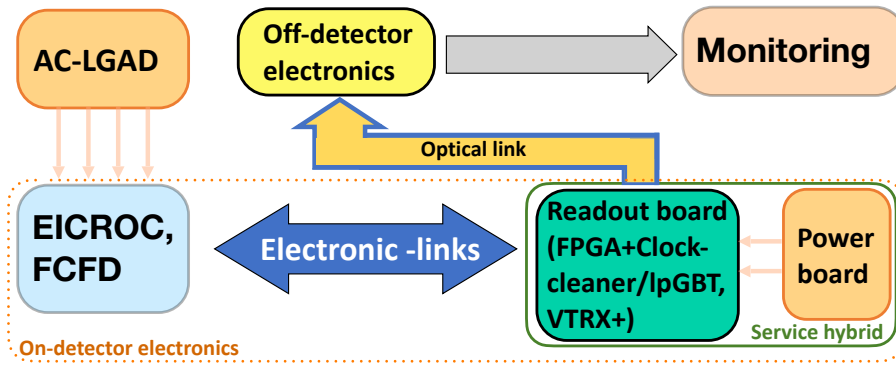


**Figure 8.92:** Schematic of the AC-LGAD subsystem readout chain. Each component is undergoing design, (pre-)prototyping, testing under various environments, and customization to meet the specific requirements of individual subsystems.

3230 The first single-channel CFD-based ASIC (FCFDv0) wire-bonded to a DC-LGAD sensor achieved  
 3231 around 35 ps timing precision during test beams, where the dominant contribution is expected  
 3232 from the intrinsic resolution of the AC-LGAD sensor. A 6-channel prototype (FCFDv1) was devel-  
 3233 oped for AC-LGAD sensors, demonstrating around 11 ps jitter in charge injection and around 50 ps  
 3234 time resolution with 0.5 cm AC-LGAD strip sensors during test beams. Ongoing efforts focus on  
 3235 optimizing the frontend design for 1 cm AC-LGAD strip sensors for the BTOF.

3236 Assemblies of  $4 \times 4$  AC-LGAD pixel sensors with  $500 \times 500 \mu m^2$  pixelation and  $30 \mu m$  thickness,  
 3237 and  $4 \times 4$  EICROC0 ASICs, were completed by the BNL, IJCLab, OMEGA, and Hiroshima groups  
 3238 on test-boards developed by IJCLab/OMEGA. Testing included scans of the analog and digital  
 3239 components using charge injection and beta particles from a Sr-90 source, resulting in a measured  
 3240 jitter of 8-9 ps for charges above 20 fC. Both wire-bonded and flip-chip assemblies were developed  
 3241 for various characterizations. Additional tests using Transient Current Technique (TCT) laser scans  
 3242 were conducted to map out charge distribution, and various tests are still ongoing.

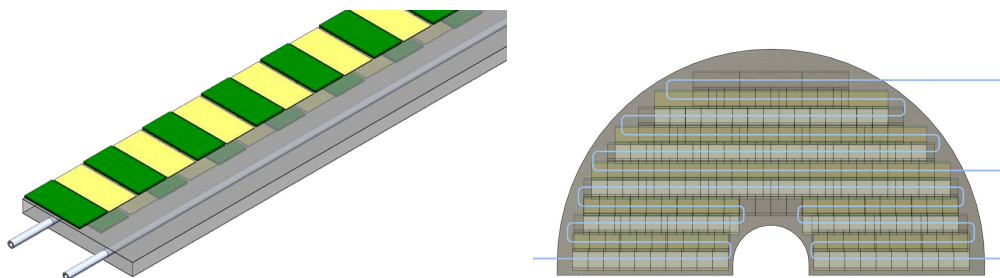


**Figure 8.93:** schematic drawings of the cooling pipes in one BTOF stave (left) and half of the whole FTOF (right). Each BTOF stave has one input line and a return line, while the FTOF has a total of 4 input lines and 4 return lines.

3243 ORNL is developing flexible Kapton PCBs for TOF applications, where sensors and mock-up ASICs  
 3244 will be glued to the stave and wire-bonded at UCSC and then co-cured onto a composite structure  
 3245 at Purdue for evaluation. Flip-chip options will be available soon, aiming to support low-cost  
 3246 sensor-ASIC hybridization techniques.

3247 In FY24, BNL, LBNL, and Rice developed a prototype board (ppRDO) for precise clock distribution  
 3248 and ASIC integration for AC-LGAD systems. Key milestones, including schematic designs, part  
 3249 orders, PCB layout, and initial testing, were completed ahead of schedule. Firmware development  
 3250 and performance tests on clock cleaning, jitter, and power distribution are ongoing. The collabora-  
 3251 tion aims to continue in FY25, focusing on developing a readout board (RBv1) and power board  
 3252 (PBv0) for AC-LGAD systems, supporting the TOF applications, and ensuring DAQ compatibility.  
 3253 The ppRDO includes three components: an FPGA, a clock cleaner, and an SFP+ module. Future  
 3254 versions will adopt an lpGBT to replace the FPGA, clock cleaner, and a VTRx+ to replace the SFP+  
 3255 module, improving performance, radiation hardness, and integration.

## 3256 Implementation

3257 **Services:** Electric power is distributed to the detector components via the Power Board (PB),  
 3258 which is part of the Service Hybrid (SH). The SH also includes the functionality of the Readout  
 3259 Board (RDO). In the case of BTOF, one SH supports 64 sensors and 128 ASICs, with SHs placed  
 3260 on both sides of the stave. For FTOF, several types of SHs are used, covering 12, 24, or 28 sets of  
 3261 sensors and ASICs. The SH is distributed on the mechanical and support disk, together with sensor  
 3262 modules.

3263 Low Voltage (LV) and High Voltage (HV) cables are connected to the PB, where multiple DC-DC  
 3264 converters step down or adjust the voltages as needed. HV is applied to groups of multiple sensors  
 3265 rather than distributed individually to each sensor. The size of each sensor group is determined by  
 3266 the design of the sensors and the electronics. Table 8.40 summarizes the services (cables and tubes)  
 3267 necessary for the TOF detectors.

3268 A liquid cooling system is employed to control the temperature of the detector. For the BTOF stave,  
 3269 one or two cooling pipes are integrated into the stave sandwich structure, with liquid flowing  
 3270 in one direction along the length of the stave. In FTOF, a winding liquid pipe is integrated into  
 3271 the support sandwich structure. The flow rate and pipe diameter are determined by the amount  
 3272 of heat generated and the detector's performance requirements; thermal finite element analysis  
 3273 determines the design. The pressure must remain below the surrounding air pressure to ensure

subsystem	item	quantity	diameter (mm)	lengths (m)	description
BTOF	288 FEE LV s.hybrid dist.	24	20	15–25	Rack to Panel, 8AWG(24 AWG sense pairs)
BTOF	FEE LV	72	6.3	8	panel-to detector, Alpha-PN: 2424C SL005
BTOF	FEE HV	18	14	15–25	Rack to Dist. Panel
BTOF	FEE HV	144x2	1.5	8	panel to sensor
BTOF	cooling tubes	144x2	5	> 2.6	supply/return from panel to stave (Aluminum)
BTOF	cooling tubes	4x2			supply/return to panel
FTOF	132FEE/sHybrids, service feeds	44	10.0	25	LV,rack-to-detector LV-dist,14AWG TC,w/24AWG-sense wires
FTOF	132FEE/sHybrids, dist.	44	9	3	18 AWG TC, 6 cond.dist. panel-to s.hybrids
FTOF	FEE HV	212	2.42	10	panel to sensor
FTOF	cooling tubes	2x2	5		supply/return from panel to detector (Aluminum)
FTOF	cooling tubes	2			supply/return to panel

**Table 8.40:** Summary of BTOF and FTOF low voltage and high voltage power supply cables to distribution panels and then to the detector FEE (the exact numbers are being checked at the time of writing).

safe operation. Fig. 8.93 shows a single BTOF stave with cooling pipe (left) and half of the FTOF structure with cooling pipes (right). Possible cooling liquid choices are either water or the NOVEC 7200 engineered fluid [63].

**Subsystem mechanics and integration:** Both the BTOF and FTOF detector systems are supported by their own support structure, which is integrated and supported by the global support tube (GST). The BTOF is a barrel geometry time-of-flight detector system located at a radius of 63 cm from  $z = -117.5$  cm to  $z = +171.5$  cm along the beam direction as shown in Fig. 8.94. The BTOF detector subsystem has a dedicated 7.5 cm space in the radial direction, and similarly, the FTOF subsystem has a dedicated 7.4 cm space along the beam direction. Three engagement rings (each 5 mm width) are made from composite materials and support the BTOF detector - they are supported by the GST. A first concept was developed for a BTOF stave mounting mechanism employing the engagement rings by clips with staves at an  $18^\circ$  angle. Staves are individually removable to ease maintenance. The FTOF detector is designed in two half-disc structures, or dee's, that are kinematically mounted to the GST. Services (readout, power, cooling) of the BTOF are routed to both ends of the barrel, while those of the FTOF are routed to the outer radius, and all are sup-

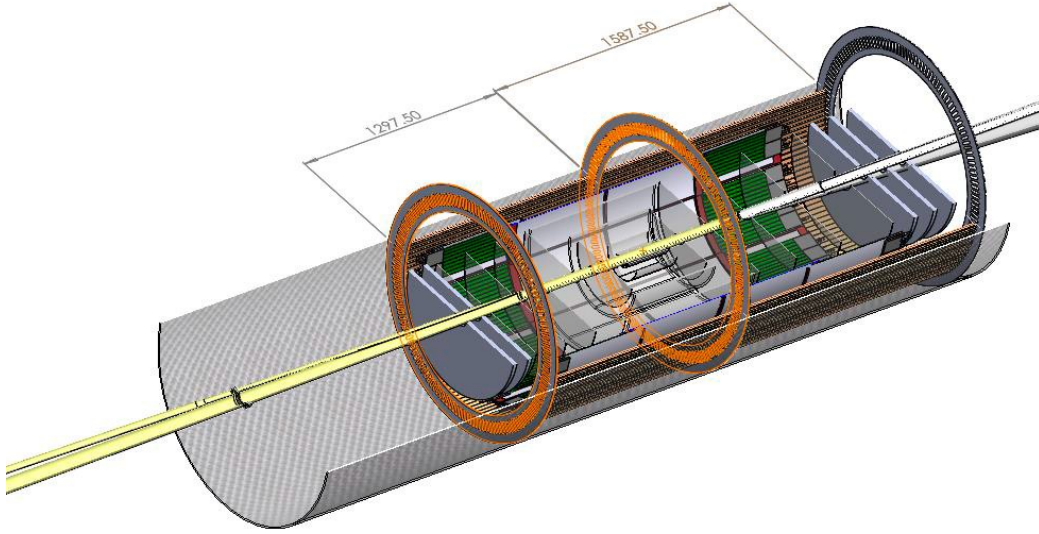


**Figure 8.94:** BTOF supporting mechanical structure with engagement rings situated and supported by the EPIC global support tube structure (GST). The width of each of the three engagement rings is 5 mm.

ported by the GST. Table 8.41 lists the positions of the BTOF and FTOF relative to the global ePIC geometry.

subsystem	$z_{min}$ (cm)	$z_{max}$ (cm)	inner radius (cm)	outer radius (cm)	stave angle
Barrel TOF	-117.5	171.5	62	69.5	$18^\circ$
Forward TOF	185	192.5	10.5	60	0

**Table 8.41:** The BTOF is designed with a barrel geometry surrounding the beam pipe and interaction point, while the FTOF is a disk geometry perpendicular to the beam direction on the hadron side (positive  $z$ ).

**Calibration, alignment and monitoring:** **Calibration and alignment:** For spacial calibration and alignment, the TOF layer is essentially treated as a layer of the overall tracking system. Therefore, spacial alignment will be carried out as part of the entire tracker. This is typically based on the match between tracks reconstructed in other layers of the tracking, then extrapolated to the TOF and the hits in the TOF. By combining the information from many tracks, high precision can be achieved.

To exploit timing in the reconstruction of the charged tracks, the different TOF channels must be synchronized to a precision of a few picoseconds. The absolute time calibration (or phase shifts relative to the beam clock) is not a particular concern, as all the event reconstruction relies on the relative time between tracks within the same collision event. The time offsets of the TOF channels can be intercalibrated using all the tracks collected online through a fast reconstruction stream.

The distribution of the reconstructed time at the vertex of these tracks – assuming they are pions – should have an rms spread of approximately 50 ps, including the time spread of the luminous region and detector resolution. The mean time of this distribution over many tracks provides the reference calibration points. Non-pion particles will contribute to the tail of the distribution, which can be cleaned up using an iterative procedure. These calibrations can be made available for the prompt reconstruction of the events and updated frequently.

**Monitoring:** In the readout scheme of the TOF, a common clock is distributed to the individual channels belonging to the same service hybrid. The time stability of the clock distribution can be monitored with a precision of a few picoseconds every second.

### Status and remaining design effort: eRD112 and eRD109

**eRD112: Sensor R&D effort** A brief summary of eRD112 activities is reported in this section, for a more detailed review of the sensor development effort consult the 2024 eRD112 report document. HPK sensors from the 2023 production have been tested at the Fermilab test beam facility; the results are summarized in Ref. [2]. HPK strip sensors from the latest full-size production were received in the fall of 2024 and are currently being characterized; HPK pixel sensors from the same production will be received by the end of the year. A summary of the best results is shown in Fig. 8.95. The same HPK production was tested in the laboratory with focused laser TCT and showed similar results as reported in Ref. [60]. The presented strip sensors (Fig. 8.95, left) show a constant time resolution of around 35 ps, which is within the requirements for the ePIC TOF (see Table. 8.36). The strip reconstructed position resolution is between 10-20  $\mu\text{m}$ , which is also within the ePIC TOF requirement of 30  $\mu\text{m}$ . The best result for pixel sensors (Fig. 8.95, right) shows a homogeneous time resolution of 20-25 ps, well within the ePIC TOF requirements. The position resolution is 20-70  $\mu\text{m}$  across the device; the charge-sharing mechanism allows for precision reconstruction between metal electrodes, but the resolution is significantly worse for hits directly on the metal electrodes.

The position resolution requirement for the FTOF is 30  $\mu\text{m}$ . Therefore, pixel technology needs to be refined to meet the requirements. The new HPK production (expected by the end of 2024) includes smaller electrode sizes and larger gaps between electrodes, which could provide good reconstruction across the sensor. However, it was observed that a larger gap decreases the total S/N between electrodes, which might degrade the overall performance of the sensors. Results from a BNL production provide a promising alternative to square metal pixels. The S/N is better across the sensor for a cross-shape electrode given the same central metal shape, allowing for better reconstruction using charge sharing. HPK did not include cross-shape geometry in the latest production, but it might be included in the next one. Another producer of cross-shaped AC-LGADs is Fondazione Bruno Kessler (FBK). The FBK prototypes were investigated with a laser TCT, and a similar behavior was observed for cross-shaped devices [61].

The sensors irradiated at the Triga Reactor with 1 MeV neutrons were received in Spring 2024 and characterized both for electrical proprieties (capacitance and current over-voltage) and with the laser TCT station. Gain degradation can be probed with measurements of capacitance over voltage by identifying the gain layer depletion point ( $V_{GL}$ ). Figure 8.96 (left) shows the change in the gain layer for the irradiated HPK AC-LGADs from several wafers, with different n+, oxide, and active thickness, up to  $1 \times 10^{15}$  Neq. In the region of interest for ePIC ( $< 10^{13}$  Neq), the gain layer is unchanged. The charge-sharing proprieties after irradiation were tested in the laboratory using a focused IR laser. As seen in Fig. 8.96 (right), the spatial response of the sensor is unchanged after irradiation up to  $5 \times 10^{14}$  Neq. The current increase in the irradiated HPK sensors is also negligible until  $< 10^{13}$  Neq, as shown in Fig. 8.96 (bottom). The measurements were done at room temperature; therefore, no cooling will be necessary to reduce the dark current, which would



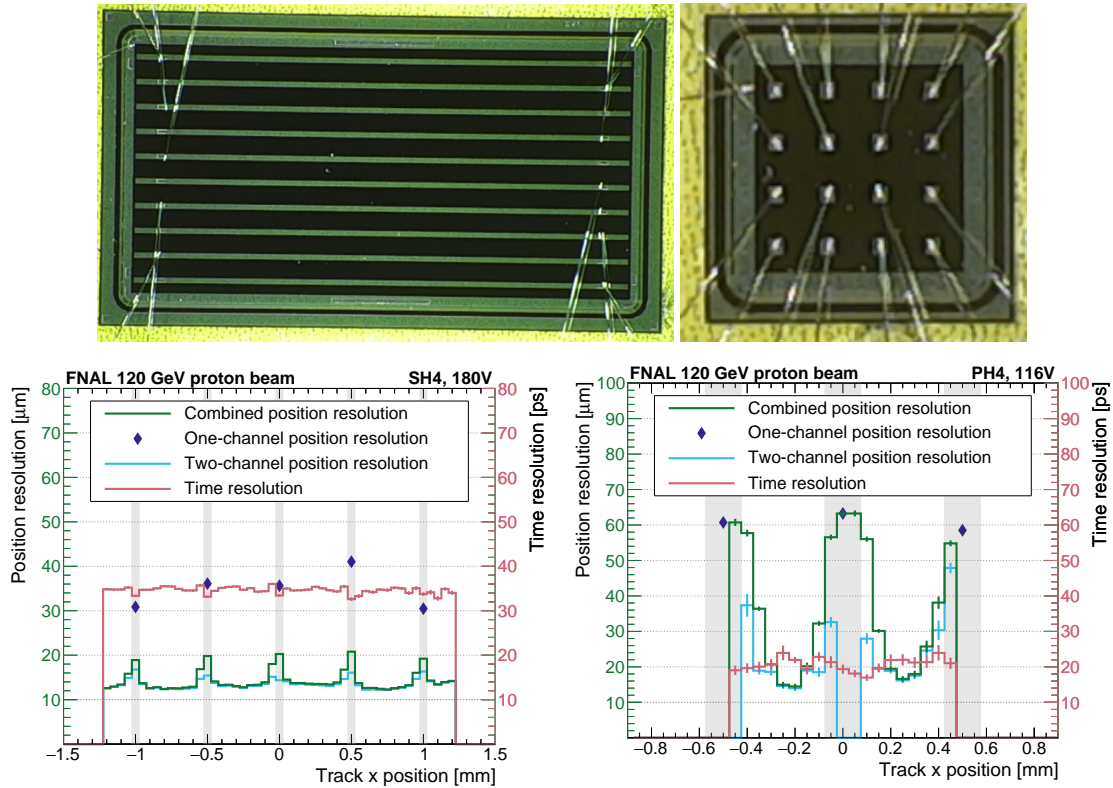


**Figure 8.95:** Left: Picture and beam test results for HPK strip sensor, 1 cm long, 500  $\mu\text{m}$  pitch, and 50  $\mu\text{m}$  metal electrode width. Right: Picture and beam test results for HPK pixel sensor, 4x4, 500  $\mu\text{m}$  pitch, and 150  $\mu\text{m}$  metal electrode width. Sensors were read out by an FNAL 16ch board, plots from Ref. [2].

3349 increase the sensor power dissipation in the ePIC. In conclusion, no change in the behavior of the  
 3350 sensors is expected during the lifetime of the ePIC detector due to radiation damage.

3351 **eRD109: readout R&D effort** A more detailed review of the electronics development effort can  
 3352 be found in the 2024 eRD109 report document. In the following section, a brief summary will be  
 3353 provided.

3354 The Fermilab team has continued the development of the FCFD ASIC prototype and, in FY23, has  
 3355 designed the first multi-channel prototype with this approach, labeled FCFDv1. Numerous techni-  
 3356 cal improvements were implemented based on the experience with FCFDv0, aimed at addressing  
 3357 the stability and performance of the system. The FCFDv1 ASIC was submitted for production in  
 3358 September 2023 and received in January 2024. A specialized readout board was designed to ac-  
 3359 commodate the FCFDv1 connected to a 0.5 cm HPK AC-LGAD strip sensor. Initial performance  
 3360 measurements were done using internal charge injections performed with an LGAD-like signal.  
 3361 With input capacitance  $\sim 3.5$  pF (mimicking AC-strip input capacitance), a jitter of around 11 ps  
 3362 was achieved, as shown in Fig. 8.97 (left). Test beam campaigns were performed in June 2024 to  
 3363 study the performance of the FCFDv1. The newly introduced amplitude readout was found to  
 3364 function well, and results show 100% efficiency when combining neighboring strips. The time re-  
 3365 solution measured from the beam test was around 50 ps. A further design improvement is foreseen  
 3366 in FCFDv1.1 to accommodate a 1 cm AC-LGAD strip sensor and improve the timing resolution.



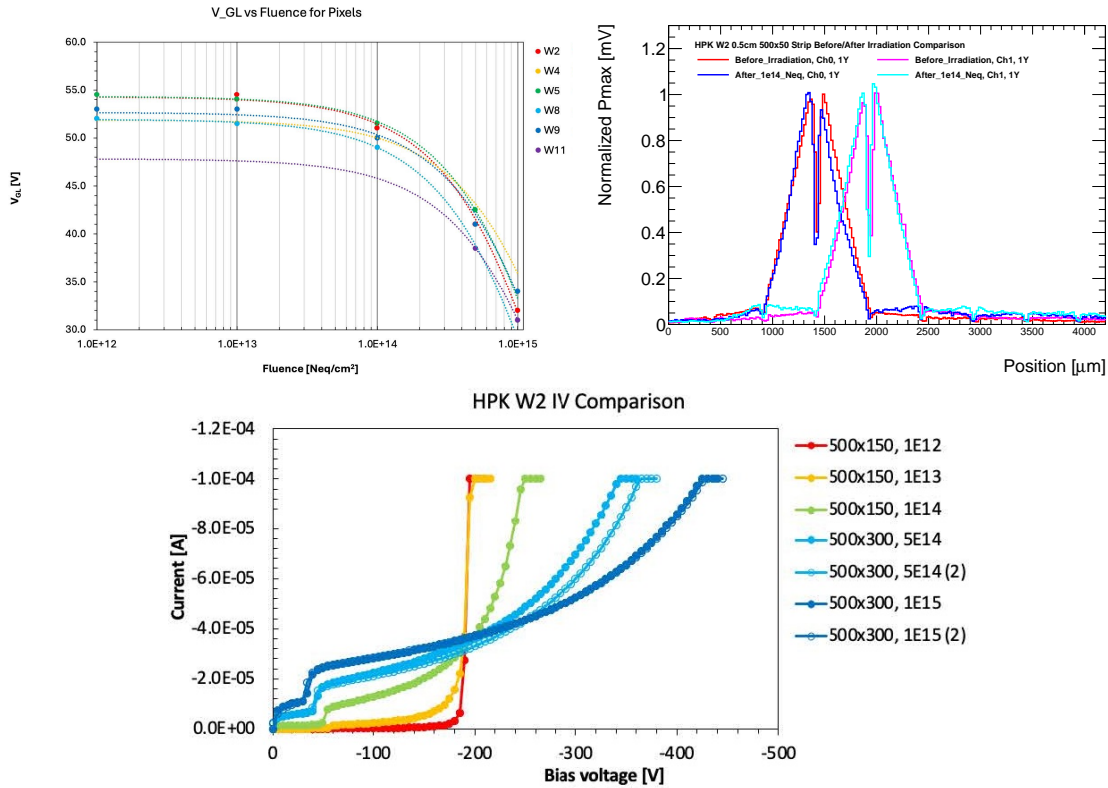


**Figure 8.96:** Left: Degradation of the gain layer for AC-LGADs of several wafers (with different  $n^+$ , oxide, and active thickness) from HPK latest sensor production, showing no change in gain layer doping up to  $10^{13} \text{ Neq}$ , which is an order of magnitude over the ePIC TOF radiation requirement. Sensors were irradiated at the TRIGA reactor (Ljubljana) with 1 MeV neutrons. Right: Normalized comparison of response profile of two nearby strips for two HPK 0.5 cm length, 500  $\mu\text{m}$  pitch, 50  $\mu\text{m}$  strip width: one before irradiation and one after  $1 \times 10^{14} \text{ Neq}$ . Even if the total signal is degraded, the charge-sharing profile will remain unchanged. Bottom: Current over voltage measurement for irradiated HPK sensors.

3367 The development of the EICROC0 chip is proceeding as planned. In 2024, an updated PCB (“2024”  
 3368 PCB) was designed by the OMEGA group in France. This updated PCB features improved testa-  
 3369 bility and grounding, as well as the removal of supplementary PLLs. The chip shows good ho-  
 3370 mogeneity between channels and jitter below 35 ps for an injected charge of  $>4 \text{ fC}$ , both for the  
 3371 preamplifier and for the discriminator output, as seen in Fig. 8.97 (left). A large correlated noise  
 3372 still remains with the updated “2024” PCBs (already observed in the “2023” PCB), which leads  
 3373 to large TDC jitters, over 50 ps, when by design, the TDC jitter is expected to be of the order of  
 3374 10 ps. Nevertheless, the intrinsic performance of the preamplifier, the TDC, and the ADC, taken  
 3375 individually, agrees with the design and within the ePIC detector specifications.

3376 The development of a pre-prototype readout board (RDO) with high-precision clock distribution  
 3377 has been completed. Figure 8.98 shows a picture of the ppRDO. It is connected with the CMS ETL  
 3378 module board v0, which consists of the full-sized ETROC2 chip for testing purposes. The ppRDO  
 3379 will be evolved into the prototype RB for the FTOF next, which consists of lpGBT and VTRx+ chips  
 3380 instead of FPGA and SFP+. Those efforts will be carried out under engineer designs as described  
 3381 later.

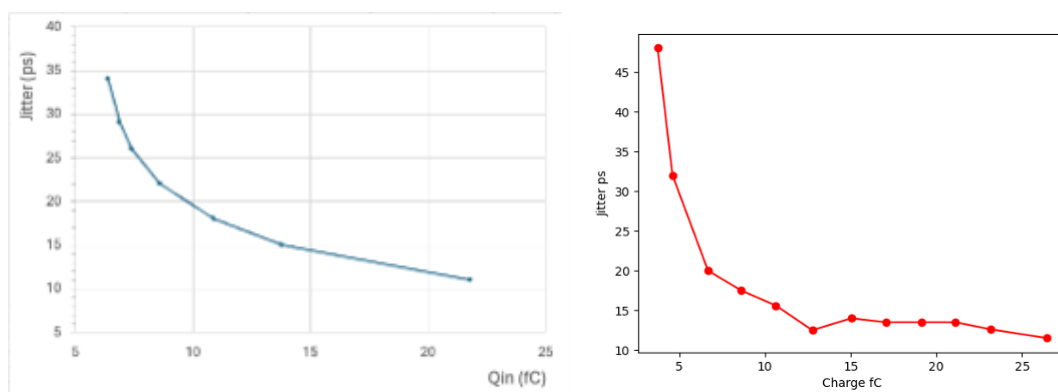


**Figure 8.97:** Left: FCFD Jitter measurements with 3.5 pF input capacitance and charge injection. Right: EICROC Discriminator jitter versus the injected charge, determined from data on an oscilloscope. Plots from the eRD112 and eRD109 2024 reports.

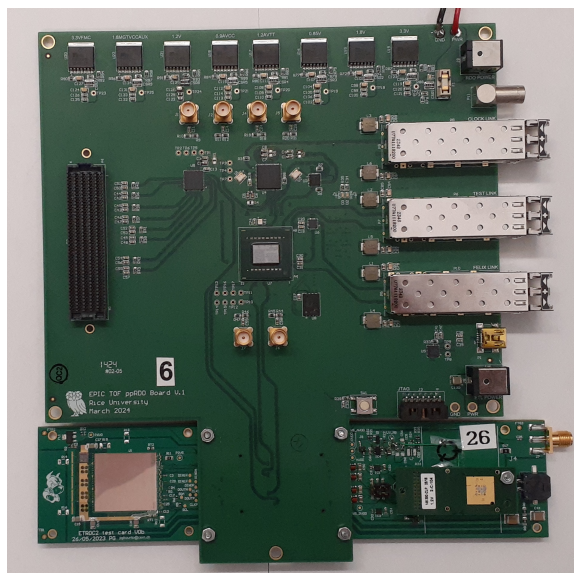


**Figure 8.98:** Picture of ppRDO connected with CMS ETL module board v0 for testing.

#### 3382 **E&D status and outlook:** E&D activities

3383 **Thermo-Mechanical demonstrator:** The fabrication of a demonstrator stave following the double-  
 3384 sided design, as seen in Fig. 8.100, is ongoing. The demonstrator will be a thermal/mechanical  
 3385 demonstrator of the assembly procedure and chip/sensor power dissipation. A mock-up stave, see  
 3386 example in Fig. 8.99, will be co-cured with a readout flex with a cooling pipe in the center. A series  
 3387 of Si heaters and full-size HPK sensors from the latest production will be glued to the stave, then  
 3388 wire-bonded together and to the readout flex. The demonstrator will probe the power dissipation,  
 3389 the temperature gradient across the stave, and the mechanical assembly procedure. Demonstrator  
 3390 results are expected by Q1 2025.



Figure 8.99: Assembled BTOF stave prototype at Purdue.

**Environmental, Safety and Health (ES&H) aspects and Quality Assessment (QA planning):** We also carried out QA long-term and stress-test reliability studies of AC-LGADs as a stepping-stone towards studies on AC-LGADs. The tests were conducted in an ambient chamber at various environmental conditions. We kept the sensors under bias voltage over periods of weeks, at different temperatures, ranging from  $-60^{\circ}$  to  $+80^{\circ}$  C, and under different humidity conditions. Under these extreme conditions, we carried out I-V scans. At intervals of time between temperature cycles, we also collected signals from  $\beta$  particles from a Sr-90 source at room temperatures to study any deterioration in noise or charge collection. The results were presented at an IEEE conference. While we saw an impact of humidity and temperature on current and breakdown voltage, the sensors recovered their original performance in subsequent cycles. In addition, we also studied the impact of passivation on sensors to minimize charge build-up and early mortality. We confirmed that passivation is critical to minimize the impact of humidity on sensors and prevent early mortality. Such tests were critical after issues had been observed in silicon sensors used for tracking detectors in other experiments, such as those at the HL-LHC. As part of our QA strategy, we also sent BNL-made AC-LGADs to colleagues of UNM to have them irradiated at various fluences in a proton beam at ITA, in a gamma beam at SANDIA and with neutrons at the TRIGA reactor. The first results are shown in the previous sections.

For both sensors and readout chips, it is imperative to evaluate the yield of the test productions to adjust the final production orders. The QA plans to evaluate the yield of the sensor productions are as follows: each produced sensor will be tested in the laboratory in a probe station with simple current over voltage (IV) and capacitance over voltage (CV) tests. AC-LGADs have a single point of DC connection on the n+, so only 1 or 2 needles are necessary for the test; a probe card is not necessary for QA. The IV test will allow us to check the current level and the breakdown voltage for each produced device; the current level has to be  $\ll 1 \mu\text{A}$ , not to introduce power dissipation issues. The breakdown voltage of all devices has to be within 10% spread to avoid issues in the HV distribution. The CV test will probe the gain layer depletion voltage and demonstrate that all devices have homogeneous gain. For LHC prototypes [58] as a reference, the gain homogeneity was within 1% spread. A selection of devices from the full production will be characterized by mounting them on analog frontend boards with laser TCT and at test beam facilities to ensure the homogeneity of the charge-sharing response.

To evaluate the yield of the chip (EICROC, FCFD) productions, a sample of chips from each batch will be tested and probed for homogeneity in all the channels using a calibration input. All channels have to be within 10% (spread) of homogeneity. A selection of chips will be coupled (wire bonded or bump bonded) with a matching working sensor and mounted on a prototype PCB to probe correct and homogeneous operation in a realistic configuration. Then, the boards will be tested with a laser TCT or at test beam facilities.

Once the state of sensors, readout chips, and flex is advanced, a fully loaded demonstrator stave is envisioned. The mounting procedure will already be tested during the assembly of the thermo-mechanical demonstrator. The full demonstrator will then be tested with radioactive sources in a laboratory or at test beams.

**Construction and assembly planning:** The BTOF detector has a cylindrical shape consisting of 144 tilted staves. These staves are assembled at designated sites within Class-7 or higher clean rooms before being transported to BNL for final construction. Each staff is approximately 270 cm long and is divided into two half-staves of 135 cm each. A half-staff includes a support structure with an integrated cooling pipe, a flexible printed circuit (FPC), sensors, and ASICs. The sensors and ASICs are mounted on both sides of the half-staff, with 64 sensors and 128 ASICs on each side. Wire bonding is used to connect the ASICs to the sensors and electronics. Only components that pass various quality inspections — such as visual checks, metrology, and electrical tests — proceed to the assembly stage. During the half-staff assembly, one FPC is glued onto the support structure; see Fig. 8.100(a). To ensure precise alignment, a specialized tool is used featuring pins and holes that guide the placement of the FPC and the correct application of glue. After assembly, the staves undergo both electrical and mechanical tests. Subsequently, sensors and ASICs are installed on the FPC surface using alignment tools similar to those used during the FPC mounting process, as shown in Fig. 8.100(b). These tools help position the components and apply adhesive. Electrical connections are verified, and in Fig. 8.100(c), the ASICs are bonded to the sensors using wire bonding, followed by wire encapsulation. Two support structures with wire-bonded sensors, ASIC, and FPC (front and back side), are attached to each other as in Fig. 8.100(d). The final round of testing is conducted after completing the installation on both sides (Fig. 8.100(e)). Fully tested staves are then shipped to BNL for integration into the global support structure of the ePIC detector, which contains 144 slots for precise alignment of the staves within the global coordinate system.

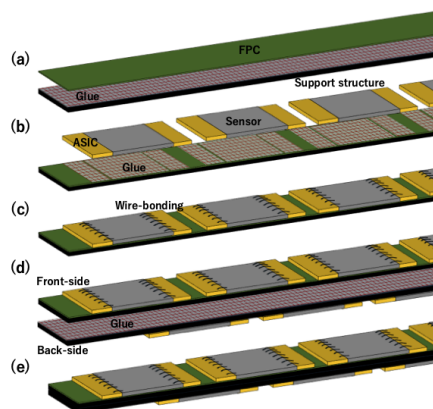


**Figure 8.100:** Assembly process of BTOF staff. The drawing is not to scale.

The FTOF is constructed in a double-sided disk shape by populating modules with dimensions indicated in Fig. 8.91. Each module includes 4 sensors, 4 ASICs, a module board, and an aluminum-nitride (AlN) base plate, which acts as a thermal conduit to the cooling system. The modules are connected to a service hybrid (SH) that consists of a power board (PB) and a readout board (RB). As mentioned earlier, three different configurations of SH are used, depending on the number of modules being supported: 3 modules (RB3), 6 modules (RB6), and 7 modules (RB7). There are about 780 modules in total to patch the disk shape. Sensor and ASIC are connected by bump-bonding. The module board is connected to the ASICs through wire bonding and has a connector to interface with the RDO. Assembly of the modules occurs in Class-7 (or higher) clean rooms, while the PB and RB can be assembled under standard conditions. The assembly of each module begins with the connection of one sensor to one ASIC using bump-bonding technology (Fig. 8.101(a)). Automated machines are used for sensor and ASIC placement, alignment, and bonding. After bonding, the electrical performance of the sensor-ASIC hybrids is tested. Following this, 4 sensor-ASIC hybrids are mounted on the module board, using a dedicated tool to ensure precise alignment (Fig. 8.101(b)). Thermal adhesive films are placed between the hybrids and the module board to

ensure efficient heat dissipation. Once mounted, the ASICs are wire-bonded to the module board, and the wires are encapsulated for protection. After the bonding process, the AlN base plate is attached to the opposite side of the hybrid (Fig. 8.101(b)), with thermal adhesive films again used between them to aid heat transfer. The thermal adhesive films are also put between them. The modules undergo thorough quality checks before moving on to SH assembly. The RBs and PBs are manufactured using standard circuit board techniques and come with dedicated connectors for integration. SHs are available in configurations supporting 3, 6, or 7 modules, with the RB and PB connected via dedicated interfaces (Fig. 8.101(c)). Once assembled (Fig. 8.101(d)), the modules and SHs are tested for connectivity and performance. After passing all tests, the modules and SHs are shipped to BNL, where they are attached to the disk-shaped support structure. Specialized tools ensure the accurate placement of the components. Modules and SHs are mounted on both sides of the support structure to eliminate acceptance gaps between sensors. A fixture maintains the required clearance between components when installing the modules and SHs on the opposite side. Finally, the fully assembled disk is installed into the ePIC detector.

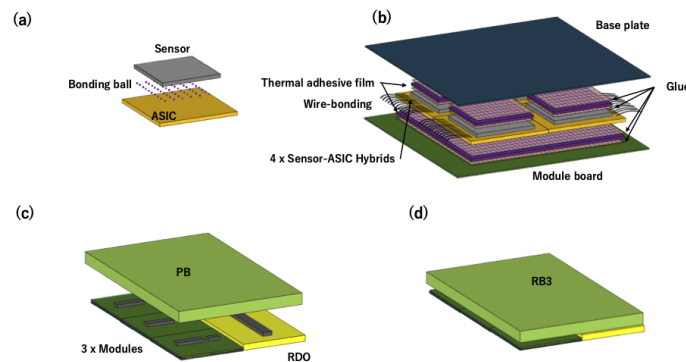


**Figure 8.101:** Assembly process of FTOF modules. RB3 type is shown as an example. The drawing is not to scale.

**Collaborators and their role, resources, and workforce:** Table 8.102 shows the participating institutes with their roles, the contact person, and potential commitments. This shows substantial participation by the international collaborators outside of the U.S.. We also anticipate substantial funding support from international collaborators for the BTOF detector.

**Risks and mitigation strategy:** Our R&D results (eRD112) show that the performance of the tested sensors would meet physics requirements for the TOF subsystems. Those studies were done with smaller chip dimensions. The production for the R&D study with a full-size sensor chip is underway. There is a potential risk that the performance of sensors with larger sizes would be worse. The mitigation is to reduce the sensor size.

The HPK sensors for R&D (eRD112) are of a small quantity. Mass production would be a risk in terms of chip yield and schedule delay. The mitigation is to explore other possible production sites (Taiwan/FBK).

FCFD ASIC design (eRD109) currently has analog signal readout only. The design and test of the digitization component is underway and is expected to have a first pass early next year. Additional resources may be needed to mitigate potential schedule delays and cost increases. In ad-



Institute	Contact Person	NOW (TDR->Project)
Brookhaven National Laboratory	Prithwish Tribedy <a href="mailto:tribedy@bnl.gov">tribedy@bnl.gov</a>	DAQ readout chain readout, <i>sensor-ASIC integration</i> , <i>sensor with FF AC-LGAD</i> ; EICROC testing
Fermi National Accelerator	Artur Apresyan <a href="mailto:Artur.Apresyan@cern.ch">Artur.Apresyan@cern.ch</a>	FCFD ASIC (no ePIC)
OMEGA	Dominique Marchand <a href="mailto:dominique.marchand@ijclab.in2p3.fr">dominique.marchand@ijclab.in2p3.fr</a>	EICROC
Los Alamos National Laboratory	Xuan Li <a href="mailto:xuanli@lanl.gov">xuanli@lanl.gov</a>	
Rice University	Wei Li <a href="mailto:wli33@rice.edu">wli33@rice.edu</a>	B/FTOF FEE?, Backend electronics (postdoc) , simulation and reconstruction
Oak Ridge National Laboratory	Oskar Hartbich <a href="mailto:hartbricho@ornl.gov">hartbricho@ornl.gov</a>	<i>sensor-ASIC integration</i> , frontend electronics (waffle probing), <i>module assembly</i>
Ohio State University	Daniel Brandenburg <a href="mailto:Brandenburg.89@osu.edu">Brandenburg.89@osu.edu</a>	BTOF/FTOF: <i>module assembly</i> ; backend electronics
Purdue University	Andreas Jung <a href="mailto:anjung@purdue.edu">anjung@purdue.edu</a>	<i>Module assembly</i>
Univ. of California, Santa Cruz	Simone Mazza <a href="mailto:simazza@ucsc.edu">simazza@ucsc.edu</a>	<i>Sensor</i> , <i>sensor-ASIC integration</i> , module assembly (no in-kind)
University of Illinois at Chicago	Olga Evdokimov <a href="mailto:mailto:evdolga@uic.edu">mailto:evdolga@uic.edu</a>	
Hiroshima University	Kenta Shigaki <a href="mailto:shigaki@hiroshima-u.ac.jp">shigaki@hiroshima-u.ac.jp</a>	FTOF EICROC testing, <i>sensor testing</i> (30%), simulation
RIKEN	Yuji Goto <a href="mailto:goto@bnl.gov">goto@bnl.gov</a>	<i>BTOF: module assembly</i>
Shinshu University	Kentaro Kawaide <a href="mailto:kawade@shinshu-u.ac.jp">kawade@shinshu-u.ac.jp</a>	<i>Sensor testing</i> , simulations
University of Tokyo	Taku Gunji <a href="mailto:gunji@cns.s.u-tokyo.ac.jp">gunji@cns.s.u-tokyo.ac.jp</a>	DAQ streaming readout
South China Normal University	Shuai Yang <a href="mailto:syang@scnu.edu.cn">syang@scnu.edu.cn</a>	
Univ of Sci. and Tech. of China	Yanwen Liu	
Indian Institute of Tech., Mandi	Prabhakar Palni <a href="mailto:prabhakar.palni@unjgoa.ac.in">prabhakar.palni@unjgoa.ac.in</a>	<i>FTOF Module Assembly/QA</i> , <i>sensor testing</i>
National Inst. of Sci. Edu. Res.	Ganesh Tambave <a href="mailto:ganesh.tambave@niser.ac.in">ganesh.tambave@niser.ac.in</a>	<i>Module Assembly</i>
National Central University		FF AC-LGAD (sensor QA)
National Cheng-Kung University	Yi Yang <a href="mailto:yiyang@ncku.edu.tw">yiyang@ncku.edu.tw</a>	Mechanics and cooling systems
National Taiwan University	Rong-Shyan Lu <a href="mailto:rslyu@phys.ntu.edu.tw">rslyu@phys.ntu.edu.tw</a>	FF AC-LGAD; <i>module assembly</i>
Univ. Técnica Federico Santa María		Simulations
LBNL	Zhenyu Ye <a href="mailto:yezhenyu2003@gmail.com">yezhenyu2003@gmail.com</a>	BTOF ASIC testing; SH
Kent State University	Zhangbu Xu <a href="mailto:zxu22@kent.edu">zxu22@kent.edu</a>	Simulation, readout test, machine shop (in-kind)
Nara	Takashi Hachiya <a href="mailto:hachiya@cc.nara-wu.ac.jp">hachiya@cc.nara-wu.ac.jp</a>	<i>BTOF module assembly/validation/FPCB</i>

**Figure 8.102:** Collaboration institutions and their potential responsibilities.

dition to the baseline chips, EICROC and FCFD, third-party ASICs are also taken into consideration: FAST (INFN Torino), AS-ROC (Anadyne Inc. and UCSC), and HPSoC (Nalu and UCSC). The most advanced one is the High-Performance System-on-Chip (HPSoC) ASIC, designed by Nalu Scientific [64], in close collaboration with SCIPP, and fabricated in 65 nm CMOS by TSMC. HPSoC includes a fast analog frontend and, unique to all other current AC-LGAD readout ASICs, will capture the full signal waveform at a sampling rate of 10-20 GS/s. Together, these are expected to address the EIC goal of 25 ps timing resolution or better per measured space point. V2b of the chip has a working digital backend and is currently under review.

We have performed heat conductivity and cooling simulations, as well as tests on the cooling capacity (currently with PED funding). Those show promising outcomes for meeting the cooling needs. The potential risk is that the cooling capacity is insufficient to maintain a stable and relatively uniform temperature. A possible mitigation strategy is to use different materials for cooling pipes with better heat conductivity and higher flow rates.

**Schedule** The schedules for BTOF and FTOF projects have been incorporated into the overall EIC project schedule. A major inter-dependence of the schedule is the sensor and ASIC designs. In the preproduction phase, 10% will be made in six months, during which quality and procedures will be confirmed. Then, during the production phase, the remaining 90% will be produced in two years.

### Additional Material

**Low-voltage and High-Voltage power supplies** Each service hybrid module will be powered by a radiation and magnetic field tolerant DC-DC regulation board as part of the hybrid module and mounted to the cooling plate. The minimum efficiency of the regulator board should be  $\geq 70.0\%$ . Input power to the DC-DC board is delivered from rack-mounted Wiener PL500 series power supplies to source  $15\text{ V DC} \pm 3.0\%$ . The current demand from the rack-mounted PSU should not exceed  $80.0\%$  of the manufacturer's rating. Each channel of the PSU will have over-current fuse protection. The power-cable size is selected to operate at  $125\%$  of the total continuous maximum load. The estimated power consumption and LV cable feed size for each detector is designated as follows: Forward TOF system LV power:  $6.0\text{ kW}$  ( $400\text{ A}$ ). LV power feeds from the platform: Custom two-conductor 12 AWG tray-rated cabling with embedded low-voltage twisted-pair sense wires.

Barrel TOF system LV power:  $15.0\text{ kW}$  ( $1,000\text{ A}$ ). LV power feeds from the platform: Custom two-conductor 8 AWG or 10 AWG (depending on LV segmentation) tray-rated cabling with embedded low-voltage twisted-pair sense wires. Custom-enclosed LV power distribution PCBs will be installed at the detector side and outside the inner detector volume. A disconnect is required for each LV output port of the distribution box. Power distribution to the service hybrids will be configured not to exceed  $10.0\%$  channel segmentation from the rack-mount power control. Multi-channel ISEG ESH series power modules will provide up to negative  $500\text{ VDC}$  bias at a current of  $10\text{ mA}$  per channel. Multiconductor cables terminated with REDEL connectors or individual coax cables terminated with SHV connectors will feed an enclosed HV distribution box. The HV bias cabling to the detector hybrids will be carried over a multi-drop cable configuration to service the sensor hybrids in small groups.

**Schedule** Although there are still many uncertain elements at this stage, the latest schedule is shown in this section. The overall progress of development depends heavily on the advancement of the sensor. For instance, since the ASIC blueprint is based on the sensor's features, the ASIC design cannot be completed before the sensor development is finalized. This was the first principle we used to set up the schedule.

At least three sensor prototypes will be produced. The first prototype, the full-size sensor prototype, has already been manufactured by HPK. Based on the characteristics of this sensor, the FCFDv2 and EICROC2 ASICs will be developed. Based on our experience, we can also expect that the time required to fabricate the sensor and the ASIC will be 4 months from submitting the design to delivery. It could be up to 6 months for the ASICs. Additionally, prototypes of the Service Hybrid (SH), electronics (FPC for BTOF and module board for FTOF), and support structure will be created based on this sensor and ASIC.

Next, the design for the second full-size sensor prototype will incorporate improvements identified from the first prototype. The design will start 2 months after starting the first sensor validation. The design of the next ASICs (FCFDv3 and EICROC2.v1) will begin as soon as the sensor design is finalized. The SH, FPC, and stave support structure will also be developed in conjunction with this



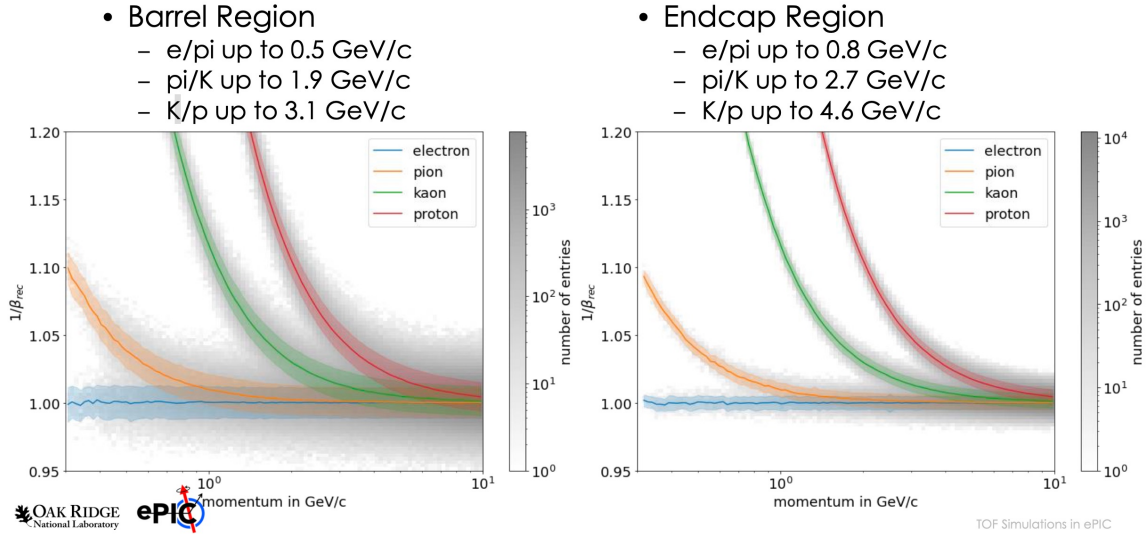


**Figure 8.103:** simulation of  $1/\beta$  as a function of particle momentum for BTOF and FTOF performance.

sensor and ASIC. Some sensor characteristics can be estimated based on accumulated knowledge, which might allow certain designs to be completed simultaneously.

The second full-size sensor prototype will be the last, but we will make another prototype as a backup and make final adjustments for mass production. Depending on the budget, additional sensor and ASIC prototypes may be ordered.

During the development phase, assembly was carried out as soon as the other components became available. However, there will be a time lag between the arrival of components and the start of assembly in the preproduction and production phases. This is because additional time is required for quality assurance (QA) and quality control (QC) procedures before the components can be shipped to the dedicated assembly sites. As a result, the preproduction and production phases will begin two months later than other phases.

**particle identification** Figure 8.103 shows an example of a single-particle response simulation of  $1/\beta$  as a function of particle momentum for BTOF and FTOF performance.

### 8.3.4.2 The proximity focusing RICH

#### Requirements

**Requirements from physics:** Particle identification capabilities in the electron going endcap region of the ePIC detector ( $-3.5 \leq \eta \leq -1.5$ ) will be provided by a proximity focusing ring imaging Cherenkov detector (pfRICH). Driven primarily by the requirements from SIDIS measurements, the pfRICH will need to provide  $3\sigma$  separation or better between pions, kaons, and protons for momenta  $p < 7$  GeV/c. The pfRICH will also play a critical role in electron-hadron separation for momenta below roughly 3 GeV/c, where hadron densities are at their maximum and the

electron ID capabilities of the backward EM calorimeter will not be sufficient to achieve the overall required electron purity. In addition to electron and hadron identification, the excellent timing resolution of the pfRICH photosensors, High Rate Picosecond Photon Detectors (HRPPDs), will allow the pfRICH to provide a high quality  $t_0$  reference for the barrel and forward endcap time-of-flight detectors.

**Requirements from Radiation Hardness:** The beam induced charged particle background impacts the pfRICH mainly via excess photons produced in the aerogel and fused silica windows of the HRPPD photo sensors. A fraction of the incoming photons are converted to photo-electrons (PE) by the photocathode according to its quantum efficiency. The amplification of PEs due to a secondary electron emission in the MCPs desorpts ions off the micro-channel walls. These ions drift towards the photocathode, and can react with or even sputter the photocathode material which leads to degradation of its quantum efficiency. HRPPD gain can also be affected due to a degradation of the secondary emission layer.

To estimate the flux of ion back flow during the expected life span of the detector, a simulation study was performed, combining the rates from DIS events and beam gas interactions. A mass-dependent minimum energy cutoff was applied so that only particles that would produce Cherenkov radiation in the aerogel plane or HRPPD window would be considered. Each particle producing Cherenkov photons in the aerogel ( $n = 1.04$ ) was assumed to produce  $\approx 10$  photoelectrons, while  $\approx 100$  photoelectrons were assumed from the HRPPD window ( $n = 1.45$ ) after factoring in the QE.

Convoluting an expected operating gain of  $10^5$  with a running period of 26 weeks/year and a luminosity of  $10^{34} \text{ cm}^{-2}\text{s}^{-1}$  yields a yearly estimate for accumulated charge of up to  $0.011 \text{ C/cm}^2$  on the photocathodes of sensors closest to the beam line. For a running period of 10 years, this will result in  $0.11 \text{ C/cm}^2$ , or  $1.1 \text{ C/cm}^2$  if one assume a higher gain of  $10^6$  to compensate the aging over time. It should be noted that the estimate of particle flux is based on realistic simulations for beam gas and DIS events. Furthermore, the rates and running period are overestimated which gives a safety factor of around 2 from the most plausible scenario. Studies to evaluate the degradation of QE with the accumulated charge are underway.

**Requirements from Particle Fluence:** Estimations of the expected data rates for the pfRICH were made using the same DIS + beam gas simulations that were used for the radiation hardness studies. The hit rates from physics and background sources as well as a noise rate of 2.34 MHz per HRPPD leads to a digitized data rate of 45 Gb/s for the entire detector. This is not divided evenly over all HRPPDs as those closest to the beamline see higher particle fluxes. The largest data rates per HRPPD are 1.5 Gb/s while the smallest are 205 Mb/s. These rates are not expected to pose a problem for the front-end electronics or data acquisition system.

### Justification

**Device concept and technological choice:** The operation of a generic proximity focusing RICH detector is based on a very simple set of principles. A charged particle passing through a thin layer of radiator (often aerogel with an appropriate refractive index) with a velocity higher than the speed of light in that medium emits Cherenkov light (photons) at an angle which is solely determined by the particle mass, momentum, and refractive index of the radiator. The 3D momentum of the particle is typically provided by a tracking system. If the average refractive index of the radiator is also known, measurements of the Cherenkov light emission angle can determine the

particle mass, thus allowing identification of different particle species, e.g. distinguishing electrons, pions, kaons, and protons.

The ePIC pFRICH was designed as a conceptually simple detector, based on proven principles, providing a high degree of performance that is practically uniform over the whole available angular acceptance in  $\eta$  and  $\phi$ . In order to reach the performance requirement of  $3\sigma$  separation or better of  $\pi/K/p$  for momenta  $p < 7 \text{ GeV}/c$ , the pFRICH design was optimized in the following ways: (1) the proximity gap length was maximized as much as possible within the volume available in ePIC; (2) the radiator thickness was taken to be small enough to reduce the contribution to the single photon angular resolution to below  $\sim 5 \text{ mrad}$ , yet produce enough photons per track to robustly reconstruct the Cherenkov angle; (3) the HRPPD pixellation was chosen such that it contributes at most  $\sim 2 \text{ mrad}$  to the angular resolution; and (4) the acrylic filter cuts off all UV light produced in the aerogel below  $\sim 300 \text{ nm}$ , where the  $dn/d\lambda$  dependency is strongest. In addition to satisfying the PID requirements in the backward direction, the small material budget of the pFRICH design minimizes the impact on the energy resolution of the endcap electromagnetic calorimeter which sits directly downstream.

### Subsystem description

General device description: The layout of the proposed ePIC pFRICH detector is shown in Fig. 8.104. It consists of a 1.3 m diameter and  $\sim 49 \text{ cm}$  long cylindrical vessel with the outer and inner walls made from a lightweight honeycomb carbon fiber sandwich and front and rear plates made of a carbon fiber reinforced plastic (CFRP). The vessel sits 123.6 cm from the nominal interaction point. Forty-two 2.5 cm thick aerogel tiles of a trapezoidal shape are installed in individual opaque compartments in a container mounted on the upstream side of the vessel. A thin acrylic filter is installed immediately after the aerogel container. The vessel is continually flushed with dry purified nitrogen. Sixty-eight HRPPD photosensors are installed in individual slots in the rear CFRP mounting plate with their fused silica windows facing the aerogel. Inner and outer conical mirrors cover the cylindrical sides of the vessel in order to increase the  $\eta$  acceptance of the Cherenkov photons produced in the aerogel radiator. Readout boards equipped with four 256-channel EICROC ASICs are mounted on the rear ceramic anode plates of each of the HRPPDs.

Sensors: An improved version of the Micro-Channel Plate Photomultiplier Tubes (MCP-PMTs) manufactured by Incom Inc. [65], the so-called High Rate Picosecond Photon Detectors (HRPPDs), will be used as the photosensor solution, see Fig. 8.105.

The sensor dimensions will be 120 mm x 120 mm, with a 104 mm x 104 mm fully efficient active area in the center (75% geometric efficiency) and will have slightly tapered 5 mm thick UV-grade fused silica windows. A DC-coupled variety of these sensors will be used, with the inner side of the anode base plate patterned into 32 x 32 square pixels, corresponding to 1024 channels per sensor, and a pitch of 3.25 mm. The sensors will be equipped with a UV-enhanced high quantum efficiency (QE) bialkali photocathode, with peak values exceeding 30% at 365 nm (see left and center panels in Fig. 8.106) [66]. The HRPPDs will be fitted with a pair of 600  $\mu\text{m}$  thick MCPs with a pore diameter of 10  $\mu\text{m}$ , open area ratio in excess of 70%, and bias angle of 13 degrees in a conventional chevron configuration. These will be operated at an amplification voltage of up to  $\sim 700 \text{ V}$  to comfortably achieve an overall detector gain above  $10^6$  if needed. The anode base plates will be manufactured from multi-layer High Temperature Co-fired Ceramic (HTCC) by Kyocera (Japan). They will have a custom design, matching the uniform 32 x 32 pixellation on the inner (vacuum) side of the sensor, short shielded traces inside of the ceramic stack, and a pattern of square pads with a smaller pitch on the outer side, matching the readout PCB design.

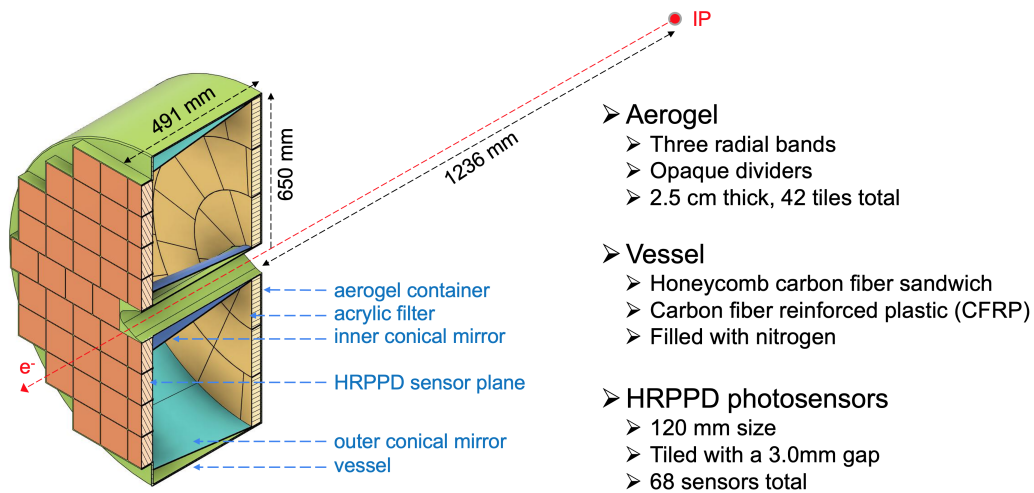


**Figure 8.104:** The proposed pFRICH detector. See the text for more details. ([Figure documentation](#))

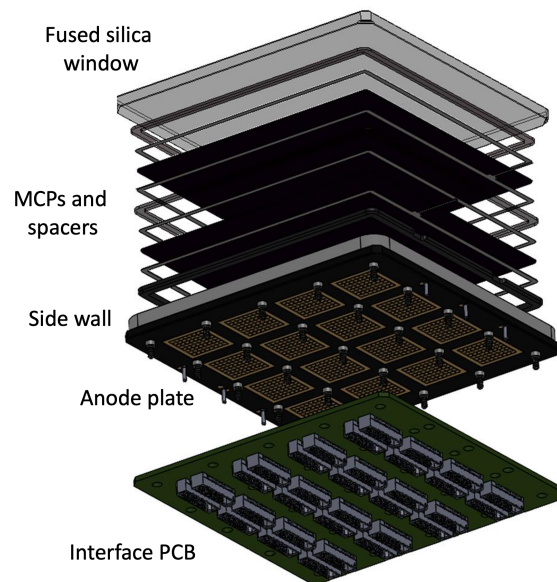


**Figure 8.105:** HRPPD photosensor CAD model with a passive interface board. Compression interposers between anode base plate and this PCB are not shown. ([Figure documentation](#))

HRPPDs have a demonstrated single photon Transit Time Spread (TTS) of  $\sim 20$  ps or better (right panel of Fig. 8.106). They have very low dark count rates (DCR), not exceeding few hundred Hz per square centimeter at a gain of  $10^6$  (see [67], slide 10). HRPPDs are expected to perform well in a 1.3 T magnetic field at the location of the pFRICH sensor plane in ePIC. Direct measurements will be performed in 2025, however the recent studies of LAPPDs with 10 micron pore MCPs indicate that HRPPD gain in a 1.3 T field should be recoverable to at least the level of  $10^6$  by increasing the MCP bias voltage [68].

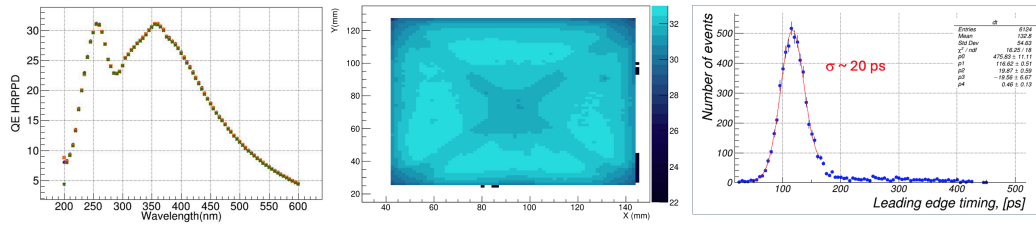


**Figure 8.106:** Left: EIC HRPPD QE as a function of wavelength. Center: QE map in the full active area at a wavelength of 365 nm. Right: Single photon timing resolution measured using Elmo 780 femtosecond laser with a wavelength of 390 nm. ([Figure documentation](#))

FEE: Each sensor will be equipped with four 256-channel EICROC ASICs [69], designed by the OMEGA group [70], each serving one quadrant of the sensor. EICROC ASICs will be built via a 130 nm technology process, with an expected power consumption of 1-3 mW/channel [69]. They will provide a Time of Arrival (TOA) and an ADC measurement with a dynamic range of 1 pC for each pixel, which should be sufficient for both single photon hits (both imaging and timing) and multi-photon hits (timing only) at a moderate HRPPD gain of a few times  $10^5$ . The ASICs will be able to measure the TOA with a resolution better than 20 ps per pixel assuming detector capacitance on the order of  $\sim 10$  pF, leading edge length of the HRPPD signal below 500 ps, and collected charge of a few dozens fC achieved by tuning the MCP gain [70]. These ballpark parameters seem to be easily within reach for pFRICH HRPPD sensors.

The ASICs will be bump bonded to the readout PCB in a “flip-chip” fashion to minimize the parasitic capacitance of the traces inside of the PCB stack. Preliminary estimates show that in such a scheme, where four  $16 \times 16$  primary pixel arrays with a pitch of 3.25 mm are first “compressed” to a 2.0 mm pitch inside the HRPPD ceramic base plate and then further reduced to a  $500 \mu\text{m}$  pad size in the readout PCB stack in order to ultimately match the EICROC ASIC pitch, the combined pad and trace capacitance should not exceed 10 pF. This is well within the expected operating range of the ASICs.

Each ASIC will be connected via a dedicated copper link to its respective readout unit (RDO), located on the outer circumference of the rear side of the pFRICH vessel. Each RDO will serve 16 EICROC ASICs, for a total of 17 RDOs. The RDOs will then be connected to a single Data Aggregation Module (DAM). The DAM board is envisioned to be a FrontEnd Link eXchange (FELIX) board [71] installed in the DAQ. The RDO will be connected to the DAM via a high speed optical link capable of at least 5 Gb/s throughput. The RDOs will follow the same design used by the ePIC pixelated AC-LGAD detectors. These boards will utilize lpGBT for aggregation of ASIC data and VTRX+ to provide the fiber interfaces. The RDO should deliver timing signals synchronized to the beam crossings with jitter  $< 5$  ps.

Other components: In addition to the vessel structure and sensors described above, two other components will be critical to the pFRICH: the aerogel radiators and mirrors. The pFRICH will be equipped with aerogel tiles produced by Chiba Aerogel Factory Co., Ltd. [72] with a nominal refractive index,  $n \sim 1.040$  and a thickness of 2.5 cm. The aerogel will be cut using a water jet technique into trapezoidal tiles providing a required radial and azimuthal segmentation with minimal dead area. This type of aerogel will replicate the performance of the material used in the Belle II experiment [73], and in particular, will be very transparent in the near UV range, with an absorption length and Rayleigh scattering length in excess of 5 mm down to  $\sim 275$ -300 nm. The aerogel tiles will be installed in segmented containers (slots) with  $\sim 500 \mu\text{m}$  thick walls and held in place with a thin filament. The container walls



will be opaque to suppress stray photons leaking out of the aerogel tile side facets, which are not expected to be of a high optical quality after water jetting.

The pfRICH will also utilize three types of mirrors to increase the active acceptance of the detector. The outer mirror cone consists of 12 segments approximately 40 cm in length which sit just inside the outer wall of the pfRICH vessel. These mirrors will recover Cherenkov photons from charged particles with large polar angles which pass through the aerogel but would exit the vessel before reaching the sensor plane. Similarly, a set of inner mirrors which wrap around the beam pipe and surrounding support structures will reflect photons emitted by small angle charged particles (close to  $\eta \approx -3.5$ ) back onto the sensor plane. Finally, small pyramidal mirrors will be placed on top of the HRPPD side walls to reflect (funnel) photons hitting this area back into the sensor acceptance. The mirrors themselves will have a reflectivity of approximately 90% for wavelengths between 300 and 600 nm and will be produced at Stony Brook University using an evaporator with the CFRP substrate material provided by Purdue University.

## Performance

Monte-Carlo simulations: The performance of the pfRICH design was studied using a custom simulation and reconstruction software suite. The geometry of the detector, along with other relevant characteristics such as the ePIC magnetic field map, aerogel optical properties, mirror reflectivity, and HRPPD quantum efficiency were modeled in GEANT4 v10.05.p01 [32]. The reconstruction made use of the Inverse Ray Tracing (IRT) library, which is part of the ePIC software stack [74], and a ROOT [75] based data structure providing access to all photo-electron, track, and event level quantities.

Parameters relevant to the performance of the pfRICH were determined by simulating single particles thrown at a variety of energies and angles. On average, roughly 11 Cherenkov photons were detected from particles at the saturation momentum, which is in agreement with first principles estimates taking into account a realistic sensor quantum efficiency. The working acceptance of the detector, defined as the region in which the ratio of tracks producing at least one detected photon over the total number of tracks is greater than 80%, was found to cover  $-3.5 < \eta < -1.5$ . Single photo-electron (SPE) and track level resolutions in the working acceptance were also determined, with the SPE resolution being roughly 5 mrad and independent of momentum, while the track level resolution improved with the number of detected photons and reached a value of 1.7 mrad.

The algorithm for event based reconstruction of the Cherenkov angles was validated using multi-particle simulations. The reconstructed Cherenkov angle (in units of mrad) as a function of particle momentum (in units of GeV/c) is shown in the left panel of Fig. 8.107 and compared to the theoretical expectations for a given mass hypothesis. It is seen that the reconstructed angles and theoretical expectations are in good agreement, confirming that the event based reconstruction is performing well. This plot also shows that the Cherenkov saturation angle is approximately 295 mrad. The  $N_\sigma$  separation count between the electron-pion and pion-kaon hypotheses as a function of momentum are shown in the middle and right panels of Fig. 8.107, respectively. It is seen that  $3\sigma$  separation is possible up to roughly 2.5 GeV/c for electron-pion and 9 GeV/c for pion-kaon hypotheses. This performance was found to be relatively uniform across the whole acceptance of the detector.

One of the main purposes of the pfRICH detector is to identify low momentum scattered electrons in the backward direction. Specifically, it will help with separating the electrons from  $\pi^-$  mesons, which are expected to dominate in the pfRICH acceptance. Using PYTHIA-6  $e+p$  collisions at  $18 \times 275$  GeV, it was shown that the pfRICH will provide good  $\pi^-$ -electron

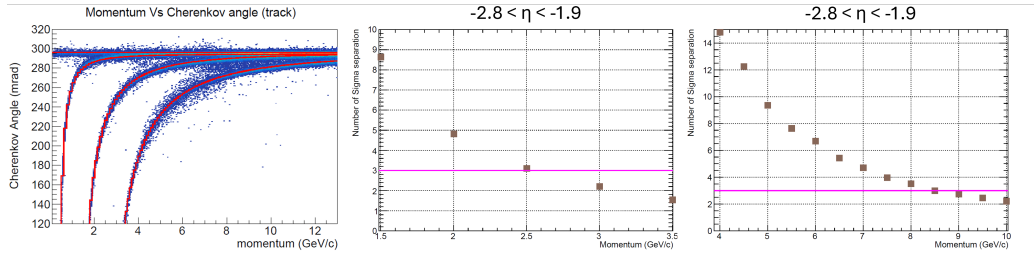


**Figure 8.107:** (Left) The reconstructed Cherenkov angle for electrons, pions, kaons, and protons as a function of momentum. (Middle)  $N_\sigma$  separation between the electron and pion hypotheses as a function of momentum. (Right) Same as the middle panel, for pion and kaon hypotheses. ([Figure documentation](#))

separation for  $p < 2$  GeV/c and decreasing separation power for momenta up to  $\sim 5$  GeV/c as seen in the left panel of Fig. 8.108. The pFRICH detector therefore plays an important role in the ePIC detector, allowing identification of the scattered electrons in kinematic region not accessible by other detectors.

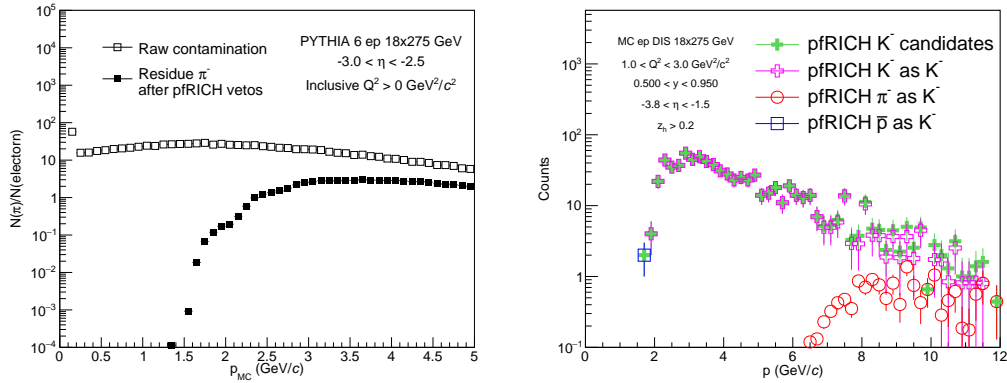


**Figure 8.108:** (left) Yield ratio of  $\pi^-/e_{\text{scat}}$  before (open black squares) and after (black full squares) pFRICH veto on  $\pi^-$  in PYTHIA 6  $e+p$  collisions at  $18 \times 275$  GeV for  $-3.0 < \eta < -2.5$ . (right) Kaon candidates identified using the pFRICH (full markers) in MC DIS  $e+p$  collisions at  $18 \times 275$  GeV in PYTHIA 8. The open markers show contributions from correctly identified kaons and other hadrons misidentified as kaons. ([Figure documentation](#))

Another important utilization of the pFRICH is hadron identification in the backward region in SIDIS studies. For that reason, the ability to separate  $\pi$ ,  $K$ , and  $p$  hadrons was studied using simulation of  $e+p$  collisions at  $18 \times 275$  GeV in PYTHIA 8. Specifically, the expected purity of leading  $K^-$  mesons was evaluated and was shown to be close to 100% up to hadron momenta of  $p < 6$  GeV/c, as shown in the right panel of Fig. 8.108. This means that pFRICH will play an important role in SIDIS studies as it can efficiently distinguish various hadron species in a wide momentum range.

**Timing performance:** A primary use of the excellent HRPPD timing resolution is providing an independent  $t_0$  reference to the barrel and forward endcap Time of Flight subsystems. However, one can make use of the  $t_0 \sim 20$  ps reference provided by the accelerator, and apply Time of Flight techniques to the pFRICH as a standalone subsystem. This functionality is



built into the Inverse Ray Tracing reconstruction algorithm (IRT 2.0) already, for both ambiguity resolution between a variety of photon optical paths for a given pair of emission and detection point candidates, and in a combined particle identification procedure using imaging and timing information at once. Numerical estimates follow, for performance illustration purposes.

The pfRICH aerogel wall and HRPPD sensor plane will be located about 1250 mm and 1650 mm from the IP, respectively, which can serve as a conservative estimate of the flight paths. An energetic charged particle will produce  $\sim 10$  detected Cherenkov photons in aerogel, and - in cases when it crosses the HRPPD fused silica window - a photon flash resulting in at least a dozen neighboring pads hit. In either case one can conservatively assume that an overall timing measurement will be of a factor of at least 3 higher than the single photon resolution. Even assuming that the HRPPD single photon resolution under real life experimental conditions will be 25-30 ps rather than 15-20 ps as bench studies using a femtosecond laser indicate (see Fig. 8.106, right), one can come to a conclusion that a standalone pfRICH time of flight measurement will be dominated by the precision of the accelerator  $t_0$  estimate at the IP. If one takes 25 ps as an overall time of flight measurement resolution between the IP and aerogel and HRPPD windows,  $3\sigma$  separation can be achieved between different particle hypothesis pairs as indicated in Table 8.42. In particular, one can clearly see that kaons and protons can be resolved at momenta far above kaon Cherenkov threshold in pfRICH aerogel. Therefore, a combined imaging and time of flight technique will provide a positive kaon identification in the whole momentum range, down to few hundred MeV/c.

	aerogel	HRPPD window
e/ $\pi$ separation	up to 0.75 GeV/c	up to 0.85 GeV/c
$\pi$ /K separation	up to 2.50 GeV/c	up to 2.85 GeV/c
K/p separation	up to 4.20 GeV/c	up to 4.80 GeV/c

**Table 8.42:** Expected pfRICH time of flight based particle identification performance. Highest momenta at which  $3\sigma$  separation for a respective pair of mass hypotheses can be achieved is quoted, for aerogel and HRPPD window radiators separately.

Hardware component evaluation: Hydrophobic silica aerogel manufactured by the Aerogel Factory [72] will be used for the radiator in the pfRICH detector. Three hydrophobic aerogel tiles, with nominal dimensions of 11 cm  $\times$  11 cm  $\times$  2.5 cm, density of 0.14 g/cm<sup>3</sup>, and refractive index of 1.04, were ordered from the Aerogel Factory to verify and assess their refractive index and transparency, two aerogel properties which are critical to the detector's performance. The refractive index was determined at Temple University by measuring the deflection of the refracted light exiting the corners of the aerogel (see QA section). The refractive index measured by Temple University ( $n_{TU}$ ) and the Aerogel Factory ( $n_{AF}$ ) were found to be in agreement, with a typical value of  $(n_{TU} - n_{AF}) / (n_{AF} - 1) \sim 2\%$ . The optical transparency was evaluated by measuring the transmittance as a function of wavelength. Transmittance curves for each tile were measured by the Aerogel Factory using a monochromator and spectrometer (Hitachi U-4100) [76], at BNL using a monochromator and spectrometer (Hitachi U-3210), and at Temple University using a LED and spectrometer setup which provides measurements at four discrete wavelengths (see left panel of Fig. 8.109). These three sets of measurements were found to be consistent with each other within the quoted errors. A sufficiently high transmittance of about 68.5% at 432 nm was found when averaging the results from three different measurements over the three produced aerogel tiles at Temple. The wavelength dependent transmittance measurements were used to extract additional information such as clarity, transmission length, and scattering length.

The mirrors will be produced by the pFRICh subsystem collaboration members, with substrates fabricated at Purdue University and coating performed at Stony Brook University. Optimization of the substrate and coating procedures is ongoing with a number of mirror samples being produced with different substrate manufacturing techniques, coating chamber settings, and coating material thickness. The reflectivity of the various mirror samples was evaluated at BNL using a dedicated test stand. The best performing mirror sample, manufactured using a  $\sim 12$  kilo-angstrom thickness aluminium coating, showed a measured average reflectivity of 0.89 for wavelengths between 300 and 600 nm (see right panel of Fig. 8.109).

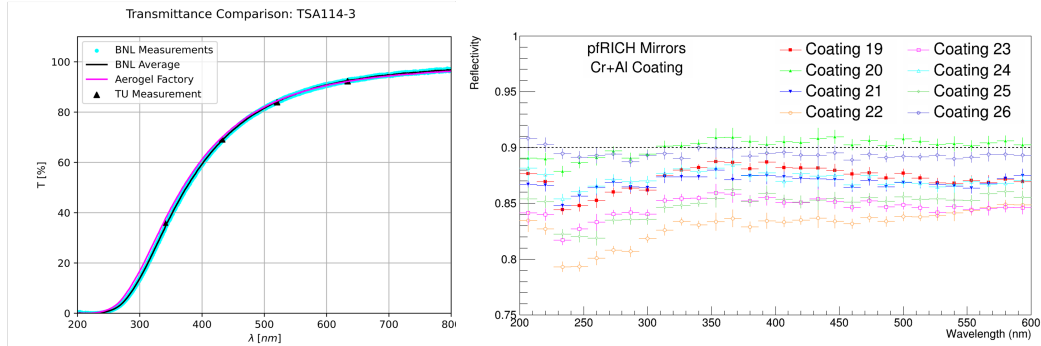


**Figure 8.109:** Left: Aerogel transmittance as a function of wavelength for factory, BNL, and Temple University measurements. Right: Mirror sample reflectivities as measured at BNL as a function of wavelength. ([Figure documentation](#))

## Implementation

**Services:** Services relevant for the pFRICh include High Voltage (HV) and Low Voltage (LV) systems to operate the photosensors and power the front-end electronics, respectively, a cooling system to regulate the temperature of the electronics and sensors, and a gas system to maintain the proper environment inside the pFRICh vessel.

The HV and LV modules will be located on the electronics platform, about 15 meters away from the pFRICh detector, in a low Total Ionizing Dose (TID) environment. Therefore, standard off-the-shelf units can be used. The high-voltage system will consist of 340 individual stackable negative HV channels. Twenty three CAEN A1515BV 16-channel 1.4kV/1mA floating ground modules [77] will be used. The HV modules will be housed in a pair of CAEN SY4527 mainframes [78], equipped with additional 1200 W power module boosters. Each of the twenty three modules will be connected to an enclosed box distribution PCB installed on the rear side of the pFRICh vessel. The box is fed from individual 15 m long multi-conductor high voltage cables. For the HV interconnect, CERN-approved 52-pin Radiall cable connectors and receptacles will be used throughout the system. The distribution PCB will arrange five of the isolated channels of the A1515BV in a manner to provide five individual stacked voltage levels and a common ground referenced return to each HRPPD. The respective five bias levels and ground will be connected to the pads on the rear side of the HRPPDs via narrow profile Teledyne Reynolds shielded 26 AWG coaxial cables, conductive vias in the Front End Board (FEB) stackup with a matching pad pattern, and custom Samtec compression interposers.

The EICROC ASICs will require 1.2 V low-voltage power. Under the assumption of up to 3 mW/channel power dissipation this corresponds to 3 W power (or up to 2.5A current) per pho-

tosensor FEB. Accounting for other electronics components present on such a FEB, and providing a 20% safety margin, we estimate the total power consumption to be less than 300 W for the whole system. This number is used as input for designing the cooling system discussed below. We will be using a single Wiener MPOD Mini LX crate with a MPOD-C controller and four MPV4008I1 4-channel LV modules [79]. One Low Voltage channel will serve four FEBs. 15 m long tray rated 10 AWG jacketed cables with 20AWG (sense wires) will run between the electronics platform and a LV distribution panel on the rear side of the pFRICH vessel. From there, 18 AWG multi-conductor cables will distribute power to the individual FEB cards.

The pFRICH cooling system will consist of several off-detector components and a few on-detector thermal interfaces and assemblies. The primary heat dissipating components will be the ASICs, which are anticipated to produce just over 1 W each (4 W per module), or about 300 W for the 68 total modules. In addition to the ASICs, the sensors are anticipated to dissipate just under 1.5 W each or 100 W total. Conservatively, the total power output will be roughly 400 W. Following the geometry, each row of sensors will have its own pair of titanium cooling tubes directly over the ASICs. The pair of tubes that contact the same row of sensors will be in series, and all rows will be in parallel with each other. The tubes will be attached to aluminum plates with thermal epoxy, and a gap pad between the plate and ASIC will maximize thermal contact. Using a stock tube of 0.25" OD and 0.218" ID and maintaining a minimal temperature gradient in the water allows the mass flow rate to be calculated. From there the Reynolds number and pressure drop can be determined, confirming the viability of the system. Additionally, a finite element analysis (FEA) was performed to confirm the water temperature difference and determine the thermal gradient across the various components. With the described configuration, the sensors reach a maximum temperature of about 32 C in the analysis.

The three primary off-detector elements of the cooling system are a Polyscience chiller, Chilldyne circulator, and a distribution panel. The Polyscience chiller will allow the water to be slightly colder than room temperature, or about 15 C, which is the lowest recommended temperature without nearing the dewpoint in the interaction region. The unit is also capable of flowing about 10 liters per minute (lpm), dissipating about 800 W at that temperature and maintaining the temperature within +/-0.1 C. The Polyscience chiller would be paired with a Chilldyne negative pressure system capable of circulating water at about 8 lpm and ~10 psi. It offers a significant advantage over a positive pressure solution, as if there is a leak in the system, it will draw air into the tube instead of letting water out and potentially damaging electrical components.

The gas system for the pFRICH detector is designed to circulate dry nitrogen at precise pressure and flow rates to remove moisture from within the pFRICH chamber. High-purity nitrogen ( $\text{H}_2\text{O} < 3$  ppm) will be supplied from cryogenic sources. To provide secondary protection, moisture traps such as silica gel dryers will be installed near the nitrogen source. The system will maintain both the required moisture levels and gas purity by ensuring that it is sufficiently gas tight and that the chamber is kept at a slight overpressure (4 mbar) above atmospheric pressure, preventing any infiltration of ambient air. A 0.5  $\mu\text{m}$  filter will be added near the source to capture dust particles. A standby nitrogen source will be available to ensure continuous operation in the event of a primary source failure. To manage fluctuations in the source pressure, a digital pressure outlet controller will be used. Additionally, nitrogen flow will be regulated by a non-pressure-limiting digital mass flow controller. The nitrogen flow rate is expected to allow several complete volume exchanges per hour, with the precise rate to be finalized later.

Pressure inside the chamber will be controlled using a tank blanketing pressure regulator, which maintains a positive internal pressure relative to varying atmospheric conditions. An overpressure protection bubbler will serve as a safeguard against excessive pressure within the chamber. To ensure uniform nitrogen distribution and prevent localized air pockets, nitrogen will be introduced

into the chamber at two locations near the top side of the pFRICH vessel, closer to the aerogel plane, and exhausted through two openings near the sensor plane at the bottom. All exhausted gases will be vented outside the experimental area. The entire gas system will undergo pressure testing at 1.5 times the operating pressure to ensure integrity. For monitoring and troubleshooting, pressure gauges and transmitters will be installed, with critical data such as chamber pressure and flow archived for reference.

**Subsystem mechanics and integration:** The shell that creates the volume of the detector will be made primarily of carbon fiber to optimize the radiation length in ePIC. Specifically, the sensor plane is intended to be made from a bulk carbon fiber layup at approximately 14.7 mm thick at its thickest point. The bulk carbon fiber will be molded and CNC-cut to allow for individual sensor frames and staves to be bonded in-place to create 68 sensor pockets along this plane of the detector. Each individual HRPPD sensor will be added into the sensor plane from the outside of the vessel and sealed in each of the sensor pockets with a face seal. The overall plane will be sealed to the cylinder at the outer and inner walls using a tightly spaced bolt-pattern and an o-ring groove on the upstream end of the sensor plane to accommodate another face seal.

On the upstream end of the vessel, the aerogel plane will be made from a carbon fiber honeycomb layup around 1/4" thick. The outer and inner circumferences of the aerogel plane will house a sealing ring made from bulk carbon fiber and an o-ring groove to create a face seal. Attached to this aerogel plane will be a web of carbon fiber that creates radial rows of pockets for the aerogel to be placed in. These tiles will be held into the pockets using a thin transparent line strung across the opening in order to contain them in place.

The cylindrical portion of the vessel includes identical end rings on the upstream and downstream end that house the threaded bolt holes and sealing surfaces for the sensor plane and aerogel plane face seals. These end rings are approximately 3/4" (on the bolting surface) and 1" in thickness (in the z-direction). They are made from bulk carbon fiber and contain threaded inserts that are placed by CNC-machining the insert locations and bonding and threading them into place. The rest of the cylinder is made from single sheets of carbon fiber on the inside and outside of the vessel, as well as a 3/4" Nomex honeycomb layer in between.

The inner wall of the cylinder is created in a similar manner to the outer wall, namely a honeycomb construction with the end rings embedded into both ends for bolting and sealing to the aerogel and sensor planes. However, the shape of the inner wall is made such that there is 5 mm of clearance (radially) from the beam pipe flange that the pFRICH will need to pass by to be installed in ePIC. This makes the shape of this inner wall similar to an egg or an avocado.

Lastly, the conical mirrors are designed such that they are attached solely to the sensor plane. This is being done to ensure that the mirrors can be controlled in relation to the sensors and will be unaffected by manufacturing misalignments and tolerance stack-up issues throughout the rest of the vessel. As such, they will hang cantilevered perpendicular to the sensor plane for both the inner and outer mirrors. The outer mirrors will be concave and the inner mirrors will be convex. The construction will be a combination of a molded, bulk carbon fiber base with a bonded Lexan sheet on top of it (which will have been coated with a mirror film).

Once the pFRICH has been fully assembled and is ready to be placed in the overall ePIC detector, it will be moved around the assembly hall on a cart. The cart will integrate lifting eyelets for the installation of the pFRICH into ePIC, rails identical to its final location, and wheels to transport, store and work on the detector when it is out of the barrel. This tooling will allow us to lift the cart with the pFRICH secured in place with the crane in the detector hall, position it against the barrel, align the rails, and transfer the pFRICH into its final position by translating it along the z-axis.

**Calibration, alignment and monitoring:** A laser-based system will be used to monitor the pfRICH performance throughout its operational life. The purpose is to monitor, on a pixel-by-pixel basis, the single photon timing resolution, the single photon pulse height amplitude (HRPPD gain), HRPPD QE, and the relative delays between channels on a few ps level. The system will also monitor the reflectivity of the conical and pyramidal mirrors. To measure the timing resolution, an array of six fibers is introduced inside the detector volume from the aerogel side which casts a broad profile of low-intensity light onto the sensor plane such that each HRPPD pixel accumulates some number of single photon hits after a given number of laser pulses. The distance between a given fiber tip and an HRPPD pixel (minimum of 40 cm) defines the flight time for photons emitted from this fiber, hence the distribution of reconstructed flight times will reveal the timing resolution for this single pixel. Similarly, a separate array of six fibers is arranged such that emitted photons reflect off of the outer mirror surface before impinging on the HRPPDs. In this case, the single photon counting rate is monitored for any degradation over time, which would indicate the deterioration of either the photocathode quantum efficiency or mirror reflectivity, or both.

The pfRICH monitoring system deploys a picosecond PiLas laser which produces a 405 nm laser beam with a nominal  $\sim 45$  ps pulse width. The beam is coupled to a custom 1-to-14 optical fiber splitter by Thorlabs, that evenly distributes the light into arrays of fibers routed into the detector vessel. Two additional fibers are connected to silicon photodiodes to provide laser signal quality verification and an initial timestamp ( $t_0$ ). A custom-sized 5 mm  $\times$  5 mm engineered diffuser is used to generate a uniform 50° square pattern to optimize the intensity profile emitted from each fiber. Additionally, a fiber delay line is added to each fiber branch to provide the ability to easily separate out in time photons originating from a given fiber. In all, there are three sets (segments) of fibers downstream of the splitter that deliver photons from the laser to the detector vessel: delay fibers, long extension fibers, and fibers mounted permanently inside the detector vessel. Finally, multiple fast photodiode sensors are used to sample the laser light before and after the splitter to monitor the light output intensity and the timing performance.

A relative alignment of the conical mirror segments inside of the vessel, and surface mapping will be performed on a fully assembled detector (up to the front wall removed) prior to the installation in ePIC, by using a 3D scanning system which is being built now for the purposes of first article mirrors QA assessment. The vessel as a whole will be aligned in ePIC after the installation, following a generic procedure developed by EIC engineers for all detector subsystems. Appropriate survey targets will be mounted on the rear and barrel sides of the vessel if required.

**Status and remaining design effort:** As shown in the previous text, the present pfRICH design fully meets the EIC Yellow Report requirements and subsequent amendments (see performance section):

- Pseudorapidity coverage from -3.5 to -1.5 in the electron-going endcap
- $\pi/K$  separation on a  $3\sigma$  level up to 7 GeV/c in this whole acceptance
- $\sim 20$  ps timing reference for ePIC ToF subsystems in the barrel and the forward endcap by combining single photon signals from aerogel and signals from multi-photon flashes of Cherenkov photons produced by charged particles in HRPPD fused silica windows

R&D effort: The pfRICH design is based mostly on proven technologies, therefore, the remaining R&D effort is fairly small. FY25 R&D activities (partly funded through the eRD110 consortium) will be limited to HRPPD aging studies, which will be performed at JLab and INFN Trieste.

E&D status and outlook: Several engineering design activities and first article productions described earlier in the text in more detail have been performed in FY24, and will continue into FY25:

- Full size mirror production and quality assessment
- First article pFRICH vessel outer shell production
- Adjustments of the production process of CFRP-based parts, mirror substrates and HRPPD pockets in the sensor plane in particular
- Fine tuning of the aerogel refractive index and bulk uniformity measurement procedure
- HRPPD sensor design modifications required after the first batch was produced
- HRPPD performance confirmation in the  $\sim 1.3$  T magnetic field typical for a pFRICH location in ePIC

Other activity needed for the design completion: The readout backplane design cannot be fully completed at this stage because of the unavailability of a final design iteration of the anticipated ASIC chip (EICROC) in either of its low channel count configurations (64, 128 or 256 channels).

The performance of the pFRICH in its anticipated configuration needs to be confirmed in a beam test for both Cherenkov photon imaging and timing in the whole momentum range required for  $e/\pi$ ,  $\pi/K$  and  $K/p$  separation. Such a beam test will be performed with electron and hadron beams at Fermilab in 2026 (contingent on facility availability), with an extensive use of first article components (outer vessel shell, aerogel, mirrors, HRPPDs).

Status of maturity of the subsystem: The design of the pFRICH subsystem is in a fairly mature state. As described in previous sections, the pFRICH consists of a cylindrical vessel with two endcap plates, an aerogel tile plane, an HRPPD sensor plane with onboard electronics, mirrors and a number of subsystems (HV and LV, cooling, gas, light monitoring). Engineering design of all of these components (except for the HRPPD ASIC backplane for the reasons stated above) is by now sufficiently advanced to be more than 60% ready by the CD-2 EIC Project phase at the end of FY26.

#### **Environmental, Safety and Health (ES&H) aspects, Quality Assessment (QA), and Construction and assembly planning:**

The environmental, safety, and health impacts of the pFRICH subsystem are expected to be minimal. When installing and integrating the pFRICH into the overall detector, all applicable safety standards (i.e. OSHA, Critical Lift procedures, etc.) will be followed and adhered to. Furthermore, the composition of the vessel itself consists mainly of carbon fiber, epoxy, and plastic and any (small) excess can be retained for future use or disposed of via standard waste streams. The operation of the detector will require a modest 400 watts of cooling power and the working gas is pure nitrogen which does not pose any greenhouse concerns.

The individual HRPPDs, mirrors, and aerogel tiles used in the pFRICH will all undergo rigorous quality assessment (QA) checks to ensure that their operation and/or properties are within acceptable limits. Beyond the testing done by the manufacturer, the performance of individual HRPPDs will be evaluated using test stands located at BNL, JLab, and possibly Yale University. While the details of the test stands differ, they all consist of a light-tight enclosure to house the HRPPD, a fiber-coupled light source (either a pulsed laser or a monochromator), an optical assembly to focus the light onto the sensor, power supplies, and readout electronics, see Fig. 8.110 (left) as an example.

The gain uniformity, quantum efficiency, photon detection efficiency, and dark count rates will be determined over the entire active photosensor area. In addition, the use of a Menlo Systems Elmo



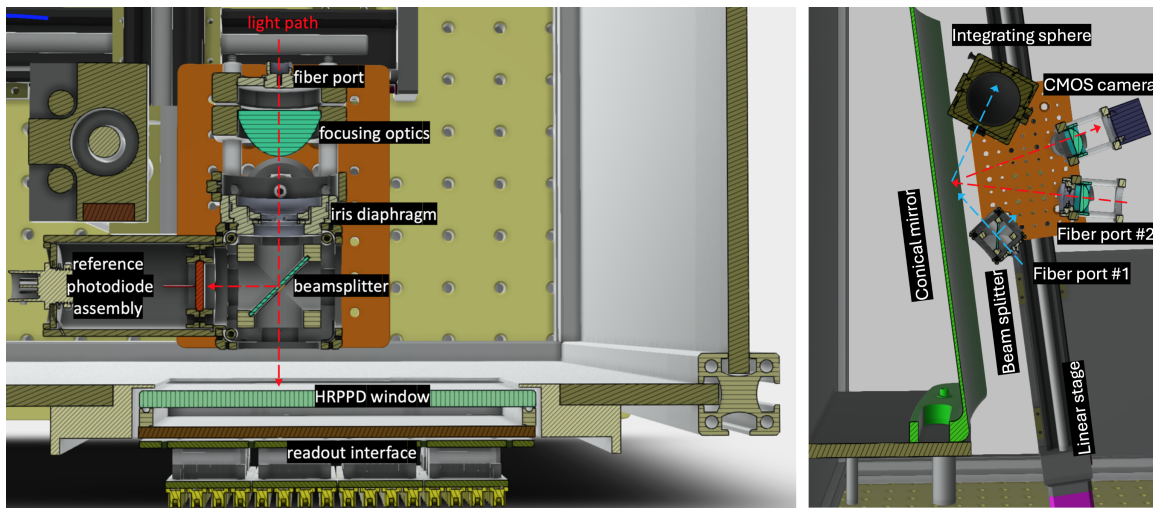


**Figure 8.110:** Left: optical setup of an existing HRPPD QA station at BNL. Right: optical table of the future full size mirror QA station at BNL. See text for more details. ([Figure documentation](#))

780 femtosecond laser at BNL will allow precision determination of the timing characteristics of the sensors.

The reflectivity of the mirror samples produced at SBU will be determined using a dedicated test stand at BNL, see Fig. 8.110 (right). The setup will consist of a large dark box with a mirror sample stand, multi-functional optical table assembly and motion control hardware implemented as a combination of rotary and translation stages.

Blue arrows in Fig. 8.110 (right) show the light path of the reflectivity measurement setup. Light from a halogen/deuterium arc lamp source located outside of the dark box will be fed via fiber with a collimating lens to a beam splitter which directs a fraction of the light to a reference photodiode and passes the remaining beam to the conical mirror sector. Reflected light gets collected in the integrating sphere and then fiber coupled into a compact spectrometer, providing a capability to measure the whole wavelength spectrum of interest at once. The reflectivity will be determined by taking the ratio of the wavelength spectra of the conical mirror under study and a calibrated small flat stock mirror located next to it. Variations in the light source intensity will be corrected using the reference photodiode.

Red arrows show the optical path of a 2D surface mapping setup. A monochromatic light will be directed onto a focusing lens through a single mode fiber with a few micron diameter core. The image of this point-like source after a reflection off the conical mirror surface will be focused onto a CMOS camera sensor. Transverse displacement of this image when the optical head is moving along the mirror surface in azimuthal and lateral directions is a measure of deviation of the mirror surface from an ideal conical shape.

The aerogel quality assessment will be performed at Temple University and include assessments of the refractive index, transparency, uniformity and mechanical specifications. So far, the refractive index has been determined by measuring the deflection of the light passing through the corner of the aerogel tile, following the procedure described in Ref. [80]. Work is currently underway to develop a setup and approach that is based on measuring changes in the polarization between



the light incident on the aerogel and the light that is reflected from its surface. This would allow for localized refractive index measurements to ensure not only the aerogel has the proper mean refractive index, but also its uniformity across the whole tile. Transparency QA will make use of wavelength dependent transmittance measurements carried out using a newly commissioned and validated UV/VIS LED-spectrometer system. The transmittance data will be fitted with the Hunt Formula [81] to extract aerogel properties such as the scattering surface coefficient and clarity, as well as the wavelength dependent properties which include the transmittance, transmission length, and scattering length. The density will be calculated by measuring the aerogel mass using a precision scale (100  $\mu$ g) and volume via caliper and touch probe. Reference jigs can be made to ensure that the aerogel mechanical specifications such as the side-to-side length, tile height, and surface planarity variations are within acceptable ranges.

The structural components of the pfRICH including the cylindrical vessel, end rings, sensor plane and aerogel wall will undergo metrology evaluations during and after construction to ensure all dimensions are within tolerances. The pfRICH has been designed such that it can be fully assembled and inserted into ePIC in one piece. Individual components such as vessel walls, sensor and aerogel planes, mirrors, HRPPDs, and aerogel tiles will be manufactured and tested at various locations and then shipped to BNL for final assembly. It is envisioned that final subsystem assembly will take place in a cleanroom or dedicated lab space within the physics building at BNL. Once assembled, the pfRICH will be transported by truck roughly 1.3 miles to the experimental hall where it will be integrated with the other ePIC subsystems.

The assembly of the pfRICH itself will proceed via the following general steps: (1) assemble the aerogel plane by fastening it to the outer and inner walls, (2) place the sub-assembly such that the upstream end is facing down, (3) add aerogel tiles and aerogel retaining system into the aerogel plane, (4) pre-assemble most of the sensor plane by affixing the inner and outer mirrors and any vessel services (i.e. inner gas tubing, laser monitoring system, etc.) to the sensor plane, (5) lift the sensor plane over the rest of the vessel and lower the sensor plane and mirrors into place, (6) fasten the sensor plane to the subassembly at the inner and outer walls, completing the cylindrical vessel, (7) systematically insert and secure the individual HRPPD modules into the back of the sensor plane, (8) lift the completed pfRICH, rotate it into its operating position, and install it onto the transportation/storage cart.

**Collaborators and their role, resources and workforce:** The pfRICH Detector Subsystem Collaboration (DSC) member institutions, as well as other affiliated groups are listed in Tab. 8.43, along with their anticipated commitments.

**Technological Challenges and Path Forward:** A reliable large area highly pixelated photosensor with a high quantum efficiency and single photon timing resolution better than  $\sim 50$  ps is a core component of the pfRICH design. The pfRICH team, together with the EIC eRD110 consortium (Photosensors) has been routinely working with one of the two manufacturers remaining on the market (Incom Inc.) for several years to help the company re-design their HRPPD sensors so they fully meet EIC specifications. The ongoing evaluation of the first seven EIC HRPPDs produced in 2024 shows that overall quality, as well as reproducibility of parameters verified so far (quantum efficiency in particular) meet the requirements. As a fallback photosensor solution, we consider Photek Auratek MCP-PMTs. Such a PMT has been ordered already, and its performance will be evaluated against the pfRICH detector needs in FY25.

Aerogel tiles of required quality can be produced in a very few places worldwide. The pfRICH team, together with the EIC Project, has been routinely working with the Aerogel Factory in Japan

**Table 8.43:** Institutions contributing to the p<sub>f</sub>RICH effort and their roles and resources. Starred entries indicate no institutional commitment.

Institution	Nation	Activities	Resources for Construction / QA
Brookhaven National Lab	USA	Project Lead  HRPPD and mirror testing  Gas Systems  DAQ Detector and physics simulation	HRPPD test stands (pico/femto-second laser, dark box with translation stages, high-performance scope, waveform digitizers) Mirror test stands (monochromator, spectrometer) Sample temperature control chamber
Chiba University*	Japan	Connection to aerogel factory	Aerogel production equipment
Duke University	USA	Detector modeling	
INFN Genova*	Italy	HRPPD B-field studies	
INFN Trieste*	Italy	Detector modeling  HRPPD aging and B-field studies	HRPPD test stand (laser, dark box, waveform digitizers)
Jefferson Lab*	USA	Mechanical design  EIC Project support HRPPD testing	HRPPD test stand (laser, dark box, translation stages, digitizers)
Ljubljana University & JSI*	Slovenia	Expert input on detector design	
Mississippi State University	USA	Laser monitoring system	
Purdue University	USA	Vessel and mirror fabrication	Machine shop and fabrication lab
Stony Brook University	USA	Vessel fabrication Mirror coating	Mirror coating chamber Vessel form
Temple University	USA	Aerogel testing and QA	Aerogel test stand
University of Debrecen	Hungary	HRPPD backplane design and fabrication	
University of Glasgow	United Kingdom	MCP-PMT evaluation	MCP-PMT test stand (laser, dark box, cosmic ray stand, electronics)
Yale University	USA	Software support  HRPPD QA	HRPPD test stand (dark box with translation stages, digitizers)

over the last two years, to make sure the quality and production capacity meet our requirements. A technical lead of the Chiba Aerogel Factory in Japan is also a member of the p<sub>f</sub>RICH DSC, see Tab. 8.43. Our simulations show, that in case Aerogel Factory cannot produce sufficiently large tiles to cover the whole front wall of the vessel in a configuration with three radial bands as shown in Fig. 8.104, one can resort to using tiles of a readily available size up to 145 mm in a four-band configuration, with an acceptable loss of performance caused by additional dead area introduced by an extra row of radial spacers between the tiles.

### 4099 8.3.4.3 The high performance DIRC

#### 4100 Requirements

4101 **Requirements from physics:** The PID system in the central section of the ePIC detector must  
 4102 provide at least 3 standard deviations of separation of  $\pi/K$  up to 6 GeV/ $c$ , and contribute to low  
 4103 momentum  $e/\pi$  identification.

4104 **Requirements from Radiation Hardness:** The anticipated radiation dose in the hpDIRC op-  
 4105 tics and its potentially sensitive readout electronics are predicted to be modest. These estimates  
 4106 are based on minimum-bias  $10 \times 275$  GeV e+p events from PYTHIA. The maximum machine lumi-  
 4107 nosity over a six-month period of annual operation at 100% machine and detector efficiency for a  
 4108 total of 10 years was assumed. Under these conditions, the total dose from electromagnetic and  
 4109 hadronic radiation is expected to be less than 100 rad. The 1-MeV-neutron-equivalent fluence is  
 4110 expected to reach  $10^{10}$  neutrons per  $cm^2$ .

4111 **Requirements from Data Rates:** The expected hit rate of 25 kHz per  $cm^2$  for the hpDIRC  
 4112 was estimated using detailed Geant4 simulations, incorporating the Pythia event generator. This  
 4113 estimation assumes the baseline MCP-PMT sensors, which typically have a dark count rate of ap-  
 4114 proximately 1 kHz per  $cm^2$ , or 0.09 kHz per pixel.

#### 4115 Justification

4116 **Device concept and technological choice:** A radially compact detector based on the DIRC  
 4117 (Detection of Internally Reflected Cherenkov light) principle, a specialized type of RICH counter,  
 4118 is appropriate. It employs solid, long, rectangular-shaped radiators made of synthetic fused silica,  
 4119 which also serve to guide the Cherenkov photons to outside the central region for readout. This  
 4120 design allows the active radiator section to remain radially compact, minimizing its impact on the  
 4121 performance of neighboring systems and simplifying the system integration.

4122 The photons are recorded by an array of pixelated photon sensors mounted on the back of the  
 4123 expansion volume. As a result of the excellent optical finish of the optical components, the emission  
 4124 angle of Cherenkov photons with respect to the particle track is maintained during the photon  
 4125 transport via the total internal reflection. This angle can be reconstructed for each track from the  
 4126 measured position of the photon on the detector surface and the measured arrival time of each  
 4127 photon.

4128 The general concept of a barrel DIRC detector was first successfully demonstrated by the BaBar  
 4129 DIRC and followed by several other experiments worldwide. The ePIC high-performance DIRC  
 4130 (hpDIRC) takes advantage of the lens-based focusing concept of the PANDA Barrel DIRC, and has  
 4131 also several other advancements to meet the performance requirements of the Electron-Ion Collider  
 4132 (EIC). The hpDIRC concept for ePIC was developed as part of the EIC generic R&D program per-  
 4133 formed by the EIC PID collaboration (eRD14) and direct EIC Project R&D eRD103 with the focus  
 4134 on extending the momentum coverage well beyond the DIRC counter state-of-the-art at that time.

#### 4135 Subsystem description:

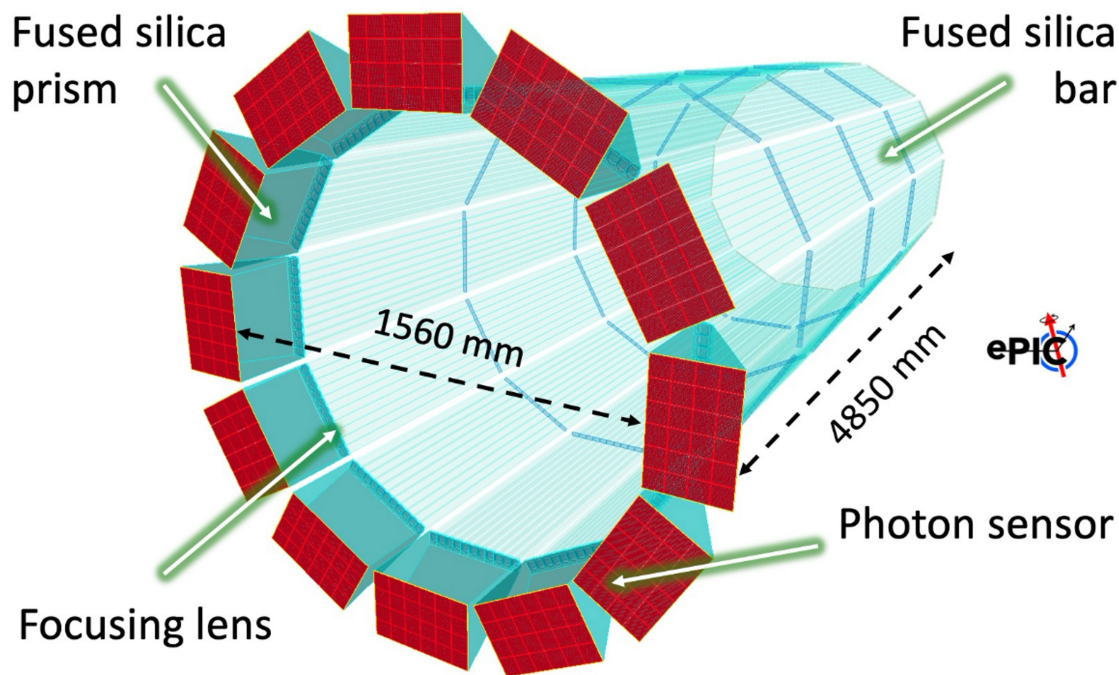


**Figure 8.111:** ePIC hpDIRC geometry in the Geant4 standalone simulation.

#### General device description:

The baseline design of the ePIC hpDIRC detector, as implemented in a detailed and test beam-validated Geant4 simulation, is shown in Fig. 8.111. It is divided into twelve optically isolated sectors, each composed of a bar box and a readout box. These 12 sectors surround the beamline in a 12-sided polygonal barrel with an inner radius of about 760 cm. Each bar box includes ten radiator bars, each made of synthetic fused silica and with a length of 4850 mm and a cross-section of 17 mm  $\times$  35 mm. The bars are placed side-by-side, separated by small air gaps, inside the light-tight bar box. Mirrors are attached to one end of each bar to reflect the Cherenkov photons towards the other (readout) end. At the readout end they exit the bar and are focused by a 3-layer spherical lens on the back surface of the prism which serves as an expansion volume.

#### Bars:

The baseline ePIC hpDIRC design envisions that the 120 long bars needed will be composed of three refurbished BaBar DIRC bars and one shorter new bar manufactured by industry. The number of bar boxes and bars per box has been optimized to the width of the BaBar DIRC bars while maximizing the azimuthal acceptance of the hpDIRC. This approach assumes that the BaBar bars can be safely extracted from the Babar boxes without compromising their optical and mechanical integrity. The disassembly and evaluation of the BaBar bar boxes are currently underway. Final information on the availability of BaBar bars for ePIC is expected by 2026.

#### Lenses:

The 3-layer spherical focusing lens is a novel component of the hpDIRC and is essential for achieving the PID performance ePIC requires. The lens design, shown in Fig. 8.112, avoids the dramatic photon loss caused by air gap transitions in standard lens systems. It does

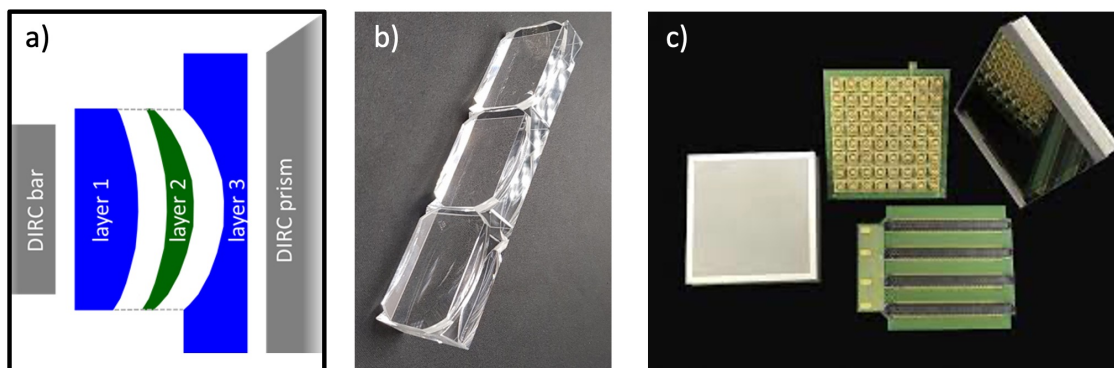


**Figure 8.112:** a) Schematic of the side view of one hpDIRC section and an exploded view of the 3-layer lens. b) Photo of prototypes of the 3-layer spherical lenses. c) Photec AuraTek MAPMT253 MCP-PMT.

this by focusing Cherenkov light through refraction at the interface between synthetic fused silica and a high-refractive-index material, such as sapphire or lanthanum crown glass. A thin layer of the high-refractive-index material is sandwiched between two layers of synthetic fused silica, with carefully optimized radii of curvature on all spherical surfaces. This design combines defocussing and focusing transitions to form a flat detector plane that accommodates a wide range of photon angles, matching the layout of the sensor array on the expansion volume prism. Several prototypes using different materials for the middle layer have been produced by the optical industry, and an example of a prototype lens is shown in Fig. 8.112b.

#### Prisms:

The prism expansion volume is made of synthetic fused silica, has a  $32^\circ$  opening angle, and dimensions of  $237 \text{ mm} \times 350 \text{ mm} \times 300 \text{ mm}$ . The detector plane of each prism is covered by an array of 24 sensors shown in red in Fig. 8.111.

#### Sensors:

The photosensors attached to the rear of the prism record the positions and arrival times of the Cherenkov photons. In the baseline design of the hpDIRC, commercial microchannel-plate photomultiplier tubes (MCP-PMTs) with a pore size of  $10 \text{ }\mu\text{m}$  or smaller were assumed. A pixel size of  $3.2 \text{ mm}$  was chosen based on Geant4 simulations as a balance between cost, performance, and expected availability as the sensor technology for the hpDIRC. Lifetime-enhanced 2" MCP-PMT tubes are commercially available from Photonis and Photek with suitable DC-coupled anode configurations. The simulation utilized Photonis Planacon XP85122 MCP-PMTs, incorporating realistic sensor characteristics including photon timing, collection efficiency, and quantum efficiency. With the termination of the production of the Photonis PMTs, the Photek MAPMT 253 sensors shown in Fig. 8.112, have been adopted as the baseline photosensor for the hpDIRC. These sensors share the same mechanical footprint and are expected to exhibit comparable performance characteristics to the Photonis tubes. High Rate Picosecond Photon Detectors (HRPPDs), currently under development by Incom, are the baseline sensor for the pFRICH detector in ePIC and are also being considered as an alternative option for the hpDIRC. Adopting a common sensor for both systems would offer significant advantages in terms of cost efficiency and streamlined integration efforts. To support an informed decision, several experimental setups are being used to conduct direct, side-by-side performance comparisons of the two sensor options, with the goal of selecting



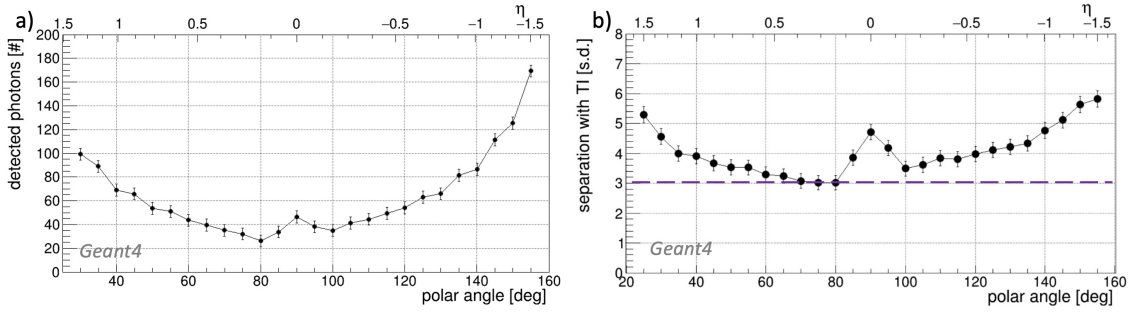


**Figure 8.113:** The expected performance of the hpDIRC as a function of the particle polar angle in terms of photon yield (a) for pions and  $\pi/K$  separation power (b). These results are based on a standalone Geant4 simulation of 6 GeV/c particles.

a unified solution for both subsystems within ePIC. More details on the HRPPD option can be found in pFRICH section 8.3.4.2.

FEE: Fast ASIC-based readout systems are being developed by the EIC project to meet the demands of various ePIC detector systems. For the hpDIRC, the readout electronics must be capable of detecting small signals (on the order of a few millivolts) from MCP-PMTs while maintaining excellent single-photon timing resolution. Additionally, the electronics need to match the channel density and sensor footprint, as they will be directly coupled to the back of the sensor to minimize distance and achieve optimal timing precision. The leading candidate for hpDIRC readout is FCFD, which is discussed in detail in Section XXX.

**Performance** Figure 8.113 presents the expected performance based on standalone Geant4 simulation studies with a tracking angular precision of 0.5 mrad at 6 GeV/c. The plots illustrate particles that are fired over a range of polar angles but with an azimuthal angle fixed at zero degrees (so perpendicular to one of the middle bars). The points represent the photon yield and separation power for 6 GeV/c charged pions and kaons as a function of polar angle with the realistic ePIC magnetic field.

The number of detected Cherenkov photons per particle (Fig. 8.113a) ranges from 40 to 150, depending on the polar angle. The sharp increase in photon yield at steeper forward and backward angles is due to the longer track lengths in the fused silica bars, with an asymmetry in forward/backward yields resulting from photon loss due to longer propagation paths at smaller polar angles. The peak in the photon yield near a polar angle of 90° occurs because a larger fraction of the photons satisfy the total internal reflection criterion near perpendicular incidence, compared to slightly larger or smaller angles.

The “separation power” for both particle hypotheses (Fig. 8.113b) is obtained from Gaussian fits to the log-likelihood differences between pairs of particle hypotheses. It is calculated as the difference between the means of the two Gaussians divided by the arithmetic average of the two widths. The slightly improved performance for polar angles above 100° is due to shorter photon paths, resulting in higher photon yields and reduced chromatic dispersion in the bar material.

Similar studies were conducted for electron-pion ( $e/\pi$ ) separation, which is primarily the responsibility of the Electromagnetic Calorimeter. However, the hpDIRC can further improve the performance at low momentum. At lower momenta, multiple scattering is severe, but assuming ePIC achieves the tracking resolution described in the Yellow Report, the hpDIRC can provide a 3 standard-deviation separation power up to 1.1 GeV/c.

The expected particle identification (PID) performance of the hpDIRC thus surpasses the ePIC PID goal, achieving more than 3 standard deviations of separation power for  $e/\pi$  identification up to 1.1 GeV/c and  $\pi/K$  separation up to 6 GeV/c across the entire polar angle range.

**Performance Systematic Studies** Most of the hpDIRC performance studies were conducted using a particle gun, providing precise control over the parameters under investigation while covering the entire required angular and momentum ranges. Detailed studies examined a range of azimuthal angles to measure the performance across the full width of the bar box. While a moderate performance deterioration was observed in some of the non-central bars, the system maintained the required 3-standard-deviation separation power. The effect of the magnetic field on hpDIRC performance was found to be negligible, as confirmed through simulations that incorporated a realistic ePIC magnetic field map.

Additionally, studies using PYTHIA-generated physics events were performed to assess the frequency and effect of multiple tracks per event within an hpDIRC module and with one bar. Even in the extremely rare cases where two or more particles are very close in momentum, polar, and azimuthal angles within a single event, the impact on performance was found to be moderate, demonstrating the robustness of the hpDIRC system.

**Simulation tools and validation** A detailed standalone Geant4 simulation, featuring realistic geometry and material properties, was developed in collaboration with the PANDA Barrel DIRC group and validated through modular prototype tests using particle beams at CERN. The simulation incorporates measured values for MCP-PMT quantum efficiency, collection efficiency, and timing resolution. It also accounts for the coefficient of total internal reflection of the DIRC radiator bars as a function of photon energy, the bulk transmission of the bars, glue, and lenses, as well as the wavelength-dependent refractive indices of the materials used, the photocathode, and the reflectivity of the mirrors. Background contributions from hadronic interactions and delta electrons in the bar, along with effects from MCP-PMT dark noise and charge sharing between anode pads, were also simulated.

All relevant resolution factors for hpDIRC performance are modeled using Gaussian smearing with conservative resolution assumptions. The total timing precision per photon, including sensor and readout electronics, is assumed to be 100 ps, and the angular resolution of the ePIC tracking system at the hpDIRC radius is assumed to be 0.5 mrad for particles with a momentum of 6 GeV/c for all studies. However, the simulation software is prepared to import and integrate a more detailed tracking parametrization when it becomes available.

Detailed hpDIRC PID Look-Up-Tables (LUTs), including the threshold mode, were generated using Geant4 simulations. These LUTs are now employed to streamline physics analyses without the need for full reconstruction.

Figure 8.114 presents photos of the modular PANDA Barrel DIRC prototype along with results obtained during the 2018 test beam campaign at CERN. Although the PANDA prototype differs significantly from the ePIC hpDIRC in terms of geometry (single bar), slower readout electronics, and lower-quality sensors with larger pixels, the studies and results are highly valuable for hpDIRC development. The same software used for all ePIC hpDIRC performance studies was employed to successfully reproduce the PANDA prototype test beam results. As shown in Fig. 8.114c and d, the agreement between the simulation and experimental data is excellent. Note that the same-size BaBar DIRC bar and the same 3-layer spherical lens prototypes were used as in ePIC.



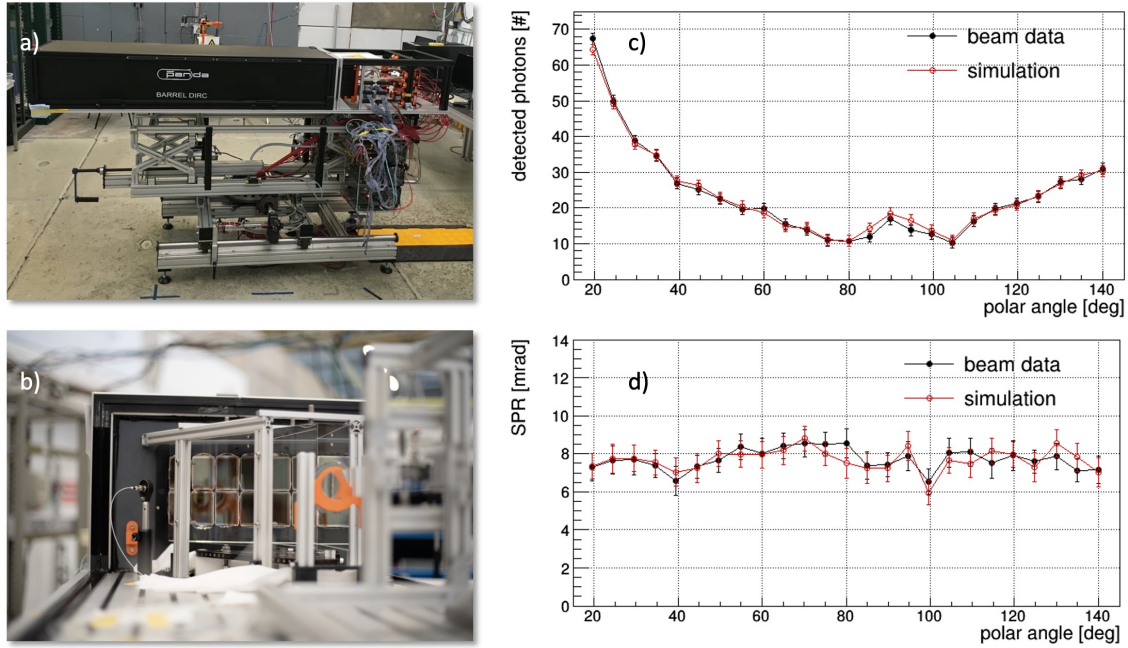


**Figure 8.114:** Photographs of the PANDA Barrel DIRC prototype (a), including a close-up of the readout section (b) taken during the CERN test beam. Performance plots illustrating the comparison between simulated and experimental data for photon yield (c) and single photon Cherenkov angle resolution (SPR) (d).

**Reconstruction methods** The hpDIRC utilizes two primary reconstruction methods for identifying particles based on Cherenkov photon detection: geometric reconstruction and time-based imaging reconstruction. These methods translate the detected photon patterns into meaningful physical information, particularly the Cherenkov angle, which allows direct particle identification.

Geometric reconstruction in DIRC detectors is based on determining the Cherenkov photon direction from the relative location of the radiator readout end and the pixel hit by the photon. This method allows direct reconstruction of the Cherenkov angle for each detected photon by utilizing both the photon direction and the beam particle direction. Photon directions in the prism are pre-calculated using full simulations, taking into account the optical materials, and stored in look-up tables (LUT). Discrete ambiguities arise due to photon reflections within the optical system, but these can be reduced by applying a cut on the difference between the expected and measured photon arrival times. The geometric method relies on the photon position, and only uses timing information to suppress ambiguities and background. The geometrical method also provides key performance variables such as the single-photon Cherenkov angle resolution, and the number of signal and background photons.

The time-based imaging reconstruction method greatly enhances the particle identification (PID) by fully utilizing both the timing and position information of the detected photons. This method compares the measured photon arrival times to expected distributions for each particle hypothesis, stored as probability density functions (PDFs) derived from experimental or simulated data. For each photon, a time-based likelihood is calculated, which is then combined with the Poissonian PDF of the number of detected photons to provide the likelihood.

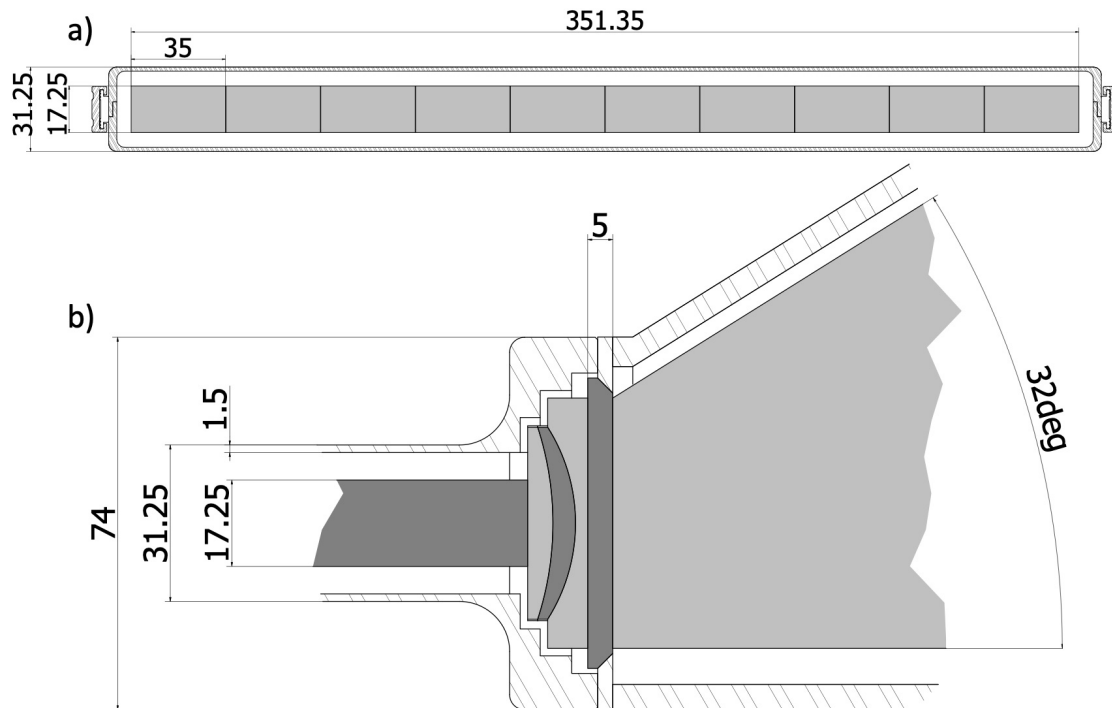


**Figure 8.115:** Technical drawings of the ePIC hpDIRC detector, showing the XY cross-section of the bar box (a) and the YZ cross-section of the connection between the bar box and the readout box (b).

## Implementation

**Subsystem mechanics and integration:** The hpDIRC consists of two primary sub-assemblies: the readout section and the bar section. Both sections are composed of 12 boxes made of carbon fiber reinforced polymer (CFRP), with varying thickness depending on the stresses expected in different regions.

The readout section includes the fused silica expansion prism, readout sensors, and front-end electronics. The expansion prism has an angle of  $32^\circ$  and maximum dimensions of 300 mm in length, 352 mm in width, and 237.5 mm in thickness. The MCP-PMTs are coupled to the 352 mm x 237.5 mm back face of the prism using silicone cookies. The sensors and associated readout electronics are mounted onto a 3D-printed frame. The rear of the readout box is sealed with a light-tight plate with ports for cables, fibers for calibration lasers, and monitoring cameras. Dry nitrogen gas is flowed through the readout box to keep the prism surface clean and free from dust and condensation. To maintain stable temperatures and cool the electronics, water circulates through tubing thermally coupled to the heat sources.

The bar box is composed of a top and bottom shell with overall dimensions of 4627 mm in length, 368 mm in width, and 31.25 mm in height. Figure 8.115a shows a dimensioned view of the XY cross-section of the hpDIRC bar box. The thicker part of the carbon fiber shell on the sides will be used during installation to slide in the bar box and hold it in place. The carbon fiber thickness is 1.5 mm except for the 3 mm sides.

Each bar box contains 10 long radiator bars, lenses, and mirrors. The radiator bars are 35 mm wide, 17.25 mm thick, and 4580 mm long, spaced 0.15 mm apart using shims to ensure optical isolation. Each long radiator bar is made up of four shorter bars bonded together with an optically transparent adhesive, similar to the BaBar DIRC construction. Three of the shorter bars, each 1225 mm long, are repurposed from the BaBar experiment, while the fourth is newly manufactured to meet the ePIC total length requirement of 893 mm. The length of the light-guide can be adjusted, based on integration constraints with no impact on the hpDIRC performance.

At one end of each long bar, a 3 mm-thick flat mirror reflects photons back toward the readout end. At the opposite end, a three-layer lens is attached to the bar using the same adhesive used to join the short bars. The lens-mirror-bar joints are kept in compression by adjustable spring plungers located behind the mirrors, which reduce stress on the joints and prevent movement during installation, and operation. The spring system also compensates for differential thermal expansion and contraction rates between the bars and the bar box. Each short bar is supported by two pairs of fixed nylon buttons along its length, which minimize stress on the glue joints and reduce photon loss by reducing contact with the radiator surface. Eight support pairs are evenly distributed along each long bar's length, with adjustable spring buttons pressing the bars against the fixed buttons to maintain secure positioning while preserving the optical isolation. Similar support mechanisms are used for the 17.25 mm-thick end of the bars, where all 10 bars are pressed against a single set of fixed buttons. To handle the additional stress at the button locations and accommodate holes for the spring buttons, the CFRP is locally thickened at these points. Like the readout boxes, the bar boxes are also flushed with dry nitrogen to protect the radiator bars surfaces with nitrogen introduced at the mirror end and vented near the lenses.

The hpDIRC consists of 12 bar boxes and 12 readout boxes. The lenses at the bar box end are coupled to a thin window that seals the box, while this window is in turn connected to the prism in the readout box using an silicone cookies during final installation. The readout box, including the prism, is compressed against the bar box window to form a tight optical seal. Figure 8.115b is a dimensioned view of the XZ cross-section of the connection between the bar box and the readout box. The 5 mm-thick window between the 3-layer lens and the prism represents an initial design, which may be adjusted following further studies of strains and forces acting on the system.

The hpDIRC is positioned radially just inside the Barrel Electromagnetic Calorimeter (BIC) and just outside the outer Micro-Pattern Gas Detector (MPGD) within the ePIC detector. Both the bar boxes and the MPGD are supported by the EM Calorimeter via rails mounted on triangular brackets extending radially inward from the calorimeter's inner surface.

**Installation:** During installation, the bar boxes are placed on a specialized lifting fixture, allowing them to be rotated into their final orientation before being transferred along rails into their designated positions. The readout boxes are supported by an external ring attached to the Hadron Calorimeter via a series of legs. Each readout box is aligned with its corresponding bar box using specialized brackets and rails, which allow the readout box to be slid into position, compressing the optical interface and forming the connection. This rail system also enables the readout boxes to be removed without disturbing the bar boxes, if necessary.

**Services:** Gas and Moisture Control: To maintain a low-moisture environment for the bars, dry nitrogen gas from liquid nitrogen boil-off will flow through each box. The nitrogen gas will be monitored for humidity and filtered through a molecular sieve and mechanical filters to remove particulates.

Power Supply and Monitoring: High-voltage supplies will be provided for each MCP-PMT sensor.

A control and monitoring system will be implemented for the readout and bar box sections. The high voltage required for each MCP-PMT will be supplied by commercially available multichannel power supply modules in crates located outside the experiment.

The low-voltage power supplies, which regulate power to the front-end electronics (FEE), need to be placed as close as possible to the detector, in racks dedicated to the hpDIRC system. A modular, multichannel approach—similar to the high-voltage system, is planned for the control and monitoring of voltages, currents, and onboard temperatures for all FEE boards. The low voltage levels will be below 50 V, with currents reaching several Amperes.

**Cooling System:** The highly integrated FEE design generates a significant amount of heat in the compact readout unit. This heat will be extracted by a water cooling system, and the necessary supply lines are included in the mechanical design of the readout boxes, although further optimization is required.

**Environmental Monitoring:** Standard commercial devices will monitor environmental parameters such as temperature and humidity at various locations inside the hpDIRC volume to ensure optimal performance and safety.

**Calibration, alignment and monitoring:** **Time Calibration:** To achieve the time resolution required for the hpDIRC, it is essential to eliminate time offsets between pixels, which may arise from differences in cable lengths and pixel-to-pixel variations within the photon sensors. A laser monitoring system will be employed to provide channel-by-channel time-zero information, which will be stored in a database. This data will be used to accurately calibrate the photon arrival times for all pixels.

**Optical Calibration and Alignment:** The exact positioning of the optical components will be determined during the hpDIRC DIRC installation, using a laser and precise survey marks. The reconstruction of the Cherenkov angle, based on the hit pattern on the MCP-PMT array, depends on the accurate relative positions and orientations of all optical elements, including the photon sensors and their individual pixels.

**In-Beam Calibration and Alignment:** After installation in the ePIC detector, the alignment of the hpDIRC will be verified using beam data. Samples of muons, pions, kaons, and protons identified by other ePIC sub-detectors or through kinematic fitting will be used to calibrate the hpDIRC measured Cherenkov angles.

Geometric reconstruction will then be used to calculate the Cherenkov angle per photon for each track and sensor pixel. Any deviation between the measured and expected Cherenkov angles in the calibration samples will be utilized to develop a correction function or multi-dimensional lookup table. This information will be stored in the configuration database to correct for residual misalignment and optimize the performance. A similar procedure was successfully employed in the BaBar DIRC, where a 10% improvement in Cherenkov angle resolution was achieved by applying per-photon corrections based on a dedicated particle calibration sample.

**Status and remaining design effort:** Preparations for the hpDIRC are progressing in line with the overall project schedule. In the chart shown in Figure 8.116, the top lines highlight the major milestones of the project from the present day to the start of the experiment and CD-4 approval. Below these milestones is a detailed breakdown of key work packages, including the optical components, readout system, and mechanical design. The hpDIRC is expected to be fully ready in advance of the installation deadline, with a substantial time contingency built into the schedule.

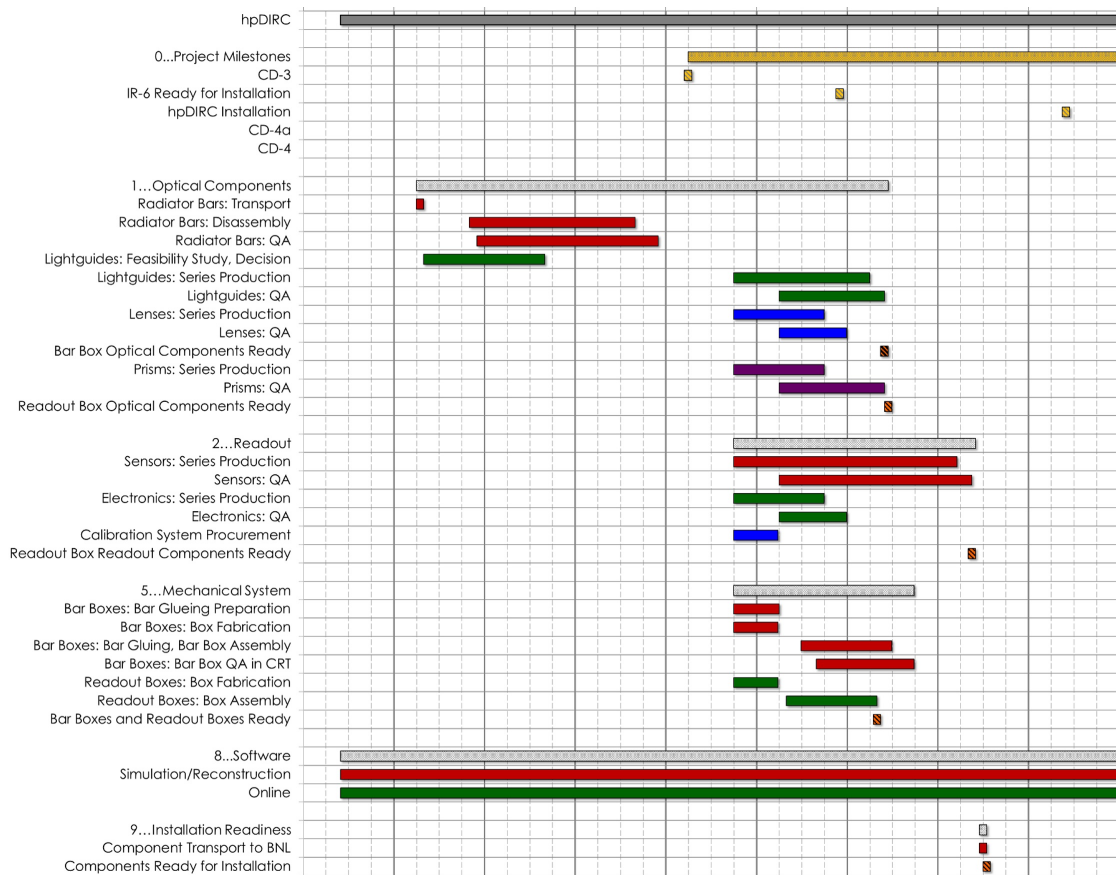


**Figure 8.116:** ePIC hpDIRC schedule chart alignment with EIC Project schedule

**Remaining R&D effort:** The primary objectives of the remaining hpDIRC R&D are to validate new components, ensure their successful integration into the hpDIRC system, and to optimize the final design. Ultimately, the goal is to achieve a validated, cost-efficient hpDIRC design for the ePIC detector, which will be demonstrated in the Cosmic Ray Telescope (CRT) setup. Several critical aspects of the hpDIRC design still require thorough study and verification to guarantee the necessary performance, mitigate risks, and explore new opportunities.

Ongoing R&D projects with a direct impact on the hpDIRC include eRD109 (focused on readout and ASIC designs) and eRD110 (focused on photosensors). The development of compact readout electronics for fast single-photon detection, using high-density sensors, must be completed and integrated into the hpDIRC prototype to validate the performance of a cost-optimized design for particle identification (PID).

The reuse of BaBar DIRC bars, another key cost-saving measure, is currently being explored with support from Jefferson Lab and the EIC Project, as discussed above.

**Environmental, Safety and Health (ES&H) aspects** The hpDIRC system is designed to operate without the use of any flammable gases or cryogenic liquids, which eliminates the risks associated with these hazardous substances. Both the bar boxes and readout boxes will be purged using boil-off dry nitrogen, which will flow at a rate of a few liters per hour per box. This method ensures





**Figure 8.117:** Photos of available setups developed during the hpDIRC R&D program that will be used for future QA of 3-layer lenses with laser setup at ODU (a), bars and other optics at Jefferson Lab (b) and readout chain including sensors and electronics and other hpDIRC components in hpDIRC prototype at CRT at SBU (c).

that the environment inside the boxes remains dry and free from contaminants, contributing to the system's safety and reliability.

In terms of electrical hazards, the sensors employed in the hpDIRC require high voltages, reaching up to 3 kV. To prevent the risk of electrical shock, the high-voltage (HV) connections will be inaccessible during normal operation. Furthermore, the HV module will be keyed off, and only trained personnel will be allowed to operate it, providing an additional layer of safety in the system's design.

The hpDIRC will also utilize a class 3B laser pulser for the calibration of sensors and electronics. Since lasers pose a radiation hazard, special precautions will be taken: the laser will be fully enclosed within optical fibers to prevent exposure, and only trained personnel will be authorized to operate the laser.

For the cooling of the readout electronics, a chilled liquid will be used, though the specific details of the liquid have yet to be determined. To avoid the risk of a chemical leak, the chilled water will circulate at sub-atmospheric pressure, which helps prevent potential leaks.

The entire hpDIRC system will comply with all applicable Environment, Safety, and Data (ES&D) standards and Occupational Safety and Health Administration (OSHA) regulations. This commitment to compliance ensures that the system adheres to the highest safety protocols, protecting both the equipment and the personnel involved in its operation.

**Quality Assurance Plan** The quality assurance (QA) plans for the hpDIRC components and modules prior to construction are centered around a combination of process control at the vendor sites and extensive in-laboratory measurements. The radiator bars and light guides will undergo

4433 vendor-provided QA to assess their mechanical properties.

4434 For newly built radiator bars and light guides, the initial QA tests will be performed by the vendors  
4435 and certificates of compliance and QA data provided. The fabrication QA data for the refurbished  
4436 BaBar DIRC bars is available.

4437 For the sensors and electronics testing, laser pulser systems will be deployed at CUA, JLab, or  
4438 USC (to be determined) to perform measurements including gain, quantum efficiency, collection  
4439 efficiency, timing precision, and dark count rate. These tests will verify the operational integrity  
4440 and performance of the sensors.

4441 The lenses will be evaluated at the laser laboratory at ODU, where the shape of the focal plane will  
4442 be analyzed to ensure proper optical alignment and focusing. Prisms will be subjected to vendor-  
4443 provided QA, followed by further checks at WSU to confirm their specifications. Similarly, the bar  
4444 boxes and prism boxes will undergo QA at the vendor sites, with additional testing and validation  
4445 at SBU, prior to the module assembly.

4446 Once the DIRC modules are fully assembled, including the coupling of the bar box to the readout  
4447 box (a vertical slice), the Cosmic Ray Telescope at SBU will be used for testing. This will ensure that  
4448 the assembled DIRC modules function as intended before final integration.

4449 After installation of the DIRC module in ePIC, a picosecond laser pulser calibration system will  
4450 be employed to fine-tune the system. Cameras will also be used to continuously monitor the op-  
4451 tical coupling between the sensors, prisms, and lenses, ensuring that the entire optical system is  
4452 correctly aligned and operational throughout the experiment.

4453 **Construction and assembly planning:** In the current plan for the ePIC hpDIRC construction,  
4454 the assembly will take place at three different locations. The bar boxes will be assembled at Jef-  
4455 ferson Lab, utilizing the existing infrastructure developed for the disassembly of the BaBar bar  
4456 boxes and the quality assurance of the bars. Short bars will be glued together to form ten long  
4457 bars per bar box, with 3-layer lenses attached, and will then be mounted inside their carbon fiber  
4458 shells. The readout boxes, along with the associated sensors and electronics, are first evaluated at  
4459 multiple sites: the University of South Carolina (USC) characterizes the sensors and matches them  
4460 with validated readout electronics before sending the paired sets to Brookhaven National Labora-  
4461 tory (BNL); Wayne State University (WSU) assesses the mechanical and optical properties of the  
4462 newly acquired expansion volume prisms and ships them to BNL; and the carbon fiber reinforced  
4463 polymer (CFRP) vendor inspects both the bar boxes and readout box structures before delivering  
4464 them to Purdue University or Jefferson Lab (JLab). Final assembly of the readout box, including  
4465 integration of the sensors and electronics, is performed at BNL. The completed readout boxes are  
4466 then temporarily integrated with the corresponding bar boxes to verify light-tightness and ensure  
4467 proper mechanical alignment prior to final installation.

4468 **Collaborators and their role, resources, and workforce:** The hpDIRC system collaboration  
4469 (DSC) consists of a core group of institutions that have long-standing experience with DIRC coun-  
4470 ters, having contributed to the BaBar, GlueX, PANDA projects, and the EIC DIRC R&D program.  
4471 Many of these groups have been involved in these efforts since 2011, bringing a wealth of exper-  
4472 tise to the development of the hpDIRC system for the ePIC detector. This collaborative network is  
4473 expected to expand, with a few expressions of interest (EoIs) from various institutions interested  
4474 in contributing to different aspects of the project closer towards construction. The process of align-  
4475 ing expertise and interest with system priorities is already underway, ensuring that the work is  
4476 distributed efficiently.



4477 Among the key collaborators, Jefferson Lab together with CUA have been handling the transport  
4478 and disassembly of BaBar DIRC bar boxes and validation the quality of the disassembled bars.  
4479 Future contributions are expected to include the QA of new bars for the light guide section as well  
4480 as the gluing of the bars and lenses and the assembly of the bar boxes.

4481 Stony Brook University (SBU) is preparing an important QA tool with their Cosmic Ray Telescope.  
4482 The initial plan is to use it for incremental integration of new components into the hpDIRC pro-  
4483 totype like disassembled BaBar bars, sensors, and electronics, but eventually, it will be used for  
4484 validation of completed bar box modules. Old Dominion University (ODU) will contribute by  
4485 evaluating the focal plane of the lenses and conducting QA procedures, ensuring the optical com-  
4486 ponents meet the required standards.

4487 On the sensor side, USC will handle QA and tests related to the readout chain, ensuring the sensors  
4488 operate within specified parameters. Wayne State University (WSU) will oversee the assembly  
4489 and QA of the readout boxes, another critical component of the system. Finally, institutions like  
4490 CUA, GSI, William & Mary, and WSU are heavily involved in simulation and reconstruction efforts,  
4491 which are essential for optimizing the performance and integration of the hpDIRC system into the  
4492 overall ePIC detector framework.

4493 This broad collaboration, with specific responsibilities assigned to various expert groups, ensures  
4494 that all components of the hpDIRC system are developed and tested by specialists, assuming more  
4495 junior workforce, like graduate students and postdoctoral researchers, can be added through exter-  
4496 nal grants.

4497 **Risks and mitigation strategy:** The disassembly procedure has been validated and is progress-  
4498 ing successfully. The first bar box has been disassembled, with the short bars extracted, cleaned,  
4499 and subjected to inspection. Preliminary measurements conducted in the laser QA laboratory con-  
4500 firm that these bars meet the performance criteria for use in ePIC. The optical quality of the remain-  
4501 ing bars will be assessed following the disassembly of the remaining bar boxes. If the fabrication  
4502 of new radiator bars or light guides is required, a vendor will need to be identified, and the pro-  
4503 curement and production process initiated. Based on the current production timeline for PANDA  
4504 Barrel DIRC radiator bars, the production of new bars for ePIC is still possible within the project  
4505 schedule.

4506 Both the baseline commercial MCP-PMTs and HRPPDs require testing and evaluation, which are  
4507 being prepared by different groups. These tests will be conducted in parallel to ensure the necessary  
4508 sensors are available within the required time before installation. The development of ASIC-based  
4509 readout electronics is being coordinated by the EIC project.

4510 **Additional Material** Add text here.

#### 8.3.4.4 The dual radiator RICH

**Requirements** The dual radiator Ring Imaging Cherenkov (dRICH) detector is part of the particle identification system in the forward (ion-side) end-cap of the ePIC detector and complements the forward time-of-flight system and calorimetry, see Figure 8.84. The dRICH has to provide acceptance in the pseudo-rapidity range defined by the ePIC beam pipe and the barrel detector and to operate within the limited envelope allowed by the rest of the compact and hermetic ePIC detector. Distinctive features of the detector are: use of aerogel and gas radiators to extend the covered momentum range, usage of silicon photomultiplier (SiPM) to ensure single photon detection capability in high and not-uniform magnetic field, non-conventional optics with curved active surfaces and compact readout electronics to fit into ePIC.

**Requirements from physics:** The dRICH is required to provide continuous hadron identification from  $\sim 3$  GeV/c to  $\sim 50$  GeV/c, and to supplement electron and positron identification from a few hundred MeV/c up to about 15 GeV/c. Such an extended momentum range imposes the use of two radiators, gas and aerogel, with a common imaging system to ensure compactness and cost-effectiveness. The radiator gas must ensure  $\pi/K$  separation at  $3\text{-}\sigma$  level up to 50 GeV/c in the most forward region, namely for  $\eta > 2$ . The aerogel radiator must cover the intermediate momentum interval, bridging the upper limit of the time-of-flight ( $\approx 2.5$  GeV/c) to the Cherenkov threshold of the dRICH gas ( $\approx 12$  GeV/c). The dRICH has to provide open acceptance in the ePIC forward pseudo-rapidity range  $1.5 \lesssim \eta \lesssim 3.5$ . To provide proper light focalization within the due volume, the dRICH active area is located behind the shadow of the barrel detector and its support ring, close to the MARCO solenoid coils. In this region, see Figure 8.85, the up to 0.6T not-uniform ePIC magnetic field imposes the use of unprecedented detectors (SiPM).

**Requirements from Radiation Hardness:** The radiation sensitive components (sensor and front-end electronics) of the dRICH detector are concentrated in a region of moderate radiation level, below  $O(10^{11}) \text{ cm}^{-2} n_{\text{eq}}$  of maximum integrated fluence where  $n_{\text{eq}}$  is a 1-MeV neutron equivalent particle, see Figure 8.86. Close to the beam line, where the integrated dose can reach a value of 15 krad, only radiation tolerant materials reside like silica aerogel [82].

**Requirements from 8xParticle Fluence:** Data rates are expected to be dominated by the intrinsic significant dark count rate of the SiPM sensor, currently of the order of 50 kHz/mm<sup>2</sup> at room temperature, that indefinitely increases with the radiation damage. To mitigate this effect, the dRICH sensors are operated at low temperature (less than  $-30^\circ\text{C}$ ) and regularly annealed at high temperature (up to  $150^\circ\text{C}$ ), in order to never exceed a maximum 300 kHz dark rate per channel. The latter value corresponds to a conservative limit taken to preserve the detector performance requirements for Physics and it is supported by present simulation studies that confirm the particle-identification capabilities of dRICH are unaffected. The corresponding maximum throughput rate of the whole dRICH is 1.3 Tbps assuming further data reduction. This will be achieved via a shutter signal on the front-end ASIC and/or via an external tagger or data reduction in dRICH DAMs using machine-learning techniques (see section 8.3.10).

**Justification** The specifications outlined above largely define the main technological choices: the momentum range dictates radiator refractive indexes that can be reliably met only by aerogel and gas, while the ePIC environment, space and magnetic field, imposes sensor characteristics that can only be met by SiPM.

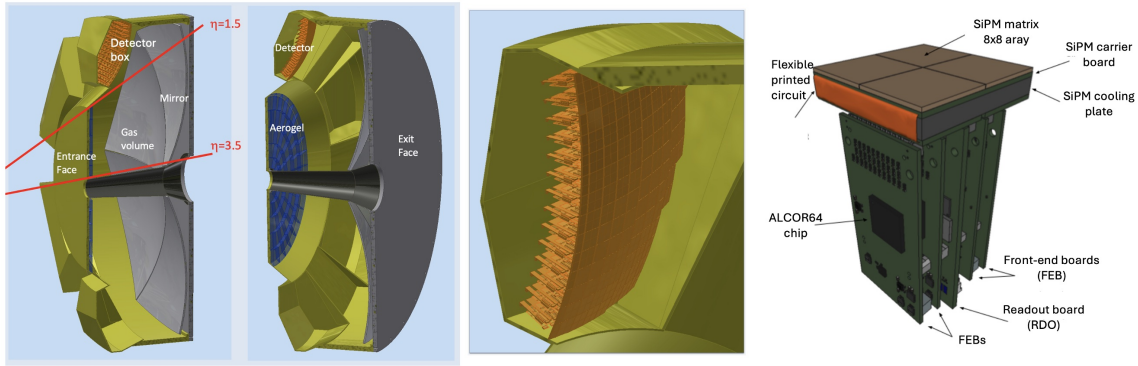


**Figure 8.118:** (Left) dRICH detector model with highlighted the major components. (Center) Model of the dRICH photodetector unit (PDU) module with its major components highlighted. (Right) dRICH detector box model with 208 PDUs forming a curved active surface.

**Device concept and technological choice:** The dRICH is a ring-shaped detector, with a length of 1.27 m and a diameter of 3.6 m, fitting inside the ePIC forward endcap, see left panel of Figure 8.118. The essential components are a layer of aerogel radiator, a volume of gas radiator, and an array of mirrors focalising the Cherenkov light into compact areas instrumented with photo-sensors. The detector is designed in a modular way, with 6 sectors around the beam line of equivalent mirror set and detection area.

The aerogel radiator is an amorphous solid network of  $\text{SiO}_2$  nanocrystals whose density regulates the refractive index and chromaticity [83]. The current manufacturing methods succeeded in improving the attenuation length  $\Lambda$  ( $\lambda = 400$  nm) up to 50 mm (e.g. aerogel for CLAS12 and BELLE-II). The selected aerogel radiator has refractive index  $n = 1.026$  at  $\lambda = 400$  nm. The chromatic dispersion has been measured during the R&D phase to be  $dn/d\lambda = 6 \cdot 10^{-6} \text{ nm}^{-1}$  at 400 nm wavelength. Aerogel is produced in tiles of few cm thickness: in order to minimize edge effects, the dRICH tile side should be greater than 18 cm, approaching the word record value of 20 cm.

The selected reference gas radiator is hexafluoroethane ( $\text{C}_2\text{F}_6$ ), which matches the requirements being characterized by refractive index  $n = 1.00086$  at STP and excellent chromatic dispersion  $dn/d\lambda = 0.2 \cdot 10^{-6} \text{ nm}^{-1}$  at light wavelength  $\lambda = 350$  nm [84].

The selected refractive indexes dictates a minimum thickness of 4 cm for the aerogel and  $\mathcal{O}(1)$  m for the gas in order to ensure enough photon yield. Mirror focalisation is necessary to minimise the consequent uncertainty on the Cherenkov photon emission point. Being inside the detector acceptance, the mirror structure is made of carbon fiber reinforced polymer (CFRP) to ensure the necessary stiffness while being light. In order to preserve the Cherenkov angle information the mirror surface should have excellent optical quality, i.e. few nm roughness and better than 0.2 mrad angular precision (reflecting in a point-like image with more than 90% of the light intensity concentrated in a disk smaller than 2.5 mm). The single mirror dimension is limited to a  $\approx 1$  m maximum diagonal when accounting for realistic forming mandrel and coating chamber dimensions. In the dRICH mirror array, the radius of curvature should be replicated within 1% of the nominal value and the reflectivity should be better than 90% in the 300-600 nm wavelength range of interest.

The dRICH photon detector surface is shaped over a sphere of radius  $\sim 110$  cm to best approach the 3D focal surface of the mirror array, see Figure 8.118 (center). The Silicon Photomultiplier (SiPM) sensor technology is selected for the photon detector. It ensures superior single-photon counting capability inside the ePIC magnetic field and compact dimensions suitable for tessellat-

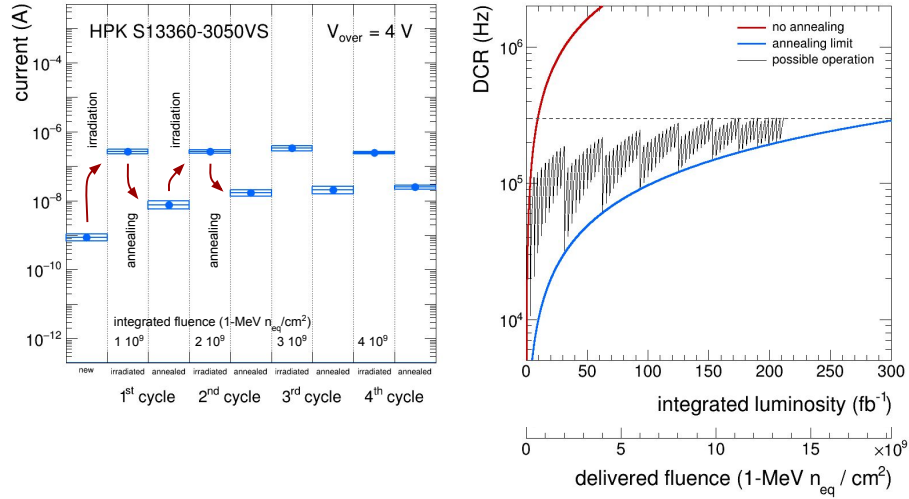


**Figure 8.119:** (Left) Dark current measurements on sample SiPM sensors for the studies of repeated irradiation-annealing. (Right) Projected increase of the DCR of SiPM as a function of the integrated luminosity (delivered fluence) for the PDU closer to the beam pipe (worst case scenario). The “no annealing” and the “annealing limit” curves show the limits of possible operations. The dashed line indicate the desired maximum DCR threshold.

ing a shaped active surface. The single SiPM sensor has a  $3 \times 3$  mm<sup>2</sup> area to provide the necessary spatial resolution with an intrinsic time resolution better than 150 ps. The selected front-end ASIC is ALCOR [85], a 64-channel chip with coupling and rate capability optimized for SiPMs, and a ToT architecture with better than 50 ps (least significant bit) resolution in order the SiPM-ALCOR readout chain could achieve an overall time resolution better than 200 ps RMS. To minimize the volume within the dRICH envelope and to maximize the active area, the photodetector is organized in compact photodetector units (PDU). The PDU integrates 256 SiPM channels with the ALCOR TDC readout provided by four front-end boards (FEB), one readout board (RDO) to interface with the ePIC data acquisition (DAQ) and detector control (DCS) systems. In addition, the PDU is designed to allow sub-zero cooling of the SiPMs as well as high-temperature annealing operations. Figure 8.118 (right) shows the conceptual design of the PDU and its main components. The present dimensions of the PDU concept are approximately  $52 \times 52 \times 140$  mm<sup>3</sup>.

### Subsystem description:

#### General device description:

Because at ePIC the electron and hadron beam collide at an angle of 25 mrad and acceptance should be provided to the far forward detectors, the common beam pipe cross-section is off-axis at the dRICH location and increasing in area with the distance from IP, imposing an asymmetric layout of the inner components. The aerogel wall is composed of five rings of tiles, each shaped in order to fit inside a 0.2 mm thin aluminum supporting structure. In each sector, focalization is provided by a compound of five mirrors covering a total area of about 2 m<sup>2</sup> with an optimized radius of curvature around 2200 mm. Six independent spherical active surfaces with curvature radius around 1100 mm, each made of 208 PDUs for a total of 53k readout channels, are mounted inside detector-boxes that provide thermal insulation, cooling for the electronics and connections to the services. Given the gas radiator open volume,

the Cherenkov photons can be reflected into different detectors depending on the parent charged particle kinematics. The aerogel and photo-detector are separated from the radiator gas by transparent septa, and immersed in a dry (e.g. purged  $N_2$ ) atmosphere to minimize contaminant absorption and prevent moisture formation. The mirrors are supported by a light carbon fiber structure that is mechanically decoupled from the vessel and allows fine alignment adjustments by means of piezo-electric motors.

#### Sensors:

The silicon photomultiplier (SiPM) [86,87] is chosen as the sensor technology for the dRICH photodetector. The main baseline specifications demand sensors with a  $3 \times 3 \text{ mm}^2$  single-channel active area, single photon detection over a broad spectral range from 300 to 900 nm and overall photodetection efficiency  $> 40\%$  at the peak sensitivity wavelength  $400 < \lambda_{\text{peak}} < 450 \text{ nm}$ . SiPMs fulfil the dRICH requirements as cost-effective and versatile devices with excellent photodetection efficiency (PDE) and time resolution. Their single-photon performance is unaffected by high magnetic fields [88,89]. SiPM sensors on the other hand have very high dark count rates (DCR) and are not radiation tolerant. The DCR in SiPM is mostly of thermal origin and it reduces significantly by lowering the SiPM temperature, typically halving every  $7\text{--}10^\circ\text{C}$  in new sensors [90]. Radiation damage in SiPM is mainly due to displacement damage in silicon, which causes a significant DCR increase [91]. At the moderate radiation levels expected at the dRICH location, no significant change in the SiPM parameters (PDE, gain, quenching resistor  $R_{\text{quench}}$ , pixel capacitance  $C_{\text{pixel}}$ , breakdown voltage  $V_{\text{break}}$ ) is observed [92]. SiPM cooling is important to keep the DCR low and it becomes crucial after radiation damage [93]. In the dRICH, the SiPMs will be operated at subzero temperature of  $T = -30^\circ\text{C}$ , or lower. A cooling block is placed in thermal contact with the back-side of the printed-circuit board hosting the SiPMs (carrier board). Cooling fluid in the cooling block will be circulated through a closed loop by a circulating thermostat with dynamic temperature control to regulate and maintain the SiPMs at low temperature. The radiation damage on SiPMs increases moderately with the integrated luminosity. At the location of the dRICH photodetector a maximum (average) fluence of  $\Phi_{\text{eq}} = 6.0 (3.6) 10^7 \text{ cm}^{-2}/\text{fb}^{-1}$  1-MeV equivalent neutrons ( $n_{\text{eq}}$  in the following) is expected from e+p interactions at the highest center-of-mass energy of the EIC (see left panel in Figure 8.120). Beam-induced background from proton beam-gas events at 35 kHz are expected to contribute bringing the total maximum (average) expected radiation damage to  $\Phi_{\text{eq}} = 6.4 (3.7) 10^7 \text{ cm}^{-2}/\text{fb}^{-1} n_{\text{eq}}$ . As shown by the “no annealing” curve in Figure 8.119 (right), the SiPM DCR is expected to increase with the integrated luminosity at a maximum (average) rate of  $31.8 (18.6) \text{ kHz}/\text{fb}^{-1}$ , reaching a DCR of 300 kHz after an integrated luminosity of approximately  $9.5 (16.1) \text{ fb}^{-1}$ . Annealing of SiPMs can be achieved exploiting the Joule effect [94]. When a SiPM is forward biased, the micro-cells composing the device behave as directly polarized diodes connected to their quenching resistors. The current flowing through the resistors eventually heats up the entirety of the sensor. In the dRICH, the circulating thermostat system used for low-temperature operation of the SiPM will be operated in heating mode to warm up the SiPM cooling plate ( $T = 100^\circ\text{C}$ , or higher) during high-temperature annealing. Therefore a low-viscosity silicone fluid is particularly suitable for cold and heat transfer. Because a fraction of the heating power is delivered by fluid, a reduced current is required to perform the “forward-bias annealing” to the SiPM. Nonetheless the required power to perform annealing at once over the full dRICH detector is excessively large and unpractical. Therefore annealing operations will be segmented in space and time across the dRICH detector and performed during periods with no Physics beam, and the temperature will be tuned up to  $T = 150^\circ\text{C}$ , depending on the DCR reduction needs. During the R&D phase it was shown that the “forward-bias mode” approach can cure approximately 97% of the radiation damage. It is therefore expected that a residual irreducible radiation damage (residual DCR) will build up during the dRICH lifetime. As



can be seen from left panel in Figure 8.120 the sensors closer to the beam line will experience a radiation damage almost a factor 3 times larger than those further from the beam line and will likely require a more frequent annealing. As shown by the “annealing limit” curve in Figure 8.119 (right), closer to the beam pipe (worst scenario) the SiPM residual DCR is expected to increase with the integrated luminosity at a rate of 950 (560) Hz/fb<sup>-1</sup>, reaching a residual DCR of 300 kHz after an integrated luminosity of approximately 310 fb<sup>-1</sup>. The “possible operation” curve shows a potential scenario for the DCR evolution for these SiPM sensors. This is based on an operation model where more frequent (every  $\sim 3$  fb<sup>-1</sup>) softer annealing cycles at lower temperature and/or of shorter duration, delivering a DCR reduction of 10 times, are interleaved by less frequent (every  $\sim 30$  fb<sup>-1</sup>) full annealing cycles to reduce DCR as much as possible. A limit in the operation scenario is reached when the annealing is not able to keep the DCR below the desired threshold or when the annealing frequency becomes too high. Beyond an integrated luminosity of  $\sim 200$  fb<sup>-1</sup> to keep the DCR below the 300 kHz threshold requires to perform full annealing cycles every  $\sim 5$  fb<sup>-1</sup>, which is not obviously a practical operation scenario anymore. Some of the SiPM sensors might be needed to be replaced at that stage with new ones or with SiPM sensors of improved performance and radiation hardness as a future upgrade of the dRICH photodetector. One has to keep in mind though that the 300 kHz limit is a conservative value that is connected to the present level of dRICH reconstruction and could be relaxed in future. Moreover, the model shown in Figure 8.119 (right) is based on measurement on Hamamatsu S13360-3050 sensors operated at  $V_{\text{over}} = 4$  V in a climatic chamber at  $T = -30^\circ\text{C}$ . Possible SiPM operation in ePIC at a lower  $V_{\text{over}}$  of 3 V and at a lower  $T$  of  $-40^\circ\text{C}$  will allow one to achieve lower DCR overall.

#### FEE:

The ALCOR (A Low Power Chip for Optical Sensor Readout) ASIC, developed by the electronics laboratory of INFN Torino, is the baseline option for the readout of the dRICH SiPM sensors. The architecture of ALCOR and its key specifications are described in Section 8.3.10. The main goal of ALCOR is to provide single-photon time tagging of the incoming signals, while being able to cope with the SiPMs inherently high DCR: a maximum DCR value of 300 kHz/ch is expected before an annealing cycle is performed. A good time resolution, better than 200 ps RMS, is required to perform DCR suppression via time gating at both hardware and software levels. A programmable hardware shutter, implemented inside the digital logic of ALCOR, can be enabled to filter out-of-time DCR and provide a significant bandwidth reduction to the system. The time window of interest is controlled off-chip by the RDO FPGA and can be adjusted using in-pixel programmable delays to compensate timing offsets among the 64 channels. Note that the shutter may be needed only when DCR becomes significant due to SiPM integrated radiation damage over time. Therefore, the first period of ePIC data taking can be used to optimize the shutter calibration. The ASIC will be integrated inside a BGA package, providing a compact and robust solution to be assembled on the FEB. A  $17 \times 17$  mm<sup>2</sup> flip-chip ball grid array (FC-BGA), with 256 balls and 1 mm ball pitch, is the option chosen for the ASIC packaging since it offers more interconnections and better performance w.r.t. standard packaging techniques and matches well with the pixel-matrix geometry of the ALCOR ASIC. Each FEB hosts one ALCOR BGA device and several components to ensure a stable and safe operation of the system. Linear regulators are employed to provide clean power supplies to the chip and are coupled to I2C interface and current monitors to control the regulators and prevent potential damage from over-current conditions. The FEB incorporates a dedicated PCB section for SiPMs bias voltage routing and also a circuit to enable the SiPM forward-biasing when annealing cycles are carried out. AC-coupling between the SiPM sensors and ALCOR inputs has been chosen to isolate them when the SiPMs are operated in forward bias.

Other components:

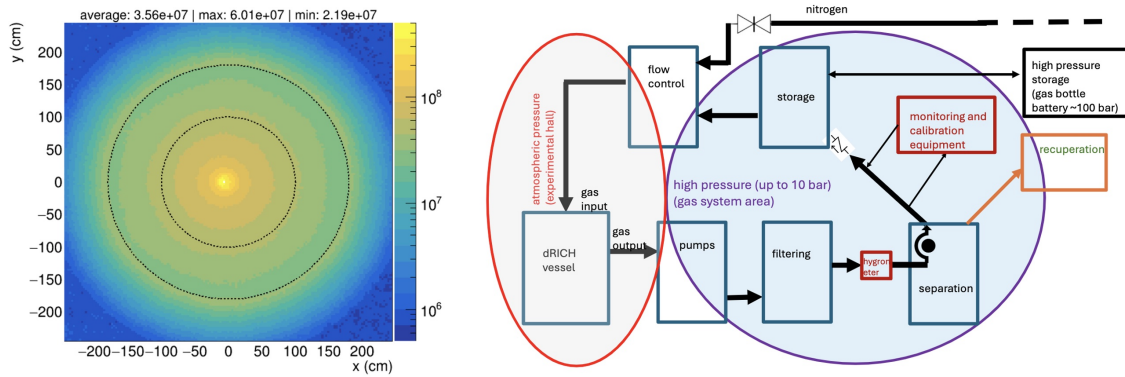


**Figure 8.120:** (Left) Transverse map of the expected 1-MeV equivalent neutron fluence per  $1 \text{ fb}^{-1}$  of integrated luminosity in e+p interactions at the maximum EIC center-of-mass energy at the location of the dRICH photodetector ( $210 < z < 260 \text{ cm}$ ). The average, maximum and minimum values within the region of the dRICH photodetector ( $100 < R < 180 \text{ cm}$ , indicated by the dashed lines) are reported. (right) Block diagram of the dRICH gas system.

The radiator gas in the RICH vessel is controlled by the gas radiator system, see right panel in Figure 8.120. Its main tasks are, during detector operation, (i) providing well controlled pressure conditions in the  $12 \text{ m}^3$  RICH vessel to avoid relevant pressure difference at the vessel walls and at the fused silica windows; (ii) removing oxygen and water vapor contaminants, in order to prevent building up impurities due to air leaks entering the gas system; (iii) performing detector vessel filling with hexafluoroethane before a data taking period and radiator gas recovery at the end of the period; the filling/recovery is from/to the storage tank. The main components of the radiator gas system are two oil-free compressors, working in parallel, which continuously extract gas from the vessel at constant rate in order to ensure the gas circulation, a pressure sensor installed on top of the radiator vessel for continuous monitoring of the internal relative pressure and to dictate the opening level of a flow control valve on the input line, adjusting the opening so to preserve the relative pressure inside the vessel. Oxygen and water vapor traces are removed by filtering cartridges with molecular sieves and Cu-catalyst, which are permanently in series in the circulation system, to maintain a contamination level better than 20 ppm (a value less stringent than for gas devices working in the VUV wavelength region). The gas temperature and pressure will be continuously monitored to correct the variation of the refractive index within an uncertainty below 0.1% in terms of  $(n-1)$ . The vessel is flushed with nitrogen during the shutdown periods. Nitrogen and hexafluoroethane separation during filling and recovery is under study and two options can be envisaged: (i) the use of osmosis via dedicated membranes or (ii) via a two-step procedure: replacing nitrogen with carbon dioxide and then performing distillation at  $-35^\circ\text{C}$ . Hexafluoroethane is a greenhouse gas and, therefore, the residual  $\text{C}_2\text{F}_6$  present in the nitrogen/carbon dioxide cannot be vented out: it must be collected and trapped for disposal with a dedicated recovery system. The control of the whole radiator gas system is performed via a Programmable Logic Controller (PLC).

## Performance

For each recorded dRICH hit, the photon path is reconstructed taking into account the charged particle trajectory and the focalising optics of the detector, in order to provide an estimate of the Cherenkov angle at the emission point. The combined information of all the Cherenkov photons



associated to a charged particle result in a precise determination of its velocity  $\beta c$  and, knowing the momentum from the ePIC spectrometer, its mass. The dRICH model is part of the ePIC simulation framework and allows complete performance studies taking into account quality of the track reconstruction, bent trajectories (by magnetic field) and multiple scattering. To bypass the complexity of such a framework, some specific study can be anyway performed with standalone simulation chains. The laboratory characterization and the numerous test-beams have provided detailed inputs for modeling in a realistic way the single components and global detector response. In the dRICH, the contributions to the single-photon (SPE) angular resolution have a different weight depending on the radiator. The dRICH has been designed in order to keep most of the contributions to the SPE angle resolution close or below 0.5 mrad, see Figure 8.121, a value dictated by the tiny Cherenkov angle difference between pions and kaons at 50 GeV/c in the radiator gas. The single SiPM readout channel has been limited to  $3 \times 3 \text{ mm}^2$  area. The MARCO coils and the dRICH position has been optimized in order to minimize the bending inside the radiator gas volume. The tracking resolution is assumed to cope with the same constrain. Note that combining  $N$  photons the angular precision scales with a maximum  $N^{-1/2}$  factor only in case of a completely uncorrelated information, a condition that is not valid for the bending and tracking contributions. The uncertainty on the emission point is not an issue for a few cm layer of aerogel, but is critical for a 1 m long gas volume, especially within the limited space available in ePIC for the optics: this remains the major contribution to the SPE resolution of the radiator gas despite the mirror focalization and the curved dRICH detector surface. Because the present model assumes a single radius for the dRICH mirrors, optimized for the forward rapidity region to boost the high-momentum reach, the resolution worsens with the polar angle increase. This is not a problem, because the average particle momentum decreases as well loosening the performance requirement. The chromatic error is well under control for gas but is the largest contribution to the angular resolution for the aerogel. This derives from the intrinsic nature of the radiator in conjunction with the quantum efficiency characteristic of the photosensor. The chromatic uncertainty limits the aerogel momentum reach to something above 15 GeV/c, a value well above the Cherenkov threshold of kaons in gas, high enough to provide the wanted overlap between the measured ranges of the two radiators.

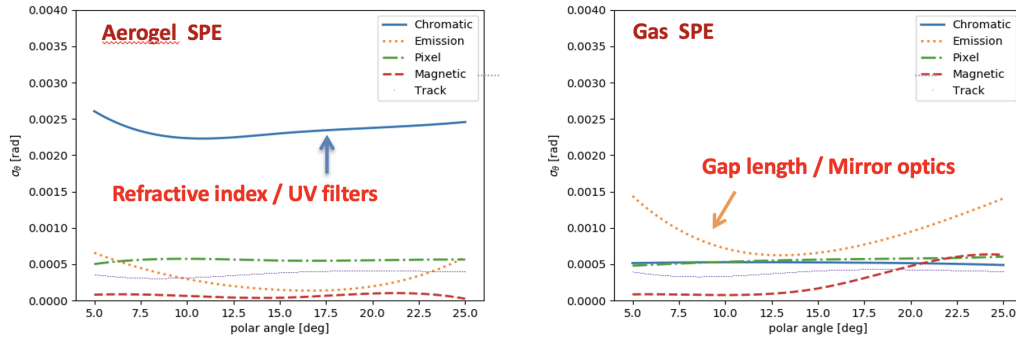


**Figure 8.121:** (Left) Contributions to the single-photon angular resolution for aerogel. (Right) Contributions to the single-photon angular resolution for radiator gas.

The number of emitted photons varies with the pseudo-rapidity due to the different path of the particle within the radiators. The mean number of recorded photons is about 18 for the radiator gas and 12 for the aerogel for a particle with momentum well above the Cherenkov threshold. In average, few charged particles per event are expected to hit the detector. With a proper pattern recognition and photon path reconstruction, the information of the two radiators can be combined to extend the hadron momentum coverage of ePIC PID from the TOF  $\approx 2.5 \text{ GeV/c}$  upper momentum limit to above 50 GeV/c, and support electron separation up to 15 GeV/c, see Figure 8.122. In

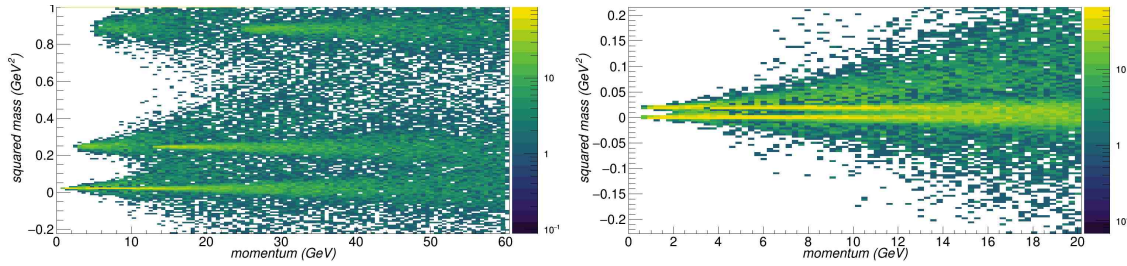


**Figure 8.122:** (Left) Reconstructed mass vs momentum for pions, kaons and protons. (Right) Reconstructed mass vs momentum for pions and electrons. Distinct values derived from aerogel and gas are shown, to highlight the complementary coverage and effective interplay of the two radiators. The study is performed at the large rapidity endpoint  $3.2 < \eta < 3.5$ .

the forward direction with optimized focalization, an identification efficiency greater than 95 % at a corresponding 5 % percent mis-identification probability, is achieved.

## Implementation

### Services:

The dRICH services are grouped into power lines for sensors, electronics and slow control monitors, gas lines for the radiator gas volume, the aerogel inert gas volume, and cooling lines for the sensors and electronics. Table 8.44 shows a list of the power services for the dRICH photodetector. Eighteen 19" wide/8U mainframes (approximately  $50 \times 40 \times 70 \text{ cm}^2$  each) capable to host 16 boards each are needed to accommodate the low-voltage and high-voltage boards. The primary power-supply channels will serve multiple modules at the same time, with a typical grouping of 1024 SiPM channels. Nonetheless, further segmentation is implemented on the detector electronics, reaching a low-voltage power segmentation of 64 SiPM channels and a high-voltage power segmentation of 32 SiPM channels. The circulating thermostat system should be capable of circulating approximately 50 l/min of fluid at a maximum pressure of 1.5 bar in a broad temperature range (from  $-60^\circ\text{C}$  to  $120^\circ\text{C}$ ). It is expected that a potential circulating thermostat system with the desired characteristics will require space in the experimental hall for a volume of approximately  $1.3 \times 0.8 \times 1.6 \text{ m}^3$ . Manifolds are needed to split the fluid from the thermostat into 6 loops, each feeding one dRICH photodetector box. A solution without manifold and 6 smaller independent thermostat units for each dRICH sector will be investigated as a possible optimization. Insulated pipes will be needed to transport the fluid from the thermostat to the detector, and back. The insula-

Name	Voltage (V)	Current (A)	Channels	Boards	AWG gauge
Analog	1.4	10.0	312	39	10
Digital low	1.4	8.5	312	39	11
Digital high	2.7	6.0	312	39	12
Master panel	5.0	5.2	6	1	13
SiPM bias	64.0	1.3	12	2	19
Annealing	12.0	3.2	1248	156	15

**Table 8.44:** List of the voltage services to the dRICH electronics, indicating the number of primary power-supply channels and boards as well as the cross-section of the cables (AWG). The number of power-supply boards is defined assuming to use commercial 8-channel low-voltage boards.

tion must guarantee no frost and no water condensation on the pipes when operating at the lowest temperatures and is also required to limit transport losses in heating/cooling capacity. Cooling for the front-end electronics is required to remove the approximately 15 kW of heat generated by the dRICH photodetector ( $\approx 2.5$  kW in each of the six photodetector boxes). Forced-air circulation in the boxes with diffusers and heat exchangers are being studied as a possible effective solution. It is important that the air-cooling system for the FEE electronics provides dry air with a dew point well below the SiPM operating temperature. A system based on forced circulation of gaseous nitrogen might be well suited also to ensure an inert environment inside the detector boxes. Gaseous nitrogen will be used to maintain the aerogel in a clean and inert environment. The radiator gas system and its related monitoring equipment require a surface of about 15 m<sup>2</sup>, in order to host 5 racks of instrumentation, the gas storage tank and a support for the spectrophotometer. Various sections of the gas system operate at a 2-3 bar pressure, while the cell to measure and monitor the gas transparency operates at 10 bar. Some gas bottles at typical high pressure (100-150 bar), organized in a battery, have to be included to provide the radiator gas at filling and house it when recovered. The pipelines connecting the gas system to the vessel can be 70 m long with a diameter of 10 cm.

### Subsystem mechanics and integration:

The dRICH structure can be described by two disks, one entrance window of 0.9 m radius supporting the aerogel radiator and one exit window of 1.8 m radius mounting the mirror system, connected by two ring-shaped structures, an outer shell that mounts the six detector boxes and one inner pipe surrounding the ePIC beam pipe. All the elements are made in composite materials, see left panel of Figure 8.123. The pipe and shell are made by a carbon fiber reinforced polymer (CFRP) bulk to provide support strength. The two windows are a sandwich of two thin carbon fiber skins and a core honeycomb to limit the material budget to about 1% of radiation length each. The shell and detector boxes are shaped in order to allow the passage of all the services of the inner barrel detectors, see central panel of Figure 8.123. The dRICH services are concentrated on the shadow of the detector boxes and do not interfere with the routing of the others. A dedicated scaffolding would be realized to allow the installation of the detector, and the roll-in and roll-out movements to the service position without interference with the beam pipe to preserve the beam vacuum, see right panel of Figure 8.123. The dRICH is suspended inside ePIC via brackets connected to the HCAL barrel.

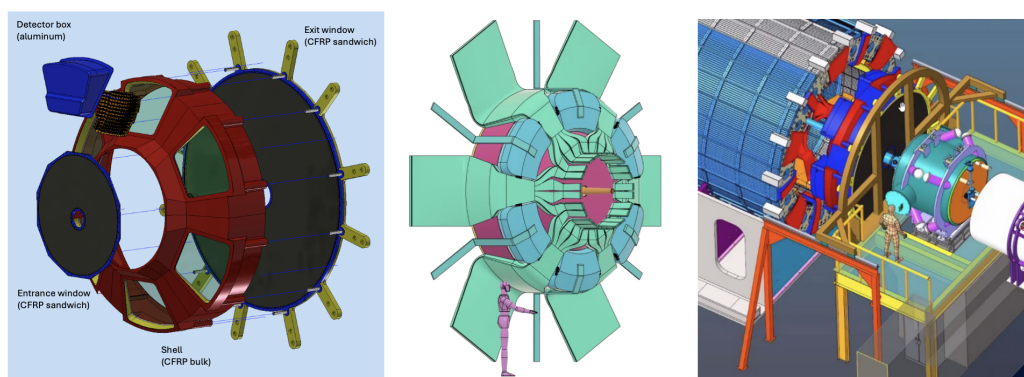


**Figure 8.123:** (Left) dRICH mechanical model. (Center) Service routing around the dRICH. (Right) Installation and extraction tool.

### Calibration, alignment and monitoring:

Dark counts in SiPMs are indistinguishable from photon-induced signals and owing to the large SiPM DCR there is no need of a dedicated system to evaluate the functioning of any given read-out channel. A measurement of the DCR as a function of the front-end electronics discrimination threshold can provide information on the actual single-photoelectron signal amplitude. Using solely the dRICH readout system it is therefore possible to measure the signal amplitude as a function of the bias voltage, hence to obtain information on sensor functioning, breakdown voltage and gain at different operation conditions. Timing calibration of the SiPM sensors can be achieved with a picosecond pulsed laser light system. The light from the laser is brought inside the dRICH volume via optical fibres. The light from the laser directly impinges on a diffuser that eventually illuminates the full area of one dRICH photodetector sector. At least one laser-fibre-diffuser system is needed for each dRICH sector. The time delay due to the different path of photons from the diffuser to the SiPM that detects the light is known and can be corrected to achieve a relative calibration of the times of SiPMs within the same sector. Absolute timing calibration can then be achieved with collision data. Sample particles from physics reactions can be used to perform fine adjustment of the calibration constants. Electron particles identified by other ePIC subsystems can be used to correct residual misalignment or calibrate the radiator refractive index thanks to the saturated Cherenkov rings. Known particles from meson decays ( $\Lambda$ ,  $\phi$ ,  $K_S$ , ...) identified by kinematics criteria can be used to verify the parameters of the dRICH reconstruction and the consequent PID performance. The calibration and monitoring equipment of the radiator gas and gas system includes a set of temperature sensors placed inside the dRICH vessel and equipment on-line in the gas circulation loop. A commercial hygrometer and a commercial oximeter, a transparency measurement system by a commercial spectrophotometer equipped with a high pressure ( $\approx 10$  bar) cell and a Jamin interferometer setup complete the set of the equipment. The interferometer, complemented with temperature and pressure sensors, will provide in real-time the refractive index of the gas in the vessel. The refractive index measurement has a twofold role: during filling/recovery, it monitors the hexafluoroethane level in the vessel, during operation it will provide in real time the refractive index of the radiator gas to make possible quasi on-line data reconstruction as foreseen in the ePIC streaming read-out model.

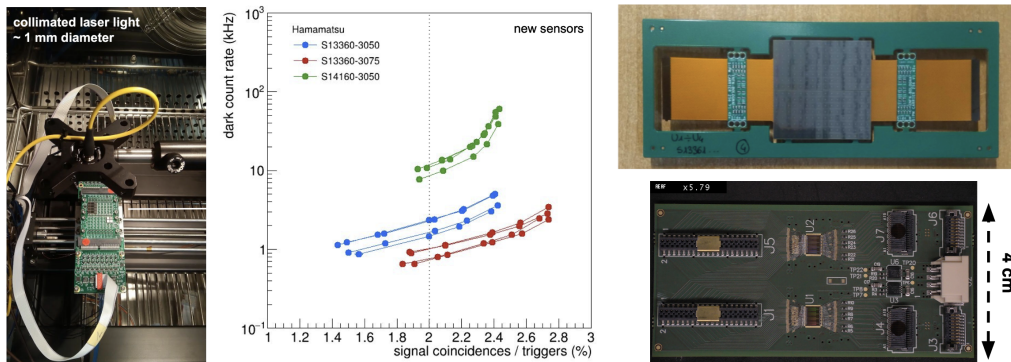


**Figure 8.124:** (Left) Test stand for SiPM characterization. (Center) Performance comparison between different SiPM models. (Right) Prototype version of the SiPM carrier board (top) and FEB (bottom).

### Status and remaining design effort:

R&D effort:



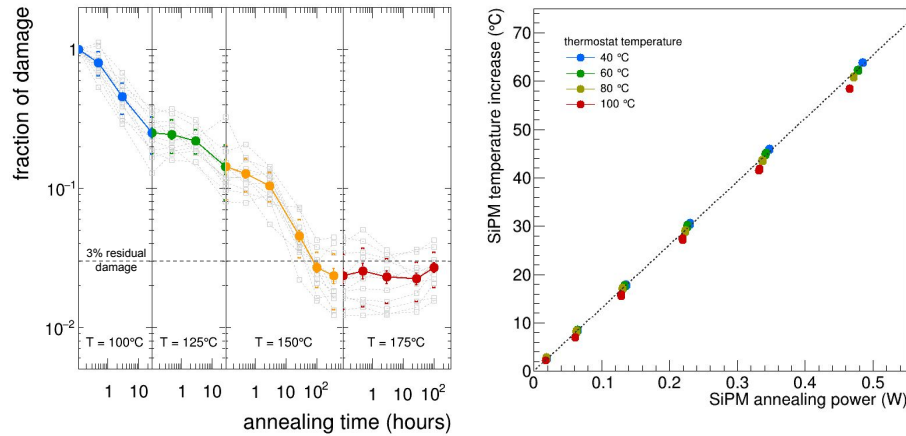


**Figure 8.125:** (Left) Fraction of residual irradiation damage measured on multiple SiPM candidate samples after “forward-bias annealing” cycles at increasing temperature and integrated annealing time. The measurements are shown for individual sensors (gray points) and as averages (coloured points, uncertainty of the average and RMS are indicated on the plot). (Right) Temperature increase of the SiPM sensor with respect to the temperature of the SiPM carrier board as a function of the “forward-bias annealing” power at different temperature values of the circulating thermostat system.

**SiPM sensors.** A station has been realized to characterize the SiPM sensors inside a climate chamber to control the working temperature, see left panel of Figure 8.124. The readout chain is based on ALCOR to reproduce the ePIC configuration. Such a station allowed detailed performance comparison between SiPMs of different manufacturers and types, see Figure 8.124 (central panel), and different ageing due to radiation and annealing. The R&D results on photosensors reported here are those obtained with Hamamatsu S13360-3050 sensors operated at  $V_{\text{over}} = 4 \text{ V}$  in a climatic chamber at  $T = -30^\circ\text{C}$ , unless otherwise specified. Nonetheless, the qualitative features of the results are valid also for other types of sensors. Irradiation tests performed to simulate a realistic experimental situation where SiPMs experience repeated irradiation and annealing cycles (see left panel of Figure 8.119) show that each irradiation cycle produces a consistent DCR increase (approximately 500 kHz for a  $10^9 \text{ cm}^{-2} n_{\text{eq}}$  irradiation) and the fraction of damage cured in the thermostatic chamber is approximately 97%. The 3% residual damage builds up after each irradiation-annealing cycle and seems to be irreducible within the details of this annealing protocol. Irradiation tests and laboratory measurements show that the “forward-bias annealing” mode can cure radiation-induced damage on SiPM (see left panel of Figure 8.125) to the same effectiveness level as the one measured for the “oven annealing” with a residual damage of approximately 3%. The benefit of the “forward-bias annealing” is significant: an extended SiPM sensors lifetime that can be achieved over the delivered radiation damage without the need to directly access the detectors in the experimental cavern. Higher temperatures and longer annealing times lead to more effective annealing. On the other hand, a limit seems to be reached already at  $T = 150^\circ\text{C}$  as annealing at a higher temperature like  $T = 175^\circ\text{C}$  does not lead to improved current reduction. Laboratory measurements performed so far show that the temperature of the SiPM increases with respect to the temperature of the SiPM carrier board proportionally to the power delivered by the forward-bias current. Figure 8.125 (right panel) shows that, as expected, the increase of SiPM temperature linearly depends on the annealing power and it is the same

at different values of circulating thermostat temperature. It is therefore sufficient to monitor the temperature of the SiPM carrier board and deliver the needed annealing power to have control of the SiPM temperature and keep the process safely under control. Laboratory measurements reported here are performed in an open environment at room temperature. With the circulating thermostat temperature set at  $T = 100^\circ\text{C}$ , a SiPM annealing temperature of  $T = 150^\circ\text{C}$  is reached with approximately a power of  $0.5\text{ W/sensor}$ , which corresponds to a forward-bias current of approximately  $60\text{ mA/sensor}$ . With the SiPM placed in a closed environment as the dRICH photodetector box, one would expect a lower power needed that will be measured during detector construction. Laboratory measurements show that for annealing temperatures up to  $T = 150^\circ\text{C}$  there is no significant degradation of the PDE up to annealing times of 150 hours. More studies will be done, but at the time of writing annealing at  $T = 150^\circ\text{C}$  can be considered safe for the expected dRICH operations.

**FE Electronics.** ALCOR has been extensively used within the ePIC dRICH Collaboration since 2021, testing it coupled to different SiPM models and assessing its single-photon time-tagging capability and time resolution. A prototype version of the SiPM carrier and FEB board have been developed, see right panel of Figure 8.124. The SiPM carrier provides electrical connections via thin kapton cables in order to bypass the sensor cooling plate. The prototype FEB hosts two 32-channel ALCOR chips which are directly wire-bonded on the PCB. It has been designed using specifications close to the ones for the final FEB, i.e. having the same dimensions and incorporating the same number of channels (64). It is served by a master-logic board that provide bias control and temperature monitor. These boards have been extensively used for the 2023-2024 dRICH activities, including two successful beam tests. ALCOR has been tested for radiation hardness with results showing only some small degradation on the TDC performance after a total ionizing dose (TID) of 300 krad, which is  $O(100)$  times the expected TID in ePIC. The single-event upset (SEU) cross section has been measured to be  $3.3 \cdot 10^{-15}\text{ cm}^2/\text{bit}$ , which corresponds to an expected mean time between failure due to SEU of about 190 hours for the entire dRICH detector. These results confirm that the technology is sufficiently radiation tolerant to be used in the ePIC dRICH environment.

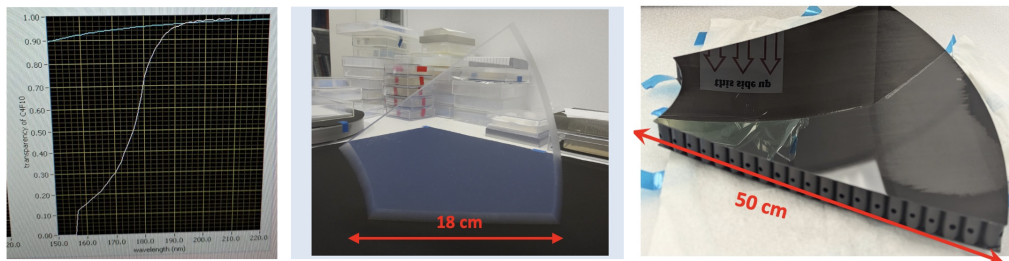


**Figure 8.126:** (Left)  $\text{C}_2\text{F}_6$  measured transmittance in the near UV-region. (Center) Aerogel tile real-size demonstrator. (Right) Mirror demonstrator with an optimized dRICH core structure.

**Radiator gas.** The transparency in the near-UV benchmark region (most sensitive to the gas quality and contaminants) has been measured with a monochromator at CERN, resulting in values above 98% for a 1.6 m column of gas at wavelengths greater than 200 nm, see left panel of Figure 8.126. The measurement has been done with a gas that was stored into bottles for about 4 years, indicating an excellent preservation with time.

**Aerogel.** The transparency of several aerogel samples from Aerogel Factory Co. Ltd (Chiba, JP) has been measured using a spectrophotometer at CERN and at INFN. Aerogel tiles with different refractive index (from  $n = 1.015$  up to 1.05) and 2 cm in thickness have been tested. At the wavelength of 400 nm, the transparency values are typically above 70% with a peak

at  $n=1.03$ . Real-size demonstrators have been realized with the baseline refractive index of  $n=1.026$ , see central panel of Figure 8.126. In general the tiles have the shape of a dome as a consequence of the production process. In the metrology laboratory at CERN, the thickness and flatness of the tile have been also measured. The measurement has been executed on a tile with  $n = 1.03$  using the touch probe system (force applied = 2 g). The measuring system is the LEITZ PMMC with  $\pm 0.3 \mu\text{m}$  of precision. There is a variation in thickness from the center to the edges, of the order of 0.4 mm, and a different planarity in the two faces, one 0.7 mm, the other 1.27 mm. These values are unexceptional but are not a reason of concern.

**Mirror.** A mid-size demonstrator (of 60 cm diagonal) has been realized with dRICH specifications, see right panel of Figure 8.126. The CFRP core structure has been optimized for preserving the surface shape accuracy and a light body: it adopts a light C-shaped cell structure (used by LHC-b) in the center, and a stronger cylindrical cell structure (used by CLAS12) on the edges. Before coating, the point-like source image test measures a D0 value, that represents a global surface quality estimator, of 1.8 mm, better than the specification of 2.5 mm. The same test indicates a radius of  $2254 \pm 5$  mm, slight above the request to be within 1% of the nominal 2200 mm value.

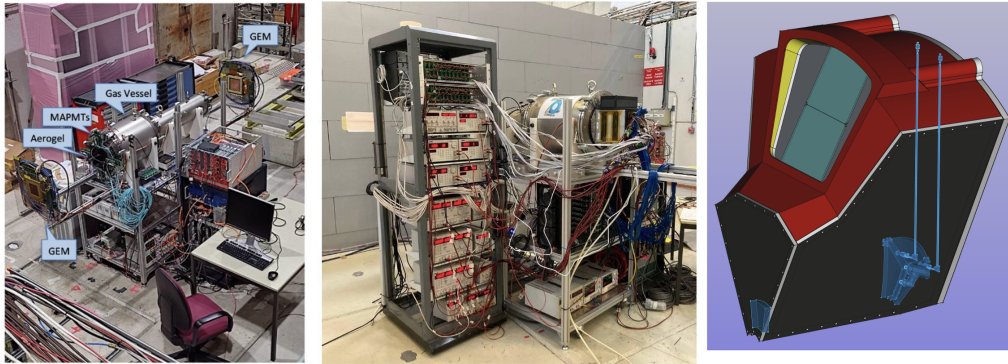


**Figure 8.127:** (Left) Baseline prototype with reference multi-anode PMT sensors at the SPS-H8 beam line of CERN. (Center) First ePIC-drive SiPM detector box under test at the PS-T10 beam line of CERN. (Right) Real-scale prototype model mimicking the basic dRICH construction unit (sector).

**Prototyping.** A baseline prototype has evolved in time to serve the dRICH R&D development for few years, see left panel of Figure 8.127. The gas vessel is a cylinder made of vacuum standards, to allow an efficient and safe gas exchange. The entrance flange can mount an external dark box separated from the inner gas volume by a UV-transparent lucite foil (or quartz window). An aerogel tile with possible additional UV filters, plus an array of alternative sensors and readout electronics, can be inserted into the dark box. Two mirrors inside the vessel have optimized focal lengths to image the Cherenkov light from the two radiators onto the limited active surface. The major achievements obtained during several test-beams have been the validation of the dual-radiator concept, the validation of the  $\text{C}_2\text{F}_6$  gas radiator (see left panel of Figure 8.128), the optimization of the aerogel refractive index (see central panel of Figure 8.128), the performance study of the SiPM-ALCOR readout chain (see right panel of Figure 8.128), and the development of an EIC-driven readout plane. A partially equipped EIC-driven plane has been realized in time for the October '23 test-beam with Hamamatsu S13360-3050 SiPM sensors of standard  $50 \mu\text{m}$  pixel pitch, see left panel of Figure 8.129. The plane has been complemented for the test-beam in May 2024 with sensors of  $75 \mu\text{m}$  pixel pitch, to verify the potential benefit in timing and photon detection efficiency.



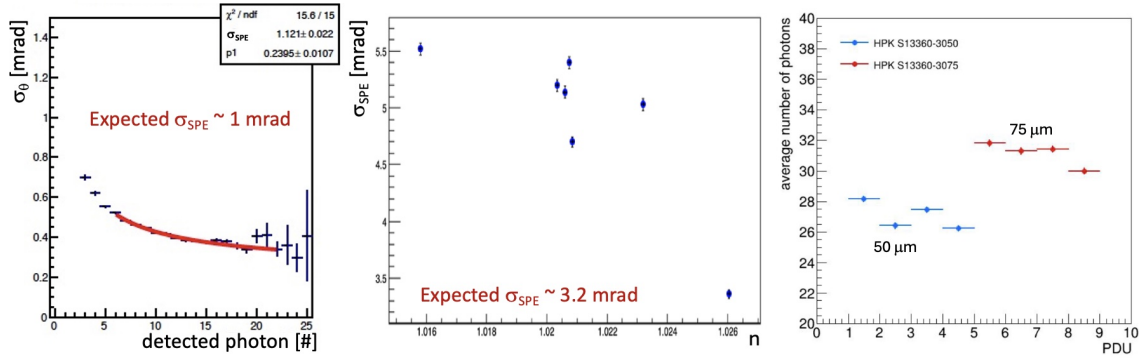


**Figure 8.128:** (Left) Cherenkov angular resolution obtained for  $\text{C}_2\text{F}_6$  as a function of the recorded number of photons. The SPE values is consistent with expectations. (Center) SPE angular resolution measured on aerogel as a function of the refractive index. The expected resolution is obtained for an index greater than  $n=1.025$ . (Right) Comparison in photon yield of sensor with different SPAD size. All the measurements has been obtained with the dRICH prototype.

This has allowed for the first time a full ring coverage, an essential requirement for precise radiator performance study and effective signal over background study, see central panel of Figure 8.129. An effective interplay between the two radiators at intermediate energies has been demonstrated, see right panel of Figure 8.129. The new detector box has allowed a preliminary study of the thermal gradients and possible effects on the gas performance, indicating that the possible temperature gradient of few degrees induced into the gas volume by the cool sensor plane can be largely mitigated by a gas re-circulation or by a double window.

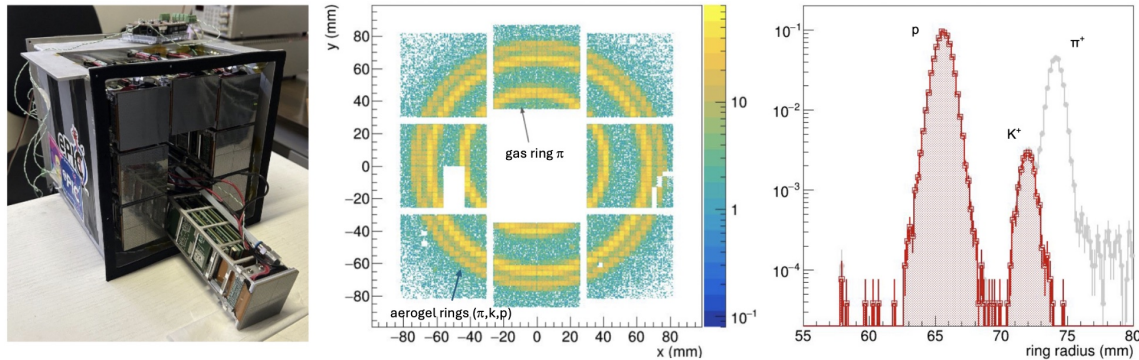


**Figure 8.129:** (Left) Prototype PDU and assembled detector plane. (Center) Cumulated ring imaging for a mixed hadron beam at 10 GeV/c. (Right) Dual-radiator interplay at 10 GeV/c: After the gas information is used to tag pions (clear histogram), an effective separation between kaon and proton is provided by the aerogel (shaded histogram).

**E&D status and outlook:** The study of SiPM performance continues with irradiation cycles of different particle type and more and more optimized annealing protocols to achieve the best PDE and time resolution preservation. A new version of the ALCOR ASIC has been designed to extend the number of channels to 64 and integrate the chip inside a BGA package with a tape-out in the first months of 2025. The design of the final version of the SiPM carrier, FEB and master-logic boards will be completed in 2025. For the radiator gas, it is required

to complete the design of the gas system and finalize the layout of the monitoring equipment. A dedicated system will be developed to measure the gas transparency in the visible wavelength range. The remaining E&D activity is expected to be completed by the end of 2026. An increase of the aerogel tile volume is instrumental to minimize the edge effects and contain the cost. During the R&D phase, tiles with side up to 15 cm and thickness up to 2 cm were realized. A feasibility study is ongoing to increase these limits towards a side of 20 cm or a thickness of 3 cm to maximize the photon yield. The aerogel production efficiency should be evaluated in conjunction with the optical quality and precise shaping obtained. This engineering work is expected to take time and not be completed before the end of 2026. Coating of the CFRP mirror substrate should be realized and compare with the benchmark performance obtained with the similar materials at CLAS12. This work will be completed by fall 2025. A real-scale prototype is being realized with composite materials and a realistic geometry (mimicking a dRICH sector). This is instrumental to validate the mechanical elements and study the assembling details (e.g. of transparent septa), the mechanical stability, the gas tightness, and the thermal aspects. One of the major goals of the real-scale prototype is also to reproduce the final ePIC working conditions, mount an extended readout plane with the designed RDO board, operate demonstrators of the optical components as results of the ongoing developments, and optimize the performance in a realistic off-axis optics configuration. To this end, a commissioning test-beam is planned for fall 2025 and a performance test-beam in spring 2026.

Other activity needed for the design completion:

Slow control, interlock and the calibration LED/laser system design is planned to start in 2026.

Status of maturity of the subsystem:

The R&D activity has been focused on the most innovative aspects of the detector that present technological challenges. These are the SiPM for single-photon detection in a strong and not-uniform magnetic field, a compact readout electronics to fit into the ePIC envelope and the use of two radiators to extend the momentum reach. The remaining effort is substantial, but is connected to more consolidated technologies, with possibly the only exception of the gas separation system for the peculiar  $C_2F_6$  gas.

### **Environmental, Safety and Health (ES&H) aspects, Quality Assessment (QA), Construction and assembly planning:**

Standard slow-control and interlock procedures will be implemented to control power and cooling while monitoring gas flow, humidity and temperature. The cooling system is complemented by a buffer tank to allow air flow and heat removal from the detector boxes in case of a failure of the recirculating system. Annealing of SiPM will be performed during technical stops and/or during the annual stops of the EIC machine. All the dRICH front-end electronics (FEE) will not be powered, with the exception of a few components needed to monitor and control the annealing operations. An interlock-based system will inhibit the FEE power-supply units during annealing. The circulating thermostat system used to cool the SiPMs will be switched to heating mode to reach a temperature of up to  $T = 100^\circ\text{C}$ . A slow heating ramp of  $< 1^\circ\text{C}/\text{minute}$  will be employed to reduce thermal stress on the system. The dRICH photodetector boxes will be thermally insulated to control heat leaks into neighbouring detectors while performing annealing. It is expected that the inner volume of the detector box can reach a temperature of  $T \lesssim 100^\circ\text{C}$  and will be monitored with temperature sensors. Temperature sensors will be placed on the outside of the photodetector boxes to monitor the external environment. Only a fraction of the dRICH SiPMs will perform annealing at a given time, to limit the total amount of power needs to about 20-40 kW. This is similar to the total power consumption of the FEE during normal operations and the same safety procedures

Component	QA station 1	QA station 2	QA detail and backup	QA Acceptance	In-depth
Aerogel	Temple U.	BNL	INFN-BA	100 %	5%
Gas	BNL		INFN-TS	2 %	2%
Mirror	JLab	Duke U.		100 %	10%
Sensor (SiPM)	INFN CS-SA-CT	INFN-TS	INFN-BO	100 %	1%
Readout	INFN-BO	INFN-FE	INFN-TO	100 %	1%

**Table 8.45:** Planned quality assurance (QA) stations, organized in order to provide redundancy and support specific characterization studies.

apply. Annealing power will be distributed evenly across the dRICH SiPM. In case of a power outage, the annealing current will be promptly removed from the SiPMs and their temperature will promptly drop to the temperature of the thermostat. The latter will eventually slowly cool down. The gas volume is maintained at +1 mbar with respect the atmospheric pressure on the top, with a consequent +5 mbar overpressure defined by the hydrostatic pressure of the radiator gas on the bottom, by means of pressure regulators connected to an UPS station and a two-way bubbler. Hexafluoroethane is non-flammable and it has limited toxicity, when below 1000 ppm level and for short exposure time [95]. In case of a major damage of the supply pipeline or of the vessel itself, 12 m<sup>3</sup> of hexafluoroethane at atmospheric pressure from the vessel ( 0.02% of the hall volume) will mix with the air present in the experimental hall, requiring the implementation of standard ODH procedures. Hexafluoroethane has a high Global Warming Potential (GWP): 12400 for a horizon time of 100 years [96] and it is, therefore, included in the group of GreenHouse Gasses (GHG). Environment protection imposes that such gases are not released in the atmosphere. This is obtained by using them in closed circuits, where leakages are minimized, and by collecting and sending for disposal the fraction of gas purged during circuit filling and gas recovery at the beginning and at the end of an operation period, respectively. Both closed circuit gas circulation and purged gas trapping are characterizing elements of the dRICH radiator gas system design. The maximum expected leakage rate during operation is about 20 m<sup>3</sup> / year assuming six-month operation.

Experience in quality assurance protocols has being gained in parallel with the R&D activity. For each critical component two stations are being organized to provide essential QA and redundancy, with a (third) station able to supports in-deep characterization on samples and serve as backup, see Table 8.45. The QA activity will be supported by workforce from all the dRICH groups. Essential QA parameters will be measured: integrity, refraction index, transparency, dimensions, and planarity of the aerogel; leak rate of the gas system (after completion); refractive index and transparency of the radiator gas (with the monitoring equipment of the gas system); dark count rate and PDE for the sensors; electrical connections, bias levels and data rate for the readout; dimensions, weight, reflectivity and D0 (point-like source image brightness) for the mirrors.

The construction and assembling plan assumes to compress all the necessary tasks in a short time period in between the presently known EIC milestones: start with CD3 (late 2027) and completion 6 months in advance of installation (in October 2032), see Figure 8.130. The 6 months contingency time before installation will be used to perform functionality tests, and complete the services in the experimental hall at IP6. The assembling of 1248 PDUs comprising SiPM sensors and cooling, front-end electronics and RDOs, and their integration with the services inside six detector boxes will be staged over 2 years (mainly 2029 and 2030) by the dRICH DSC in Italy. This organized effort requires a timely procurement, starting with the ALCOR chip (wafer and packaging) followed by sensors, readout electronics, and box mechanics. Cooling infrastructure and DAQ system are expected to run in parallel to the detector box construction and be mainly covered by the EIC Project. First articles of DAQ, power supply and slow control could be used for the initial functionality tests of each single detector box, but the main effort on such services is concentrated on a later stage of the plan during assembling at BNL. The detector boxes will be completed in time to be shipped

to BNL and mounted on the dRICH in the second half of 2031. The dRICH vessel construction, a joint venture of the dRICH DSC and the EIC Project, will start in 2029 in order to be ready for detector assembly mid 2031. Mirror production is expected to take 2 years and is staged as soon as possible, subject to the funding profile of the EIC Project, to reduce the sole source risk. The engineering of the aerogel production is expected to extend beyond the TDR, with the consequent production led by the dRICH DSC not happening before 2029 and lasting for at least 2.5 years. An early procurement of the  $C_2F_6$  gas by the EIC Project is planned in order to reduce the risk of a market price increase. The basic design of the radiator gas system will be completed by the end of 2026 by the dRICH DSC. The executive drawings and the system realization by the EIC Project engineering team supported by adequate technical personnel is expected during years 2029 and 2030. The layout finalization and validation of the monitoring equipment will be completed by the end of 2027, with its realization by the dRICH DSC planned by the end of 2028. This equipment will be interfaced with the gas system in 2029, via synergistic effort between the EIC Project engineering team and the dRICH DSC. This combined group will perform the QA assessment of the gas system in 2030.

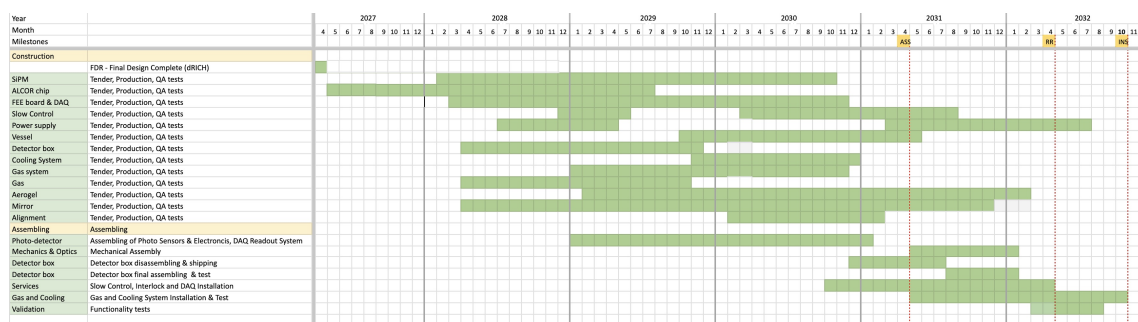


**Figure 8.130: dRICH construction timeline**

5064 **Collaborators and their role, resources and workforce:**

The overview of the collaborating Institutes and their roles in the dRICH activity is presented in Table 8.46. INFN has agreed on a substantial in-kind contribution and the corresponding workforce has taken corresponding responsibilities in the construction within the DSC. The INFN in-kind will cover the design, production and quality assurance cost of the SiPM sensors, of front-end ASIC (ALCOR), of the front-end board (FEB), of the readout boards (RDO) as well as the assembly of the above components in a compact Photo Detector Unit (PDU), including the cooling circuitry and related mechanics. It will cover the cost of the realization of the six detector boxes (containing the 208 PDUs of each sector) with the control panels and the electronic services attached (for HV/LV/daq links routing). It will contribute to the design and realization of the main vessel, the design/supervision of the powering and monitoring systems, the dRICH tagging system and data filtering in streaming mode, see Sec. 8.3.10, and to the definition of specifications and quality assurance (QA) of all the other components and services (i.e. gas, power and cooling plants). Secondments of personnel from all the DSC groups will be organized to support the QA activity in US and the assembling phase at BNL. The EIC Project is expected to cover the procurement effort that can be more efficiently based on US, and all the safety, infrastructural and integration aspect that require specific engineering background. This include the cost of the gas, of the mirrors, of the installation tools, of the power-supply systems, of the cooling plant and the gas plant, and of the FELIX cards receiving the data from the RDO.

Institution	Nation	Main Activity
INFN-FE	Italy	Mechanics, detector box and control panels
INFN-BO	Italy	Photosensors, photodetection unit PDU and readout board RDO
INFN-TO	Italy	ALCOR and front-end board FEB
INFN-BA	Italy	Aerogel radiator
INFN-CS-SA-CT	Italy	SiPM quality assurance
INFN-GE	Italy	dRICH tagger
INFN-LNS	Italy	Mechanical design
INFN-RM1-RM-TV	Italy	Online data reduction
INFN-TS	Italy	Radiator gas, gas system and software, SiPM quality assurance
DUKE-U,	USA	Mirror and mirror characterization
JLab	USA	Mechanical design and mirror characterization
BNL	USA	Mechanical design, integration, infrastructure
Temple U.	USA	Aerogel quality assurance
M.S. Ramaiah U.	India	Simulations and performance study
NISER	India	Performance study
Central U. of Haryana U.	India	Performance study
Central U. of Karnataka U.	India	Performance study

**Table 8.46:** Overview of Institutes and roles in the dRICH activity.

### Technological Challenges and Path Forward:

The dRICH gas radiator is a greenhouse gas with high GWP. A more severe restriction or ban on the usage of hexafluoroethane can result in an increase in cost or difficult procurement. The only alternative option to preserve the dRICH performance would be an eco-friendly gas with a very similar refractive index, an option not available in nature at atmospheric pressure. Argon at  $\approx 3$  bar absolute pressure mimics with great accuracy the hexafluoroethane characteristics. It is also non-expensive, non-toxic and non-flammable. R&D activity has been performed within the EIC generic R&D program and is now pursued within the DRD4 initiative (see below) to establish the validity of this approach. Radiation damage reduces the lifetime of the SiPM as good photodetector for the dRICH performance. Estimates of the radiation level on the dRICH photodetectors are expected to be accurate. The DCR model shown in Figure 8.119 (right) is for the sensors experiencing the largest radiation levels (closer to the beam line) and for detector operation at  $V_{\text{over}} = 4$  V and  $T = -30^\circ\text{C}$ . Operation at lower  $V_{\text{over}} = 3$  V and/or lower temperature  $T = -40^\circ\text{C}$  would reduce the DCR without loss in performance, hence allowing one to accommodate larger integrated radiation levels (up to a factor 2-3) than those reported in the figure. The addition of small thermoelectric cooling (TEC) modules will be evaluated as a potential approach to boost the cooling performance, allowing one to reach an even lower operation temperature of  $T = -50^\circ\text{C}$  and avoid possible dishomogeneities. Current R&D on new SiPM technologies for improved performance and radiation hardness are being followed up as an optimization strategy and as a potential upgrade for the dRICH photodetector in the late 2030's or in the early 2040's. For two components, optical aerogel and carbon-fiber mirror, there is only one known supplier able to deliver the wanted specifications at the present stage. An early procurement should limit the risk of a market discontinuity. Within the ePIC RICH Consortium, the recently initiated R&D on mirrors at Purdue University are being followed up as potential sources of cost mitigation in the long term period, if the adaptation to the dRICH needs will be proven feasible. DSC members are part of the recent DRD4 initiative, that aims to create a worldwide collaborative environment to foster new technological breakthroughs in Cherenkov particle identification and photon detectors. Within DRD4, there are many development areas of interest for the dRICH program, in particular gasses or mixtures alternative to the greenhouse fluorocarbon gasses and radiation hard SiPM.

5113 **8.3.5 Electromagnetic Calorimetry**

5114 Add text here.



### 5115 8.3.5.1 The backward endcap electromagnetic calorimeter

5116 The concept of ePIC places the backward endcap electromagnetic calorimeter inside the central de-  
 5117 tector. The requirements from physics outlined below require a homogeneous scintillator material.  
 5118 The basic requirements on this scintillator material are compactness to minimize the radial thick-  
 5119 ness of the calorimeter, reasonably fast response, and high energy resolution and efficiency over  
 5120 a wide range of energies given by the physics program, and finally adequate radiation hardness.  
 5121 To fulfill these requirements even a compact geometrical design must provide high granularity re-  
 5122 sulting in a relatively large quantity of crystal elements. Their fabrication relies on existing proven  
 5123 technology for mass production to guarantee the necessary homogeneity of the whole calorimeter.  
 5124 Presently there is no alternative material available besides lead tungstate.

### 5125 Requirements

5126 **Requirements from physics:** The electron-end-cap calorimeter (EEEMCal) will cover a dy-  
 5127 namic energy range of 0.5–18 GeV for electromagnetic showers of the scattered electron based on  
 5128 e+p Pythia simulations at  $18 \times 275 \text{ GeV}^2$ . Detection down to 0.1 GeV is needed for decay photons  
 5129 and radiated photons that improve the scattered electron reconstruction. The EEEMCal is a high-  
 5130 resolution ECal designed for precision measurements of the energy of scattered electrons and final-  
 5131 state photons in the electron-going region. The requirements for energy resolution in the backward  
 5132 region is driven by inclusive DIS where precise determination of the scattered electron properties  
 5133 is critical to constrain the event kinematics.

5134 An excellent energy resolution of  $\sigma_E/E \approx (2 - 3)\%/\sqrt{E} \oplus (1 - 2)\%$  is required for the backward  
 5135 endcap electromagnetic calorimeter over a large dynamic range of photon energies [8].

5136 **Requirements from Radiation Hardness:** The EEEMCal detector must operate at a radiation  
 5137 level of  $\sim 3 \text{ krad/year}$  ( $30 \text{ Gy/year}$ ) electromagnetic and  $10^{10} \text{ n/cm}^2$  per year hadronic at the EIC  
 5138 top luminosity.

5139 **Requirements from Particle Fluence** The high-resolution EEEMCal has the following basic  
 5140 requirement: Interaction rate capability up to  $0.5 \times 10^6 \text{ Hz}$  requiring reasonably fast scintillation  
 5141 kinetics.

### 5142 Justification

5143 **Device concept and technological choice:** The EIC physics program requires high-precision  
 5144 detection and identification of the scattered electrons emitted in the electron-going direction, as  
 5145 well as final-state photons. The backward endcap electromagnetic calorimeter (EEEMCal) provides  
 5146 a compact solution with excellent energy resolution over a large dynamic range and with high  
 5147 granularity.

5148 In general, for high-precision electromagnetic calorimetry, the following areas are of relevance:  
 5149 smaller radiation length for smaller longitudinal size, smaller Moliere radius allowing higher gran-  
 5150 ularity, smaller decay time, better energy resolution and larger number of photoelectrons per MeV  
 5151 to reach higher resolution, smaller constant term contribution to energy resolution, mainly due to



Parameter/ Material	Density (g/cm <sup>3</sup> )	Rad. Length (cm)	Molière Radius (cm)	Decay time (ns)	Light Yield (%)	dLY/dT (%/°C)	Rad. Hard. (krad)
NaI(Tl)	3.67	2.59	4.13	245	100	-0.2	1–2
CsI(Tl)	4.51	1.86	3.57	1220	165	0.4	1
CsI	4.51	1.86	3.57	35/6	3.6/1.1	-0.6/-1.4	1
BaF <sub>2</sub>	4.89	2.03	3.1	650/0.9	36/3.4	-1.9/0.1	>50
CeF <sub>3</sub>	6.16	1.70	2.41	30	5	~0.1	>100
(BGO) / Bi <sub>4</sub> Ge <sub>3</sub> O <sub>12</sub>	7.13	1.12	2.23	300	21	-0.9/-1.6	> 1000(recovery)
(PWO-II)/PbWO <sub>4</sub>	8.3	0.89	2	30/10	0.6	-3.0	> 1000
SciGlass	3.7–4.5	2.2–2.8	2–3	20–50	0.3	None	> 1000

Table 8.47: Table of crystal properties.

non-uniformity and gaps or due to readout and noise, reasonable temperature dependence to light yield, and higher radiation hardness.

Lead tungstate meets the requirements of an extremely fast, compact, and radiation hard scintillator material providing sufficient luminescence yield to achieve good energy resolution. We are here referring to a new material labeled PWO-II available since the late 2010's, which provides improved luminescence compared to the PWO as developed for CMS. PWO-II with its increased structural perfection and optimized activation with luminescent impurity centers as well as reduced thermal quenching of the luminescence process meets all the requirements of the EEEMCal. Full size crystals with 200 mm length deliver an average light yield of 18 photoelectrons per MeV (pe/MeV) at 18 degrees Celsius measured with a photomultiplier with bi-alkali photocathode (quantum efficiency ~ 20%).

The specifications are based on a large quantity of full-size crystals and are similar to those achieved with detectors at Jefferson Lab. Detailed specifications as well as a quality control program have been developed, taking into account the experience from CMS, PANDA, and the Jefferson Lab detectors.

The quality crystal can be provided at the moment by the Czech Republic manufacturer Crytur. The only alternative producer SICCAS in China has not yet succeeded producing full size PWO-II crystals.

The EEEMCal meets the experiment requirements of fast timing to handle an interaction rate up to 500 kHz and acceptable radiation hardness. Furthermore, the EEEMCal achieves the required clean electron identification for energies greater than 1 GeV with a rejection factor better than  $10^4$  when combined with other detector subsystems (tracker and pFRICH). The EEEMCal has been reviewed and passed the EIC Project Calorimetry Technical Review on December 2022.

A drawing of the EEEMCal mechanical design is shown in Figure 8.131. The EEEMCal will be located at a distance of 175 cm from the EIC interaction point where it is installed around the beam line in a roughly cylindrical geometry. It will cover a pseudo-rapidity range of  $-3.5 < \eta < -1.5$ . The particles of interest impinge on the front face of the detector and pass through a radiator with adapted geometrical dimensions to contain the major part of the electromagnetic shower. The produced scintillation photons are detected at the back of the radiator by means of an array of Silicon PhotoMultipliers (SiPMs) and their readout electronics. The entire detector is enclosed in a mechanical structure that also provides services such as thermal monitoring, cooling and light monitoring. The entire assembly weighs on the order of three metric tonnes, which is consistent with the specifications of the EIC experimental area at IP6.

Based on extensive simulation and experimental studies, the preferred material for the EEEMCal radiator is lead tungstate (PWO), an extremely fast, compact, and radiation-hard scintillator pro-

Parameter	Unit	EEEMCAL Required	Q&A Inform. Source
Light Yield (LY) at RT (for all sides polished crystals)	pe/MeV	$\geq 15$	Test with $\gamma$ -source
LY(100ns)/LY(1 $\mu$ s)	%	$> 90$	Test with $\gamma$ -source
Longitudinal Transmission at $\lambda = 360$ nm	%	$\geq 35$	Optical Measurement
Longitudinal Transmission at $\lambda = 420$ nm	%	$\geq 60$	Optical Measurement
Longitudinal Transmission at $\lambda = 620$ nm	%	$\geq 70$	Optical Measurement
Transverse Transmission and LY uniformity along crystal	%	10	Optical Measurement
Inhomogeneity of Transverse Transmission $\Delta\lambda$ at T=50%	nm	$\leq 5$	Optic. Measure.
Induced radiation absorption coefficient $\Delta k$ at $\lambda = 420$ nm and RT, for integral dose $> 100$ Gy	$\text{m}^{-1}$	$< 1.5$	Irradiate with different sources
Mean value of $dk$	$\text{m}^{-1}$	$\leq 1.0$	Test
Tolerance in Length	$\mu\text{m}$	$\leq \pm 0, -100$	Measure.
Tolerance in sides	$\mu\text{m}$	$\leq \pm 50$	Measure.
Surface polished, roughness Ra	$\mu\text{m}$	$\leq 0.02$	Vendor
Tolerance in Rectangularity ( $90^\circ$ )	degree	$\leq 0.1$	Measure.
Purity specific (raw material)			Vendor
Mo contamination	ppm	$< 10$	Vendor
La, Y, Nb, Lu contamination	ppm	?	Vendor

Table 8.48: PWO specifications.

5187 viding sufficient luminescence yield (15 - 25 photoelectrons/MeV) to achieve good energy reso-  
 5188 lution. This material has been widely used for high-precision measurements of electromagnetic  
 5189 particles in a variety of experiments, such as at multiple setups at JLAB and also at PANDA/GSI.  
 5190 To achieve good energy resolution including the so-called constant term typically requires 20 or  
 5191 more radiation lengths ( $X_0$ ). For PWO in the EEEMCal we have  $22X_0$  (20 cm). The transverse  
 5192 block dimensions of  $2 \times 2 \text{ cm}^2$  are matched to the Moliere radius to capture the major part of the  
 5193 transverse shower. It has been shown that a PWO calorimeter can achieve an energy resolution  
 5194  $\sigma_E/E \approx 2\%/\sqrt{E} \oplus 1\%$  [97] when all the system parameters are carefully controlled. To pinpoint  
 5195 the electron scattering kinematics, the EEEMCal provides a position resolution of  $\sim 2\text{mm}$  at 1-3  
 5196 GeV. The technology for mass production of PWO crystals that guarantees the needed homogene-  
 5197 ity of the whole calorimeter has been well established with recent experiments, most recently with  
 5198 the Neutral Particle Spectrometer at JLab [98,99].

5199 The relatively low energy threshold for the EEEMCal requires the usage of excellent photodetectors.  
 5200 The magnetic field of the EIC detector precludes the use of conventional photomultipliers. To solve  
 5201 this a photosensor insensitive to magnetic fields and with a small response to ionizing radiation  
 5202 has to be used. Furthermore, the photosensor should have an internal gain as PWO has a relatively

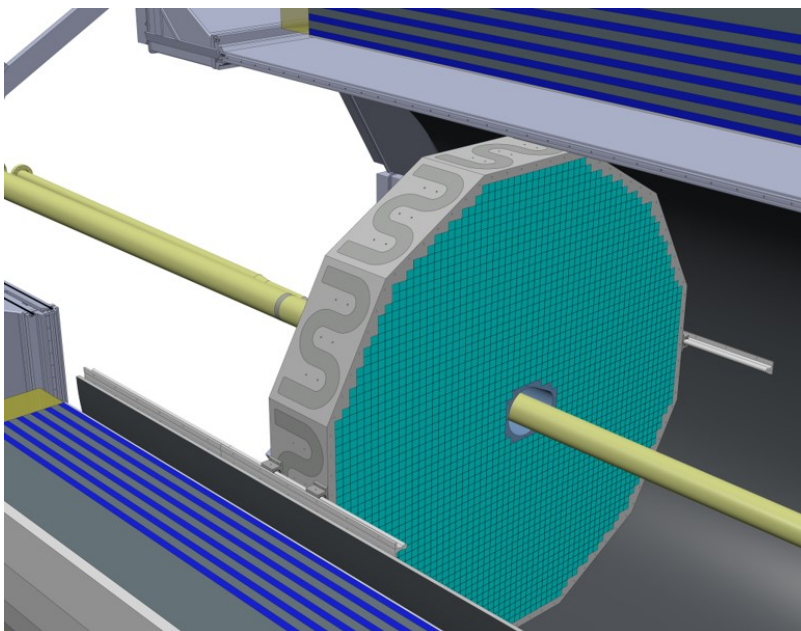


**Figure 8.131:** CAD drawing of the backward ECal attached to the Global Support Tube (GST) by means of rails. The outer structure shows the external cooling using Friction Stir Welding (FST) technology. The shape of the inner support structure is optimized to maximize the pseudo-rapidity coverage around the beam pipes.

low light output.

An effective way to read out the EEEMCal is through SiPMs that offer several advantages, e.g., a high gain and a medium photodetection efficiency of about 30%. Furthermore, SiPMs can be operated in the magnetic field of order few hundred Gauss expected at the location of the EEEMCal. Individual devices are grouped into an array to maximize surface coverage of the PWO blocks. In a recent beam test campaign, the readout concept was validated to work well with a Streaming Readout setup, the method of choice envisioned for the EIC [100].

#### Subsystem description:

General device description: In the EEEMCal the PWO crystals are arranged in the mechanical support structure (Fig. 8.132). This provides the infrastructure to attach the readout components, cooling system, and cables, as well as the installation fixtures to mount the detector in the experimental hall. The support for the crystals is provided by a frame that is installed in the mechanical structure. Photosensors are located at the backend of the crystals, and their photosensors are attached to a grating in the mechanical structure. The crystals are stacked with carbon fiber plates at front and back that allow one to guide the crystal into position. The cooling system provides thermal stabilization, which is important for crystal performance. Based on initial thermal calculations, this stabilization can be achieved with a combination of internal and external cooling aided by airflow.

Radiator: The radiation detectors are composed of lead tungstate scintillating crystals and thin reflector sheets.

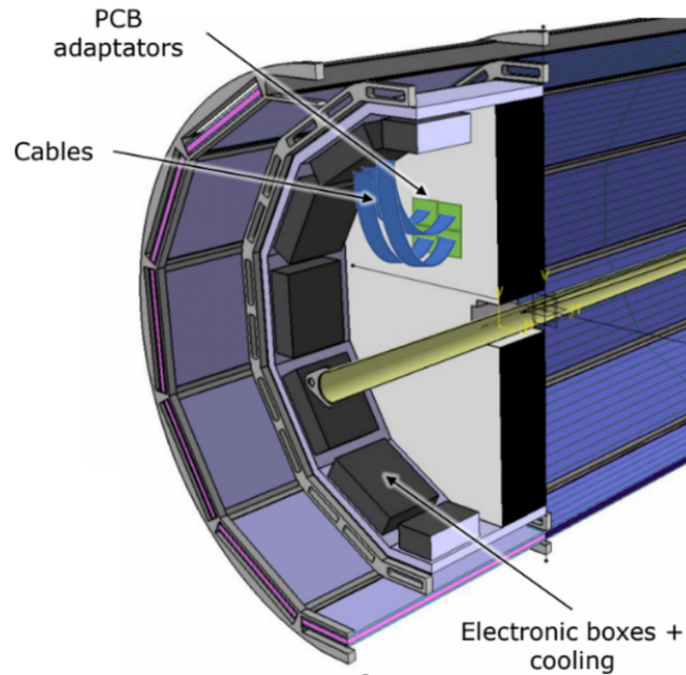


**Figure 8.132:** Conceptual design of the ePIC electron endcap electromagnetic calorimeter support.

Sensors: Hamamatsu S14160-3015 SiPMs have been identified as the optimal choice for the EEEMCal. Their gain of  $3.6 \cdot 10^5$  and relatively low dark current rate (0.7 MHz) allow the measurement of very small signals, close to the single photo-electron (Fig. 8.133, left), while its high pixel density provided by a  $15\text{-}\mu\text{m}$  pixel pitch provides very good linearity over several orders of magnitude (Fig. 8.133, right).

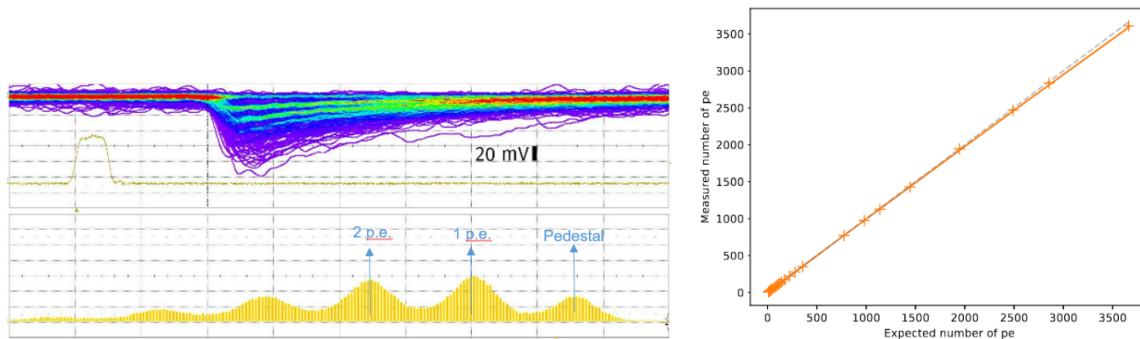


**Figure 8.133:** Left: waveform (top) and integrated signal (bottom) showing single photo-electron signals in Hamamatsu  $15\text{ }\mu\text{m}$  pixel SiPMs. Signals are produced with a low-intensity LED. Right: Linearity measurement, showing 2% linearity up to 3500 photo-electrons.

FEE: All calorimetry in ePIC will use SiPMs for their readout. However, the number of channels and input signals and capacitance varies greatly from detector to detector. The require-

ments of the EEEMCal are particularly stringent in terms of energy resolution, which in particular requires the detection of low energy signals (down to 5 MeV per crystal). The readout should provide sufficient dynamic range to accommodate for signals of energy up to 18 GeV.

A discrete readout solution based on commercial devices is currently the baseline for the forward and backward ECals. However, a readout based on the existing H2GCROCv3 chip (developed for the CMS HGCal) is currently under investigation for the backward ECal. It presents many advantages, in addition to exploiting the synergies with most of the other calorimeters in ePIC. Using an ASIC in the readout of the calorimeter is a very cost effective, more radiation tolerant and cooler (i.e. consuming less power) solution. The H2GCROCv3 chip was developed by the Omega group for the primary use for the High Granularity Calorimeter (HGCal) for the CMS detector at LHC, making it a great fit for any calorimeter readout. The ASIC requirements for the EEEMCal are very low noise level, low power consumption and very good ( $< 1\%$ ) linearity throughout a very large dynamic range. The chip also has a current conveyor where each channel's bias voltage can be fine-tuned from the ASIC itself. A variation of the H2GCROCv3 chip (CALOROC) is currently under development by OMEGA in order to make it compatible with EIC.

A particular challenge for the EEEMCal (which is common for any readout solution) is the high capacitance of the photosensors (530 pF per SiPM; 8.5 nF if all 16 SiPM of a crystal are read in parallel). If we require to readout each SiPM individually in order to meet the energy resolution and time response of the detector, the number of readout channels for the EEEMCal will be  $\sim 48,000$ .

LED monitoring system: the individual response of each calorimeter channel will be monitored using a dedicated LED light source integrated onto the PCB and positioned adjacent to the SiPM matrix of each crystal (see Fig. 8.134). These LEDs will provide a controlled light pulse that enables continuous monitoring of the channel gain and stability over time. By tracking the LED-induced signal over time, it is possible to detect and correct for variations due to temperature changes, radiation damage, or electronic drift. An effort is ongoing to identify an LED model that is radiation-hard and suitable for this purpose.

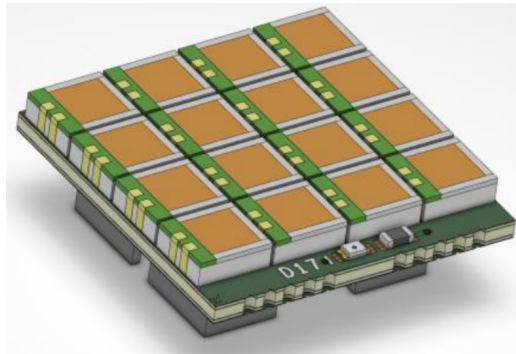


**Figure 8.134:** PCB holding the 16 SiPMs of a PWO-II crystal. An SMC LED is mounted on each PCB (the white component centered at the bottom of the board in this figure).

**Performance** Our group has performed extensive simulations of the detector performance in the ePIC geometry, including a realistic material budget in front of the detector, which directly affects its resolution and PID capabilities. Figure 8.135 shows the performance of two key parameters: the energy resolution and the pion rejection factor. For this resolution result, a conservative, energy-independent 2% smearing was applied on the simulated deposited energy values to account for



effects of digitization and randomness of the optical photon yield. Results fulfill the physics requirements as outlined in the Yellow Report [8] and NAS study [11].

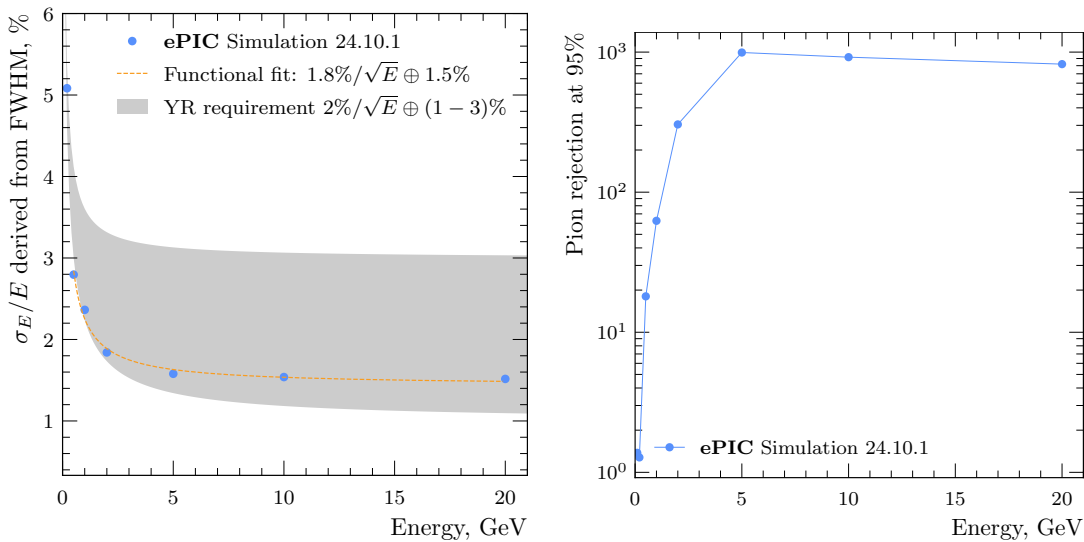


**Figure 8.135:** EEEMCal performance estimated from single particle simulations using the full ePIC detector geometry. Left: energy resolution as a function of the incident particle energy. Right: pion rejection factor as a function of energy and different values of electron efficiency. (Performance plots were produced by the [backwards.ecal](#) benchmark)

**Implementation** The EEEMCal project has been organized into a well-defined Work Breakdown Structure (WBS). The WBS contains the work necessary to complete the project scope and will form the basis of planning, executing, and controlling project activities. The WBS ensures that no portions of the estimate are omitted. The level of the WBS reflect a logical breakdown of the work by major system as shown in Table 8.49.

The EIC-DOE project dictates the window of installation of the EEEMCal. The EEEMCal assembly at BNL and full system cosmic tests are projected for 2029-2030. Installation in the ePIC detector is currently projected to be in the calendar year 2031.

**Services:**  $\text{PbWO}_4$  crystals are sensitive to temperature changes with a variation of  $2\%/^{\circ}\text{C}$  in light output. Thus, the specification is to keep the crystal temperature stable within  $\pm 0.1^{\circ}\text{C}$ . Temperature control is also needed for SiPMs, whose response is sensitive to temperature as well. To ensure temperature stability the additional heat generated by the electronics needs to be removed and the following cooling structures are being considered. As internal cooling structure several machined copper blocks with internal coolant circulation will be used around the beam pipe. To reduce the spatial extend support structures the EEEMCal consortium is moreover planning to use cooling plates in between the readout cables which are linked to the support structure surrounding the EEMC with tubes. This system is composed of 12 plates with a 5-8 mm spacing in which water can be circulated. The cooling near the crystals will likely not be enough to meet specification. These challenges could be overcome by outside cooling with standard cooling blocks with airflow in front of the electronics or additional cooling added at the back of the assembly.

ANSYS simulations are being performed to quantify the efficiency and guide the design of the

WBS	WBS Title	WBS description
2.00	EEEMCAL Project	Construct the EEEMCAL. The EEEMCAL is an electromagnetic calorimeter for measurement of the inclusive process physics in the electron-going direction at the EIC
2.01	Radiator	Radiation detectors consisting of scintillating crystals (PWO) and thin reflector sheets. These provide the detection of energetic electrons
2.02	Photosensor	Photosensors consisting of multi-pixel photon counters grouped into an array to maximize surface coverage of the PWO blocks.
2.03	Mechanical	Mechanical structure including installation fixtures and a cooling system providing thermal stabilization, which is important for crystal performance.
2.04	Signal Processing/DAQ	Signal Processing/DAQ providing the front-end electronics to transmit the signals to the data analysis modules
2.05	Simulation/Software	Simulations/Software providing the software libraries and infrastructure foundation for extracting the physics from the detector

Table 8.49: EEEMCAL WBS Structure

cooling system. Figure 8.136 show the temperature distribution of crystals in stationary state with room tempertaure at 26° C and cooling plates at 19° C assuming a uniform heat source of 1 kW behind the crystal, corresponding the current estimate of the FEBs power dissipation.

Steady-state simulation at different room temperatures have been performed to quantify the effect of the temperature fluctuation in IP6. Figure 8.137 shows the effect of a 3° C variation. Results of transient-state simulations are shown in Fig. 8.138 and demonstrate that crystal temperatures will remain within  $\pm 0.1^\circ$  C with the expected FEB power dissipation of FEBs and typical room temperature variations in IP6. This has also been confirmed experimentally by a recent and similar cooling-concept calorimeter built and operated by the EEEMCal consortium: the NPS calorimeter at JLab consisting of 1080 PWO crystals with readout electronics dissipating 500 W. Figure 8.139 show the crystal temperature variation within  $\pm 0.1^\circ$  C during a 24-hour period.

**Subsystem mechanics and integration:** The EEEMCal installation fixtures are shown in Fig. 8.140. They include a mechanical structure that mounts the detector and positions it in the EIC experimental hall at the appropriate height above ground. The structure is envisioned to ride on rails for the installation. The rails could be on the floor as shown, but could also be within the cylindrical structure. In the latter case the outer structure would be bolted to the floor. Having the rails extend from the cylindrical structure has the advantage that it would not require rails on the floor of the experimental hall, which could interfere with other hall infrastructure, e.g., the magnet.

**Calibration, alignment and monitoring:** To achieve the required energy and spatial resolution of the electromagnetic calorimeter it is essential to precisely calibrate the individual crystal



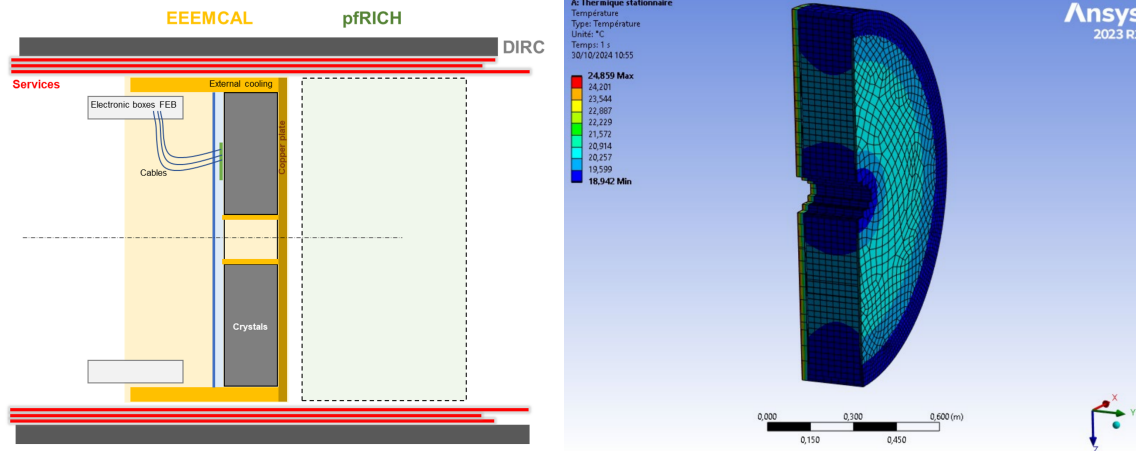


**Figure 8.136:** Left: Layout of the EEEMCal subsystem showing the external and internal cooling plates (yellow), a front copper plate, and some insulating barrier (blue) between the crystals and the heat source (FEBs, inside cooled boxes). Right: Simulated temperature distribution of crystals in stationary mode with plates at 19° C and room temperature of 26° C. A uniform heat source of 1 kW is assumed behind the crystals.

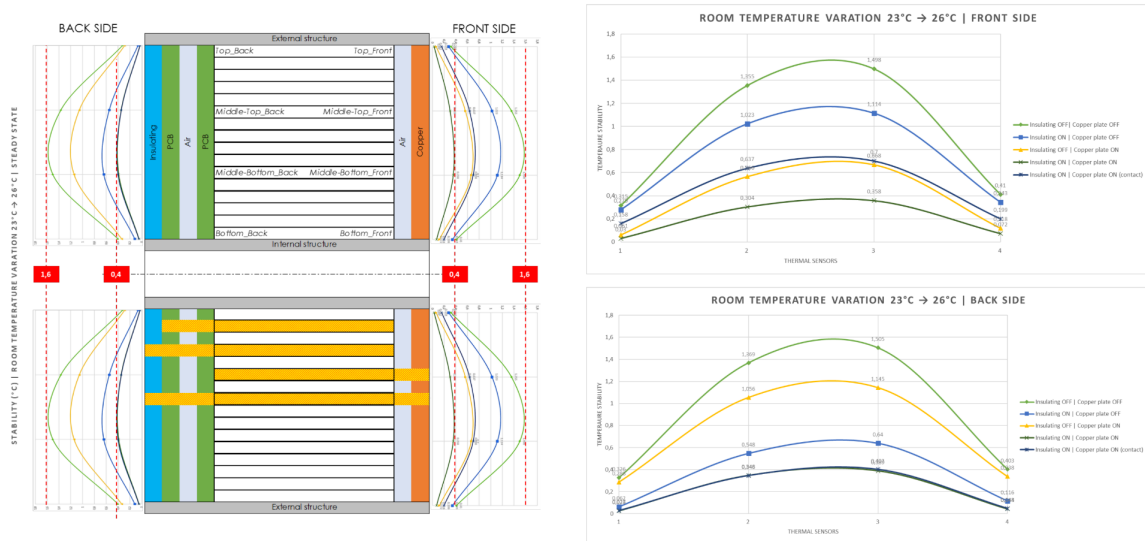


**Figure 8.137:** Steady-state simulation at 2 different room temperatures. Data show the temperature difference across the detector for different configurations of the cooling system. The nominal configuration (dark green) shows the best performance and yields a maximum temperature variation of 0.4° C in the central crystals.

channels. Time dependent variations of the calibration factors are expected due to several effects: change in light transmission, change in the coupling between the crystal and the photodetectors and variations in the photodetectors itself and the following electronics. Both the scintillation of the crystals and the amplification of the SiPMs depend on the temperature. Therefore stable cooling at the level of 0.1 degrees Celsius is required. Long term variations in the temperature need to

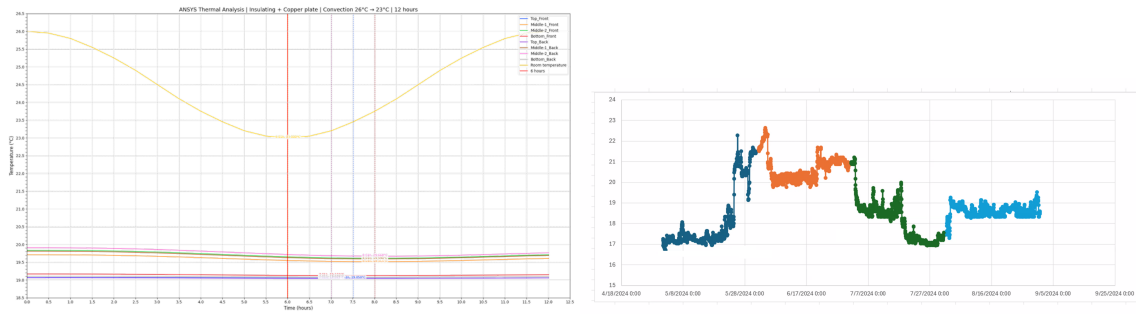


**Figure 8.138:** Left: Transient-state simulation showing the temperature variation of crystals as a function of time for a room temperature variation from  $26^{\circ}\text{C}$  to  $23^{\circ}\text{C}$  in 6 hours. The thermal inertia of crystals is sufficiently high that the temperature variation of all of them is below  $0.1^{\circ}\text{C}$ . Right: typical temperature variations in IP6 as measured by the STAR experiment. Temperature is constant within  $\pm 1.5^{\circ}\text{C}$  within a few hours.

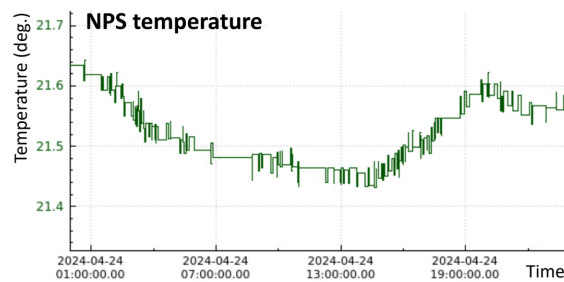


**Figure 8.139:** Temperature variation of PWO crystals measured in the NPS calorimeter, consisting of 1080 PWO crystals and 500 W FEBs. The cooling concept used for this detector is similar to the one planned for the ePIC backward ECal, and shows that the required crystal temperature stability is achieved.

5311 be tracked by the calibration. Given an energy resolution between 1% and 2% at energies above 1  
 5312 GeV, the precision of the calibration needs to be at the sub-percent level. For the calibration several  
 5313 methods performed in stages are planned: 1) Precalibration at test beams and with cosmic muons  
 5314 at the level of 10%, 2) In situ calibration with physics events (neutral mesons and electrons), 3)  
 5315 Continuous monitoring with a light-pulsar system

#### 5316 Status and remaining design effort:

5317 R&D effort: there are no ongoing R&D efforts for the EEEMCal.

5318 E&D status and outlook: there are no ongoing efforts regarding the overall design choices.  
 5319 Ongoing activities relate to the integration and eventual impact on the design.

5320 Other activity needed for the design completion: the test of engineering articles is required  
 5321 for the final choice of the readout electronics chain. Beam test campaigns are being prepared  
 5322 to address this.

5323 Status of maturity of the subsystem: The EEEMCal subsystem is mature.

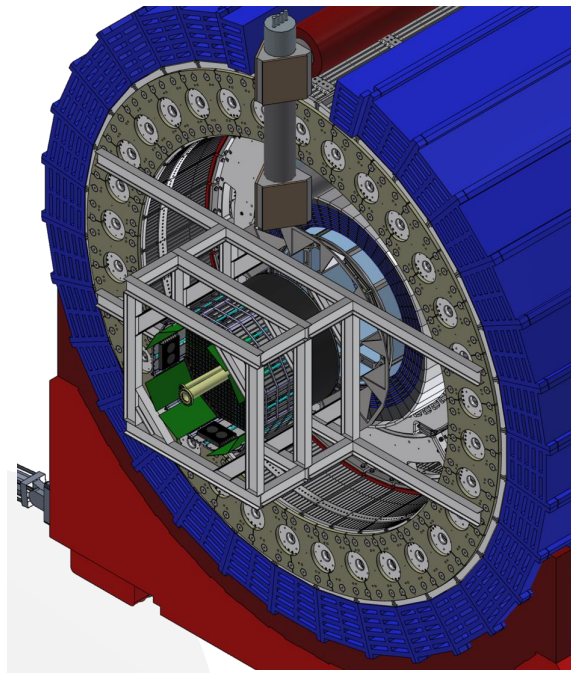


**Figure 8.140:** EEEMCal installation fixtures that allow for installing the detector safely into the ePIC detector barrel.

5324 **Environmental, Safety and Health (ES&H) aspects and Quality Assessment (QA), Con-**  
 5325 **struction and assembly planning** Quality Assurance (QA) is an integral part of effective  
 5326 project management and will be employed throughout the design, procurement, and construction  
 5327 of the project. An EEEMCal Project-specific Quality Assurance Plan has been developed to estab-  
 5328 lish all applicable QA requirements for the design, construction, and operation of the EEEMCal,  
 5329 consistent with the EIC Quality Assurance Plan that implements the ten criteria defined in DOE  
 5330 Order 414.1D.

5331 Upon completion of its construction and initial testing, the EEEMCal will be situated at BNL. The  
 5332 EEEMCal collaboration leaders will coordinate the required equipment readiness for experiment  
 5333 and final integration of the EEEMCal into the EIC beamline with the EIC Project Management,  
 5334 the ePIC collaboration, and the BNL and JLAB Technical leads. This is necessary for successful  
 5335 integration. For example, a special external support frame will be provided, installed, and surveyed  
 5336 by the BNL technical staff for this purpose. All installations and the integration of the EEEMCal  
 5337 will be handled by BNL technical staff with expert's assistance to ensure appropriate interfacing of  
 5338 infrastructure and fulfillment of installation and operation protocols.

5339 Once installed in the EIC experimental hall the EEEMCal will be operated and maintained by the  
 5340 EEEMCal team and its stakeholders in collaboration with technical teams at BNL. The normal oper-  
 5341 ating resources will be provided by BNL. The physics resources to operate and maintain the EEEM-  
 5342 Cal will be provided through research grants. These resources are critical for tasks that are not  
 5343 directly related to the construction of the calorimeter, but instead to the integration of the EEEM-  
 5344 Cal into the ePIC detector. Examples include developing readout software and trigger algorithms,  
 5345 implementing online GUIs and the slow controls interfaces required to operate and monitor the  
 5346 detector during data taking, as well as designing clustering algorithms and calibration tools and  
 5347 integrating them into the ePIC workflow.

5348 **Collaborators and their role, resources and workforce:** The participating institutions are  
 5349 briefly described and characterized by their expertise gathered in previous or ongoing research  
 5350 activities.

5351 AANL (H. Mkrtchyan): the group has long-standing experience in constructing calorimeters and  
 5352 evaluating scintillating materials for different projects. For example, the group has built the lead  
 5353 glass based HMS and SHMS electromagnetic calorimeters in Hall C at Jefferson Lab.

5354 ACU (L. Isenhower): the group has long standing experience with electronic signal digitization  
 5355 and readout systems.

5356 Augustana (N. Grau)

5357 Charles U./Prague (M. Finger): the group has long-standing expertise evaluating lead tungstate  
 5358 crystals for different projects.

5359 CUA (T. Horn): the group has longstanding experience in crystal calorimetry. It has been leading  
 5360 the construction of the Neutral Particle Spectrometer at Jefferson Lab. In collaboration with Giessen  
 5361 U. the group contributed in the development of PWO-II

5362 FIU (H. Szumila): the group has long-standing experience in running experiments at Jefferson  
 5363 Lab with focusing spectrometers and a variety of detectors including calorimeters. The group has  
 5364 experience with electronic signal digitization and readout systems.

5365 JMU (I. Niculescu): The group has long-standing experience in the application of scintillation de-  
 5366 tectors and photo sensors.

5367 Kentucky (R. Fatemi): the group has longstanding experience in experiments and detector con-  
 5368 struction at STAR. The group is leading simulation and software development efforts at the EIC.

5369 Lehigh (R. Reed): the group performs research at BNL and has experience in detector construction  
 5370 and studies of photo sensors and readout systems.

5371 MIT (R. Milner): the group has long-standing experience mounting large experiments and detector  
 5372 mechanical design and construction. The group has experience in response studies of scintillators  
 5373 using electron accelerators.

5374 Orsay (C. Munoz-Camacho): the group has long-standing experience in mechanical and electronics  
 5375 engineering and the construction of large-scale detector systems. The group has played a leading  
 5376 role in the construction of the NPS.

5377 LLR (M. Nguyen): the group has long-standing experience with readout electronics. The group  
 5378 has been strongly involved with the EMCal of CMS and, more recently, with the high granularity  
 5379 calorimeter upgrade for Phase-2 of the LHC.

5380 OU (J. Roche, J. Frantz): the group's expertise covers many aspects of electromagnetic calorimeters,  
 5381 photo sensors, and readout systems.

5382 W&M (C. Fanelli): the group has major experience in AI-assisted optimization of detector systems.

5383 **Technological Challenges and Path Forward** Radiation exposure over time will induce dam-  
 5384 age in the SiPMs used for the backward ECal, leading to an increase in their dark current and asso-  
 5385 ciated dark rates. As dark rates rise, affected channels may begin to trigger more frequently, and in  
 5386 extreme cases, almost continuously, resulting in excessive data rates and potential degradation of  
 5387 overall detector performance. To mitigate this, it will become necessary to raise the discriminator  
 5388 thresholds for the noisiest channels, particularly those located at very high pseudo-rapidity, closer

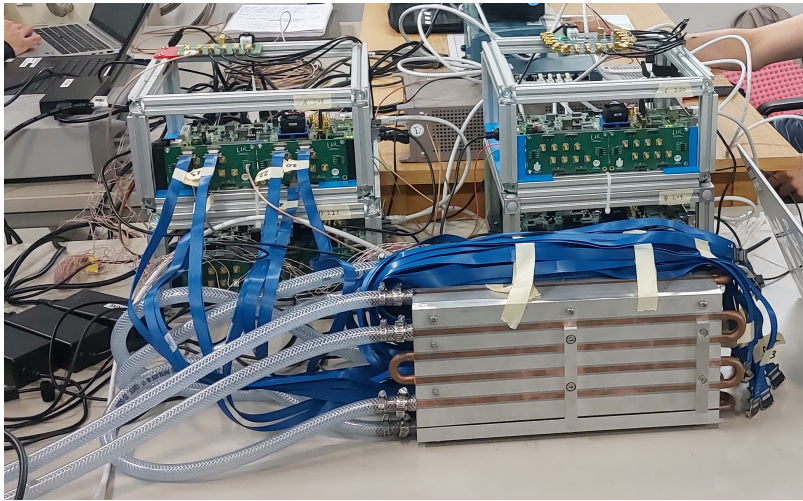


**Figure 8.141:** Backward ECAL  $5 \times 5$  crystal prototype and full readout 400-channel electronic chain based on the HGCROC chip.

5389 to the beam pipe, where radiation levels are highest.

5390 We are also evaluating the impact of such threshold increases on the physics performance of the  
 5391 calorimeter. Raising thresholds can reduce sensitivity to low-energy deposits and may introduce  
 5392 non-uniformities in the detector response, which could affect energy resolution and reconstruction  
 5393 efficiency in certain regions. Quantifying these effects is essential to ensure that physics goals can  
 5394 still be met as radiation damage accumulates.

5395 To inform our mitigation strategy, studies are currently underway combining irradiation cam-  
 5396 paigns on SiPM prototypes with simulations of trigger behavior as a function of dark current. These  
 5397 efforts aim to determine when performance degradation becomes significant and which channels  
 5398 are most vulnerable.

5399 In the long term, the backward ECal has been designed with a modular architecture that enables  
 5400 targeted maintenance. Individual SiPMs can be accessed and replaced during scheduled shut-  
 5401 downs of the ePIC detector, allowing for restoration of performance in the most affected regions  
 5402 and ensuring the longevity and reliability of the calorimeter system.

5403 **Additional Material: prototype and beam tests** After validation of the choice of scintillat-  
 5404 ing material (PWO) and photosensor (Hamamatsu S14160-1315), a  $5 \times 5$  prototype (Fig. 8.141) has  
 5405 been designed and built at IJCLab in order to test the full readout chain in a realistic experimental  
 5406 environment. It includes cooling plates to maintain crystals at constant temperature ( $\pm 0.1^\circ \text{C}$ ).

5407 The readout chain is based on a protoboard developed within the EIC project R&D (eRD109) by  
 5408 the ORNL (Oak Ridge National Lab) group, driven by a Xilinx KCU105 board. The interface board  
 5409 between the ORNL board and the SiPMs was designed at LLR. It has been tested with LED sig-  
 5410 nals injected into the crystals and more recently at CERN with electrons in the T09 line of the PS  
 5411 (see Figure 17). Figure 8.142 shows the waveforms of the 16 SiPM of a crystal as readout by the  
 5412 H2GCROCv3 chip. Signals show a rise time of 25-50 ns and a fall time of  $\sim 100$  ns (the scintillating  
 5413 PWO signal typically has a rise time of 20 ns with a fall time of  $\sim 50$  ns).

5414 Additional beam tests were performed at DESY in 2025 and are currently under analysis.

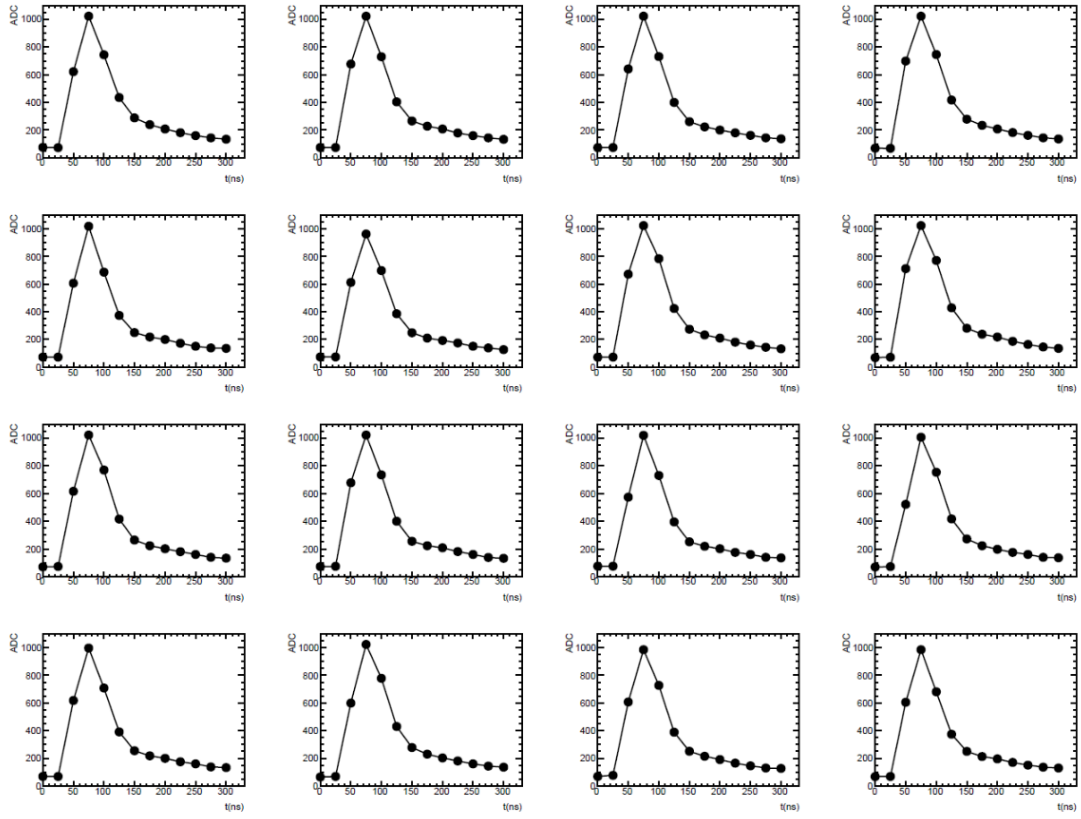


**Figure 8.142:** Waveforms for a 5-GeV electron in the 16 SiPM of a PWO crystal



### 8.3.5.2 The barrel electromagnetic calorimeter

#### Requirements

**Physics requirements:** The Barrel Electromagnetic Calorimeter (BEMC) must meet the following physics requirements: It needs to identify scattered electrons and measure their energy, particularly in high  $Q^2$  events, and also detect decay electrons from vector or heavy flavor meson decays, and DVCS photons. Electron identification, including electron-pion separation, is required up to 50 GeV and down to 1 GeV, with an energy resolution better than  $10\%/\sqrt{E} \oplus (2-3)\%$ . Additionally, the BEMC must provide photon reconstruction from 100 MeV to 10 GeV. The system must also achieve photon-pion discrimination ( $\gamma/\pi^0$  separation) up to 10 GeV, with the ability to distinguish two showers with an opening angle down to 30 mrad. Furthermore, the BEMC will assist with muon identification and provide a charged tracking point behind the DIRC to help with charged hadron PID, with a spatial resolution of less than 150  $\mu\text{m}$ . Lastly, the system must have sufficient dynamic range to detect MIP signals, such as those from muons.

**Radiation hardness requirements:** The BEMC must be designed to operate in an environment where it may experience radiation levels of up to approximately  $3.2 \times 10^9$  1-MeV neutron equivalent per  $\text{cm}^2$  over the first 15 years of running (corresponding to  $140 \text{ fb}^{-1}$ ), and ionizing doses of less than 1 krad over the BEMC's lifetime.

All components, including sensors, electronics, and structural materials, must be sufficiently radiation-hardened to maintain performance under these conditions. This includes ensuring that the sensor response, energy resolution, and position reconstruction capabilities remain stable throughout the detector's operational lifetime.

**Data rate requirements:** The BEMC and its readout technology must be designed to handle the high event rates expected at full luminosity, ensuring stable performance under expected background conditions, including radiation doses and neutron flux. The system must provide sufficient timing resolution to accurately discriminate between different bunch crossings, ensuring precise event separation. The chosen detector and readout technologies must be capable of processing the high data rates without compromising performance or data integrity. Furthermore, noise levels in the combined detector/readout system need to be low enough to enable detection of MIPs. The expected rates in the detector are presented under [Performance](#) and [Readout Electronics and Data Acquisition](#).

#### Justification

**Device concept and technological choice:** The ePIC BEMC is called the Barrel Imaging Calorimeter (BIC). The BIC combines two proven technologies to meet the stringent requirements of the EIC physics program: The first is a lead-scintillating fiber (Pb/ScFi) sampling calorimeter read out with SiPMs, providing robust energy measurement through light collection, based on the well-established GlueX Barrel Calorimeter (BCAL) design [101]. This technology offers a reliable solution for high-resolution energy measurements, benefiting from its extensive use in other experiments. The second is a silicon tracker using AstroPix [102, 103] sensors, monolithic active pixel sensors (MAPS) based on HV-CMOS technology, interleaved with the Pb/ScFi layers to provide precise 3D imaging of calorimeter shower development. This hybrid approach delivers excellent



spatial resolution and position reconstruction, essential for separating particle showers and achieving accurate photon and electron identification, while preserving the superior energy performance of sampling calorimetry. The AstroPix sensors, developed for the NASA space mission AMEGO-X, offer low power consumption, radiation tolerance, cost-effectiveness, and scalability, making them ideal for large-area applications in a high-radiation environment. We selected the combination of Pb/ScFi for energy resolution and AstroPix for spatial resolution to balance performance, cost-effectiveness, and long-term reliability under the expected operational conditions at the EIC.

**Subsystem description:** The Barrel Imaging Calorimeter has a cylindrical geometry consisting of 48 trapezoidal sectors, with End-of-Sector Boxes (ESBs) at each end for services and readout, including the SiPMs for two-ended readout of the scintillating fibers and electronics front end boards. The trapezoidal sectors are fully active, with no dead areas of the Pb/ScFi matrix at their boundaries. This design allows the sectors to maintain a simple trapezoidal shape, projective to the solenoid axis, without requiring a tilt. The calorimeter spans approximately 17.1 radiation lengths ( $X_0$ ) at central pseudorapidity, with the first layer consisting of an AstroPix imaging layer that provides a tracking point behind the DIRC. Each sector has six slots for AstroPix imaging layers, separated by about  $1.43 X_0$  of Pb/ScFi at  $\eta = 0$ . In the baseline configuration, slots 1, 3, 4, and 6—counting radially outward—are filled with AstroPix sensors, while slots 2 and 5 are designated for future upgrades. Figure 8.143 presents the overall structure of BIC and its sectors and Figure 8.144 shows the imaging AstroPix layers components. A sketch of the mechanical envelopes of the ESB is presented in Figure 8.145. Table 8.50 summarizes the main BIC detector parameters and Table 8.51 summarizes the structure of AstroPix and Pb/ScFi layers.

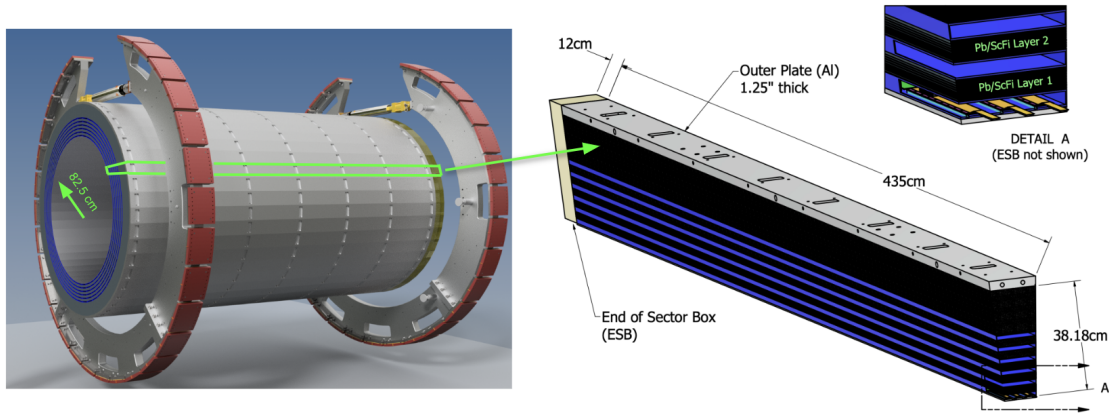


**Figure 8.143:** On the left, a 3D rendering of the Barrel Imaging Calorimeter with its 48 sectors. The central drawing shows the structure of a single sector, featuring interleaved Pb/ScFi layers and slots for trays holding AstroPix chips, followed by the Pb/ScFi bulk section. On the right, a zoomed view of the first radially layers is presented.

**Scintillating fibers for Pb/ScFi:** The Pb/ScFi calorimeter system, similar to the GlueX BCAL, has its fibers positioned parallel to the z-direction with 2-sided readout for energy measurement and position reconstruction along the fiber. We will use scintillating fibers with 1 mm diameter embedded in lead and glue to provide reliable energy measurement through light collection. For the scintillating fiber parameters refer to Table 8.54.

**Sensors for Pb/ScFi:** The light from the scintillating fibers is subdivided into 12 rows of 5 columns per sector-end by light guides, which are optically coupled with silicon rubber



5492 chained AstroPix sensors are glued on a base plate and read out on a flexible PCB to form a  
 5493 module, providing high-resolution spatial information for 3D imaging and particle identifi-  
 5494 cation. For the AstroPix chip parameters refer to Table 8.52.

5495 **Staves and trays:** Each stave is formed by daisy-chaining 12 AstroPix modules. A tray holds  
 5496 6–7 staves based on the (radial) layer position, with each tray being half of the sector length  
 5497 and read out at its respective end in the ESB. This modular structure allows for flexible scaling  
 5498 and future upgrades to the system.

5499 **End-of-Tray Card (ETC):** The ETC functions as the RDO unit in the ePIC DAQ scheme (see  
 5500 also RDO). Each ETC is responsible for a full tray of AstroPix staves. It manages signal pro-  
 5501 cessing, data formatting, and communication with the DAM, ensuring efficient and reliable  
 5502 data flow from the sensors. Note that within the module-stave-tray design, the ETC commu-  
 5503 nicates directly with each 9-chip module.

Detector parameters	Value
Active length (z-direction)	435 cm
Inner radius	82.5 cm
Number of sectors	48
$\eta$ coverage	$-1.71 \lesssim \eta \lesssim 1.31$
Radiation length $X_0$	1.45 cm
Total depth in $X_0$	between 17.1 ( $\eta = 0$ ) and 42 ( $\eta = -1.55$ )
Molière radius	4.5 cm
Total sampling fraction of the entire Pb/ScFi system	about 9.5%, see Figure 8.146
Total sampling fraction of the entire AstroPix system	$< 0.4\%$
ScFi diameter	$\varnothing 1$ mm
ScFi radial separation	1.22 mm (between fiber centers)
ScFi azimuthal separation	1.35 mm (between fiber centers)
Light guide length	5 cm
Number of light guides	60 per sector per side
Monitoring system	Blue LED, one LED per light guide
SiPMs	$1.2 \times 1.2$ cm <sup>2</sup> arrays, 50 $\mu$ m pixel
Number of SiPMs	60 arrays per side for each sector
Number of scintillating fibers per sector	about 20k

Table 8.50: Selected BIC Parameters.

5504 **Performance** The BIC design meets the stringent energy and particle separation requirements  
 5505 for the EIC scientific program. We optimized the BIC design and validated its performance through  
 5506 a combination of detector simulations, beam tests, and bench measurements. We analyzed key  
 5507 metrics, including energy resolution, angular resolution, and particle identification, to ensure that  
 5508 the detector meets or exceeds the required specifications. The results presented here highlight the  
 5509 detector’s capabilities and its ability to operate efficiently under EIC conditions. While the BIC may  
 5510 seem to exceed requirements in metrics such as energy and position resolution, this reflects a design

AstroPix layer (radially out)	Number of staves per sector-layer	Number of modules per sector-layer	Number of chips per sector-layer
1	$6 \times 2$	144	1296
2	-	-	-
3	$7 \times 2$	168	1512
4	$7 \times 2$	168	1512
5	-	-	-
6	$7 \times 2$	168	1512

Pb/ScFi layer (radially out)	Number of ScFi sublayers radially	Thickness in $X_0$	Readout channels per sector-layer
1–12	17	about 1.43	$5 \times 2$

**Table 8.51:** AstroPix and Pb/ScFi layer parameters. The first table presents the parameters for the AstroPix layers, while the second table outlines the Pb/ScFi layer configuration. Radially outward, the calorimeter begins with AstroPix layer 1, followed by interleaved Pb/ScFi and AstroPix layers. Beyond AstroPix layer 6, the bulk section of the calorimeter consists of Pb/ScFi layers 6–12.

Parameter	Specification
Pixel size	$500 \mu\text{m} \times 500 \mu\text{m}$
Power usage	$< 2 \text{ mW}/\text{cm}^2$
Energy resolution	10% @ 60 keV
Dynamic range	25–700 keV
Passive material	$< 5\%$ on the active Si area
Design time resolution	3.125 ns
Si Thickness	$500 \mu\text{m}$
Active area per chip	$2 \text{ cm} \times 2 \text{ cm}$

**Table 8.52:** AstroPix chip parameters for BIC.

5511 tailored to meet more demanding performance needs, including electron-pion separation, neutral  
5512 pion-photon separation, and the dynamic range required for detecting MIPs. These challenging  
5513 requirements drive the superior energy resolution and the enhanced position resolution, which are  
5514 critical for reconstructing event topologies where particles are closely spaced.

5515 **Energy resolution:** We estimated the energy resolution of the Pb/ScFi layers based on de-  
5516 tailed simulations in various rapidity ranges and photon/electron energies. Figure 8.146 (a)  
5517 presents the energy resolution for photons, extracted from the Gaussian core of a Crystal  
5518 Ball fit to the expected energy losses in Pb/ScFi. Table 8.55 shows the fitted stochastic and  
5519 constant terms  $a$  and  $b$  of the energy dependence  $\sigma/E = a/\sqrt{E} \oplus b$ . The stochastic term,  
5520 ranging from 5.8% to  $6.6\%/\sqrt{E}$ , and the constant term, between 0.6% and 1.2%, depend-  
5521 ing on rapidity, meet the detector’s energy resolution requirement of better than  $10\%/\sqrt{E}$   
5522  $\oplus 2\text{--}3\%$ . Figure 8.146 (b) shows the sampling fraction, defined as the energy deposited in

Parameter	Specification
Active Area	3 mm x 3 mm (4 x 4 array) Preassembled array covering 1.2cm x 1.2cm
Pixel Size	50 $\mu$ m
Package Type	Surface Mount
Peak Sensitivity	450 nm
PDE	$\sim 50\%$
Gain	$> \sim 2 \times 10^6$
DCR (Dark Count Rate)	Typ.: $\sim 500$ kHz / SiPM Max: $< 1.5$ MHz / SiPM (DCR applies to each SiPM in the 4 x 4 array)
Temperature Coefficient of Vop	$< 40$ mV/C
Direct Crosstalk Probability	$< \sim 7\%$
Terminal Capacity	$\sim 500$ pF / SiPM (Applies to each SiPM in the 4 x 4 array)
Vop Variation within a Tray	$< 200$ mV
Recharge Time	$< 100$ ns
Fill Factor	$> 70\%$
Protective Layer	Silicone (n $\sim 1.5$ -1.6)

Table 8.53: SiPM specifications for BIC.

Parameter	Specification
Light yield	$> 3.5$ photoelectrons (measured using Sr-90 source with blackened opposite end)
Diameter	$1.00 \pm 0.01$ mm (RMS $\leq 0.02$ mm)
Attenuation length	$> 4$ m (for blue light)
Batch-to-batch variation of light yield	$< 15\%$
Batch-to-batch variation of attenuation length	$< 10\%$
Emission spectrum	Blue-green light
Scintillation decay time	$< 3$ ns
Total length	4900 km of fibers
Delivery method	In canes, length of fibers 4.55 meters $\pm 0.01$ m

Table 8.54: Scintillating fiber specifications for BIC.

the scintillating fibers divided by the true energy of generated photons. Our energy performance results align well with beam test data using a positron beam at Jefferson Lab. See the [Additional Material](#) for more details, including results on the contribution of the low-energy tail of the energy loss.

**Angular resolution:** We estimated the angular resolution for photons using the AstroPix layers, based on detailed detector simulations for various rapidity ranges and photon en-

$\eta$ range	$a/\sqrt{E}$ [%]	$b$ [%]
$(-1.7, -1.3)$	$6.60 \pm 0.03$	$0.66 \pm 0.04$
$(-1.3, -0.88)$	$6.11 \pm 0.01$	$1.24 \pm 0.01$
$(-0.88, -0.4)$	$5.91 \pm 0.02$	$1.24 \pm 0.02$
$(-0.4, 0)$	$5.85 \pm 0.01$	$0.88 \pm 0.02$

**Table 8.55:** Fitted energy resolution parameters for photons in BIC for different  $\eta$  ranges.

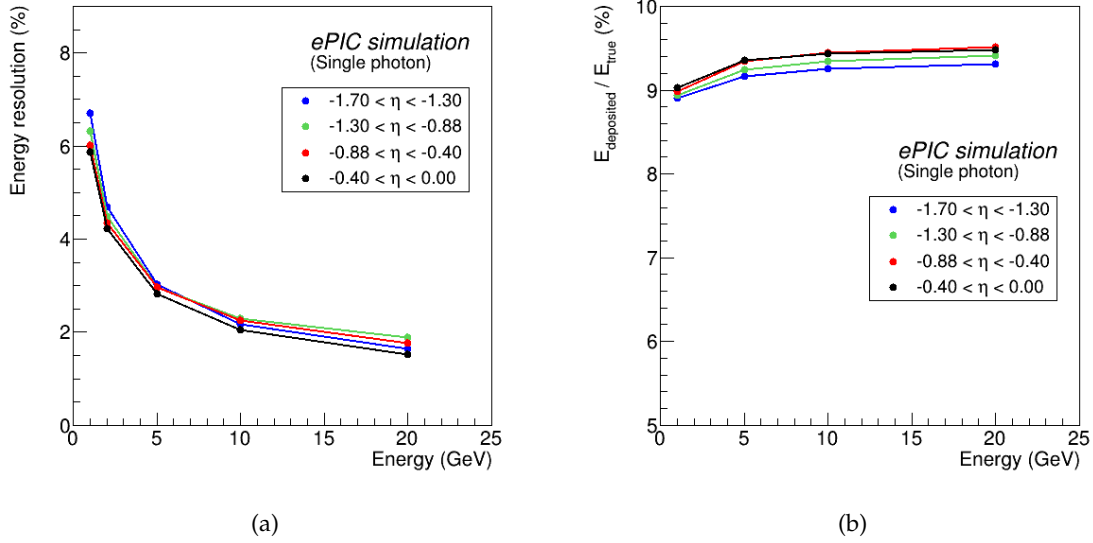


**Figure 8.146:** (a) Simulated energy resolution from the Pb/ScFi calorimeter, extracted as the standard deviation ( $\sigma$ ) of the Gaussian core of a Crystal Ball fit to the photon energy deposits in various rapidity ranges of the BIC. The performance in the positive  $\eta$  region is similar to that in the negative region; for clarity, only the negative region is shown. (b) Sampling fraction for photons, defined as energy losses in scintillating fibers divided by the true photon energy, as a function of photon energy in different rapidity ranges. [Source code for figures](#)

ergies. We extracted the difference between the true and reconstructed polar ( $\theta$ ) and azimuthal ( $\phi$ ) to estimate the FWHM resolution. In the current reconstruction algorithm, the angles are reconstructed from the hit with the maximal energy deposit in the AstroPix layer where the shower started. The resolutions for  $\theta$  and  $\phi$  are presented in Figure 8.147. The results indicate a small dependence of the angular resolution on  $\eta$ . In all regions, the angular resolution remains well below 0.1 degrees, which is on the level of single pixel resolution. The example fit of the  $\theta$  resolution in the rapidity region of  $-0.88 < \eta < -0.4$  gives  $(0.040 \pm 0.004) \text{ deg}/\sqrt{E} \oplus (0.016 \pm 0.003) \text{ deg}$ . The  $\phi$  resolution is worse than the  $\theta$  resolution due to the smearing of shower particles by the magnetic field. Overall, the results show significantly better performance than what can be achieved with any tower-like calorimetry systems and fulfills the requirements for the barrel electromagnetic calorimetry for the EIC.

**Electron-pion separation:** The design of the barrel calorimeter aims to provide high  $\pi^-/e^-$



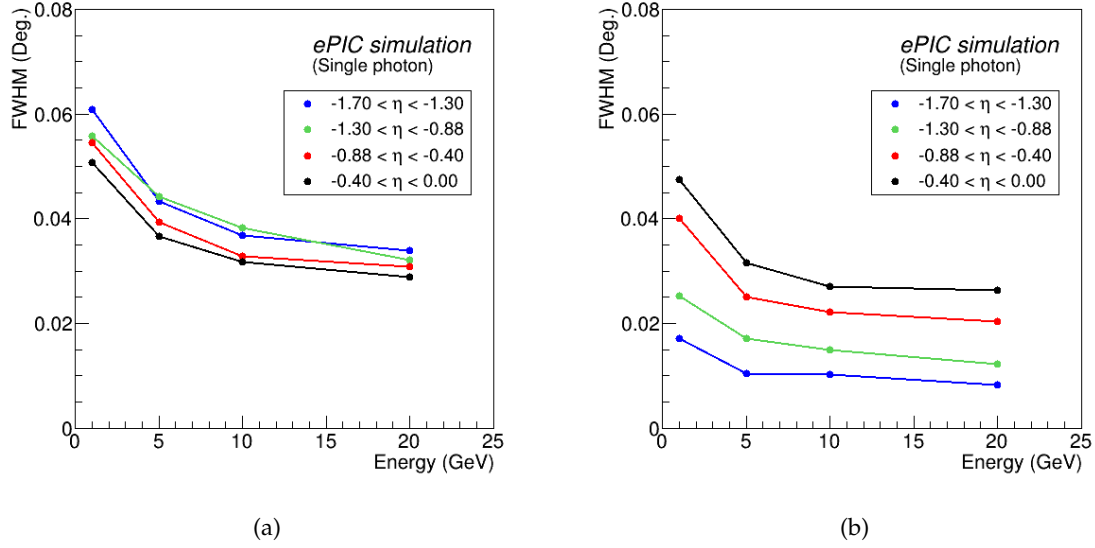


**Figure 8.147:** Simulated angular resolution for photons at different energies for the  $\phi$  (a) and  $\theta$  (b) angles reconstructed from the maximal-energy pixel from the first AstroPix layer where the shower started. The resolution is taken as FWHM from the distribution of the difference between true and reconstructed angle. [Source code for figures](#)

separation, particularly in the momentum region below 5 GeV. The AstroPix layers capture snapshots of electromagnetic and hadronic showers, allowing for the reconstruction of a 3-dimensional profile of the shower development, supported by the longitudinal energy profiles from the Pb/ScFi layers. Charged pion rejection is a two-step process. First, we apply an  $E/p$  cut to the cumulative energy deposit in the Pb/ScFi layers. This cut is deliberately loose to ensure high electron efficiency. The “cleaned” samples, following the  $E/p$  cut, are then fed into a classification neural network for inference. We used a 10-layer Visual Geometry Group-style Convolutional Neural Network [104] using the combined AstroPix and Pb/ScFi detector response. The network utilizes energy and position features from both technologies capturing energy and spatial shower details. Future improvements may come from using more advanced reconstruction techniques based on Graph Neural Networks [105] or Point Clouds [106]. Figure 8.148 (a) illustrates the charged pion suppression factor at  $\eta = 0$  rapidity for a target 95% electron efficiency. The rejection exceeds  $10^3$  at low to mid energies, where it is most critical.

**Photon- $\pi^0$  separation:** Figure 8.148 (b) shows the upper limit of the probability of merging two  $\gamma$ s from a  $\pi^0$  decay into a single cluster at  $\eta = 0$ . Simulations were performed for neutral pions decaying into two  $\gamma$ s with various momenta. For the calorimeter technologies based on tower geometry, as outlined in the EIC Yellow Report [8], the separation probability is defined by the criterion requiring the two  $\gamma$ s to be separated by at least one tower size. In contrast, the BIC technology, leveraging granular position information from AstroPix, employs a different criterion. The probability of merging two  $\gamma$ s was determined using a separation of six times the FWHM of the shower profile, measured at the third imaging layer. This layer registers at least one hit for more than 90% of photons with energies above 0.5 GeV, ensuring a conservative estimate. This limit for  $\gamma/\pi^0$  separation is expected to be well above 10 GeV, based on studies incorporating AstroPix’ position resolution and shower profile data. Addi-

tionally, initial results from a neural network approach for neutral pion identification, similar to the  $e^-/\pi^-$  studies but simplified, were applied using full detector simulations. These initial findings indicate a  $\pi^0$  rejection of approximately 82% at 90% photon efficiency for 10 GeV particles, reflecting the current status of model training.

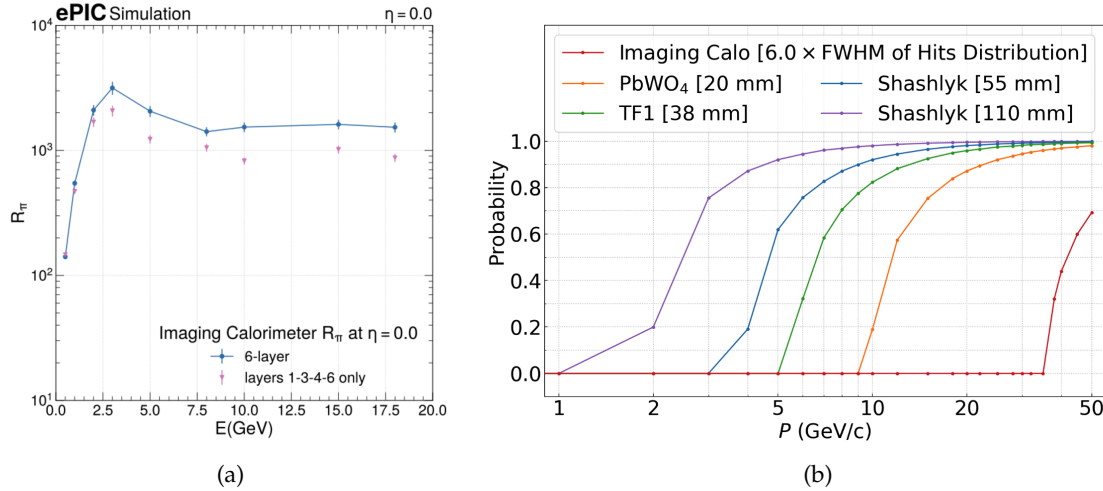


**Figure 8.148:** Simulated performance on particle identification from BIC. (a) The charged pion suppression factor for  $\eta = 0$  rapidity for 95% electron efficiency as a function of particle energy  $E$ . Pink points show the baseline performance where slots 1, 3, 4, and 6, counting radially, of imaging layers are filled with AstroPix trays, blue points show performance with 6 imaging layers. (b) Upper limit on cluster merging at  $\eta = 0$  (shortest distance for particles to travel about 80 cm) from 2 photons from  $\pi^0$  decay at particular  $\pi^0$  momentum  $P$ . For calorimeter technologies based on tower geometry from [8] the separation by at least one tower size, marked in the plot legend, is required. For BIC the separation based on shower profile was assumed (see text). [Source code for figures](#)

**Low-energy response:** We evaluated the performance of the BIC for detecting MIPs through simulations using 5 GeV muons at various rapidities. The deposited energy per readout cell, represented by the most probable value of the MIP peak, was extracted from simulations with Kuraray fibers that meet the Final Design Review fiber specifications. This was compared against the 4-sigma pedestal peak from S14161-3050-04 SiPM array simulations, which is one of SiPM models that fulfill Final Design Review specifications. Even with the dark count rate corresponding to the irradiation level of  $1 \times 10^9$  1-MeV neq/cm<sup>2</sup> (performed for ePIC by the INFN Bologna group) at 5°C, the MIP signal remains well-detectable with a 4-sigma cut on the pedestal. Figure 8.149 shows the extracted most probable value (MPV) of the MIP peak in terms of the number of photoelectrons (nphe) for muons at  $\eta = 0$ , which is the case where we observe the least photoelectrons from muons due to the combination of the distance the light has to travel in the fibers and the energy muons deposit at this angle in one Pb/ScFi layer. The pedestal 4-sigma value is marked in red and the electron-going and proton-going end results are presented. An example pedestal and MIP signal spectrum for 9 and 12 phe MIP signals assuming same sample size for the pedestal and the signal, showing the worst-case scenario for the back Pb/ScFi layer of the BIC, is also presented. The BIC demonstrates the capability to detect minimum ionizing particles for calibration purposes in the Pb/ScFi layers, with the MIP peak from 5 GeV muons remaining well-separated from

the pedestal, even after realistic irradiation doses. This separation is maintained through careful application of threshold cuts in each channel, ensuring that the MIP signal remains distinguishable from the noise. If necessary, we can lower readout thresholds, as the ASIC provides enough headroom, and employ a coincidence logic (e.g., requiring two neighboring readout cells to fire) for further zero suppression to ensure stable MIP performance over the lifetime of the detector.

We also evaluated the response to low-energy photons using simulations. For 100 MeV photons—the lowest energy required to be detected in the BIC according to the EIC detector requirements—we observe performance that meets the energy resolution requirement with high efficiency. The GlueX BCAL has demonstrated the capability to detect and reconstruct photons down to the nominal threshold of 100 MeV, with certain physics-channel analyses lowering it to 50 MeV for which typical clusters contain two fired readout cells [101]. Our simulations indicate that for 100 MeV photons, the energy resolution achieved will be approximately 15%, with an efficiency of firing at least two readout cells per shower on both sides of the calorimeter of 94% for photons at  $\eta = 0$  and 73% at  $\eta = 1$ . See the [Additional Material](#) for more details.

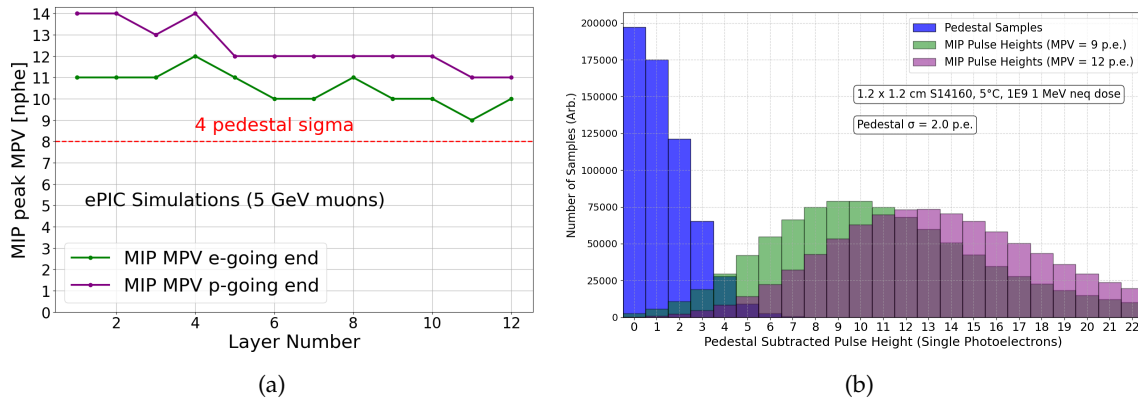


**Figure 8.149:** Simulated performance on MIP response in BIC. (a) The most probable value of the MIP peak in terms of the number of photoelectrons for 5 GeV muons at  $\eta = 0$  at each of the 12 BIC layers. The red line corresponds to 4 sigma of the pedestal simulated with realistic S14160 family SiPM responses at 5 degrees Celsius, irradiated with a dose of  $1 \times 10^9$  1-MeV neq/cm<sup>2</sup>. The green line corresponds to the electron-going end, while the purple line corresponds to the proton-going end readout cells. (b) An example spectrum of the pedestal and MIP pulses at 9 and 12 phe signals, showing the worst-case scenario from plot (a) for the back Pb/ScFi layer of the BIC at  $\eta = 0$ . [Source code for figures](#)

**AstroPix sensor performance:** The AstroPix chip has been extensively tested in both bench and beam environments. The AstroPix\_v3, the first full-size chip with a 500  $\mu\text{m}$  pixel pitch and row-and-column readout (35 rows and columns in a strip-like format), has demonstrated strong performance, as summarized, for example, in [103]. Key tests included a noise study and a radiation source test. In the noise study, less than 0.5% of the pixels exhibited a noise rate exceeding 2 Hz, at the threshold of approximately 25 keV. These results meet the BIC’s requirements for low energy thresholds and masked pixel yield. The radiation source test, using isotopes with calibration points ranging from 22.2 keV to 122 keV, as shown in Figure 8.150, showed that 44% of pixels met the 10% energy resolution requirement at 59.5 keV, and 92.4% of pixels achieved the required 25 keV sensitivity for BIC. Although the AstroPix\_v3 chip is not fully depleted, it demonstrated promising performance. The upcoming

AstroPix.v5, designed with a dynamic range extending to 700 keV, is expected to meet energy resolution requirements for all pixels.

**AstroPix beam test results:** We used beam tests at Fermilab Test Beam Facility (FTBF) to further validate the AstroPix.v3 chip in both single- and double-layer configurations. In the single-layer test, data collected with a 120 GeV proton beam was used to match corresponding row and column hits, using matching timestamps and ToT to reveal a hit map that showed the proton beam profile presented in Figure 8.150 (a). Although the AstroPix.v3 has a daisy-chained row and column readout and does not yet have an individual pixel buffer (which is implemented in AstroPix.v4 and higher versions), it demonstrated a precise hit-pixel reconstruction. In the double-layer configuration, two daisy-chained layers of AstroPix.v3 were tested, successfully reading events in coincidence and pinpointing hit-pixel locations, providing a proof-of-concept for layer integration in a beam environment.

In summary, the characterization of AstroPix.v3 is ongoing, with specific tests designed to meet the ePIC detector requirements. Remaining improvements, including enhanced dynamic range and energy resolution, will be addressed in the upcoming AstroPix.v5, which is expected to be fabricated by late 2025.

**Simulation performance validation:** The BIC performance results presented in this work are based on a full simulation of the system within the ePIC detector, using realistic geometry and a framework validated through bench tests and beam data from FTBF and Jefferson Lab Hall D (see [107] for FTBF results). The Pb/SciFi matrix was modeled in detail, with embedded scintillating fibers in lead and glue. AstroPix layers were implemented as realistic staves, accounting for dead areas and material contributions from sensors, electronics, cables, insulation, and support structures. Realistic digitization and reconstruction were applied throughout. For the Pb/SciFi component, we implemented an effective model incorporating fiber attenuation, photoelectron statistics, light guide efficiency, and SiPM thresholds, based on data and optical simulations. AstroPix digitization was modeled at the pixel level, while each Pb/SciFi readout unit corresponded to one light guide with an attached SiPM.

We present more details on select benchmarks of realistic simulation results against measurements in the supplemental material.

**Expected Data Rates:** Based on global ePIC studies of rates from signal and background [108], the channel maximum, channel average, and total data rates for the BIC are presented in Table 8.56. For the imaging layers, one channel corresponds to one chip, while for the SciFi/Pb layers, one channel corresponds to one SiPM array. For electron-proton DIS, rates have been estimated from the  $18 \times 275$  GeV simulations, where  $0 < Q^2 < 1$ , and the collision rate has been scaled to the highest luminosity (500 kHz), corresponding to the  $10 \times 275$  GeV beam energy configuration. In beam background simulations, the highest channel rates are achieved for the hadron and electron beam backgrounds at  $10 \times 275$  GeV.

## Implementation

**Subsystem mechanics and integration:** The 48 BIC sectors are arranged in a self-supporting Roman arch configuration. Once assembled, the full calorimeter rests on the solenoid cryostat support rings. In the hadron-going direction a small gap must be bridged between the end of the BIC and the support ring, while in the lepton-going direction the system slightly overhangs, creating a cantilevered structure.

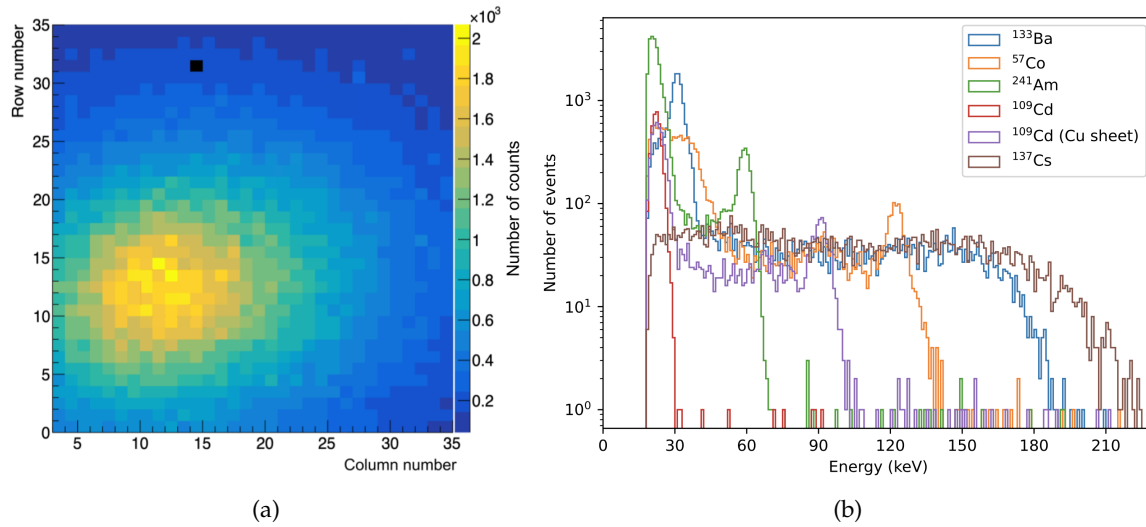


**Figure 8.150:** (a) Beam hit map recorded in the 120 GeV proton run in Fermilab Test Beam Facility with a AstroPix.v3 chip. The masked pixel has been marked in black. [Source code for figure](#). (b) Calibrated energy responses form an example pixel of a AstroPix.v3 chip. Plot from [103].

	DIS	Electron Beam Background	Proton Beam Background	All Sources
<b>ScFi/Pb Layers</b>				
Channel Max	7.4 kHz	8.8 kHz	430.0 Hz	15.2 kHz
Channel Avg	2.8 kHz	875.1 Hz	132.5 Hz	3.8 kHz
Total	16.1 MHz	5.0 MHz	763.4 kHz	21.9 MHz
<b>Imaging Layers</b>				
Channel Max	794.7 Hz	389.2 Hz	51.8 Hz	924.8 Hz
Channel Avg	179.9 Hz	36.8 Hz	7.8 Hz	224.5 Hz
Total	11.7 MHz	2.4 MHz	509.2 kHz	14.6 MHz

**Table 8.56:** Expected data rates for ScFi/Pb and Imaging layers of the BIC. For the imaging layers, one channel corresponds to one chip, while for the ScFi/Pb layers, one channel corresponds to one SiPM array.

5658 A BIC sector consists of six carbon fiber frames for the imaging layers, interleaved with five  
 5659 single layers of a Pb/ScFi matrix (each 17 fibers tall), followed by a bulk segment consisting of seven  
 5660 Pb/ScFi matrix layers. The back of the sector consists of an aluminum support plate with connec-  
 5661 tors designed to link the sectors together, affix the ESB, and integrate with the global BIC support  
 5662 structure. The sector is constructed as a monolith, with all components epoxied together to ensure  
 5663 structural integrity.

5664 The inner face of each BIC sector consists of a 0.5 cm thick aluminum plate, designed to connect the  
 5665 inner support rails to the detector. The inner support rails hold the inner detector support structure,  
 5666 maximizing the use of available space while avoiding obstruction of the ESBs (the readout boxes),

ensuring that individual imaging layers can be added or removed as necessary for future upgrades or servicing. Hence, the BIC plays a critical role in supporting the overall inner detector structure.

Detailed Finite Element Analysis to validate the mechanical integrity of the sector design is ongoing. The design of the support that connects the BIC to the solenoid cryostat support rings is still under development, ensuring it meets the mechanical stability requirements while maintaining accessibility to readout electronics and other critical components.

**Calibration, alignment and monitoring:** The BIC calibration approach treats the Pb/ScFi and AstroPix imaging layers as two separate systems, each calibrated independently. For the Pb/ScFi calorimeter, we will follow well-established in-situ calibration methods, starting with MIP-based calibration, then refining with meson decays, electrons, and kinematic techniques successfully used in many other experiments including experiences with GlueX and HERA experiments (See, e.g., [101]). The energy calibration is further refined using decay photons from neutral pion events ( $\pi^0 \rightarrow \gamma\gamma$ ).

For the AstroPix layers, the calibration process occurs in three steps. First, an absolute pixel energy calibration is performed during stave assembly using a radioactive source. Next, in-situ position and alignment calibration will be conducted similarly to standard tracker procedures, utilizing cosmics. Finally, the overall imaging cluster energy calibration will be matched with the Pb/ScFi calorimeter, leveraging the energy reconstruction methods described above.

We will use metrology for alignment during installation, but precise alignment of the full BIC detector is not critical due to the calorimeter's purpose. Sub-millimeter physical alignment of the entire detector is unnecessary, except for potential requirements driven by the alignment needs of the inner detector, which the BIC supports. However, subcomponent alignment is more stringent: AstroPix modules and staves require alignment at the 100  $\mu\text{m}$  level. The alignment requirements for the carbon fiber frames holding the AstroPix trays are still under evaluation but are likely to fall within a few hundred microns. We will calibrate the relative positioning of detectors and sensors using cosmic and physics events to ensure accurate reconstruction.

Calibration stability during operation for Pb/ScFi will be ensured by using LED-based relative light monitoring systems, along with additional checks on linearity and timing using both cosmics and dedicated calibration runs for both AstroPix and Pb/ScFi layers.

**Services:** The Pb/ScFi part of BIC, which utilizes SiPMs, requires two LV lines (plus ground) of 1.2 V and 2.5 V for each H2GCROC3-based front-end board (FEB), along with one HV line (plus ground) operating at less than around 50V for biasing SiPMs. The SiPM bias voltage is 38V and operating voltage is 38V+2.7V. In order to fill the LV needs, the current ESB design has a single 30 V line arriving at the FEB, where it will be stepped down to the required voltages for the SiPM board, AstroPix ETCs, and the FEB itself. The system features a total of 5,760 readout channels distributed across 48 sectors, with one FEB per sector per side, each managing 60 readout channels. Each FEB is connected to the RDO through four lines: two data lines, one clock line, and one slow control line, and 1 RDO maintains 24 FEBs.

For the AstroPix sensor layers, the LV services include two 1.8 V to power the analog and the digital part of the chip and the HV of 200-400 V distributed to each stave. Each stave within an AstroPix tray connects to the data acquisition system through an FPGA-based End-of-Tray Card (ETC, one per tray) connected to DAM via an optical link. In total, each sector will include 27 staves per side. Each ETC will receive power from the Pb/ScFi FEB.

The SiPMs require cooling to maintain a temperature of 7°C in order to keep the dark noise at an



acceptable level for detecting signals from MIPs. Refer to the simulations as detailed in the *Performance* section, which show that after radiation doses corresponding to about one year of running at top luminosity, MIP peaks remain distinguishable at temperatures around 5°C. Each ESB will have in/out lines for cooling water and a dry air or N<sub>2</sub> system to prevent condensation. The estimated heat load per ESB is projected to be under 100 W, necessitating effective heat management. Liquid water cooling will be utilized for the SiPMs, their readout boards, and the ETCs. AstroPix sensors are highly heat efficient, consuming less than 2 mW/cm<sup>2</sup>. The baseline cooling strategy involves thermal coupling to dissipate heat through the staves and trays, with cooling occurring at the edges along with the ETCs. If additional cooling is required, circulating liquid through the staves will be employed as a mitigation measure. The ongoing PED program includes detailed thermal simulations toward a preliminary cooling design.

**Status and remaining design effort:** High-level schedule for the BIC design and production phase is available in [Additional Material](#) (See Figure. 8.151).

**R&D effort:** The R&D efforts for BIC focus on demonstrating the combined performance of Pb/ScFi and AstroPix in EIC-like environments. This involves measuring higher than GlueX energy response up to about 10 GeV, benchmarking high-energy electron and pion simulations, testing AstroPix in high-rate environments, and integrating the Pb/ScFi with AstroPix sensor layers. In FY23, responses to 6 GeV positrons in 60 cm long Pb/ScFi prototype (termed *Baby BCAL*) were measured in Hall D of Jefferson Lab, showing a constant term of about 2%, consistent with simulations. The Baby BCAL was commissioned with proton, pion, and electron beams during a June 2024 FBTF test, where data collected allowed for pion simulation benchmarking [107]. A proof-of-concept synchronization of AstroPix with Baby BCAL was achieved by triggering on the AstroPix analog signal. With extensive data from previous AstroPix tests in FY23, and the multi-layer Pb/ScFi and AstroPix bench tests, the R&D program has been concluded in FY25.

**E&D status and outlook:** The Project Engineering Design phase of our project that started with granting the funding to the participating institutions starting Q4 2024, encompasses a detailed roadmap for the design, testing, and integration of key components for BIC. Early milestones focus on the design and development of Pb/ScFi sectors, including short and long test articles and the structural framework needed for housing these components. Alongside this, efforts are directed toward the design and prototyping of the end-of-sector box, which includes light guide and light monitoring system integration. The tracking layer, which features AstroPix sensors, undergoes simultaneous development. This includes tracker mechanical design, cooling design, performance characterization of the AstroPix chips, module design and assembly, and testing of components such as bus tapes and end-of-tray cards. By mid-PED-phase, both the Pb/ScFi and tracking layers will undergo rigorous integration testing to ensure seamless functionality within the full detector system. The final phase focuses on validating the designs and performing full integration testing of staves, modules, and tracking layers. Quality control procedures will be established for each component, ensuring that everything meets performance specifications before final assembly. The PED phase is setup to exceed 90% design maturity by Q1-Q2 FY26.

**Other activity needed for the design completion:** Within the small-scale R&D and design funding in Korea, a focused effort is underway during the period from August 2024 to April 2027, covering the PED phase and pre-production phase. The primary objectives include the development of testing and assembly systems for the AstroPix chip, particularly emphasizing automatic wafer testing and module assembly. Additionally, this work involves

5757 designing the readout box for the Pb/ScFi system and producing test modules to conduct  
5758 performance studies.

5759 **Status of maturity of the subsystem:** The maturity of BIC is currently estimated to be at least  
5760 60%, with some components, such as the scintillating fibers and SiPMs advanced beyond  
5761 the final design review level. The entire BIC underwent an incremental Preliminary Design  
5762 Review (PDR2) in September 2024. The Final Design Reviews for both the scintillating fibers  
5763 and SiPMs were successfully passed in September 2023. The first and second batches the  
5764 scintillating fibers were included in CD3a and CD3b. The vendor selection is complete and  
5765 the contract for the scintillating fibers has been finalized.

## 5766 Construction and assembly planning:

5767 **Pb/ScFi Sectors Construction:** The production of Pb/ScFi sectors will take place at Argonne,  
5768 where there will be two production lines. The sectors will be constructed by embedding  
5769 scintillating fibers in lead sheets, arranged in a stepped “Mayan pyramid” configuration,  
5770 following the GlueX model. Carbon fiber frames will be integrated with the sector as it  
5771 is built, with each frame assembled from two C-channel-like sides and a top and bottom  
5772 plate. The sector construction process will proceed at a pace of 0.5 to 1 matrix layer per  
5773 day, with the ability to build two sectors in parallel. Once the matrix lay-ups have been  
5774 completed, an external machine shop will trim and polish the ends and machine the sides to  
5775 the desired trapezoidal shape. Upon return to Argonne, the sector will undergo metrology  
5776 and QC before being prepared for shipment to BNL.

5777 **ESB Manufacturing:** The construction process for the ESB is still in development. ESB con-  
5778 struction will include large-scale SiPM testing, SiPM mounting, light-guide manufacturing,  
5779 light-monitoring system integration, construction of structural and cooling components, and  
5780 manufacturing of electronics boards. There will be likely two ESB production sites: one in  
5781 Canada at U. Regina and one in Korea. After the ESB assembly is completed, they will be  
5782 shipped to the production site at BNL for installation (see Assembly Planning).

5783 **AstroPix Sensors and Wafers:** The AstroPix sensors were originally developed for NASA-  
5784 GSFC’s AMEGO-X mission. Although we collaborate closely with NASA-GSFC on AstroPix,  
5785 the external dependency is minimal at this advanced stage of chip development. The As-  
5786 troPix engineering runs are nearly complete, with the only remaining dependency being the  
5787 AstroPix v6 engineering run, which is covered by NASA for the ComPair project.

5788 The AstroPix sensors will be fabricated at the AMS foundry. Due to the large scale of the  
5789 detector, automatic wafer-level testing will be conducted at two sites: PNU (South Korea)  
5790 and Argonne. This testing will ensure the functionality of each chip before dicing, includ-  
5791 ing IV-CV measurements, ASIC performance, noise levels, and defect detection early in the  
5792 production process. After testing, the wafers will be diced into individual AstroPix chips.

5793 **AstroPix Modules and Trays:** AstroPix chips will be assembled into modules at three pro-  
5794 duction sites: Argonne, UC Santa Cruz, and PNU (South Korea). Each module will consist  
5795 of nine daisy-chained AstroPix chips, readout on flexible PCBs. After assembly, each module  
5796 will undergo initial testing to ensure proper chip-to-chip communication, pixel functionality,  
5797 and noise levels. Modules that pass this stage will be integrated into staves, with 12 modules  
5798 per staff. To keep the production process scalable and efficient, only one flavor of staff will  
5799 be used across the entire system. The staves will then undergo additional QC testing. Once  
5800 validated, the staves will be integrated into trays. There are two flavors of trays: one for  
5801 the first imaging layer and the other for layers 3, 4, and 6. The hadron-going side and the  
5802 lepton-going side trays of the detector are mirror images of each other. Each tray will contain

6 staves in layer 2 and 7 staves in the outer three layers. These trays will then undergo final QC prior to shipping to BNL. The entire production and QC procedure is designed to catch any defects early and ensure that the trays are fully operational before final integration into the BIC sectors.

**Assembly Planning:** The assembly of the BIC will follow a carefully planned sequence. Upon arrival at the integration site, the Pb/ScFi sectors will be unpacked and prepared for assembly. The first step will involve attaching the light guides to the sectors. Once the initial sectors have been prepared, we can begin the barrel assembly while continuing to unpack and attach light guides to the remaining sectors. The BIC barrel will be assembled next to the solenoid and then inserted into the solenoid using existing sPHENIX tooling. Following the installation of the barrel at BNL, the imaging layer trays will be inserted using specialized tooling that is still under development. After all trays are installed, the ESB will be mounted to complete the installation. This phased approach ensures that all components are properly integrated (and tested) prior to integration testing.

**Quality Control (QC) Planning:** QC will be implemented at multiple stages of the BIC production and assembly process to ensure system integrity and performance. The system, particularly the imaging layers, is designed with both modularity and scalability in mind, allowing for efficient production, easier upgrades, and reworkability. Key QC procedures include:

**Pb/ScFi Sector Assembly:** The Pb/ScFi sectors will undergo thorough inspection during assembly. Scintillating fibers and lead sheets will be inspected for defects before embedding. After each matrix layer is completed, visual and metrological inspections will ensure proper alignment and uniformity in matrix growth thickness (height of the build). Final metrology checks will be performed after external machining to confirm dimensions prior to shipment.

**AstroPix Wafer Testing:** Automatic wafer-level testing will be conducted to assess chip functionality, including chip performance, noise levels, and defect detection. Once tested, wafers will be diced, followed by additional metrology and electrical/non-electrical QC on individual AstroPix chips to ensure reliability before moving to the module assembly phase. We are currently exploring an alternative possibility to leverage experience in our collaboration in automated chip-level testing as part of our ongoing engineering design studies.

**Module and Tray QC:** Modules will be assembled from AstroPix chips and undergo functional tests to verify chip-to-chip communication, pixel functionality, and noise levels. Defective modules will be identified and replaced before progressing to stave assembly. Staves will be tested for electrical continuity, power consumption, and thermal performance under load. QC for staves and trays will use the actual End-of-Tray Card (ETC) readout electronics to perform these tests. Once integrated into trays, final testing will check for alignment, electronic connectivity, and cooling performance, ensuring that trays operate as intended under operational conditions.

**ESB QC:** SiPMs will undergo rigorous testing to ensure proper photon detection efficiency, dark count rates, and timing precision before being integrated into the ESB, while, component-wise optical tests will characterize the light guides and optical cookie system. Furthermore, the QC procedure at the production site will include a full system test of the electrical connections, readout electronics, cooling system, and light tightness. The full-chain tests will be repeated during installation at BNL.

**Final Integration and Barrel Assembly at BNL:** After attaching light guides to the Pb/ScFi sectors, alignment and metrology checks will be conducted during barrel assembly to ensure

sector and tray alignment within tolerances. Electrical and cooling system checks will be completed post-installation of the ESBs on assembled barrel to confirm proper functionality. System-wide tests, including cosmic ray runs and electronic readout, will validate the entire system before commissioning.

**Environmental, Safety and Health (ES&H) aspects** The BIC design incorporates standard safety and environmental practices across all production sites. We will strive for standardized safety protocols while adhering to internal work planning and control processes at each institution to identify hazards, implement mitigations, and document safety procedures. Main hazards associated with the BIC include:

**Lead handling:** The handling of lead sheets for the Pb/ScFi matrix requires careful consideration. We are working closely with experts to determine the appropriate safety steps. These steps may include specific protocols to mitigate any hazards and the potential enrollment of personnel in continuous health monitoring programs to ensure long-term safety.

**Epoxy usage:** Standard procedures for handling, mixing, and applying epoxy will be followed, with work conducted in fume hoods to ensure safety. Part of our PED work aims to deploy a custom mixing nozzle to reduce air contaminants and epoxy waste while improving consistency in the application process.

**Scintillating fibers:** The fibers are made of flammable polystyrene, and with the total fiber mass exceeding 3.9 tons, proper fire safety measures and storage protocols are essential.

**Pinch/nip hazards:** Automated systems, such as robots for wafer probing, pick-and-place, and glue application, present pinch hazards. Controls, such as PPE, gloves, guards, and procedures, will be in place to mitigate these risks.

**Crush hazards:** The use of presses and swaging equipment introduces crush hazards during assembly processes. Strict safety protocols, including the use of guards and operator training, will mitigate these risks.

**Radioactive sources:** The use of radioactive sources for calibration introduces additional handling requirements, and proper shielding and storage protocols will be implemented as necessary.

**Electrical safety:** Electrical safety procedures will also be applied for all electronics and power systems associated with the BIC production tooling and detector components.

**Collaborators and their role, resources and workforce:** The full BIC WBS org chart is available in [Additional Material](#) (see Figure 8.156). BIC is supported by a diverse and robust international collaboration, with institutions from the United States, Canada, Korea, and Germany. These collaborators bring together a wealth of expertise and resources, working collectively to advance the development of the BIC, and has the necessary workforce and expertise to execute the BIC design on schedule.

In the United States, several institutions play a key role across multiple aspects of the project. Argonne National Laboratory is leading several crucial areas, including the design and assembly of modules and staves, sector production, cooling systems, and system testing and QC, while also overseeing the software, simulation, and benchmarks. Oklahoma State University leads efforts on stave bus assembly, and the University of California, Santa Cruz (UCSC) supports module design and assembly efforts. NASA Goddard Space Flight Center (GSFC) contributes via the ETC components, ensuring that electronic testing is integrated into the system.

Canadian institutions play a critical role, especially in the production and quality control of ESB. The University of Regina contributes to multiple efforts, including the QC of scintillating fibers, SiPM integration, light guides, and electrical design, while also contributing to the system's demonstration and testing. The University of Manitoba provides leadership in cooling system development and supports the SiPM integration efforts. Mount Allison University focuses on ESB production, aiding in the overall electronics support infrastructure.

Korean institutions are heavily involved in various production, design, and testing processes. Collaborators from Kyungpook National University (KNU) support both electronics and SiPM integration. Yonsei University plays a key role in the sector production process and testing, while Sungkyunkwan University (SKKU) focuses on sector development and production. Pusan National University (PNU) leads efforts on wafer testing and supports software development and simulation. Additionally, Hanyang University, Korea University, and other Korean institutions provide significant contributions across assembly, installation, and testing.

The Karlsruhe Institute of Technology (KIT, Germany) is responsible for the AstroPix chip development, and provide essential chip support and communication with the foundry.

#### Risks and mitigation strategy:

A potential risk in the production of AstroPix chips is related to the feasibility of using 12-inch wafers, which offer a more modern and cost-effective solution. However, if this option proves unviable, we will need to use 8-inch wafers, increasing costs. This is budgeted in the risk registry.

The schedule has sufficient time built in to accomodate an additional iteration of AstroPix beyond v6 if needed.

Risks on production-delays due to the availability of scintillating fibers and SiPMs were mitigated through CD3a/b long-lead procurement ensuring the timely availability of these components.

As outlined in the Construction and assembly planning paragraph, in the default scenario, sector production will take place at Argonne using two production lines, with one staffed by Korean collaborators. ESB production and quality control will be managed by Canada and Korea. Wafer testing will occur in both Korea and the US. AstroPix module and stave production will be distributed across three or more sites in the US and Korea. The baseline plan includes producing four AstroPix layers, with the possibility to fill the two additional slots as a later upgrade. In the unlikely event of no in-kind funding from Canada and Korea, the project will cover all sector production labor costs, including Korean collaborators, and consolidate production to a single ESB site (Canada) and a single wafer testing site (US). AstroPix module/stave production will be limited to two sites in the US, requiring an increased workforce at each site or potentially facing a one-year delay to deliver the four baseline layers.

#### Additional Material

**Schedule** High-level BIC schedule can be found in Figure 8.151.

#### Performance

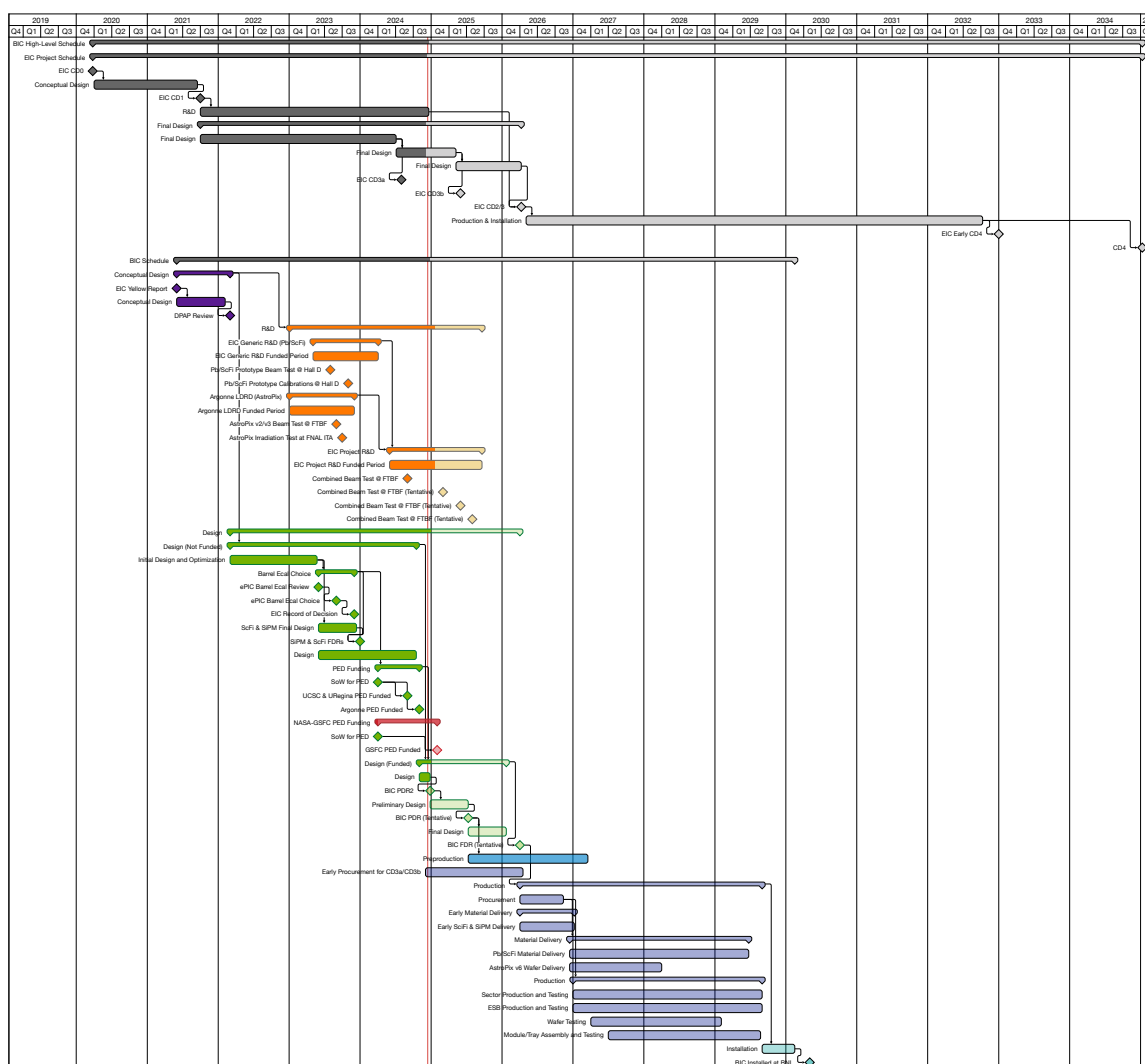


**Figure 8.151:** Barrel Imaging Calorimeter high-level schedule for design and production phases.

**Energy Response Measurement and Simulations** The realistic BIC geometry was implemented, including a detailed Pb/SciFi matrix with scintillating fibers embedded in lead and glue, following the GlueX model. The AstroPix layers were implemented as staves, with AstroPix chips placed in realistic dead areas, and materials accounted for the sensors, electronics, cables, insulation, glue, and support structure. Realistic digitization and reconstruction were applied. For the Pb/SciFi component, an effective model for light attenuation in the fibers, photoelectron statistics, light guide efficiency, and SiPM thresholds was implemented based on beam and bench measurements as well as optical simulations of the light guide response. For AstroPix, each digitized readout unit corresponds to one pixel, while for the Pb/SciFi component, each readout cell covers the area of one light guide with an attached SiPM.

The contribution of the low-energy tail of the energy losses was quantified by calculating the difference between the area under the fitted Crystal Ball function and that of its Gaussian core marked in



red in Figure 8.152 (a). The tail contribution to the overall energy loss area is shown in Figure 8.152 (b) and (c) for electrons and photons, respectively. In addition to the energy resolution and total sampling fraction as a function of energy presented for photons in Figure 8.146, the results for electrons are presented in Figure 8.153.

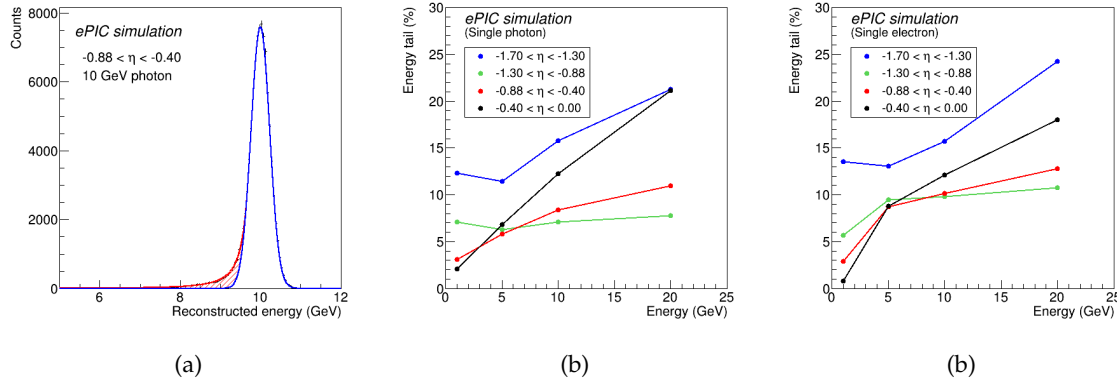


**Figure 8.152:** (a) Simulated energy losses in scintillating fibers of BIC for 10 GeV photons in the rapidity range  $-0.88 < \eta < -0.4$ . The distribution has been fitted with the Crystal Ball function; the Gaussian core of the function is marked in blue, and the power-law tail area is marked in red. (b) Percentage contribution of the low-energy tail—red area in plot (a)—to the overall area under the Crystal Ball fit to the energy losses of photon in Pb/ScFi as a function of photon energy and rapidity. (c) Same as (b) but for electrons. [Source code for figures](#)

5946

The low-energy photon response has also been evaluated based on simulations, as described in the [Performance](#) section. Two example plots for low-energy photons at  $\eta = +1$  are shown, which represent a highly asymmetric situation where the photon shower develops close to the p-going end of the BIC, far from the e-going end. As shown in Figure 8.154, left plot shows the number of fired readout cells for 100 MeV photons with a threshold of 6 phe, and right plot shows the energy resolution extracted from each end of the BIC and the combined resolution for photons below 0.5 GeV. We observe performance that meets the energy resolution requirement with high efficiency.

Energy response to both electromagnetic and hadronic showers has been tested in the beam test environment with a 60 cm long and  $15.5 X_0$  deep Pb/ScFi bulk-section prototype based on GlueX BCAL geometry, termed *Baby BCAL*. At Hall D of Jefferson Lab, Baby BCAL was exposed to 3-6 GeV positrons hitting it at different impact angle and position depending on beam energy. Figure 8.155 (a) presents the measured energy resolution measured in those conditions. Note that the highest energy points reflect positrons hitting the prototype close to the end and at the impact angle that causes partial shower leakage. At Fermilab Test Beam Facility, Baby BCAL was exposed to mixed electron-pion-muon beam at energies of 4, 6, 8 and 10 GeV. The energy response to pion beam has been benchmarked in simulation of Baby BCAL implemented in ePIC environment, same as used for the BIC simulations. Figure 8.155 (b) shows comparison between collected data and simulations benchmarking their realism.

**Particle identification** The following section provides details of the AI-based particle identification performance described in the [Performance](#) section.

For our  $\pi^-/e^-$  separation studies, we utilized a 10-layer Visual Geometry Group (VGG)-style Convolutional Neural Network (CNN) to process combined data from the AstroPix and Pb/ScFi parts

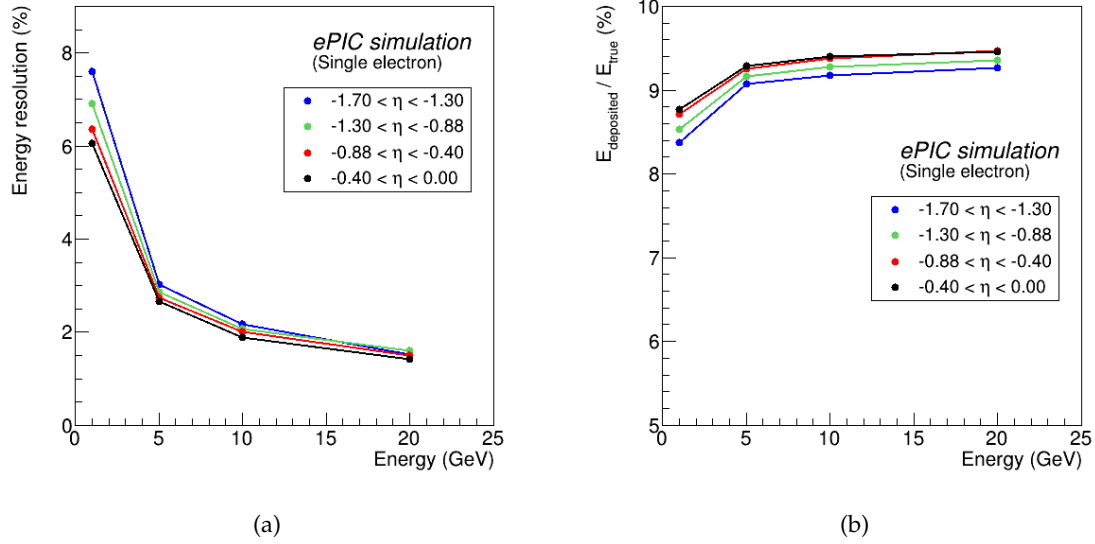


**Figure 8.153:** (a) Simulated energy resolution in from Pb/SciFi extracted as a  $\sigma$  of the Gaussian core of the Crystal Ball fit to the energy deposits of electrons in different rapidity ranges at BIC. (b) Sampling fraction for electrons, defined as energy losses in scintillating fibers divided by the true electron energy, as a function of electron energy in different rapidity ranges. [Source code for figures](#)

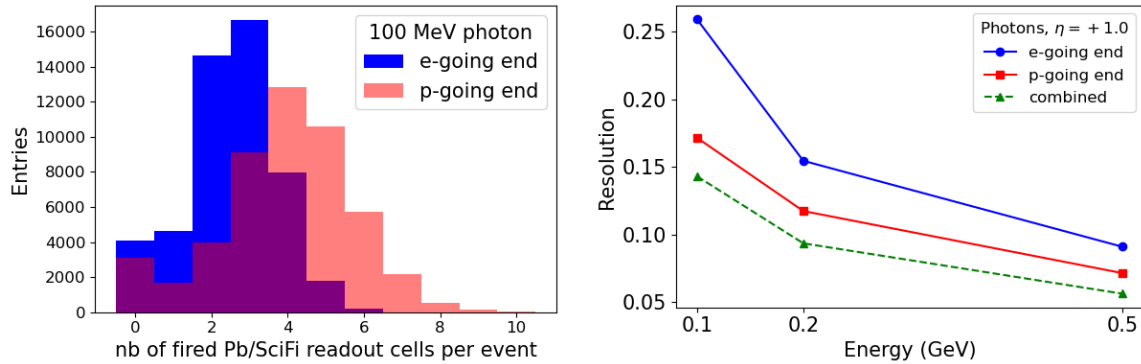


**Figure 8.154:** Simulated, low-energy photon response in BIC at  $\eta = +1$ . (left) Expected number of fired Pb/SciFi readout cells for 100 MeV photons with a threshold of 6 phe. (right) Energy resolution extracted for both ends of the BIC and the combined one for photons below 0.5 GeV. [Source code for figures](#)

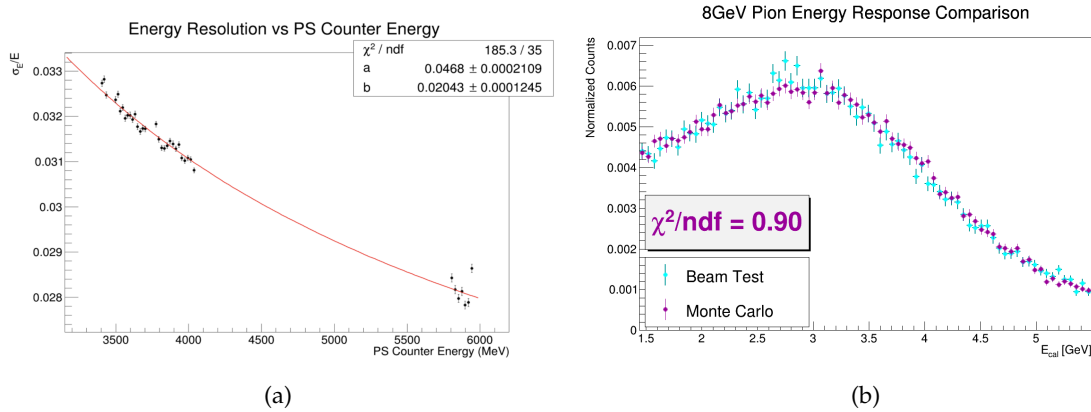


**Figure 8.155:** (a) Preliminary energy resolution of Baby BCAL exposed to 3–6 GeV positrons at Hall D of Jefferson Lab, with varying impact angles and positions depending on beam energy. The highest energy points correspond to positrons striking near the end of the prototype and at angles causing partial shower leakage. Red line shows the fitted function  $\sigma/E = a/\sqrt{E} \oplus b$ . [Repository to be added](#) (b) Preliminary energy response of Baby BCAL to an 8 GeV pion beam at the Fermilab Test Beam Facility. The plot compares the collected data (light blue) with simulations (purple) implemented in the ePIC environment, as used for BIC simulations, benchmarking the realism of the simulation model. [Source code for figures](#)

of the calorimeter. This CNN architecture consists of 5 convolutional layers interspersed with 2 pooling layers, followed by 3 fully connected (dense) layers. Each event is formatted into an input array with dimensions  $N_{\text{layers}} \times N_{\text{hits}} \times N_{\text{features}}$ , where 4 primary features: energy deposit,  $\eta$ ,  $\phi$ , and radial position of the hit inside the calorimeter, to capture both energy deposition and spatial information about the particle shower.

We trained the network using supervised learning with a data set composed of a 10:1 ratio of pions to electrons. This ensured a sufficient number of pions remained after applying the energy-over-momentum ( $E/p$ ) cut, which was crucial for training accuracy. Each training cycle consisted of 20 epochs, with data split into 70% for training, 10% for validation, and 20% for testing. On average, between 100,000 and 200,000 events were included in each training set, drawn from over 2TB of official singles productions simulations.

The CNN’s performance is measured with uncertainties based on binomial statistics, providing robust estimates of classification accuracy. A similar but simplified approach was used for neutral pion identification. Initial results demonstrate promising pion rejection rates, which could be further enhanced by implementing algorithmic improvements. Future iterations of the model may explore Graph Neural Networks or Point Clouds to better capture the spatial and relational data inherent in these complex events.

**Collaborators and their role, resources and workforce:** The full org chart for the BIC Detector Subsystem Collaboration is presented in Figure 8.156.

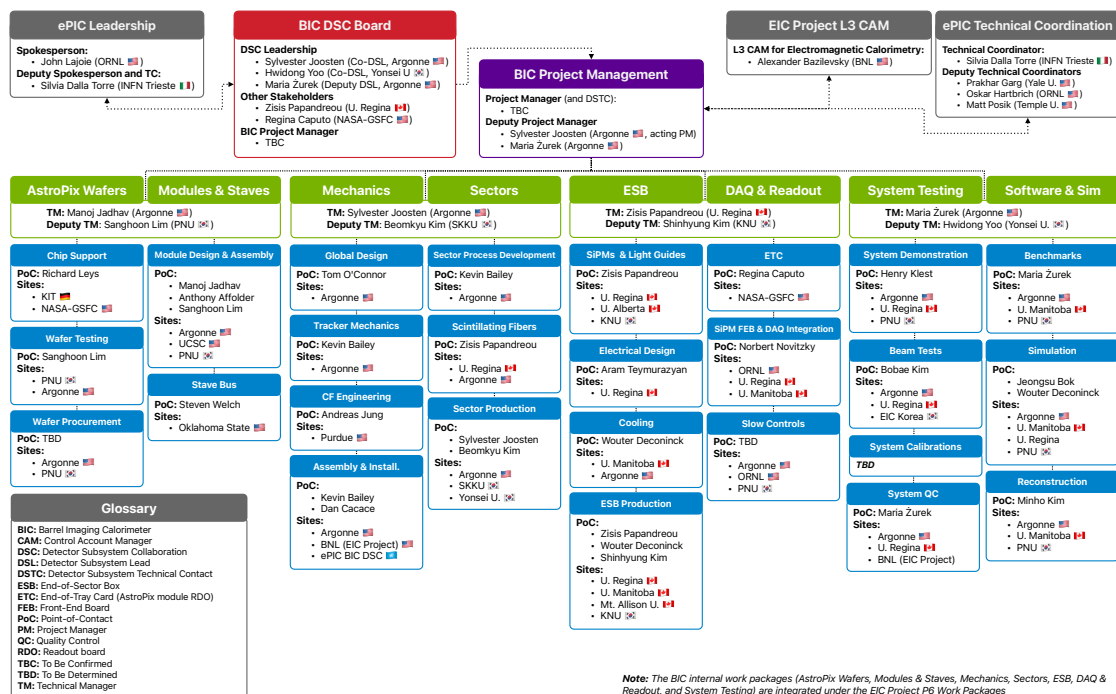


Figure 8.156: Barrel Imaging Calorimeter org chart.

### 8.3.5.3 The forward endcap electromagnetic calorimeter

**Introduction** The ePIC forward electromagnetic calorimeter (FEMC) is part of the hadron end-cap calorimeter system, complementing the forward hadronic calorimeter. Complete electromagnetic calorimetric coverage in ePIC is essential for detecting photons and electromagnetically decaying mesons, which are crucial for reconstructing parton-scattering kinematics through jets and to identify DVCS photons. FEMC provides full azimuthal coverage within a pseudorapidity range of approximately  $1.4 \lesssim \eta \lesssim 3.9$ . At lower pseudorapidity, FEMC overlaps with BEMC, ensuring continuous coverage by electromagnetic calorimeters in the hadron side of the ePIC detector. Coverage at higher pseudo-rapidity is restricted due to mechanical limitations (clearance required to accommodate the accelerator beam pipe).

The design requirements for the FEMC were established through extensive studies of various detector concepts proposed for the EIC over the past decade. These concepts originated from the designs presented in the EIC White Paper [9] and Yellow Report [8], evolving through the ECCE [12] and ATHENA [13] proposals and culminating in the ePIC detector concept discussed here. It was concluded that an energy resolution of approximately  $12\%/\sqrt{E} \oplus 2\%$ , along with high granularity needed to distinguish single photons from DVCS events and photon pairs from  $\pi^0$  decays up to 50 GeV, would meet the EIC's measurement objectives.

Though numerous electromagnetic calorimeter technologies were considered, as noted in the EIC Yellow Report [8], the stringent space limitation in ePIC detector (an integration length of only 27 cm along the Z-axis for FEMC) ruled out all but one technology for the FEMC: WScFi. This technology, developed during the generic EIC detector R&D program [109], has also been successfully implemented in the recently constructed barrel electromagnetic calorimeter of the sPHENIX experiment [110], which is comparable in scope with the ePIC FEMC.

Some of the key requirements and parameters for the FEMC are summarized in Tab. 8.57. The most critical challenges include the limited integration space and the need for a very large dynamic range, approaching 7000:1. Radiation doses and neutron fluxes are not expected to pose significant challenges for current technologies. For instance, the forward calorimeter system (FCS) constructed for the STAR experiment at RHIC has been successfully operational since 2021 under conditions—both in terms of radiation and neutron flux—similar to those anticipated at the highest luminosities of the EIC. The choice of photodetectors and front-end readout electronics for the FEMC is partially based on the readout system developed for the STAR FCS.

**Device concept and technological choice:** Figure. 8.157 depicts the front face of the ePIC hadron end-cap in its closed position, which is divided into two halves to allow access to the inner ePIC detectors in its open position. The end-cap features 1,145 FEMC installation blocks, each of which is mounted to a one-inch-thick steel plate situated between the hadronic and electromagnetic calorimeters. Each installation block comprises 16 FEMC towers and weighs approximately 18 kilograms, bringing the total weight of the FEMC to around 21,000 kilograms. A 0.250 mm air gap separates each FEMC installation block to accommodate production and installation fixtures tolerances. The readout system for the FEMC is located at the front face of the blocks, ensuring easy access to the electronics. Cables and utilities run horizontally along each row of blocks to the perimeter of the FEMC, where they bunched and passed through few openings in the light-tight external shell and connected to the RDOs positioned on the sides of the hadron end-cap.

Each FEMC installation block is composed of four “production blocks,” with each production block consisting of a  $2 \times 2$  arrangement of towers. All production blocks are identical, and precise mechanical tolerances are ensured by using identical production molds fabricated to high tolerances,

**Table 8.57:** Some requirements on performance of FEMC and its parameters

Parameter	Requirements	Comments
Geometrical Acceptance	$1.4 \lesssim \eta \lesssim 3.9$	$R_{out} \sim 190$ cm, $Z_{frontface} \sim 341$ cm Hole for the beam pipe $30 \times 30$ cm <sup>2</sup>
Integration envelope	$R_{max}=205$ cm, Depth = 27 cm	
$E_{min}$ in a single tower	15 MeV	Minimal shower energy 50 MeV
$E_{max}$ in a single tower	100 GeV	$18 \times 275$ GeV, ep
Maximum rate in a single tower	10 kHz	$E_{thr}=15$ MeV, $10 \times 275$ GeV ep 500 kHz collision rate
Radiation doses	15 kRad	Integrated over 10 years
Neutron fluxes	$4 \times 10^{11}$ n/cm <sup>2</sup>	1 MeV eq, integrated over 10 years
Energy resolution	$\lesssim 12\%/\sqrt{E} \oplus (2)\%$	Verified in the test beams
$\gamma/\pi^0$ separation	up to 50 GeV	$\sim 5\%$ mis-identification at 50 GeV
Depth	$23 X_0$	Minimize leakages
Detector parameters	Units	Comments
$X_0, R_m$	7 mm, 19 mm	Rad. length, Moliere radius
$f_{samp}$	2%	$e/h \simeq 1$ above 10 GeV
Scintillating Fibers	$\varnothing$ 0.47 mm	Single clad sc. fibers
Light yield	$\sim 1600$ pixels/GeV	Test beam results.
Transverse size of tower	$2.5$ cm $\times$ $2.5$ cm	Matches $R_m$
Transverse size of installation block	$10$ cm $\times$ $10$ cm	Block of 16 towers
Total number of towers	18320	
Photodetector	S14160-6015PS	Four $6 \times 6$ mm <sup>2</sup> SiPMs per tower 15 $\mu$ m pixels size
Monitoring system	Blue LED	LED integrated on SiPM board. One LED per four towers

within a few tens of micrometers. The epoxy layer between production blocks is typically less than 100 micrometers thick. These thin epoxy layers, along with air gaps between installation blocks, represent the only dead material within the FEMC volume. These dead zones have a negligible impact on the overall performance of the FEMC.

The primary reason for using tungsten powder and scintillating fiber technology for FEMC is that it is the only practical method to meet the stringent requirements outlined in Tab. 8.57. Specifically, the desired energy resolution with extremely compact tower dimensions can only be achieved by combining a small sampling fraction with a high sampling frequency. This high sampling frequency is attained by using 780 thin, 0.47 mm diameter scintillating fibers in each tower, arranged in a staggered pattern with a center-to-center distance of approximately 0.955 mm. Both the fiber diameter and spacing were optimized through Monte Carlo simulations to ensure FEMC is nearly compensated and maintains the required energy resolution. Tungsten powder is used as the base material for the absorber structure to make the technology viable in practice. A set of specifications for tungsten powder and scintillating fibers for ePIC were established during generic detector R&D program for EIC and experience of constructing sPHENIX barrel EMCal utilizing WScFi technology.



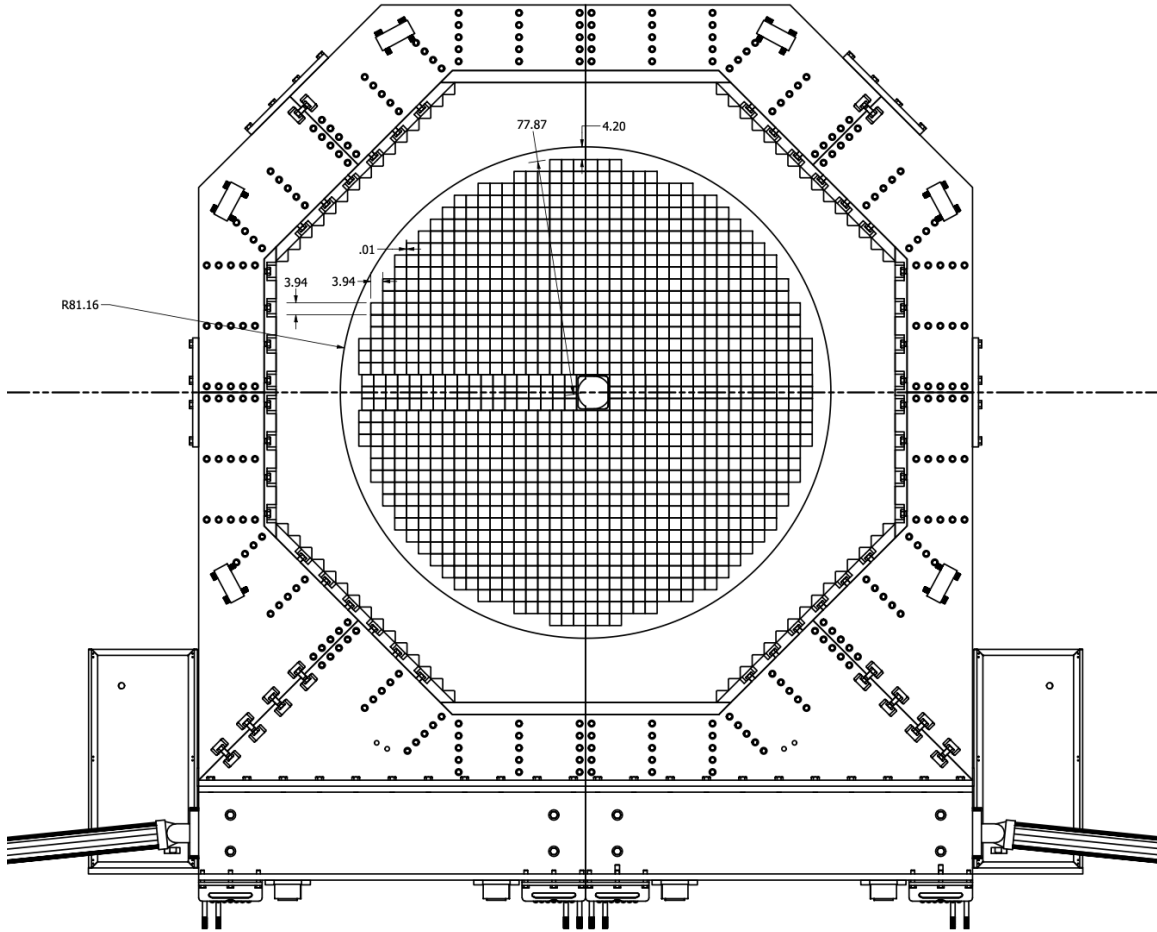


Figure 8.157: The front face of the ePIC hadron end-cap.

Despite the apparent simplicity of fiber calorimeters, constructing them is not straightforward. Detector components must be produced with extremely tight tolerances to maintain uniformity. Historically, techniques like extrusion, machining, or rolling were used to manufacture absorber plates, but these processes were complex and often required the creation of specialized machinery and tools. Building fiber calorimeters has traditionally been a labor-intensive process, with individual detector elements being handled one at a time, driving up costs compared to scintillating plate detectors. Moreover, traditional methods face challenges with increasing sampling frequency, as thinner absorber layers and fibers become more difficult to produce and manage. We refer to the example of the H1. Construction and assembly techniques for the H1 fiber calorimeter detailed in [111].

Our approach differs in that we first create a matrix of fibers and then pour the absorber material into the matrix. Unlike previous methods, this technique eliminates the need to handle individual calorimeter elements separately. Fig. 8.158 shows a matrix of scintillating fibers and image of tungsten powder used to build FEMC prototypes. This powder has a particle size distribution of 90% between 70 and 160 microns, a tap density of  $11.5 \text{ g/cm}^3$ , and a purity of  $W \geq 99.9\%$ , with Fe, Ni, and Co combined at  $\leq 0.1\%$ . Additionally, this tungsten powder demonstrates exceptional fluidity, a critical characteristic for our application. It is stored in a humidity-controlled environment prior

to its use in block production, as humidity can impact epoxy impregnation. The only other step required for the absorber material is accurately measuring the specified amount of powder before pouring it into the fiber matrix.



**Figure 8.158:** Matrix of scintillating fibers prepared to build production FEMC blocks and SEM image of tungsten powder.

The second key element is a straightforward method for forming the scintillating fiber matrix. This matrix is defined by a set of precision brass meshes produced via photo-etching. These meshes have mechanical tolerances of 30 microns on their overall dimensions for 300-micron thick meshes and about 15 microns for the center-to-center distances between the holes for the scintillating fibers. The fibers are cut to the desired length using a thermo-cutter, which melts the fiber ends to form small drops that act as stoppers, preventing the fibers from slipping through the mesh holes. Once the meshes are stacked, approximately 500 fibers at a time can be dropped into the container holding the meshes, and with slight tapping, the fibers will flow through the set in seconds. For our recent prototypes, a trained student could form a fiber matrix for a 2x2 tower production block with 3,120 fibers in around 30 minutes.

The total production volume of scintillating fibers for the forward EMCal (FEMC) is 3,000 km. Only two companies, KURARAY and Luxium (formerly St. Gobain, BICRON), are capable of producing the necessary fibers. Both companies' fibers were previously used to construct and beam-test several WScFI EMCal prototypes for the EIC, with St. Gobain fibers also utilized by the sPHENIX collaboration for their barrel EMCal. Recently, Luxium optimized the composition of their standard BCF-12 fibers specifically for the shorter 17 cm fibers required for FEMC, resulting in a 20% improvement in light yield compared to their standard fibers. This was achieved by adjusting the concentrations of primary and wavelength-shifting fluors, bringing them to the same performance level as KURARAY fibers. Tab. 8.58 outlines the technical specifications and requirements for the FEMC fibers.

To create a scintillating fiber matrix, it is essential that the fibers remain straight when placed into the mesh framework. Fibers processed from spools tend to retain a bend due to "memory," which leads to significant friction between fibers flowing through a set of meshes, which complicates the

**Table 8.58:** Requirements and Technical specifications for FEMC scintillating fibers.

Parameter	Requirements	Comments
Light Yield (LY)	$\geq 8000$ photons per MeV	Acceptance QA with Sr90 source Compared to a standard sample
Nominal Diameter	$0.47 \text{ mm} \pm 0.0094 \text{ mm RMS} \leq 0.02 \text{ mm}$	QA sampled on 10% boxes 100% at ramp-up prod. stage
Attenuation Length	$\geq 3 \text{ m}$	QA with UV LED
Batch-to-batch LY variation	$\leq 10\%$	QA with Sr90
Emission spectrum	Blue-green light	To match QE of SiPMs
Scintillation Decay Time	$\leq 3 \text{ ns}$	Bunch structure at EIC
Delivery Method	In canes, length of fibers +2%, -0%	Length $\geq 1 \text{ m}$ , increment 20 cm

assembly process. Among suppliers, only Luxium agreed to a delivery method that addresses this issue, making them the sole provider of fibers for the FEMC. These scintillating fibers are a long lead procurement item, with a pre-production batch expected to arrive at ePIC by the end of 2024, followed by monthly deliveries of the remaining fibers. Both the production and acceptance sites will adhere to agreed-upon QA and acceptance protocols to ensure that the fibers meet FEMC specifications. Some of these QA steps are outlined in Tab. 8.58.

The concept of using tungsten powder as an absorber was briefly explored by the UCLA group in 2003, when they constructed and tested a small electromagnetic prototype at SLAC. At the time, the tower structure required a thin-walled brass container to hold the dry powder and fibers in place. However, this assembly technique proved imperfect, leading to significant transverse non-uniformities in detector response due to variations in the sampling fraction and potential displacement of fibers during packing. A compact calorimeter demands strict mechanical tolerances and a highly uniform internal structure to achieve theoretical energy resolution. To address these issues, we introduced intermediate meshes to secure fibers along the towers and developed a vacuum-assisted method to infuse epoxy into the tungsten powder/fiber assembly. Once assembled, the structure becomes rigid, eliminating the need for external containers and dead material in the tower. The homogeneity of the WScFi structure was confirmed by cutting multiple samples into small pieces for analysis. The results showed a uniformity better than 1%, ensuring a negligible effect on energy resolution. The mechanical properties of the WScFi structure (Young's, shear and bulk modulus) were measured and they are comparable to construction steel.

This refined technique, with slight variations, was then employed in constructing the sPHENIX barrel EMCal and all recent FEMC R&D prototypes.

**Light Collection scheme and Photosensors** The light collection scheme and photosensor setup adhere to the general requirements outlined in Tab. 8.57. The back of each installation block features a thin layer of optical epoxy (1.8 mm thick) mixed with 10%  $\text{TiO}_2$ , which acts as a diffuse optical reflector for the scintillating fibers and provides a surface for bonding the 13 mm-thick aluminum "strong back." This strong back plate is then bolted to the steel interface plate connecting the EMCal and HCal. On the front side of the installation block, a 21 mm-long light guide (LG) plate is attached. Fabricated from a single piece of optically clear cast acrylic, this LG plate features 64 trapezoidal light guides designed to channel light from the fibers to the SiPMs. Specialized tools were developed and refined during the R&D phase to optimize the machining of these light guides. Additionally, a post-machining light polishing process, which enhances light collection efficiency by approximately 10% compared to non-polished guides, will be implemented during production.

6125 The front and back views of the LG plate with SiPMs attached can be seen in Fig. 8.159. The light  
 6126 collection efficiency of this setup is approximately 80%, which is sufficient to detect 15 MeV in a  
 6127 single tower, corresponding to 24 fired pixels. However, due to the short length of the light guide  
 6128 (typically much longer in fiber calorimeters), light “mixing” from individual fibers is minimal, re-  
 6129 sulting in spatial non-uniformities in light collection at the 10% level, as measured with a point  
 6130 light source.

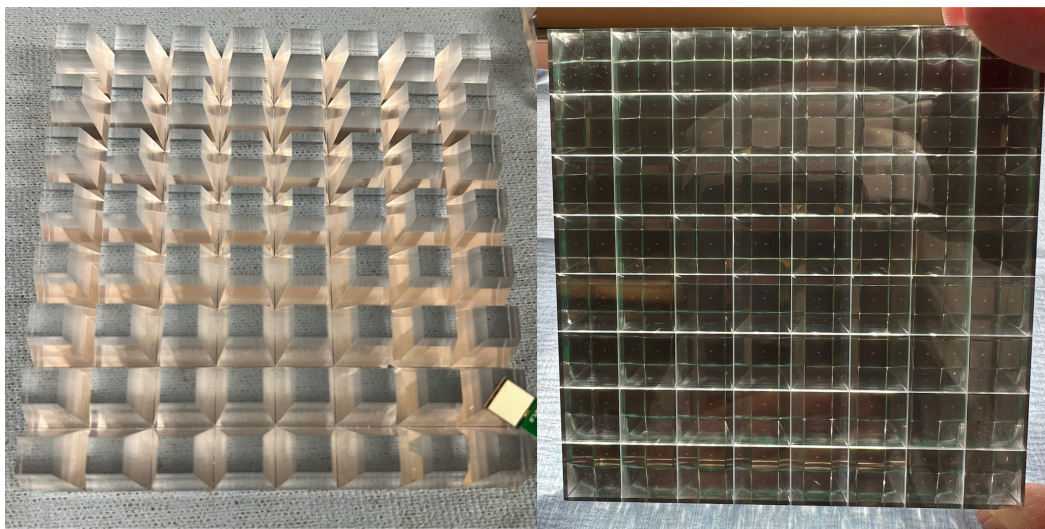


**Figure 8.159:** Front and back views of LG plates with installed SiPMs.

6131 The chosen photodetector for the FEMC is the SiPM (Silicon Photomultiplier). Over the past 15  
 6132 years, extensive R&D programs across the globe—including the generic detector R&D program for  
 6133 the EIC—have worked to bring SiPM technology to a mature and reliable level. Today, hundreds  
 6134 of thousands of SiPMs are in use in various high-energy physics and nuclear physics experiments.  
 6135 These detectors are extremely compact, robust, and well-suited for calorimetry readout in moder-  
 6136 ate radiation environments, such as the forward region of the ePIC detector, as shown in Tab. 8.57.  
 6137 The failure rates of SiPMs in calorimeter operations at facilities like JLab, BNL, and CERN have  
 6138 been remarkably low, typically less than  $\approx 0.1\%$ . Notably, the STAR Forward Calorimeter System  
 6139 (FCS) experienced zero SiPM failures (out of  $\sim 10\text{k}$  SiPMs) during three years of operation under  
 6140 conditions similar to those expected in the high-luminosity EIC. Although neutron-induced dam-  
 6141 age will lead to increased leakage current and noise levels, these effects remain within tolerable  
 6142 limits. For example, it is anticipated that the equivalent noise level for FEMC at ePIC will rise to  
 6143 around  $\approx 6$  MeV after 10 years of operation, particularly in areas near the beam pipe. This projec-  
 6144 tion is based on scaling from the results observed in the STAR FCS. After this period, replacement  
 6145 of some of the SiPM boards near the beam pipe may be necessary. These considerations guided the  
 6146 design of the FEMC readout system, ensuring simple and seamless integration with the detector, as  
 6147 well as facilitating maintenance of electronics and replacement of SiPM boards during shutdowns  
 6148 if necessary. The technical specifications and performance details of the SiPMs for the FEMC are  
 6149 summarized in Tab. 8.59.

6150 **Mechanical Integration** The mechanical integration, installation procedures, and structural  
 6151 tests for the FEMC were validated using installation blocks at BNL. These blocks were produced



**Table 8.59:** Requirements and Technical specifications for FEMC SiPMs.

Parameter	Requirements	Comments
Active Area	6 mm $\times$ 6 mm	Efficiency of light collection, $E_{min}$ 15 MeV
Pixel Size	15 or 20 $\mu$ m	Dynamic Range, $E_{max}$ 100 GeV
Peak Sensitivity	$\sim$ 420 nm	Match scintillating fibers spectra.
PDE	$\geq$ 30%	Efficiency of light collection, S/N
Gain	$\sim 2 \times 10^5$	at 3 V overvoltage, S/N
DCR	$\leq$ 3000 kcps	at 3 V overvoltage, 25 C, S/N
Temperature Coefficient	$\leq$ 40 mV/C	Stability, Uniformity
Direct Cross Talk	$\leq$ 1%	
Terminal Capacitance	$\leq$ 2.5 nF	FEE coupling
Packing Granularity	Multiple of 4 per tray	4 SiPMs per tower at same $V_{op}$
$V_{op}$ variation within a tray	$\pm$ 0.02 V	Uniformity of response

following the final production protocols and using the same components that will be used for the  
 actual installation. Structural tests on smaller samples demonstrated that the safety factor for the  
 proposed mounting scheme is greater than 48. A full structural test Fig. 8.160 was conducted by  
 mounting an installation block on a mockup plate and applying five times the expected load. The  
 deflections at the readout end of the FEMC block were measured to be less than 100  $\mu$ m, confirming  
 that each installation block is self-supporting and does not exert any load on the blocks beneath it.  
 Simple installation fixtures were designed, and the installation procedures were verified to ensure  
 safety. Specifically, it was crucial to confirm that the FEMC blocks could be safely installed with  
 the SiPM-carrying boards glued to the LG plates. The tests confirmed that the blocks can be safely  
 mounted onto the hadron end-cap without causing any damage to the SiPM boards.

**Figure 8.160:** Structural and installation tests at BNL.

**Performance** The performance of the FEMC prototypes has been tested in several test beams at FNAL over the past few years, initially as part of the generic detector R&D for the EIC and later as part of the ePIC R&D program. In the summer of 2024, one installation block featuring the latest version of the light guide (LG) and SiPM readout was tested at FNAL. Energy scans were conducted at various impact angles covering the entire FEMC acceptance range. As expected, some variation in response across the surface was observed, as shown in Fig. 8.161, due to the compact nature of the LG. However, this variation represents an improvement compared to earlier versions [112]. Position-dependent corrections, based solely on the data from FEMC, were applied to account for non-uniformities. This method is similar to the approach used in the 2014 test [112] and for the sPHENIX barrel EMCal. As anticipated, the uniformity of response improves with shallower impact angles. The energy resolution, shown in Fig. 8.161, corroborates previous measurements with this type of electromagnetic calorimeter [112] and aligns with the performance requirements outlined in Tab. 8.57. The measured absolute light yield is 1580 pixels/GeV.

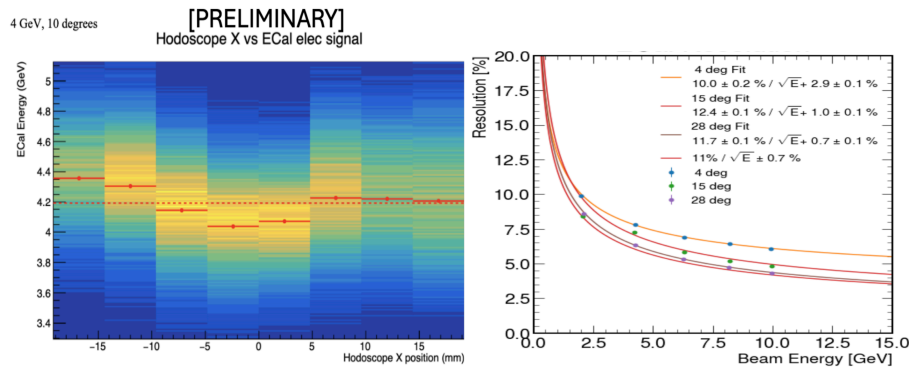


**Figure 8.161:** Response of calorimeter vs position in hodoscope (left panel). Energy resolution for different impact angles (right panel).

The remaining performance parameters were extensively tested using MC simulations, incorporating the full ePIC simulation chain with the latest detector geometry updates. A material scan indicated the presence of approximately  $0.2 X_0$  of “dead” material in front of the FEMC in ePIC, but its impact on performance was found to be negligibly small. Simulations conducted with PYTHIA8, using minimal  $Q^2$  cuts for all energy configurations at the EIC, examined occupancy, rates, and dynamic range. These studies informed the set of requirements listed in Tab. 8.57.

An initial investigation into  $\gamma/\pi^0$  separation, based on the traditional shower shape analysis method outlined in the EIC Yellow Report (Fig. 11.46, [8]), revealed potential for improvement. A significant enhancement in  $\gamma/\pi^0$  separation was achieved by applying machine learning algorithms. As shown in Fig. 8.162 (left panel), the misidentification rate at 60 GeV dropped to approximately 10%, compared to 80% with traditional methods [8].

**Readout Electronics** The FEMC readout electronics face three primary challenges: achieving a large dynamic range of 7000:1, ensuring precise discrimination for streaming small signals (24 pixels) amidst dark counts of up to 45 GHz caused by radiation damage to SiPMs, and integrating everything within a compact space—around 5 cm for SiPM boards, front-end boards (FEBs), cooling, and cables. Tab. 8.60 summarizes requirements for the FEB.

Building on the successful design of the STAR FCS readout, FEMC’s readout system transfers SiPM signals to a low impedance load, shapes and amplifies the resulting voltage, and digitizes the waveform. Hits are detected in the digital waveform via threshold crossing (which may be filtered). In

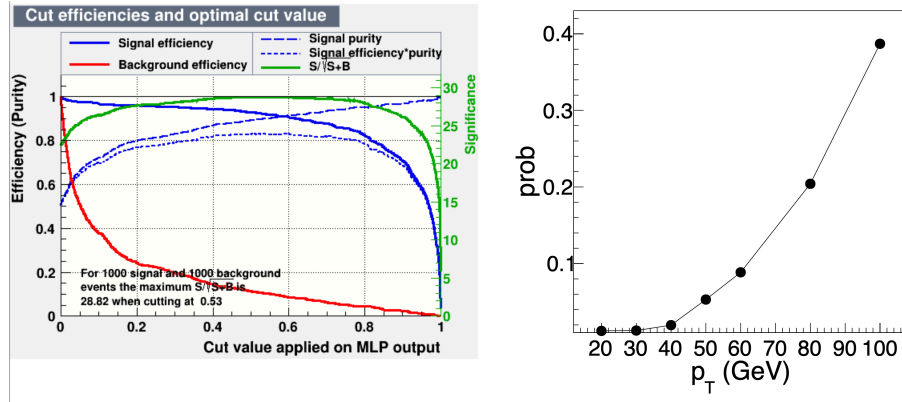


**Figure 8.162:** Signal (single photon) efficiency and background (merged di-photons) contamination for different cut value of the NN output for 60 GeV (left panel). Probability of misidentifying  $\pi^0$  as a single photon vs energy (right panel)

**Table 8.60:** Requirements for the FEB

Parameter	Requirements	Comments
SiPM & overvoltage	4xS14160-6015PS, 2-3V	
Min signal	15 MeV (@ 1.6 pix/MeV)	
Max signal	100 GeV	
Hit rate	10 kHz	per channel
Charge reso.	$\sim 210\% / \sqrt{npix} \oplus (0.9)\%$	contribute $\leq 10\%$ of FEMC resolution
Charge nonlinearity	$\leq 1\%$	
Time resolution	$\ll 10$ ns	for $\geq 100$ MeV signals only
SiPM bias voltage stability	$\leq 10$ mV	including T compensation
Bias voltage setting range	33 to 47 V	sufficient for meaningful IV curve
Bias current range & mon. resolution	2 mA, $\leq 200$ nA	4 SiPMs per tower at same $V_{op}$
LED drive control	var. amplitude, masks	fired by global command

streaming readout mode, regions of interest in the digital waveform are identified, timestamped, and sent to an output FIFO/merging scheme, before being transmitted to the readout (RDO) board. At the RDO, data from up to 16 FEBs are buffered, merged, and sent to the DAM. Feature extraction, converting raw waveform samples to estimated pulse amplitude and timing, may be done either at the FEB or RDO level to reduce data volume. If hardware feature extraction is not used, this will be performed during preliminary online analysis.

Waveform digitization for FEMC will operate at either 39.4 MSPS or 49.25 MSPS. The digitization clock must be phase-locked to the beam bunch crossing clock at 98.5 MSPS to extract hit timestamps in real-time within the streaming DAQ system. Sampling at 98.5 MSPS is not feasible due to power and FPGA resource constraints. To meet the 15 MeV readout threshold and achieve the dynamic range, the ADC resolution must be 14 bits. The analog waveform will be shaped before digitization to achieve a peaking time of approximately  $2.8/f_{SAMPLE}$ , which ensures less than 1% error in pulse amplitude measurement while minimizing noise from dark count pileups. For instance, a 57 ns peaking time is optimal at 49.25 MSPS.

The FEB will individually regulate bias voltage for each tower, providing temperature compensa-



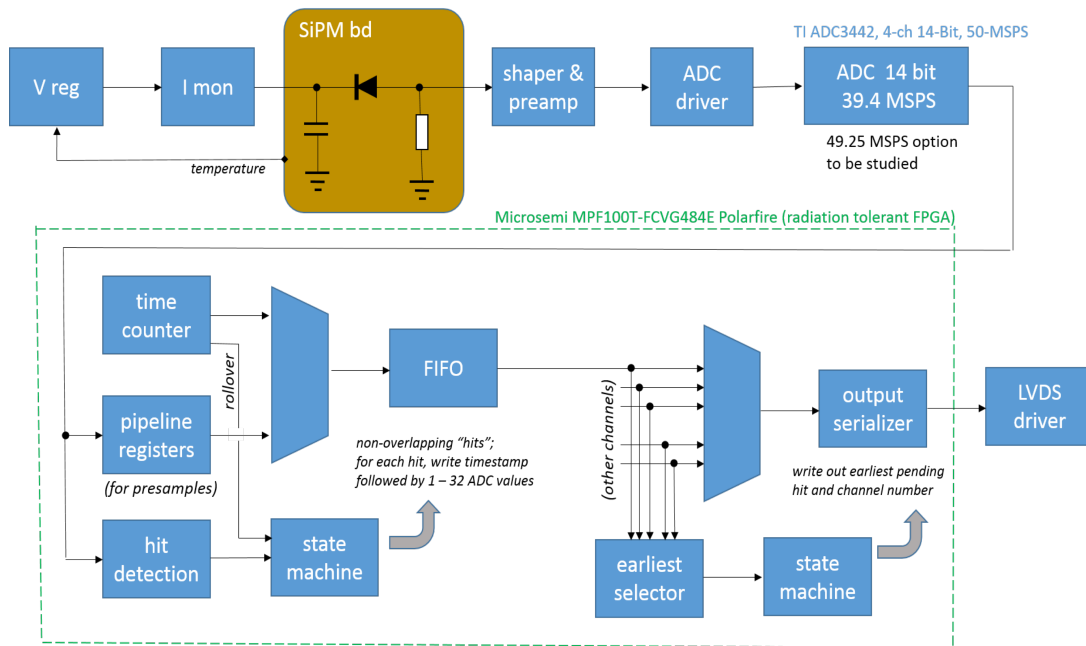


**Figure 8.163:** FEMC front end electronics.

tion for each SiPM board (covering  $2 \times 2$  towers) and monitoring current with built-in protective current limits. Each tower's four SiPMs will be connected in parallel, sharing a common bias voltage, requiring precise matching of the breakdown voltages ( $V_{BR}$ ) among the four SiPMs to ensure uniform gain. The bias regulation circuits, developed from the STAR Forward Calorimeter, have proven effective, though radiation sensitivity in a voltage reference IC was noted. To mitigate this, FEMC's bias regulator will use a remote reference on the power distribution boards, ensuring the required 0.03% stability. Less critical internal voltage references require only 1% stability. The bias regulation channels provide sharp current limiting to protect the SiPMs from overload, maintaining 10 mV bias voltage stability up to the current limit (2 mA).

Signal routing from the SiPM boards to the FEBs is achieved through board-to-board connectors, eliminating the need for cables. These connectors can accommodate mechanical tolerances of  $\pm 0.5$  mm between the FEB and SiPM boards and overlap with space allocated for the cooling water tube. Should radiation damage impact the innermost FEBs, a backup plan would route SiPM signals via 2m coaxial cable bundles to FEBs mounted at the block periphery.

Connections between the FEBs and RDO will use shielded Cat6 Ethernet cables, routed horizontally through the FEB rows and out of the magnet to racks housing the RDOs. One rack will be placed north of the north detector half, and another south of the south detector half. Cable lengths are estimated at 15 meters, and it has been confirmed that LVDS signals can be properly received at 200 Mb/s over this distance, meeting performance requirements.

Each rack will also house a Wiener MPOD crate with low-voltage (LV) power supplies, with one crate serving the north half and one for the south half of the detector. Each FEB will require approximately 250 mA at +16 V, 180 mA at -2 V, and up to 67 mA (depending on SiPM radiation damage) at +50 V.

The FEBs will be cooled conductively via a copper bracket attached to the main board (housing the ADCs, FPGA, and power supply circuits) and connected to a water cooling line. The water line will

consist of standard 1/4" inch (potentially 3/16 inch) diameter copper tubing. A negative pressure system will mitigate the risk of water leaks. Two rows of FEBs will be served by a single water line in a U-shaped loop, with no fittings at each FEB, only at the loop ends. Reliable flare fittings will be used for the connections. Custom water manifolds, located in the "service gap" at the outer perimeter of the calorimeter blocks, will manage water distribution. The arrangement will likely consist of two supply and return manifold sets—one for the upper and one for the lower half of the detector.

Each water circuit will need to cool about 750 W of power from 148 FEBs, requiring chillers with at least 1.5 kW capacity for each half of the detector. One chiller will serve the north half and another the south, cooling two water circuits each.

Slow controls for FEMC will fall into two categories: hardware registers on the FEBs (communicated through DAQ software and the DAM/RDO) and controls for commercial equipment such as the water chillers and power supplies (Wiener MPOD), connected via Ethernet. SoftIOC interfaces will manage EPICS variables, providing GUI control, logging, and alarms.

Tab. 8.61 summarizes the control and status registers for the FEB.

**Table 8.61:** Control and status registers on the FEB

Function/description	Qty per FEB	R/W	Notes
SiPM bias voltage (base)	32	R/W	
Bias temp. comp. slope	1	R/W	
actual compensation	8	R	i.e. temperature
SiPM current monitor	32	R	extra diagnostic info
input LV supply monitor	2	R	
FEB temperature monitor	3	R	
FEB & SiPM board serial numbers	9	R	read once at startup
firmware revision	1	R	read once at startup
firmware update interface	1	R/W	maintenance use only
hit threshold channel mask	32	R/W	
hit detection options registers	4	R/W	
LED firing mask	1	R/W	
hit scalers	32	R	
fifo overrun scalers	32	R	
ADC configuration interface	1	R/W	might be internal use only

**Calibration** The FEMC faces the hadron beam, and at mid to high energies, its signals will predominantly come from photons produced by  $\pi^0$  decays. Tower-by-tower absolute energy calibration of the forward electromagnetic calorimeter will be performed by reconstructing  $\pi^0$  mesons through the invariant mass of two photons from  $\pi^0$  decays. It is expected that  $\pi^0$  calibration for each tower can be achieved in approximately one day of data collection, followed by semi-online analysis using only forward FEMC data. The method involves associating reconstructed  $\pi^0$  mesons with the tower showing the highest response, adjusting the tower's gain based on the  $\pi^0$  mass location, and repeating the process over several iterations. This technique has been successfully implemented in forward calorimeters at RHIC, including the STAR FCS.

Electrons from DIS events, combined with tracking information, can be used to cross-check the

calibration. However, this approach requires a large dataset and will be performed offline. Additionally, Minimum Ionizing Particle (MIP) signals from hadrons can be utilized for calibration at the low-energy end. For high energies, where the two photons from  $\pi^0$  decays are too close together for the forward EMCal to distinguish them,  $\eta$  mesons can be used to verify energy non-linearity.

**Monitoring system** An LED system will be installed on the FEE boards to illuminate four towers using a trigger pulse. The LEDs will be preselected to provide equal light output to the towers, serving as a critical monitoring system. This will be essential for initial testing during installation, verifying mapping, and ensuring long-term stability of the detector, SiPMs, and FEE board gain, as well as detecting any potential radiation damage. A dedicated short LED run will be performed daily to monitor the calorimeter's performance.

Additionally, the current and voltage on the FEE boards will be continuously monitored. Periodic I-V curve measurements will be conducted, on a weekly or bi-weekly basis, to assess the health of the SiPMs and FEE boards.

#### Status and remaining design effort:

R&D effort: eRD106 will be completed in early 2025 with finalizing analysis of the test beam data.

E&D effort: Detailing of mechanical design, and formalizing production drawings.

Other activity needed for the design completion: Produce and test first versions of final design FEB and SiPM boards.

Status of maturity of the subsystem:  $\sim 70\%$

**Environmental, Safety and Health (ES&H)** The project will strictly adhere to all Environment, Safety, and Health (ES&H) regulations to ensure the safety of personnel, the integrity of the equipment, and the protection of the environment throughout the construction and operation phases. Comprehensive risk assessments will be conducted for all activities, including the handling of hazardous materials, electrical components, while implementing proper controls to minimize exposure to risks. Personnel will receive specialized training in safety protocols and emergency response procedures, and regular audits will be conducted to ensure compliance with ES&H standards. Additionally, the design of systems such as power management will prioritize environmentally friendly practices, incorporating energy-efficient technologies and minimizing waste and emissions. Continuous monitoring of environmental impact and adherence to radiation safety guidelines will be maintained to ensure the long-term safety and sustainability of the project.

**Collaborators and their role, resources and workforce:** Collaboration plays a pivotal role in the success of this project, as it brings together a diverse group of experts from various institutions, each contributing specialized knowledge and skills. The development of the FEMC detector, for instance, relies on coordinated efforts between physicists, engineers, and technicians working on different aspects such as design, testing, and integration. Collaborative efforts ensure that challenges in areas like electronics, cooling systems, and data acquisition are addressed through shared expertise and innovative problem-solving. Additionally, partnerships with other research labs, such as BNL and international institutions, allow for the exchange of ideas, the pooling of resources, and the sharing of key R&D advancements. This collaborative environment fosters a

6299 culture of learning and inclusivity, which is critical for the project's long-term success, allowing it  
6300 to meet both scientific and technical goals.

### 8.3.6 Hadronic Calorimetry

Add text here.

#### 8.3.6.1 The backward endcap hadronic calorimeter

The backward hadronic calorimeter, here called **nHCal** (meaning Negative-eta/Neutral Hadronic Calorimeter), is a tail catcher calorimeter to be installed in the electron-going negative-z direction. As illustrated in the ePIC detector schematic 8.14, the nHCal is surrounded by an outer collar, backed by a flux return plate and has an oculus ring placed in front. Experience from the H1 experiment at HERA demonstrates the need for such a calorimeter for low-x measurements [113, 114].

#### Requirements

**Requirements from physics:** The main requirements for nHCal originate from physics processes in events with low  $Q^2$  and low  $x \sim 10^{-3} - 10^{-2}$  as well as high inelasticity  $y$ . This requires the acceptance of  $-4.14 < \eta < -1.18$ .

The processes of interests include diffractive vector meson overproduction  $J/\psi \rightarrow \mu^+\mu^-$ ,  $\phi \rightarrow K_L K_S$ ,  $\phi \rightarrow K^+ K^- \rightarrow \mu^+\mu^-$  and diffractive dijets. It will be also used as a veto for jet studies with neutral energy component and help in scattered electron identification along with backward EMCAL. Finally, it will be used as a hadron beam background veto for dRICH in conjunction with LFHCAL for which a good timing resolution is required. In order to measure vector meson production with muons a good  $\mu/\pi$  separation of tracks with MIP signal in calorimeters is required. Low-energy neutron detection for neutral jet identification demands low hit thresholds to achieve greater than 90% detection efficiency for 2 GeV neutrons. Moreover, neutral clusters must be identifiable after charged hadron correction, necessitating track matching and cluster position resolution capable of distinguishing showers separated by 30 cm. This resolution is achievable with tiles of up to 25 cm size.

**Requirements from Radiation Hardness:** In general, the radiation dose in the electron endcap area is expected to be low. A study was performed and summarized by ePIC background study group [31].

The low radiation dose compared to the forward region makes the use of SiPMs and FEE safe. SiPMs are required to maintain a low dark count rate after 10 years of operation. This is possible with the selected Hamamatsu S14160-1315PS model. Radiation tests [115] show that non-avalanche starts to increase above the level of  $10^{-10}$  MEQ neutron fluence, which is expected to be reached after 10 years of operation.

**Requirements from Data Rates:** Data rates were studied by considering the following sources:

- Deep Inelastic Scattering (DIS)
- Synchrotron Radiation
- Electron Beam Gas

bkg. type	hit rate in detector [kHz]	max single channel hit rate [kHz]
DIS	$\sim 10^3$	1.23324
Synchrotron rad.	$\sim 2 \cdot 10^1$	-
e+gas	403.899	6.6448
h+gas	$\sim 7 \cdot 10^2$	0.303781

**Table 8.62:** Maximum expected background rates for backward HCal. The assumed threshold is 170 keV.

- Hadron Beam Gas

The values are taken from background studies found here:

- <https://wiki.bnl.gov/EPIC/index.php?title=Background>

### Justification

**Device concept and technological choice:** Sampling calorimeter design featuring 10 layers of steel absorber and plastic scintillator tiles was selected as nHCal, because of low cost and simplicity. SiPMs and WLS fibers are going to be used for the light collection. The design, similarly to LFHCAL, is inspired by CALICE [116] collaboration, which allows mass production and easy handling of same type of detector modules.

### Subsystem description:

General device description:

The nHCal is planned to be a sampling hadronic calorimeter with 10 layers of alternating steel and plastic scintillator, 4 cm and 0.4 cm thick, respectively. This arrangement provides compensation. The structure of the calorimeter will be a flattened cylinder with an outer radius of 276 cm and an inner radius of 14 cm to accommodate the hadron and electron beam pipes. The total thickness along the beam direction will be 45 cm. The detector will be placed at a position of  $-395$  cm from the interaction point in the electron-going direction. The plastic scintillator layer will consist of tiles with a size of  $10 \text{ cm} \times 10 \text{ cm}$  (TBD). Two light collection solutions are under consideration: either the use of WLS fibers with SiPM readout or the SiPM-on-tile design, similar to that used for the LFHCAL, which was developed by CALICE [116]. The SiPM-on-tile approach is feasible with smaller tiles near the beam ( $\eta \sim -4$ ), while larger tiles will require the WLS+SiPM combination. Tiles and absorber plates will be assembled into modules inspired by LFHCAL modules, with dimensions of  $10 \text{ cm} \times 20 \text{ cm} \times 45 \text{ cm}$  in the  $y, x$ , and  $z$  directions, respectively.

Sensors:

The Hamamatsu S14160-1315PS SiPMs will serve as light sensors. They will either be connected to the WLS fibers or placed directly on the tiles.

FEE:

The HGCROCv3 will be used as a Front-End Electronics (FEE) system, similar to other calorimetry systems in ePIC. The FEEs will be placed in front of the modules.



Other components:

The nHCal will also feature a calibration system based on LEDs as well as a temperature monitoring via sparsely placed temperature sensors. This is described in more detail in 8.3.6.1.

**Performance:** The performance of the nHCal was studied using single particle simulations in dd4hep with GEANT4 used for particle transport. Neutron detection thresholds were evaluated against kinetic energy and integration time. Figure 8.164 illustrates the neutron detection efficiency as a function of energy threshold and integration time. Good performance is achieved with 100 ns integration time, and further increases offer minimal improvement. Additionally, a low threshold of  $0.25E_{MIP}$  already provides a good detection efficiency 70% at 300 MeV.

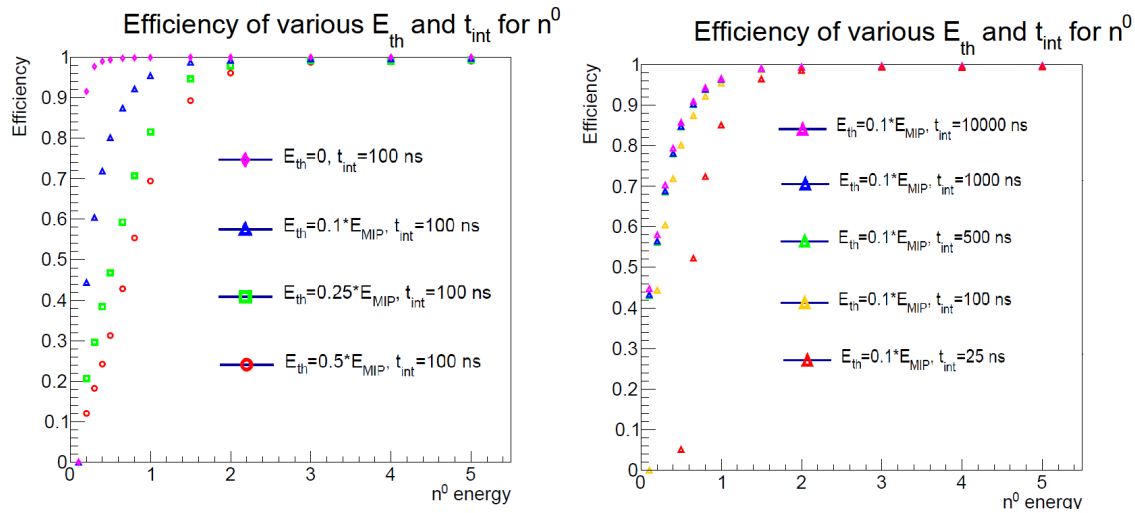


**Figure 8.164:** Left: Neutron detection efficiency vs. kinetic energy  $E_{kin}$ , dependence on threshold as a fraction of MIP energy deposit. Right: Same as left, but showing dependence on integration time. Repository: [https://github.com/OSUNuclearPhysics/ePIC\\_preTDR\\_nHCal\\_thresholds](https://github.com/OSUNuclearPhysics/ePIC_preTDR_nHCal_thresholds)

Studies of  $e/h$  response with  $e/\pi$  simulation show that the ratio of steel and scintillator achieves compensation within uncertainties as presented in Fig. 8.166.

**Simulated DIS events:** One of the basic studies is a check of energy and momentum distributions going into backward HCal. This study used DIS  $e + p$  events at  $18 + 275$  GeV with  $Q^2 > 1 \text{ GeV}^2$ . The Fig. 8.167 shows total energy  $E$  and  $p$  distributions of each particle species in the nHCal acceptance  $-4.0 < \eta < -1.0$ .

Energy and momentum distributions of particles within nHCal acceptance in  $e + p$  DIS events at  $18 + 275$  GeV with  $Q^2 > 1 \text{ GeV}^2$  were studied using the full official simulation of the ePIC detector. These distributions are presented in Fig. 8.167 as well as versus  $\eta$  in Fig. 8.168, Fig. 8.169 and Fig. 8.170. This analysis was used to determine the average energy of neutrons and optimize the detector geometry and thresholds.

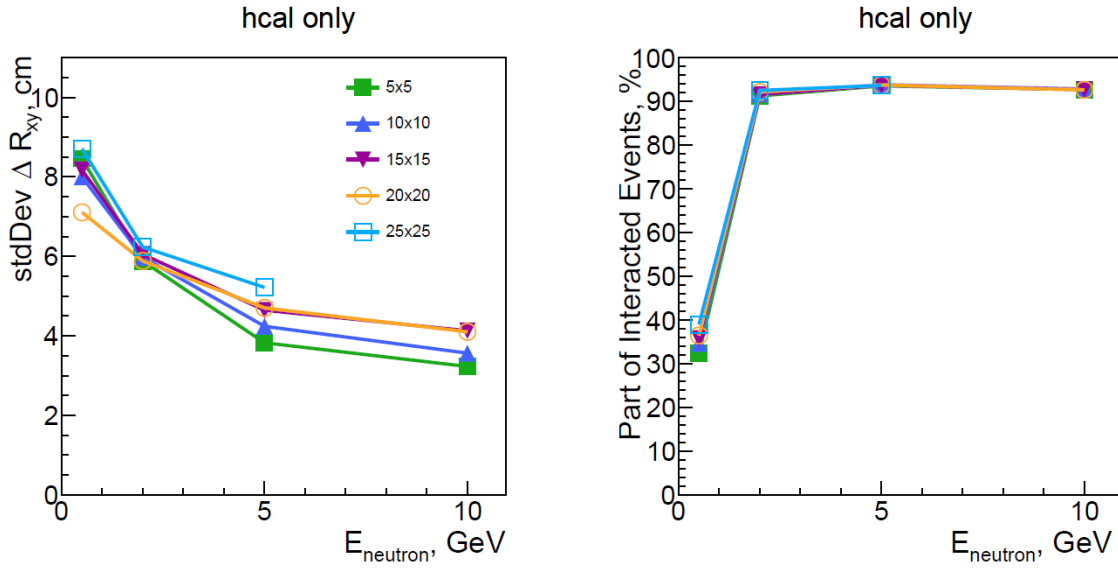


**Figure 8.165:** Position resolution  $R_{xy}$  and cluster efficiency vs.  $E$  for different tile sizes. Repository: [https://github.com/OSUNuclearPhysics/ePIC\\_preTDR\\_nHCal\\_TileScaling](https://github.com/OSUNuclearPhysics/ePIC_preTDR_nHCal_TileScaling)

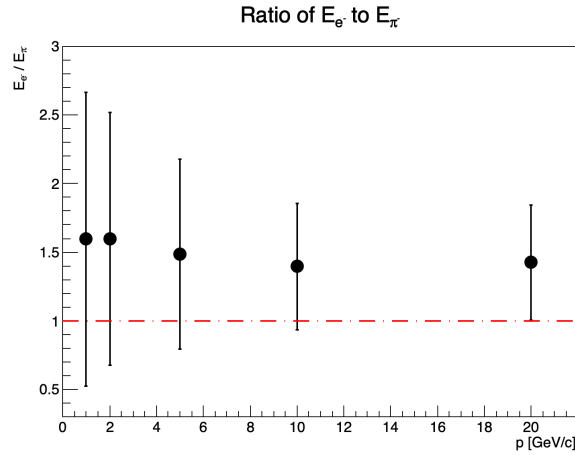


**Figure 8.166:** Ratio of  $e/\pi$  response vs.  $E$ . Repository: [https://github.com/OSUNuclearPhysics/ePIC\\_preTDR\\_nHCal\\_eh-ratio](https://github.com/OSUNuclearPhysics/ePIC_preTDR_nHCal_eh-ratio)

6387 **Vector meson reconstruction:** Vector meson reconstruction and acceptance were studied in  
 6388  $e + p$  and  $e + A$  events using a standalone Sartre simulation, focusing on exclusive diffractive pro-  
 6389 duction. A large fraction of the  $J/\psi$  cross section was found to be produced in the backward direc-  
 6390 tion, highlighting its importance. It should be noted that the  $J/\psi$  study is one of the major goals  
 6391 of EIC, as listed in the Yellow Report [41]. The acceptance of  $J/\psi$  is shown in Fig. 8.171 versus  $-t$ ,  
 6392 Bjorken  $x_{BJ}$ , and Pomeron  $x_P$ . The figure also illustrates the acceptance when decay daughters are  
 6393 measured in different hadronic calorimeters. A similar study was performed for  $e + A$  collisions  
 6394 and is presented in Fig. 8.172. Studies of  $\Phi \rightarrow K^+ K^-$  were also performed as shown in Fig. 8.173

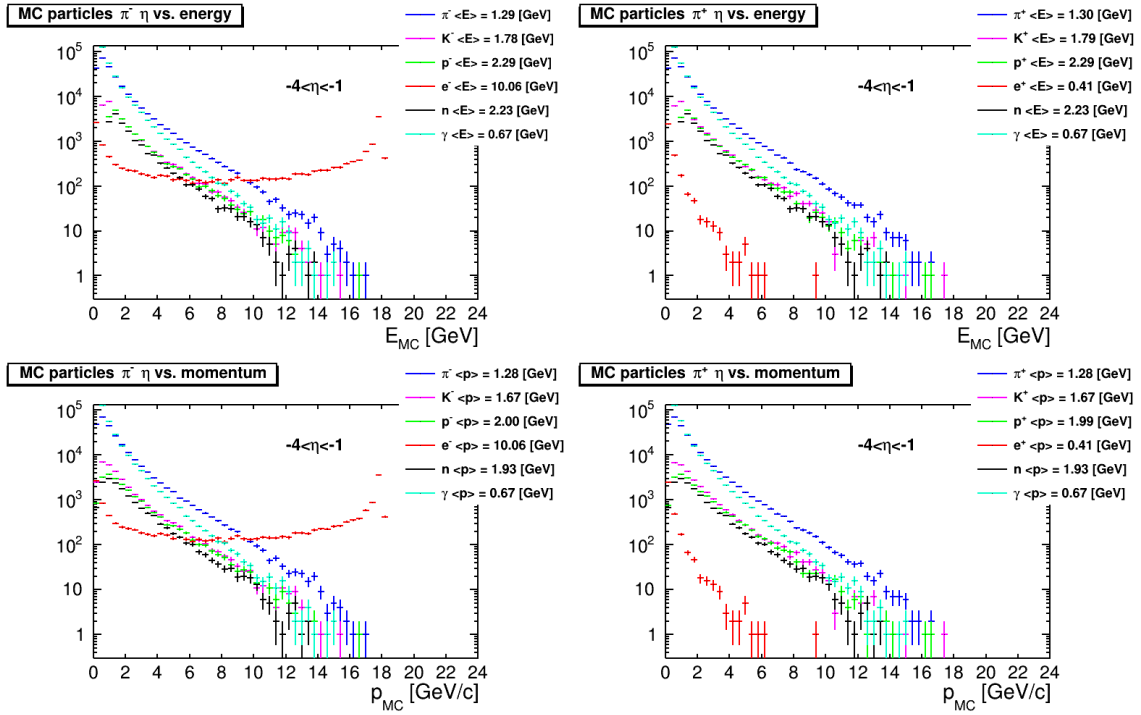


**Figure 8.167:** **Top:** Primary, generated particle  $E$  distributions in nHCal acceptance  $-4.0 < \eta < -1.0$ . **Bottom:** Primary, generated particle  $p$  distributions in nHCal acceptance  $-4.0 < \eta < -1.0$ . Repository: [https://github.com/OSUNuclearPhysics/ePIC\\_preTDR\\_nHCal\\_DIS\\_MCPart](https://github.com/OSUNuclearPhysics/ePIC_preTDR_nHCal_DIS_MCPart)

for  $e + p$  and in Fig. 8.174 for  $e + A$  collisions. These studies indicate that nHCal is needed to measure  $J/\psi$  and  $\phi$  in events with  $x \sim 10^{-3}$  and lower.

Vector meson reconstruction was also studied with Sartre and Pythia generated events with full EICrecon reconstruction output and ePIC geometry. The results are qualitatively consistent and are summarized in a technical report [117].

**Jets with neutral component:** Another purpose of the nHCal is to help identify jets with neutral energy component, especially low energy neutrons of around  $E = 2.23$  GeV total energy. This is an average neutron energy as indicated by the DIS study mentioned above. By selecting charged only jets and vetoing those containing neutral hadrons, the jet energy resolution can be improved. This was studied with a full ePIC simulation and track matching to MC particles or clusters using MC information. The jet energy resolution for the cases of inclusive (squares) and charged-only jets (triangles) is compared in Fig. 8.175. Results show a  $\sim 20\%$  improvement in jet energy resolution with the nHCal present.

**Diffraction dijet measurement:** Diffractively produced dijets [118] are a key area of study for the nHCal. With integrated luminosity  $10 - 100 \text{ fb}^{-1}/\text{year}$  it is expected that  $10^8 - 10^9$  diffractive dijet events will be produced at ePIC. Preliminary studies indicate that 1.8% of diffractive dijet events contain one of the jets in the nHCal acceptance. This increases to 4.8% for jets shared between

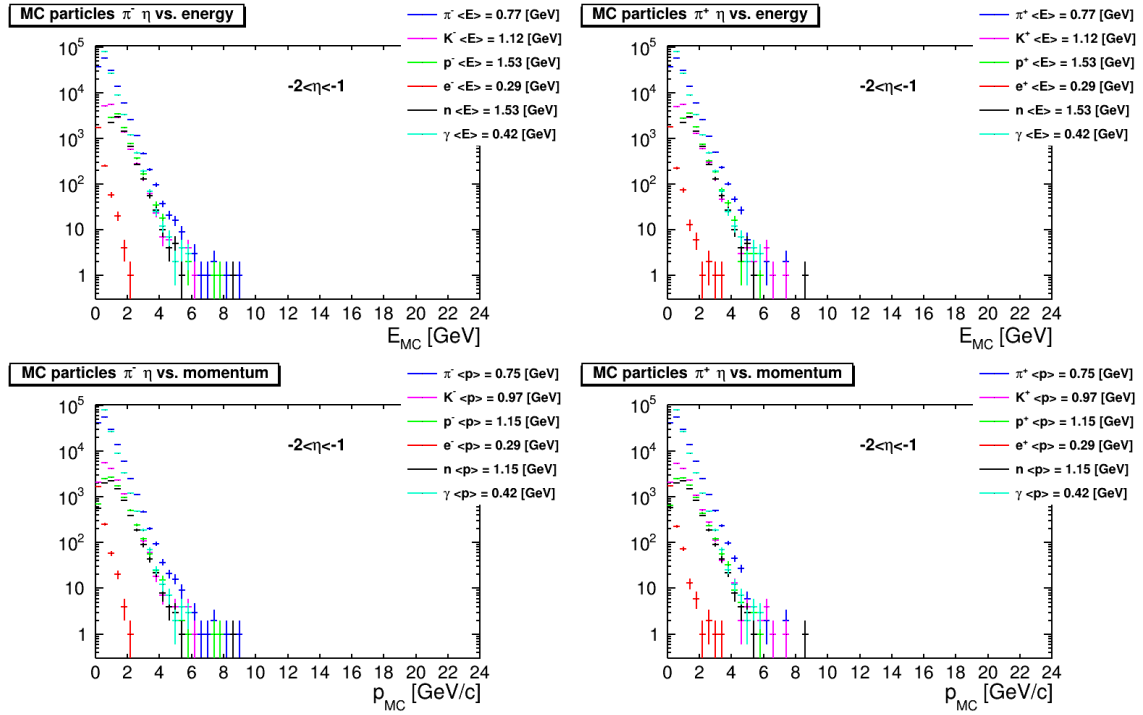


**Figure 8.168:** Top: Primary, generated particle  $E$  distributions in  $-2.0 < \eta < -1.0$  range. Bottom: Primary, generated particle  $p$  distributions in  $-2.0 < \eta < -1.0$  range. Repository: [https://github.com/OSUNuclearPhysics/ePIC\\_preTDR\\_nHCal\\_DIS\\_MCPart](https://github.com/OSUNuclearPhysics/ePIC_preTDR_nHCal_DIS_MCPart)

nHCal and barrel HCal. Such events have  $x \sim 10^{-3}$ , so are important to study the structure of protons and nuclei. This is illustrated in Fig. 8.176 vs. Bjorken  $x$  and inelasticity  $y$  for different number of jets with thrust axis in the nHCal acceptance.

In order to investigate the required position resolution to distinguish charged and neutral hadrons the momentum vectors of pairs of MC particles were projected onto the surface of nHCal and their separation was calculated. This provides an approximate estimate of the particle density per event in nHCal. A normalized distribution of the distances for all particle pairs is shown in Fig. 8.177 (left). The fraction of pairs that are separated by less than 30 cm is 1.8%. This includes secondaries produced in the detector material. On the other hand, the distance between neutron and any other particle is different and presented in Fig. 8.177 (right). The fraction of such pairs drops to 0.7%, which means it will be much easier to separate neutrons from other particles.

After full reconstruction with EICrecon it was possible to also investigate the distance ( $R_{xy}$ ) between clusters of neutrons paired with clusters of any other particles (X). This provides constraints on the position resolution required to distinguish charged and neutral hadrons. Fig. 8.178 presents the dependence of the fraction of such cluster pairs per cm on the distance between their centers. The Fig. 8.178 (left) shows MC truth clusters, while Fig. 8.178 (right) shows reconstructed clusters. The effect of merging is visible for distances below 20 cm. On the MC truth level, a 22% of clusters fall below 30 cm, which provides an upper limit on the fraction of clusters affected by merging. On the other hand, only 5% of reconstructed clusters are within 30 cm. Overall this means that the nHCal will be able to separate clusters which are separated by 30 cm between their centers.

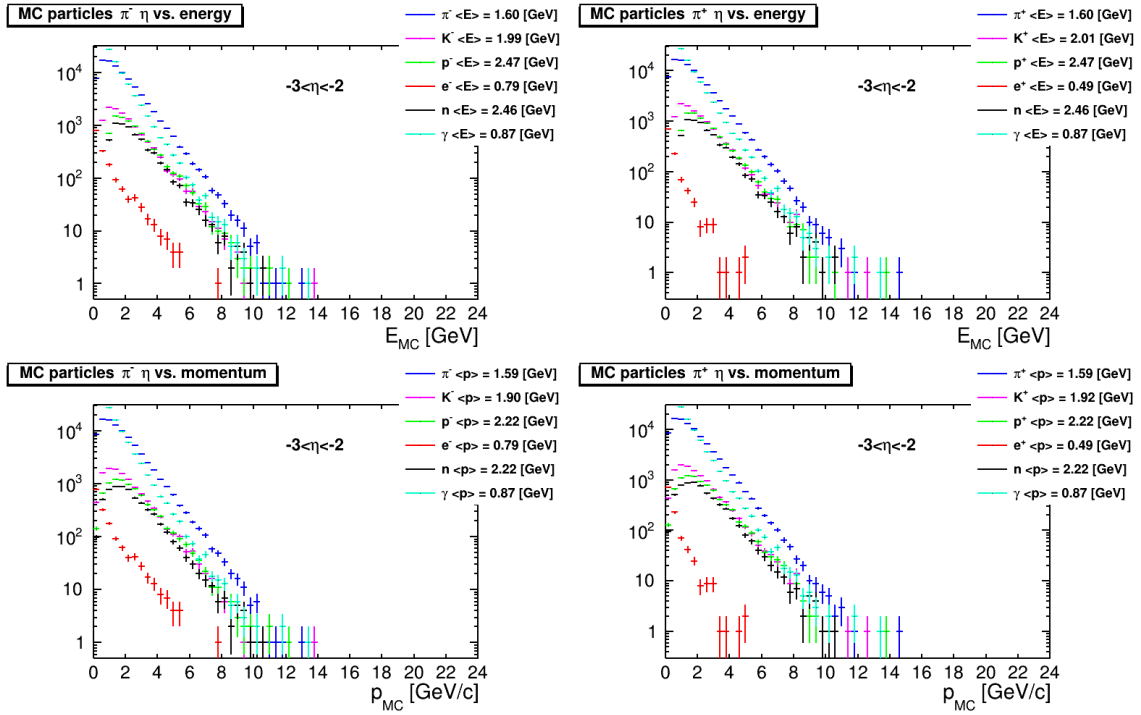


**Figure 8.169: Top:** Primary, generated particle  $E$  distributions in  $-3.0 < \eta < -2.0$  range. **Bottom:** Primary, generated particle  $p$  distributions in  $-3.0 < \eta < -2.0$  range. Repository: [https://github.com/OSUNuclearPhysics/ePIC\\_preTDR\\_nHCal\\_DIS\\_MCPart](https://github.com/OSUNuclearPhysics/ePIC_preTDR_nHCal_DIS_MCPart)

6432 **Scattered electron identification:** The nHCal will augment the backward EMCAL in scattered  
 6433 electron identification, by increasing the  $e/\pi$  rejection.

6434 **Hadron beam background veto for dRICH:** Another important function of the nHCal is to  
 6435 serve as a hadron beam background veto along with the LFHCAL. Such background is problematic  
 6436 for dRICH. Experience from STAR experiment shows that 30% of events may be due to background.  
 6437 Further studies need to be performed in order to understand the impact of beam background.

6438 **Cluster reconstruction:** Clusters are reconstructed using the standard island clustering algo-  
 6439 rithm [119, 120]. To distinguish between charged and neutral clusters, track-cluster matching must  
 6440 be employed. The neutral energy component is obtained by subtracting the expected energy of  
 6441 charged particles, determined from the momentum measurement via tracking. The overlap of  
 6442 clusters was studied using two-particle simulations of neutrons and pions with  $E = 1$  GeV. This  
 6443 is illustrated in Fig. 8.179 as a function of  $x, y$  position of the reconstructed clusters. The legends  
 6444 indicate the emission angles of the neutrons and pions.

6445 Initial studies show that neutron and pion clusters can be distinguished when separated by  $\approx 30$  cm  
 6446 or  $\approx 4.5$  degrees.

6447 In order to check the performance of neutron energy reconstruction and isolation, a charged hadron  
 6448 correction was applied on the total reconstructed energy  $E_{total}^{reco}$ . This is done by subtracting the

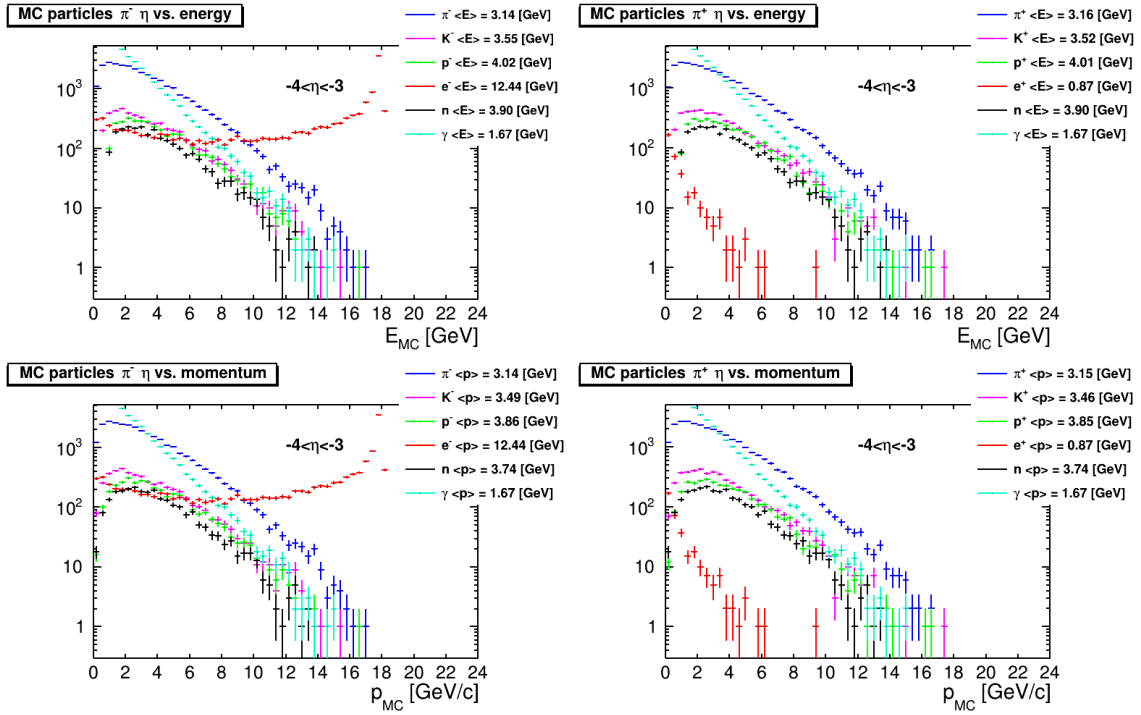


**Figure 8.170: Top:** Primary, generated particle  $E$  distributions in  $-4.0 < \eta < -3.0$  range. **Bottom:** Primary, generated particle  $p$  distributions in  $-4.0 < \eta < -3.0$  range. Repository: [https://github.com/OSUNuclearPhysics/ePIC\\_preTDR\\_nHCal\\_DIS\\_MCPart](https://github.com/OSUNuclearPhysics/ePIC_preTDR_nHCal_DIS_MCPart)

6449 pion momentum with the formula  $E_{neutral}^{reco} = E_{total}^{reco} - p_{\pi}$  when  $|\frac{E_{charged}^{reco} - p}{\sigma_{E_{charged}^{reco}}}| > 3$  otherwise, just the  
6450 energy of the isolated charged pion cluster  $E_{charged}^{reco}$  is subtracted using  $E_{neutral}^{reco} = E_{total}^{reco} - E_{charged}^{reco}$ .  
6451 The performance of neutral energy reconstruction is quantified by the ratio  $\frac{E_{neutral}^{reco}}{E_{neutral}^{MC}}$  presented in  
6452 Fig. 8.180 for different values of neutron and pion impact point separation. The overlap of the  
6453 2 showers starts impacting neutron energy reconstruction at a separation of 33.9 cm with serious  
6454 effects below 25.6 cm. For distances smaller than 8.7 cm, the distribution is almost flat meaning that  
6455 the energy is associated randomly between pion and neutron and the showers are not separable in  
6456 this way. The distribution has a large tail at lower values due to shower fluctuations. This impacts  
6457 the reconstruction performance depending on how much energy was deposited by neutron. This  
6458 is visible in Fig. 8.181 when plotting  $\frac{E_{neutral}^{reco}}{E_{neutral}^{MC}}$  as a function of  $E_{neutral}^{MC} \times f$ , which corresponds to the  
6459 original neutron energy deposits in the scintillators by factoring out the sampling fraction  $f$ . As  
6460 expected, the fraction reaches unity when the energy deposit is large, because it's easier to pass the  
6461 thresholds and obtain a stronger signal.

6462 This confirms that good neutral energy separation should be possible between clusters which are  
6463  $\approx 30$  cm apart.

## 6464 Implementation



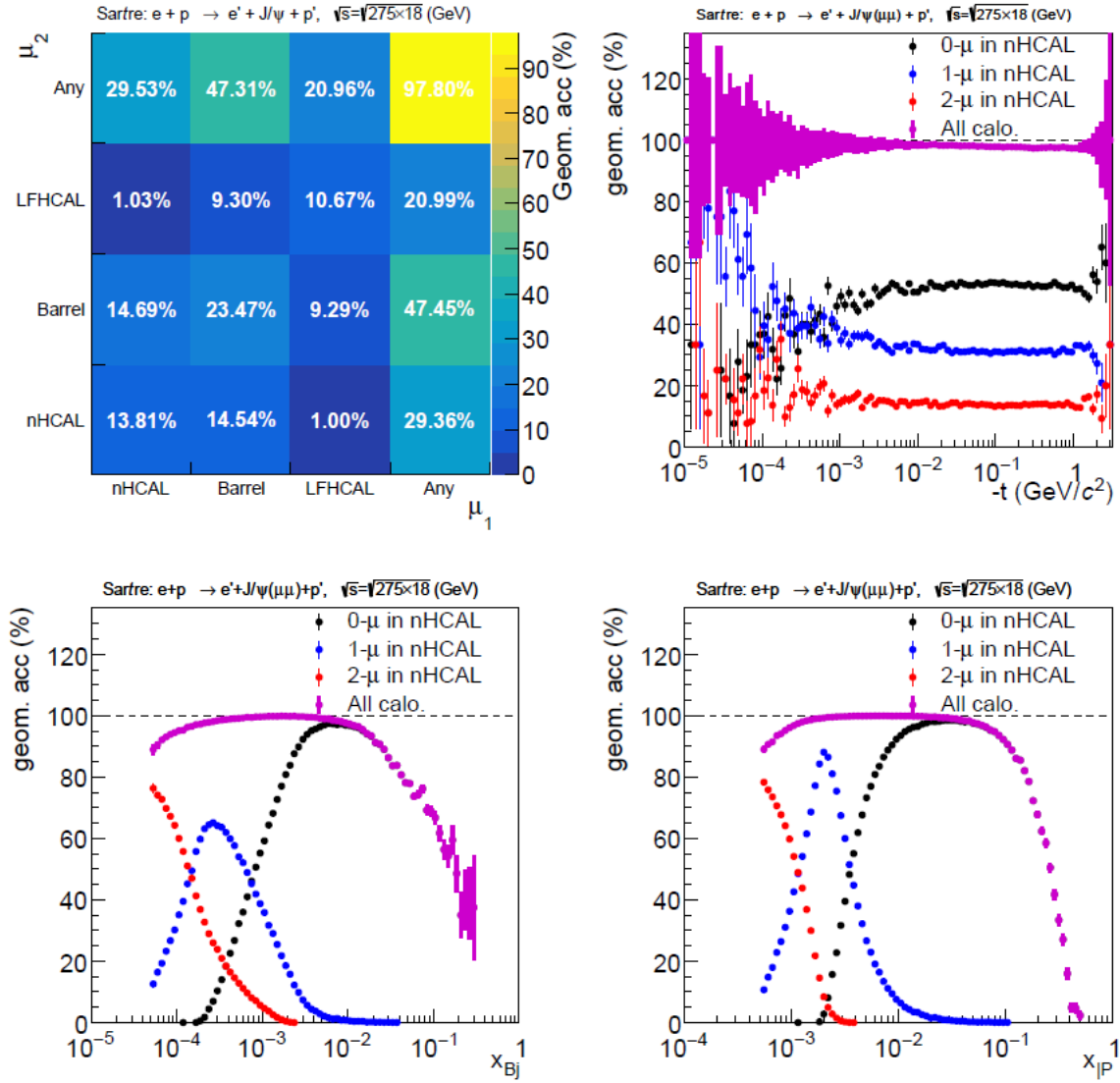


**Figure 8.171:** Acceptance of photoproduced  $J/\psi \rightarrow \mu^+\mu^-$  in  $e + p$  collisions at 18 + 275 GeV. **Top left:** Acceptance vs.  $\mu_1$  and  $\mu_2$  hitting different HCals. **Top Right:** Acceptance vs.  $-t$  for different number of  $\mu$  in nHCAL. **Bottom Left:** Acceptance vs. Bjorken  $x_{bj}$  for different number of  $\mu$  in nHCAL. **Top Right:** Acceptance vs. Pomeron  $x_P$  for different number of  $\mu$  in nHCAL. Repository: [https://github.com/OSUNuclearPhysics/ePIC\\_preTDR\\_nHCal\\_VM\\_Sartre\\_kine](https://github.com/OSUNuclearPhysics/ePIC_preTDR_nHCal_VM_Sartre_kine)

6465 **Services:** All services will be provided through the service gap in front of the endcap, including  
 6466 power supply cables for the FEEs and SiPMs, as well as data connections to the FEEs. Depending on  
 6467 the final chosen granularity of the nHCal readout channels, it will have to be investigated whether  
 6468 a small cooling system to dissipate the heat produced by the ASICs will have to be integrated,  
 6469 similarly to the LFHCAL as described in Subsec. 8.3.6.3.

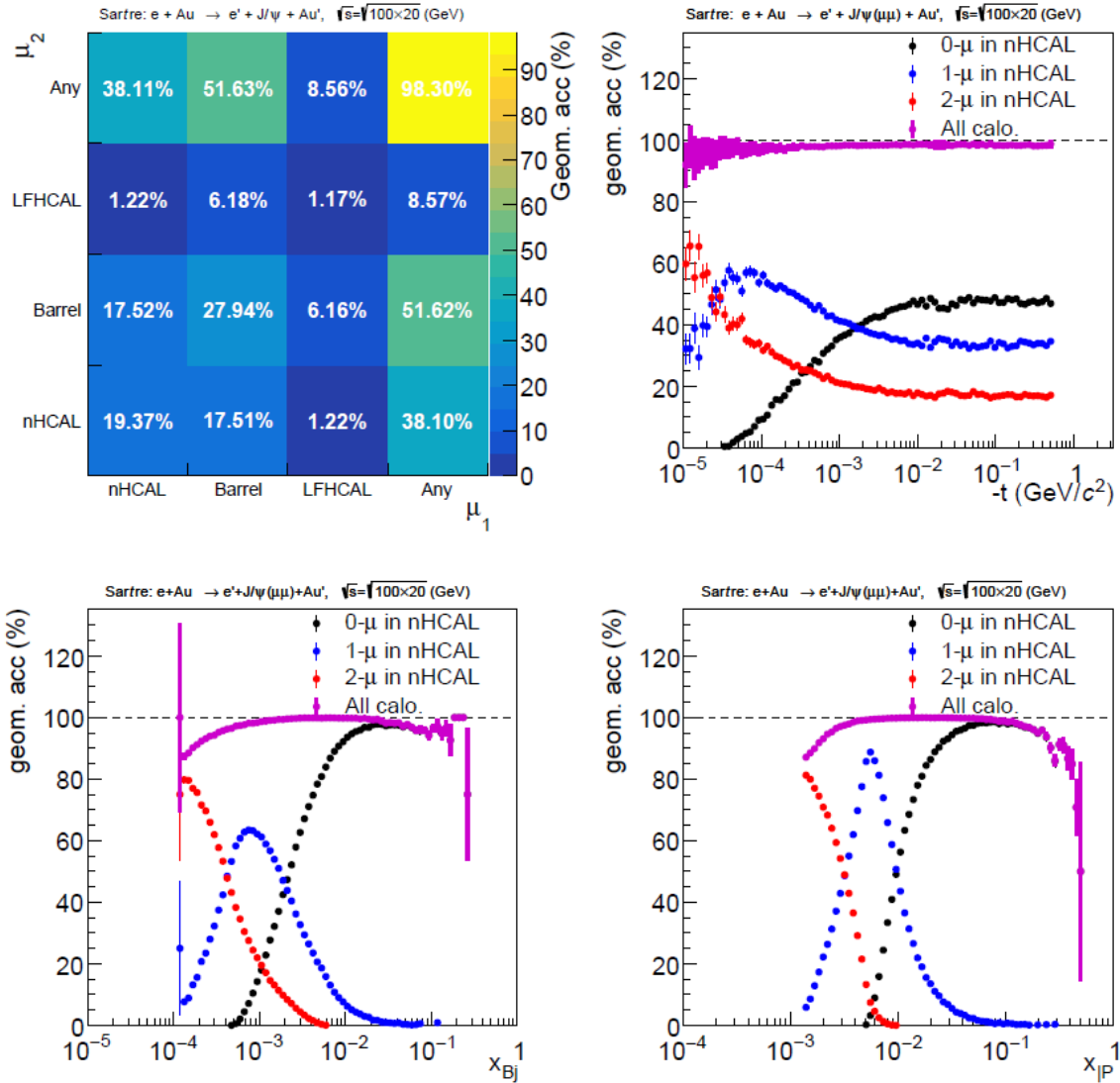


**Figure 8.172:** Acceptance of photoproduced  $J/\psi \rightarrow \mu^+\mu^-$  in  $e + p$  collisions at 20 + 100 GeV. **Top left:** Acceptance vs.  $\mu_1$  and  $\mu_2$  hitting different HCals. **Top Right:** Acceptance vs.  $-t$  for different number of  $\mu$  in nHCAL. **Bottom Left:** Acceptance vs. Bjorken  $x_{bj}$  for different number of  $\mu$  in nHCAL. **Top Right:** Acceptance vs. Pomeron  $x_P$  for different number of  $\mu$  in nHCAL. Repository: [https://github.com/OSUNuclearPhysics/ePIC\\_preTDR\\_nHCal\\_VM\\_Sartre\\_kine](https://github.com/OSUNuclearPhysics/ePIC_preTDR_nHCal_VM_Sartre_kine)

6470 **Subsystem mechanics and integration:** The backward HCal modules will be stacked on top  
 6471 of each other similarly to the LFHCAL. Communication with the calibration system will be handled  
 6472 by the HGCROCv3 ASIC on FEE board through I<sup>2</sup>C.

6473 **Calibration, alignment and monitoring:** Calibration will be performed using LEDs on the  
 6474 tiles or additional clear fibers to guide laser/LED light (similar to the STAR EEMC calibration

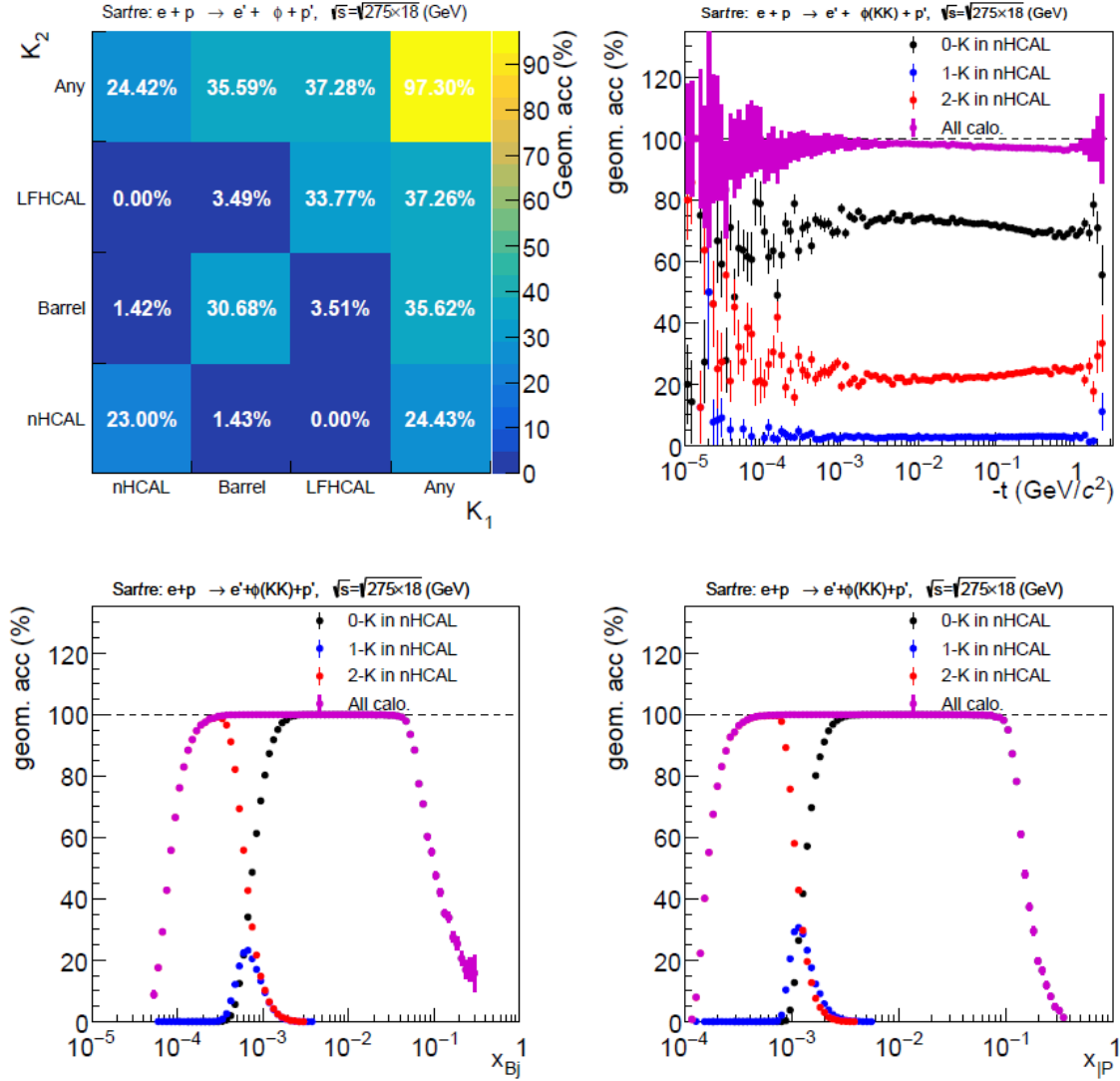


**Figure 8.173:** Acceptance of photoproduced  $\Phi \rightarrow K^+K^-$  in  $e + p$  collisions at  $18 + 275$  GeV. **Top left:** Acceptance vs.  $K_1$  and  $K_2$  hitting different HCals. **Top Right:** Acceptance vs.  $-t$  for different number of K in nHCAL. **Bottom Left:** Acceptance vs. Bjorken  $x_{bj}$  for different number of K in nHCAL. **Top Right:** Acceptance vs. Pomeron  $x_P$  for different number of K in nHCAL. Repository: [https://github.com/OSUNuclearPhysics/ePIC\\_preTDR\\_nHCAL\\_VM\\_Sartre\\_kine](https://github.com/OSUNuclearPhysics/ePIC_preTDR_nHCAL_VM_Sartre_kine)

system) to the scintillator tiles. The system will enable the simulation of custom shower shapes, similar to the LFHCAL. The response will be studied and used to calibrate the SiPM gains by adjusting the bias voltage to compensate for variations in response, differences between SiPMs, and potential radiation damage to the SiPMs and tiles. This approach allows for system monitoring during operation.

Alignment will be performed during assembly. During operation, physics events and cosmic rays

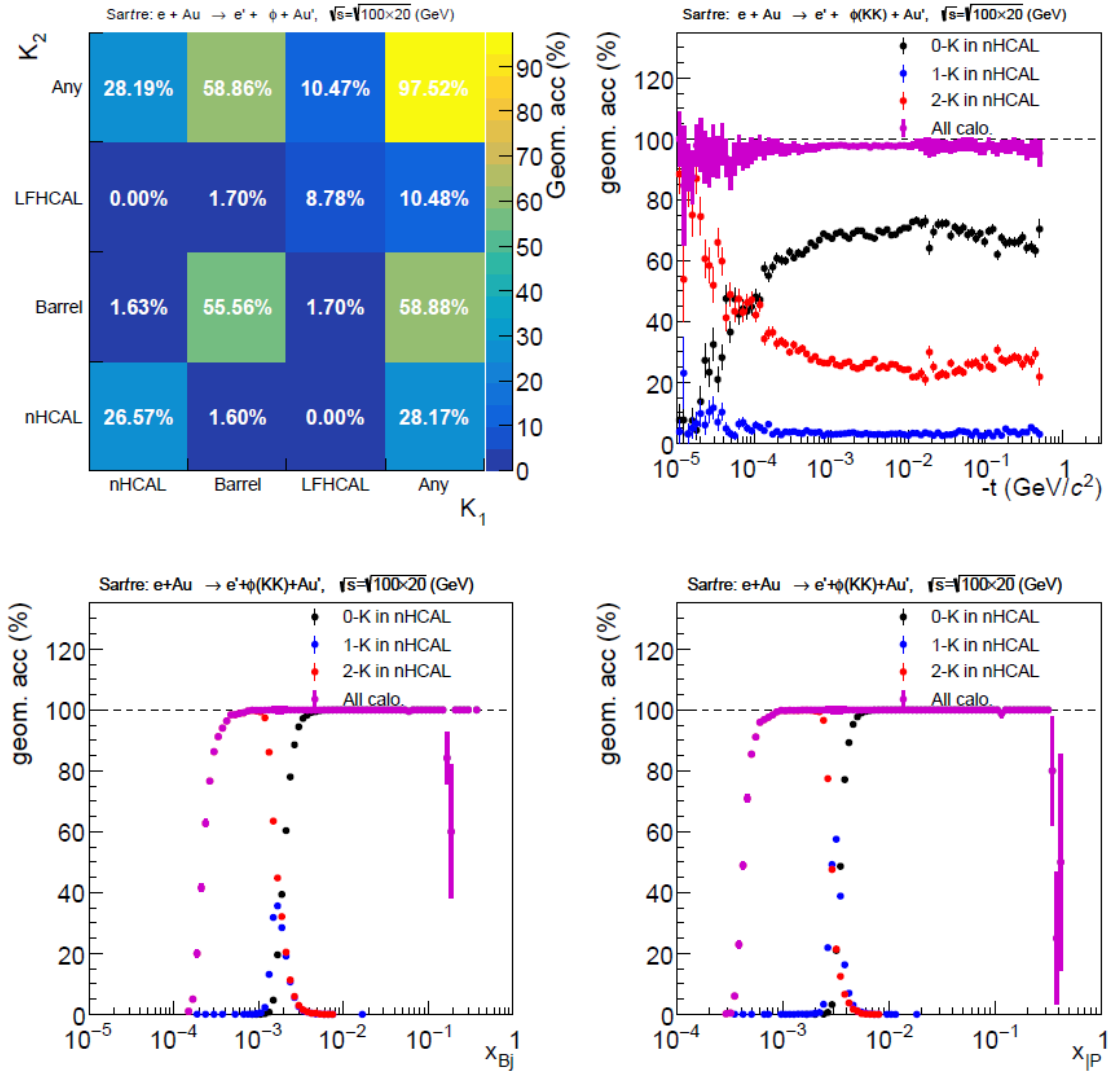


**Figure 8.174:** Acceptance of photoproduced  $\Phi \rightarrow K^+K^-$  in  $e + p$  collisions at 20 + 100 GeV. **Top left:** Acceptance vs.  $\mu_1$  and  $\mu_2$  hitting different HCals. **Top Right:** Acceptance vs.  $-t$  for different number of  $K$  in nHCAL. **Bottom Left:** Acceptance vs. Bjorken  $x_{bj}$  for different number of  $K$  in nHCAL. **Top Right:** Acceptance vs. Pomeron  $x_p$  for different number of  $K$  in nHCAL. Repository: [https://github.com/OSUNuclearPhysics/ePIC\\_preTDR\\_nHCal\\_VM\\_Sartre\\_kine](https://github.com/OSUNuclearPhysics/ePIC_preTDR_nHCal_VM_Sartre_kine)

will be used to study the relative position of the calorimeter with respect to the trackers. We will follow standard alignment procedures used in many collider experiments.

Since SiPM gains are sensitive to temperature variations, a temperature monitoring system with thermocouples will be employed. These only need to be placed coarsely, as SiPMs generate very little heat. Additionally, the absorber steel, with its high thermal conductivity, will help distribute

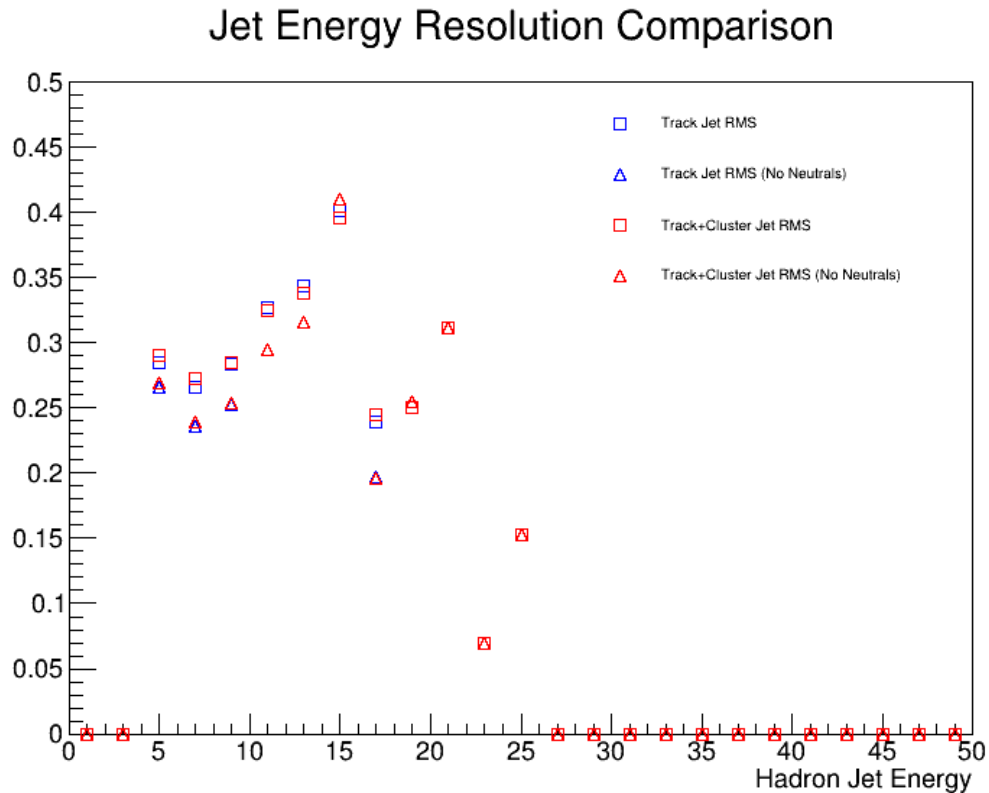


**Figure 8.175:** Energy resolution of jets vs. jet energy  $E$  compared for inclusive jets(squares) and jets with neutral veto(triangles). Track only jets(blue) are also compared to track and nHCal cluster jets(red). Repository: [https://github.com/OSUNuclearPhysics/ePIC\\_preTDR\\_nHCal\\_neutralJetRes](https://github.com/OSUNuclearPhysics/ePIC_preTDR_nHCal_neutralJetRes)

6486 heat over large volume.

#### 6487 **Status and remaining design effort:**

6488 R&D effort: Finalize simulations and confirm optimal tile size.

6489 E&D status and outlook: Design of support structures to follow the confirmed tile design.

6490 Other activity needed for the design completion: Finalize simulations to confirm the tile size  
6491 and design.

6492 Status of maturity of the subsystem: Technologies and design are mature. Dependent on the  
6493 outcome of performance simulations.

6494 **Environmental, Safety and Health (ES&H) aspects and Quality Assessment (QA plan-**  
6495 **ning:** We will follow standard ES&H procedures observed at all participating institutions. Qual-  
6496 ity of the tile, fiber and SiPM interfaces as well as optical isolation will be tested after assembly of  
6497 individual modules. This will be performed with the calibration system of the nHCal.

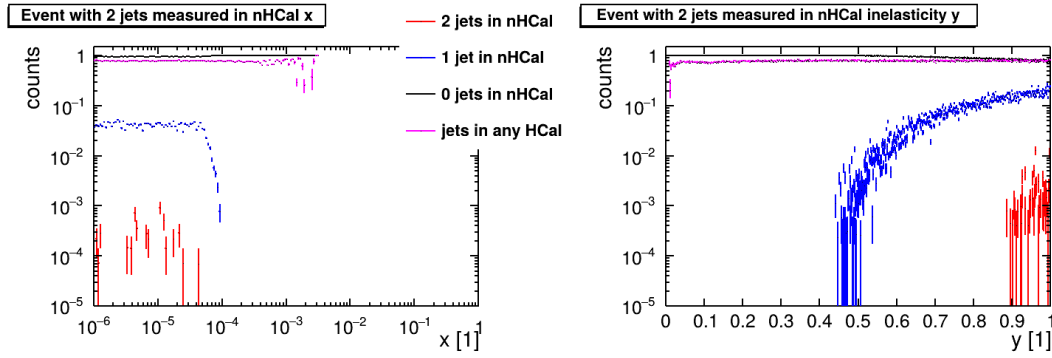


**Figure 8.176:** Left: Acceptance vs.  $x$  for 2, 1 and no diffractively produced jets with thrust axis in nHCal acceptance. Right: Acceptance vs. inelasticity  $y$  for 2, 1 and no diffractively produced jets with thrust axis in nHCal acceptance. Repository: [https://github.com/OSUNuclearPhysics/ePIC\\_preTDR\\_nHCal\\_Diff2Jet\\_Pythia](https://github.com/OSUNuclearPhysics/ePIC_preTDR_nHCal_Diff2Jet_Pythia)

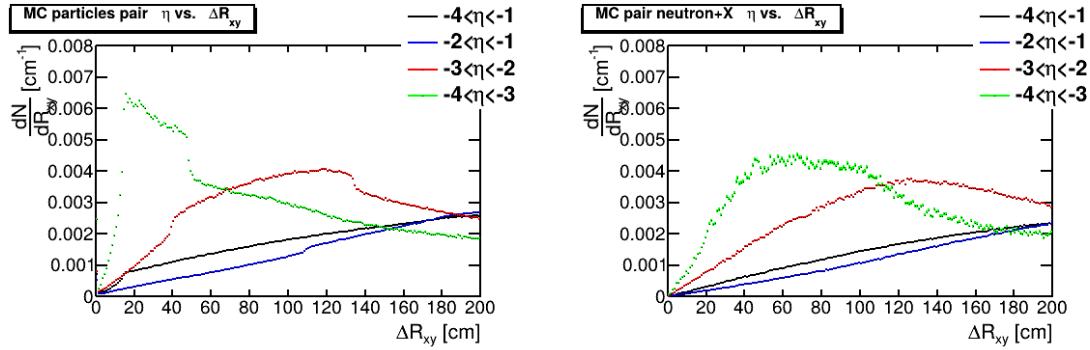


**Figure 8.177:** Left: Fraction of MC particle pairs per cm as a function of distance between straight line projections of particle pairs onto nHCal surface. Right: Fraction of MC particle pairs per cm as a function of distance between straight line projections of neutron paired with X(any particle) onto nHCal surface. Repository: [https://github.com/OSUNuclearPhysics/ePIC\\_preTDR\\_nHCal\\_Diff2Jet\\_Reco](https://github.com/OSUNuclearPhysics/ePIC_preTDR_nHCal_Diff2Jet_Reco)

6498 **Construction and assembly planning:** The 294 nHCal modules will each contain  $2 \times 10$  scin-  
 6499 tillator tiles and 10 steel absorber plates. They will be produced using electron beam welding  
 6500 technique in a vacuum. The modules will be assembled in a similar way as it is described for  
 6501 LFHCAL.

6502 The tiles will be wrapped in a highly reflective foil using a machine being developed for CMS  
 6503 collaboration or by hand with the help of students.

6504 **Collaborators and their role, resources and workforce:** There are a few institutes partici-  
 6505 pating in nHCal development and construction including The Ohio State University (OSU), Czech  
 6506 Technical University in Prague (CTU), University of Illinois Urbana-Champaign (UIUC). There  
 6507 is also help from Brookhaven National Laboratory (BNL) and Oak Ridge National Laboratory  
 6508 (ORNL). The organization structure of work is shown in the chart in the Fig. 8.182. The tasks la-



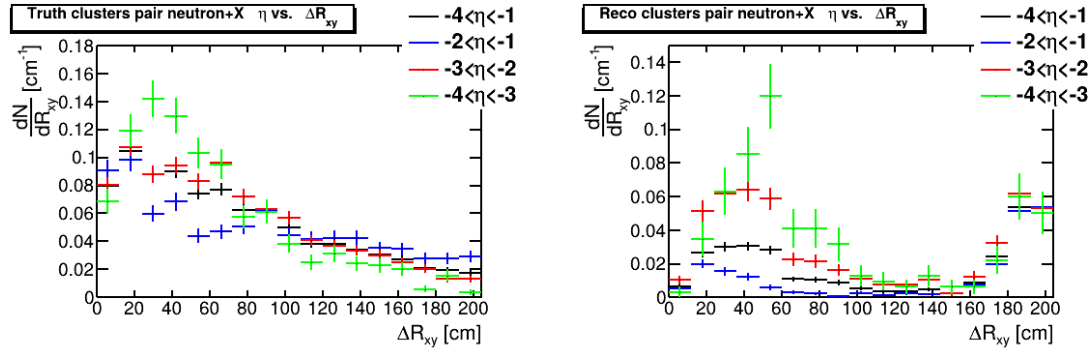


**Figure 8.178:** Left: Fraction of MC truth cluster pairs per cm as a function of distance between clusters created by neutron paired with X (any particle). Right: Fraction of reconstructed cluster pairs per cm as a function of distance between clusters created by neutron paired with X (any particle). Repository: [https://github.com/OSUNuclearPhysics/ePIC\\_preTDR\\_nHCal\\_Diff2Jet\\_Reco](https://github.com/OSUNuclearPhysics/ePIC_preTDR_nHCal_Diff2Jet_Reco)

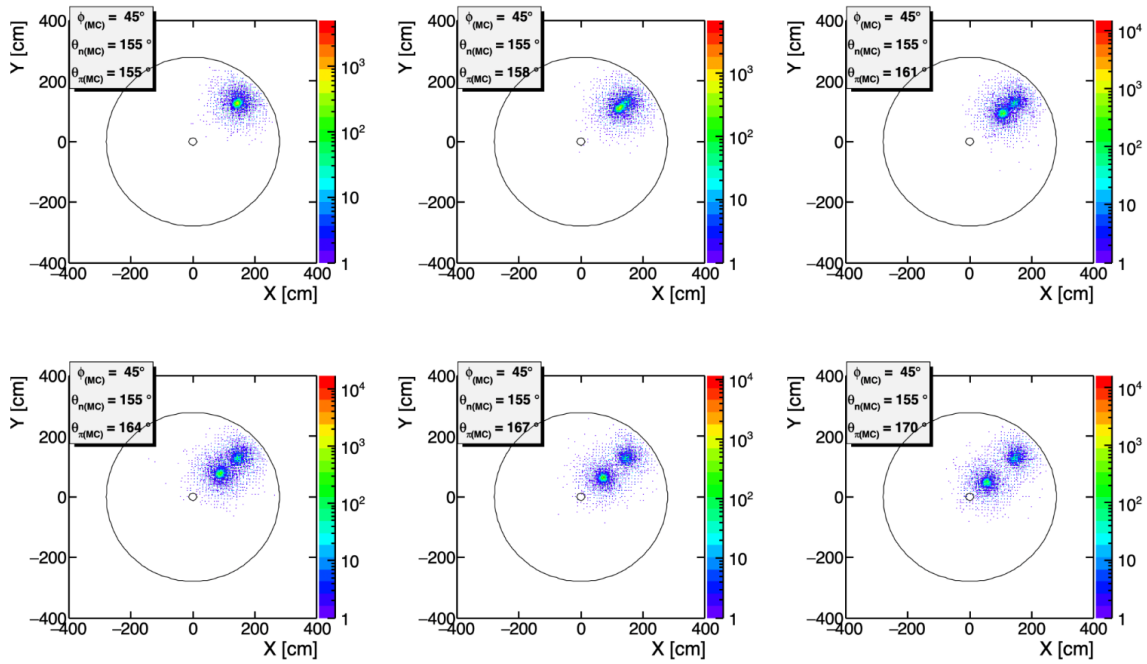


**Figure 8.179:** Position of the reconstructed clusters in  $x, y$  for 2-particle position resolution study. Repository: [https://github.com/OSUNuclearPhysics/ePIC\\_preTDR\\_nHCal\\_PosRes](https://github.com/OSUNuclearPhysics/ePIC_preTDR_nHCal_PosRes)

6509 beled as TBD can be filled by additional institutions joining the effort or sharing work and expertise  
6510 with other ePIC groups.

6511 **Risks and mitigation strategy:** Each nHCal module needs to be tested before assembly to  
6512 make sure that the LEDs, SiPMs and connectors work properly. Such work can be performed by

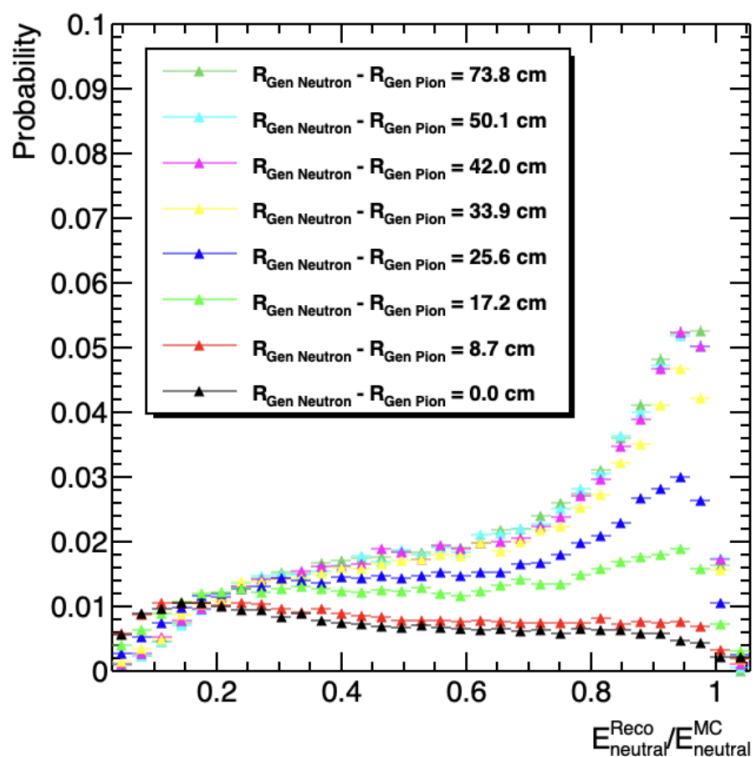


**Figure 8.180:** Ratio of reconstructed, charged hadron corrected cluster energy to the sum of neutron MC energy deposits for different values of the distance between neutron and pion impact points on the nHCal surface. Repository: [https://github.com/OSUNuclearPhysics/ePIC\\_preTDR\\_nHCal\\_PosRes](https://github.com/OSUNuclearPhysics/ePIC_preTDR_nHCal_PosRes)

6513 experts with the help of students.

6514 **Additional Material** Add text here.

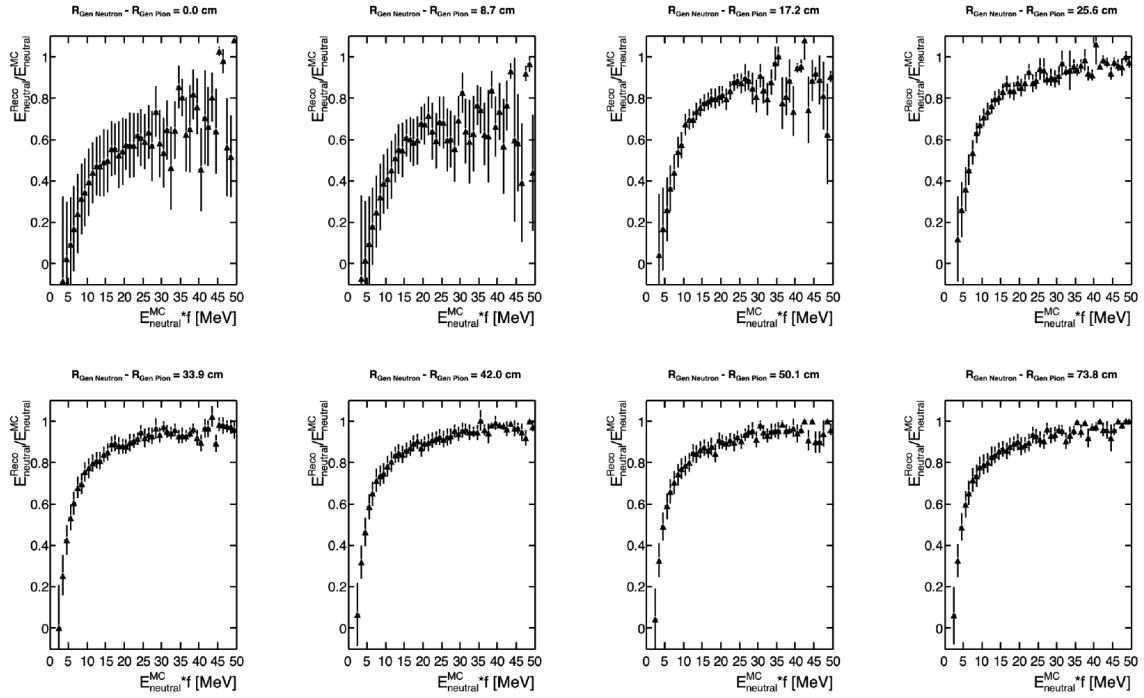


**Figure 8.181:** Ratio of reconstructed, charged hadron corrected cluster energy to the sum of neutron MC energy deposits vs. neutron MC energy deposits in scintillator tiles only. Comparison for different values of the distance between neutron and pion impact points on the nHCal surface. Repository: [https://github.com/OSUNuclearPhysics/ePIC\\_preTDR\\_nHCal\\_PosRes](https://github.com/OSUNuclearPhysics/ePIC_preTDR_nHCal_PosRes)

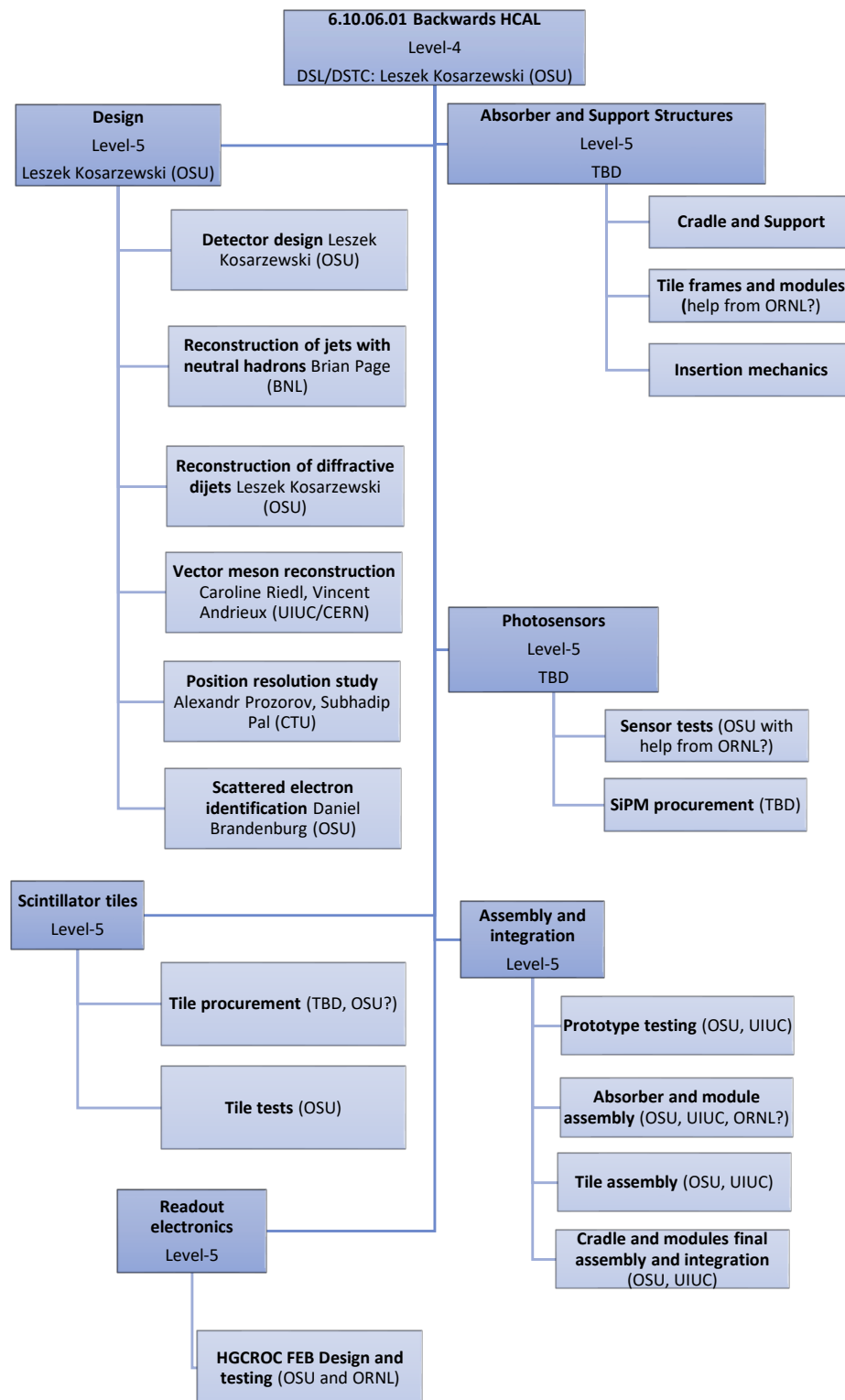
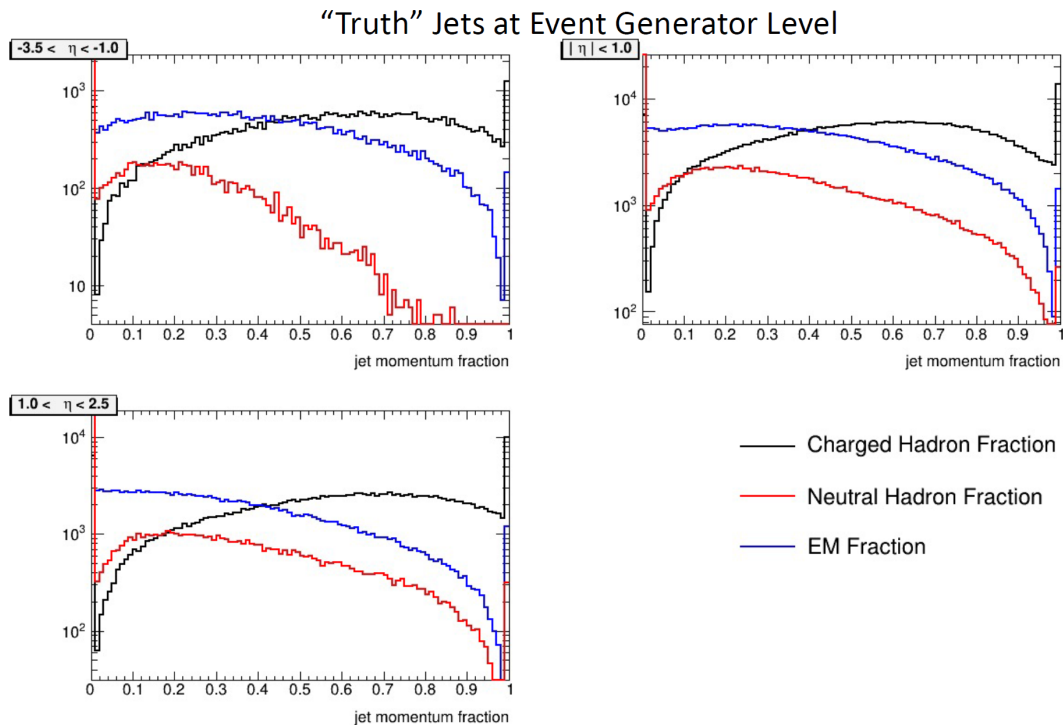


Figure 8.182: Work organization structure of nHCal project within ePIC.

### 8.3.6.2 The barrel hadronic calorimeter

**Requirements** The yellow report states the energy resolution of the mid-rapidity hadron calorimeter should be  $85\%/\sqrt{E/\text{GeV}} + 7\%$ . This requirement is driven by single jet measurements. While approximately 90% of the jet energy will be measured in the high precision tracking and electromagnetic calorimetry, the hadronic calorimeter is crucial for capturing the neutral hadron contribution.

The importance of measuring this contribution at mid-rapidity is demonstrated by 8.183, which shows the charged, neutral EM, and neutral hadronic momentum fractions of jets as a function of the pseudorapidity  $\eta$  in the lab frame. For  $|\eta| < 1$ , while sub-dominant, there is still a significant population of jets with a substantial neutral hadronic component.



**Figure 8.183:** The charged (black lines), neutral EM (blue lines), and neutral hadron (red lines) fractions of jets at the truth level in  $\eta \in (-3.5, 1.0)$  (upper left panel),  $|\eta| < 1$  (upper right panel), and  $\eta \in (1.0, 3.5)$  (lower left panel). Received from John Lajoie in private communication. **THIS IS A PLACEHOLDER**

**Requirements from Radiation Hardness:** Compared to LHC detectors, the various subsystems of the ePIC detector have moderate radiation hardness requirements. The Yellow Report states that at the calorimeters, the radiation level will be up to  $\approx 3$  krad/year electromagnetic and  $10^{11}n/\text{cm}^2$  hadronic at top luminosity. However at the BHCAL, the radiation level will be only 10 rad electromagnetic and 0.1 rad hadronic, orders of magnitude lower than, *e.g.*, at the fHCAL.

The on-detector electronics (SiPMs, H2GCROC3) are radiation tolerant. While the read-out boards (RDOs) contain FPGAs and therefore are radiation sensitive, they will sit well outside the detector, and therefore there is no concern for single-event upsets (SEUs). The neutron fluence will be low enough that it is not an issue for SiPMs. The neutron fluence is lower than in sPHENIX, where the dark current increase after the first year of running is consistent with expectations. Since the H2GCROC3s are used for the other calorimeter systems as well, there is no concern for the BHCAL.

## Justification

**Device concept and technological choice:** The sPHENIX outer HCal, which was demonstrated to have a single particle energy resolution of  $75\%/\sqrt{E} \oplus 14.5\%$ , will be repurposed for the EIC. It generally satisfies the requirements described in the previous section.

The absorber material for the central hadronic calorimeter will also serve as the flux return for the solenoid magnet.

**Subsystem description:** [Derek, 07.12.2025] I apologize for not catching this in my 1st read-through; but as far as I can tell, the discussion of the LED system is the only time we note that in ePIC we read out each tile vs. reading out 5 tiles in sPHENIX. This is a big change from sPHENIX and I feel it would be useful to foreground this in the general subsystem description.

General device description: The sPHENIX Outer HCal will be used as the basis of the ePIC Barrel HCal. The sPHENIX OHCal design was developed and optimized through a series of simulation and prototype studies. The sPHENIX hadronic calorimeter system consists of two longitudinal compartments of calorimeter, one inside the solenoid, filling the gap between the magnet and the electromagnetic calorimeter, and one outside the solenoid. In the ePIC design the electromagnetic calorimeter will fill the space before the magnet. Therefore only the sPHENIX Outer HCal will be adopted in ePIC.

The basic calorimeter concept is a sampling calorimeter with tapered absorber plates tilted from the radial direction to provide more uniform sampling in azimuth. Extruded tiles of plastic scintillator with an embedded wavelength shifting fiber are interspersed between the absorber plates and read out at the outer radius with silicon photomultipliers. The tilt angle is chosen so that a radial track from the center of the interaction region traverses at least four scintillator tiles as shown in Figure 8.184.

Each tile has a single SiPM. In the sPHENIX design, the analog signal from five SiPMs are combined at a single preamplifier channel to form a calorimeter tower. In ePIC, each SiPM will be read out individually. Twelve tiles span 1.1 units of pseudorapidity in each direction as shown in Figure 8.185. Therefore the overall segmentation is  $\Delta\eta \times \Delta\phi \sim 0.1 \times 0.02$ .

Scintillator description:

The properties of the HCal scintillating tiles are listed in Table 8.63. There are 12 different shaped tiles which span half of the  $\eta$  range of the detector. The detector is mirror-symmetric in  $\eta$  except in the region where the chimney for the cooling of the magnet reduces the depth of the HCal.

A wavelength shifting (WLS) fiber is embedded in the tile to direct the light to the SiPM. The Kuraray single clad fiber was selected due to its flexibility and longevity which are critical for



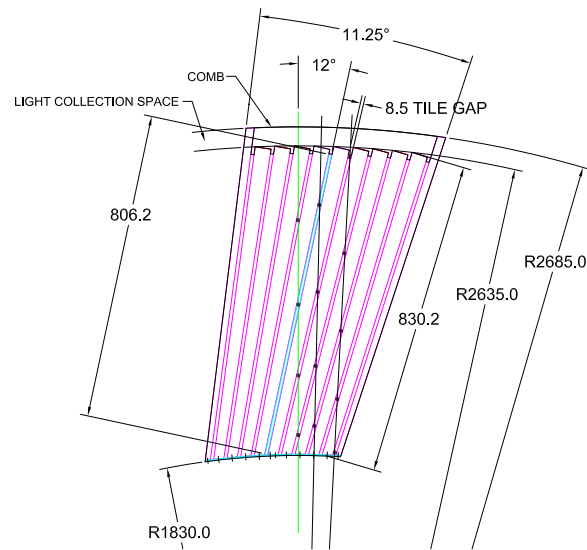


**Figure 8.184:** Transverse cutaway view of an sPHENIX Outer HCal module, showing the tilted tapered absorber plates. Light collection and cabling is on the outer radius at the top of the drawing.

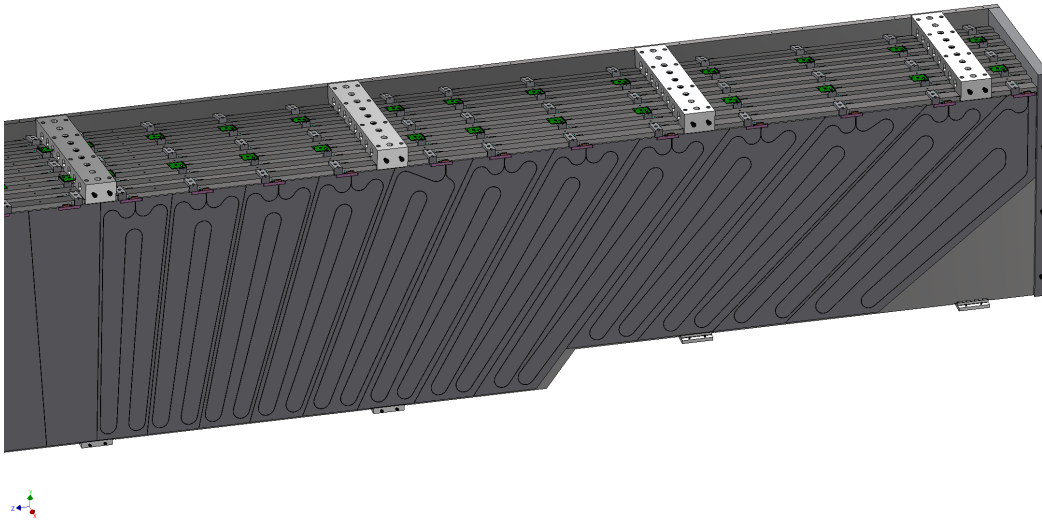


**Figure 8.185:** Scintillator tiles in a layer of the Outer HCal.

6570 the multiple fiber bends in the design. The routing of the fiber was carefully designed to max-  
 6571 imize the uniformity of light collection across the various tile shapes and avoid light leaks in  
 6572 the bends. The properties of the HCAL wavelength shifting fibers are listed in Table 8.64.  
 6573 The fiber routing was designed so that any energy deposited in the scintillator is within  
 6574 2.5 cm of a WLS fiber to minimize the pathlength of the light through the tile to the fiber and

Component	Description
Plastic	Extruded polystyrene
Scintillation dopant	1.5% PTP and 0.01% POPOP
Reflective coating	Proprietary coating by surface exposure to aromatic solvents
Reflective layer thickness	50 $\mu$
Wrapping	one layer of 100 $\mu$ Al foil, one layer of 30 $\mu$ cling-wrap, one 100 $\mu$ layer of black Tyvek
Attenuation length in lateral (with respect to extrusion) direction	$\sim$ 2-2.5 m
Wavelength shifting fiber	Single clad Kuraray Y11
Fiber size	1 mm round
Fiber core attenuation length	$> 2$ m
Optical cement	EPO-TEK 3015

**Table 8.63:** Properties of HCal scintillating tiles.

Property	Description
Fiber diameter	1.0 mm
Formulation	200, K-27, S-Type
Cladding	single
Cladding thickness	2 percent of d (0.02 mm)
Numerical Aperture (NA)	0.55
Emission angle	33.7 deg
Trapping Efficiency	3.1 percent
Core material	polystyrene (PS)
Core density	1.05 g/cc
Core refractive index	1.59
Cladding material	Polymethylmethacrylate (PMMA)
Cladding density	1.19 g/cc
Cladding refractive index	1.49
Color	green
Emission peak	476 nm
Absorption Peak	430 nm
Attenuation length	$> 3.5$ m
Minimum bending radius	100 mm

**Table 8.64:** Properties of Kuraray Y-11 (200) wavelength shifting fibers.

6575 maintain uniformity in the response of energy depositions throughout the tile and across  
6576 various tile shapes. In addition, the bend radius of any turn in the fiber has been limited to  
6577 35 mm. These parameters on the fiber routing where based on T2K and the sPHENIX R&D  
6578 experience with test tiles. Since there are 12 different tile shapes, the routing for each tile  
6579 shape was uniquely designed to satisfy these conditions.

6580 The two ends of a fiber are brought to the outer radius of a tile where a small plastic holder

carries a 3 mm  $\times$  3 mm SiPM at 0.75 mm from the end of the polished fibers.

Parameter	Units	Value
Inner radius (envelope)	mm	1820
Outer radius (envelope)	mm	2700
Length (envelope)	mm	6316
Material	1020 low carbon steel	
Number of tiles in azimuth ( $\Delta\phi$ )		320
Number of tiles in pseudorapidity ( $\Delta\eta$ )		24
Number of electronic channels	$320 \times 24 = 7680$	
Number of modules (azimuthal slices)		32
Total number of absorber plates	$5 \times 64 = 320$	
Tilt angle (relative to radius)	$^{\circ}$	12
Absorber plate thickness at inner radius	mm	10.2
Absorber plate thickness at outer radius	mm	14.7
Gap thickness	mm	8.5
Scintillator thickness	mm	7
Module weight	kg	12247
Sampling fraction at inner radius		0.037
Sampling fraction at outer radius		0.028
Calorimeter depth	$\lambda$	3.8

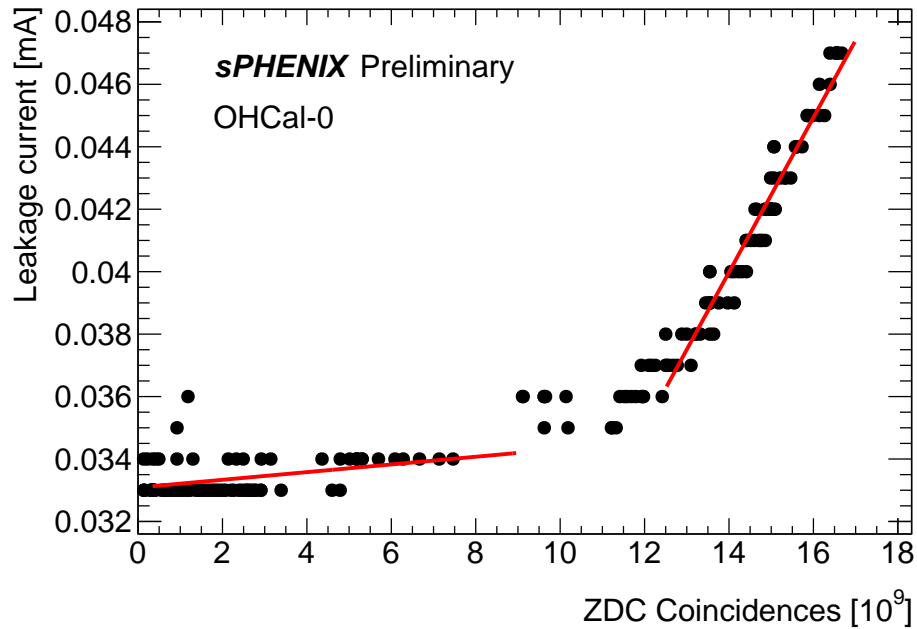
**Table 8.65:** Design parameters for the Barrel Hadronic Calorimeter w/o additional absorber, based on the sPHENIX Outer Hadronic Calorimeter.

Table 8.65 summarizes the major design parameters of the HCAL, which is illustrated in Figure 8.184.

The Outer HCAL SiPM sensors and electronics are to be arranged on the outer circumference of the detector which reduces the radiation exposure of the SiPMs.

**Sensors:** The SiPMs used in sPHENIX will be replaced with newer S14160-3015PS Hamamatsu SiPMs. The SiPMs are still 3 mm  $\times$  3 mm and will be attached to a board that will fit in the same plastic connectors used in sPHENIX to mount the SiPM to the tile. Each SiPM will be read out individually via the CALOROC. The electronics developed for the BHCAL is similar to other calorimeters and are described in a separate section.

**LED system:** An LED system injects light into each tile. This allows for testing the entire functionality of the detector and read-out chain starting all the way from the SiPMs. The LED system can also be used to track time dependent changes of the SiPM gain. We will re-use the existing (from sPHENIX) fiber distribution system, which is comprised of five bundles of 25 fibers each (24 tiles per fiber bundle plus one spare) for each half sector. (The separation in five bundles, each driven by an individual LED, was necessary in sPHENIX to test each individual SiPM due to the read-out of towers consisting of five tiles. In EPIC, this is not necessary since each tile is read out individually. But the separation into five bundles does not constitute any disadvantage (except that five LEDs are needed instead of a single one) and allows for the re-use of the already installed fiber system. The polished fibers end in a ferrule plugged and held in place in the light blocker glued to the tile. A hole in the light blocker allows for the LED light to hit the diffusely coated surface of the tile. The CALOROC allows for LEDs to be pulsed at a defined rate. An LED board will be designed that will be



**Figure 8.186:** Leakage current in HCal measured once per fill as a function of total number of ZDC coincidence hits

6604 driven by the CALOROC. One LED board per half sector will have five LEDs each in cans  
6605 into which the fiber bundles plug in.

6606 **Performance** The performance of the BHCAL for ePIC has been studied in simulation as well as  
6607 tested through the experience of the HCals in sPHENIX. The sPHENIX HCal system has performed  
6608 very well in Au+Au and p+p collisions. One concern with using SiPM sensors is the potential ra-  
6609 diation damage in high energy collisions. The radiation exposure causes an increase in the leakage  
6610 currents and the measured noise. The leakage current measured in the commissioning run for  
6611 sPHENIX shows that leakage currents even when extrapolated are well below the limit. This is  
6612 expected since the large amount of material in front of the SiPMs reduces their radiation exposure.

6613 **Physics performance:** As mentioned above, the yellow report requirements on the BHCAL are  
6614 driven primarily by single jet measurements. However, the BHCAL will provide significant addi-  
6615 tional capabilities in terms of performance. These capabilities include:

- 6616 - Identification of muons,
- 6617 - Reconstruction of neutral hadrons such as neutrons,
- 6618 - Constraining the jet energy scale and resolution by precise measurement of the jet neutral  
6619 component,
- 6620 - Reconstruction of event kinematics and the hadronic final state,
- 6621 - And tagging of charged-current DIS events.

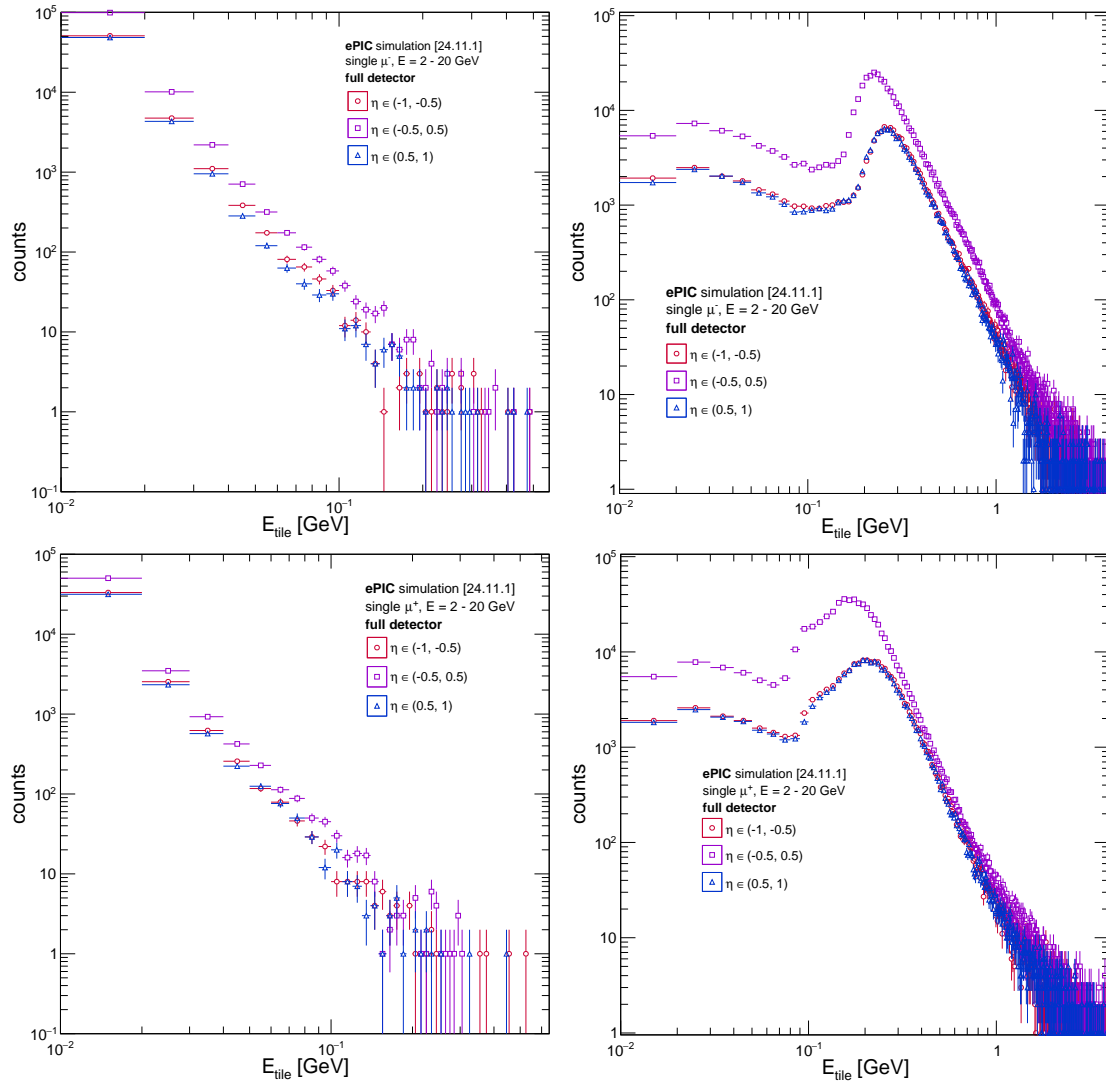


**Figure 8.187:** Energy deposited on BHCAL tiles (left panels) and reconstructed tile energies (right panels) by single  $\mu^-$  (top row) and  $\mu^+$  (bottom row) as a function of tile pseudorapidity. Muons were simulated using the 2024.11.1 simulation geometry with energies between 2 and 20 GeV. Repository: <https://github.com/ruse-traveler/EpicBHCALPTDRStudies>

One way the BHCAL can aid in muon identification is by the identification of MIPs as muons will typically MIP through both an EMCal and an HCal. Being able to reliably measure this signal is one motivation for reading out individual tiles rather than groups of tiles.

To assess the performance of the BHCAL in this category, single  $\mu^\pm$  with energies between 2 - 20 GeV were thrown with  $|\eta| < 1$ . Figure 8.187 illustrates the energy deposited on a given scintillator tile (i.e. the sum of G4 hits for a tile) and their reconstructed energies. A clear peak at 250 MeV can be observed in the reconstructed tile energies, well above the minimum energy anticipated to be measured by the BHCAL.

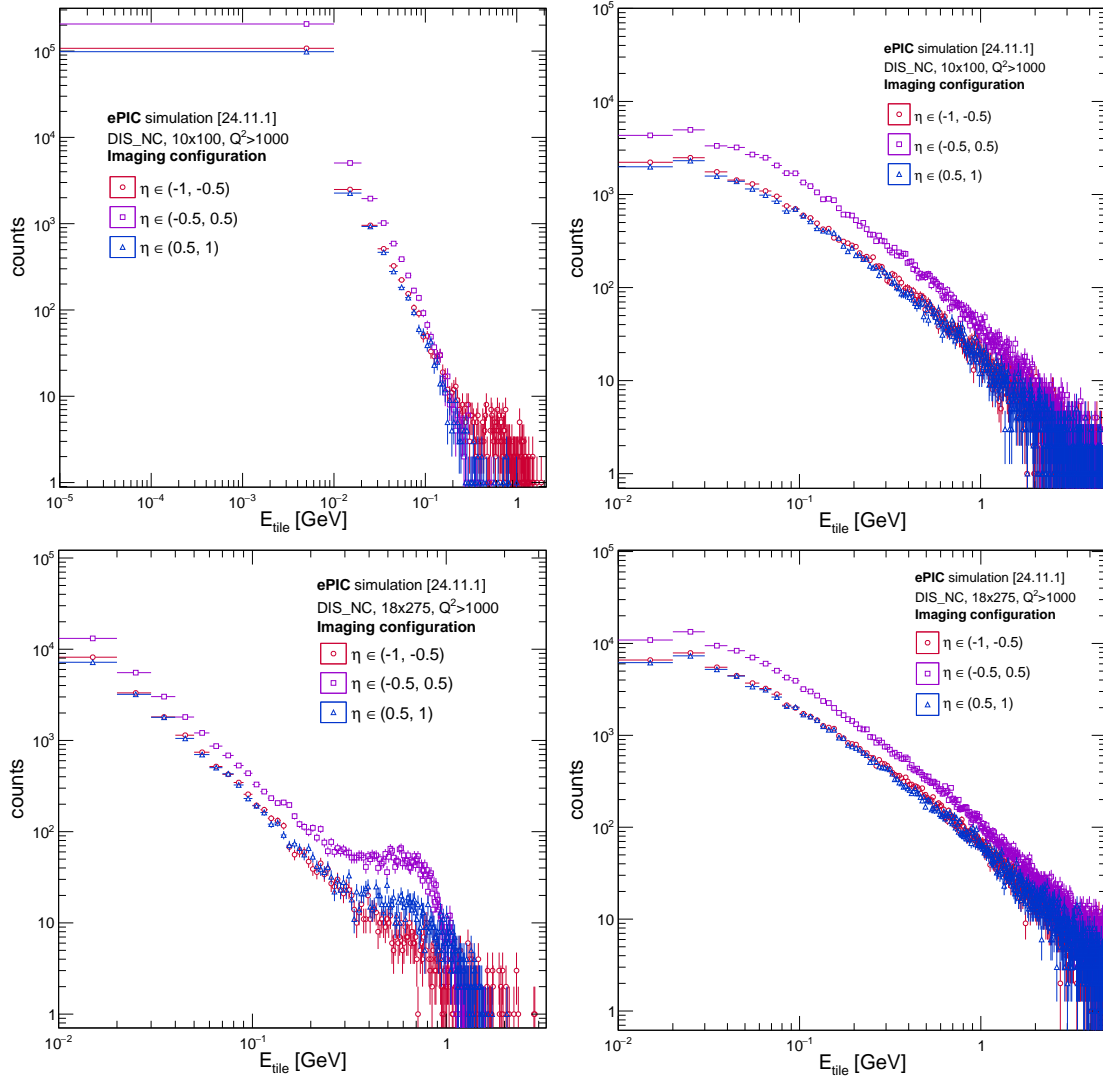


**Figure 8.188:** Energy deposited on BHCAL tiles (left panels) and reconstructed tile energies (right panels) by all particles in  $10 \times 100$  (top row) and  $18 \times 275$  (bottom row) NC DIS events as a function of particle pseudorapidity. Distributions were simulated using the 2024.11.1 simulation geometry with  $Q^2 > 1000 \text{ GeV}^2$ . Repository: <https://github.com/ruse-traveler/EpicBHCALPTDRStudies>

To contrast this, the same quantities are shown in figure 8.188 for all particles in NC DIS events for beam energies of  $10 \times 100$  and  $18 \times 275$ . As one would expect, this sample is dominated by particles which do not MIP through both calorimeters, and the clear MIP peak in the reconstructed tile energies is washed out. This figure also demonstrates the typical reconstructed energies on a tile-by-tile basis.

To measure hadron energies, clusters are formed from individual tiles. Figure 8.189 shows the reconstructed energy of the leading (highest energy) cluster in single  $\pi^\pm$  simulations of only the BHCAL. Note that these energies are shown at the EM scale, i.e. are corrected for the sampling



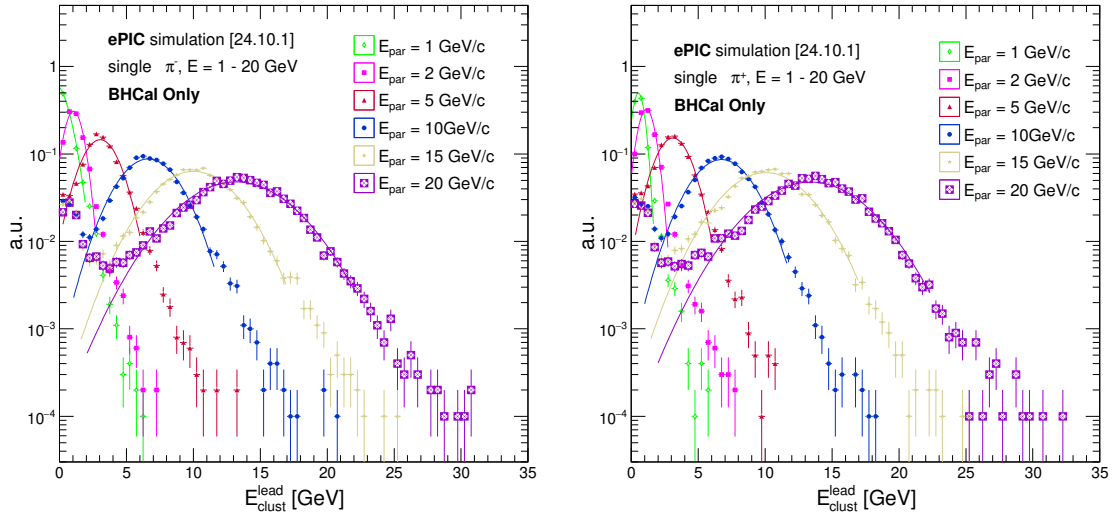


**Figure 8.189:** Reconstructed energy of leading BHCAL cluster for 1 (green) - 20 GeV (purple) single  $\pi^-$  (left) and  $\pi^+$  (right) in BHCAL-only simulations. Pions were simulated using the 2024.10.1 simulation geometry. Solid lines are Gaussian fits. Repository: <https://github.com/ruse-traveler/EpicBHCALPTDRStudies>

fraction.

The pions were simulated with energies between 2 - 20 GeV, and clear gaussian peaks are observed for each pion energy. The solid lines in the figure are Gaussian fits to the main peak of the energy spectra. This demonstrates that the simulation of the BHCAL produces reasonable hadronic energy spectra.

**TODO:** add a plot comparing the BHCAL-only energy resolution in the BHCAL-only vs. sPHENIX test beam data, and a plot of the BHCAL-only linearity.

However, the reconstructed energy of a hadron in an HCal will be significantly smeared by energy loss in dead material and due to nuclear binding, fluctuations in the hadronic shower, and clustering inefficiencies. These effects can already be seen in the BHCAL-only simulation of fig. 8.189.

These effects will be exacerbated when the full detector is present. This can be seen in the upper row of fig. 8.190, where the Gaussian peaks of the BHCAL-only single  $\pi^\pm$  simulations are washed out. Thus, hadron energies measured with the BHCAL will need to be further calibrated from the EM scale to the hadronic scale utilizing information from additional subsystems.

This calibration is carried out using two simple machine-learning models, a Linear-Discriminant (LD) and a Multi-Layer Perceptron (MLP), implemented in the ROOT TMVA package [Citation = CERN-OPEN-2007-007 (arXiv:physics/0703039)]. In both cases, the models are trained to perform a regression on the simulated particle energy using the leading BHCAL and BIC (ScFi + imaging) cluster energy, and the sum of energy in the 6 imaging (AstroPix) and 12 ScFi layers of the BIC.

The single  $\pi^\pm$  energies calibrated by the LD model and the MLP model can be seen in the middle and bottom rows of fig. 8.190 respectively. The Gaussian shape of the energy spectra is clearly recovered by the models, except for the MLP-calibrated 20 GeV  $\pi^-$  which displays some pathologies.

[Note to reviewers: this is currently being worked on.]

Figure 8.191 shows the linearity and energy resolution of the calibrated  $\pi^\pm$ . Also shown in fig. 8.191 is what the linearity and resolution would be if one simply summed all of the clusters in the BHCAL. This illustrates the impact of the calibration, and that the BHCAL adequately meets the yellow report requirement for energy resolution.

To gauge the performance of the BHCAL in reconstructing neutral hadrons, the calibration procedure was repeated for single neutrons. Figure 8.192 shows the uncalibrated and calibrated neutron energies, and fig. 8.193 shows the linearity and resolution of the calibrated neutron energies.

Note that even after calibration, there are distinct low energy tails in the energy spectra. These could be due to either cluster splitting, fluctuations in the hadronic shower, or inadequacies in the model. Efforts to understand and ameliorate these tails are ongoing.

Towards understanding the role of cluster splitting, fig. 8.194 shows the ratio of uncalibrated lead BHCAL clusters to the sum of all BHCAL clusters for single neutrons. **TODO: add same plot for pions.**

[Derek, 07.12.2025] I've commented out the JES/R plot from the Yellow Report. I had initially included it as an example of a previous study of the JES/R for full jets and as a placeholder. I'm a little skeptical of the veto approach, and I think it would be prudent to avoid foregrounding it until we've carried out a more systematic study.

As discussed, the BHCAL provides an additional handle of the neutral hadronic component of jets, and thus aids in constraining the jet energy scale (JES) and jet energy resolution (JER). This is illustrated in fig. 8.195.

**Note to reviewers: a redo of this study with ePIC software and geometry is ongoing.**

Furthermore, measurement of neutral hadrons will be crucial for precise measurements of the hadronic final state and of event kinematics, particularly in CC DIS.

Figure 8.196 shows the DIS kinematic variables  $x$ ,  $y$ , and  $Q^2$  reconstructed using the Jacquet-Blondel method at the truth and reconstructed level for two different acceptances,  $|\eta| < 3.5$  and  $|\eta| < 4$ . **TODO: the different acceptances can be dropped when we redo this study.**

Lastly, fig. 8.197 shows the truth vs. reconstructed missing  $E_T$ ,  $E_T^{\text{miss}}$ , the total transverse energy relevant. This quantity could be useful in tagging CC DIS events.

**Note to reviewers: a redo of these studies with ePIC software and geometry are ongoing.**

## Implementation

**Subsystem mechanics and integration:** The BHCAL is the outermost central detector and will need to be installed first. The steel serves as the flux return for the solenoid magnet.

**Calibration, alignment and monitoring:** The sPHENIX HCal was calibrated to the electromagnetic scale using cosmic ray muons by matching the the ADC distribtution in data to the energy deposition in a realistic simulation. To account for imperfections in the simulation from not including material outside the main sPHENIX detector, a tower slope method in collision data was used to symmetrize the response in  $\phi$   $\eta$  bin by  $\eta$  bin. Further, gain variations with time due to changing ambient temperature was corrected for by measuring the temperature as a function of time can applying the corresponding temperature dependent correction. Alternatively, the LED system can

be used to correct for the time dependence of the gain. Currently, the calibration to the hadronic scale relies on HIJING simulations propagated through Geant, with reweighting of the HIJING particle spectra based on experimental measurements. In the future, the hadronic scale calibration will be further improved by photon (or high fragmentation  $z$  hadron)-jet balancing and studying the calorimeter response to isolated hadrons measured with the sPHENIX tracking system. In ePIC we plan to pursue a similar calibration strategy.

#### **Status and remaining design effort:**

R&D effort: The basic design is set by reusing the sPHENIX outer HCal. However, the electronics and details of the LED system are still being developed. There are plans to utilize the sPHENIX prototype, which was used to demonstrate the energy resolution from beam tests, to test the readout of individual tiles instead of tiles. Related simulation studies are also underway. Additional tests include measuring the potential noise for longer cables to transmit the signal from the SiPM to HGCROCs located at the end of the sector.

#### **Environmental, Safety and Health (ES&H) aspects and Quality Assessment (QA planning):**

**Construction and assembly planning:** Once RHIC operations conclude, the sPHENIX detector will be disassembled. During this process, each outer HCal sector will be removed from sPHENIX, and the SiPMs for each tile within the sector will be replaced with ePIC SiPMs. Following installation, the cables will be connected and integrated with a dedicated electronics test setup to verify that each tile can be read properly. To ensure accurate calibration, cosmic-ray tests will be performed on each sector. These tests will confirm the relative calibration factors on a tile-by-tile basis.

Currently, three test stands are being constructed at BNL, Georgia State University (GSU) and the University of New Hampshire (UNH). These facilities will be used to train students in the assembly and testing procedures. Following the disassembly of sPHENIX, the students will travel to BNL to perform these tests. The assembly process at BNL will be overseen by Stefan Bathe from Baruch College. Dr. Bathe previously served as the Level 3 Manager for the sPHENIX HCals and was responsible for the assembly of both the inner and outer HCals for sPHENIX.

**Collaborators and their role, resources and workforce:** There are several collaborating institutions working on the BHCals. The co-DSLs are Prof. Stefan Bathe and Prof. Murad Sarsour. Stefan Bathe is the PI of the Baruch College, CUNY, group. One postdoc in that group, Dr. Anjaly Menon, works on testing the read out and setting up the prototype for test beam. Stefan Bathe has extensive experience with the sPHENIX HCal as former Lvl3 manager for the assembly and testing of the HCal in the sPHENIX project, Operations Manager for the sPHENIX HCal, and co-convenor of the calorimeter calibrations group in sPHENIX. Murad Sarsour is co-PI at Georgia State University. GSU is a large group (with co-PIs Megan Connors and Xiaochun He) and several postdocs and graduate students. GSU was responsible for the tile testing in sPHENIX. Brookhaven National Lab is involved, mainly with Dr. Eric Mannel (former Lvl2 manager for the calorimeter electronics in sPHENIX) and Dr. Martin Purschke (data acquisition and calorimeter expert). The BNL group has extensive experience with the HCal, in particular with multiple test beam campaigns for sPHENIX. Groups not previously involved in sPHENIX are the University of New Hampshire with PI Prof. Nathaly Santiesteban, postdoc Dr. David Ruth, and a graduate student. UNH is now leading the

6741 simulations effort (previously led by Dr. Derek Anderson (then ISU), who has recently moved on  
6742 to a new position) David Ruth will join the University of New Mexico and start a new HCal group  
6743 there, focusing on the design of the LED system and simulations. Oak Ridge National Lab is de-  
6744 veloping the electronics and collaborating on testing the electronics with the HCal prototype. The  
6745 electronics development is led by Dr. Norbert Novitzky.

6746 **Risks and mitigation strategy:** The BHCAL depends on previously tested technologies which  
6747 minimizes the risks associated with it. A limited number of spare tiles were stored at GSU; however,  
6748 these tiles are currently being used in the HCal prototype that is being prepared for beam test.  
6749 Therefore, it is essential to procure additional tiles to ensure replacements are available in case any  
6750 tiles are damaged during the HCal refurbishment process. We anticipate needing 20 tiles of each  
6751 shape, for a total of 240 tiles. There are two ways we can monitor the tiles once they are installed  
6752 into EPIC. The LED system is useful for quickly testing the tiles on a regular basis while the cosmic  
6753 ray studies require a long time to collect sufficient data.

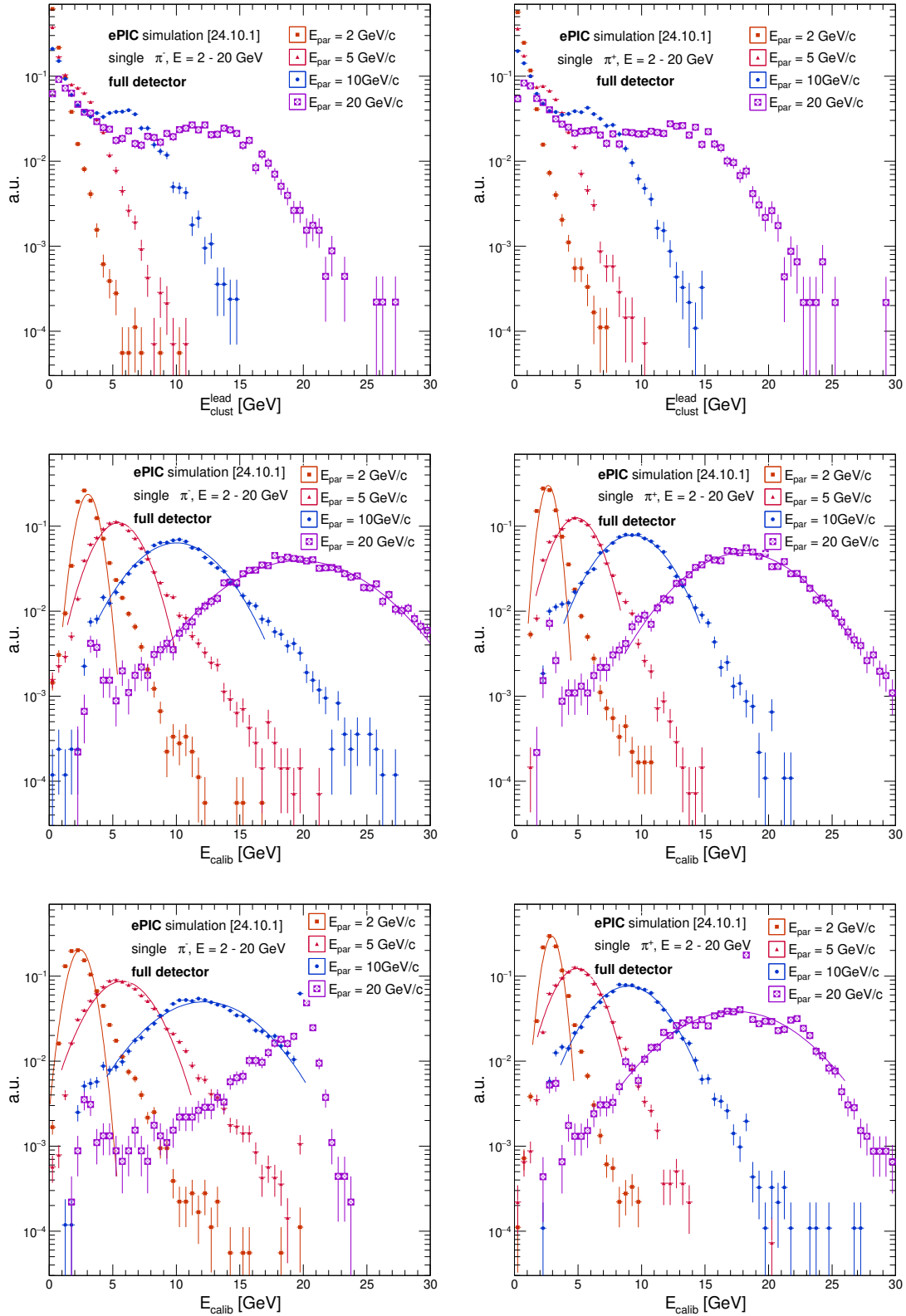


**Figure 8.190:** Uncalibrated (top row) vs. LD-calibrated energy (middle row) and MLP-calibrated (bottom row) of lead BHCAL clusters for 2 (orange), 5 (pink), 10 (blue), and 20 GeV (purple)  $\pi^-$  (left column) and  $\pi^+$  (right column). Distributions were simulated using the 2024.10.1 simulation geometry. Repository: <https://github.com/ruse-traveler/EpicBHCALPTDRStudies>

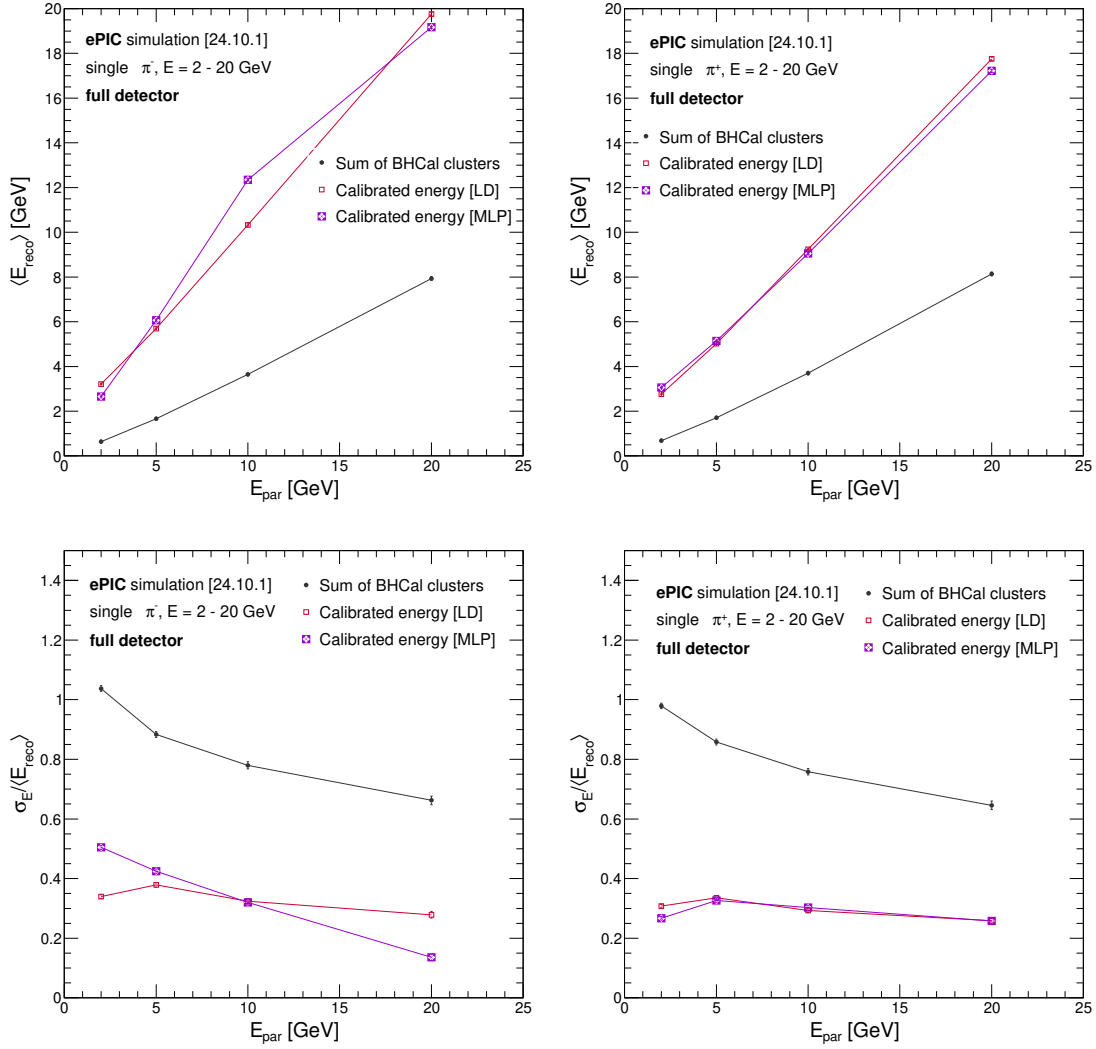


**Figure 8.191:** Linearity (top row) and energy resolution (bottom row) of calibrated single  $\pi^-$  (left column) and  $\pi^+$  (right column). Red lines indicate LD-calibrated energies, purple lines indicate MLP-calibrated energies, black lines indicate the linearity, resolution of summing BHCAL clusters without calibration. Distributions were simulated using the 2024.10.1 simulation geometry. Repository: <https://github.com/ruse-traveler/EpicBHCALPTDRStudies>



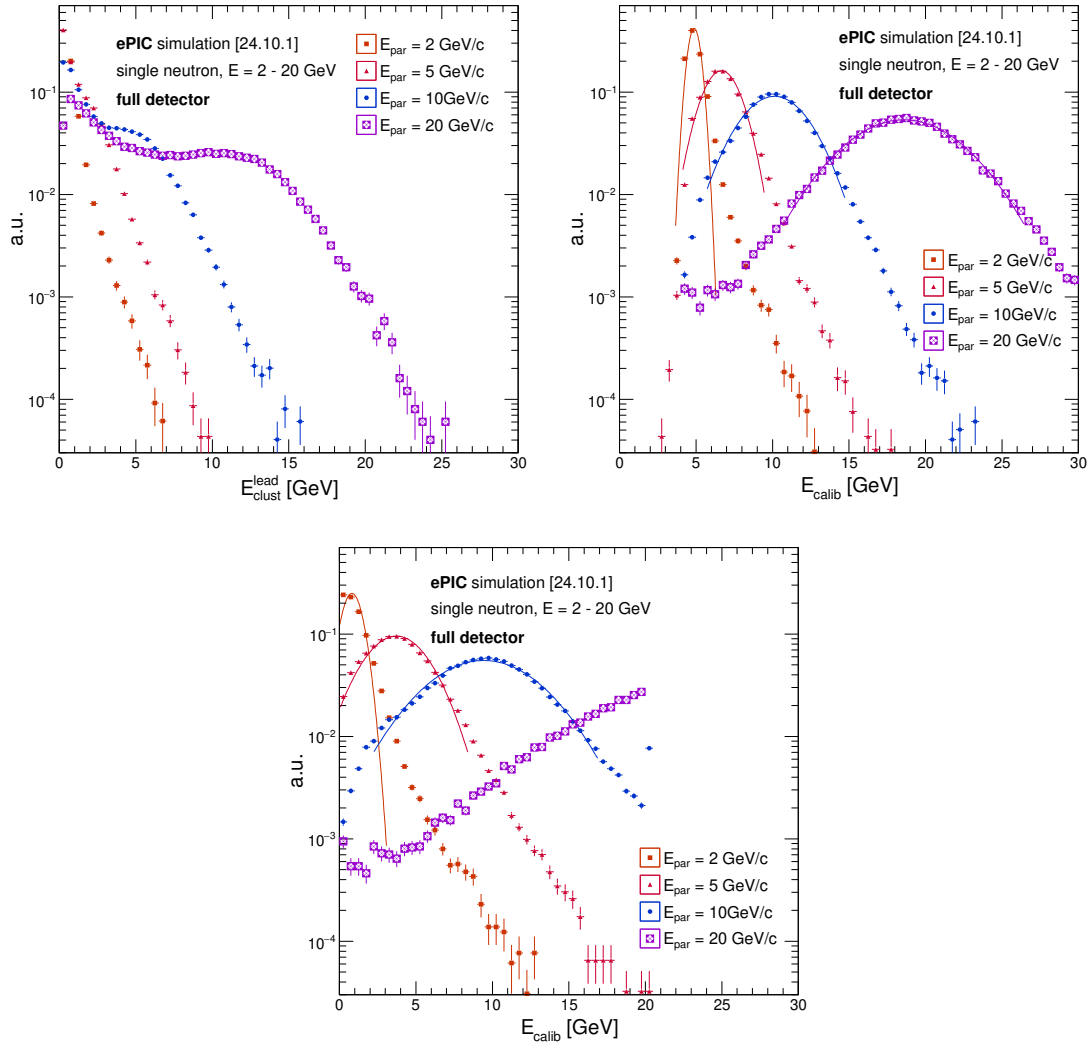


**Figure 8.192:** Uncalibrated (to left) vs. LD-calibrated energy (top right) and MLP-calibrated (bottom) of lead BHCAL clusters for 2 (orange), 5 (pink), 10 (blue), and 20 GeV (purple) neutrons. Distributions were simulated using the 2024.10.1 simulation geometry. Repository: <https://github.com/ruse-traveler/EpicBHCALPTDRStudies>

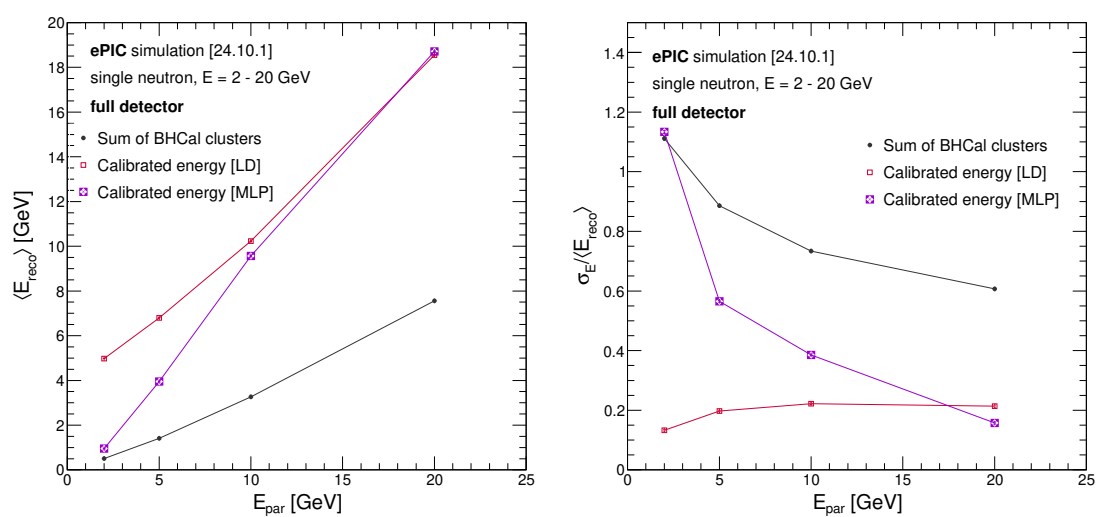


**Figure 8.193:** Linearity (left) and energy resolution (right) of calibrated single neutrons. Red lines indicate LD-calibrated energies, purple lines indicate MLP-calibrated energies, black lines indicate the linearity, resolution of summing BHCAL clusters without calibration. Distributions were simulated using the 2024.10.1 simulation geometry. Repository: <https://github.com/ruse-traveler/EpicBHCALPTDRStudies>

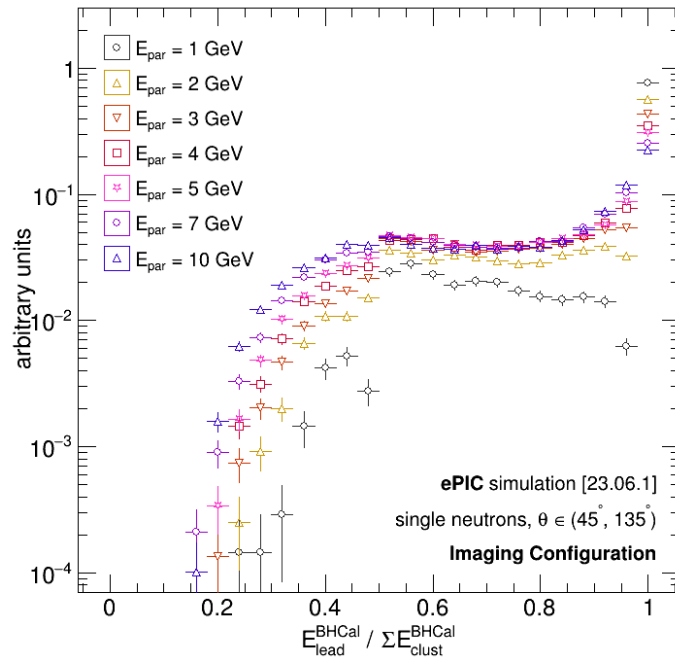


**Figure 8.194:** ratio of uncalibrated lead BHCAL cluster to the sum of all BHCAL clusters for 2 (grey) - 10 GeV (blue) single neutrons. Distributions were simulated using the 2023.06.1 simulation geometry. Repository: <https://github.com/ruse-traveler/EpicBHCALPTDRStudies>

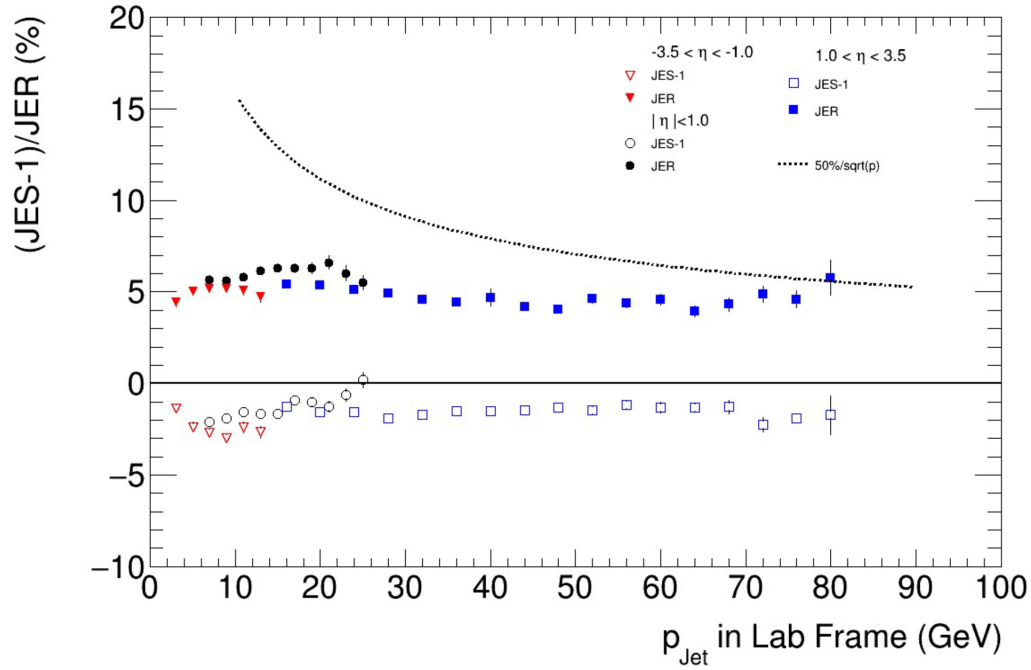


**Figure 8.195: JES/R for full (tracks + ECal + HCal):** The  $JES - 1 = \langle \Delta p/p \rangle$  (open markers) and JER (closed markers) plotted as a function of  $p_{jet}$  in the lab frame for jets in  $\eta \in (-3.5, 1.0)$  (red points),  $|\eta| < 1$  (black points), and  $\eta \in (1.0, 3.5)$  (blue points). In the barrel region, jets are constructed from reconstructed tracks and ECal clusters *without* a nearby track. Neutral hadrons are included in the jets by smearing the particle energy by the measured energy resolution of the sPHENIX OHCAL. Jets are reconstructed via the Centauro algorithm ( $R = 0.8$ ) and transformed back into the lab frame. Jets are required to have at least 2 particles, and exclusively charged or neutral jets are rejected. From ECCE responses to the EIC DPAP Panel; received from John Lajoie in private communication. **THIS IS A PLACEHOLDER**

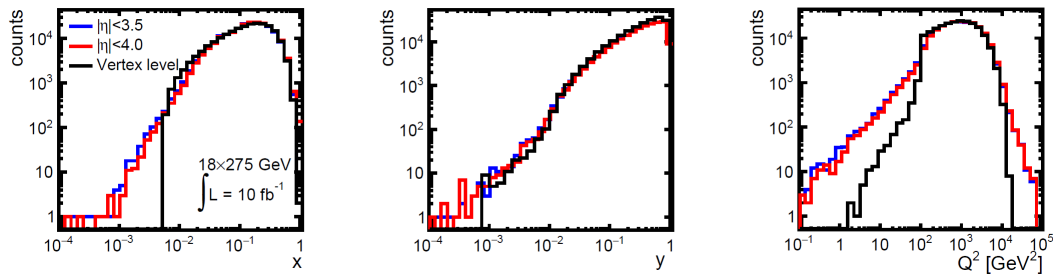


**Figure 8.196: JB variables at truth ("vertex", black) and reconstructed level for particle  $|\eta| < 3.5$  (blue) and  $|\eta| < 4$  (red) in  $18 \times 275$  CC DIS events.** Detector simulation and reconstruction was carried out using a fast simulation using Delphes. Figure 8.21 from the **EIC Yellow Report**. **THIS IS A PLACEHOLDER**

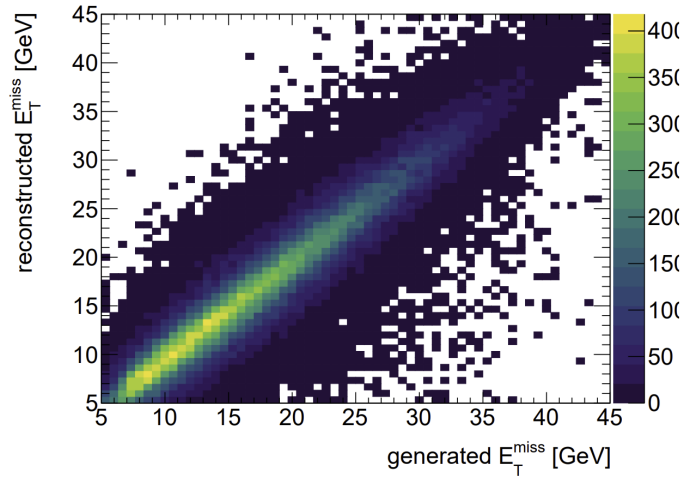


**Figure 8.197: Truth vs. reconstructed  $E_T^{\text{miss}}$ :** the truth (x-axis) vs. reconstructed (y-axis)  $E_T^{\text{miss}}$  for  $10 \times 275$  CC DIS events. Detector simulation and reconstruction was carried out using a fast simulation using Delphes. Figure 4 from [arXiv:2006.12520](https://arxiv.org/abs/2006.12520). **THIS IS A PLACEHOLDER**

### 8.3.6.3 The forward endcap hadronic calorimeter

#### Requirements

**Requirements from physics:** In electron-proton ( $ep$ ) or electron-ion ( $eA$ ) collisions, many highly-energetic hadrons are created in the process of probing the partonic structure of the target proton or ion using the electron. However, since the incoming proton/ion has a significantly larger kinetic energy than the incoming electron, most of the hadrons are emitted in the same direction as the hadron beam, into the hadron end cap, which is defined as the “forward” direction at the EIC.

Thus, jets of particles, with single-particle energies of up to 150 GeV, are expected to reach the forward hadronic calorimeter, e.g. based on simulated PYTHIA events for  $e+p$  collisions at  $18 \times 275$  GeV<sup>2</sup>. Typical jets consist of 10-12 particles contained within a jet radius of  $R = 1$ , with  $R$  being the angular distance  $\sqrt{\eta^2 + \phi^2}$ . These jets also contain nontrivial substructure within this cone, which carries important information about QCD dynamics. Unfortunately, the tracking momentum and angular resolution worsen rapidly above  $\eta = 3$ . Because of this, the hadronic and electromagnetic calorimetry in that region are required to provide both excellent energy resolution and sufficient spatial resolution to resolve particles within the jets. Thus, the forward calorimeter system has to be finely-segmented and built with minimal dead space in between the towers. This design will provide shower containment for highly energetic particles while still providing good energy resolution down to low energies.

**Requirements from Radiation Hardness:** In the forward region the radiation dose the detector is exposed to varies significantly as a function of radius. Three different regions are considered:

**A:**  $R > 1$  m which is exposed to less than  $5 \cdot 10^9$  neq cm<sup>-2</sup>year<sup>-1</sup>

**B:**  $0.2 \text{ m} < R < 1 \text{ m}$  which is exposed to less than  $10^9 - 10^{11}$  neq cm<sup>-2</sup>year<sup>-1</sup>

**C:**  $R < 0.2$  m which receives around  $10^{11}$  neq cm<sup>-2</sup>year<sup>-1</sup>

The maximum radiation dose is received closest to the beam pipe and closest to the interaction point. Consequently, the primary concern will be the radiation hardness of the silicon photo multipliers (SiPM) within each layer and a secondary concern are the ASICs used to read out their signals and all other components for calibration or control, which will be sitting behind the calorimeter. It is not expected that the scintillator or steel will experience significant deterioration due to the radiation.

#### Requirements from Data Rates:

#### Justification

**Device concept and technological choice:** The ePIC forward HCal (LFHCal) will be a steel-plastic scintillator sampling calorimeter, read out in transverse and longitudinally separated segments. The design is based on the SiPM-on-tile concept first introduced by CALICE collaboration [121], which is now being further developed for the CMS HGCal upgrade [122]. The SiPM-



on-tile concept allows for high readout granularities with low dead space between scintillator tiles in a design that enables largely automated assembly of individual layer modules.

The LFHCal baseline readout granularity has been adapted to satisfy the physics performance requirements of the EIC Yellow Report [8], leading to a readout granularity of 5x5 cm in transverse direction and about 10-20 cm in the longitudinal direction. The innermost section closest to the beam pipe will be populated by an high-granularity insert [123, 124] with geometry tailored to maximize acceptance up to  $\eta = 4.0$ .

Figure 8.198 shows an overview of the LFHCal design and the main parameters are given in Table 8.66.

parameter	LFHCal 8M & 4M modules	insert modules
inner x,y (R)	$-20 \text{ cm} > x > 40 \text{ cm},$ $-30 \text{ cm} > y > 30 \text{ cm}$	$R > 17 \text{ cm}$
outer R (x,y)	$R < 270 \text{ cm}$	$-20 \text{ cm} > x > 40 \text{ cm},$ $-30 \text{ cm} > y > 30 \text{ cm}$
$\eta$ acceptance	$1.2 < \eta < 3.5$	$3.5 < \eta < 4.4$
tower information		
x, y	5 cm	$\approx 4.2 \text{ cm}$ (layer 1-20) $\approx 6.5 \text{ cm}$ (layer 21-60)
z (active depth)	120 cm	120 cm
z read-out	$\approx 8.4 \text{ cm}$	$\approx 8.4 \text{ cm}$
# scintillator plates	60 (0.4 cm each)	60 (0.3 cm)
# absorber plates	60 (1.52 cm)	60 (1.52 cm)
interaction lengths	$5.8\text{-}6.5 \lambda/\lambda_0$	$5.8 \lambda/\lambda_0$
# towers	8752	
# modules		2
8M	1058	
4M	72	
# read-out channels	$7 \times 8752 = 61264$	$\approx 7000$

**Table 8.66:** Overview of the calorimeter design properties for the LFHCal.

6798

### 6799 Subsystem description:

**General device description:** The LFHCal is positioned at  $z = 3.68 \text{ m}$  from the interaction point, with a radius of about 2.7 m and a total depth of  $\Delta z = 1.32 \text{ m}$ . It is constructed in alternating layers of 1.52 cm steel absorber and 0.4 cm plastic scintillator, see details in Table 8.66.

The LFHCal is largely constructed from mechanical assemblies housing 60 layers of 2x4 ("8M" modules) or 2x2 ("4M" module) tile layers. Alongside each assembly module, a multi-layer PCB picks up the analog pulses from each SiPM and passively transports them towards the end-face of the LFHCal. This analog signal transport approach differs from the latest CALICE/CMS designs, where the signal is digitized with ASICs placed near the SiPMs. Similar to the approach first proposed in Ref. [123], it simplifies the SiPM-carrying boards, saves longitudinal space in the detector's active area, and eliminates the need for cooling to counteract heat generated by the ASICs. In order to reduce the number of readout channels of the

6810

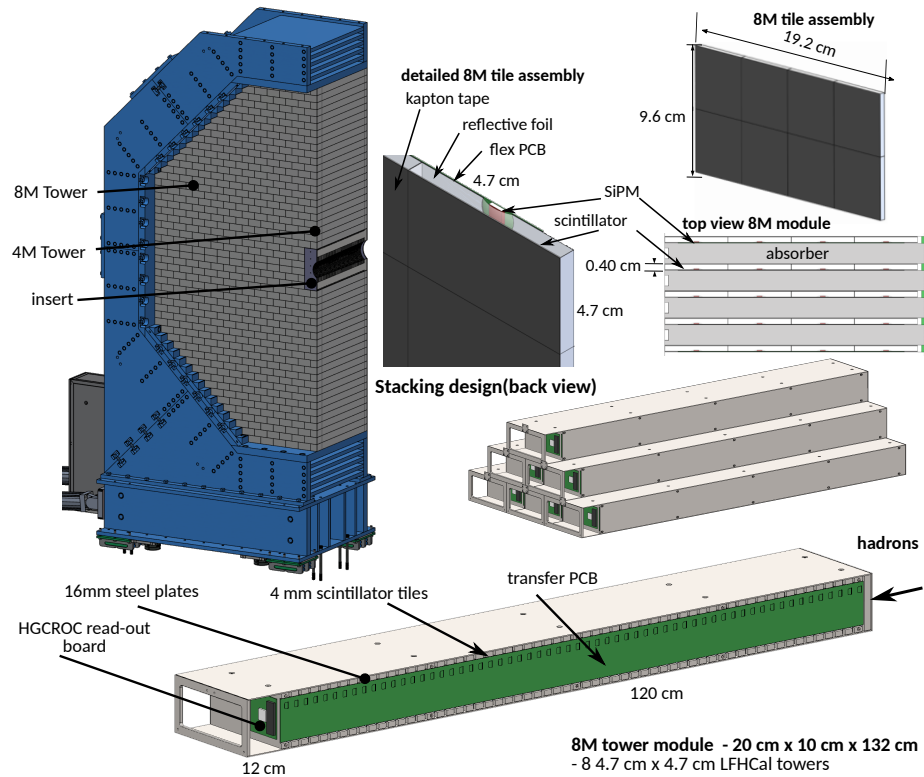


**Figure 8.198:** Renderings of the forward calorimeter assembly (top left), tile assembly of 8 scintillator tiles of the LFHCal with the SiPMs sitting in a dimple on each tile, detailed stacking example (middle right) and 8-tower module design (bottom).

LFHCal, SiPM signals from tiles in 5-10 consecutive layers are summed up before digitization by the readout electronics placed on the rear end of the LFHCal, facing away from the interaction point. Following [123], to increase the geometrical acceptance around the beam pipe and allow access to the scintillator layers during extended shutdowns for SiPM replacement or annealing, the modules surrounding the beam pipe are designed to be larger and include a conical cut-out for the beam pipe, as shown in Figure ?? (left).

The majority of the active scintillator layers are segmented into  $5 \times 5 \times 0.4\text{cm}$  tiles, individually wrapped in reflective foil, as depicted in Figure 8.200. The scintillation light generated in each tile is detected by a SiPM placed inside a circular “dimple” depression in the center of the tile. Tiles and SiPMs are assembled on thin, flexible printed circuit boards which carry the electrical signal of each SiPM to the side of an assembly module. In the insert region hexagonal tiles of two different sizes are used in order to maximize the acceptance and simultaneously reduce the number of read-out channels. Consequently, the first 20 layers are equipped with hexagonal tiles of 4.2 cm width which are arranged in a staggered pattern repeating every four layers and the subsequent layers are tiled with hexagonal tiles of 6.5 cm width. This staggering pattern creates overlaps among neighboring cells, which can improve position resolution for hadronic showers when applied in sub-cell reweighting algorithms, such as HEXPLIT [125], or with AI/ML methods. In the insert region, each tile is read out separately to maximize the position resolution of individual showers and to facilitate cell-by-cell calibration and monitoring in high-radiation environments, where radiation levels are expected to be inhomogeneous in both radial and longitudinal positions.

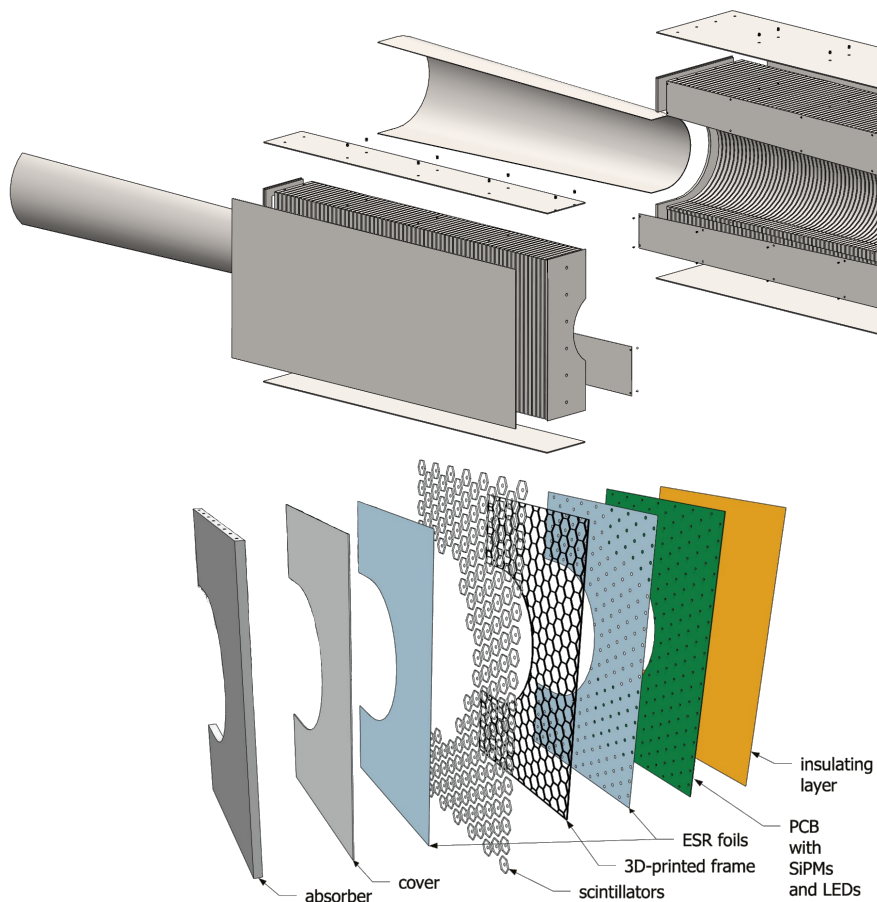


**Figure 8.199:** Renderings of the absorber structure for the insert modules surrounding the beam pipe (top) and their individual layer composition (bottom).

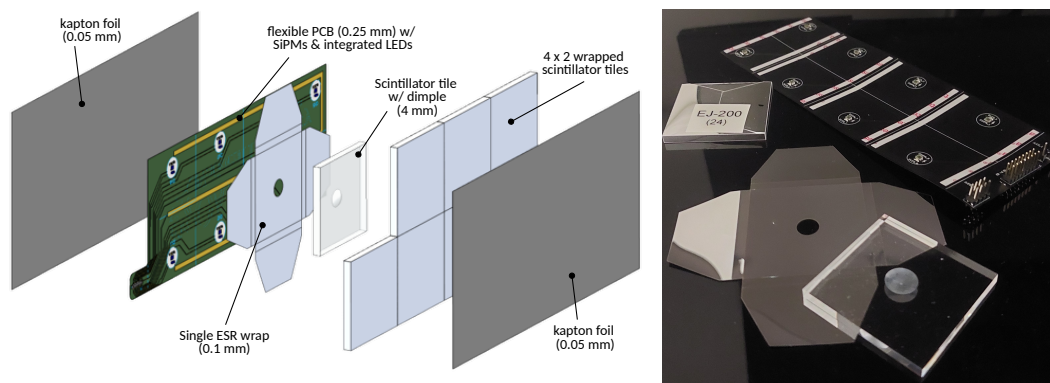


**Figure 8.200:** Left: Visualization of 8M-scintillator assembly with its individual components. Right: Samples of the individual components used for the 2024 test beam campaign.

The full LFHCal consists of 68264 readout channels. Out of these about 7000 channels are located in the insert modules and the remaining channels are contained in the 1058 “8M” modules and 72 “4M” modules. They are grouped into 8752 towers of  $5 \times 5 \text{ cm}^2$  transverse size with each 7 read-out segments.

**Scintillator:** The majority of the LFHCal will be instrumented with injection molded plastic scintillator tiles developed and produced by the Fermilab Scintillator Manufacturing Facility. While the light yield of injection molded plastic scintillator is found to be 20-25% lower than that of otherwise comparable commercially available cast sheet plastic scintillators, injection molded scintillator tiles are at least one order of magnitude more economical on the scale of the full LFHCal.

Only for the LFHCal segments that will be exposed to the highest radiation doses ( $R < 1 \text{ m}$ ) and inaccessible during the yearly maintenance intervals tiles machined from cast plastic scintillator stock will be used to increase the light yield in order to maintain enough signal-to-noise ratio to distinguish single MIP signals from the background noise.

**Sensors:** Simulations and test bench studies have shown that SiPMs with an active area of  $1.3 \times 1.3 \text{ mm}^2$  and pixel sizes around  $20 \mu\text{m}$  (i.e. Hamamatsu S13360-1325PE or S14160-1315PS) will yield enough light yield, gain and dynamic range even after full irradiation over the whole projected lifetime of the LFHCal. However, as neither the scintillator tiles nor the SiPMs are accessible after assembly, larger SiPMs with an area of  $3 \times 3 \text{ mm}^2$  (ie. Hamamatsu S13360-3025PE or S14160-3015PS) for radii below 1 m in order to provide an additional operational safety factor in the S/N ratio towards the end of its lifetime. For example, Ref. [126] demonstrated that an S14160-3015PS, operated at 40.5 V ( $\approx 2 \text{ V}$  over-voltage), yields a most-probable value of approximately 60 photoelectrons per MIP when coupled with an EJ-212 scintillator cell with an area of  $8 \text{ cm}^2$ .

**FEE:** The electrical signals from all SiPMs in the LFHCal are routed towards the end-face of the LFHCal using a passive transfer board, where they are picked up by a summing board that forms analog sums of 5 – 10 channels located consecutive layers of the same position. The following text will need to be adapted with the details of the CALOROC. The summed signals are then digitized by an ASIC based on the CMS HGCROC chip designed and produced by OMEGA. Each HGCROC can read out up to 72 individual SiPM channels. It features a 12bit ADC for low amplitude hit digitization, complemented by a 16bit time-over-threshold counter for larger amplitude signals. Individual signal arrival times are tagged with a 20 ps time-of-arrival counter. The HGCROC chip family features trimmable bias voltage in the range 0 – 2.5 V for each input channel, greatly reducing the number of required high voltage power supply channels to operate the LFHCal.

While the HGCROC chip family is well advanced in its design, it is designed for the externally triggered environment of the CMS experiment. A self-triggered variant of the HGCROC concept named CALOROC will be developed for the use in ePIC, which will natively support the ePIC streaming readout model. [122].

**Performance** The minimum requirements for the LFHCal performance are driven by the energy and position reconstruction of hadronic particles within a jet of 5 – 250 GeV. These requirements, however, must be evaluated as a combined resolution of the electromagnetic and hadronic calorimeter responses, as a significant fraction of the energy may already be deposited in the electromagnetic calorimeter, which has an equivalent depth of one interaction length. Since these two calorimeters have different  $e/h$  values, their combination must account for this to achieve a linear response with optimal resolution. Moreover, as the hadronic calorimeter is not compensated at the hardware level (i.e., given its Fe/Sc design, the response differs for electromagnetic and hadronic

depositions, with  $e/h \approx 1.2$ ), optimal energy reconstruction requires a shower-by-shower weighting approach. This is necessary because the electromagnetic content of hadronic showers varies on a shower-by-shower basis on an energy-dependent manner. This weighting procedure, dependent on particle energy and angle, is commonly referred to as “software compensation” or “offline compensation”. As noted in Section 11.4.1 of the Yellow Report [8], this approach requires fine granularity in the hadronic calorimeter, including in the longitudinal direction. This was demonstrated in previous experiments, such as H1 at HERA, which used a Pb/Fe liquid argon calorimeter, and in test beams with the CALICE Fe/Sc calorimeter.

Rather than following a traditional minimization approach to achieve the weight functions to implement software compensation, we rely on AI/ML methods, which provide a more efficient and optimal way. Specifically, we used a graph neural network approach, following the method applied in EIC calorimetry studies in Refs. [3, 7], which builds on prior work by the ATLAS collaboration [127]. Similar advancements were recently presented by the CALICE collaboration using test beam data [5]. This graph network approach effectively implements software compensation through shower-by-shower weighting at the cell level, using the shower structure encoded in graphs to achieve a linear response that is independent of both energy and the electromagnetic energy fraction of the hadronic shower, thereby yielding optimal energy resolution.

Figure 8.201 shows the combined energy resolution of the forward electromagnetic and hadronic calorimeter for single pions within the primary acceptance of the LFHCal as a function of  $\eta$ , obtained using the aforementioned graph network approach. The resulting combined energy resolution of  $\sigma_E/E = 27\%/\sqrt{E} \oplus 3\%$  surpasses the required resolution of  $\sigma_E/E = (35 - 50)\%/\sqrt{E} \oplus (7 - 10)\%$ , as specified in the Yellow Report [8].

The combined position resolution of the LFHCal and forward electromagnetic calorimeter for single pions can be found in Figure 8.202. Both the  $\varphi$  and  $\theta$  resolution are found to be better than 4 mrad for pions with an energy larger than 5 GeV within the full acceptance. A mild energy dependence can be observed for the  $\theta$  resolution increasing as a function of energy down to 2.5 mrad. For the  $\varphi$  no clear energy dependence can be claimed. While the  $\theta$  resolution appears to be largely  $\eta$  independent, the  $\varphi$  improves with increasing  $\eta$  to better than 2.5 mrad

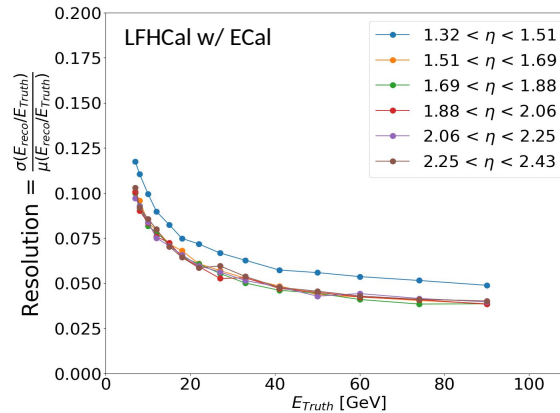


**Figure 8.201:** Combined energy resolution of the forward calorimeter system as a function of pseudo rapidity  $\eta$  for single pions, evaluated within the primary LFHCal acceptance. These results are obtained using the graph-neural network approach described in Ref. [3].

## Implementation

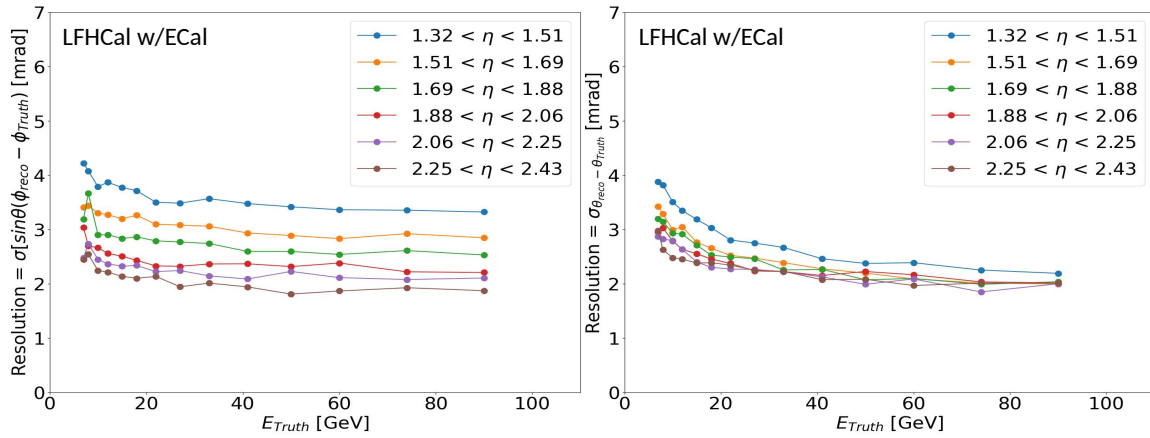


**Figure 8.202:** Combined position resolution of the forward calorimeter system as a function of pseudo-rapidity  $\eta$  for single pions, evaluated within the primary LFHCal acceptance. These results are obtained using the graph-neural network approach described in Ref. [3].

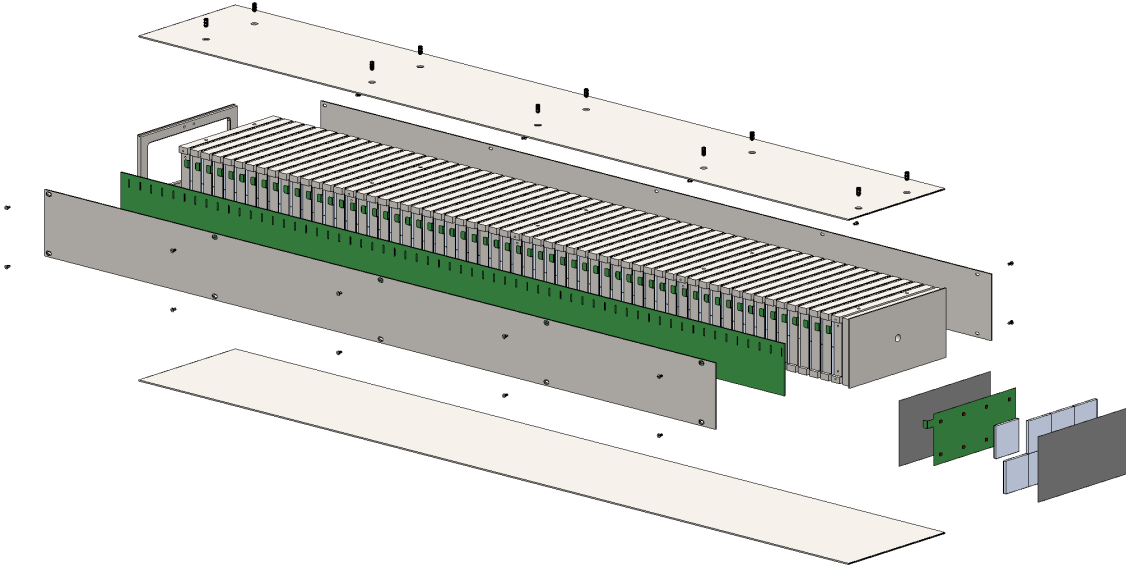


**Figure 8.203:** Visualization of the individual components of an 8M module.

**Subsystem mechanics and integration:** The primary construction component of the LFHCal are the 1052 8M modules, as depicted in Figure 8.203. These modules are constructed out of an electron beam welded and nickel-plated absorber structure out of AISI-1020 carbon steel, consisting of the 60 absorber plates, the front and back plate and the top and bottom plate. Inside the resulting slots inbetween the absorber plates 8M scintillator assemblies (Figure 8.200) are placed, which are connected to a long transfer PCB running along the side of the 8M module. The module is closed by two screwed side panels out of AISI 304 stainless steel. The read-out electronics is placed in a rear compartment of about  $19.5 \times 9.5 \times 8.5 \text{ cm}^3$ , which is accessible from the rear though a cut-out window in the back plate.

The individual absorber plates are welded on the top and bottom using alternating stitch welds of



two times 63.5 mm and 88.78 mm length with a minimum penetration depth of 0.5 mm over the full length. For the front and back plates, as well as, the those plates to which the strong back for transportation is anchored the available maximum weld length is used to ensure maximum stability. Afterwards, the fully welded structure is nickel electroplated to reduce the effects of corrosion and the stainless steel side covers are installed. This production mechanisms allows for minimal distortions during construction and thus allows for a maximization of the available active detector surface.

The active layers are inserted and tested together with the long transfer board at the various assembly locations. The FEE-cards at the rear of each module can be installed during the same assembly process or could be mounted prior to installation at Brookhaven National Laboratory depending on the production readiness of the CALOROCs.

A similar construction procedure will be followed for the half sized 4M modules, where the staggering of the welds will not be necessary. For the two individual modules we envision the same construction technique, however, due to its weight and corresponding necessary rigidity it will most likely need to be welded also on the outer straight edge of each module to correctly disperse the load of the modules stacked on top of the respective inserts.

The LFHCal will be stacked in two half shells surrounding the beam pipe, as shown in [Figure 8.204](#) (top), which are situated on rails and movable using Hillman rollers and linear actuators, which are detailed in the same drawing on the bottom. During assembly each module is lifted into place and then adjusted horizontally and vertically using different sized stainless steel shims. Afterwards it is fixated in place using bracket at the rear of each module as seen in the detailed stacking pictures in [Figure 8.198](#). Moreover, each module is bolted to the 2.54 cm plate covering the full front face of the each half of the LFHCal. This steel plate will simultaneously serve as mounting plate for the forward electromagnetic calorimeter.

**Services:** Apart from the SiPM sensors integrated into each scintillator tile layer, all active LFHCal electronics are located on the end-face of the LFHCal, fully accessible in between active beam runs of the EIC. As such, there are no significant bottlenecks in terms of maximum permissible occupied cross section of service channels.

The total number of readout ASICs is expected to be around 1000 at a power dissipation of an estimated 2 W per ASIC distributed over the entire end-face of the LFHCal, which is cooled with a small liquid cooling system.

The overall cross section of low voltage supply cable conductors is estimated to be around 1000 mm<sup>2</sup> from the required current rating (up to 1 kA at 2.5 V), which can be supplied by a few units of off-detector low voltage power supplies in a common crate area with the appropriate air flow, mains power connection and electrical safety facilities.

The HGCROC readout ASIC supports channel-individual trimming of SiPM bias voltages, reducing the overall number of required high voltage bias supply channels. For the start of the operation of ePIC, we expect not more than 16 channels of high voltage supplies in the voltage range 50-80 V. When more significant adjustments to the bias voltages will have to be made due to the varying effects of radiation damage across the LFHCal volume, more channels might have to be added.

Since the LFHCal is planned to be assembled in two individual half-discs, all cables and other services are separated along the same axis and cannot reach across the central separation gap of the LFHCal, which is either reflected in individual cable trees from the power supplies to individual halves of the LFHCal, or potentially entirely separate power supplies located on different sides of the experimental hall.



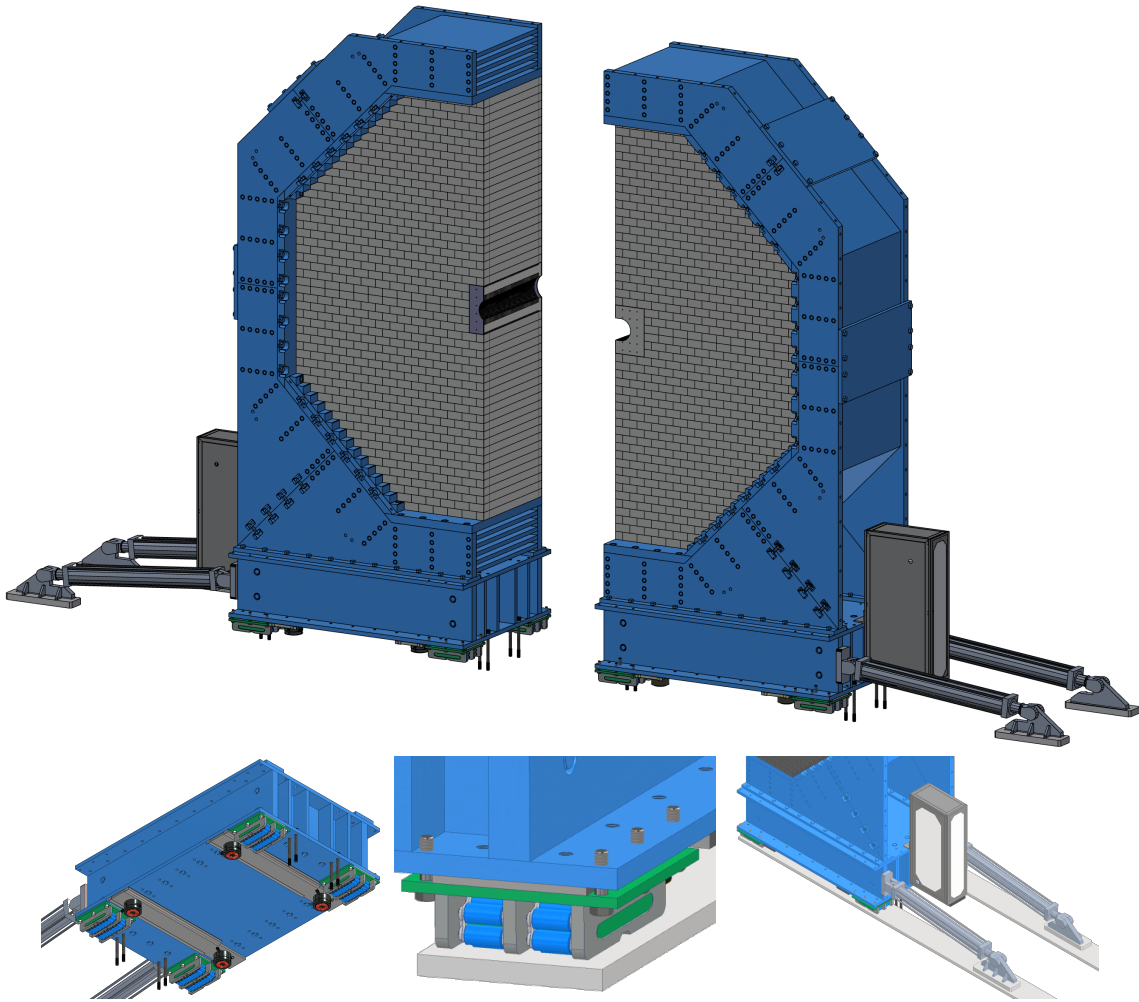


**Figure 8.204:** Visualization of the full LFHCal in its cradle (top) and details of its moving mechanism (bottom).

6963 **Calibration, alignment and monitoring:** The gains of individual SiPMs will be monitored  
 6964 and calibrated by means of an integrated LED calibration system providing short, low amplitude  
 6965 flashes of light into each sensor. This gain calibration scheme does not depend on the exact ampli-  
 6966 tude of each LED pulse and is thus robust to changes in ambient conditions and very cost effective.  
 6967 The front-end electronics include a charge injection mechanism that can calibrate its own ADC and  
 6968 ToT scales with respect to each other.

6969 Using the calibrations in sensor gain and readout electronics scales, the light yield of each tower of  
 6970 summed scintillator tiles will be monitored from the deposits of minimum ionizing tracks produced  
 6971 in EIC collisions during the operation of the accelerator, as well as with cosmic muons in between  
 6972 run periods.

6973 Initial parameters for module alignment will be provided from the metrology during and after the  
 6974 stack-up of the LFHCal modules into the full LFHCal detector. No significant relative movement of  
 6975 LFHCal modules is expected during its lifetime, however the absolute position of each half-cradle  
 6976 will need to be validated each time the cradles are moved out and back into their positions.

### 6977 **Status and remaining design effort:**

6978 R&D effort and status: The primary R&D effort for the LFHCal has been concluded in 2024.  
 6979 The remaining activities focus on the readout electronics as well as the analog summation  
 6980 of the signals for consecutive individual layers and the long passive transfer board. First  
 6981 prototypes of a summation test board have been received and are currently being tested. The  
 6982 long transfer board is in its design phase and a first prototype should become available middle  
 6983 of 2025.

6984 Other activity needed for the design completion: To validate the simulated performance of  
 6985 the different LFHCal module types several test beam campaigns are planned during 2025-  
 6986 2028 with increasingly larger prototypes. The first of which have been completed in 2023 and  
 6987 2024 with particle or single modules.

6988 Status of maturity of the subsystem: The a large fraction of the LFHCal components has  
 6989 reached 90% design maturity and thus the steel structures for the 8M- and 4M-modules as  
 6990 well as the necessary SiPMs have been included in CD3-A as part of the long lead procure-  
 6991 ment items. The first preproduction items are evaluation and are largely compliant with  
 6992 the given specifications. The remaining mechanical components, as well as, the SiPM carrier  
 6993 boards are currently under evaluation and are being considered for inclusion in the CD3-  
 6994 C procurement, as the assembly of the 8M- and 4M-modules will take about 2 years after  
 6995 receiving the various components.

6996 **Quality Assessment (QA) and Control (QC) planning:** The quality assessment of the LFH-  
 6997 Cal components will be structured similarly to the construction process. The following processes  
 6998 are currently foreseen:

6999 **Absorber structure:** During the production of the absorber structures of the 8M and 4M mod-  
 7000 ule, at random 5% of the modules will be inspected with full GD&T, while for the remaining  
 7001 modules only the external dimensions will be inspected and the slots cross-checked using  
 7002 a go-no-go-gauge after welding. The subsequent nickel plating thickness will be evaluated  
 7003 at for a random 5% of the modules following standard industry techniques. For the insert  
 7004 modules full GD&T will be performed on both individual modules and the thickness of the  
 7005 nickel plating will be evaluated. Should any of these evaluations be outside the specified  
 7006 limits the module badge of modules will be rejected and the production parameters adjusted  
 7007 as necessary.

7008 **Silicon photomultipliers:** The quality control of the SiPMs will be performed in a two step  
 7009 process. The vendor guarantees that within one badge of about 520 SiPMs a maximum vari-  
 7010 ation of the break down voltage of 0.1V for the 8M and 4M-modules can be expected, whilst  
 7011 for the ~20k SiPMs necessary for the insert a variation of 0.05V will be guaranteed. Out of  
 7012 each badge 5% of the SiPMs are tested at random and their break down voltage is measured  
 7013 as well as their gain dependence and noise levels. Should the respective SiPMs fail to comply  
 7014 with the desired specifications the full badge shall be rejected and replaced by the vendor.

7015 **Assembled SiPM-flex boards:** As per industry standard connectivity tests for all SiPM-flex  
 7016 board assemblies will be performed by the vendor.

7017 **Assembled Scintillator layers:** All assembled scintillator layers will be visually inspected  
 7018 regarding light tightness by flashing the internal LEDs. These will be followed by a go-  
 7019 no-go gauge approach for checking the external dimensions. Moreover, connectivity tests  
 7020 as well as single photon spectra measurements will be performed for every assembly, prior

7021 to installation in the absorber structure. Each assembly will receive a unique identification  
7022 number and the collected data will later be used as basis for the calibration of the full module.

7023 **Long-transfer-board:** Each long-transfer board will be tested for connectivity as well as level  
7024 of cross talk among the different lines.

7025 **FEE-card:** Each FEE-card will be exposed to a series of functionality tests prior to installation  
7026 in the module.

7027 **Full Modules:** After the assembly of each module first electrical connectivity test for each  
7028 SiPM layer will be performed and afterwards cosmics data will be taken in order to assess  
7029 the performance of the module. The same procedure will be repeated once the modules are  
7030 put in place in the experimental hall prior to installing the next layer.

7031 **Environmental, Safety and Health (ES&H) aspects:** The LFHCal design follow the best  
7032 practices established within the national laboratories regarding standard safety and environmental  
7033 concerns. We will strive to implement these practices at all production sites by standardizing the  
7034 safety protocols, while adhering to local constraints and control processes specific to each institu-  
7035 tion. Consequently, for each site the potential hazards will be identified, mitigation strategy will be  
7036 developed and the appropriate safety procedures will be documented.

7037 The primary hazard during construction of the LFHCal have been identified as:

7038 **Handling of absorber structure:** The different modules of the LFHCal range in weight from  
7039 74 kg up to 1.3 t. None of them should be lifted without a lifting fixture (strongback) and the  
7040 appropriate lifting equipment for the respective weight. They will need to be uncrated for  
7041 assembly and lifted on top an appropriate assembly table which can support the respective  
7042 weight during installation and testing of the individual components. In particular, for the  
7043 lifting operations specific protocols in compliance with the local safety rules will need to be  
7044 established in order to prevent accidents.

7045 **Storage of absorber structure during assembly:** While the modules are being assembled a  
7046 large fraction of the 8M modules will need to be stored at the different assembly sites. Thus  
7047 in order to mitigate excessive space requirements a storage solution which allows stacking  
7048 of crate modules (2-3 crates) or similar solutions will need to be pursued. This will require  
7049 additional safety measures to prevent collaps of the crates or other stacking previsions as  
7050 well as lifting the modules accordingly in their crates.

7051 **Laser operation hazards:** The ESR foil wraps will need to be cut with a laser-cutter. Controls  
7052 and measures will be implemented to ensure the corresponding device cannot be operated  
7053 without interlocks and following the laser safety guidelines of the respective institution.

7054 **Pinch/nip hazards:** Automated systems, such as robots for wafer probing, pick-and-place,  
7055 and glue application, present pinch hazards. Controls, such as guards and procedures, will  
7056 be in place to mitigate these risks.

7057 **Crush hazards:** The use of presses and swaging equipment introduces crush hazards during  
7058 assembly processes. Strict safety protocols, including the use of guards and operator training,  
7059 will mitigate these risks.

7060 **Radioactive sources:** The use of radioactive sources for calibration introduces additional  
7061 handling requirements, and proper shielding and storage protocols will be implemented as  
7062 necessary.

7063 **Electrical safety:** Electrical safety procedures will also be applied for all electronics and  
7064 power systems associated with the LFHCal production tooling and detector components.

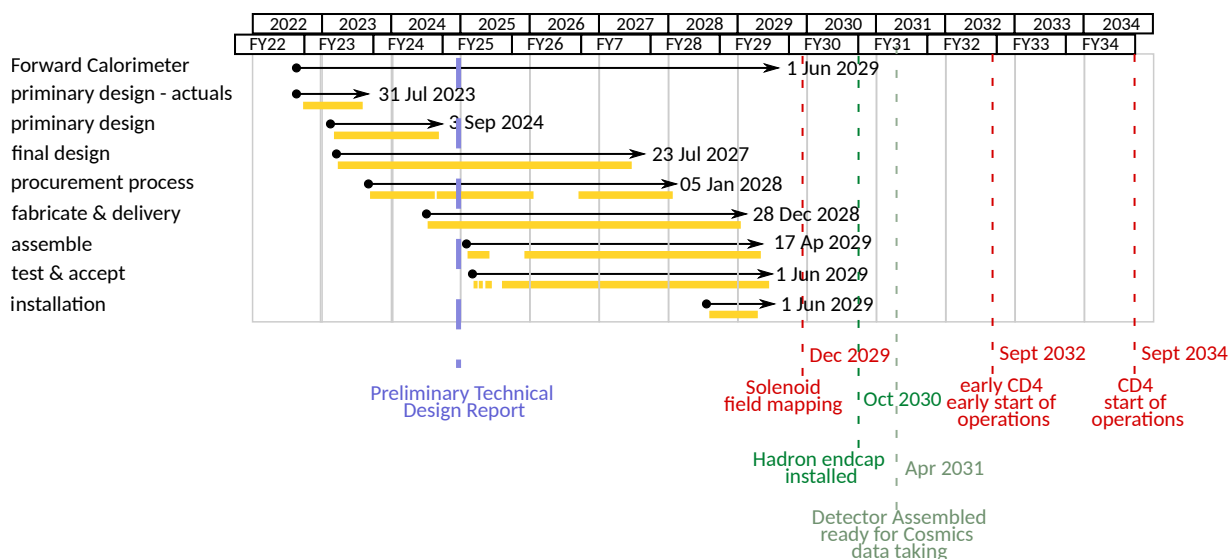


**Figure 8.205:** General timeline of the LFHCAL design, construction and assembly.

**Flammable liquid handling:** For cleaning the different electrical components ethanol might be used, these bottles will need to be handled with care and their storage will follow the institutional safety protocols. Handling will only be done with appropriate gloves.

**Construction and assembly planning:** The LFHCAL construction is divided into several phases, which are partially happening in parallel:

**Absorber structure fabrication:** The individual 8M, 4M and insert module absorber structures are assembled out of 66 individual pieces each, excluding screws, as seen in [Figure 8.203](#). Out of these 64 pieces are welded together using electron-beam welding after having been preassembled and fixated in a specially designed jig for the weldment. It has been currently estimated that a maximum of 12-20 8M modules and 4M modules could be produced within a 5-day work week. The limiting factor being the availability of the large vacuum welding chamber and a full weldment cycle lasting about 2/hour per weldment. The weldments are afterwards electroplated with nickel to prevent corrosion and reduce the wearing on the outer surface due to transportation and handling. At full capacity this would require a full year of production time for the 1058 8M weldments not factoring in any delays in the supply chain. With the LFHCAL also serving as flux-return for the MARCO magnet and the need to be available for the powering tests currently scheduled for December 2029, has led us to acquire the LFHCAL modules as part of CD3-A and CD3-B long lead procurement starting in fiscal year 2024. In order to reduce the storage needs at the respective vendors and allow for a staggered further assembly the delivery of these modules will be done in badges of 50-100 modules during 2025 and 2026.

**Scintillator layer assembly:** The assembly of the individual scintillator layers for the 8M and 4M modules can be completely decoupled from the absorber structures fabrication. In order to assemble a single 8M-scintillator layer one fully equipped flexible SiPM-carrier board, 8 wrapped tiles and two layers of Kapton foil will be needed. For the main body of the LFHCAL (1058 8M and 72 4M) modules a total of 63480 8M scintillator layers and 4320 4M scintillator layers will be required, leading to at least 525120 wrapped scintillator tiles.

About 10 – 12% of the tiles will be produced out of cast sheets, while the remaining  $\approx 90\%$  of the tiles will be injection molded out of scintillator plastic using the facilities at Fermilab. Producing all tiles out of cast material is cost and schedule prohibitive, despite having an about 20% higher light yield. The production time at Fermilab has been estimated to be about 6/month of nominal operations, which can be done in batches in order to reduce the storage overhead. The tiles produced using injection molding have to be degreased and subsequently wrapped in highly reflective foil (i.e. ESR foil). Given the tight tolerances of the LFHCAL modules and the amount of tiles to be wrapped it is currently envisioned to perform the wrapping using a specifically designed tile-wrapping setup similar as for the CMS HGCal.

Afterwards, the wrapped tiles are assembled into  $4 \times 2$  or  $2 \times 2$  scintillator assemblies backed by a flexible SiPM-carrier board and sandwiched into two adhesive sheets of thin kapton foil, as seen in [Figure 8.200](#). The assembled layers are subsequently tested and packaged into groups of 60 assemblies to ease storage and assembly during the module assembly.

For the two insert modules each layer will need to be assembled individually due to their unique shape and hexagonal tile arrangements. The around 7000 hexagonal tiles will need to be painted on their edges individually with  $\text{TiO}_2$ -paint and then subsequently embedded in their 3D printed frame for each layer. The frame is mounted to a kapton backed SiPM carrier board which is covered with a pre-cut ESR sheet in order to accommodate the SiPMs and LEDs for each tile. After installing another sheet of ESR-foil on top of the scintillator layer the assembly is completed by a thin cover. Due to their unique shapes and placements the insert module layers have to be assembled manually and then tested. These layers are constructed with a significantly larger rigidity than the 8M assemblies in order to allow for removal during the extended year end shutdowns and possible replacement of annihilation.

**Module assembly and testing:** The assembly of the individual 8M- and 4M-modules requires: 1 steel absorber structure, 60 tile-assemblies, 1 long-transfer-board and 1 FEE-card. For the assembly the absorber structure will be placed on a flat surface using its lifting fixtures and afterwards the 60 tile assemblies will be inserted in the corresponding slots. They are then connected to the long-transfer-board by connecting the 60 individual latches with the connectors through the prepared slots in the long transfer board. Afterwards, the FEE-card is connected in the rear of the module and a connectivity test for all layers is executed. Then the side-panels are installed and the module can be placed on its front face for cosmic testing in a vertical position. Should the FEE production be delayed a test board instead of the final FEE could be installed for the tests and removed afterwards. In this case the final FEE's would be installed prior to installation in the experimental hall at BNL.

The insert module assembly follows a similar procedure except that each layer of tile assemblies is unique and thus should be placed in the correct order for these two modules.

**LFHCAL assembly:** The LFHCAL assembly will be done in the Point 6 experimental hall at BNL in its support cradle. Each half of the LFHCAL is going to be assembled separately by placing one module at a time with a crane and chiming it in place using the prepared chims, layer by layer. At the same time the cradle is growing around it as the number of layers grows. The large front plate to mount the ECal is installed simultaneously to anchor the LFHCAL modules in place in front.

**Collaborators and their role, resources and workforce:** The full LFHCAL WBS organizational chart is available in the additional material ([Figure 8.206](#)). The LFHCAL consortium consists of a diverse list of institutions under the leadership of Oak Ridge National Laboratory (ORNL). Currently the majority of the leadership team is situated at ORNL, in particular regarding mechanical, electrical and read-out design as well as scintillator testing. System testing and Software and

Simulation design are headed by Brookhaven National Laboratory (BNL) and the University of Riverside, respectively.

#### Risks and mitigation strategy:

Each LFHCal scintillator tiles has to be wrapped in a suitable foil, ensuring the wrapping fulfills the requirement in light-tightness as well as geometric tolerances after wrapping. The LFHCal tiles for lab tests and testbeam studies so far have been wrapped manually. The CMS collaboration is developing an automated wrapping machine, following two similar concepts at Northern Illinois University and DESY, Germany. We are in close contact with these groups and plan to adapt one of their designs to the needs of the LFHCal design. If their final designs turns out to be unsuitable to wrap LFHCal tiles, we will require additional R&D efforts to adapt the existing design to the LFHCal or potentially develop our own. If all automated wrapping developments fail to produce reliable results, all tiles can be manually wrapped with the help of already existing 3d-printed and a sufficient number of e.g. students to perform the wrapping under supervision.

The readout ASIC of the LFHCal (as well as other ePIC detectors) is expected to be based on the HGCROC design with modifications enabling a self-triggered streaming readout named CALOROC. In case the CALOROC developments are not successful, HGCROC can be operated to be quasi self-triggering by adding additional FPGA logic close to the readout electronics that locally generates external triggers based on the streaming trigger output that already exists in the HGCROC. This mitigation would require additional electronics on the LFHCal end-face and greatly increase the number of differential data links required, which increases system complexity and cost.

Stacking the 1168 LFHCal modules into two coherent half-discs requires each module to adhere to the defined tolerances after assembly. Ongoing tests of the electron-beam welding procedures achieve tolerances very close to the requirements, but scaling the production to the required volume still needs to be demonstrated and validated. If the tolerances for individual modules can not be ensured, more shimming is required during the module stackup.

A number of critical components of the LFHCal are not accessible after the modules are stacked up into the full LFHCal. All connectors and PCBs buried into the LFHCal volume must thus be thoroughly validated for electrical and mechanical functionality and longevity. If certain connector types are found to be unsuitable e.g. in past and future testbeam campaigns, different connectors need to be selected or, if not possible, additional fastening mechanisms need to be introduced to ensure no readout channel is lost to bad or worsening connectors over the lifetime of the LFHCal.

#### Additional Material

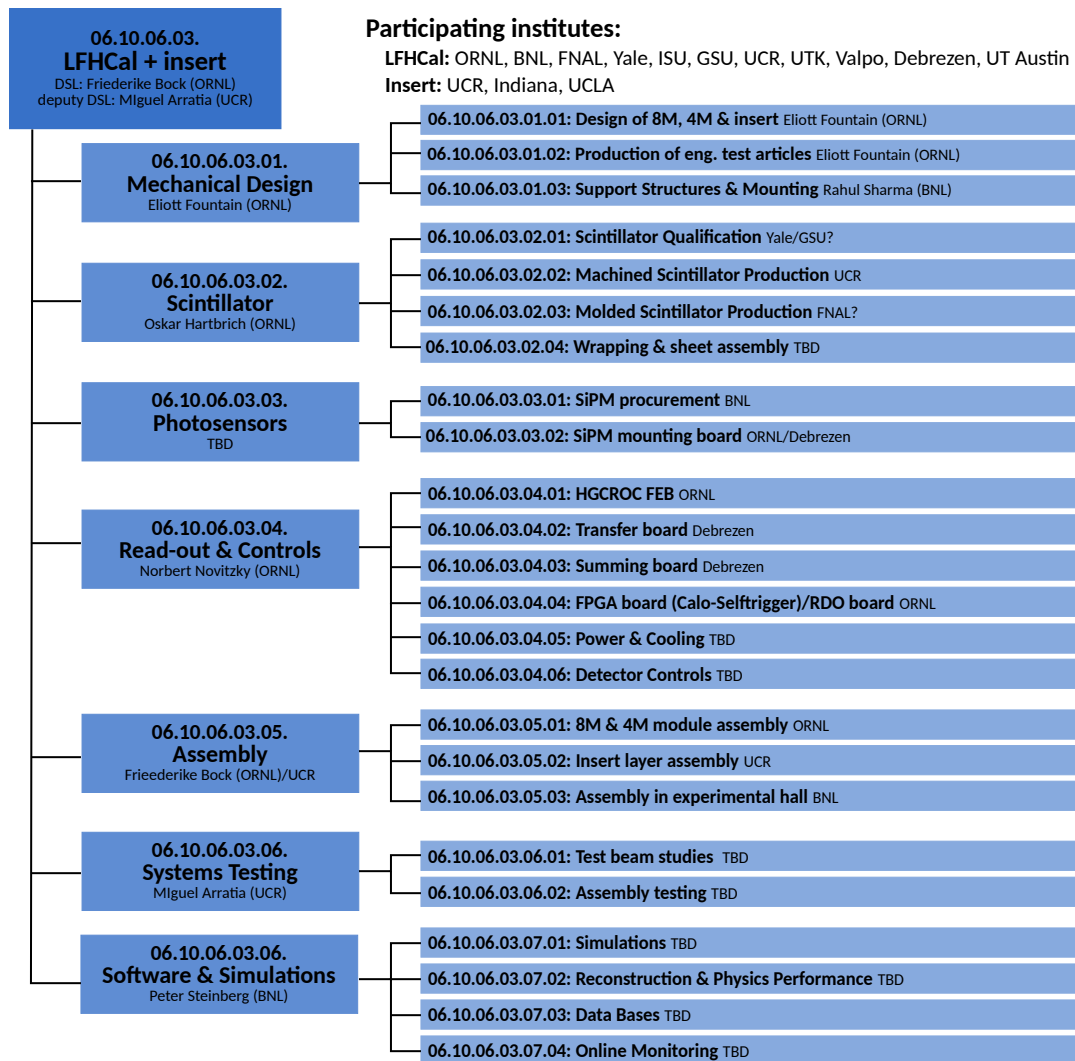


**Figure 8.206:** Organizatorial chart of the LFHCal & insert consortium, indicated by the numbers are the associated WBS structures.



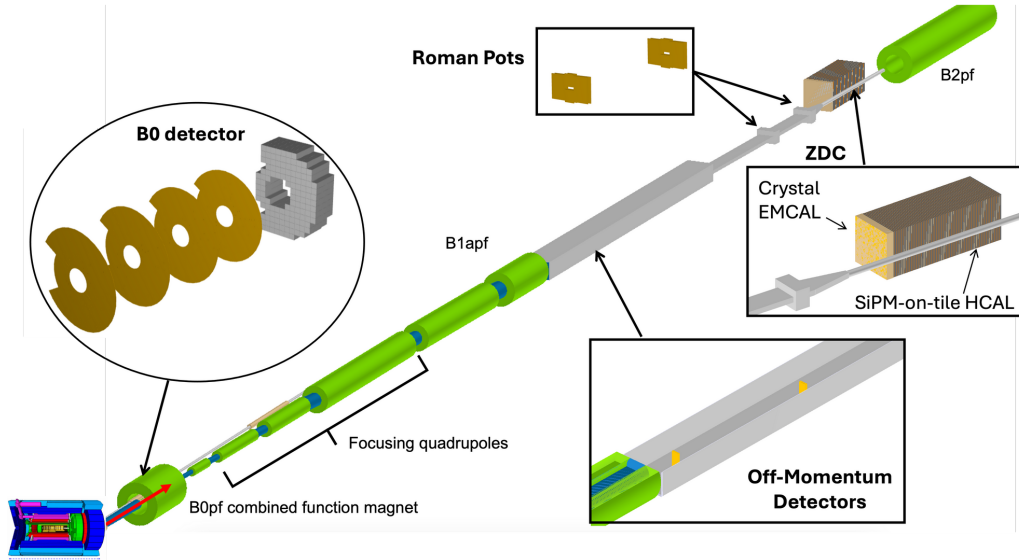


**Figure 8.207:** All four far-forward subsystems in the outgoing hadron beam direction. The green cylinders are accelerator dipole and quadrupole magnets.

### 8.3.7 Far-forward detectors

The ePIC far-forward detectors are required to enable essentially the entirety of the exclusive physics program at the EIC, where final-states involve protons, neutrons, photons, and various other particles at  $\eta > 4.5$ . There are four subsystems, all integrated with the outgoing hadron beamline between  $\sim 5.5$  and 39 meters from the interaction point. The far-forward subsystems are summarized in Fig. 8.207, and details are presented in subsequent subsections.

#### 8.3.7.1 The detectors in the B0 bending magnet

##### Requirements

**Requirements from physics:** The B0 magnet bore will contain two detectors: a charged particle tracker and an electromagnetic calorimeter. Both will have acceptance covering the angular region from 5.5 to 20 mrad. Given the mechanical constraints imposed by the detectors' location in the magnet (and respecting the beam lines themselves) the detectors will be highly asymmetric for angles greater than  $\sim 13$  mrad. To maximize acceptance it's required that there be minimal dead areas in the instrumentation especially for angles less than  $\sim 13$  mrad. The tracker should have momentum resolution up to 6% for protons, and timing precision sufficient to properly associate tracks with their vertex,  $\sim 35$  ps. The calorimeter should have a large dynamic range with sensitivity to both soft,  $O(100 \text{ MeV})$ , and hard,  $O(100 \text{ GeV})$ , photons. The energy resolution should be less than  $8\%/\sqrt{E} \oplus 4\%$ , with position resolution  $\lesssim 10 \text{ mm}$ . We note that for some analyses the calorimeter will function as a photon 'tagger' rather than an actual calorimeter, and so in some regions of acceptance (where the mechanical constraints are acute) this resolution may not be achieved but having the acceptance instrumented is still valuable to tag the event as containing a forward photon even with only imprecise knowledge of the photon's energy.

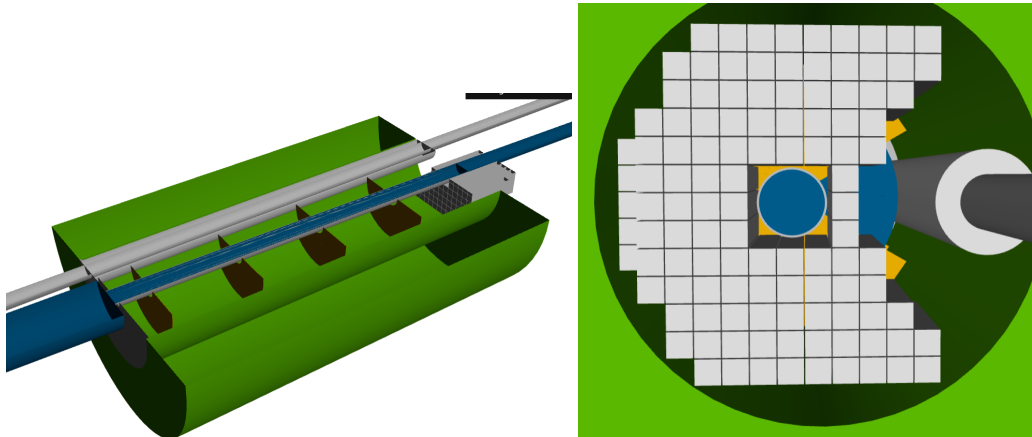


**Figure 8.208:** Left: A cutaway view of the detectors in the B0 magnet. The beam pipes are shown in blue and gray, the four tracking detectors are dark brown and the calorimeter is gray (the figure orientation is such that IP is to the left of the magnet). Right: The transverse profile of the calorimeter in the B0 magnet. Both figures are from the DD4HEP implementation of the detectors.

**Requirements from Radiation Hardness:** The expected non-ionizing radiation dose at a longitudinal distance of 692 cm from the interaction point (near the fourth tracking layer and the front of the calorimeter) is approximately  $3.1 \times 10^{11}$  1 MeV neutron equivalent per square centimeter for  $100 \text{ fb}^{-1}$ . At this location the ionizing dose can reach  $\sim 100 \text{ kRad}$ .

## Justification

**Device concept and technological choice:** The charged particle tracker will be composed of four layers instrumented with silicon. The layers are approximately equidistantly placed at distances between 590 and 690 cm from the interaction point, to enable measurement of the protons with resolution  $\lesssim 6\%$ . The electromagnetic calorimeter is composed of 112 scintillating  $\text{PbWO}_4$  crystals, each  $2 \times 2 \times 20 \text{ cm}^3$  (the long direction is on the z axis). We note that the crystals are the same as those used in the EEMCal as discussed in Section 8.3.5.1.

## Subsystem description:

General device description: Each tracking layer has a transverse layout to cover as much of the angular acceptance as possible given the mechanical constraints. The transverse geometry of each layer may be very roughly thought of as a ring with inner radius of 5 cm and outer radius of 15 cm, however there is a significant “cut-out” of the ring to accommodate the beam pipe as well as other deviations from the radial geometry due to mechanical constraints inside the magnet. The crystals of the calorimeter are arranged in a similar transverse geometry. A cutaway view of the detectors in the magnet as well the transverse profile (shown for the calorimeter) are illustrated in Figure 8.208.

Sensors: For the tracking detectors AC-coupled low-gain avalanche diodes (AC-LGADs) are chosen for their capability to provide both high-precision space and time information. To meet the momentum resolution performance requirements a spatial resolution of  $\sim 20 \mu\text{m}$ . To

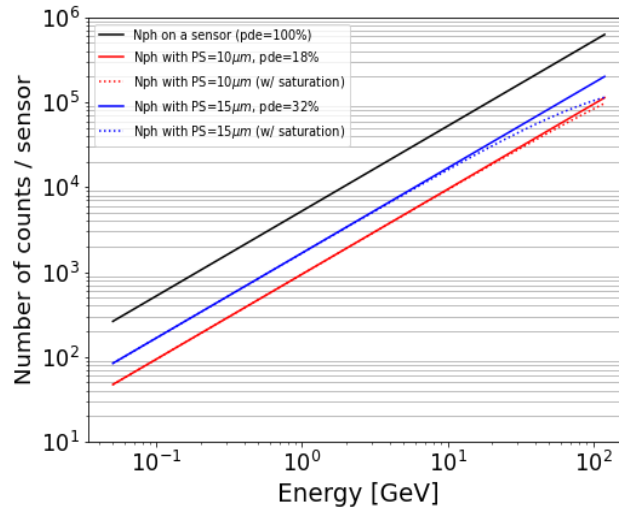


**Figure 8.209:** A simulation of the expected number of pixel hits for a  $6 \times 6 \text{ mm}^2$  SiPM coupled to a  $\text{PbWO}_4$  crystal as function of the energy of a photon impinging on the crystal. An ideal SiPM response is shown as well as the response of a  $10 \mu\text{m}$  pitch SiPM with 18% photo-detection efficiency and a  $15 \mu\text{m}$  pitch SiPM with 32% photo-detection efficiency (matching the specs of S14160-6010PS and S14160-6015PS). The realistic SiPM responses are shown with and without occupancy effects.

achieve this with the AC-LGADs charge sharing must be implemented in the reconstruction. We note that this technology is broadly in use within ePIC, and its particular implementation for the B0 detectors is very similar to the Roman Pots/Off Momentum Detectors and a more detailed description of the sensors may be found in Section 8.3.7.2. Assuming identical or similar staves as those used in the Roman Pots/Off Momentum Detectors, each tracking layer will be composed of approximately 30 staves with 4 modules per staff. The tiling scheme has not yet been fixed.

For the calorimeter the  $\text{PbWO}_4$  crystals produce light peaking at  $\sim 420 \text{ nm}$ , which will be read out by SiPMs. Unlike most scintillating crystal calorimeters the light will be read out from the front face of the crystal. Either four  $6 \times 6 \text{ mm}^2$  SiPMs or sixteen  $3 \times 3 \text{ mm}^2$  SiPMs will be used per crystal. The sensors will be a mixture of  $15 \mu\text{m}$  pitch and  $10 \mu\text{m}$  pitch SiPMs (likely Hamamatsu S14160-6015PS and S14160-6010PS or S14160-3015PS and S14160-3010PS), in a ratio of 3:1. Compared to the higher pitch SiPMs the larger pitch SiPMs have higher efficiency but fewer pixels, and are thus more prone to non-linearity due to occupancy as shown in Figure 8.209. Given this the smaller pitch SiPMs are appropriate for smaller signals, whereas the smaller pitch SiPM will be utilized for the higher energy particle signals. Using them together provides energy resolution in line with the requirements (as shown in Figure 8.213 below).

**FEE:** Following the Roman Pots/Off Momentum Detectors, the ASICs will be readout using lpGBT in-place of FPGAs due to the high-radiation environment in which these detector will be located. AC-LGAD + ASIC modules will be connected to the lpGBT, which will be coupled to a VTRX+ to convert the signals to a fiber to send off to the DAW system. The electronics to process the SiPM signal are still to be worked out but expected to follow closely the scheme of the EEMCal.

**Other components:** For both detectors the front-end board, power distribution, and cabling schemes are all still in development.

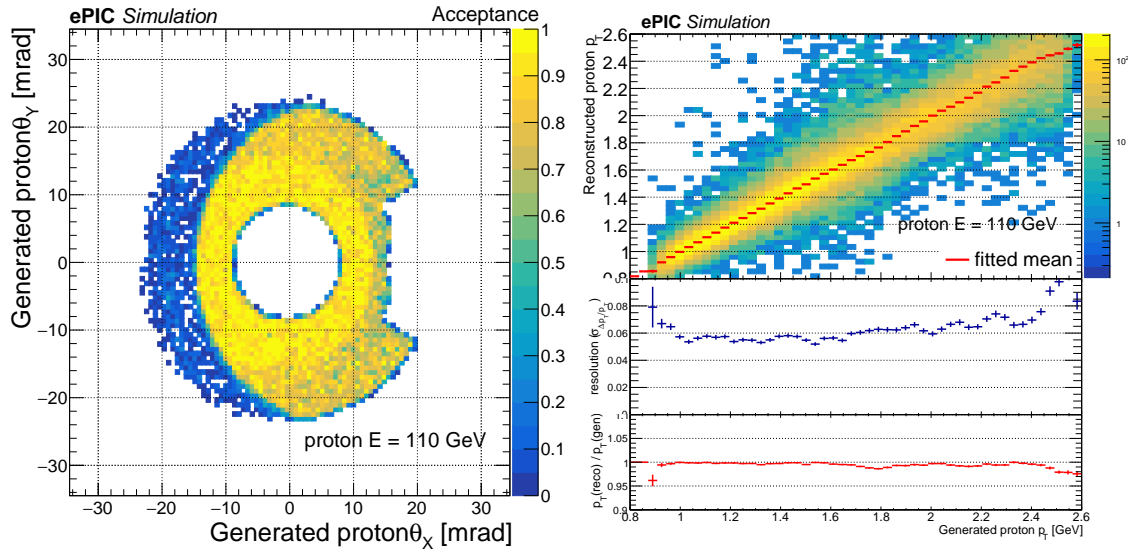


**Figure 8.210:** Left: The B0 tracker’s acceptance of protons ( $E=110$  GeV), as a function of  $\theta_x$  and  $\theta_y$ . Right: The top panel shows the reconstructed vs generated proton  $p_T$ . Each slice of this distribution is fit to a Gaussian function and from this fit a resolution (middle panel) and bias (bottom panel) are extracted.

**Performance** The key physics task of the B0 tracker system is the measurement of protons, and this is summarized by the acceptance and transverse momentum resolution shown in Figure 8.210. We note that the precise longitudinal position and transverse acceptance of each layer is not finalized, and so the figure should be considered a tentative performance estimate. To contextualize the B0 tracker’s proton measurements in the larger ePIC context, Figure 8.211 shows the acceptance for forward protons as a function of pseudo-rapidity in the central tracker, B0 tracker, and Roman Pots. The B0 calorimeter’s acceptance for photons is shown in Figure 8.212. The calorimeter seeks to measure photons over a very large range. The performance of the detector, in particular the energy resolution, is shown separately for low and high energy photons in Figure 8.213. The higher energy photons are evaluated based on a signal to a single  $6 \times 6$  mm<sup>2</sup> SiPM with 10  $\mu$ m pitch, whereas the lower energy photon performance assumes readout of the light using three  $6 \times 6$  mm<sup>2</sup> SiPMs with 15  $\mu$ m pitch.

## Implementation

**Services:** For the trackers low voltage ( $\sim 3$ V) and high voltage ( $\sim 150$ V) supplies for the operation of the ASICs and the bias supply, as well as slow controls for the voltages and the DAQ system. We assume The SiPM for the calorimeter need a bias of ( $\sim 5$ V). The cooling system is still to be worked out, but is expected to be air based (unlike the in-vacuum challenge of similar instrumentation for the Roman Pot/Off Momentum Detectors). Temperature stability

**Subsystem mechanics and integration:** The integration of the detectors into the B0 magnet bore is a significant undertaking. The space for the detectors (and services) is quite limited and the installation procedure introduces more constraints. After the vacuum valve is closed there is only about 10 cm of clearance in front of the magnet and this precludes installation of the 20

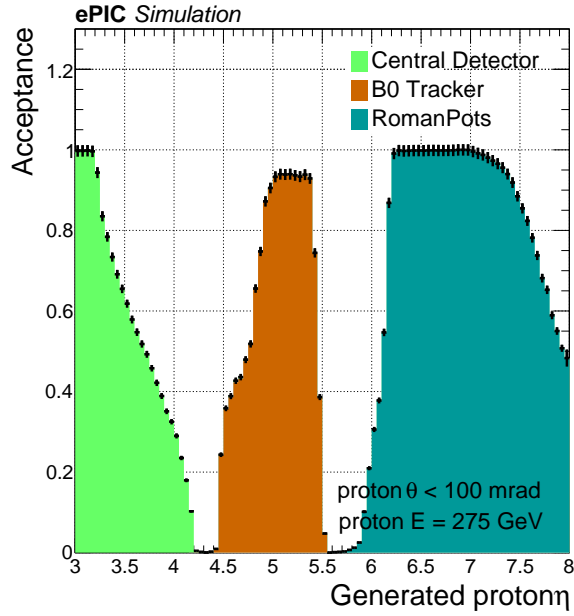


**Figure 8.211:** Proton acceptance as a function of  $\eta$  spanning the central tracker, B0 tracker, and Roman Pots.

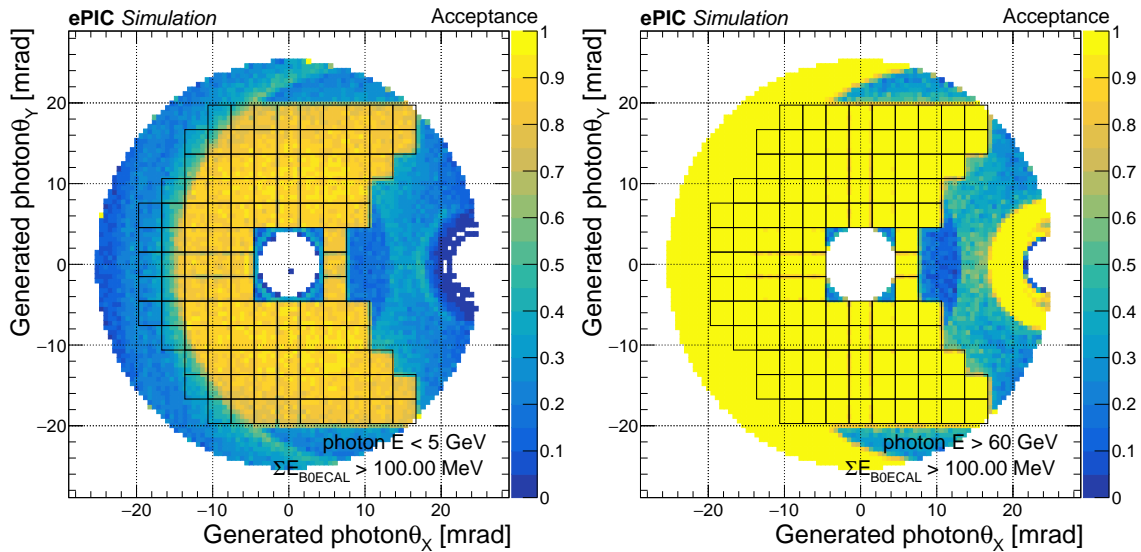


**Figure 8.212:** The B0 EM calorimeter's acceptance of photons shown for soft (less than 5 GeV) and hard (greater than 60 GeV) photons. Acceptance is defined as more than 100 MeV deposited in the calorimeter. The position of the calorimeter crystals is indicated as a grid. The un-instrumented regions which nevertheless high nominal acceptance, correspond to upstream interactions whose shower products are visible in the B0 calorimeter.

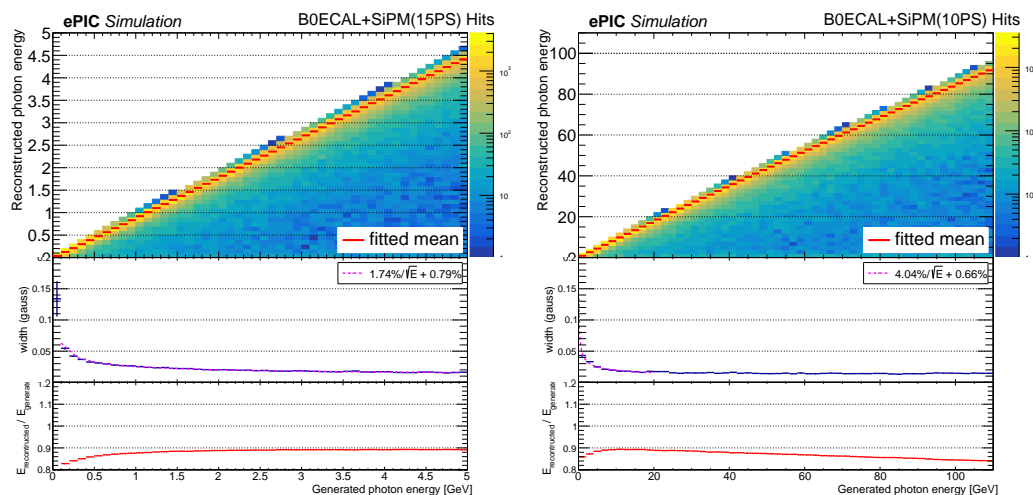


**Figure 8.213:** The energy reconstructed and associated resolution for the B0 EM calorimeter of photons with  $\theta < 13$  mrad in the soft (left) and hard (right) energy reconstruction regimes. The top panels show the reconstructed photon energy vs the generated energy. Each slice of this distribution is fit to a Gaussian function and from this fit a resolution (middle panels) and energy scale shift (bottom panels) are extracted.

cm crystals. To address this difficulty, the crystals -themselves less radiation delicate than other components - will be installed prior to the valve closing and the beam commissioning. At this point *only* the crystals will be installed to avoid the risk of damaging other components during the commissioning. The crystals themselves are Following this, the SiPMs and electronics of the calorimeter will be installed. Both installations, as well as the final positioning of the detectors, will be via a rail system: detector components will be loaded onto the rails system outside the magnet and inserted in to it. We note that each tracking layer and the calorimeter is composed of multiple components installed individually.

**Calibration, alignment and monitoring:** During operation an in-situ calibration based on pions and/or rho mesons will be employed. The calorimeter will utilize LED signals shined onto the crystals and a thermistor, both integrated into the front end board, for monitoring.

#### Status and remaining design effort:

R&D effort: There is still work to be done for full detector operation. For the trackers especially, demonstrating effective reconstruction using charge sharing and for the calorimeter the multi-SiPM readout. For both the trackers and calorimeter this includes optimizing the acceptance in concert with the installation procedure.

E&D status and outlook: Engineering design is still very preliminary, but necessary design choices are being evaluated as engineering support becomes available. A full thermal and mechanical study is still needed for both detectors.

Other activity needed for the design completion: Completion of the mechanical rail system and an installation procedure is underway. For both the tracker and the calorimeter the front

end electronics are still being finalized (with as much overlap as possible with other subsystems).

Status of maturity of the subsystem: Both detectors in the subsystem have (intentionally) large overlap with other subsystems and the maturity of the B0 detectors thus follow to a large extent this common development. There are, of course, particulars of the implementation for the B0 detectors and these are progressing in line with the shared development.

**Environmental, Safety and Health (ES&H) aspects and Quality Assessment (QA planning):** The detectors placement inside the magnet bore as well as the staged installation procedure will require somewhat special considerations for integration with the accelerator complex. All the detector component and services must be coordinated with the magnet.

**Construction and assembly planning:** The tracking system should benefit from the local BNL expertise, production capabilities for AC-LGAD, and from there ‘directly’ to installation readiness. The calorimeter sub-components may be prepared either on or off site, but in any case the final assembly can not be separated from the installation procedure.

**Collaborators and their role, resources and workforce:** The Israeli ePIC consortium, in particular BGU and TAU, are playing the main role in the detector development and this will continue through installation and operation. Both the BGU and TAU groups have one PI, several graduate students and postdocs expected to contribute. Local resources in both groups allow in lab testing but not significant fabrication capabilities. There is also very significant participation from BNL generally and especially for the common AC-LGAD instrumentation.

**Risks and mitigation strategy:** For the trackers the largest risk is the necessity to utilize charge sharing in the reconstruction to obtain the needed momentum resolution. Other detection technologies have been considered to mitigate this risk (with smaller pixels) but to this point none have been identified as an appropriate alternative. For both detectors, and even more acutely for the calorimeter, the installation challenge risks limiting the detector acceptance.

### 8.3.7.2 The roman pots and the off-momentum detectors

#### Requirements

**Requirements from physics:** The Roman pots (RP) and off-momentum detector (OMD) subsystems are both intended to tag far-forward protons and reconstruct their momenta. These detectors are based on the same technology and are implemented in a very similar way, so throughout this subsection they will often not be differentiated unless an aspect of the discussion is specific to one of the two subsystems.

Measurement of protons with scattering at angles  $< 5$  mrad requires tracking detectors integrated directly into the outgoing hadron beamline. In previous and current experiments, silicon detectors meeting these basic criteria have been implemented in the form of Roman pots (RP) subsystems, and the EIC will take a similar approach. However, since the EIC will also aim to tag and reconstruct protons which arise from the breakup of light nuclei (deuterons, helium-3, etc.), another



set of silicon detectors which are optimally placed for capturing these protons is required. These off-momentum detectors (OMD) enable tagging and reconstruction of spectator protons whose momentum is significantly smaller than that of the hadron beam itself. We classify the various far-forward protons based on their magnetic rigidity, which determines their trajectories through the seven magnets (four dipoles for bending/steering; three quadrupoles for focusing) between the interaction point and the drift region where the RP and OMD systems are located. For the sake of simplicity, the ratio of the longitudinal momentum of the proton with the total momentum of the beam itself is used to determine if the proton is within the RP or OMD fiducial acceptance, and defined as  $x_L = p_{z,proton} / p_{beam}$ . As an example, a proton from the breakup of a deuteron has an  $x_L \sim 50\%$ , on average. The RP acceptance is for  $x_L > 65\%$ , while the OMD covers a region between  $25\% \lesssim x_L \lesssim 65\%$ , with the lower bound being determined heavily by the scattering angles in question, since low- $x_L$  particles will not follow the design beam orbit and will often be lost in the magnets before reaching the OMD. The RP and OMD are placed to have a small overlap in  $x_L$  to aid in alignment of the detectors, and calibration of the matrices used to reconstruct the particle's momentum. Figure 8.214 shows an illustration of the proton envelopes relevant for the RP and OMD placement.

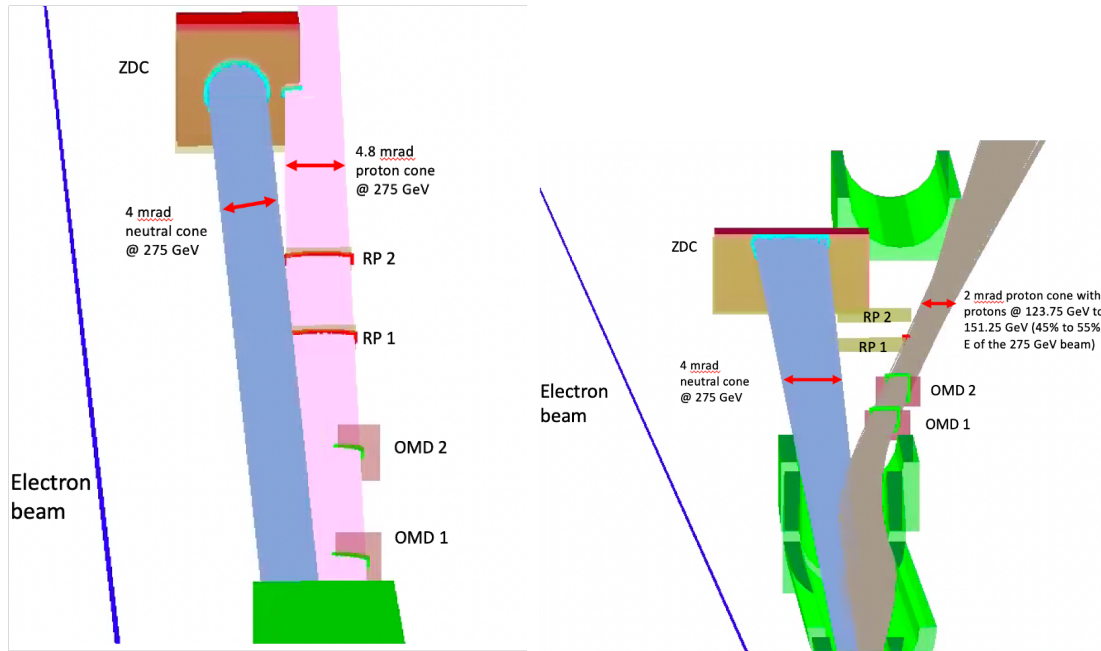


**Figure 8.214:** Depiction of the envelopes from protons with  $x_L \sim 1.0$  (left) and with  $x_L \sim 0.5$  (right). The RP and OMD systems are placed to obtain an almost-continuous acceptance of protons across a broad range of proton rigidities.

A particular challenge for the Roman pots (true for any Roman pots detector) is achieving acceptance down to 0 mrad (or,  $x_L = 1.0$ ). This is impossible due to the presence of the hadron beam itself, so the low- $\theta$  (low- $p_T$ ) acceptance is essentially entirely driven by the focusing quadrupoles (driven by the choice of machine optics) before and after the interaction point. If the RP sensor planes approach too close to the core of the beam, they would see an extremely high particle incidence and be rapidly damaged (the beam itself would also not be able to operate with the detectors that close to the beam core).

For IP-6, the choice of low- $\beta^*$  optics to maximize luminosity (so-called “high divergence”) means

the transverse beam size,  $\sigma_{x,y} \approx \sqrt{\beta_{x,y}(z_{RP}) \times \epsilon_{x,y}}$ , where  $\beta_{x,y}(z_{RP})$  are the beta-functions in (x,y) at the Roman pots location and  $\epsilon_{x,y}$  is the emittance for the machine, is larger, providing maximal luminosity at the expense of low  $p_T$  acceptance at the Roman pots. Generally,  $10\sigma_{x,y}$  is the average “safe distance” for the Roman pots to operate and is used as the assumed “nominal” position for data-taking, although this distance is adjusted based on operation beam conditions, in reality. For reference, at the top hadron beam energy, these translate to  $10\sigma_x = 1.6$  cm and  $10\sigma_y = 0.27$  cm. Conversely, a choice can be made to reduce luminosity to improve low- $\theta$  (low- $p_T$ ) acceptance at the Roman pots location, normally referred to as “high acceptance” optics. Given this set of operational parameters for the machine itself, it is required that the sensor packages have minimal dead area at the edges to take maximum advantage of the machine optics during data taking runs.

It should be noted that the OMD don’t suffer from the same trade-off between luminosity and acceptance, because they are centered on the location for a  $x_L = 0.5$  proton with a 0 mrad scattering angle, which places them at more than  $20\sigma$  from the core of the beam. This means that off-momentum protons can be tagged at 0 mrad (or,  $p_T = 0.0$  GeV/c), allowing for tagged-DIS measurements to be carried out to arbitrarily low- $p_T$ .

For momentum resolution, the detectors must deliver  $p_T$ -resolution better than 10% for  $p_T \sim 1$  GeV/c. These requirements are detailed on the EIC Wiki page [128], along with numerous links to supporting studies done for ePIC.

**Requirements from Radiation Hardness:** Maximal radiation doses for the RP and OMD are shown to be  $< 10^8$  cm<sup>-2</sup> 1 MeV neutron equivalent for NIEL fluence per fb<sup>-1</sup> of integrated luminosity, while total ionizing doses are  $\sim 10 - 100$  Rads for the same integrated luminosity, for a combination of minimum-bias and hadron beam+gas events. It should be noted that these numbers do not include estimates from the hadron beam halo, as no simulations are yet available to study the impact of this source of background. These doses and fluences are far below the operating limits of the AC-LGADs, but these doses and rates will need to be assessed further with simulations that can approximate the beam halo.

**Requirements from Data Rates:** Rates during normal operations, with expected vacuum of  $10^{-9}$  mbar, are a few Hz/channel. However, the beam halo could potentially provide rates of 30-50kHz at  $\sim 10\sigma$  from experience of Roman pots at STAR. While the EIC hadron beam will have many differences to the RHIC hadron beam, it’s hard to estimate the full rate impact of the beam halo without an appropriate simulation. This is something to be done in the coming year as the machine develops.

## Justification

**Device concept and technological choice:** The basic concept of Roman pots detectors for measuring protons near the beam is not new and has been employed at HERA, RHIC, and the LHC, among other collider facilities. In the case of the EIC, the Roman pots (and OMD) need to be able to make measurements with challenges different to those in previous facilities. Studies from the EIC generic R&D program [129], in particular eRD24, demonstrated that the RP detectors need to have both high spatial ( $\sim 140\mu\text{m}$ ) and timing ( $\sim 35\text{ps}$ ) resolutions, a challenge to deliver with one sub-system. In previous studies, the beam effects (e.g. angular divergence, beam-momentum spread, vertex smearing from crab cavity rotation) were shown to be the dominant source of smearing for momentum reconstruction. The spatial resolution requirement for the RP and OMD is chosen such

that when the effects are separated and added in quadrature, the smearing coming from the detector spatial resolution is subdominant. It should also be noted that there are various different optical configurations for the machine, as noted above, and as the smearing components driven by the beam are decreased, the detector-driven portion becomes dominant and can be a limiting factor for momentum reconstruction. This is something unique to the beamline detectors, where normally negligible beam smearing effects become a major factor impacting momentum reconstruction. Finally, the B0 tracking system has the most-stringent requirement for spatial resolution to meet the physics requirements, and the RP and OMD need to use the same sensor as the B0 to ensure efficient cost savings and the ability to use the same ASIC for reading out the sensor.

The silicon detector technology which meets our requirements is the AC-coupled low-gain avalanche diode (AC-LGAD), an evolved version of the DC-coupled Low Gain Avalanche Diode (DC-LGAD) sensor, normally used for high-resolution timing detectors. The AC-LGADs allow for finepixilization and can meet the requirements of the RP and OMD subsystems, as was the goal of eRD24.

An additional challenge with operation of the RP and OMD systems is the usage of these detectors in vacuum. The subsystems themselves are large enough to prohibit use of the conventional “pot” vessels used to protect the detectors in other colliders, and therefore necessitate the inclusion of the sensor planes directly into the machine vacuum, providing unique challenges for cooling and shielding.

#### Subsystem description:

General device description: The Roman pots and off-momentum detectors are both vacuum-based silicon sensors arranged into two stations for fully reconstructing protons at various magnetic rigidities, where rigidity here refers to the fraction of the momentum the proton has with respect to the steering dipoles design orbit momentum.

Sensors: AC-LGADs are the technology of choice for these two subsystems due to their capability to provide both high-precision space and time information [59]. These sensors were originally introduced into the EIC efforts with an expected application to beamline detectors.

FEE: ASICs will be readout using low-power gigabit transceivers (lpGBTs) in-place of FPGAs due to the high-radiation environment in which these detectors will be located (as stated above, the radiation doses calculated are based collision rates, not on the beam halo and other backgrounds which are not yet simulated). Up to sixteen AC-LGAD + ASIC modules will be connected to a single lpGBT, which will be coupled to a VTRX+ to convert the signals to a fiber to send off to the data acquisition system. The stave design is aimed to have a minimal amount of components inside the vacuum to ensure smooth operations and ease of access during maintenance periods.

Other components: Design of the front-end board and power distribution is still in a very early stage for the RP and OMD systems. The current plan is to reuse as much of the design for the forward time-of-flight as is possible to reduce costs.

**Performance** The performance of the Roman pots and Off-Momentum Detectors is summarized in Fig. 8.215. The overall momentum resolution is also affected by the detailed understanding of the hadron magnet lattice, which is used to be able extract the normal transfer matrices used to reconstruct momenta in Roman pots detectors. There is also a software solution in place using deep neural networks to further improve the momentum resolution performance, especially for

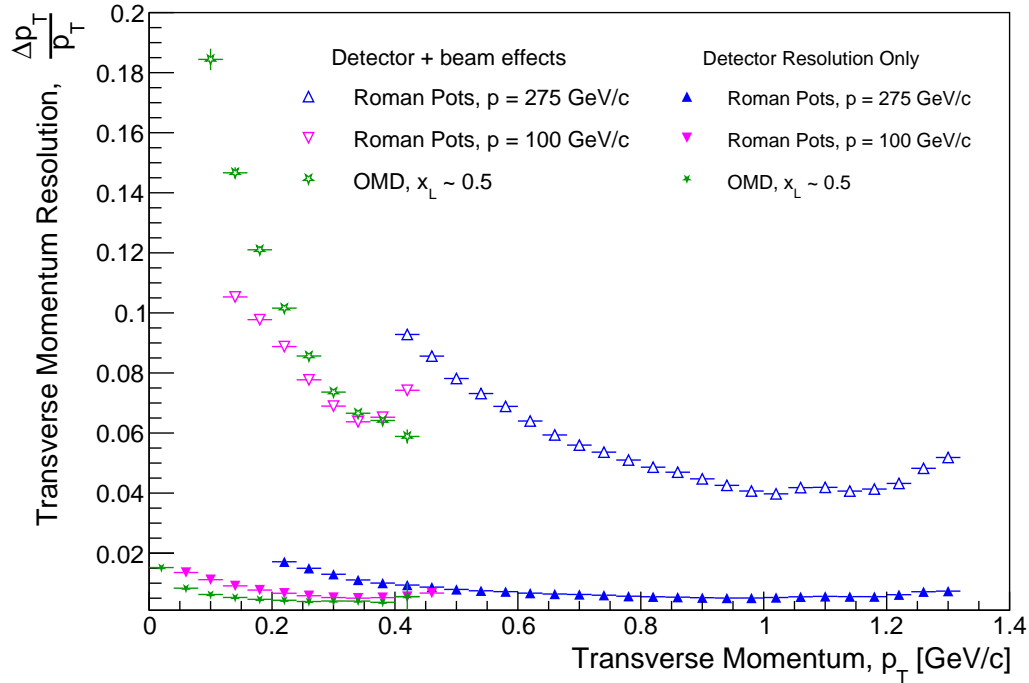


**Figure 8.215:** Summary of transverse momentum resolutions for the Roman pots and off-momentum detectors using stand-alone detector simulations. Contributions are separated by those induced by intrinsic detector choices (e.g. pixel sizes) and those from beam effects (e.g. angular divergence), which have an outsized impact on momentum measurements at very-forward rapidity.

the off-momentum detectors. This solution is presently being integrated into the ePIC software framework.

**Implementation** The basic detector component will be a “stave” which contains 3 “modules” consisting of bump-bonded AC-LGADs and ASICs attached to a PCB, arranged in a 1x3 layout with modules on either side of the PCB to enable partial transverse overlap of the sensors to cover the dead area at the edges (e.g. guard ring location). The staves only contain the sensors and ASICs, plus cooling services, with all other services coming from a readout board placed outside the vacuum which contains the lpGBT and VTRX+ components and power distribution. The details of this concept still need to be properly worked out with engineering support, but strawman versions of these concepts can be found in Figs. 8.217 and 8.218. A full layout of the sensors in the 1x3 stave configuration is shown in Fig. 8.219, while the DD4HEP implementation for the “high acceptance” optics configurations for the three proton beam energies is shown in Fig. 8.220. The RP and OMD subsystems will both be immersed directly into the machine vacuum to maximize acceptance and minimize impact to the machine. This technically makes the name Roman pots incorrect to describe these detectors, since they are literally potless tracking systems operating in vacuum.

The OMD system will be much simpler than what is needed for the Roman pots, with the staves

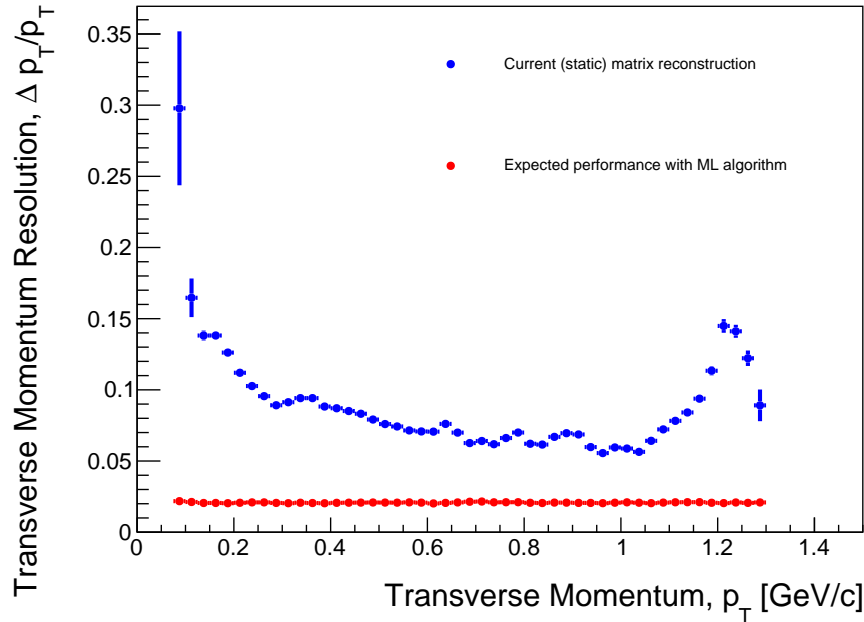


**Figure 8.216:** Transverse momentum resolution for Roman pots using the full ePIC simulation framework. This plot is from the ePIC framework, where Fig. 8.215 shows performance from standalone simulations which include beam effects and optimized matrix reconstruction, shows both the nominal performance with the current reconstruction algorithm (in blue), and (in red) the expected improvement from the machine learning model which has been developed and tested in standalone simulations. This ML algorithm (based on deep neural networks) is currently being implemented in ePIC. A presentation on this work and the resulting performance of the model was presented at the Deep-Inelastic Scattering conference in 2023 [4]. Work is underway to integrate this model into the ePIC framework for RP and OMD reconstruction.

7451 arranged into a rectangle with the dimensions 10cm x 20cm and inserted horizontally into the  
 7452 vacuum of the beamline.

7453 **Services:** The Roman pots and OMD have the same essential needs for services, which include  
 7454 cooling using conductive strips coupled to an external chiller to allow cooling in-vacuum, low volt-  
 7455 age ( $\sim 3V$ ) and high voltage ( $\sim 150V$ ) supplies for the operation of the ASICs and the HV bias supply  
 7456 for the sensor, and slow controls to control both voltages and the DAQ system, and also to control  
 7457 the moving stages necessary for the detector operations. There will also need to be communication  
 7458 between the slow controls and the machine for safety interlocks for fast beam abort systems, and  
 7459 for permits to enable motion control of the detectors when beam conditions are stabilized.

7460 **Subsystem mechanics and integration:** The primary support systems only need to be able to  
 7461 support very light staves with 3-4 modules per PCB. However, the entire subsystem needs to be  
 7462 on a motor-driven rail system to enable movement near the hadron beam, especially in order to  
 7463 achieve acceptance at very low  $p_T \sim 0.2$  GeV/c.

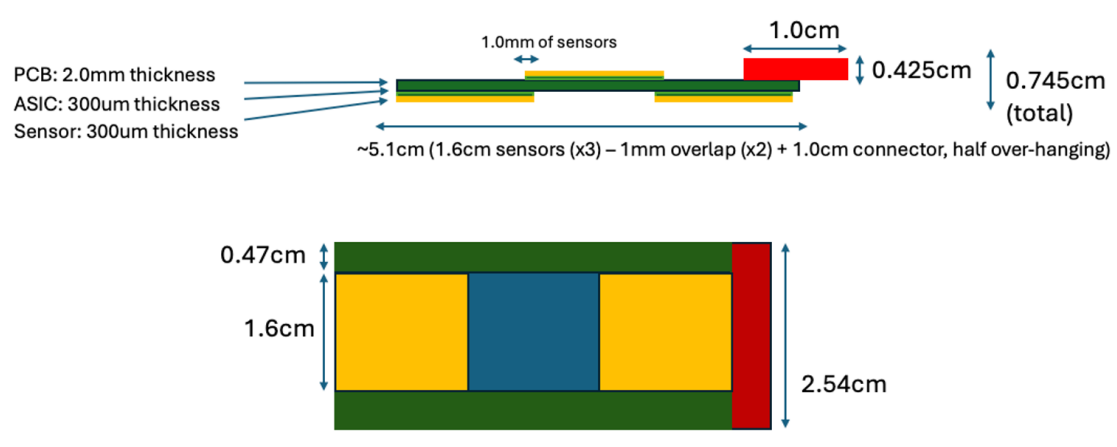


**Figure 8.217:** Strawman concept for the layout of the RP and OMD sensor staves. Work is ongoing to get the necessary electronics engineering support to design the final PCB. The connector on the end of the PCB is presently assumed to be a TE connectivity Erni 354096-E 32 pin serial connector. Work is still needed to understand how to apply thermal cooling to the staves without using compressed gases or liquids (not allowed in the primary machine vacuum). Presently, cooling plates/heat sinks which are thermally coupled to outside the vacuum and cooled with an LN2 chiller are assumed, but only preliminary thermal analysis has been carried out.

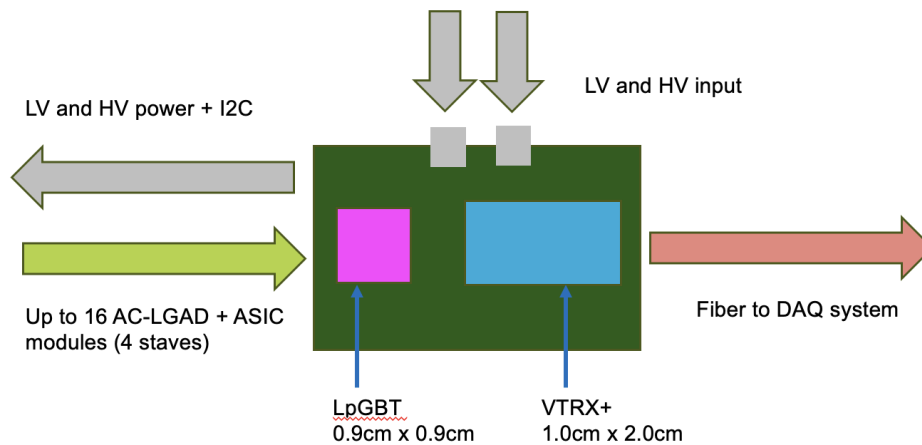


**Figure 8.218:** Strawman concept a readout board concept to communicate with and readout RP and OMD sensor staves. Work needs to be done to solve the issue of power distribution, and to ensure the EICROC ASIC can indeed be readout by the lpGBT.

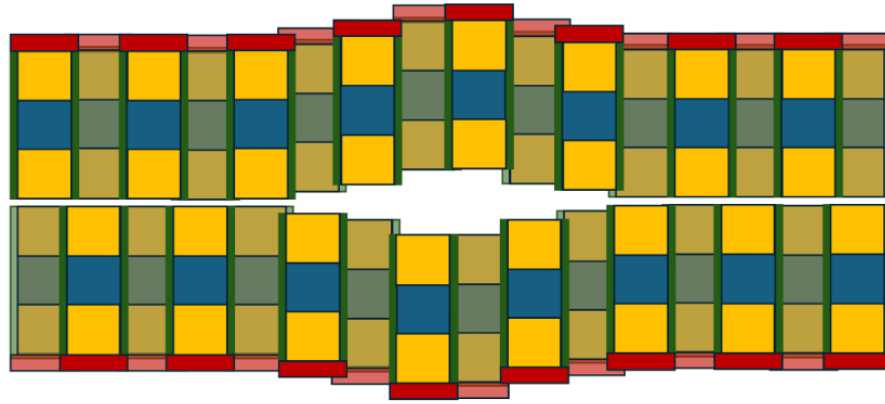


**Figure 8.219:** Current layout of a single RP layer using a 1x3 stave configuration, with the staves following the concept shown in Fig. 8.217. This configuration leads to a full detector layer with dimensions  $\sim 26\text{cm} \times 10\text{cm}$ , with some work to be done to finalize the exact amount of overlap between individual staves to provide uniform acceptance in the transverse plane.

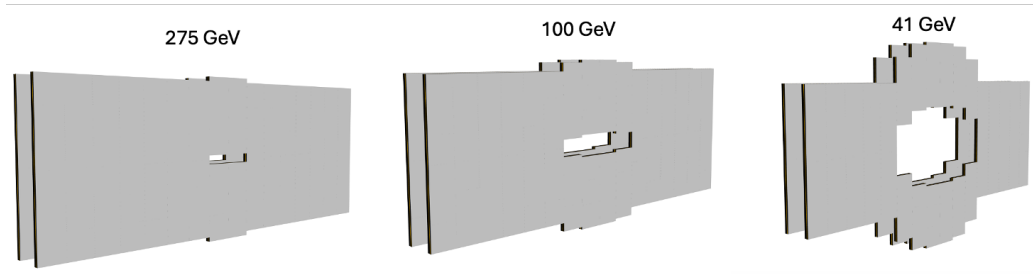


**Figure 8.220:** Depiction of the location of the RP sensor packages for the three different “main” EIC hadron beam energies, all in the optics configuration with the maximal low- $p_T$  acceptance. Optimization of the stave layout and movement stages is still underway to ensure best fiducial acceptance.

7464 **Calibration, alignment and monitoring:** AC-LGAD sensors will be calibrated with MIPs,  
 7465 while alignment of the detector systems will need to be carried out using beam-based alignment  
 7466 with dedicated, short, very-low luminosity runs, which enable the detectors to approach the beam  
 7467 much closer than the standard  $10\sigma$  distance such that the beam halo itself can be seen on the sensor  
 7468 planes. This, combined with conventional survey information used to align the motion system to  
 7469 the machine should enable alignment at a level much less than 1mm, where 1mm is the minimum  
 7470 precision required to avoid introducing additional smearing effects competitive with those from  
 7471 other sources.

#### 7472 **Status and remaining design effort:**

7473 R&D effort: Much work is still needed to demonstrate full system operations with full size  
 7474 sensors + ASICs, and the cooling concept using conductive strips. As of now, only 4x4 chan-  
 7475 nel versions exist and have been tested, but 32x32 channel versions of the ASICs necessary  
 7476 to perform tests of AC-LGADs with the same channel count are expected in Fall 2025. These



versions will not have the fully optimized digital backend or power consumption, but will still enable most of the tests needed for necessary design maturity, and will allow for close to final design of the carrier PCB for the sensor modules to be completed.

E&D status and outlook: Engineering design is still very preliminary, but necessary design choices are being evaluated as engineering support becomes available. This is especially needed for the stave design to carry the sensor modules, and for the support substructure and cooling for both subsystems.

Other activity needed for the design completion: The design of the front-end PCB which carries the sensors, ASICs, and necessary services needs to be carried out. Presently, only a strawman concept which will meet our requirements exists.

Status of maturity of the subsystem: The design of the RP and OMD subsystems are aimed for 60% design maturity by end of calendar year 2025. The main components which need to be developed to realize that timeline are the PCB design for the stave, a cooling solution for the staves, and more-advanced design of the vacuum system and support structure for the two subsystems. The first two items are already in-progress, while the final item is in-progress, but still needs several iterations, as it does not concern just the RP and OMD subsystems, but also the HSR machine design in that region 30 meters from the IP.

**Environmental, Safety and Health (ES&H) aspects and Quality Assessment (QA) planning:** Since these detectors are embedded directly into the machine vacuum, special considerations must be made for integration with the machine. We expect that the detectors will be interlocked against operation until permits are received from the machine, pending stable operations of the machine in terms of stable beam losses, collisions at the IP, and background conditions. The cooling system will also have to be integrated with the machine envelope, which requires coordination with the machine group.

**Construction and assembly planning:** AC-LGAD sensors and EICROC ASICs will be manufactured in different foundries, but bump-bonding of the sensors + ASICs can be done for the far-forward subsystems at BNL, since these detector subsystems are very small compared to other ePIC subsystems. The assembly will have to take place in stages which include the following steps. First, preparation of stave PCBs will be carried out, which will include the production of the bump-bonded sensor + ASIC assemblies, adhesion of these modules to the PCB, and the wire-bonding of the ASICs to the pads on the PCBs. Each stave will then need to be integrated into the support structure for the RP and OMD detector layers, and tested. These final modules would then be installed into the respective motor-driven insertion systems for usage. It should be noted that these detectors will not be installed on “day one” since the machine will need to be commissioned and stabilized before detectors approaching so close to the beam can be installed and tested safely.

**Collaborators and their role, resources and workforce:** BNL and JLAB will take the primary role in constructing the Roman pots and off-momentum detectors, with engineering support for cooling design supplied by IJCLab in France. The RP and OMD subsystems will leverage the work on AC-LGAD development which originated from efforts to apply this technology to these detectors (EIC generic R&D project 24), and have grown to include applications to time-of-flight subsystems and generic particle tracking in ePIC. The larger AC-LGAD effort covers several subsystems, and includes work from collaborators from Los Alamos National Laboratory, Hiroshima University, Rice University, the University of Illinois at Chicago, Lawrence Berkeley National Laboratory, and the University of California at Santa Cruz. While these groups will not participate

in the construction of the RP and OMD subsystems, they are instrumental the overall AC-LGAD efforts. The work on the EICROC ASIC development is lead by OMEGA and IJCLab in France, and testing is done by all institutions listed.

**Risks and mitigation strategy:** The primary risks to the successful construction of the Roman pots and OMD are late receipt of the final 32x32 channel EICROC ASICs and issues with the bump-bonding and construction of the final staves. These risks are fairly minor given the large interest in successful implementation of AC-LGADs in ePIC, and given the small size of the RP and OMD subsystems. Much of the contruction work can take place with a small laboratory space at BNL. There are additional risks related to machine integration, which are hard to fully quantify at the present moment, but will be better understood in the coming year (e.g. operating and cooling the detector in the machine vacuum). These risks are all under evaluation and work is being done to develop studies to identify solutions to outstanding problems.

**Additional Material** Extra details, including links to numerous studies on aspects of the far-forward detectors can be found on the ePIC Wiki page [128] for the far-forward detectors. This material is being migrated to the ePIC Zenodo page.

### 8.3.7.3 The Zero Degree Calorimeter

#### Requirements

**Requirements from physics:** The ZDC must achieve energy and polar-angle resolutions for neutron showers better than  $50\%/\sqrt{E}$  and  $3\text{ mrad}/\sqrt{E}$  as specified in the Yellow Report [130]. For electromagnetic showers, it must achieve  $20\%/\sqrt{E}$  resolution [131,132]. The ZDC also needs to tag photons in the  $\mathcal{O}(10\text{--}100\text{ MeV})$  range in  $eA$  collisions.

These requirements originate from the extensive physics program enabled by the ZDC in  $ep$ ,  $ed$ ,  $eH^3$  and  $eA$  collisions that need measurements of neutral particles such as neutrons, photons, neutral pions, neutral lambda baryons, and other neutral mesons and baryons at near-zero polar angle with respect to the hadron beam. Table 8.67 summarizes the reactions that yield these signatures; they are briefly discussed below.

Reactions in  $ep$  collisions that produce signals in the ZDC include various channels. The highest cross sections are for inclusive processes involving leading neutrons (e.g.,  $ep \rightarrow eXn$ ), which were measured at HERA to be about 10% of all DIS events [133]. Leading neutrons can originate either from scattering off the pion cloud (the Sullivan process) or from regular beam fragmentation in DIS, which serves as a background to the Sullivan process that probes pion structure.

In contrast, inclusive Lambda production ( $ep \rightarrow eX\Lambda^0$ ), predicted to have a cross section about five times smaller than that of leading neutrons, can probe the kaon cloud and enable measurements of kaon structure, although target fragmentation in DIS also contributes to the inclusive reaction. The Lambda channel was not measured at HERA.

Channels with lower cross sections include exclusive processes such as deeply exclusive meson production (DEMP), e.g.,  $ep \rightarrow e\pi^+n$  and  $ep \rightarrow eK^+\Lambda(n\pi^0)$ ; backward  $u$ -channel DEMP (e.g.,  $ep \rightarrow e\pi^0p$ ); and DVCS ( $ep \rightarrow e\gamma p$ ) [131,132].

**Table 8.67:** Examples of reactions that yield high-energy neutral particles within the ZDC acceptance. In each case, the leading particle’s energy and polar scattering angle are used to constrain the Mandelstam variables  $t$  or  $u$ . The azimuthal angle can also be exploited for spin-dependent modulation measurements and for studying  $\Lambda^0$  polarization and deuteron structure. While these reactions are labeled as having an electron in the final state, it should be understood that they can correspond to either the electroproduction (large  $Q^2$ ) or photoproduction ( $Q^2 \approx 0$ ) regime. The references provided are representative of the literature discussing the corresponding channel, although they do not constitute an exhaustive list.

Name	Refs.	Reaction	Signal in ZDC	$E$ of interest
Inclusive leading $n$	[133–135]	$ep \rightarrow eXn$	$n$	10–275 GeV
Inclusive leading $\gamma$	[136]	$ep \rightarrow eX\gamma$	$\gamma$	10–275 GeV
Inclusive leading $\Lambda$	[137]	$ep \rightarrow eX\Lambda$	$\Lambda^0 \rightarrow n\pi^0 \rightarrow n\gamma\gamma$	10–275 GeV
$t$ -channel DEMP	[130]	$ep \rightarrow e\pi^+n$	$n$	10–275 GeV
	[138]	$ep \rightarrow eK^+\Lambda^0$	$\Lambda^0 \rightarrow n\pi^0 \rightarrow n\gamma\gamma$	10–275 GeV
	[138]	$ep \rightarrow eK^+\Sigma^0$	$\Sigma^0 \rightarrow \Lambda^0\gamma \rightarrow n\gamma\gamma\gamma$	10–275 GeV
$u$ -channel DVCS	[132]	$ep \rightarrow e\gamma p$	$\gamma$	10–250 GeV
$u$ -channel DEMP	[132]	$ep \rightarrow e\pi^0 p$	$\pi^0 \rightarrow \gamma\gamma$	10–275 GeV
	[131]	$ep \rightarrow e'\omega^0 p$	$\omega^0 \rightarrow \gamma\gamma\gamma$	10–275 GeV
Sullivan DVCS off $\pi^+$	[139]	$ep(\pi^+n) \rightarrow e\gamma\pi^+n$	$n$	10–275 GeV
Sullivan DEMP off $\pi^+$	[139, 140]	$ep(\pi^+n) \rightarrow e\rho\pi^+n$	$n$	10–275 GeV
	[141]	$ep(\pi^+n) \rightarrow e\phi\pi^+n$	$n$	10–275 GeV
	[141]	$ep(\pi^+n) \rightarrow eJ/\psi\pi^+n$	$n$	10–275 GeV
Sullivan DIS dijet off $\pi^+$	[142, 143]	$ep(\pi^+n) \rightarrow ejjXn$	$n$	10–275 GeV
CC DEMP	[144]	$ep \rightarrow \nu_e\pi^0n$	$n$	10–275 GeV
$n$ -tagged DIS	[145]	$ed \rightarrow eX(n_s)$	$n$ (spectator)	10–135 GeV
Di-tagged $J/\psi$	[146]	$ed \rightarrow eJ/\psi pn$	$n$ (active or spectator)	10–135 GeV
Di-tagged DVCS	[146]	$ed \rightarrow e\gamma pn$	$n$ (active or spectator)	10–135 GeV
$p$ -tagged DEMP	[147]	$ed \rightarrow e\pi^0n(p_s)$	$n$ (active)	10–135 GeV
		$ed \rightarrow eK^0\Lambda^0(p_s)$	$\Lambda^0$ (active)	10–135 GeV
$n$ -tagged DEMP	–	$ed \rightarrow e\pi^+n(n_s)$	$2n$ (active and spectator)	10–135 GeV
	–	$ed \rightarrow eK^+\Lambda^0(n_s)$	$\Lambda^0$ (active) and $n$ (spectator)	10–135 GeV
Quasi-coherent $J/\psi$	[148]	$eA \rightarrow eA^*J/\psi$	$\gamma$ emission from $A^*$	$\mathcal{O}(100)$ MeV
Incoherent $J/\psi$	–	$eA \rightarrow eXJ/\psi$	$n$ and $\gamma$ de-excitation	$\mathcal{O}(100)$ MeV to $\mathcal{O}(100)$ GeV
eA DIS (centrality)	–	$eA \rightarrow eX$	Spectator neutrons	$\mathcal{O}(1)$ TeV

7559 For all these measurements, the ZDC must provide a standalone determination of the energy and  
7560 angle of the particle in question, which is used to constrain the Mandelstam variables  $t$  or  $u$ .

7561 A parallel set of measurements to those described above can be carried out with deuteron beams  
7562 to probe e.g. neutron structure. This relies on the “spectator tagging,” technique. For example,  
7563 inclusive DIS on a deuteron with spectator tagging [145] can be performed with proton tagging (in  
7564 trackers) to yield “free-neutron” structure measurements, albeit with theoretical extrapolations.  
7565 This method can be validated by the neutron-spectator case, which yields “free-proton” struc-

ture measurements that can be compared with proton-beam data. Neutron tagging requires the ZDC: measurements of the spectator neutron constrain the proton's momentum in the deuteron-rest frame, and low-momentum configurations approximate a "free-proton" structure. Differential measurements at higher neutron momentum select specific nucleon configurations or studies of short-range correlations and modified bound-proton structure, which also serve as references for studies in  $eA$  scattering.

Similarly, spectator tagging with deuteron beams can be used for diffractive or exclusive channels. In the method of Tu et al. [146], a "double-tagging" approach is proposed in which both the proton and the neutron from the deuteron breakup are measured to reconstruct  $t$ . This is necessary because, unlike in a proton beam, the incoming momentum of the proton bound in a deuteron is not known from the beam momentum. For example, Tu et al. apply this method to study incoherent diffractive  $J/\psi$  production off a deuteron, with either a proton or neutron spectator. They further argue that it can be used to study incoherent DVCS off a deuteron—probing bound neutron or bound proton structure depending on which nucleon is the spectator. A conceptually similar approach, with both proton and neutron tagging, was first performed by the CLAS collaboration to study neutron DVCS [149]. The same concept of double-tagging could be extended to DEMP off a neutron with proton spectator, which in the neutral-meson channels ( $\pi^0$ ,  $K^0$ , etc.) yields neutron signals in the ZDC [147].

The ZDC has also an important role as veto detector for the study of production of exclusive vector mesons in diffraction processes from  $eA$  collisions. For the coherent processes, where the nucleus remains intact, the  $t$ -dependent cross section can be related to the transverse spatial distribution of gluons in the nucleus, which is sensitive to gluon saturation. In this case, however, the coherence of the reaction needs to be determined precisely. Incoherent events can be isolated by identifying the break-up of the excited nucleus. The evaporated neutrons produced from the break-up in the diffraction process can be used in about 90% of the cases to separate coherent processes. In addition, photons from the de-excitation of the excited nuclei can help identify incoherent processes even in the absence of evaporated neutrons. Therefore, to identify coherent events over a wide  $t$  range, neutrons and photons must be accurately measured near zero degrees.

An interesting limiting case that bridges coherent and incoherent diffraction is the "quasi-coherent" process, in which the final-state nucleus remains intact but is excited and then de-excites via photon emission [148]. In the nucleus rest frame, these photons have very low energies ( $\mathcal{O}(1)$  MeV or lower), but the Lorentz boost to the laboratory blue-shifts them to  $\mathcal{O}(100)$  MeV—within the range measurable by the crystal section of the ZDC. Tagging specific photon energies (i.e.,  $\gamma$ -spectroscopy) could identify the lowest excited states and thus link coherent and incoherent measurements. This process lies beyond the traditional Good-Walker paradigm and is currently in theoretical limbo [148]. Moreover, in principle,  $\gamma$ -spectroscopy could support additional programs in nuclear fragmentation studies.

Another key role of the ZDC is to measure the number of spectator or evaporated neutrons from  $eA$  DIS. Each of these neutrons carries similar energy (around 110 GeV for the case of 250 GeV  $Pb$  beam). Thus, overlapping showers from several or even dozens of neutrons can produce large energy depositions, reaching up to the TeV scale. These measurements can be used to constrain the geometry of the collision, which is important for understanding the characteristics of each event in  $eA$  collisions. It has been proposed that collision geometry can be studied by tagging it with the multiplicity of forward neutrons emitted near zero degrees. Determining the geometry of the collision, such as the "travel length" of the struck partons in the nucleus, which correlates with the impact parameters of the collision, is very useful in the study of nuclear matter effects. Determining the geometry of the collision will allow us to understand the nuclear structure with greater accuracy.

**Requirements from Radiation Hardness:** In the ePIC radiation doses and particle fluences, the ZDC neutron fluence is smaller than  $10^{12}$  1-MeV equivalent neutron/cm<sup>2</sup> for 6 month operation. At this fluence degradation may occur for crystals due to radiation. The SiPMs are expected to suffer a considerable increase in the dark current [150]. This consideration is addressed in the design, which ensures adequate light yield for an acceptable signal-to-noise ratio and allows for high-temperature annealing of SiPMs to mitigate neutron fluence effects [150].

**Requirements from Data Rates:**

## Justification

**Device concept and technological choice:** The ZDC system consists of two subsystems: a crystal calorimeter and a sampling calorimeter. The crystal calorimeter measures low to medium energy photons (0.1 GeV to 10 GeV) during  $eA$  running for tagging and vetoing purposes, while the sampling calorimeter covers high energy (10 to 250 GeV) neutrons, photons, neutral pions, and neutral lambda baryons, and can detect multiple neutrons from  $eA$  collision remnants.

Because the crystal calorimeter is not required for every run, it is mounted on a retractable table and can be removed when not needed.

The crystal calorimeter is constructed from PbWO<sub>4</sub> crystals. The sampling calorimeter is a high-granularity iron-scintillator detector with SiPM readout, often called “SiPM-on-tile.” Both the crystal and sampling calorimeters are employed in larger ePIC systems: the crystal calorimeter in the backward electromagnetic calorimeter and the sampling calorimeter in the forward hadronic calorimeter, respectively.

The high granularity of the sampling section is motivated by the requirements associated with high energy neutrons and neutral lambda baryons in DEMP, which enable measurements of the momentum transfer variable  $t$ .

## Subsystem description:

### Crystal calorimeter

**General device description:** The first section of the ZDC is designed with a layer of crystal calorimeter towers, each with 8 radiation lengths ( $X_0$ ) thick. This layer is composed of  $2 \times 2$  cm<sup>2</sup> crystals arranged in a  $30 \times 30$  grid. LYSO is chosen as the crystal material for its high light yield and suitability for measuring low energy photons.

**Sensors:** The gain of SiPMs is on the order of  $10^5$  with an operational bias of 25–30 V, while for APDs (avalanche photodiodes), the gain ranges from 1 to 50. Given the high light yield of LYSO crystals, APDs are a more suitable choice to avoid signal saturation. However, an operational bias of 150–200 V is required. If SiPMs are selected as the photodetector, a filter would need to be installed between the crystals and photodetectors to reduce the light yield and prevent saturation.

**FEE:** Under consideration.

**Other components:** Under consideration.

**Sampling calorimeter** The design and simulated performance of the sampling-calorimeter section of the ZDC is described in Ref. [7] and is briefly summarized here.

This ZDC section uses SiPM-on-tile approach, in which SiPMs directly couple to tile in the active layers of the calorimeter. This technology is used in the forward HCAL. The absorber structure, which is self-supporting, is composed of iron-blocks whereas the active layers correspond to tiles of plastic scintillator of size  $50 \times 50 \text{ mm}^2$  mounted on PCBs with SiPMs and no other component besides capacitors for passive filtering and connectors for flat cables.

One or more active layers will be placed in front of the first iron blocks to serve as a hodoscope for vetoing charged particles produced, for example, by neutrons interacting with upstream material. Charged-particle veto capabilities were also used in conjunction with the HERA ZDCs [133, 134]

Sensors: The SiPMs to be used are Hamamatsu 3 mm size, model S14160-3015PS, which are among the models to be used in the forward HCAL and Insert.

FEE: The raw analog signals from the SiPMs are transported to the back of the calorimeter to FEE boards using flat cables. The FEE boards will be identical to those used in the forward HCAL.

Other components:

#### Performance Crystal section performance:

The first test beam experiment for crystal calorimeter prototype was performed in February 2024 using 50 to 800 MeV positron test beam at the ELPH facility (now the RARiS facility) in Tohoku University in Japan and its data analysis is underway. The prototype modules have been made by the Taiwan group. Two simulation calculations and evaluations are ongoing;  $\Lambda$  identification and low energy photon identification. Angular resolution is a common thread. It has been less emphasized early on, but absolute requirements for successful exclusive physics program should be given.

#### Sampling calorimeter section performance:

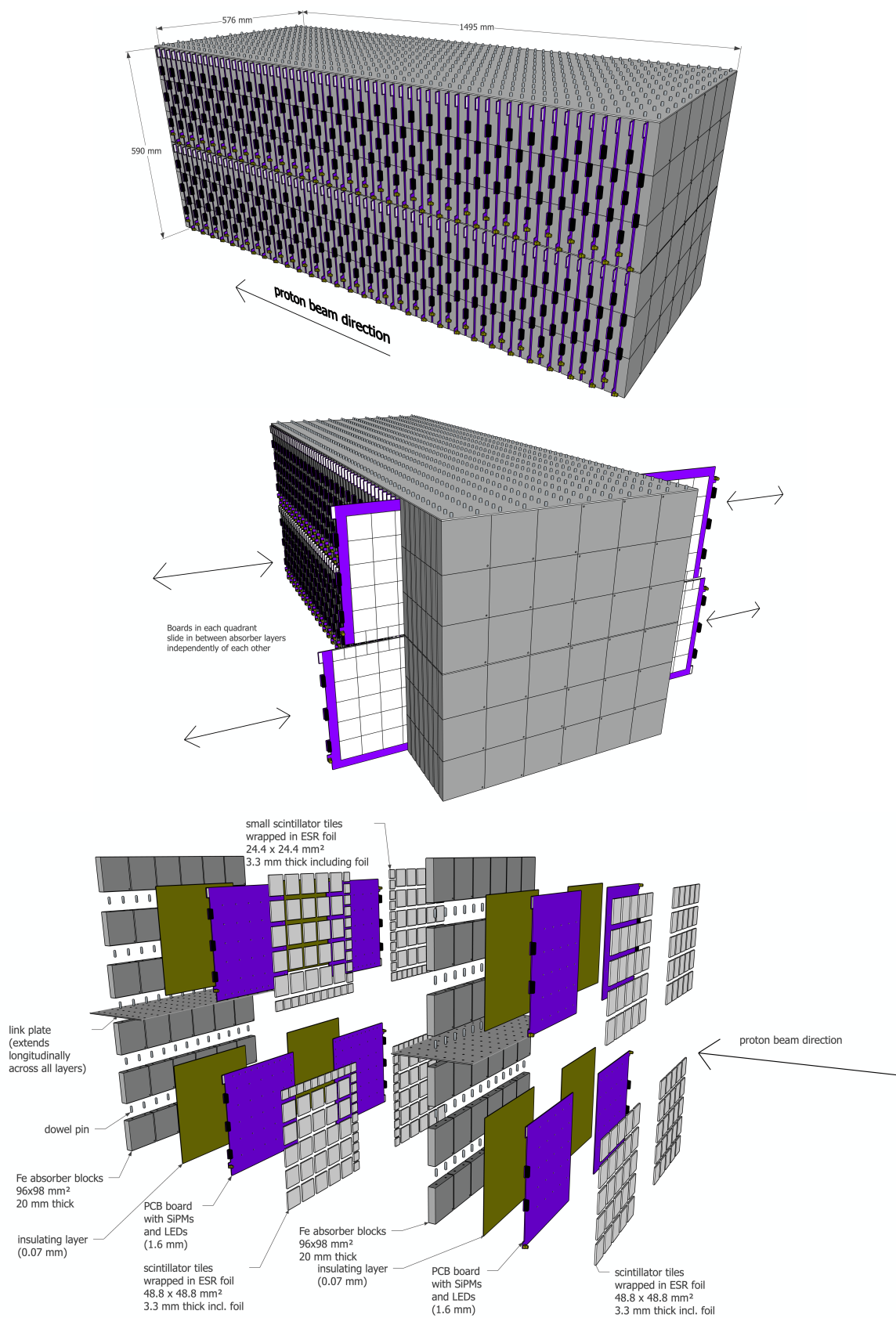
The standalone performance of the SiPM-on-tile section of the ZDC has been simulated for the following single-particles: neutrons, lambda baryons, photons and neutral pions. The range of interest for all of these is 10–250 GeV. Studies have been published elsewhere, and are reproduced here in a summarized fashion. All performance studies below reflect the performance of the SiPM-on-tile system without the crystal calorimeter in front, since this will be removed when not needed.

Arguably, the most challenging channel for ZDC reconstruction is the neutral-decay channel of neutral lambda baryons:  $\Lambda^0 \rightarrow n\pi^0$  (branching ratio 36%). As depicted in Figure 8.228, this measurement necessitates estimating the  $\Lambda^0$  displaced vertex, which is expected to range from meters to tens of meters. We addressed this challenge using an iterative method that explicitly estimates the displaced vertex, called IDOLA [6], as well as a graph-neural network approach that resolves it implicitly.

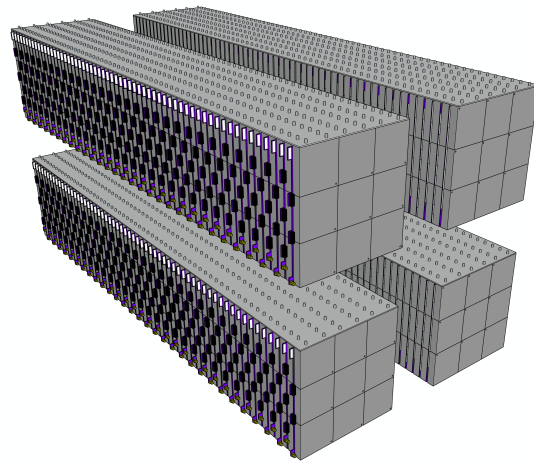
**Implementation** The ZDC implementation will benefit from a creative approach; for example, non-static configurations which can adapt to different running conditions. The crystal-calorimeter needs depend on physics channel. Some level of conflict in the final states and associated require-



Figure 8.221: SiPM-on-tile ZDC.







**Figure 8.222:** SiPM-on-tile ZDC modular design is composed of quadrants.



**Figure 8.223:** ZDC mechanical

ments. Having the ability to bring the crystal calorimeter in and out of configuration as needed, would provide clear benefit to specific physics needs.

**Services:** Add text here.

**Subsystem mechanics and integration:** Each LYSO crystal will be wrapped in ESR, a high-reflectivity foil. Each crystal tower, composed of a  $5 \times 5$  array of crystals, will be either wrapped in aluminum foil or placed into an aluminum support structure to ensure stability. In total, there will be 36 towers. An additional thin aluminum support structure will be added around the crystal calorimeter for extra reinforcement.

The assembled crystal calorimeter will be housed in an aluminum container, which will be securely mounted to the table in the ZDC area using screws. This design allows for easy removal of the crystal calorimeter when necessary.

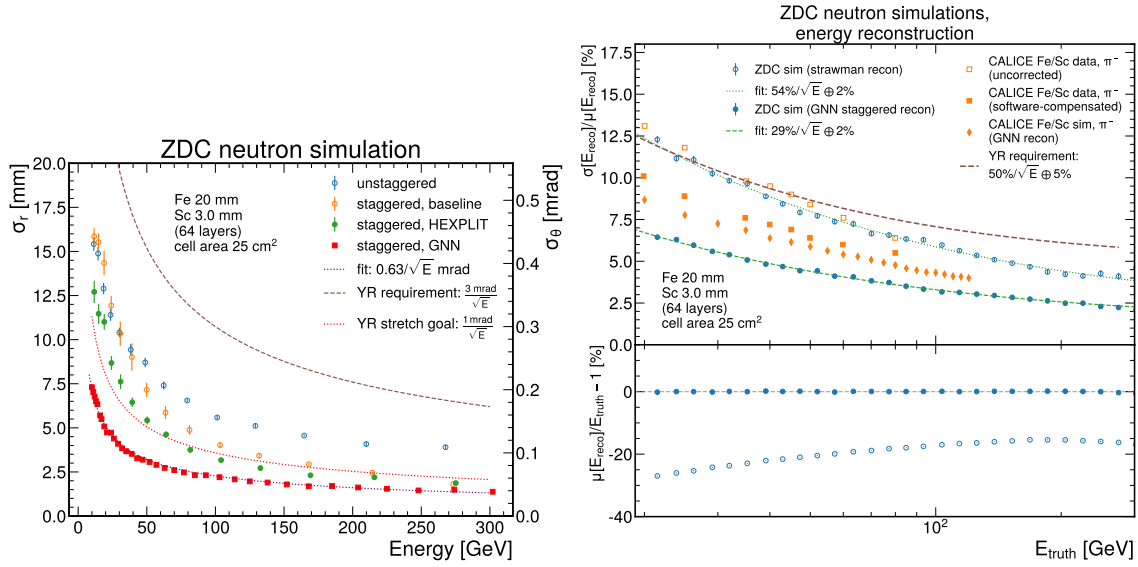


**Figure 8.224:** Left: ZDC neutron-shower position resolution for neutrons as a function of the generated energy. Results are shown with an untagged layout (blue) and staggered layout with the positions reconstructed with the baseline (orange), HEXPLIT (green), and GNN (red) reconstruction algorithms. Right: Energy resolution (top row) and scale (bottom row) obtained with the strawman (open symbols) and GNN (filled symbols) for simulated single neutrons. The resolutions are compared to those of the CALICE beamtest [?] (orange squares) with (filled) and without (open) software compensation, as well as the CALICE GNN reconstruction (orange diamond) [5].

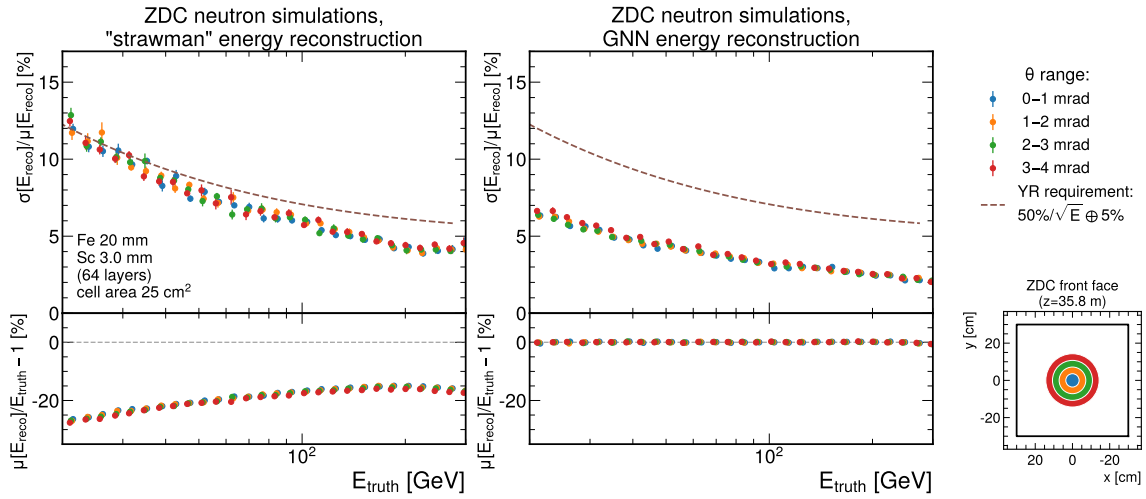


**Figure 8.225:** Energy resolution (top row) and scale (bottom row) obtained with the strawman (left) and GNN (right), at various ranges in  $\theta$ . The positions on the face of the detector corresponding to each color are visualized in the inset.

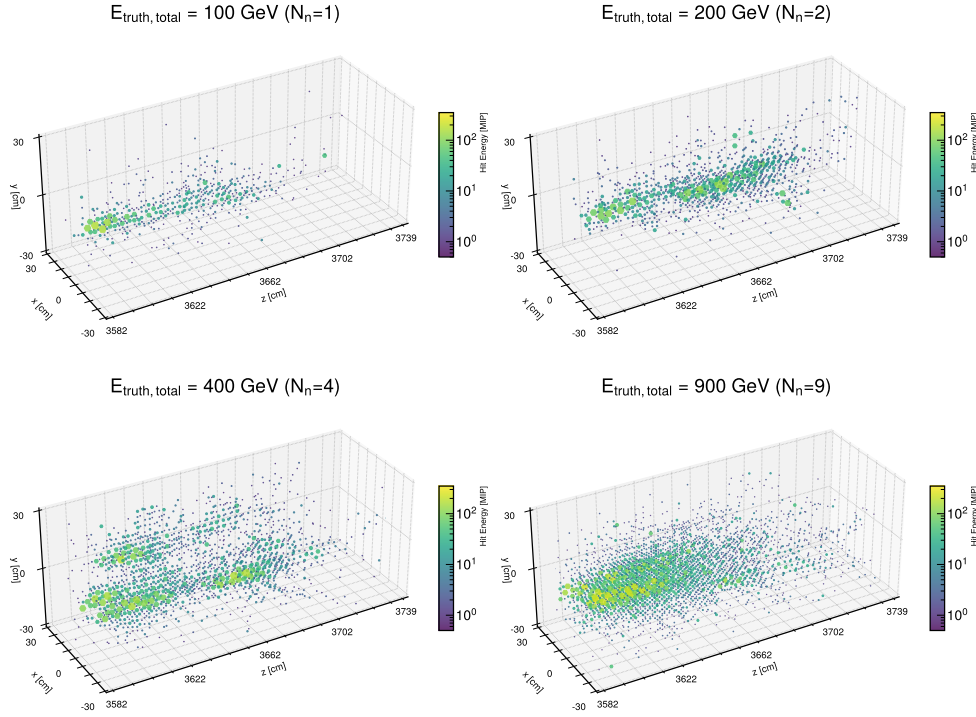


**Figure 8.226:** Examples of 4 reconstructed 3D shower shapes in the ZDC for events with 1 neutron ( $N_n = 1$ ), 2 neutrons ( $N_n = 2$ ), 4 neutrons ( $N_n = 4$ ), and 9 neutrons ( $N_n = 9$ ). The color code represents hit energy in terms of  $E_{\text{MIP}}$ . The marker size is displayed proportionally to hit energy for display purposes.

Precision cooling for the crystals and power cooling for the electronic readout will be achieved using water-cooling circuits. The cooling needs for individual crystals will be addressed through a thermal conduit extending from the crystal's rear face, through metal inserts, to the interface plate and support elements. A front thermal screen will also be installed to maintain the crystals at a controlled temperature.

The crystals will undergo pre-calibration using beam test facilities. In-situ calibration with physics events will be conducted using the process  $\pi^0 \rightarrow \gamma\gamma$ .

A light monitoring system will be implemented to continuously measure the relative light transmission and the full photodetector gains across all channels. Light pulses will be injected into each crystal to assess the optical transmission near the scintillation spectrum peak of LYSO crystals.

Sampling section:

The calibration of the detector is carried out with MIPs channel by channel. The self-supporting mechanical structure of the detector.

**Status and remaining design effort:**

R&D effort:

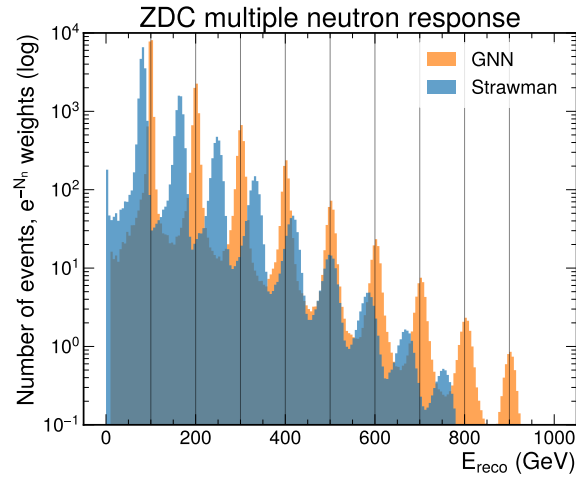


**Figure 8.227:** Energy measured for each integer number of neutrons with energy equal to 100 GeV, reconstructed with GNN (orange) and strawman (blue). The events are weighted by a factor of  $e^{-N_n}$ . The black, vertical lines are drawn at the total true energies of events with different numbers of neutrons. Here we show events containing up to nine neutrons. This performance illustrates just instrumental effects, excluding nuclear effects like smearing caused by Fermi motion and fission. In the laboratory frame, these nuclear effects would contribute in quadrature about 5 GeV per 100 GeV neutron, according to BEAGLE [?], which happens to be similar to the widths of the strawman reconstruction shown here.

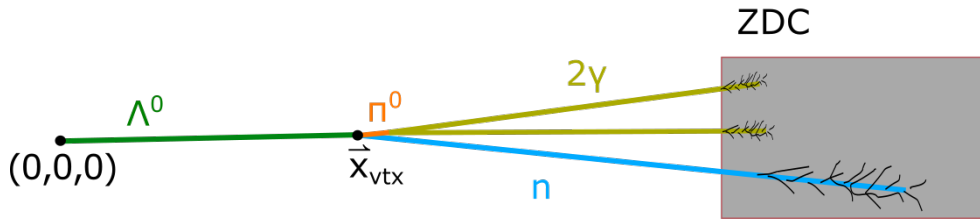


**Figure 8.228:** Topology of  $\Lambda^0$  decay in neutral-channel decay. Not shown to scale. Figure reproduced from Ref. [6].

7724 E&D status and outlook: Add text here.

7725 Other activity needed for the design completion: Add text here.

7726 Status of maturity of the subsystem: Add text here.

7727 **Environmental, Safety and Health (ES&H) aspects and Quality Assessment (QA plan-**  
 7728 **ning:** The quality assurance for each crystal and the assembly of each crystal tower will be con-  
 7729 ducted in Taiwan. Each tower will undergo pre-calibration using beam test facilities before being  
 7730 assembled into the final detector in Japan, after which it will be shipped to BNL for in-situ installa-  
 7731 tion.

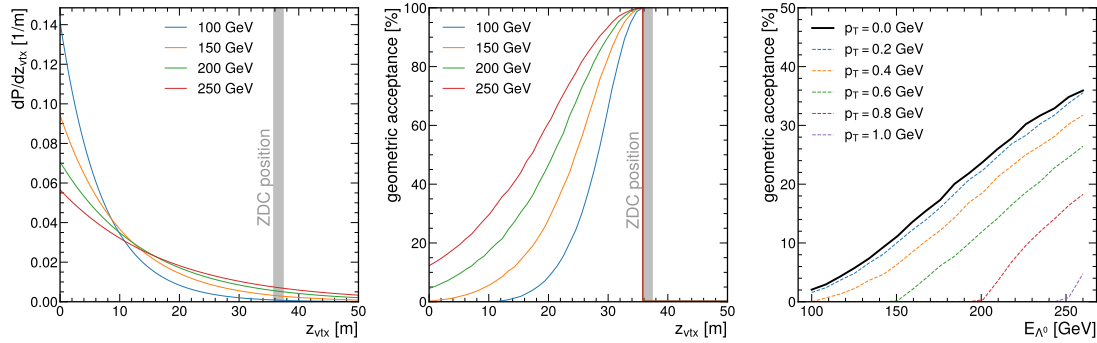


**Figure 8.229:** Left: Decay position distribution, for different  $\Lambda^0$  energies. Middle: acceptance as a function of energy and decay position. Right: Acceptance as a function of energy, integrated over decay position, for  $\Lambda^0$ 's along the proton axis (black solid curve) and with varying amounts of transverse momentum (colored dashed curves). Figure reproduced from Ref. [6].

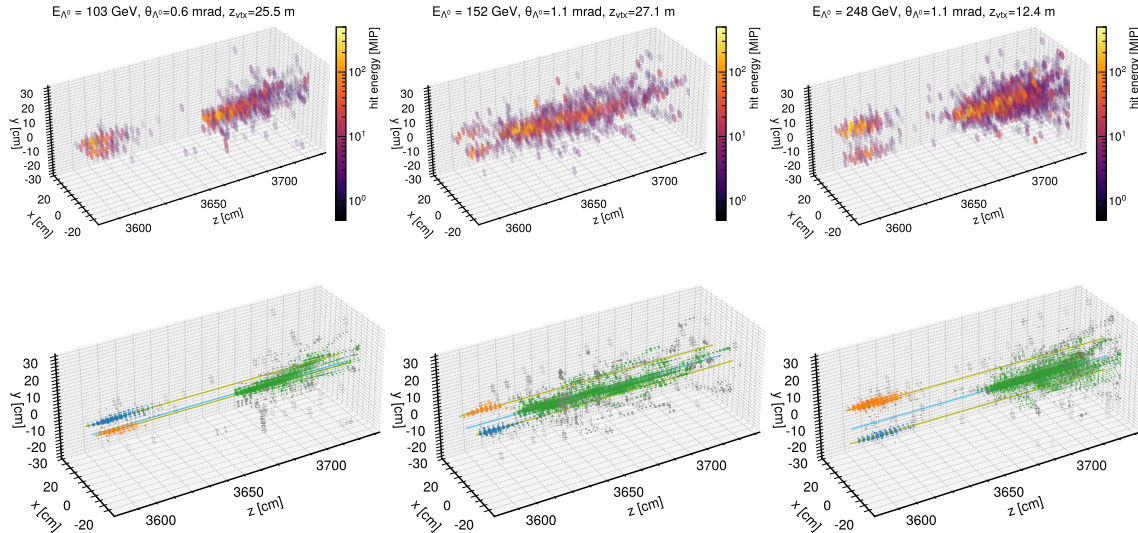


**Figure 8.230:** Top row: event display for example events, with the hits color coded by energy deposited, in units of MIPs. Bottom row: the same events, with subcell hits from HEXPLIT algorithm color-coded by which cluster the subcell hits have been assigned to by the 3D topological clustering algorithm. The olive (cyan) line(s) represent the truth-level trajectories of the incident photons (neutron). Figure reproduced from Ref. [6].

7732 **Construction and assembly planning:** The self-supporting mechanical structure of the SiPM-  
 7733 on-tile section will be assembled at BNL. The construction process will follow a method similar to  
 7734 that shown in Figure ??, which depicts a prototype with an area one-quarter that of the full ZDC and  
 7735 a depth of 23 layers. This prototype includes a total of 575 channels, representing approximately  
 7736 10% of the total number of channels in the full-size ZDC.

7737 In this modular assembly method, a baseplate with drilled holes serves as the mounting surface,  
 7738 where Fe blocks are connected using dowel pins. Each Fe block on the baseplate supports two  
 7739 additional blocks stacked above, also linked with dowel pins. Thin aluminum sheets are then used

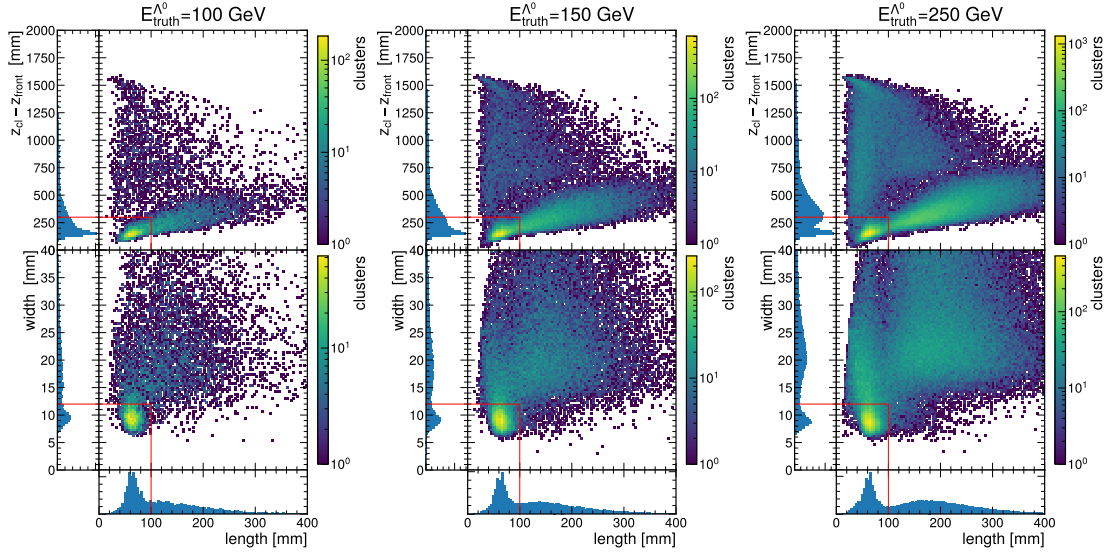


**Figure 8.231:** Distribution of the cluster shape parameters, at three different  $\Lambda^0$  energies. The red lines show the cuts used to identify the photon clusters.

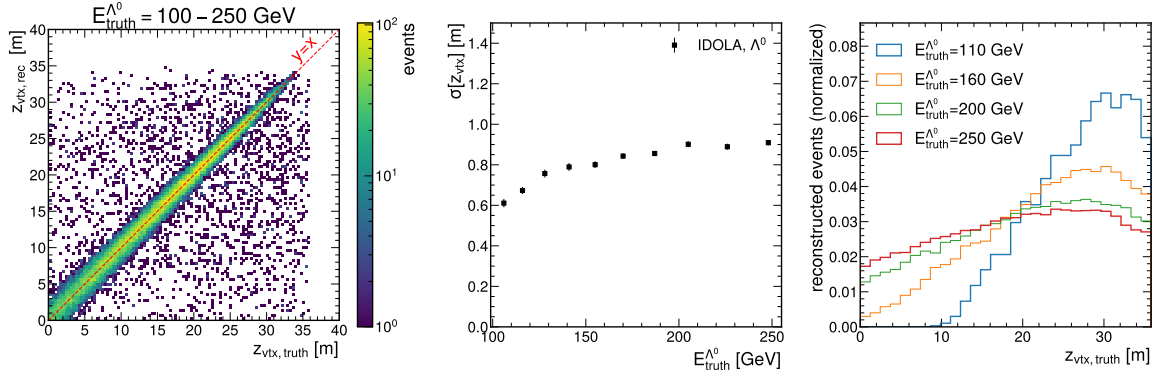


**Figure 8.232:** Left: truth decay position of  $\Lambda^0$  ( $x$  axis), compared to the reconstructed values ( $y$  axis). A thin red dashed line is shown at  $y = x$ . Middle: the decay position resolution as a function of the  $\Lambda^0$  energy. Right: distribution for the decay positions of reconstructed events for different  $\Lambda^0$  energies. Figure reproduced from Ref. [6].

7740 to connect the vertical  $3 \times 3$  columns. This modular process is repeated until the entire  $6 \times 6$  array  
 7741 and all 64 layers of the ZDC are completed.

7742 The modular construction design was adapted from the successful design and deployment from  
 7743 the STAR forward HCAL construction.

7744 **Collaborators and their role, resources and workforce:** Academia Sinica and National Cen-  
 7745 tral University in Taiwan, RIKEN, Kobe University, Shinshu University, University of Tsukuba,  
 7746 Tsukuba University of Technology and Nihon University in Japan, and Sejong University in Korea  
 7747 will contribute to the R&D, assembly, beam tests, and operation of the ZDC crystal calorimeter.  
 7748 The Taiwan team will collaborate with a crystal producer in Taiwan for LYSO crystals and develop



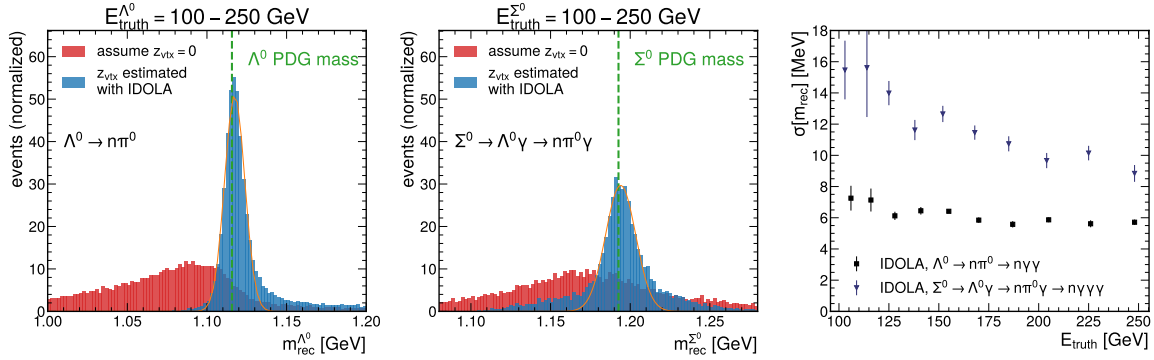


**Figure 8.233:** Left: distribution for the reconstructed  $\Lambda^0$  mass before (red) and after (blue) fitting the vertex position with the IDOLA algorithm. Middle: Same for the reconstructed  $\Sigma^0$  mass. Right: the  $\Lambda^0$  ( $\Sigma^0$ ) mass resolution as a function of the  $\Lambda^0$  ( $\Sigma^0$ ) energy. Figure reproduced from Ref. [6].

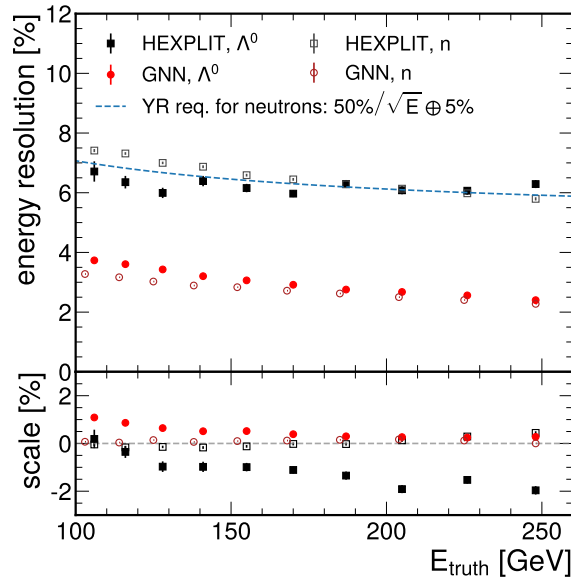


**Figure 8.234:** Energy resolution as a function of the  $\Lambda^0$  energy. For comparison, the values obtained in Ref. [7] for single neutrons are shown in gray. Figure reproduced from Ref. [6].

7749 electronic readout circuits and mechanical support. Currently, the Taiwan team consists of three  
7750 faculty members, five postdoctoral researchers, and three students.

7751 University of California, Riverside, University of Kansas, University of Connecticut, and Jefferson  
7752 Laboratory in US will contribute to the R&D, assembly, beam tests, and operation of the ZDC  
7753 SiPM-on-tile section.

7754 **Risks and mitigation strategy:** Radiation damage to the SiPMs poses a risk to the performance  
7755 of the ZDC and must be mitigated. The expected dark current has been measured for the spec-  
7756 ific SiPMs intended for use in the ZDC [150]. The primary mitigation strategy involves high-



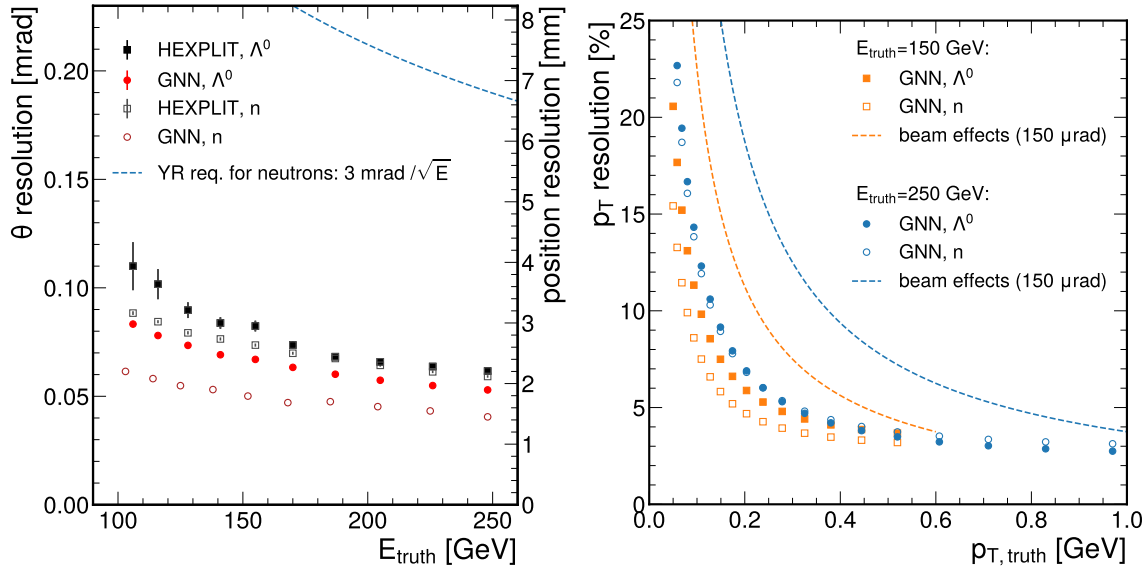


**Figure 8.235:** Left: Polar angle resolution for  $\Lambda^0$  (filled symbols) and neutrons (open symbols) with baseline reconstruction and GNN reconstruction. Right: The resolution for reconstructing the transverse momentum for  $\Lambda^0$  (filled symbols) and neutrons (open symbols) using a GNN at 150 GeV (blue) and 250 GeV (orange). These values reflect the resolution without beam effects. The beam effects terms for  $\sigma_{\text{beam}}=150 \mu\text{rad}$  are shown as dashed curves. Figures reproduced from Ref. [6].

temperature annealing of the SiPM boards. For these SiPMs, a 20-hour annealing session at 120°C reduces the dark current by a factor of two [150].

The design of the sampling section allows the SiPM boards to be removed from the mechanical structure for annealing treatment, which will be carried out in an environmental chamber in a BNL lab. High-temperature annealing can therefore be performed as needed between runs. This process requires removing the plastic scintillator tiles from the boards, as they would be damaged by the high temperature. Although delicate and labor-intensive, the procedure for removing and reattaching the scintillator tiles is straightforward.

From a mechanical standpoint, appropriate risk mitigation strategies include using a weight-rated table to support the detector and a crane if needed. The self-supporting structure closely follows that of the STAR forward HCAL, minimizing risks related to construction tolerances and structural integrity. Nevertheless, appropriate checks will be conducted, and custom support materials may be implemented to bracket the ZDC structure and provide additional reinforcement if necessary.

**Additional Material** Add text here.

### 8.3.8 Far backward detectors

The luminosity system at the Electron-Ion Collider plays a critical role in achieving high-precision measurements in nuclear physics experiments. By determining, monitoring and optimizing the number of particle collisions, the luminosity system ensures that the collider operates at peak per-

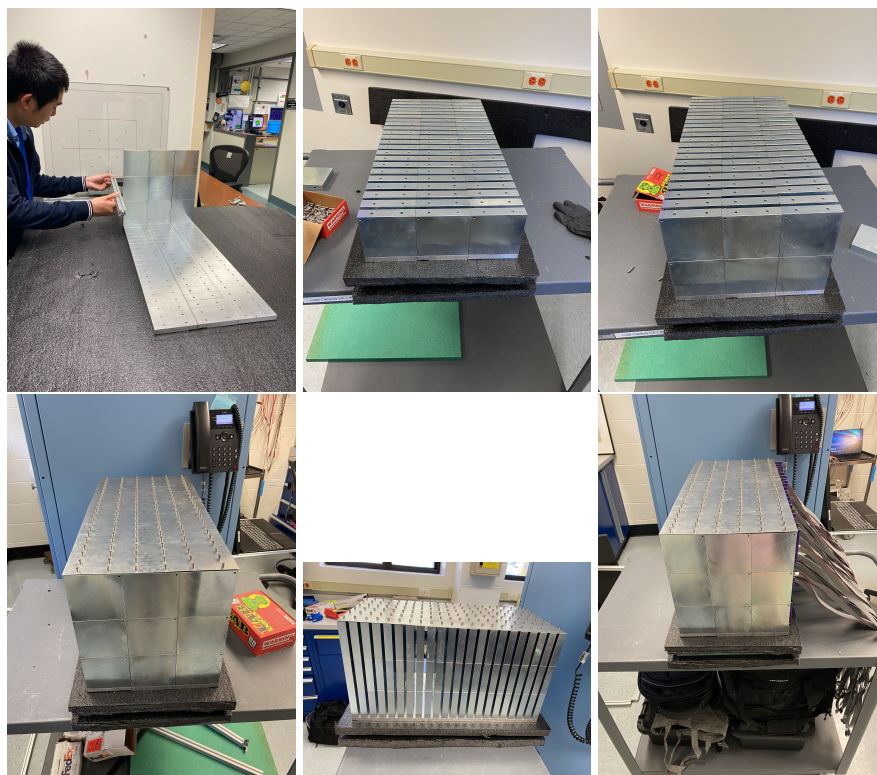


**Figure 8.236:** Assembly of a ZDC prototype representing approximately 10% of the full ZDC size.

7775 formance, enabling detailed exploration of the structure of matter. When electrons collide with  
 7776 protons or nuclei, Bremsstrahlung (BH) photons are generated, with a well know cross section [].  
 7777 This process thus provides us with the mean to indirectly determine the luminosity by accurate  
 7778 and precise determination of the Bremsstrahlung photons generated in the interaction region of  
 7779 the collider.

7780 Accurately determining luminosity is essential for addressing the fundamental physics questions  
 7781 that underpin the construction of the Electron-Ion Collider. The Yellow Report specifies the EIC  
 7782 requirements for luminosity determination to be 1% in absolute uncertainty and  $10^{-4}$  in relative  
 7783 luminosity [8]. This requirement will be fulfilled by two complementary detectors in the lumi-  
 7784 nosity monitoring system: the Pair Spectrometer (PS) and the Direct Photon Detector (DPD). It was  
 7785 demonstrated at HERA – the first electron-hadron collider – that the bremsstrahlung process can be  
 7786 successfully used to precisely measure the luminosity of high-energy  $ep$  collisions (ZEUS achieved  
 7787 an absolute uncertainty of 1.7% [?, ?]). The luminosity monitors designed for the EIC utilise the  
 7788 same approach with implementation that mitigates large systematic uncertainties.

7789 The two subsystems, Pair Spectrometer, and Direct Photon Detector, are sensitive to different sys-  
 7790 tematic effects; on one hand the Direct Photon detector is placed downstream the photon beam with  
 7791 full acceptance, but within the synchrotron radiation fan and needs to be shielded. In addition,  
 7792 at nominal luminosities planned for the EIC several photons will hit the DPD in each bunch cross-  
 7793 ing. Thus the counting of bremsstrahlung photons is done through the total energy determination  
 7794 deposited in DPD and is associated with systematic uncertainties related to gain stability. On the  
 7795 other hand, the PS is outside the synchrotron radiation fan and overall rates can be controlled

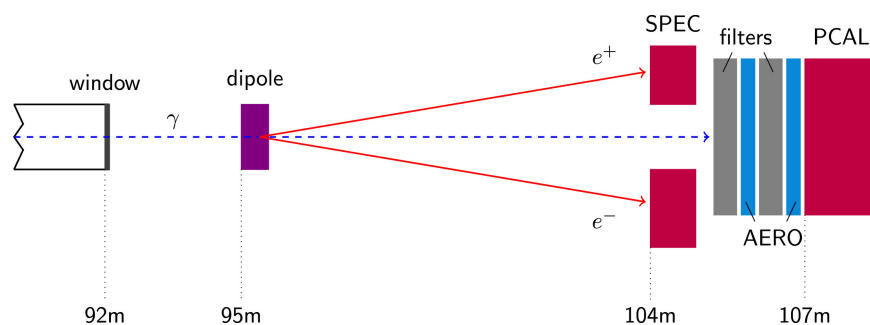


**Figure 8.237:** The layout of the luminosity monitor in the ZEUS experiment [?].

with a dedicated converter. The luminosity determination from the PS is sensitive to systematic effects related with the acceptance determination.

The PS and DPD detectors in the ZEUS luminosity monitor are shown in figure (8.237). The PS system consists of an analysing dipole magnet and two electromagnetic calorimeters, while the DPD system includes absorbing plates and an electromagnetic calorimeter. BH photons generated in the interaction region exit the vacuum chamber through a thick exit window. About 10% of these photons (depending on the window's thickness) undergo pair conversion into electron-positron pairs, which are then detected by the PS calorimeters. The remaining unconverted photons are detected by the downstream DPD. Additionally, the luminosity monitor includes a collimator positioned just after the exit window to produce a uniform, narrow cone of photons and pair-converted particles. This simple steel block also protects the PS system components from direct synchrotron radiation (SR), BH radiation, and unwanted stray particles.

The PS was needed at ZEUS due to challenges introduced by upgrades to the HERA accelerator, which significantly increased luminosity and, consequently, the rate of BH events [?]. The stronger beam focusing and increased synchrotron radiation (SR) — radiation resulting from the bending of electrons by the magnet—led to a higher pile-up of photons in the DPD, increasing the uncertainty in luminosity measurements from 1% to 3% [?]. The PS, positioned outside the SR fan and unconverted photon flux, experienced a lower pile-up due to fractional pair conversion. This introduction reduced the uncertainties in rate measurement to 2% [?], and additionally both detectors were utilized to monitor real-time detector inefficiencies and manage systematic uncertainties.

### 8.3.8.1 The luminosity system

**Introduction** The luminosity system at the Electron-Ion Collider plays a critical role in achieving high-precision measurements in nuclear physics experiments. By determining, monitoring and optimizing the number of particle collisions, the luminosity system ensures that the collider operates at peak performance, enabling detailed exploration of the structure of matter. The luminosity measurement provides the required normalization for all physics studies, allowing us to determine absolute cross sections and the proper scaling for different polarisation states enabling precise asymmetry measurements.

When electrons collide with protons or nuclei, bremsstrahlung (BS) photons are emitted, with a well known cross section due to Bethe-Heitler [?]. Thus, this process provides us with the means to indirectly determine the luminosity by accurate and precise determination of the bremsstrahlung photons produced in the interaction region of the collider. This approach was successfully implemented at HERA, measuring the luminosity of high-energy  $ep$  collisions [?, ?]. The experimental

conditions at the EIC (expected luminosities of  $10^{33} \text{ cm}^{-2}\text{s}^{-1}$ ), with a wide range of electron beam energies, and a variety of (polarized) targets complicate the precise determination of the luminosity. For example, beam-size effects suppress the bremsstrahlung process due to the finite transverse size of the beam overlap relative to the typical impact parameter [?]. In addition, the large cross section of the Bethe-Heitler process, which increases with  $Z^2$  of the target for nuclear beams, results in a large amount of photons (over 20 for electron-proton scattering), complicating the determination of the rate of generated photons, which is also sensitive to event pileup. This direct measurement of the rate of generated photons at the interaction region is further affected by the strong synchrotron radiation background, which has a similar angular distribution as bremsstrahlung.

**Beam Size Effects:** The Bethe-Heitler process in electron-proton collisions is notable for its extremely small momentum transfers between the radiating electron and the proton. It is kinetically possible for both particles to continue along their initial paths without angular scattering, while the Bethe-Heitler photon is emitted in the direction of the electron's momentum. This specific configuration results in the smallest virtuality ( $Q_{\min}^2$ ) of the exchanged photon [?]. At high-energy colliders, this minimal photon virtuality becomes very small. For instance, at HERA, the  $Q_{\min}^2$  for a photon energy of 1 GeV the photon virtuality can be as low as  $10^{-8} \text{ eV}^2$ . Consequently, the typical transverse momentum transfer ( $q_{\perp}$ ) reaches values around  $10^{-4} \text{ eV}/c$ . Since the Bethe-Heitler differential cross section is proportional to  $Q^{-4}$ , photon virtualities near  $Q_{\min}^2$  dominate the process and allows for the approximation,

$$Q^2 = Q_{\min}^2 + q_{\perp}^2.$$

Analyzing the process in impact parameter space reveals that these small  $q_{\perp}$  values correlate to large impact parameters ( $b = \hbar/q_{\perp}$ ), explaining the precision of Bethe-Heitler cross-section calculations in the Born approximation.

The derivation of the two-particle rate ( $R$ ) relation with the collision luminosity ( $L$ ) and cross-section ( $\sigma$ )

$$R = L\sigma, \tag{8.1}$$

assumes both beams to be modeled as simple plane waves with a uniform impact parameter distribution. However, this assumption falls short when beams are strongly focused at the interaction point, since focusing suppresses large impact parameters. Consequently, for the head-on collisions the Bethe-Heitler differential cross section is predominantly "over-sampled" at low impact parameters where the cross-section value is smaller. This results in an effective suppression of the Bethe-Heitler process. This is particularly pronounced at lower photon energies, since typical  $q_{\perp}$  is proportional to  $E_{\gamma}$ .

Relative corrections to the standard Bethe-Heitler cross-sections due to the beam-size effects is shown in Fig. 8.238. The observed suppressed Bethe-Heitler cross-section is related to the Bethe-Heitler cross-section as  $(d\sigma_{\text{obs}}/dy) = (d\sigma_{\text{BH}}/dy) - (d\sigma_{\text{corr}}/dy)$ . It is worth noting that the beam-size effects will be higher at EIC as compared to HERA due to the stronger focused beam evident from the beam-size parameters. In a recent study, the understanding of corrections due to the beam-size effects is proposed to be verified by a precise measurement of the Bethe-Heitler spectra as a function of lateral beam displacements (indirectly the impact parameter) at the interaction point. This will be achieved using Van der Meer scans, commonly performed at hadron colliders. This involves systematically varying the beam positions to find the  $L$  as a function of lateral beam displacement, which can be described by the formula

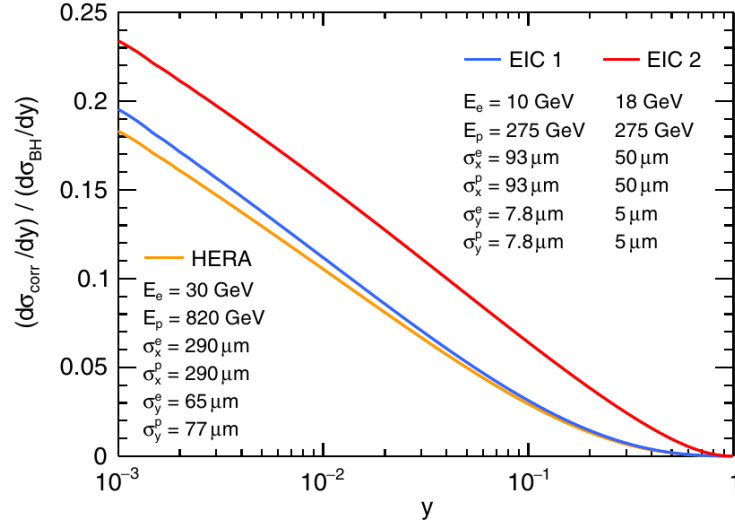


**Figure 8.238:** Relative suppression due to the beam-size effects  $(d\sigma_{\text{corr}}/dy)/(d\sigma_{\text{BH}}/dy)$  is shown as a function of  $y = E_\gamma/E_e$  for three cases of collider parameters, HERA, EIC 1 & EIC 2. The corresponding beam energies and Gaussian lateral beam sizes at the interaction point are listed. Figure from Ref. [?].

$$L(B) = L(0) \exp\left(-\frac{B}{2(\sigma_1^2 + \sigma_2^2)}\right).$$

Here,  $B$  represents the lateral displacement of one of the beams within either the horizontal or vertical plane,  $\sigma_1$  and  $\sigma_2$  are the two Gaussian widths in a given plane, often assumed to be equal, and  $L(0)$  corresponds to the luminosity of nominal, head-on collisions. However, in the case of Bethe-Heitler, its photon spectrum will also be modified in a very specific manner, reflecting the beam size effects.

**Beam Polarisation:** The electron and light ion beams at the EIC will be polarized both longitudinally and transversely. A recent study investigated the impact of longitudinal beam polarisation on the bremsstrahlung cross-section in the low- $Q^2$  region [?]. Calculations revealed that the polarised component is very strongly suppressed compared to the unpolarised component, by a factor of about  $m_e^2/(E_e E_p)$ . Figure 8.239 illustrates the unpolarised component first calculated by Bethe-Heitler, alongside the polarized component. Studies that extend this calculation to transversely polarised beams, including nuclear recoil effects need to also be performed to ensure negligible contributions.

**Bremsstrahlung event rates:** The Bethe-Heitler process is associated with high rates. Table 8.68 shows the  $ep$  bremsstrahlung cross sections in mb (and the corresponding event rates in GHz for the nominal EIC luminosities) for different selection criteria. Taking into account the bunch crossing rates, one gets about 20 photons per bunch crossing, with this number scaling with  $Z^2$  for collisions with heavy ions. These high rates result in significant power deposited in the calorimeter that detects the bremsstrahlung photons. This also means that the counting of bremsstrahlung pho-



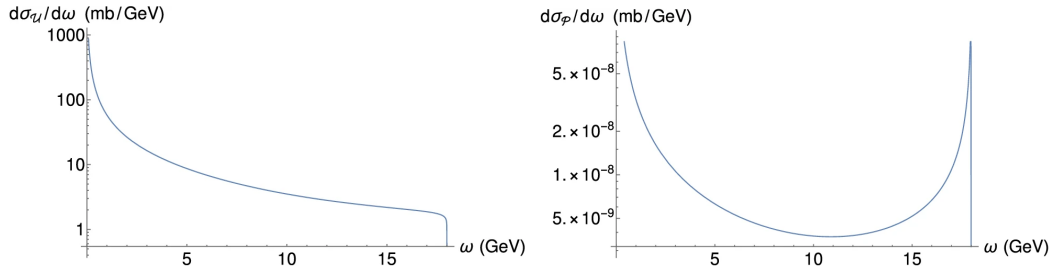


**Figure 8.239:** Unpolarised Bethe-Heitler cross-Section (left panel) and the polarised component (right panel), calculated in Ref. [?]

$E_e$	$E_p$	$E_\gamma/E_e > 0.01$	$1 > E_\gamma/E_e > 0.7$	$0.1 > E_\gamma/E_e > 0.1$
18	275	237 (0.36)	11.6 (0.018)	65.2 (0.10)
10	275	230 (2.3)	11.1 (0.11)	63.2 (0.63)
5	100	209 (0.77)	9.81 (0.036)	57.1 (0.21)

**Table 8.68:** Bethe-Heitler  $ep$  bremsstrahlung cross section in mb (and the corresponding event rates in GHz, for the nominal EIC luminosities), for various beam energies in GeV and three selection criteria. Table from Ref. [?].

tons effectively becomes an energy measurement in the photon calorimeter with all of the related systematic uncertainties (e.g. gain stability).

**Synchrotron radiation:** The magnet which bends the electrons away from the hadron beam-line, serves as an analyzing magnet for forward scattered electrons and is a source of a large synchrotron radiation flux. Synchrotron radiation is emitted at very small angles ( $\sim m_e/E_e$ ) and has a similar angular distribution as bremsstrahlung. This means that the dedicated system for the direct bremsstrahlung photon measurement will be exposed to this synchrotron radiation fan.

**Luminosity monitors at the EIC** The challenging conditions at the EIC dictate a complementary approach to the determination of the luminosity. A method that utilized the pair production from bremsstrahlung photons on a thin converter was also effectively employed at HERA [?]. This indirect approach that utilizes the detection and energy reconstruction of the  $e^+e^-$  pair, results in lower rates, which can be controlled from thin converters and an analyzing magnet. This approach is less sensitive to event pileup and insensitive to synchrotron radiation. This is due to the reduced rates ( $\sim 1\%$ ) from pair production (conversion foil of 1% radiation length) and the placement of the pair spectrometer calorimeters, which will be installed outside the primary synchrotron radiation fan. On the other hand, a detailed knowledge of the detector acceptance and the conversion rate is needed for a precise determination of the luminosity. A direct photon detector, which sits in the direct synchrotron fan, provides a full acceptance of the bremsstrahlung photons but is also exposed to high rates and sensitive to event pileups. At the EIC, the luminosity will be determined using both approaches – direct photon detection (Direct Photon Detector, DPD), and detection of pair-produced photons (Pair Spectrometer Calorimeter, PSCal) – allowing us to reduce the associated systematics.

## Requirements

**Requirements from physics:** An accurate determination of luminosity is essential for addressing the fundamental physics questions that underpin the construction of the Electron-Ion Collider. The Yellow Report specifies the EIC requirements for luminosity determination to be 1% in absolute uncertainty and  $10^{-4}$  in relative luminosity [?]. Proper figure from Physics studies that highlight the requirement.

**Requirements from Radiation Hardness:** The DPD, which is exposed to the direct synchrotron radiation fan and the high bremsstrahlung rates has more stringent requirements than the PSCal, which sits outside the synchrotron radiation fan and only sees  $\sim 1\%$  of the events in the DPD. Geant4 simulations were performed to study the 3D distribution of doses due to bremsstrahlung only, which estimated a maximum annual local dose of about 7 MGy (assuming  $100 \text{ fb}^{-1}$ ). Furthermore, a special ultra-fast synchrotron radiation event generator was developed to simulate hard part of synchrotron radiation spectra ( $E_\gamma > E_{cr}$ ). It was found that for an 18 GeV beam a 35 cm of graphite (which is less than 2 radiation lengths), would be sufficient in shielding the DPD.

**Requirements from Data Rates:** The high cross-section of the Bethe-Heitler process drives the data rate requirements. As discussed above, the DPD will be exposed to high rates of about 20 photons per bunch crossing (at nominal luminosities) for  $ep$  collisions, with the rates scaling with  $Z^2$  for heavy ion collisions. The requirement for the PSCal, is much less stringent as rates are expected to be much lower and can be controlled with the position of the calorimeters, the analyzing magnet, and the converter. The vertical position of the PSCal is as such that it does not affect the acceptance of the DPD (at least  $5\sigma$  of the beam size at the position of the calorimeters).

**Systematic Uncertainties -** Past experience from ZEUS dictate that efforts to reduce/minimize systematic uncertainties in our system are needed. The systematic uncertainty in the ZEUS luminosity measurement at HERA II was 1.7 %, and our goal is to reduce this value to below 1 %. Table 8.69 summarises the main systematic uncertainties that contributed to the ZEUS luminosity determination. In our current design, we ensure we mitigate the largest of these sources with the introduction of trackers for the PS, that would enable an accurate determination of the detector acceptance and beam size effects, and a sweeper magnet that allows us to have more control on the converted pair rates in the PS.

Source	DPD detector (%)	PS detector (%)
Acceptance	1.0	1.0
x-position of photon beam	1.2	1.2
Pair conversion in EW		0.7
RMS Cut Correction		0.5
Pedestal Shifts	1.5	
Pile up	0.5	
Total	2.2	1.8

**Table 8.69:** Summary of systematic uncertainties at ZEUS DPD and PS detector. [?]

7939

**Justification** The detector and beamline component layout for the luminosity system is illustrated in Fig. 8.240. A sweeper magnet is utilized to remove pair conversions primarily from the



**Figure 8.240:** Luminosity system layout showing the Direct Photon Detector and Pair Spectrometer, as well as the sweeper and analyzing magnets.

relatively thick exit window and conversion in air between the exit and sweeper magnet. This reduces the systematic uncertainty related to the photon conversion rate and allows us to control the rate at the PSCal and estimate systematics. A vacuum beam pipe also minimizes photon conversion in air. Converter foils will be located between the analyzing and sweeper magnet. The analyzing magnet bends the  $e^+e^-$  pairs away from the photon beam direction so that they can be detected by the PSCal. A set of trackers (PSTrack) is positioned in front of the PSCal and enables the detailed determination of the detector acceptance as well as the reconstruction of the beam spot profile. The DPD sits just behind the PSCal. Graphite absorbers are placed in front of the DPD to shield the detectors from the low-energy synchrotron radiation. The luminosity system described here would allow us to determine the luminosity at the required precision, minimizing contributions from systematic uncertainties.

**Device concept and technological choice:** Below we provide a description of each detector subsystem and the technology of choice that would enable us to meet all requirements as set above.

#### PSCal Subsystem description:

General device description: The Pair Spectrometer Calorimeters are based on the same technology as the fEMCal, and builds upon R&D studies [References from <https://arxiv.org/html/2408.11075v1> and applied in the sPHENIX experiment [References from <https://arxiv.org/html/2408.11075v1>. The calorimeters are composed of 20 layers, with the fibers oriented in alternate directions – parallel to either the  $x$ -direction or  $y$ -direction in the transverse plane. This alternating orientation and the orientation of the fibers perpendicular to the beam direction aids in reconstructing the shower profile of hits in all three dimensions, thereby enhancing the position resolution of hits and enabling the detection and reconstruction of multi-hit events. This feature becomes more important for the DPD (lower rate) and low- $Q^2$  taggers where multi-hit events are obtained even at low luminosities. Each layer has a thickness of 0.9 cm and a transverse size of  $18.06 \times 18.06 \text{ cm}^2$ . Additionally, the layers are segmented into three modules, each with a width of 6.02 cm. This is illustrated in Fig. 8.241, where the two PSCal are illustrated with their layers and components. The location of the two calorimeters are :Top (0.0, 15.76, -6408.6) and Bottom (0.0, - 15.76, - 6408.6). Each module contains 448 scintillating fibers, grouped in bundles of 16 ( $4 \times 4$ ). All production modules will be identical, and precise mechanical tolerances are ensured by using production molds fabricated to high tolerances.

Sensors: Each bundle of 16 fibers are read out by  $3 \times 3 \text{ mm}$  SiPMs (Hamamatsu S14160-3015PS). Each module is read out by 28 SiPMs providing us with information on the shower profile as a function of depth allowing for position resolution. This additional information allows the reliable reconstruction of multi-hit events.

FEE: A bespoke PCB board that host the 28 SiPM has been designed. Each PCB board provides individual bias to each SiPM and host a temperature sensor for correcting gains. Connectors between this sensor PCB and a bespoke ASIC is implemented. Details on the ASIC will be finalised and provided at a later stage.

Other components: A light-tight enclosure is designed to hold all modules at position and provide support for the PCB and ASICs.

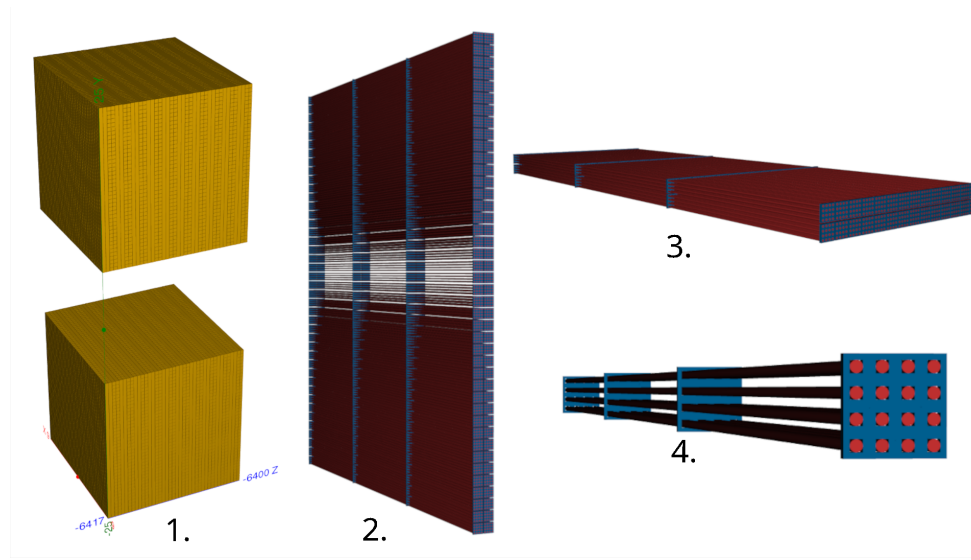


**Figure 8.241:** Pair Spectrometer calorimeters and their components: (1) The two Pair spectrometer calorimeters; (2) one layer, made out of three modules, with the fibers oriented perpendicular to the beam direction (the orientation of the fibers alternate from horizontal to vertical); (3) one module; (4) zoomed-in view of a set of 16 fibers which are read out by a SiPM.

#### 7983 PSTrack Subsystem description:

7984 General device description: Two layers of AC-LGADs with pixelated sensors, for each  
 7985 calorimeter, constitute the Pair spectrometer trackers. The trackers adopt the technology of  
 7986 FTOT trackers and a detailed description can be found in that section. The pitch between the  
 7987 readout pads, set at  $500\ \mu\text{m}$ , is expected to provide approximately  $70\ \mu\text{m}$  position resolution  
 7988 at the detector plane and around  $2\ \text{mm}$  at the vertex (conversion foil).

7989 Current estimations indicate that, in order to achieve acceptance uncertainties below  $1\%$ , the  
 7990 vertex resolution in the dispersive direction must be less than  $6\ \text{mm}$ . With a  $500\ \mu\text{m}$  pitch,  
 7991 the number of readout channels is estimated to be about  $130,000$  per plane. To minimize  
 7992 the number of DAQ channels, the number of pixels in the non-dispersive direction could be  
 7993 combined.

7994 Their location is: Module 1 : Top  $(0.0, 15.76, -6397.6)$  and Bottom  $(0.0, -15.76, -6397.6)$ , and  
 7995 for Module 2 : Top  $(0.0, 15.76, -6407.6)$  and Bottom  $(0.0, -15.76, -6407.6)$ . Their dimensions  
 7996 are  $(18.06, 18.06, 0.044)$ , covering the full front face of the PSCal, with a thickness of around  
 7997  $2\%$  radiation lengths.

7998 Sensors: Sensor, and FEE information for the trackers is provided in the FTOD section.

#### 7999 DPD Subsystem description:

8000 General device description: Details on the DPD will be given by the Krakow group. Two  
 8001 detector systems, one for nominal luminosities and one for low luminosities, will comprise  
 8002 the Direct Photon Detector systems. The low luminosity calorimeter will be of the same  
 8003 technology of the Pair spectrometer, utilizing its capabilities for multi-hit reconstruction.

8004 Sensors: Add text here.  
 8005 FEE: Add text here.  
 8006 Other components: Add text here.

8007 **Performance** The performance of the PSCal has been evaluated and tested using MC simula-  
 8008 tions. These simulations utilized the ePIC DD4HEP framework with the full geometry of the lumi-  
 8009 nosity system, including analyzer and sweeper magnets, in place. The field map for these magnets  
 8010 was also incorporated. Simulations were conducted by generating a bremsstrahlung photon spec-  
 8011 trum, applying beam effects, and then propagating this photon to the conversion foil and convert-  
 8012 ing it utilizing a photon splitting function (see Eq 34.31 of the PDG [?]). Converting the photons in  
 8013 this manner significantly reduces computation times for this simulation.

8014 MC simulations for the PSCal demonstrate that the current design will meet design requirements.  
 8015 Simulations indicate that the design achieves a uniform sampling fraction of  $\sim 2\%$ , as seen in  
 8016 Fig. 8.242. The sampling fraction is defined as the total energy deposited in sensitive elements of the  
 8017 calorimeter divided by the total energy of the incident particle. Figures 8.243 & ?? also demonstrate  
 8018 that energy resolutions of 5 to 8% – stochastic term of 10% – (in the 3 to 18 GeV electron energy  
 8019 range) are also achievable with the current design. The energy resolution is about (stochastic term).

**Figure 8.242:** PSCal sampling fraction as a function of incident electron energy. Events inci-  
 dent on the top or bottom 2cm of the front face of the calorimeter have been excluded in this  
 sample. This selection cut removes events where the full shower is not contained within the  
 calorimeter.

**Figure 8.243:** PSCal energy resolution as a function of generated electron energy. In this  
 study, monoenergetic electrons (at the discrete values shown) were generated at the front face  
 of the calorimeter.

8020 Figure 8.244 shows the expected rates at the Pair spectrometer detector subsystems for different ion  
 8021 and energy combinations. The highest rate of coincidence events, at the highest luminosity runs, is  
 8022 approximately one coincidence event for every ten bunch crossings, or every 100 ns [?], with single  
 8023 hits having slightly higher rates.

8024 The current design, which allows the 3D shower reconstruction allows us to further increase these  
 8025 rates, by reducing the magnetic field of the analyzing magnet while still being able to reconstruct  
 8026 the photon energy spectrum from multi hit events. This additional information allows us to better  
 8027 understand systematic uncertainties and constrain them.

8028 Test beam runs to evaluate the performance of detector electronics and the uniformity of the  
 8029 calorimeter blocks are planned for late 2024/early 2025. Initial testing is planned at the Mainz  
 8030 A2 facility followed by tests in Jefferson Lab Hall D. Testing of individual module responses using  
 8031 cosmic ray data is already underway at the University of York.

8032 The PStrackers are capable of providing very precise position resolution for electron/positron  
 8033 tracks. This exceeds the required position resolution and utilizes technology (AC-LGAD) from  
 8034 other detector subsystems.

8035 Studies that would estimate systematic uncertainties and how the current design meets all require-  
 8036 ments will be provided at a later stage (currently investigated).

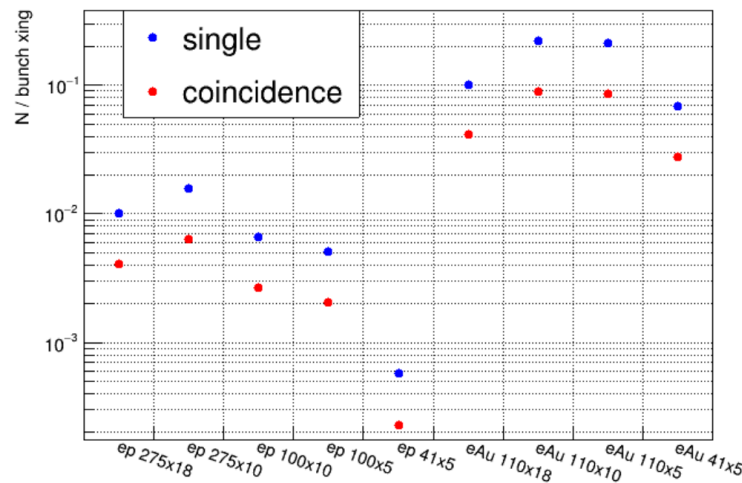


Figure 8.244: Rate of single and coincidence events for the PS detectors.

## Implementation

**Services:** Subsystem services information will be provided at a later stage.

**Subsystem mechanics and integration:** Subsystem mechanics and detector integration is being prototyped and will be provided at a later stage.

**Calibration, alignment and monitoring:** Calibration of the PSCal is required for the accurate determination of the energy of the electron-positron pair and from that the energy of the bremsstrahlung photon. Corrections will have to be made to account for non-uniform SiPM responses to the same photon load, and other irregularities that might arise from the construction of the detector. Whilst initial calibration can be done on individual SiPMs and sections of the detector before installation in the beam enclosure, this will not be sufficient to ensure optimal performance of the detector. Further calibration will have to be carried out in dedicated calibration runs, as well as during regular operation of the machine.

The detectors are to be built in modules or tiles, with sixty of these tiles making up a single detector. Each module will be tested individually using cosmics, allowing for the characterization and correction of non-uniform SiPM responses. SiPMs are grouped in each module based on the operating voltage, and visual inspection will be carried out before their installation. Fibers will also be inspected.

LED benchmark tests will be carried out to characterize the module response before installation and compared with a reference module. These initial tests will be carried out at the University of York. The PSCal will be calibrated using dedicated runs and a tight collimator, allowing us to select electron-positron pairs with a well-defined energy. This can then be used to calibrate the detector response.

In-operation calibration will make use of the bremsstrahlung electron, as well as the photon. This electron will be detected by the low  $Q^2$  taggers, and coincidences between the two systems al-

low us to continuously monitor the detector response. The pointing and position resolution of the PStrackers also allows us to continuously monitor the PSCal detector response and provide continuous calibrations.

#### Status and remaining design effort:

R&D effort: Curr.

E&D status and outlook: Add text here.

Other activity needed for the design completion: Add text here.

Status of maturity of the subsystem: Add text here.

**Environmental, Safety and Health (ES&H) aspects and Quality Assessment (QA planning:** ES&H aspects from construction and use. QA testing - Test beams for uniformity, signal baseline from cosmics at York/BNL?

**Construction and assembly planning:** The construction of the calorimeters for the PS and DPD systems will involve plastic scintillating fibers embedded in a mix of tungsten powder and epoxy, this technique was developed by Prof. Tsai [?]. Fibers will be threaded through four thin brass meshes, which will hold them at even distances apart, shown in Fig. 8.245. The fibers and meshes will be placed in a mould with the meshes separated to form three sections of equal length. Tungsten powder will then be poured into the mould and leveled using weights and a vibrating table to ensure the mould is filled evenly and packed well. Epoxy will then be slowly poured into the mould before the mould and contents are placed into a low-temperature oven to cure the epoxy. A test module, consisting of only tungsten powder and epoxy is shown in Fig. 8.246a, with Fig. 8.246b showing a cross-section of a broken piece. The epoxy permeates well through the module, forming a solid and durable brick. A larger amount of force, applied with a hammer, was needed to produce the piece seen in the figure.

**Figure 8.245:** Multiple fibers threaded through a pair of brass meshes.

(a)

(b)

**Figure 8.246:** (a) Tungsten powder and epoxy-only test module. (b) A section of another test module showing the interior.

**Collaborators and their role, resources and workforce:** The main collaborating institutions for the PS calorimeter are York and Houston. The roles of each institution are outlined below -

- University of York, United Kingdom
  - Design and construction of calorimeters
  - Calorimeter simulation
  - Calorimeter reconstruction and analysis

- 8090           – DAQ and electronics for calorimeter
- 8091       • University of Houston, Texas, USA
- 8092           – Calorimeter simulation
- 8093           – Calorimeter reconstruction software
- 8094           – Calorimeter design support
- 8095       • Tel Aviv University, Israel
- 8096           – Design and integration of PS trackers.
- 8097           – Simulation.

8098 Additional workforce is required for the detailed design of the two magnets, collimators, and exit  
8099 windows, as well as the beam pipe and support structure.

8100 The workforce at each institution comprises -

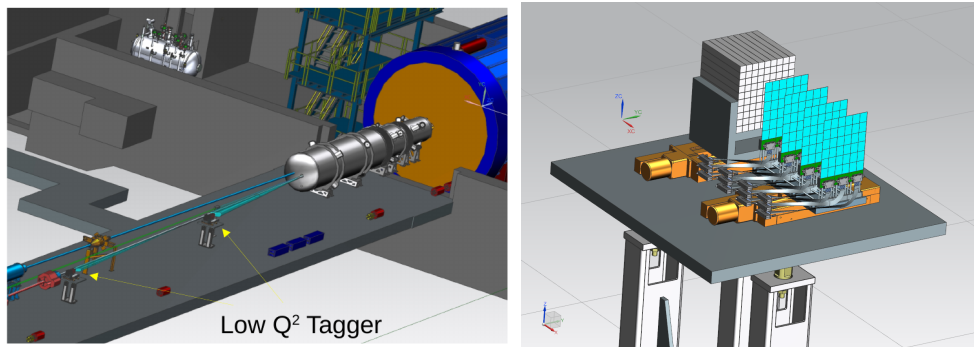
- 8101       • University of York, United Kingdom
- 8102           1. Dan Watts, academic staff (20-25 % FTE)
- 8103           2. Nick Zachariou, academic staff (25-30% FTE)
- 8104           3. Mikhail Bashkanov, academic staff (10-15% FTE)
- 8105           4. Stephen Kay, PDRA (100% FTE)
- 8106           5. Alex Smith, PG Student (100% FTE)
- 8107           6. Pankaj Joshi, academic support staff (5% FTE)
- 8108           7. Julien Bordes, Geant4/simulation support (10-15% FTE)
- 8109           8. Technical Support Staff
- 8110               – Electrical engineer
- 8111               – Mechanical engineer
- 8112               – CAD support
- 8113       • University of Houston, Texas, USA
- 8114           1. Aranya Giri, PG Student (100% FTE)
- 8115       • Tel Aviv University, Israel
- 8116           1. Igor Korover, academic staff (15% FTE)
- 8117           2. Avishay Mizrahi, Mechanical engineer (50% FTE).

8118 **Risks and mitigation strategy:** Add text here.

8119 **Additional Material** Add text here.

### 8120 8.3.8.2 The low $Q^2$ taggers

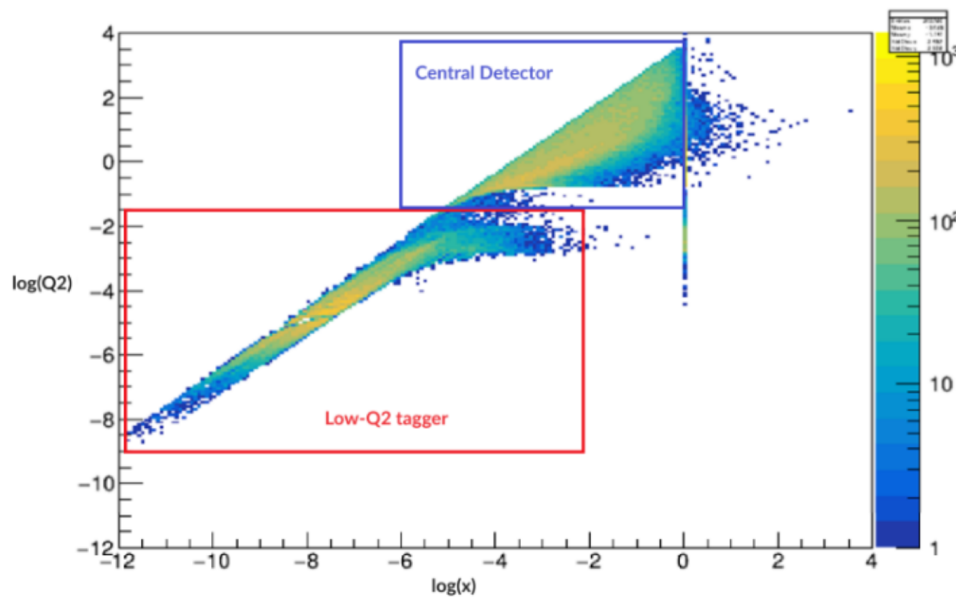
8121 **Requirements** The Low- $Q^2$  Tagger is required to measure the momentum of low-angle scattered  
8122 electrons. The Tagger sits close to the electron beamline and consists of two modules, each with  
8123 silicon trackers and a calorimeter. This is shown in Figure [8.247](#).



**Figure 8.247:** Left: Low- $Q^2$  taggers in relation to beamlines and central detector. Right: Tagger module with calorimeter and tracker from recent CAD model.

**Requirements from physics:** The acceptance for the low- $Q^2$  tagger should complement the central detector to reach the coverage close to the limits given by the divergence of the beam and beamline magnets. Low- $Q^2$  tagger will have one or more stations to cover the maximum momentum acceptance.

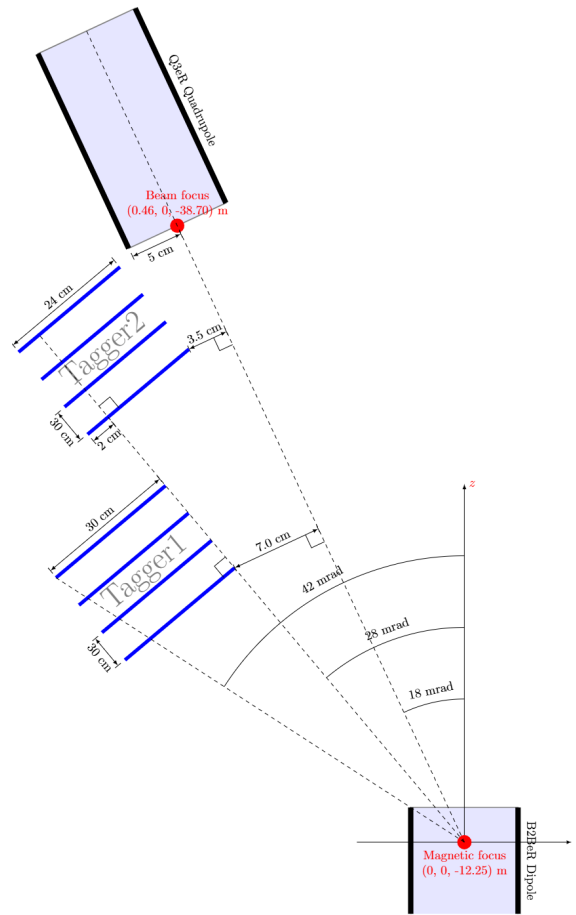
The Low- $Q^2$  tracking system shall have a spatial resolution providing a momentum resolution  $< 5\%$  with  $Q^2$  acceptance between 0 and  $0.1 \text{ GeV}^2$ . The acceptance ranges of the Central Detector and Low- $Q^2$  Trackers as function of  $Q^2$  and Bjorken  $x$  are shown in Figure 8.248, and the positions and angular acceptances of the tracker are illustrated in Figure 8.249.



**Figure 8.248:** Acceptance ranges of the Central Detector and Low- $Q^2$  Trackers as function of  $Q^2$  and  $x$ .

More on resolution here? Too much here on spectroscopy - maybe reduce and more from the ArXiv paper blurb. Or add other sections with other physics titles. I added two.



Figure 8.249: Low- $Q^2$  tagger coverage.

8134 **TCS** Add text

8135 **Vector Meson production** Add text

8136 **Spectroscopy** Reduce - only want to know how it influences the detector requirements.  
 8137 Electron-ion collisions, where the electron is scattered through a very shallow angle, correspond  
 8138 to the case where the exchanged photon is almost real. Such photoproduction processes are of in-  
 8139 terest in their own right, but also can enable a program of hadron spectroscopy. Furthermore, as  
 8140 the virtual photon flux is highest in this region, yields may be relatively high or rare states may be  
 8141 searched for.

8142 A topic of particular interest is the photoproduction of exotic charmonium-like mesonic states.  
 8143 Commonly referred to as XYZ spectroscopy, these states were originally seen in decays containing  
 8144  $J/\psi$  mesons and additional products. Despite there being many missing charmonium states these  
 8145 states do not fit the quark model expectations in terms of numeracy, masses or widths. While the  
 8146  $Z_c^+$  states were manifestly exotic as their charge required additional constituent quarks to a  $c\bar{c}$  pair.

8147 The production cross section of these states is expected to be low, of order 1 nb and branching ratios

to particles that can be detected can also be small. Therefore tagging a large fraction of the virtual photon flux is essential for making measurements of exclusive production of these states. The energy of the tagged photon can be used to determine the reaction invariant mass,  $W$ , and provide exclusivity discrimination when combined with the measured meson state from the central detector and hadron from the far-forward region.

Reconstruction of the azimuthal angle for the electron would provide an effective linearly polarised photon beam, with polarisations up to 1 when the tagger electron energy is close to the beam energy. Reconstructing this angle will be challenging and probably only possible with sufficiently high scattering angles. Provided this information alongside the virtual photon degree of polarisation, which will mainly depend on the measured energy, would allow additional constraints to be used in partial wave analysis of the meson decay allowing the production amplitudes to be determined.

The  $Q^2$  of the scattering is not directly of use for these reactions, however ultimately it can be used to reject bremsstrahlung electrons which would improve the analysis.

Count rate estimates were performed for a number of exotic states in [?] including branching ratio through to detected particles and using the models developed in [?] . To summarise for the charmonium-like XYZ states they are expected to be of the order 1000 per day at luminosities of  $10^{34} \text{cm}^2 \text{s}^{-1}$ , while for double  $J/\psi$  or  $Z_b$  decays there may be 10s per day.

Given just providing evidence of the existence of these states in photoproduction would be a great result, as few of these states have been seen in more than one production mechanism, tagging efficiencies of 10% would be sufficient. However to perform detailed physics studies to determine quantum numbers and production amplitudes, which may provide insight into their exotic nature, or to measure rarer states such as the  $Z_b$ , large data samples would be required.

#### Requirements from Radiation Hardness:

The Low- $Q^2$  trackers are in the far backward region, where the incident flux is predominantly from bremsstrahlung electrons (MIPS). This means there is no requirement for a radiation hard classification for the trackers. However, the intensity is focused on a narrow band in the bend plane (see Figure 8.250), particularly close to the beam line, and trackers should be designed to spread the load by period vertical translation, and exchange of modules.

#### Requirements from Data Rates:

The Low- $Q^2$  system must operate at a full projected EIC luminosity.  
 The Low- $Q^2$  system must operate in extreme background conditions (synchrotron radiation, bremsstrahlung events and beam gas) at the levels specified by the simulation studies.  
 The Low- $Q^2$  trackers shall provide timing resolution sufficient to resolve 10 ns beam buckets.  
 The Low- $Q^2$  tagger will be able to measure the momentum of more than 10 electrons per bunch crossing.

The rate distributions, based on simulation, are illustrated in Figure 8.250. It is clear that the raw rates on the detectors are dominated by bremsstrahlung, with increasing intensity closer to the bend plane, and to the beam line. These results can be used to calculate the integrated data rates for DAQ and storage, and the bottom right plot can be used to estimate the maximum rate which the tracker must be able to handle, in terms of pixel, column, sensor and board. The rates are summarised in Figure 8.251.

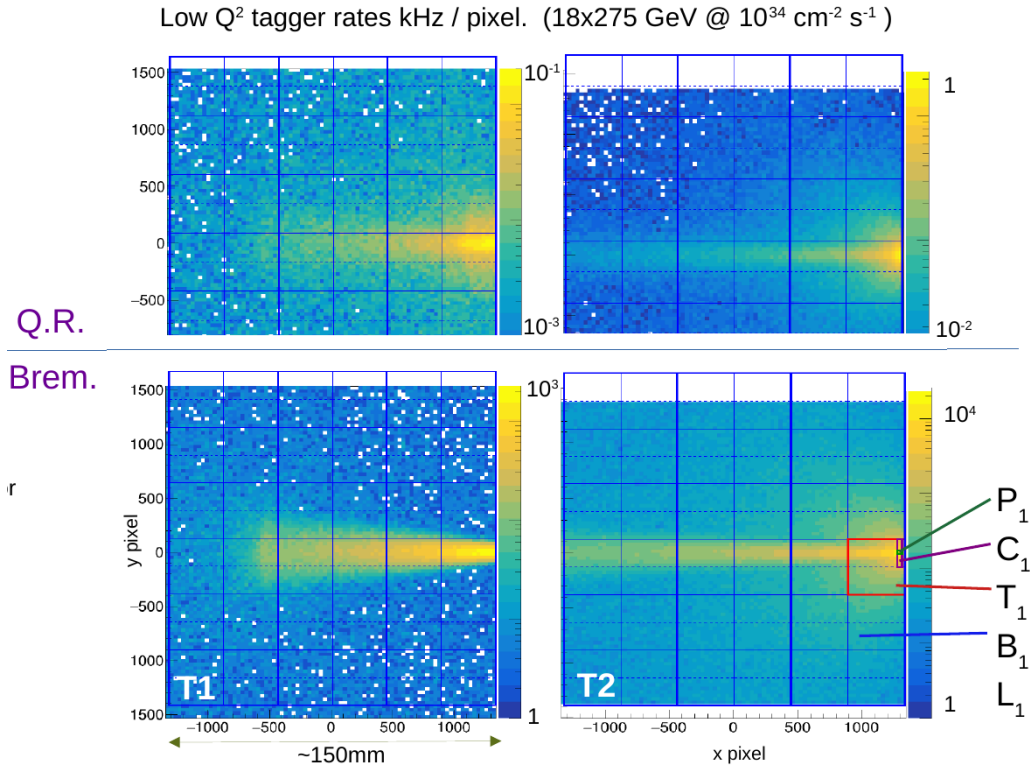


**Figure 8.250:** Hit rates on tracker layers for Quasi Real (Top) and bremsstrahlung (bottom) electrons, incident on Tagger 1 (left) and Tagger 2 (right). This design is based on layers with three carrier boards, each containing twelve Timepix4 hybrid sensors. The dashed lines indicated the centre lines of the Timepix4 ASICs, where the vertical columns terminate.

## Justification

**Device concept and technological choice:** As described above, the Low- $Q^2$  detector will consist of two separate taggers, each with a silicon tracker and a calorimeter. For the trackers, the positions and layer spacing are still to be optimised on the basis of simulations. The essential characteristics are angular resolution (since all other quantities are derived from polar and azimuthal angles), rate capability and background rejection. For pixel detectors, the angular resolutions relate to pixel size, or, more precisely, to the position resolution of the centroids of pixel clusters. From the simulations it is clear that  $55 \mu\text{m}$  pixels (Timepix4 pixel size) would provide very good resolution. Bigger pixels would still provide acceptable resolution, but high segmentation is even more important for rate capability, where the efficiency for separating multiple tracks within a single event needs to be as high as possible: For an electron-proton collision event, at maximum luminosity there are typically ten background bremsstrahlung electrons within the same beam bucket, each passing through all layers of a tagger and creating hits. Furthermore, in each layer there will be *singles* resulting from rescattering, or synchrotron radiation, together with hits from detector noise. However, we already have enough information to set some constraints on detector and readout technologies. We have used Timepix4 as the template for much of the development, and have had its dimensions, readout and rate capabilities as a strong influence in the development of the current design. However, where possible, we used *generic* pixel detectors - particularly in the Geant4

Maximum rates		
Pixel (P1)	70 kHz	
2 column (C1)	8 MHz	
Tpix4 (T1)	600 MHz	38 Gb/s
Board (B1)	1500 MHz	96 Gb/s
Layer (L1)	2500 MHz	160 Gb/s
Total integrated rates		
Tagger 1	2 GHz	130 Gb/s
Tagger 2	7 GHz	480 Gb/s
<b>Total</b>	<b>9 GHz</b>	<b>600 Gb/s</b>
Data buffered & filtered:	need a hadron in main detect	
Trigger rate: 500 kHz:	99.4% rejection (brem only)	
Data rate (signal):	4 Gb/s	
<b>Data rate</b> (incl BG and rand sample)	<b>&lt;20 Gb/s</b> To tape	

**Figure 8.251:** Maximum and integrated rates for Low- $Q^2$  trackers.

simulations, with the aim of being able to evaluate other current, or emerging, technologies.

It is already clear, both from a basic knowledge of the kinematics of bremsstrahlung and quasi-real events, and from preliminary simulations, that the intensity of electrons passing through the trackers will be distributed in a highly non-uniform way, with the bulk of the events close to the plane of the accelerator, and the flux increasing strongly towards the electron beamline. In particular, the rates on Tagger 2 are significantly higher than Tagger 1, with the hottest zone closest to the beamline (Figure 8.251). For an estimate of the relevant rates we focus on the bremsstrahlung distribution in Tagger 2 and superimpose a tracking layer geometry based on three boards, each consisting of 12 Timepix4 hybrids, as shown in Figure 8.250. The six Timepix4 detectors running across the centre of Tagger 2 take the bulk of the events, with the very highest on the one closest to the electron beam (T1). The small vertical offset between the centre of the board and the accelerator plane is to ensure that the centre line (dashed), where the top and bottom vertical 255 pixel columns meet, does not coincide with the very high rate band. The maximum rate estimates can be obtained by integrating over the relevant bins of the 2D histogram, and are shown in Figure 8.251. Although the dimensions of pixels and sensors are from Timepix4, these rates are *detector agnostic*, in the sense that they merely quantify numbers of electrons passing through the  $55\mu\text{m}$  pixels in the tracking plane. After comparison with other technologies with other technologies proposed for the ePIC detector (MAPS, AC-LGAD) it became clear that Timepix4 is the only solution which can provide the required combination of rate capability, timing resolution and position resolution. **The calorimeter ..... paragraph.**

The final configuration and position of the Low- $Q^2$  tagger is still to be decided, since it depends on the position and structure of the magnets and beamline configuration in the backward regions. These are not yet finalised.

#### Subsystem description Tracker :

There are two trackers, each consisting of four layers on pixel sensors. The sensors are mounted on carrier boards (12 sensors per board) which connect to a readout modules. Read-

8235 out modules perform some presorting and pass data to cluster and tracking modules and  
 8236 data buffers. Tracks which are in coincidence with a hadron in the central detector are saved  
 8237 in the main DAQ readout.

8238 Sensors: Timepix4 ASIC with Silicon sensor.

8239 FEE: SPIDR4 readout to custom FPGA clustering and tracking modules.

8240 Other components: Frame / infrastructure with cabling and cooling for layers with remov-  
 8241 able carrier boards. Cabling from boards to readout modules (housed below on platform).

8242 **Subsystem description Calorimeter:** Main purpose of the calorimeter is direct energy mea-  
 8243 surement for cross check with energy obtained from trackers, where it is measured indirectly via  
 8244 ML methods. Also alignment and fake-track reduction will benefit from the use of the calorimeter.

8245 General device description: In the initial running at lower luminosity when in-bunch pileup  
 8246 from Bethe-Heitler bremsstrahlung is relatively small it is assumed to share the same technol-  
 8247 ogy as luminosity pair spectrometer, i.e. scintillating fibers embedded in tungsten-powder  
 8248 epoxy (SciFi), read-out by SiPMs. General layout of the SciFi calorimeter is indicated in  
 8249 Fig. 8.252, giving tower arrangement of 4 layers. Total perpendicular size is given by the  
 8250 trackers. The towers are arranged perpendicular to shower axis. Fibers inner radius is  
 8251 0.25 mm, fiber spacing is 1 mm. Optical photons are detected by SiPMs, shown as yellow  
 8252 rings at the end of each fiber. It is assumed that groups of 4x4 fibers in the same cell act as  
 8253 a single SiPM. Opposite ends of the fibers are ended by aluminum mirrors, shown as green  
 8254 caps.

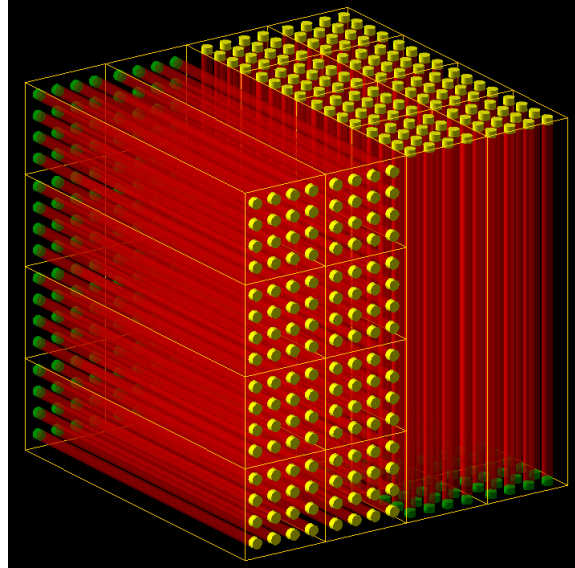


**Figure 8.252:** Layout of SciFi calorimeter.

8255 For the case of nominal collider luminosity, reached in later runs, the in-bunch pileup from  
 8256 Bethe-Heitler bremsstrahlung will cause calorimeter rates to reach bunch crossing frequency,  
 8257 giving some signal every 10 ns at top luminosity for 10x100 GeV beams. Calorimeter tech-  
 8258 nology will be shared with luminosity direct photon detector, where only Cherenkov fibers  
 8259 can fulfill the rate requirement. Expected energy resolution is shown in Fig. 8.253

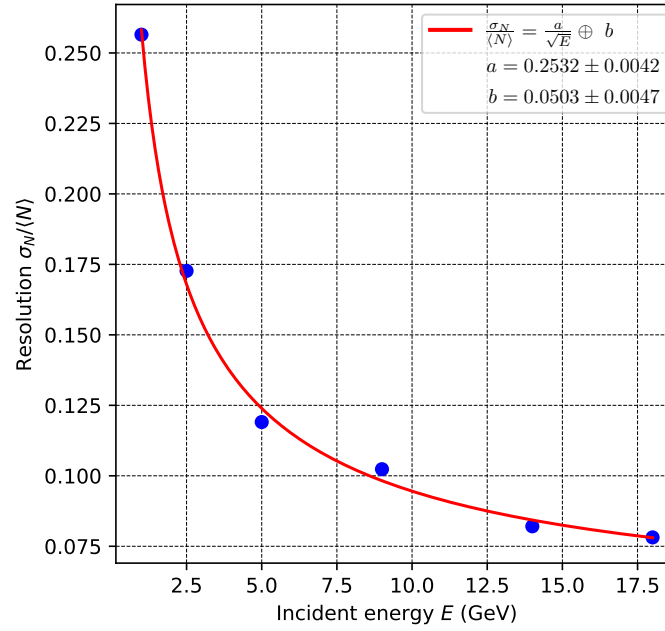


**Figure 8.253:** Energy resolution for Cherenkov fiber calorimeter.

8260 Diameter for quartz fibers 1.5 mm, fiber spacing is 2.5 mm. The resolution is mainly driven  
 8261 by limited Cherenkov photon yields. Photon detection efficiency of 0.41 is included.

8262 Sensors: SiPM, specific SiPM with fast capacitive coupling is required for nominal luminosity,  
 8263 possible example is Onsemi 30035 series.

8264 FEE: fADC250 (flash ADC, 250 MSPS, 12 bit) for nominal luminosity

8265 Other components: Add text here.

8266 **Performance** Figures 8.254, 8.255 and 8.256 show the performance of the Trackers based on cur-  
 8267 rent simulation.

8268 **Implementation**

8269 **Services:** No special services.

8270 **Subsystem mechanics and integration:** The taggers are housed on platforms which need to  
 8271 be movable in vertical and horizontal (towards beamline) directions. Lower platform for readout  
 8272 modules in close proximity for readout modules. Bias and LV per board (24 total). Chiller (800W)  
 8273 per tagger.

8274 **Calibration, alignment and monitoring:** Procedures for calibration and equalisation of indi-  
 8275 vidual sensors are already well established within the Medipix collaboration. These will be mapped

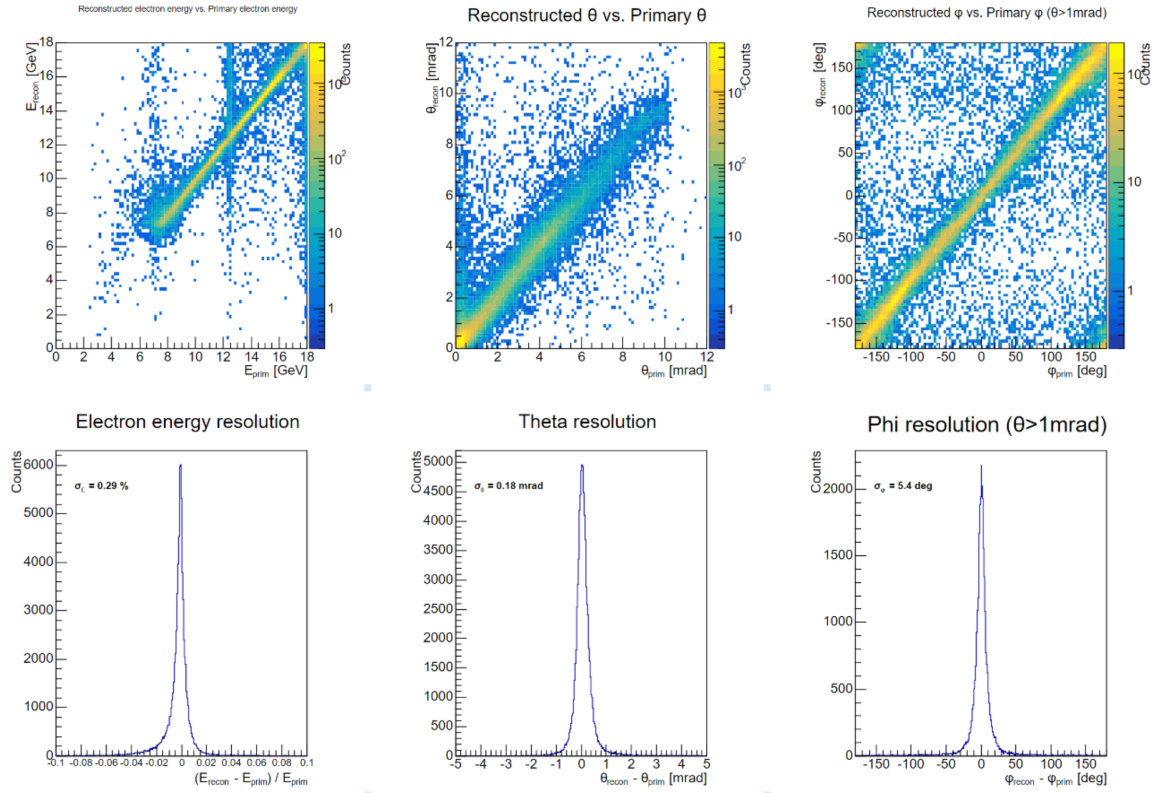


**Figure 8.254:** Top - Reconstruction of the initial electron energy,  $\theta$  and  $\phi$  angles from fitted tracks. Bottom - Integrated reconstruction difference.

8276 to a dedicated Slow Controls interface for the tracker. Alignment and timing calibrations require  
 8277 tracks; they can be developed locally using cosmic rays and more rigorously tested in beam at Jlab  
 8278 or one of the European facilities.

#### 8279 Status and remaining design effort:

8280 **More a total effort not just R&D**

8281 R&D effort:

8282 Electron tracker

8283 Total expected from UK Infrastructure project in FTE years:

8284 Academic 1.5

8285 Senior Researchers 2.5

8286 Postdocs 10.0

8287 Technical 3.0

8288 PhDs 10

8289 Additional Requirement: Postdoc 6 FTE Years

8290

8291 R&D status and outlook:

8292 Electron tracker:



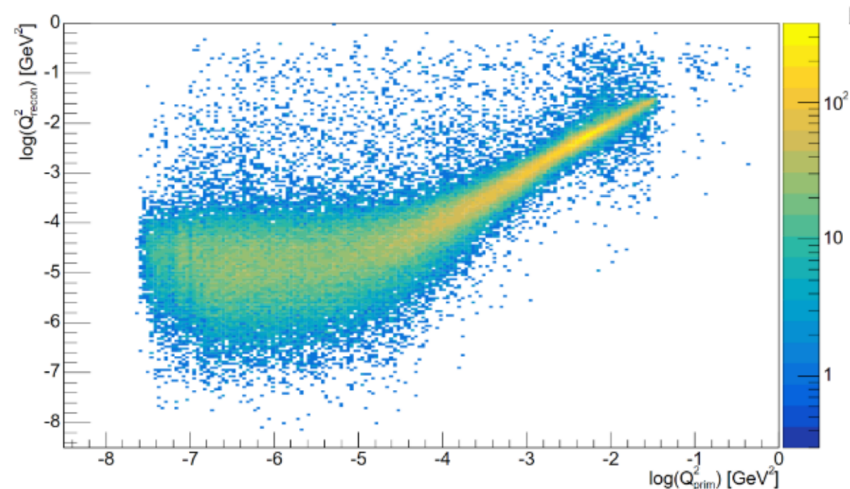


**Figure 8.255:** Reconstruction of the initial electron as a function of  $Q^2$ .

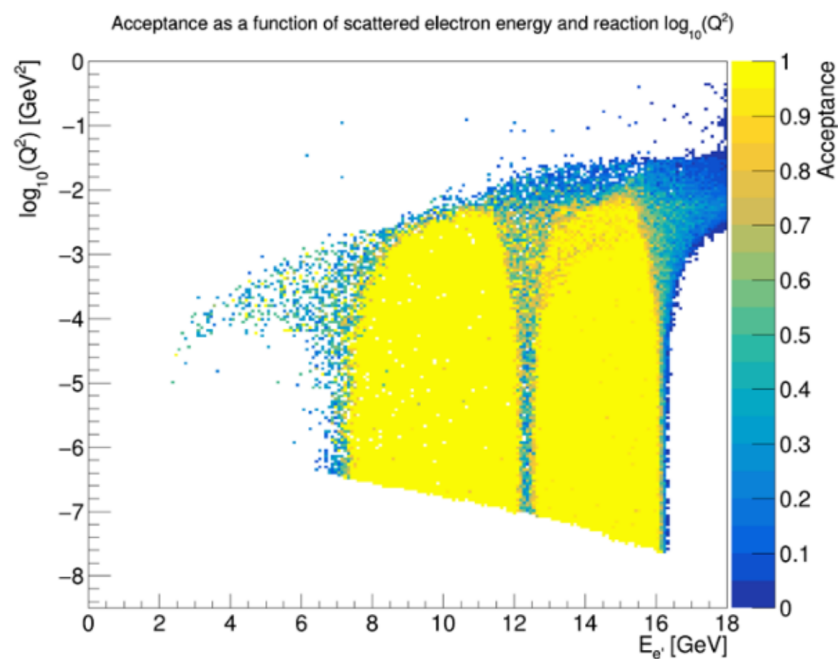


**Figure 8.256:** Acceptance as a function of  $Q^2$  and  $E_{e'}$ .

8293 A test rig with SPIDR4 and Timepix4+Si sensors is complete, and fast readout tested. The  
 8294 development of prototype tracker with single sensor layers in progress. To be tested in stand-  
 8295 alone mode in Mainz, Dec24, with a further test using preliminary ePIC DAQ at Jlab in  
 8296 2026. Carrier board for 12 x Timepix4 sensors to be developed and approved by Dec 2027.  
 8297 Procurement and fabrication of layers from Jan 2028 - 2030. Completion of taggers including

8298 mechanical infrastructure, cooling, readout to be completed in Glasgow by Dec 2030 with  
8299 delivery to BNL Jan 31.

8300 Other activity needed for the design completion  
8301 Final decision on positioning, layer dimensions and spacing is still to be made. The requires  
8302 completion of designs for magnets, beamline and vacuum windows in the backward region.

8303 Status of maturity of the subsystem:

8304 Electron tracker

8305 The Timepix4 sensor is well established, and is the latest in a series of detectors by the CERN  
8306 Medipix collaboration. Current applications used the wire-bonded readout mode, but the  
8307 TSV (through silicon vias) mode is in fast development, and we anticipate having a test setup  
8308 within the next few months. The TSV mode is required to allow 4-side buttability, and fabri-  
8309 cation of the layers with no dead space. The current readout uses SPIDR4 from the NIKHEF  
8310 group in Amsterdam. We will collaborate with the developers to make an upgraded version  
8311 of their carrier boards and readout to handle the data from the 12 sensor layer modules.

8312 **Environmental, Safety and Health (ES&H) aspects and Quality Assessment (QA plan-**  
8313 **ning:** We will follow all procedures laid out by BNL and other labs where production test and  
8314 development are carried out. During the engineering design phase, we will include production of  
8315 mockups and engineering test articles to insure the proper functionality and quality, and will have  
8316 full production chain tests for each sub-system.

8317 For operation with HV and cooling we will ensure that these are mechanically secure and not a  
8318 trip hazard, have proper warning signs and follow the lab procedures for electrical safety, and  
8319 for operation near the beam-pipe and vacuum, anyone working near the far-forward/backward  
8320 detectors will wear ear protection, and will post signage to that effect.

8321 **Construction and assembly planning:** The tracker modules will be constructed assembled  
8322 and tested in Glasgow as Work Package 2 (WP2) of the UK's EIC Infrastructure project. We will  
8323 follow closely the fabrication and quality control procedures developed for the LHCb Velopix and  
8324 ATLAS ITK detectors by the Glasgow experimental particle physics group.

8325 **Collaborators and their role, resources and workforce:** The electron trackers are a *deliver-*  
8326 *able* within the UK's EIC Infrastructure project. The resources for constructing and delivering the  
8327 trackers are expected to be mostly met by this. However, the project is still to be passed through a  
8328 peer review panel and the costings for the tracker work package officially approved. As outlined  
8329 above, we anticipate that we need and additional 6 FTE postdoc years for simulation, analysis and  
8330 thermal modelling relating to detector development.

8331 **Risks and mitigation strategy:** The Timepix4 tracker is being developed in close collaboration  
8332 with colleagues in the Medipix collaboration. We will use suppliers and services recommended  
8333 by them for wafers and production. For local production, fabrication and testing we have a team  
8334 trained in bonding and quality control in case of staff changes. Our maximum rates have been  
8335 calculated on the basis of EIC maximum proton luminosities, so in the initial running we will be  
8336 well below capacity.

8337 **Additional Material** Add text here.

### 8.3.9 Polarimeters

Add text here.

#### 8.3.9.1 The electron polarimeters

The electron polarization will be measured in two locations in the EIC accelerator complex. The first polarimeter will be in the Rapid Cycling Synchrotron (RCS) and will be primarily used for setup of the accelerator, and hence has rather modest performance requirements. The second will be in the Electron Storage Ring (ESR), near the ePIC detector. The performance requirements for this polarimeter are more challenging. Both systems will employ Compton backscattering and will be described in the following sections.

#### Requirements

**Requirements from physics:** The measurements made using the ePIC detector will require high precision, non-destructive measurement of the electron beam polarization. In particular the, Compton polarimeter in the ESR will measure the electron beam polarization with systematic uncertainty of  $dP/P < 1\%$ . This implies that the measurement must be made for each electron bunch in the ring individually (since the polarization can vary bunch-to-bunch) and that the polarimeter must measure both the longitudinal ( $P_L$ ) and transverse ( $P_T$ ) components of the beam polarization (since the polarimeter cannot be located between the spin rotators due to space constraints). Due to the short amount of time that bunches will be stored in the ESR at the highest energy, the system must also be able to make polarization measurements of a single bunch within  $\approx 2$  minutes. The need to measure the polarization bunch-by-bunch, also places challenging requirements for the detector and electronics response time due to the small time (10 ns) between bunches at 5 and 10 GeV.

The primary purpose of the RCS polarimeter will be to monitor the evolution of the electron polarization between the electron source (which injects electron bunches into the RCS) between the injection energy of 750 MeV and the ESR energies of 5, 10, or 18 GeV. The required absolute systematic uncertainty requirements are less challenging ( $dP/P < 2 - 3\%$ ) and the measurement need not be made for each bunch separately. In addition, since bunches are injected into the RCS at 1-2 Hz, the detector rate requirements are much easier to meet.

**Requirements from Radiation Hardness:** Add text here.

**Requirements from Particle Flow:** Add text here.

#### Justification

**Device concept and technological choice:** Add text here.

**8370 Subsystem description:**

8371       General device description: Add text here.

8372       Sensors: Add text here.

8373       FEE: Add text here.

8374       Other components: Add text here.

**8375 Performance****8376 Implementation**

8377 **Services:** Add text here.

8378 **Subsystem mechanics and integration:** Add text here.

8379 **Calibration, alignment and monitoring:** Add text here.

**8380 Status and remaining design effort:**

8381       R&D effort: Add text here.

8382       E&D status and outlook: Add text here.

8383       Other activity needed for the design completion: Add text here.

8384       Status of maturity of the subsystem: Add text here.

8385 **Environmental, Safety and Health (ES&H) aspects:** Add text here.

8386 **and Quality Assessment (QA), Construction and assembly planning:** Add text here.

8387 **Collaborators and their role, resources and workforce:** Add text here.

8388 **Technological Challenges and Path Forward:** Add text here.

**8389 8.3.9.2 The proton polarimeters****8390 Requirements**

8391 **Requirements from physics:** Add text here.

8392 **Requirements from Radiation Hardness:** Add text here.

8393 **Requirements from particle Flow:** Add text here.

8394 **Justification**

8395 **Device concept and technological choice:** Add text here.

8396 **Subsystem description:**

8397       General device description: Add text here.

8398       Sensors: Add text here.

8399       FEE: Add text here.

8400       Other components: Add text here.

8401 **Performance**

8402 **Implementation**

8403 **Services:** Add text here.

8404 **Subsystem mechanics and integration:** Add text here.

8405 **Calibration, alignment and monitoring:** Add text here.

8406 **Status and remaining design effort:**

8407       R&D effort: Add text here.

8408       E&D status and outlook: Add text here.

8409       Other activity needed for the design completion: Add text here.

8410       Status of maturity of the subsystem: Add text here.

8411 **Environmental, Safety:** Add text here.

8412 **Quality Assessment (QA), Construction and assembly planning:** Add text here.

8413 **Collaborators and their role, resources and workforce:** Add text here.

8414 **Technological Challenges and Path Forward:** Add text here.

## 8415 **8.3.10 Readout Electronics and Data Acquisition**

### 8416 **8.3.10.1 Requirements**

8417 The electronics and data acquisition systems are required to digitize and readout the data provided  
8418 by the sensors of all ePIC detectors. The electronics must tag hits with a time resolution sufficient to  
8419 identify the bunch crossing (10.16 ns) and provide high resolution time reference. The most strin-  
8420 gent timing requirement is 5 ps of clock jitter in order to meet the 25 ps overall timing requirement  
8421 for the forward TOF (see section 8.3.4.1). The readout system must provide high data volume links  
8422 to read data from the front end electronics up to 10 Gb/s for selected components. The readout  
8423 system must provide very high live times, with the goal of zero system-wide downtime in normal  
8424 operation, despite the possibility of by-channel downtime according to the specific readout technology  
8425 of each detector.

8426 The Data Acquisition will group streaming data into time frames of  $O(600\text{ ns})$ . The readout systems  
8427 are expected to digitize up to  $O(2\text{ Tb/s})$  and must be capable of reducing this data volume to an  
8428 output rate of  $O(100\text{ Gb/s})$  using techniques to compress signal and remove noise with minimal  
8429 impact to signal integrity. The data from all running detectors for each time frame will be gathered  
8430 together in a single buffer for transfer to the Echelon 1 computing facilities located at BNL and  
8431 JLAB for archive and analysis.

8432 **8.3.10.1.1 Requirements from Physics** The requirement for the ePIC readout system is to  
8433 successfully collect data at the Electron Ion Collider for physics analysis. In turn, the expected  
8434 performance and mode of operations of the collider impact the design of the readout system. The  
8435 collision and background rates are detailed in section 8.2.2. The maximum event rates are expected  
8436 to be as high as 500 kHz for DIS, 3.2 MHz for electron beam gas, and 32 kHz for hadron beam gas.  
8437 These rates are of primary interest within DAQ to estimate the data volumes and will be discussed  
8438 in section 8.3.10.1.3.

8439 A second consideration is that individual bunch crossings can have different polarization states.  
8440 This implies that the luminosity and polarization of the beams must be tracked by bunch and  
8441 produces the requirement that events must be associated to the bunch crossing from which they  
8442 originated.

8443 Each ePIC detector has its readout organized into Front-End Boards (FEB) hosting ASICs to pro-  
8444 vide digitization, Read-Out Boards (RDO) providing aggregation and transmission of FEB data to  
8445 the central DAQ system, and Data Aggregator and Manipulation Boards (DAM) (This scheme is  
8446 further detailed later in section 8.3.10.2, see Figure 8.260). The scale and technology of the different  
8447 ePIC detectors is summarized in Tables 8.257 and 8.258, where the large channel counts combined  
8448 with low occupancy lead to the need for multiple levels of aggregation.

8449 **8.3.10.1.2 Requirements from Radiation Hardness** The electronics installed in the ePIC  
8450 detector will be subjected to significant radiation doses. Radiation doses are described in section  
8451 8.2.2. Electronics placed in the central detector (SVT, eTOF, bTOF, and MPGDs) will utilize radiation  
8452 hard components to minimize the effect of radiation.

8453 Electronics must be chosen and placed to minimize failure rates. The electronics must be tested

Detector System	Channels	ASIC	FEB	RDO	Gb/s (RDO)	Gb/s (Tape)	DAM Boards	Readout Technology	Notes
Si Tracking: Inner Barrel (IB) Outer Barrel (OB) Backward Disks (BE) Forward Disks (FE)	1.8B Pixels 5.0B Pixels 4.7B Pixels 4.7B Pixels	160 495 462 462	592* 1870* 1744* 1744*	24 55 52 52	2.36 3.52 4.68 4.68	2.36 3.52 4.68 4.68	1 2 2 2	ITS-3 sensors & ITS-2 staves / w improvements	ASIC corresponds to VTRX+ counts FEB corresponds to detector fiber RDO is off detector Fiber aggregator
MPGD tracking: Electron Endcap Hadron Endcap Inner Barrel Outer Barrel	16,384 16,384 32,768 98,304	256 256 512 1536	64 64 128 384	16 16 32 96	2.86 4.01 4.10 15.81	0.58 0.80 0.82 3.16	1 1 1 2	uRWELL / SALSA uRWELL / SALSA MicroMegs / SALSA uRWELL / SALSA	VTRX+ based FEB
Forward Calorimeters: LFHCAL 8K HCAL Insert ECAL W/SciFi 18,320 HCAL 1,536 ECAL SciFi/PB 5,760 ECAL ASTROPiX 500M pixels 3,256 Backward Calorimeters: NHCAL 2,852 ECAL (PWO)	63,280 8K 18,320 1,536 5,760 500M pixels 3,256 2,852	1130 142 142 28 102 58 102	1130 142 574 28 102 58 102	74 9 72 2 4 340 13	18.54 17.72 14.75 0.87 11.45 1.25 3.46 2.00	2.47 2.36 7.36 0.12 1.52 1.25 0.47 0.99	2 1 2 1 1 8 1 1	SIPM / CALOROC SIPM / CALOROC SIPM / Discrete SIPM / CALOROC SIPM / CALOROC Astropix SIPM / CALOROC SIPM / Discrete	CALOROC: 56 Ch/CALOROC 16 CALOROC / RDO  Discrete: 32 Ch/FEB, 8 FEB/RDO conservative (16 estimate).
Far Forward: B0: Crystal Calorimeter 4 AC-LGAD layer 2 Roman Pots 2 Off Momentum ZDC: Crystal Calorimeter HCAL	135 688,128 524,288 294,912 900 9,216	672 512 288 165	5 168 128 72 30 165	1 42 32 18 4 11	2.3 12.75 14.53 3.53 2.30 0.22	2.3 2.1 2.1 0.7 4.5 -22	1 1 1 1 1 1	SIPM/APD / Discrete AC-LGAD / EICROC AC-LGAD / EICROC AC-LGAD / EICROC SIPM/APD / Discrete CALOROC	4 layer x 42 module x 4 EICROC x 1024 ch 2 stations x 2 layer x 32 module x 4 EICROC x 1024 ch 2 stations x 2 layer x 18 module x 4 EICROC x 1024 ch
Far Backward: 2 x Low Q Tagger 2 x Low Q Tagger Cal 2 x Lumi PS Calorimeter 2 x Lumi PS tracker Direct Photon Lumi Cal	66M pixels 420 3,360 128k 100	3456 672 512 288 1000	288 168 128 72 250 24	24 1 1 64 24*	37 - 19 45 200	.3 - 7 2 7	10 1 1 2 1	Timepix4 SIPM / CALOROC SIPM / Discrete AC-LGAD: FCDF or EICROC SIPM / ADC250	Firmware Trigger to reduce output rate Low Q Calorimeter doesn't run at high luminosity  Direct Photon: commercial digitizer, no RDO
PID-TOF: Barrel Endcap	2,359,296 3,719,168	18,432 3,632	288 212	288 212	15.95 33.92	4.79 7.34	8 6	AC-LGAD: FCDF or EICROC AC-LGAD: EICROC	bTOF 128 ch/ASIC, 64 ASIC/RDO eTOF 1024 pixel/ASIC, up to 28 ASIC/RDO
PID-Cherenkov: dRICH pRICH DIRC	317,952 69,632 73,728	4968 544 576	4968 68 144	1242 17 24	1240 24 11	13.5 12.5 6	30 1 1	SIPM / ALCOR HRPPD / FCDF or EICROC MCP-PMT / FCDF or EICROC	Worse case after radiation. Includes 30% timing window. Requires further data volume reduction Firmware trigger

Figure 8.257: ePIC DAQ component counts



Detector Group	Channels					Det Fiber Down	Det Fiber Up	RDO	Fiber Pair (DAQ)	DAM	Data Volume (RDO) (Gb/s)	Data Volume (To Tape) (Gb/s)
	MAPS	AC-LGAD	SIPM/PMT	MPGD	HRPPD/MCP-PMT							
Tracking (MAPS)	16B					183	5863	183	183	7	15	15
Tracking (MPGD)				164k		640	2560	160	160	5	27	5
Calorimeters	500M		100k					522	522	17	70	17
Far Forward		1.5M	10k					80	80	6	36	12
Far Backward	66M	128k	4k					60	82	14	301	16
PID (TOF)		6.1M				500	1364	500	500	14	50	12
PID Cherenkov			318k		143k			1283	1283	32	1275	32
<b>TOTAL</b>	<b>16.6B</b>	<b>7.7M</b>	<b>432k</b>	<b>164k</b>	<b>143k</b>	<b>843</b>	<b>9,787</b>	<b>2,788</b>	<b>2,810</b>	<b>95</b>	<b>1,774</b>	<b>109</b>

Figure 8.258: ePIC DAQ component count summary

Detector	Channel Max Hit Rate (Hz)	Noise To RDO (gbps)	Noise Per RDO (gbps)	Noise To Tape (gbps)	RDO (max) (gbps)	RDO_max / with Noise (gbps)
SiBarrelTracker	4.13E-04	3.25	0.06	3.25	0.00	0.06
SiBarrelVertex	5.22E-03	1.15	0.05	1.15	0.17	0.21
SiEndcapTracker	2.78E-03	6.02	0.06	6.02	0.23	0.29
BackwardMPGDEndcap	2.19E+02	1.74	0.11	0.35	0.42	0.52
ForwardMPGDEndcap	4.44E+02	1.74	0.11	0.35	0.86	0.97
MPGDBarrel	8.67E+01	3.26	0.10	0.65	0.04	0.14
OuterMPGDBarrel	1.29E+01	15.23	0.16	3.05	0.01	0.17
LFHCAL	2.10E+04	10.33	0.14	1.38	1.30	1.44
HcalEndcapPInsert	6.18E+04	1.31	0.15	0.17	2.78	2.93
EcalEndcapP	1.51E+05	0.78	0.01	0.35	2.69	2.70
HCcalEndcapN	7.81E+04	0.53	0.13	0.07	2.64	2.77
EcalEndcapN	8.07E+04	0.14	0.01	0.06	1.06	1.07
HcalBarrel	1.30E+03	0.25	0.13	0.03	0.08	0.21
EcalBarrelImaging	2.92E-02	0.32	0.00	0.32	0.01	0.01
EcalBarrelSciFi	1.52E+03	0.94	0.07	0.13	2.69	2.76
TOFBarrel	1.74E+00	13.59	0.05	4.53	0.01	0.06
TOFEndcap	8.34E-01	32.13	0.15	7.14	0.07	0.22
hpDIRC	2.35E+02	3.22	0.13	1.07	0.00	0.13
pfrICH	4.99E+02	3.05	0.18	1.02	0.00	0.18
dRICH	1.09E+02	1220.94	0.98	6.10	0.00	0.98
B0 Crystal Calorimeter	2.66E+05	0.00	0.00	0.00	0.00	0.00
B0 AC-LGAD	1.72E+01	5.95	0.20	1.32	0.00	0.20
RP	3.31E+01	4.53	0.21	1.01	0.00	0.21
OM	5.93E+00	2.53	0.21	0.56	0.00	0.21
ZDC Crystal Calorimeter	7.81E+04	0.02	0.00	0.02	0.00	0.00
ZDC HCAL	3.39E+01	0.20	0.02	0.20	0.00	0.02
DirectPhoton	2.00E+08	0.00	0.00	0.00	0.00	0.00
LowQ2Tracker	8.76E+00	0.04	0.00	0.04	0.00	0.00
LowQ2Calorimeter	0.00E+00	0.01	0.01	0.01	0.00	0.01
PairSpectrometerTracker	2.44E+02	0.74	0.07	0.25	0.00	0.07
PairSpectrometerCalorimeter	3.26E+04	0.07	0.07	0.07	0.00	0.07
Total		1334.01		40.67		

Figure 8.259: Maximum data volume per RDO with noise estimates by detector. (Data Rate evaluation: <https://github.com/jml985/epicJTools>)

8454 against Single Event Latchup and the power system must have built-in protection mechanisms  
8455 against latchup. There are commercial IP cores available for FPGAs that can support recovery from  
8456 single event upsets (SEUs). Transient failures due to radiation remain possible, so automatic failure  
8457 sensing must be implemented to allow recovery procedures such as automated reset and reload for  
8458 FEBs and RDOs.

Detector	Noise (Hz/channel)
ITS3, ASTROPIX, TIMEPIX	0.01
AC-LGAD	30
HRPPD	230
dRICH(initial)	3000
dRICH(Max)	300,000
All Others	$4.5\sigma = 340$

Table 8.70: Noise Estimates

	Noise (Gb/sec)	Synchrotron Radiation (Gb/sec)	Electron Beam Gas (Gb/sec)	Proton Beam Gas (Gb/sec)	Collision Signal (Gb/sec)	Aggregate (Gb/sec)
Digitized	1,600	tbd	48	40	530	2220
To Tape	32	tbd	4.5	1.0	62	109

Table 8.71: Expected worse case data rate contributions for the ePIC detector. (<https://github.com/jml985/epicJTools>)

**8.3.10.1.3 Requirements from Data Rates** The triggerless readout of the ePIC detector uses zero-suppression to help manage the volume of data read out. The streaming model's sensitivity to noise, beam background, and collision data make the understanding of these effects critical. Collision, synchrotron radiation and beam gas backgrounds from both the electron and hadron beams have been studied extensively by the ePIC collaboration, and the methods are presented in section 8.2.2. The hits have been converted to data volumes using our current understanding of zero suppression and data formats of each detector readout. Furthermore, the distribution of hits to each component has been estimated by arbitrarily assigning readout components to the sensitive planes of the detectors in order to estimate the impact of potential bottlenecks.

The hit rate for the collision signal is taken from simulated hits for DIS events generated by the ePIC physics and detector simulations. The simulated data set was taken for 18x275 GeV collisions with  $Q^2 > 0$  with luminosity  $1.54 \times 10^{33} \text{ cm}^2\text{s}^{-1}$ . The hit rates were scaled to the maximum rate of the EIC collider of 500kHz. Hadron and electron beam gas events were generated using the simulated vacuum profile after 10,000 Ah of pumping.

Noise calculations are currently based on the ePIC detector group expert estimates and shown in table 8.70. Generally, the noise level can be controlled with thresholds. The thresholds for each detector will be set according to the physics requirements as balanced against bandwidth limitations.

One additional factor that must be considered is dark currents in the SiPM detectors which increase with radiation damage. In particular, this issue affects the dRICH, in which the SiPM threshold must remain low enough to be sensitive to single photons. There are several features planned to reduce these dark currents including annealing, and implementation of timing windows to synchronise readout with collision times. These are described in section 8.3.4.4. The DAQ system must be designed with the capability to manage the highest rates expected by the dRICH and must also apply filters to reduce the dRICH noise, either by applying high level selection criteria or by using specialized AI algorithms to determine which hits correspond to a dRICH physics signal.

The expected maximum data contributions of data digitized and stored to tape are summarized in table 8.71. The data volume expected, including collisions, background and noise for the worse

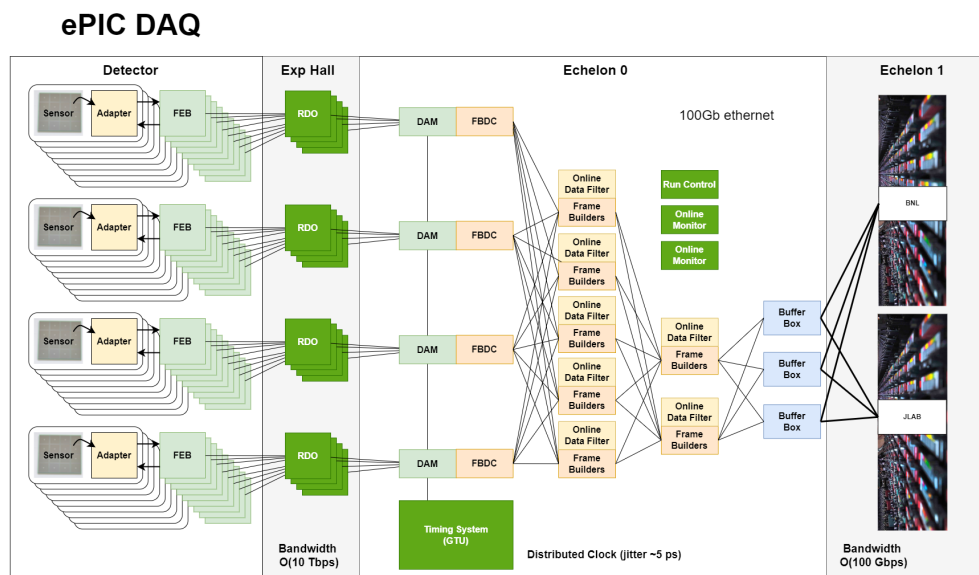


Figure 8.260: Schematic of the ePIC Streaming DAQ

case RDO by detector, is shown in Figure 8.259.

### 8.3.10.2 Device Concept and Technological choice: Streaming Readout

The ePIC readout system will implement a flexible, scalable, and efficient streaming DAQ as outlined by the EIC Yellow Report [41]. This design will provide the advantages of streaming include the replacement of custom L1 trigger electronics with commercial off-the-shelf (COTS) computing, virtually deadtime-free operation, great flexibility in event selection using full event data along with offline analysis, and the opportunity to study event backgrounds in detail. These advantages come at the cost of greater sensitivity to noise and background. A schematic of the readout system is shown in figure 8.260.

Readout will be accomplished using detector specific front end sensors and adaptors. Even though the organization of the front end electronics varies by detector needs the custom electronics of each system generically referred to as Front End Boards (FEBs). There is no global trigger system in ePIC, instead each FEB is required to self-trigger, providing a stream of hit data. Digitization and zero-suppression is typically handled with ASIC support. Each FEB has similar needs for clocks, configuration, and serial data links. These needs are provided by Readout Boards (RDOs). In some cases the RDO-FEB link is direct using LVDS signals, and in other cases the transmission is accomplished by lpGBT serializer/deserializer devices [151] over fiber. The RDOs also aggregate data from the FEBs. The RDO serves as an interface between custom, technology driven, readout schemes of specific detectors and the ePIC DAQ. While there are a number of variations of the RDOs depending upon the FEB technology, all of the RDOs support a unified ePIC DAQ fiber protocol. They distribute high-resolution time reference, configuration, and control to the FEBs and transmit hit data and monitoring information to the Data Aggregation and Manipulation Boards (DAM).

The DAM boards have significant processing available for implementing high level data selection criteria and other data reduction algorithms. They also provide further aggregation and function as

Implementation	Detector/Sensor	Key Attributes
Discrete	Calorimeter/SiPM	COTS devices, 14-bit digitization
CALOROC	Calorimeter/SiPM	ASIC, 10-bit digitization
EICROC	AC-LGAD, pixel	ASIC, High-precision timing for Cd < 5 pF
FCFD	AC-LGAD, strip	ASIC, High-precision timing for Cd < 10 pF
ALCOR	dRICH/SiPM	ASIC, uses shutter for 1 p.e. sensitivity
SALSA	MPGD	ASIC, peaking time to 50 ns, includes DSP

Figure 8.261: ePIC Electronics and ASICs summary

the interface between the electronics and the first level of COTS computers called the Frame Builder Data Collectors (FBDC). The farm of COTS DAQ computers dedicated to readout, data reduction, logging, monitoring, QA, data buffering, and data transfer to data centers is integrated in the ePIC computing model and referred to as Echelon 0.

Synchronizing the front end electronics and providing high resolution time reference to beam crossings is an important requirement of the streaming DAQ. The Global Timing Unit (GTU) is the interface to the EIC collider controls. It receives the 98.5Mhz bunch crossing clock, orbit information, and beam polarization information and distributes it via the DAM boards to the RDOs and FEBs. The GTU is the only global source of real time information provided to the FEB/RDOs, so it must provide information a trigger system would normally provide. These functions include the ability to synchronize data from different detectors, to send flow control signals, to pass bunch information such as spin orientations and bunch structure, the ability to provide user defined signals for signaling special data formatting or calibration needs, and the ability to implement a hardware trigger for debugging or as a fallback option to solve unforeseen readout issues.

The communication between the RDOs, DAM, and GTU will use an unified ePIC data protocol to coordinate data transfer. This protocol will be discussed in more detail in section 8.3.10.3.6.

### 8.3.10.3 Subsystem Description (components)

**8.3.10.3.1 ASICS and digitization PCBs** Readout electronics are being developed based on the sensor technologies. Common requirements among various sub-detectors have been identified to maximize synergy. In most cases the digitization solutions take the form of ASICs, but we also use PCB solutions with COTS components. Each component supports the ePIC streaming readout model with triggerless operation and serial interfaces. To facilitate calibration and debugging, capability for triggered operation is also implemented. The solutions and their characteristics are summarized in figure 8.261.

The scope of each project is summarized in figure 8.262, which shows the number of readout channels, technologies employed and institutions developing these readout solutions.

It is noted that the pFRICH and the hpDIRC detectors benefit from the FCFD and the EICROC developments due to their timing precision requirements. The FCFD is, however, the nominal choice due to its lower channel density packaging for these applications with higher detector capacitance, which enable tailoring their timing performance via detector bias adjustment.

**Discrete** The Discrete readout refers to custom PCBs using commercial (COTS) components. Discrete readout addresses calorimeters with SiPMs where high resolution digitization (14 bit) is required.. The design and technologies will be validated for the radiation level expected in the

	# Ch	# Ch/ Unit	#ASICs/ Wafer	#Wafers	Node (nm)	Package	Institution
Discrete/COTS	24 k	32	NA	740 Digitizers	COTS	NA	IU
CALOROC	97 k	64	480	5	130	BGA	OMEGA/IN2P3/IJCL/ORNL
EICROC	5.2 M	1024	160	42	130	Wafer Bump	OMEGA/IN2P3/IJCL/CEA- IRFU/AGH
FCFD	2.6 M	128	180	149	65	Wire Bond	FNAL
ALCOR	318 k	64	800	8	110	BGA	INFN
SALSA	202 k	64	500	9	65	BGA	CEA-Saclay/U of Sao Paulo

Figure 8.262: Scope of the electronics and ASICs developments

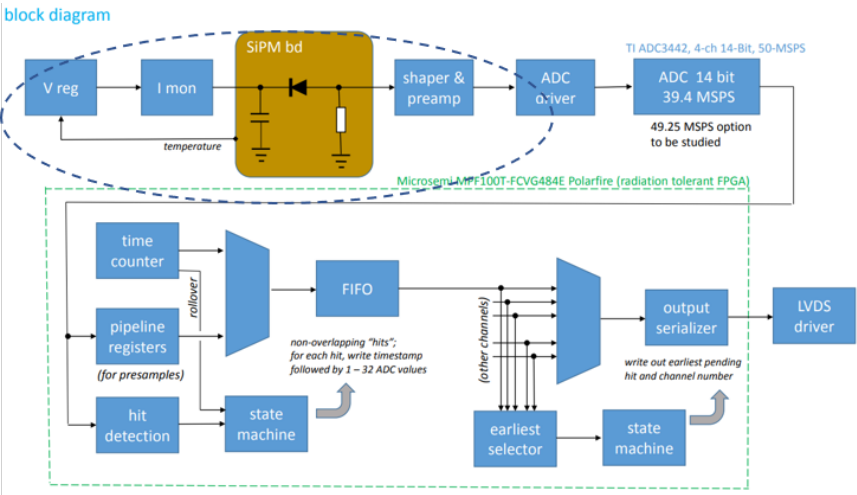


Figure 8.263: Discrete block diagram

specific positions of readout electronics within the ePIC detector. The block diagram is shown in figure 8.263.

The circled area in fig. 8.263 delineates the Adapter section with SiPMs and bias circuitry; the remaining parts make up the FEB PCB, which includes signal conditioning, ADCs and readout logic. The Adapter and FEB PCBs are located at the detector, as a stack, and CAT6 cables are employed for serial interfaces. Key specifications are shown in figure 8.265. Prototypes of the Adapter and FEB PCBs are shown in figure 8.264.

**CALOROC** The CALOROC ASIC is being developed from the H2GCROC (HGCROC-SiPM) [152]. The CALOROC will address readout from calorimeters with SiPMs and for which a 10-bit resolution digitization with wide dynamic range capabilities is applicable. The H2GCROC ASIC digitizes SiPMs with similar characteristics as needed in ePIC. But the CALOROC updates the digital backend with interfaces, conforming to the needs of the streaming readout approach at the EIC. In parallel, tests with the H2GCROCv3 chip continue to provide input and validation into the design of the CALOROC ASIC. There are, however, two frontend variants being considered: CALOROC1A uses an ADC, a TOA and a TOT for wide dynamic range, similar to the H2GCROC; CALOROC1B uses a different frontend architecture making use of dual gain switching techniques to extend its dynamic range. The CALOROC block diagram is shown in figure 8.266 and its speci-

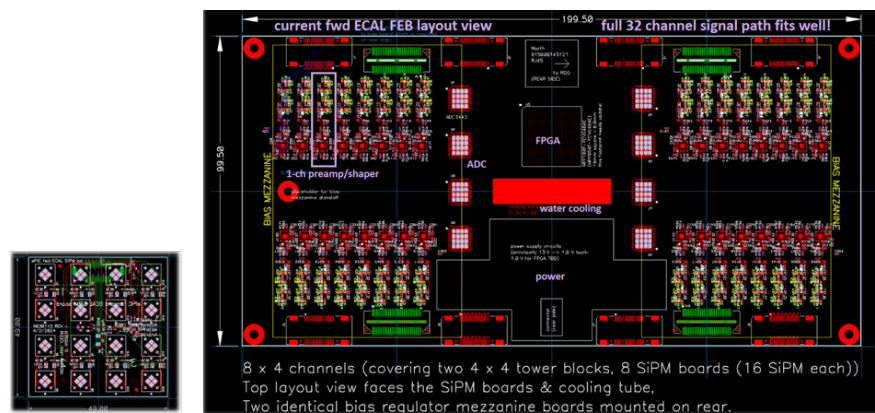


Figure 8.264: Discrete Adapter (left) and digitizer FEB PCBs

Function	Waveform digitizer with COTS devices
Channels	32
Digitizer	TI ADC 3422
Resolution	14-bit (12-bit also available)
Shaping	80 ns peaking time
FPGA	Microsemi MPF100T-FCVG484E Polarfire (Rad Hard)
Power	DC-DC converter (bPOL12V, bPOL48V, LTC36xx)
Cooling	Liquid
Cabling	CAT6

Figure 8.265: Discrete key specifications

8561 fications summarized in figure 8.267.

8562 **EICROC** The EICROC ASIC will address readout from AC-LGAD pixel detectors with low de-  
8563 tector capacitance ( $C_{din}$ ) and very stringent timing precision requirements. The EICROC design

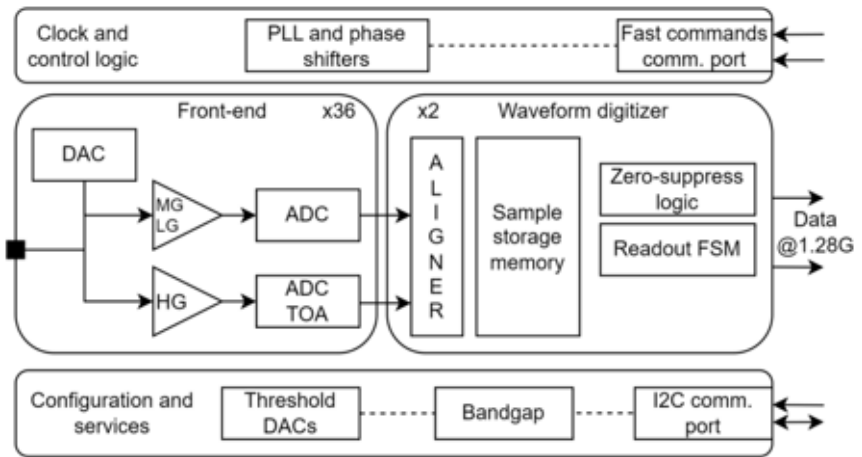


Figure 8.266: CALOROC block diagram



Function	Charge and timing digitization from SiPMs
Tech Node	130 nm CMOS
Channels	64
C <sub>din</sub>	500 pF – 10 nF
Digitization	Charge: 10-bit ADC, 15-bit TOT; Timing: <500 ps TOT (1 MIP)
Dynamic Range	Up to 12 nC
Clock	39.4 MHz operation from BX 98.5 MHz
Links	1260.8 Mbps @ 39.4 MHz, multiple
Power	10 mW/ch
Package	BGA
Rad Tolerance	Radiation hard

Figure 8.267: CALOROC Key Specifications

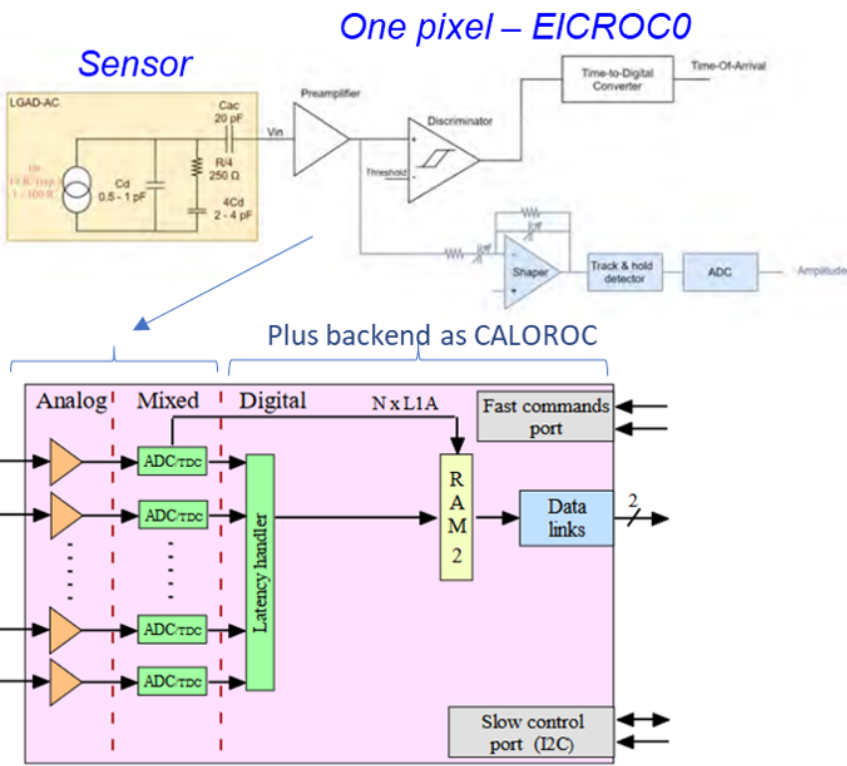


Figure 8.268: EICROC block diagram

is based on the existing HGCROC-Si ASIC [152] for Si and PMTs with similar characteristics and timing requirements as the AC-LGAD pixel sensors. The EICROC updates the digital backend with interfaces conforming to the needs of the streaming readout approach at the EIC. The same digital backend is already being designed for the CALOROC. Main IP blocks consist of preamp, discriminator, TOA, ADC and TDC. The EICROC block diagram is shown in figure 8.268 and its specifications are summarized in figure 8.270. Figure 8.269 shows the EICROC timing performance with varying charge from input signals.



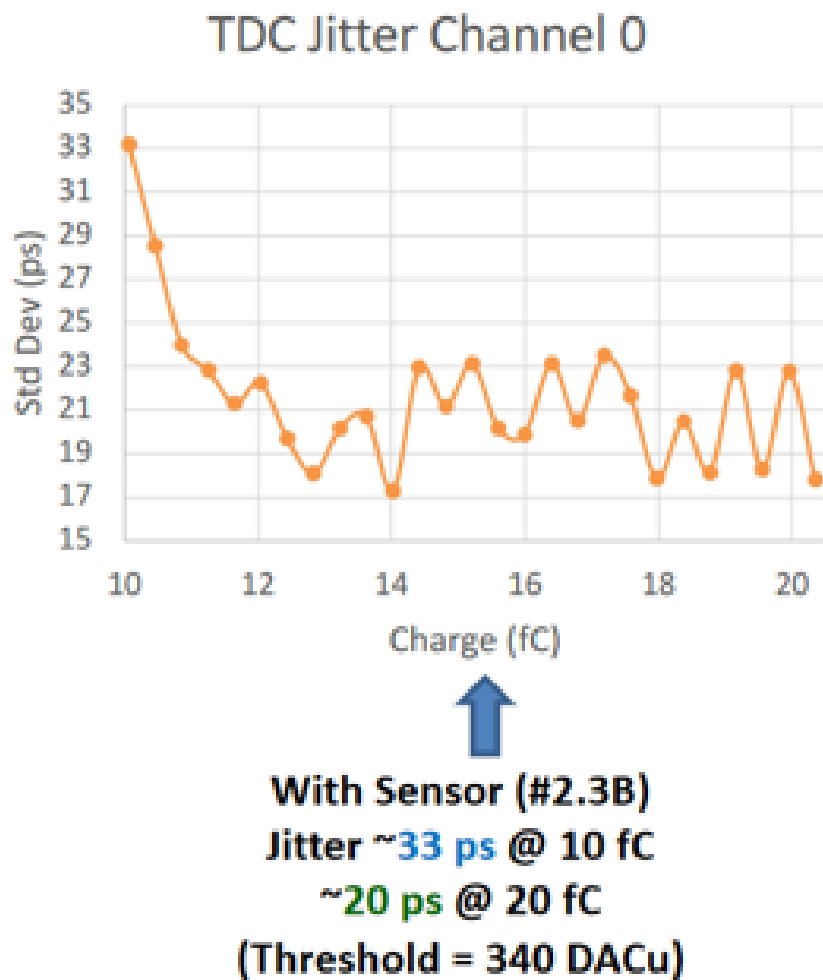


Figure 8.269: EICROC timing performance

Function	Timing digitization from AC-LGAD pixels
Tech Node	130 nm CMOS
Channels	1024 (32x32)
Cdin	1 – 5 pF
Digitization	ADC: 8-bit, TDC: 10b; Timing: 30 ps
Dynamic Range	1 – 50 fC
Clock	39.4 MHz operation from BX 98.5 MHz
Links	1260.8 Mbps @ 39.4 MHz, multiple
Power	<2 mW/ch
Package	Bump + wire bonds
Rad Tolerance	Radiation hard

Figure 8.270: EICROC Key Specifications

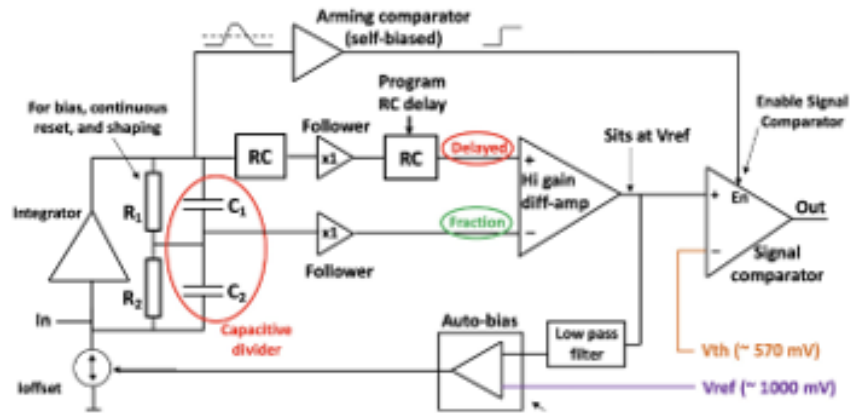


Figure 8.271: FCFD block diagram of the frontend

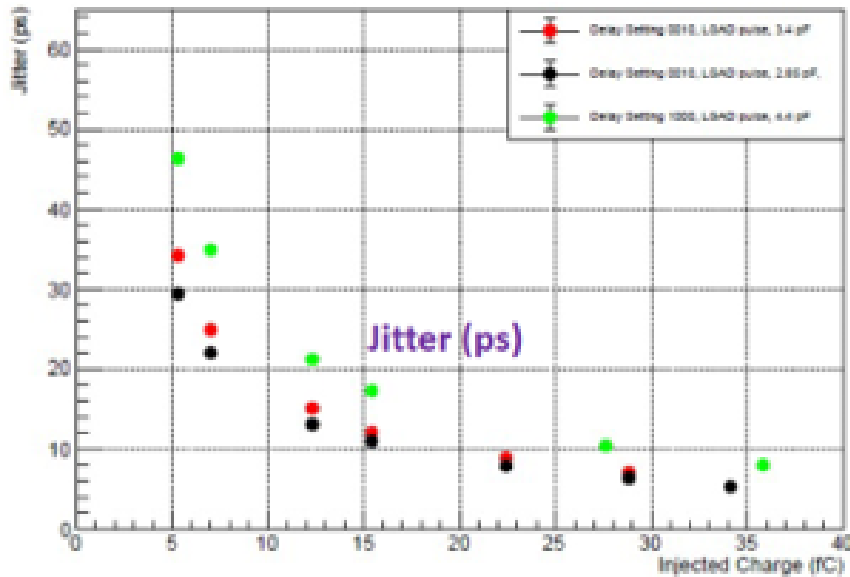


Figure 8.272: FCFD timing performance

**FCFD** The FCFD ASIC is currently under development to address readout from AC-LGAD strip detectors with medium detector capacitance ( $C_{din}$ ) and very stringent timing precision requirements. The FCFD design implements the constant fraction discriminator technique for high precision timing without time-walk corrections. The backend, which is currently being considered, may be based on the existing ETROC ASIC [153] or the EICROC development. The FCFD block diagram is shown in figure 8.271 and its specifications are summarized in figure 8.273. Figure 8.272 shows the FCFD timing performance with varying charge from input signals.

**ALCOR** The ALCOR ASIC is currently under development specifically for the readout of the dRICH detector with SiPMs due to its single photo-electron sensitivity requirement. The ALCOR design includes trans-impedance amplification (TIA) with regulated common gate (RCG) bias for

Function	Timing digitization from AC-LGAD strips
Tech Node	65 nm CMOS
Channels	128
C <sub>din</sub>	<15 pF
Digitization	TBD; Timing: 10 - 30 ps
Dynamic Range	5 – 40 fC
Clock	39.4 MHz operation from BX 98.5 MHz
Links	1260.8 Mbps @ 39.4 MHz, multiple
Power	<2 mW/ch
Package	Bump + wire bonds
Rad Tolerance	Radiation hard

Figure 8.273: FCFD Key Specifications

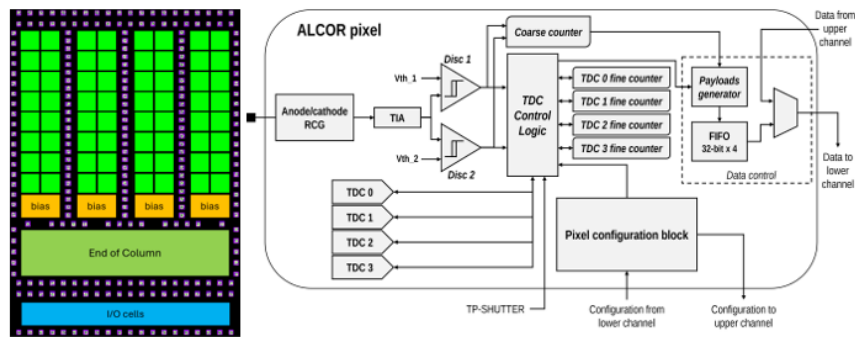


Figure 8.274: ALCOR Si Die (left) and block diagram

low noise, inhibit or shutter operation to limit contribution from dark-rate SiPM noise and TDCs to allow for single-photon tagging or time and charge digitization. The shutter function is a critical aspect of this ASIC and it is programmable for width and latency. The ALCOR die and block diagram are shown in figure 8.274 and its specifications are summarized in figure 8.275.

**SALSA** The SALSA chip is an ASIC being developed based on the SAMPa [154], [155]. It will readout the MPGD trackers, namely the barrel cylindrical Micromegas, the barrel  $\mu$ RWELL and

Function	Digitization from SiPMs with 1 p.e. sensitivity
Mode	Single-photon tagging or time and charge
Tech Node	110 nm CMOS
Channels	64 (8x8), dual polarity
C <sub>din</sub>	<1 nF
Digitization	20-40 ps TDCs, TOA + TOT; Timing <150 ps
Shutter	Width: 2–3 ns, programmable latency
Input Rate	<2.4 MHz (up to 5 MHz on single channel)
Clock	394.08 MHz operation from BX 98.5 MHz
Links	788 Mbps LVDS, SPI configuration
Power	12 mW/ch
Package	BGA
Rad Tolerance	Radiation hard

Figure 8.275: ALCOR Key Specifications

the end-cap  $\mu$ RWELL detectors. The purpose of SALSA is to amplify, shape and digitize signals coming from the MPGD detectors, and then perform basic data processing on the digitized samples before to transmit them to the next element of the data acquisition chain. It gathers in a single die a CSA pre-amplifier, a shaper and an ADC for each of the 64 channels, followed by a DSP which performs baseline corrections, digital shaping and a zero-suppression in order to reduce the output data bandwidth. Furthermore, to reduce data output even more, a peak finding algorithm is implemented to extract from samples information like amplitude and time of detected hits. It will be able to work both in the streaming readout environment foreseen at EPIC, and in a triggered environment.

The characteristics, performances and configurability of SALSA are designed to make the ASIC very versatile, being able to be adapted to several kinds of MPGD detectors and to several applications. It will be able to work with a large range of signal amplitudes, a large range of electrode capacitance and large range of signal rise times. Its target specifications are summarized in the Table 8.72.

Specification	Values	Remarks
Number of channels	64	Reasonable gain up to 1 nF
Input capacitance	50-200 pF	
Peaking time range	50 - 500 ns	
Max gain range	50 fC to 5 pC	Fast CSA reset
Max input rate	100 kHz/channel	
Signal polarity	Negative and positive	
ADC max sampling rate	50 MS/s	More than 10 effective bits
ADC dynamics	12 bits	
DSP processing	Baseline correction, filter, zero-suppression, peak finding	
Readout modes	Streaming readout, triggered	1 only used at EPIC
Output data links	4 Gigabit links	
Die technology	TSMC 65nm	
Die size	$\sim 1 \text{ cm}^2$	
Power consumption	$\sim 15 \text{ mW/channel}$	
Radiation hardness	Up to 300 Mrad and $10^{13} n_{eq}/\text{cm}^2$	

**Table 8.72:** Main specifications of the SALSA chip.

**8.3.10.3.2 FEB** The Front End Boards (FEB) are customized to the space, power, radiation load, and cooling requirements of each detector. However each FEB has similar needs for clocks, serial links, power, configuration, and control. The FEB usually uses ASICs to provide functionality, so efforts related to the FEB design has focused primarily on components to be shared by most or all FEBs.

**FEB Components: DC/DC converters** DC/DC converters are employed throughout ePIC for the efficient distribution and regulation of the various sub-systems. The bPOL12V and bPOL48V

Target Detector	Input	Output	technology
TOF Pre-Prototype, Calorimeters	copper	SFP+ fiber	FPGA
dRICH	copper	VTRX+ fiber	FPGA
Fiber Aggregator (SVT, MPGD, AC-LGAD)	fiber	fiber	FPGA
Imaging Calorimeter	copper	fiber	FPGA
Low $Q^2$ Tagger	copper	up to 12 fiber	FPGA
Direct Photon Detector	copper	fiber	Flash ADC250

Table 8.73: Types of RDO

DC/DC modules are selected for their radiation hardness and high magnetic field tolerances. Designs based on the LTC36xx family of devices will also be employed after proper validation.

**FEB Components: lpGBT** In some cases the serial links from the FEB to the RDO is direct, using Low-Voltage Differential Signaling (LVDS) or SFP+ fiber links. However, in the central detector region where radiation load is highest, and space and material budgets are most constrained the links will be accomplished using the low power Giga-Bit Transceiver devices (lpGBT) [151]. These devices operate at the 40 MHz LHC clock which has consequences for the ePIC fiber protocols (See sections 8.3.10.3.6 and 8.3.10.3.5) The lpGBT is a radiation hard part with Serializer/Deserializer (SERDES) functionality. The downlink transceiver operates at 2.5 Gbps, whereas the data uplink transceiver operates at 10.24 Gbps.

**FEB Components: VTRX+** The VTRX+ [156] module is an electro-optical receiver/driver used to interface to multi-mode optical fibers with MT optical connectors. The VTRX+ is radiation hard and it is tolerant to high magnetic fields; it has a small footprint, has low power consumption and interfaces directly to the lpGBT transceiver devices. One (1) receiver Rx (2.5 Gbps) and four (4) transmitters Tx (10 Gbps) are implemented.

**8.3.10.3.3 RDO** The RDO aggregates digitized ASIC data from the multiple front end boards, and ships this data to the DAM Boards. The RDO also has the function of delivering a high resolution clock ( $\leq 5$  ps jitter) to the front end boards. This clock is reconstructed from the data on the downlink fiber. The final function of the RDO is to act as the interface between the detector specific function of the ASICS to the global ePIC DAQ fiber protocol (See section 8.3.10.3.6).

Several detectors — the SVT, the MPGD based detectors, and all AC-LGAD based readouts — will make use of lpGBT or lpGBT-like aggregation using VTRX+ transceivers. The lpGBT aggregates ASIC information, delivers a high resolution reconstructed clock, and gives a transparent, simplified interface to the ASICS via serial links. It does not have, however, the capability of implementing the full ePIC protocol. For these RDOs the protocol will be implemented at the next level, either inside the DAM board or in a second level fiber to fiber RDO.

There will be several versions of the RDO depending on the needs of the specific detectors. The different RDO types are summarized in table 8.73

**RDO Subtypes: TOF pre-prototype** The TOF pre-prototype RDO was designed to use elements common to most ePIC detector RDOs. These elements include Xilinx Ultrascale+ Artix FPGA, SFP+ fiber optics interface, clock cleaner PLLs, and clock recovery. The pre-prototype has



Figure 8.276: TOF pre-prototype RDO

8639 been produced and is undergoing measurements of power usage and clock jitter. The board is  
8640 shown in figure 8.276.

8641 **RDO Subtypes: dRICH** The dRICH RDO is part of the dRICH Photo Detector Unit PDU (see  
8642 section 8.3.4.4, 1248 PDUs will serve the dRICH). It provides read-out of four 64-channel ALCOR  
8643 ASIC, installed each on a separate FEB. The space constraints are particularly demanding: the  
8644 total RDO area is  $40 \times 9 \text{ mm}^2$  - quite similar to a credit card - requiring a devoted design, given  
8645 the high integration of data buses and services within the PDU. The FPGA providing readout of  
8646 the ALCOR is an AMD Artix Ultrascale+ AU15P-SBVB484, complemented by a PolarFire FLASH-  
8647 based FPGA MPF050T-FCSG325. The latter will support remote programming and continuous  
8648 scrubbing of configuration bits of the SRAM-based AMD FPGA, to protect against SEU. Given the  
8649 space constraints and the need to curb power consumption (total RDO power is expected  $\approx 4 \text{ W}$ )  
8650 the VTRX+ optical transceiver has been selected, directly connected to the AMD FPGA SERDES.  
8651 The maximum throughput per link (reached at maximum radiation damage before annealing) is  
8652 expected to be about 1 Gbps, safely within VTRX+ specifications. The ALCOR will be read out at  
8653 394 MHz, with a clock multiplier and jitter-attenuator (Skyworks Si5326) deriving this clock from  
8654 the reconstructed EIC clock. A Microchip microcontroller provides power management and acts as  
8655 watchdog against SEL. The first prototype of this card is under production and will be intensively  
8656 tested during 2025, including irradiation tests. A 3D-rendering of the card is shown in Fig. 8.277.

8657 **RDO Subtypes: Fiber Aggregator** The fiber to fiber RDO is to be used with lpGBT-like FEBs  
8658 to convert the transparent ASIC interface to the ePIC DAQ protocol. They are also necessary to  
8659 further aggregate the fibers, particularly in the case of SVT and bTOF large numbers of low-data  
8660 utilization fibers are required.

8661 **RDO Subtypes: Astropix End of Stave Card** This RDO is to be used by the Barrel Imaging  
8662 Calorimeter. It is expected to be an updated version of the Astropix end of stave card developed

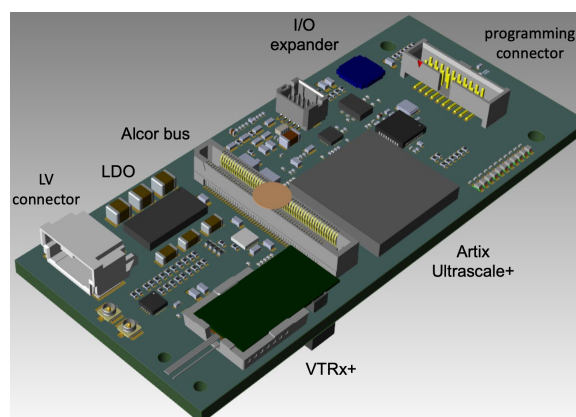


Figure 8.277: 3D model of dRICH RDO

8663 by NASA.

8664 **RDO Subtypes: Low  $Q^2$**  This is a RDO specifically for the low  $Q^2$  taggers. It is expected to be  
 8665 an updated version of the Spyder3 board. These use the timepix sensor and have high potential  
 8666 data volumes, requiring several uplink fibers per RDO.

8667 **RDO Subtypes: Direct Photon Detector** The Direct Photon RDO is a specialized interface  
 8668 expected to use the JLab Flash ADC250. This detector has only about 100 channels, but is expected  
 8669 to have very high occupancy, and as such the appropriate technology is to digitize all channels at  
 8670 200 MHz and stream it directly to the DAM boards which will summarize the information, writing  
 8671 out only the summed energy deposited each bunch crossing, or histograms of the bunch crossing  
 8672 energies according to bunch number.

8673 **8.3.10.3.4 DAM - Data Aggregation and Manipulation Hardware** For the ePIC DAQ sys-  
 8674 tem the DAM boards will be used as the primary aggregation point for the “raw” detector data  
 8675 streams. Because these boards are also the final aggregation points for the front-end (hardware  
 8676 managed) DAQ, there will need to be some well-defined but configurable algorithms for merging  
 8677 streams and managing potential congestion and data loss both for the incoming detector streams  
 8678 and the outgoing aggregated streams being queued up for online processing.

8679 In Addition, the DAM boards will interface with the Global Timing Unit (GTU) hardware via a  
 8680 proprietary communication protocol that supports a synchronized EIC clock distribution to all sub-  
 8681 systems and general DAQ/Run control and configuration. Finally, the DAM will act as the slow  
 8682 control interface for configuration and monitoring of all detector subsystem front-end boards (e.g.  
 8683 ASICs and other digitizing electronics).

8684 We have identified an ideal candidate for the DAM hardware. An updated version of the FELIX  
 8685 board [157] (Model FLX-155) is currently being developed at BNL for ATLAS at the HL-LHC. The  
 8686 board is show in figure 8.278. The features and updated components ensure a longevity of pro-  
 8687 duction, performance, and support that match very well with the EIC timeline. The board is built  
 8688 around the Xilinx Versal ACAP. This will facilitate using the board both as a PCIe device (sup-  
 8689 porting both PCIe Gen4 and Gen5 standards) in a server or as a standalone “smart” “aggregation”  
 8690 switch running a Linux OS. It can support up to 48 serial links to RDOs at the front-end running at



## FELIX 155

- Versal Premium: XCV1552-VSVA3340
- Support PCIe Gen4 x16, 2 Gen5 x8
- 48 FireFly data links (10/25 Gb/s)
- 4 LTI links (10/25 Gb/s)
- 100GbE (4\*25Gb/s)
- DDR4
- GbE
- White Rabbit
- Electrical IOs (single-ended)

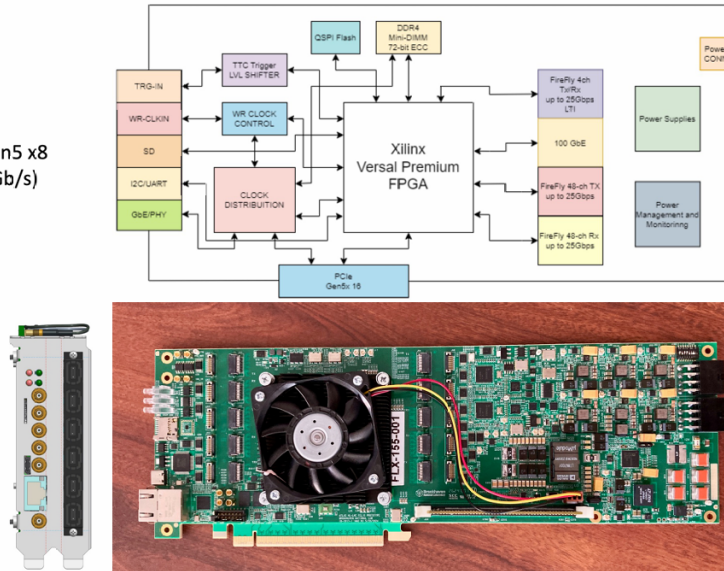


**Figure 8.278:** The FLX-155 board identified for use as a DAM board

speeds up to 25 Gbps as well as an LTI interface (8 fibers) supporting a high-resolution direct clock along with our GTU-DAM communication protocol. There is also a separate 100 Gb ethernet link off the board. A DDR4 RAM slot is available to support buffering and more complex algorithms for data reduction or interaction tagging. The board supports JTAG and I2C communications.

We expect to procure several FLX155 boards for testing and software/firmware development in 2025.

**8.3.10.3.5 GTU - Global Timing Unit** The design of the global timing distribution system (GTU) will be central to the operation of the streaming readout model. The timing system must provide signals to ensure that the data from different detectors can be synchronously aggregated. It must provide a copy of the accelerator bunch crossing clock (running at 98.5Mhz) to all front-end systems. A subset of these systems (e.g. TOF) will require a phase aligned system clock with a jitter of <5 ps in order realize required timing resolutions for these detectors (20-30 ps).

The GTU is also the only source of real time information provided to the FEB/RDOs, so it must provide information a trigger system would normally provide. These functions include the ability to synchronize data from different detectors, to send flow control signals, to pass bunch information such as spin orientations and bunch structure, the ability to provide user defined signals for signaling special data formatting or calibration needs, and the ability to implement a hardware trigger for debugging, calibration or as a fallback option to solve unforeseen readout issues.

**Precision Clock Distribution** The ePIC clock distribution must support both 98.5 MHz and 39.4 MHz components both of which will reconstruct their clock from the data transferred on the fiber and require < 5 ps jitter and phase stability. In order to naturally support both frequencies the GTU will distribute clock synchronized to 10 bunch crossings at 9.85 Mhz to all DAM boards. The DAM boards will recover 98.5 MHz and 39.4 MHz clocks by multiplying by 10 and 4 respectively.

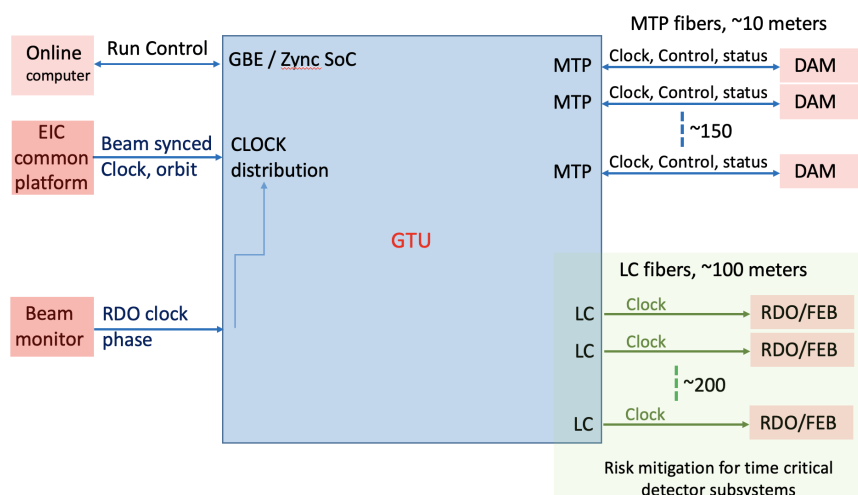


Figure 8.279: Schematic layout based for the GTU

8714 The frequency multiplications will be done synchronously (i.e. the clock edge should be aligned  
8715 with the 9.85 MHz clock).

8716 We tested this scheme using the Si5344H evaluation board (Skyworks) to emulate the ePIC clock  
8717 source (EIC common platform), Jlab's Trigger Interface board with Analog Devices' AD9510 chip  
8718 to emulate the GTU, Finisar's FLT410 optic transceiver for the dedicated optical fiber distribution,  
8719 and the Si5394A evaluation board (Skyworks) to emulate the DAM clock recovery.

8720 We re-synchronize the clock divider (AD9510) and the clock recovery (Si5394A) every 1,073,741,830  
8721 (98.5 MHz) clock cycles. The recovered clocks (98.5 MHz and 39.4 MHz) are always phase aligned  
8722 with the original clock (before the clock divider and multiplication). The measured phase difference  
8723 uncertainty for this is about 1.5 ps (std). This uncertainty includes the recovered clock jitter, and  
8724 the clock phase shift.

8725 For the 98.5 MHz clock distribution, from DAM to RDO, our tests with the ppRDO shows that the  
8726 jitter of the MGT recovered clock is less than 3 ps (std) and the phase can be aligned to picosecond  
8727 precision with the pseudo clock technique.

8728 For the 39.4 MHz clock distribution, from DAM to lpGBT, both the lpGBT ASIC production tests  
8729 and our tests using a VLDB+ board (a CERN development board with VTRx+ optical receiver and  
8730 lpGBT) show that the lpGBT recovered clock is phase aligned with the DAM (emulated by the  
8731 kcu105 FPGA evaluation board from AMD, and the Si5344H evaluation board from Skyworks).  
8732 The source clock and the lpGBT recovered clock have very low jitter. The uncertainty of the phase  
8733 difference (including the clock jitter and the phase shift) is less than 2 ps (std).

8734 **GTU hardware design** Figure 8.279 shows a schematic layout based on required functionality  
8735 of the GTU. The physical concept is shown in figure 8.280. The GTU will be custom rack-mounted  
8736 hardware in the DAQ room with a base board and multiple plug-in optical interface modules. It  
8737 will be based on a multi-FPGA architecture including a single Zync SoC FPGA supporting gigabit  
8738 ethernet and a full Linux OS to facilitate both ePIC Run Control and other user-based applications.  
8739 It will include an interface for the EIC Common platform (Clock, beam orbit and other collider  
8740 information) and an interface for feedback from the local IP-6 beamline to support bunch crossing  
8741 clock phase corrections

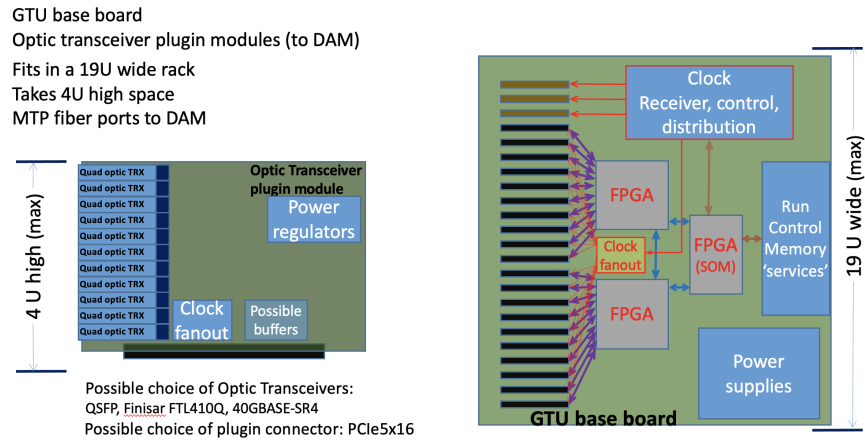


**Figure 8.280:** Physical concept for the fiber distribution for the GTU

type	clock (MHz)	downlink rate (Gb/s)	downlink word length (ns)	downlink word width (bits)
Standard	98.5	10	10.15	64
VTRX+	98.5	2.56	10.15	16
VTRX+	39.4	2.56	25.375	64

**Table 8.74:** RDO downlink words

8742 The jitter-cleaned and phase corrected clock then is fanned out for distribution to all DAM boards  
8743 via a multi-fiber communications link (We intend to support up to 150 of these links for current  
8744 needs as well as potential future requirements). In addition we plan to support up to 250 direct  
8745 clock links to the RDO/FEB electronics. This is to mitigate potential limitations with the distribu-  
8746 tion of the low jitter (<5 ps) clock via the DAM path communication protocol.

8747 **8.3.10.3.6 Protocols** The ePIC fiber protocol is used to communicate information between the  
8748 GTU, DAM and RDO boards. The DAM to RDO communications are limited by the type of inter-  
8749 face, and can be described in three categories as shown in table 8.74.

Decoded Synchronous Command Structure							
[0:7]	[8:15]	[16:23]	[24:31]	[32:39]	[40:47]	[48:55]	[56:64]
Flexible Command Data Encoding				FAST CMD		Comma	
type	type specific			FAST CMD		Comma	

**Table 8.75:** DAM/RDO Decoded Synchronous Command Structure. This structure is defined to allow continuous availability of the critical beam related bits and more rare commands. The data in the 40 bits worth of flexible command data encoding remains flexible but must contain enough control bits to select what structure it has. The "type", "type specific" division is an potential holding this flexibility

The ePIC fiber protocol depends upon a synchronous command structure (table 8.75). The need for links with separate clock rates and with separate downlink speeds requires careful attention to the encoding of commands, which to the extent possible will share the same synchronized command format among all detectors. Detectors with faster links can support additional features and higher bandwidth for configuration and ASIC control. In order to synchronize data in all detectors it is necessary to demand that synchronous commands are sent on 5 bunch crossing (50.75 ns) intervals when the 98.5 MHz and 39.4 MHz clock edges coincide.

The protocol will delimitate streaming data into timeframes. The maximum length, in bunch crossings will be defined to fit within  $2^{16}$ , which implies a time frame length of  $\sim 600$  us. This is also a convenient time as it corresponds to a manageable maximum time frame size of  $\sim 10$  MB.

The bandwidth available for transmitting data from the FEBs to the DAM depends upon adequate zero-suppression. This implies the potential for data loss if the front ends produce unexpected levels of data. This potential must be mitigated by sensing, and tagging any data loss, by implementing flow control mechanisms, and by providing mechanisms for resetting and disabling problematic FEBs and RDOs.

The features that must be encoded in the Synchronous command protocol are

- The distribution of real-time control information to the RDO and FEBs.
- The distribution of a high-resolution beam crossing timing signal to the RDO and FEBs.
- Synchronize and verify synchronization of bunch counters among all detector readouts
- Define the time frame boundaries
- Provide RDO and DAM Data processing flags
- High performance ( $\sim 10$  Gbps) transfer of hit data and monitoring information from the FEBs and RDO to their DAM boards.
- The distribution of configuration information to the RDOs and FEBs.
- Firmware based high level selective readout
- Flow control
- Error detector and recovery
- Transfer Slow Controls Data from the FEB to soft IOCs in the DAM board or readout computer to pass slow controls information to Slow Controls.

**High Level Selective Readout** One example of the operation of the protocol is to allow a high level trigger criteria to reduce dRICH noise. This is not a global trigger to exclude events from the readout of the ePIC detector. Instead, this trigger criteria will be used to selectively omit data from particular detectors with unusually high data volumes. In this example, the dRICH.

The path of the commands sent is show in figure 8.281. Data arrives at DAM boards with 10us from digitization. It is stored in the DAM boards. After 10us FPGA based algorithms provide a description of the data (for example number of hits above a specified threshold) from each fHCAL DAM board. This information is encoded into 64 bits and sent to the GTU which aggregates data from fHCAL DAM boards and sends the keep/drop bunch bit to the dRICH DAM boards. The dRICH DAM boards drop or transmit data based upon this message. The decision comes after a fixed latency of about 11us which is very small compared to the buffering available on the DAM board.

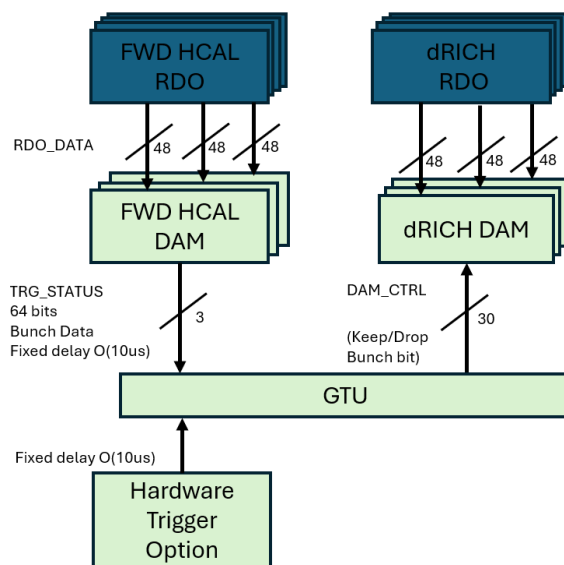


**Figure 8.281:** Operation of firmware trigger under assumption that the trigger decision for the dRICH depends upon data from fHCAL

Note that a similar approach can be implemented with a hardware signal into the GTU. In this case a fixed delay is applied to the hardware signal, but the decision mechanism uses the same data path.

**dRICH data algorithms** There are also additional schemes for implementing dRICH data reduction using only dRICH data or aggregated data from different sub-detectors. This is currently under investigation by the dRICH groups at INFN. One possibility would be to perform such reduction on the network of interconnected dRICH DAMS using the APEIRON framework [158], which implements a multi FPGA ML algorithm with deterministic time. The results of this calculation are transmitted to the GTU in the same manner as for cross detector selection criteria. The DAM buffering capacity is exploited in this scheme. Another possibility is to use instead, Online Data Filter algorithms in the servers receiving the aggregated data (see Fig. 8.260), exploiting xPU resources. Given the noise rate in the dRICH will increase with the radiation damage (see section ??), this will provide an opportunity to develop and test carefully such systems.

Resource	Totals
DAM/FELIX boards	136
EBDC Servers	92
DAQ Compute Nodes	108
File Servers (Buffer Box)	6

**Table 8.76:** DAQ Computing Resources

**8.3.10.3.7 DAQ/Online Computing - Echelon 0** Table 8.76 outlines the planned resources for the ePIC detector DAQ and Online computing needs. This is based on the elements shown in

the DAQ schematic in Figure 8.260. Several thousand fibers from the RDOs will be aggregated in the DAM boards and presented to the Online Farm. To be clear each online farm node represents one multi-core server. The expectation is that they will minimally support 32-64 cores, and selected nodes will support PCIe-based GPUs and/or FPGAs in addition to the DAM boards in the FBDC (Frame Building Data Concentrator) nodes. The high performance DAQ network is expected to support 100/400 Gbps bandwidth connections. As the majority of the Online computing is expected to be COTS hardware, much of it will be acquired as late as is reasonable in the construction phase.

All Echelon 0 resources are fully dedicated to operation of the ePIC Detector and are included as part of the EIC Project. One open question under consideration, however, is to split these resources between the DAQ Room at IP-6 and the SDCC (BNL main data center) and to integrate them as a single enclave under ePIC control. There are several advantages to this configuration. First it will reduce the overall cost of infrastructure upgrades to the DAQ Room cooling systems. Also, having a subset of ePIC computing resources available in the SDCC will allow better network access to DAQ and electronics labs during construction (when the DAQ Room will not be available. Finally, during operations having DAQ tiered storage of production data in the SDCC will facilitate distribution of that data to both Echelon 1 processing sites (BNL and JLAB).

At the DAM stage the aggregated data streams will have substantial buffering and available network bandwidth for online processing that will be primarily focused on event identification and background/noise reduction. While we do not currently have solid estimates on the necessary computing resources to complete the required tasks, we have tried to provide conservative estimates of computing resources that would allow a full reconstruction of a 500 kHz event rate of events from similar scale detectors that exist now (e.g. GlueX and CLAS12 at Jefferson Lab and sPHENIX at RHIC). More likely the necessary computing resources for online filtering to get the expected data rates of O(100 Gbps) to files will be somewhat smaller.

**Time Frame Building** In the streaming model, the primary consideration is ensuring that enough bandwidth and buffering will be available to handle the digitized data at each stage of the DAQ. At the front-end stage time frames for the individual streams are created, managed and aggregated. Given current background and noise estimates the planned bandwidth off the detector to the DAM boards O(10 Tbps) should be more than sufficient.

Streams at the DAM boards will support time frames using a 16 bit bunch crossing counter which would represent a configurable time window of up to  $65536 \times 10.15 \text{ ns} = 665 \text{ us}$ . Although the front-end DAQ will be synchronized using a single common clock from the EIC, not all ASICS/digitizers at the FEBs will be running at the same frequency. Hence the timestamps coming from hits in different detectors will need to be wrapped in smaller "time slices" within the full time frame to establish an absolute time for each hit.

Time frames buffered at the DAM boards will be able to utilize the online farm to complete a full build of complete time frames with data from all detectors. Effectively N streams from the DAM boards will generate  $M < N$  streams of time frames containing the time frame fragments from the N original streams. This will greatly facilitate additional event identification and processing at both the Echelon 0 and Echelon 1 stages.

**Data Processing** The ePIC readout system must support data reduction techniques. The implementation of high level selective readout has already been described, but there are many additional techniques that might be implemented in Echelon 0. These include zero loss techniques like aggregation of headers from ASICS or DAM board data. It could include standard or ML based compres-



sion techniques. It could involve analysis techniques such as cluster finding or track reconstruction. There could also be ML based noise reduction techniques. And there could be analysis done for specific purposes such as the creation of scalers for monitoring or collider feedback.

The framework for the code generating these features must allow the code to be shared with the offline software, for operational transparency, and for algorithm evaluation.

The results of the code must be incorporated into the time frame data using data formats that allow for independent data banks to co-exist. The policy of ePIC is expected to be to avoid dropping any data unless data volumes make it necessary. There should also be a sample of unprocessed data even if the readout of raw data banks are suppressed due to data volume limits. This implies that the write out of specific data banks be controlled by configurable prescales.

**Configuration Databases** Configuration information must be stored and made accessible to the ePIC Collaboration.

**Slow controls interface to RDOs/FEBs** The primary configuration and slow control communications interface to all the ASICs and other digitizing electronics (FEBs) will be through our proprietary data link between the DAM board and the RDOs. Our current plan is to take advantage of the Versal SoC FPGA dual-core ARM Cortex processor. All DAM boards will support a full LinuxOS and gigabit ethernet access. This will facilitate running an EPICS soft IOC as well as user-based server applications for local and remote communication with the front-end electronics.

Slow control communication on the DAM-RDO link must be bidirectional which means that slow control communications must share the link with streaming data coming from the detectors. The protocol must ensure that adequate bandwidth is available for digitized hits from the detector and slow controls readouts. The flow control provisions must enforce this requirement.

Software and firmware development of drivers and libraries necessary to access all the FEB “flavors” is supported as part of the Project. The majority of the FEBs will support standard I2C/SPI control communications.

**Monitoring / Logging** A unified system for centralized logging of informational and error messages is required. These messages should be ideally be available and archived in web-accessible form.

A unified system for monitoring of the real time behaviour and utilization of online components is also needed.

**Interface to Echelon 1** As will be discussed in Section 8.3.11, the ePIC DAQ (Echelon 0) is an integral part of the computing system, and the output of the DAQ data triggers the calibration and reconstruction pipeline in Echelon 1, located at the computing centers of the host labs. From the DAQ buffering disks, two identical copies will be sent to the buffer file system at the BNL SDCC via a dedicated fiber link and at the JLab Data Center via the 400 Gbps ESnet link, respectively. Each data center’s data buffer has the capability of about three weeks’ ePIC data taking to allow for multiple iterations of calibration jobs and reconstruction passes. Data will also be copied to permanent archival storage (presumably HPSS-like tape system), one copy at each site, which allows for reprocessing of the data in the future in case a problem identified in the prompt reconstruction pass or an improved reconstruction becomes available in the future. Nevertheless, in a steady state, the



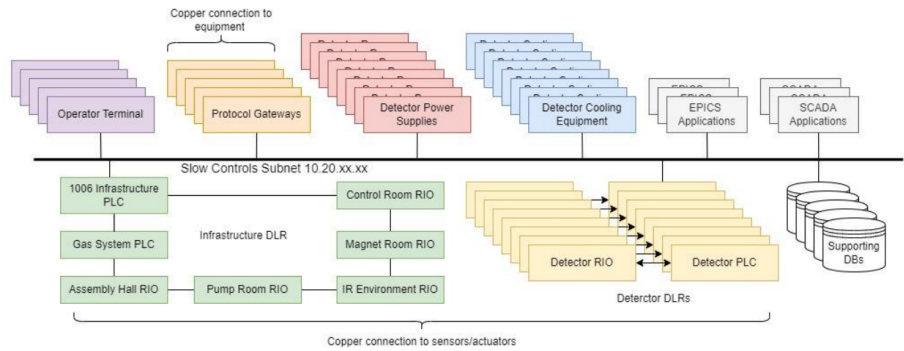


Figure 8.282: Proposed ePIC slow controls network topology

Scenario	Yearly Database Storage (TB)	Network Traffic (Mbps)
estimated	53.9	22.8
worst case	173.5	73.4

Table 8.77: Slow Controls data volume and network traffic

prompt calibration and production are expected to make the final analysis-ready data for physics working groups within days of the data taking, significantly expedited compared to many ongoing Nuclear Physics experiments.

**8.3.10.3.8 Slow Controls** There will be a myriad of slow controls information associated with both the EIC collider and the ePIC detector. These include various systems associated with the beamline, magnets, detector biases, gas flows, temperatures, pressures, etc... While the design and implementation of these slow control systems will be driven by the relevant subsystems they are associated with, it is the defined responsibility of the DAQ to provide software tools to facilitate the integration of all this information with the streaming physics data. This will include synchronizing the times associated with readout of slow control systems and the bunch-crossing clock that will be driving the DAQ system. Online slow control databases to support calibration and reconstruction processing will also be developed. Finally, a general network infrastructure in the experimental hall and control room, independent of the high performance DAQ network, will be provided to support integration of all slow control systems

A schematic of the proposed slow controls network topology is shown in figure 8.282. The implementation uses EPICS 7 on an ethernet network to control detector operation and read and archive conditions information. Allen-Bradley PLCs are to be used for controlling power to racks in the IR and for detector interlocks.

Resource requirements for the slow controls system were obtained by surveying detector managers. These resulted in approximately 500,000 channels to be read and stored. The yearly storage estimates and network traffic estimates are show in table 8.77.



Figure 8.283: DAQ/Computing schedule

#### 8.3.10.4 Implementation

#### 8.3.10.5 Calibration, alignment and monitoring:

During run time, predetermined calibration and alignment will be used in configuring the readout electronics and data reduction computing tasks. These calibration and alignment are managed by detector groups, extracted from dedicated prior-to-beam calibration runs, such as pedestal runs and zero field runs. When necessary, such as changes in detector condition, new calibration will be extracted and updated to be used in data taking. The calibration constant used will be archived in the run database and made available for reference in the offline analysis.

Constant monitoring for detector status and data pipeline healthiness is key to high-efficiency data taking and a successful run. We expect a multi-level of monitoring that includes monitoring the metrics on (1) detector statues (2) each stage of the data pipeline (3) sampled data content for decoding and analysis. In addition, in the Echelon 1 computing facility, full reconstruction will be performed for a small fraction of time frames expediently to provide holistic feedback of the experiment capability down to analysis level observable such as pi0 and K0s.

#### 8.3.10.6 Status and remaining design effort:

R&D effort: ASIC R&D to continue through 2025

E&D status and outlook: The bulk of the engineering design efforts still required for the readout electronics are centered around the development of RDO and FEB designs needed to support all the detector subsystems. This information is needed to establish baseline costs and better define construction and testing schedules. Project Engineering design for a GTU engineering article can be completed prior to CD2/3. Finally, we expect to procure several FLX155 engineering articles in 2025 to support further timing and communication protocol testing and initial firmware development.

Status of maturity of the subsystem: Electronics and DAQ held a second PDR in June 2024. We expect to hold a third PDR in 2025 on track to an FDR in 2026. There are CD-3B items in the Electronics for VTRX+ and lpGBT. The FDR was held in June 2024, and will be presented during the CD-3B review in January 2025.

#### 8.3.10.7 Environmental, Safety and Health (ES&H) aspects and Quality Assessment (QA planning:

#### 8.3.10.8 Construction and assembly planning:

Figure 8.283 shows the current project schedule for DAQ/Computing. It is broken down into four general categories: Design/Procurement, Fabricate and Delivery, Test and Accept and Installation. Early in the construction phase there is a heavy focus on building and testing custom hardware (GTU, DAMs, RDOs) in order to facilitate detector subsystem testing and DAQ firmware/software development.

Once IP-6 infrastructure upgrades have been completed (DAQ and Control rooms, Wide Angle Hall), we can begin the main trunk fiber pulls into the hall and tunnels and install required patch panels and terminate fibers. At this time we can also start installation of the general IP-6 network infrastructure in the Hall, DAQ and Control Rooms.

Computing hardware procurement and installation are scheduled in three phases during the course of construction. Phase I at the beginning of construction will be for a small subset of machines for development and evaluation. They will be placed in both the DAQ/Electronics development labs as well as in the SDCC. Phase II will be primarily in the DAQ Room as part of the DAQ subsystem installations and will provide the opportunity for full chain large scale testing of the DAQ as well as for detector subsystems as they begin to be installed at IP-6. Finally Phase III will be implemented at the end of the full ePIC detector installation as we have a better understanding of the required resources needed for initial Physics operation. This hardware will be installed at both the DAQ Room and in the SDCC which will define the full Echelon 0 enclave.

#### 8.3.10.9 Collaborators and their role, resources and workforce

The institutions specifically developing the readout electronics and ASICs are listed under the electronics section. Figure 8.284 lists the institutions which have expressed interest in participating in the design of various other parts of the readout chain. Formal agreements committing engineering and technical personnel have not been officiated.

### 8.3.11 Software and Computing

This section provides an overview of the ePIC computing model, as presently conceived many years before datataking begins. Although ePIC datataking is distant, software and computing is an active and vital part of the ePIC development program today, supporting ongoing detector design optimization, studies of detector and physics performance, and the development of reconstruction and analysis software that will be the foundation for the ePIC physics program. A well-developed software stack and computing capability is also needed early in order to develop an understanding of the complete workflows and their operating scales sufficient to deliver the ePIC physics program, thereby establishing the S&C requirements for the experiment. A capable S&C infrastructure is also needed to support a steady R&D program such that when ePIC datataking begins, it will be with a modern, sustainable software stack that is effective and economical in using the computing facilities of the day; that effectively utilizes the globally distributed computing resources available to the Collaboration; and that strongly leverages the available community software within and beyond nuclear and particle physics. This section addresses these aspects of the computing model and use cases for the present and near term, and the longer term towards datataking. In a future

Detector System		Channels	SensorTechnology	Readout Technology	Institution
Si Tracking					
	3 vertex layers	7 m <sup>2</sup>	MAPS	ipGBT, VTRX+	STFC, UK, ORNL
	2 sagitta layers	368 pixels	MAPS	ipGBT, VTRX+	STFC, UK, ORNL
	5 backward disks	5,200 MAPS sensors	MAPS	ipGBT, VTRX+	STFC, UK, ORNL
	5 forward disks		MAPS	ipGBT, VTRX+	STFC, UK, ORNL
MPGD Tracking					
	Barrel, e & H Endcaps	202 k	URWELL, MicroMegas	SALSA	CEA, OMEGA, JLab
Forward Calorimeters					
	LFHCAL	63,280	SIPM	CALOROC	ORNL, Debrecen
	HCAL Insert	8 k	SIPM	CALOROC	ORNL, Debrecen
	pECAL W/SciFi	16,000	SIPM	Discrete	IU
Barrel Calorimeters					
	HCAL	7,680	SIPM	CALOROC	ORNL, Debrecen
	ECAL SciFi/Pb	5,760	SIPM	CALOROC	U Regina, ORNL
	ECAL Imaging Si ASTROPiX	500 M pixels	Astropix	Astropix	KIT,NASA (GSFC), ANL
Backward Calorimeters					
	nHCAL	3,256	SIPM	CALOROC	ORNL
	ECAL (PWO)	2,852	SIPM	Discrete	IU, EEMCAL Consortium
Far Forward					
	B0: 3 Crystal Calorimeter	135	SIPM/APD	Discrete	IU, JLab
	B0: 4 AC-LGAD layers	688,128	AC-LGAD Pixel	EICROC	UCLab, OMEGA, BNL, ORNL, Rice
	2 Roman Pots (RP)	524,288	AC-LGAD Pixel	EICROC	UCLab, OMEGA, BNL, ORNL, Rice
	2 Off Momentum (OMD)	294,912	AC-LGAD Pixel	EICROC	UCLab, OMEGA, BNL, ORNL, Rice
	ZDC: Crystal Calorimeter	900	SIPM/APD	Discrete	IU, JLab
	ZDC: HCAL	9,216	SIPM	CALOROC	ORNL, Debrecen, JLab
	Low Q Tagger 1	33,030,144	Timepix4	Timepix4	U. Glasgow
	Low Q Tagger 2	33,030,144	Timepix4	Timepix4	U. Glasgow
Far Backward					
	Low Q Tagger 1+2 Cal	420 (2x210)	SIPM	CALOROC	U. York
	2 Lumi PS Calorimeter	3,360 (2x1680)	SIPM	Discrete	U. York
	2 Lumi PS Tracker	128,000 (2x64,000)	AC-LGAD Strip	FCFD/EICROcX	FNAL, OMEGA, Hiroshima, NTU, ORNL, UIC, UH, Rice, KSU, Tokyo
	Lumi Direct Photon Calorimeter	100	SIPM	Flash250	AGH Krakow, JLab
PID-TOF					
	Barrel bTOF	2,359,296	AC-LGAD Strip	FCFD/EICROcX	FNAL, OMEGA, Hiroshima, NTU, ORNL, UIC, Rice, BNL, KSU, Tokyo
	Hadron Endcap fTOF	3,719,168	AC-LGAD Pixel	EICROC	UCLab, OMEGA, BNL, ORNL, Rice
PID-Cherenkov					
	dRICH	317,952	SIPM	ALCOR, VTRX+	INFN (BO, FE, TO)
	pRICH	69,632	HRPPD	FCFD/EICROcX	BNL, FNAL, JLab
	hpDIRC	73,728	MCP-PMT or HRPPD	FCFD/EICROcX	BNL, FNAL, JLab

Figure 8.284: Electronics and DAQ Resources

revision, details regarding the software, as well as the preservation of data and analysis, will be included.

**Computing Use Cases** In this section, we outline the computing use cases for the Streaming Computing model. In Sec. 8.3.11, the use cases are associated with the four tiers of the ePIC Streaming Computing Model computing fabric, Echelons 0 through 3. Echelon 0 refers to the ePIC experiment. Echelon 1 pertains to the host labs. Echelon 2 encompasses global processing and data facilities. Echelon 3 concerns home institute computing.

**Interface between DAQ and Computing** Where the interface lies between “online” and “offline” in the ePIC streaming data and processing flow is still a matter of discussion. The working definition for the purposes of this document is the point at which data flows to archival storage. In aspects both technical and sociological, this is the point at which substantial differences exist on the two sides. All processing prior to delivering the archival stream is at risk of permanently losing data in case of error or reduced live time. Post archival, the requirements and latencies are less stringent, the environment is more open.

This Section describes the computing use cases on the offline side of this definition, beginning with the stored data stream and its associated monitoring.

8996 **Stored Data Streaming and Monitoring** The first and foremost responsibility of the data  
8997 stream processing as it receives archive-ready raw data from DAQ is to archive it. ePIC's butterfly  
8998 model provides for geographically separated replicas of raw data as it is archived, by symmetri-  
8999 cally receiving the raw data stream at both BNL and JLab facilities, and archiving to tape at both  
9000 sites. The data is also retained on disk at both sites for near real time workflows such as calibra-  
9001 tion and prompt processing, discussed below. Monitoring of the raw data stream and other data  
9002 and metadata received from DAQ provides for examination, validation and alarming of the data  
9003 stream, both by automated means and via UI. Monitoring can also consume the reconstructed ob-  
9004 jects produced by prompt reconstruction. Background analysis and subtraction can take place to  
9005 ready the data stream for subsequent processing.

9006 **Alignment and Calibration** ePIC aims for rapid turnaround from data taking to full calibrated  
9007 reconstruction, making a prompt alignment and calibration loop vital. It will operate off the same  
9008 buffered raw data stream (and prompt reconstruction data set) that is available at each site, and  
9009 will be as automated and autonomous as possible in its operation. Workflows may ingest raw data  
9010 or (by definition incompletely calibrated) reconstructed data as input. Alignment and calibration  
9011 data products as used in the reconstruction and other downstream workflows are delivered to a  
9012 conditions database available globally, and refined until final, ready for final reconstruction. Ini-  
9013 tial prompt reconstruction based alignment and calibration is restricted to Echelon 1 (like prompt  
9014 reconstruction itself). Refinements towards a final calibration can proceed elsewhere as well.

9015 **Prompt Reconstruction** A defining characteristic of ePIC's streaming data model is the events  
9016 are reconstructed in near real time from the streaming data, modulo time varying calibrations that  
9017 will require later reprocessing for a final fully calibrated reconstruction. The prompt availability  
9018 of reconstructed data, and concurrent calibration cycle consuming it, is a crucial element of ePIC's  
9019 objective to have a rapid, near real time turnaround of the raw data to production, as expressed in  
9020 the software principles [?]. The stringent low latency and high availability requirements of prompt  
9021 reconstruction, together with the locality of its inputs at the Echelon 1 sites, makes this a processing  
9022 activity limited to Echelon 1. Prompt reconstruction uses streaming based processing described in  
9023 Section 8.3.11 below, taking time frames as produced by the DAQ as input and producing event  
9024 (single interaction) based data as output, for processing by analysis software.

9025 **First Pass Reconstruction** It is expected that the Echelon 1 facilities will have insufficient com-  
9026 pute resources to perform the complete first pass reconstruction for incoming data. The prompt  
9027 reconstruction workflow at Echelon 1 will process, at a minimum, the sample necessary for moni-  
9028 toring, diagnostics, quick-turnaround calibration and so on. The remaining first pass reconstruction  
9029 processing will be shared with Echelon 2 facilities. The maximum acceptable completion time is  
9030 about 2-3 weeks. This timescale is driven by calibrations. Given the expectation of relatively low  
9031 data rates during commissioning and early running, and the need to commission, validate and sta-  
9032 bilize the use of Echelon 2s for first pass reconstruction, it is likely that Echelon 2s will be integrated  
9033 after the first pass reconstruction workflow at Echelon 1 is operating smoothly and Echelon 2s are  
9034 validated as ready.

9035 **Reprocessing** The reprocessing use case can take several specific forms: full reprocessing from  
9036 time frames (expected to be infrequent, after commissioning), re-reconstruction of event-factorized  
9037 data with updated reconstruction and calibration (as soon as calibrations are available, plus a few  
9038 more times per year), and regeneration of analysis object data as selections against the full data

sample evolve (frequent). The analysis object data will be compact enough to “take home”. All reprocessing workflows are amenable to batch style processing and can utilize Echelon 1-2 and opportunistic resources.

**Simulation** Monte Carlo simulation in ePIC will encompass physics simulation (event and background modeling) and (with physics simulation as input) detector simulation, both fully detailed (Geant4) and fast (parameterized, ML based). At least one order of magnitude more simulated events than data will be needed for ePIC’s various run configurations in order to estimate systematic uncertainties, ensuring simulation will remain a substantial production workload and resource consumer after datataking is underway. The output of simulation and subsequent digitization will have the frame-based streaming structure matching that of real data, such that the reconstruction operates on simulated data exactly as it does on real. (This is not yet implemented.) However in its production, simulation data has more in common with conventional batch processing than streaming. That said, we aim to set up the simulation workflows to mimic streaming data production workflows in an active attempt to gain experience with these workflows prior to datataking.

From a workflow and resource utilization perspective, reconstructing the simulated data within the same workflow is preferable, e.g. avoiding a storage-consuming output stage after the simulation, and avoiding the complication of distinct MC simulation/production workflows. Technical and sociological considerations may however separate these workflows at certain times, for example if the lifetime of simulated data (slow release cycle, determined mainly by experimental setup changes and major software releases) is substantially longer than for reconstructed data (fast release cycle determined by rapidly evolving reconstruction algorithms). Both workflow configurations should be foreseen. Simulation workflows can utilize Echelon 1-2 and opportunistic resources.

**Analysis** The EIC has a broad science program. The analysis effort in ePIC categorizes its studies into inclusive, semi-inclusive, and exclusive measurements, the investigation of jet and heavy-flavor physics, and the exploration for physics that goes beyond the standard model. Each category encompasses numerous observables under examination. The feasibility of analysis prototyping and some types of analysis aligns with the capacities of Echelon 3. Nonetheless, many studies, such as imaging the quark-gluon structure of the nucleon, necessitate the computing resources of Echelon 2 or 1. The traditional approach for these analyses is rooted around immediate data reduction of large amounts of detected particles into multi-dimensional histograms. Corrections for experimental effects, such as background effects, limited detector acceptance and resolution, and detector inefficiencies can then be deconvoluted from the observable of interest through simple arithmetic and matrix transformations. This procedure of deconvoluting experimental effects from histogrammed observables is referred to as unfolding. In contrast, there are emerging analysis techniques at the event level. The event-level approach requires a reversal of the traditional procedure of correcting and unfolding measured histograms: here, idealized events from theory have to be folded with the relevant experimental effects. After folding, the theoretical calculations can then be directly compared with the experimental events at the detector level. The accuracy and precision of these methods depend on intricate simulations in the unfolding scenario and detailed modeling of experimental effects in the folding scenario.

**Modeling and Digital Twin** The streaming data will be used as input for modeling the background for detailed studies of the background under various conditions of the EIC and ePIC detector. Furthermore, ePIC plans to use the complete information from the experiment to create a digital twin of the experiment. This digital twin will complement the detailed detector simulations. It will provide a model of the experiment to be used as input for experimental control in situations where

immediate feedback from the model is necessary. The digital twin also offers a model that can be easily shared, facilitating the reproduction of results without the necessity of running computationally intensive detector simulations. The digital twin also allows for the exploration of different scenarios, providing complementary information to gain deeper understanding and optimization of experimental conditions. This, along with the data analysis and detector simulations, will offer valuable insights into improving run plans and potential upgrades for the experiment. Modeling workflows can utilize Echelon 1 and Echelon 2.

## Computing Resources

**The Computing Model's Resource Requirements** Figure 8.285 shows the Butterfly Computing Model that will be used for ePIC. In this model the detector together with the DAQ system constitute Echelon 0. Two Echelon 1 sites are located in the computing centers of the host labs BNL and JLab, with the capability to serve as functional peers for host-site ePIC computing, both providing storage and processing resources. Echelon 2 sites contribute processing resources and may also provide storage resources convenient for access by distributed collaborators (see Section 8.3.11 for details).

The computing resources needed for all phases of data processing after the raw stream leaves Echelon 0 will be distributed across multiple facilities. The overall resource requirements are therefore cumulative among them, together with the networking required for robust distributed operation.

Overall, Echelon 0 will need to send raw data at 200Gbps and each Echelon 1 site will need to be able to receive data at 100Gbps. Additional bandwidth will be needed at the Echelon 1 sites to send data to Echelon 2 sites for processing and to receive the results. Storage bandwidth and volumes are driven by these rates and are detailed in the following sections.

The resource requirement estimates are based on the EIC/ePIC timeline and expected luminosity ramp as of Fall 2024. The expected maximum luminosity of the EIC for ePIC is  $\approx 10^{34} \text{cm}^{-2}\text{s}^{-1}$ . It will take some years beyond the start of physics operations to attain this level. Present planning puts the luminosity target for initial 'Phase 1' physics operations at  $\approx 10^{33} \text{cm}^{-2}\text{s}^{-1}$ . The resource estimations below are based on this Phase 1 scenario, unless specified otherwise, taking 2034 as a nominal Phase 1 datataking year. The computing model is designed to ultimately serve the full luminosity delivered by the EIC, while tailoring the deployed scale to current needs at any given time, thereby gaining cost savings from computing cost reductions over time.

**Echelon 0: The Stored Data Stream** The maximum EIC luminosity of  $10^{34} \text{cm}^{-2}\text{s}^{-1}$  is expected to correspond to a nominal data egress rate from DAQ of  $\approx 100 \text{Gbps}$  (see sec. ??). During early Phase 1 running at lower luminosity the rate is expected to be circa 1/3 of that, the lower luminosity counterbalanced by a larger volume of detector data used for debugging and developing a detailed understanding of detector behavior. Given the uncertainties, for the purposes of resource estimation we use the full 100Gbps rate.

This is an instantaneous rate that will be reduced to the average rate via a data buffer in Echelon 0 just prior to the exit. While the average rate may be around 50% of the maximum, the system will be designed to accommodate the full 100Gbps bandwidth between Echelon 0 and each of the Echelon 1 sites. This will allow for closer to real-time processing of the data offsite. Both of the host labs will therefore receive the full storage-level data stream in real time.

Thus, Echelon 0 will use 200Gbps of outgoing bandwidth. A small amount of additional outgoing



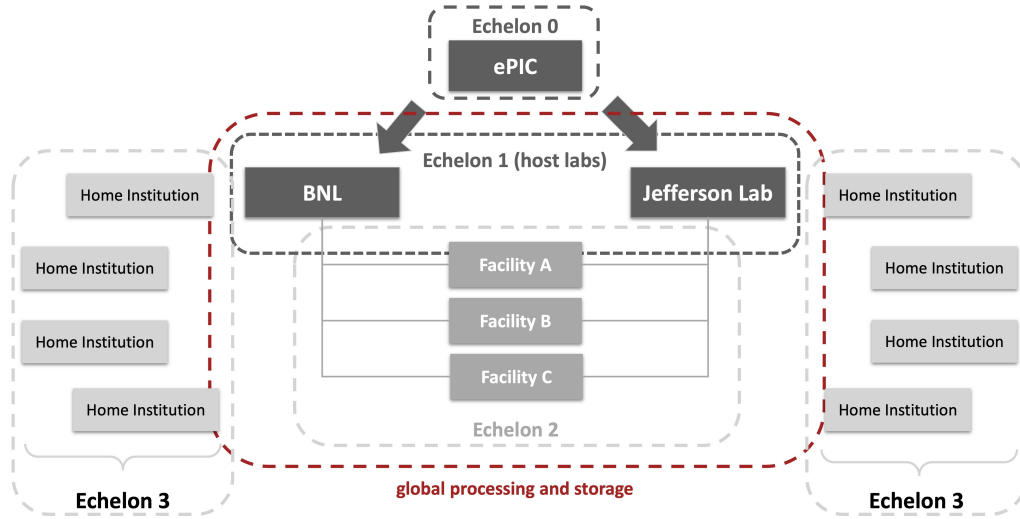


Figure 8.285: Butterfly Computing Model *see text for details*).

bandwidth will be needed for monitoring streams, slow controls data, and misc. metadata artifacts. These are expected to contribute  $\leq 1\%$  to the total. The utilized bandwidth on the network should not exceed 50% of the maximum throughput, putting the network bandwidth requirement out of Echelon 0 at 400Gbps.

A summary of the Echelon 0 rates can be seen in Table 8.78.

The incoming bandwidth to Echelon 0 is expected to be small by comparison to the total outgoing bandwidth. This will include incoming monitoring data from higher Echelons and relevant calibration values.

The Echelon 0 storage will be primarily short term disk in the form of the output Data Buffers. The buffers will serve to smooth out fluctuations in the DAQ rate as well as provide a means to store data for a short period of time in the event of a temporary loss of communication to the Echelon 1s. The buffer will be sized to hold at least 24 hours of raw data produced at the full 100Gbps rate, corresponding to on the order of 1PB.

Resource	Type	Amount
Outgoing bandwidth	raw data	200Gbps
	Monitoring, slow controls, misc. meta data	$\leq 1\text{Gbps}$
	Capacity headroom	$\approx 200\text{Gbps}$
	<b>TOTAL</b>	<b>400Gbps</b>
Incoming bandwidth	monitoring, calibration	$\leq 1\text{Gbps}$
Storage	Disk (outgoing data buffer w/ 24hr)	1PB

Table 8.78: Echelon 0 networking and storage requirements.

**Echelon 1: ePIC Computing at the Host Labs** The host labs at Echelon 1 will each receive a full copy of the data. Current planning calls for the bandwidth, storage and compute requirements to be the same for both Echelon 1 sites. An Echelon 1 site will need to be capable of receiving 100Gbps and permanently storing both the raw data and the reconstructed data for the full data set.

The following Subsections describe the computing resource requirements for networking, storage and processing at Echelon 1, necessarily describing also the proportion of computing not done at Echelon 1. Processing not performed at Echelon 1 will primarily be done at Echelon 2s, described in the next Section. The ePIC Collaboration will also draw on opportunistic resources for computing needs that can be met away from the Echelon 1 centers; opportunistic and special resources are discussed in a later Section. -----

**Echelon 1 Networking** The Echelon 1 sites will require sufficient incoming bandwidth to receive 100 Gbps of raw data and outgoing bandwidth to serve the Echelon 2 sites they connect to.

Preliminary plans have the near real-time computing for reconstruction of the raw data stream ('prompt processing') being split equally between each of the Echelon 1 sites. Over time, prompt processing is likely to be shared also with Echelon 2 sites. At any rate, Echelon 2 sites will also collectively host some number of raw data copies for reprocessing and calibration. This means each Echelon 1 site will need additional outgoing bandwidth at a level of at least 1/6 of the total raw data stream or  $\approx 35\text{Gbps}$  with capacity headroom for steady state running.

The calibration, monitoring, and slow controls data will be needed by each Echelon 2 site. While the bandwidth for all of these combined is small relative to the full raw data stream, the Echelon 1 sites will need to supply multiple Echelon 2 sites with copies of those values.

Resource	Type	Amount
Outgoing bandwidth	Raw data <i>-immediate</i> ( $\frac{1}{6}$ of total)	17Gbps
	Raw data <i>-replay</i> (contingency)	50Gbps
	monitoring, slow controls, misc. meta data	1Gbps
	<b>TOTAL</b>	<b>68Gbps</b>
Incoming bandwidth	monitoring, calibration, slow controls (from E0, E1, and Echelon 2)	1Gbps

**Table 8.79:** Echelon 1 networking requirements. Values shown are for a single E1 site.

The bandwidth requirements for each Echelon 1 site to the Echelon 2 sites it serves is shown in Table 8.79.

**Echelon 1 and 2 Storage** Each Echelon 1 site will require enough archival and disk storage to hold the entire raw data set as well as the Echelon 1's share of downstream data processing and simulation. The estimated raw data size for one year of running during Phase 1 is  $\approx 70\text{PB}$ . The total Echelon 1 storage required across all workflows for a year of data is  $\approx 200\text{PB}$ . This assumes that the Echelon 1s between them hold a complete simulated data sample ( $\approx 100\text{PB}$ ), a complete first full reconstruction dataset and one re-reconstruction dataset (each  $\approx 10\text{PB}$ ).

Fast disk access will be needed to store raw data while calibrations are done and data is processed at either an Echelon 1 or 2 site. Raw data files will not be deleted from disk until their corresponding reconstruction artifacts are stored in both Echelon 1 tape archives. This process is currently esti-

9172 mated to take up to 3 weeks allowing for an extended calibration period. The prompt processing  
 9173 sample, currently estimated (conservatively) as 50% of the full sample, also will have a steady-state  
 9174 disk presence. These disk resident samples are expected to total about 5 – 10PB in Phase 1.

9175 The raw data as well as simulation and reconstruction data may be primarily tape resident in order  
 9176 to economize on disk, with a ‘data carousel’ workflow used to dynamically orchestrate the place-  
 9177 ment of a sliding window of tape-resident data on disk for processing. This approach has been  
 9178 used successfully for many years at RHIC and ATLAS, for example.

9179 Additional disk space will be required for individual user analyses. Some of this will be distributed  
 9180 throughout the Echelon 2 sites, but it is anticipated that the Echelon 1 sites will also be used for  
 9181 this purpose. To estimate this, we assume these analyses will require an additional 10% of the  
 9182 reconstructed data volume (1% of the raw data volume) and that it will be distributed amongst the  
 9183 Echelon 1 and 2 sites in the same proportions. This is considered negligible for the purposes of this  
 9184 estimate, smaller than the uncertainties.

9185 Echelon 2 sites will be important contributors to all workflows apart from raw data streaming  
 9186 and (at least in early running) prompt reconstruction. We use the following estimates of their  
 9187 participation share for the purposes of this resource estimation.

Fraction of alignment/calibration done outside Echelon 1	50%
Fraction of first full reco done outside Echelon 1	40%
Fraction of reprocessing reco done outside Echelon 1	60%
Fraction of simulation done outside Echelon 1	75%

**Table 8.80:** Fractions of production workflows performed outside of Echelon 1 sites (i.e. at Echelon 2 and opportunistic sites)

Storage Estimates by Use Case [PB]	Echelon 1	Echelon 2
Streaming Data Storage and Monitoring	71	35
Alignment and Calibration	1.8	1.8
Prompt Reconstruction	4.4	-
First Full Reconstruction	8.9	3.0
Reprocessing	9	9
Simulation	107	107
<b>Total estimate storage</b>	<b>201</b>	<b>156</b>

**Figure 8.286:** Storage resource estimates aggregated over Echelon 1 and Echelon 2 sites, for a nominal Phase 1 datataking year.

9188 Storage resource requirement estimates are summarized in Figure 8.286.

9189 **Echelon 1 and 2 Compute** Determining the scale of the ePIC Streaming Computing and plan-  
 9190 ning for computing resource needs during the commissioning and operation of the experiment are  
 9191 essential. For a dependable estimate, a prototype for the holistic reconstruction of physics events  
 9192 from time slices is required. This reconstruction needs to include jet reconstruction and the identi-  
 9193 fication of leptons and hadrons using all PID systems in the ePIC Detector. It is important to have

reliable estimates of the fraction of background events in the data stream and their impact on the reconstruction performance in the time slices, and to understand how quickly these background events can be discarded without the need for full reconstruction. Defining the alignment and calibration methods for each subsystem and having detailed discussions about fast alignment and calibration techniques are crucial to estimate the computing resources required for alignment and calibration.

Substantial progress has been made in the year since the first release of this report, and while much work remains to be done and the uncertainties remain large (and will remain so for many years), we provide here a first estimate of the processing resources required by ePIC. Important steps during the year making this estimate possible were the implementation of time slice based track reconstruction; a careful examination of the physics and background rate environment; a similar examination of the data and processing flow of the raw stream from DAQ; and a detailed survey of alignment and calibration methodologies and timelines (during datataking) across ePIC's detector subsystems. As for the storage estimates above, the benchmark is a nominal Phase 1 year,  $10^{33} \text{cm}^2 \text{s}^{-1}$  luminosity, circa 2034.

Processing resource requirement estimates are summarized in Figure 8.287. Raw data streaming to storage and real-time monitoring requires a relatively small amount of processing, smaller than the uncertainties. Alignment and calibration processing is estimated based on a 50/50 participation of E1 and E2; this is very approximate, the main point is that calibration and alignment processing will engage both Echelons. Prompt reconstruction will take place at Echelon 1 only in the early years, potentially extending to Echelon 2s later. The capacity estimate includes a factor of two for headroom sufficient to catch up if prompt processing is interrupted. The Echelon proportions for first full reconstruction, reprocessing and simulation are as for the storage case above. Note that the total processing numbers are an overestimate given that not all workflows are active at any given time, and all available computing resources will be applied to active workflows.

Processing by Use Case [cores]	Echelon 1	Echelon 2
Streaming Data Storage and Monitoring	-	-
Alignment and Calibration	1,182	1,182
Prompt Reconstruction	11,820	-
First Full Reconstruction	14,184	9,456
Reprocessing	9,456	14,184
Simulation	24,280	72,839
<b>Total estimate processing</b>	<b>60,921</b>	<b>97,661</b>

**Figure 8.287:** Processing resource estimates aggregated over Echelon 1 and Echelon 2 sites, for a nominal Phase 1 datataking year.

**Echelon 2: Global ePIC Computing** The ePIC Collaboration is international and its computing will be as well. This is expressed in the computing model as soon as it extends beyond the Host Labs to become global, at Echelon 2. An essential component of ePIC computing, relied upon to achieve the computational scale necessary to meet the experiment's scientific goals, will be the resources contributed formally by ePIC's collaborating institutions around the world, which represent the Echelon 2 component. The computing model must be designed to effectively integrate these resources and manage their productive use, wherever they may be located, dependent of

9226 course on factors such as network connectivity.

9227 The dual Echelon 1 structure of the ePIC computing model, the “butterfly model”, already places  
 9228 distributed computing requirements on the model. Effectively integrating and leveraging globally  
 9229 distributed resources at Echelon 2 extends this requirement. The experience of the LHC experi-  
 9230 ments, well represented within the ePIC Collaboration, is relevant and applicable to developing an  
 9231 effective model for ePIC. Because Echelon 2 resources will be formally relied upon to meet com-  
 9232 puting requirements, they must come with appropriate MOUs specifying service requirements and  
 9233 assuring technical implementations compatible with the ePIC computing model. The ePIC Collab-  
 9234 oration for its part commits to a joint effort on facility integration, and the provisioning of sufficient  
 9235 testing/validation protocols, monitoring and diagnostics to convey to the Echelon 2 facility, in suf-  
 9236 ficient detail to guide remediation, the faults and performance lapses that occur.

9237 Connectivity of the Echelon 2 sites to Echelon 1 will be the same to both Echelon 1 sites (Host Labs).  
 9238 The connectivity will ultimately be to the ESnet network backbone to which the Host Labs are both  
 9239 connected. Echelon 2 sites will not have connectivity just to one or the other Echelon 1. Similarly,  
 9240 the Echelon 2 sites themselves will be interconnected as determined by their network environment,  
 9241 and these connections will be exploited by the computing model, e.g. for data replication among  
 9242 sites. A clear lesson from the LHC, which evolved from a hierarchical model to an interconnected  
 9243 mesh as experience was gained, is that the latter is far more effective.

9244 **Echelon 3: Home Institute Computing** The Echelon 3 component of the computing model is  
 9245 where the ePIC collaborator doing analysis or developing software directly encounters the comput-  
 9246 ing system. People will access ePIC computing from their institutional cluster, their work desktop,  
 9247 their personal laptop, and so on. Serving these use cases is the role of Echelon 3, and the Echelon  
 9248 1 and 2 based services that support the Echelon 3s (like access to data). Like Echelon 2, Echelon  
 9249 3 resources are global, as well as local to the user. These resources are numerous, diverse, often  
 9250 volatile and opportunistic, restricted in their use, and not suited to be managed as Collaboration  
 9251 resources. Rather the Collaboration will provide the tools, interfaces, connection points, data ac-  
 9252 cess mechanisms and support mechanisms to make such resources effective portals and analysis  
 9253 processing resources for ePIC analysis.

9254 **Opportunistic and Special Resources** Among the software and computing principles [?]   
 9255 guiding ePIC are those expressing the importance of leveraging as many computing resources for  
 9256 the collaboration as is possible and practical. ePIC software should be able to run on the archi-  
 9257 tectures and platforms available, effort permitting, while leveraging system characteristics such as  
 9258 the presence of accelerators (GPUs, TPUs, etc.), again effort permitting. ePIC S&C should support  
 9259 distributed workflows on the computing resources available to the worldwide EIC community,  
 9260 leveraging not only conventional cluster “high throughput computing” (HTC) but also high per-  
 9261 formance (HPC) systems with good usability and thereby a rewarding cost/benefit calculation.

9262 The most productive computing resource currently used by ePIC is the Open Science Grid (OSG),  
 9263 where a concurrent core count of 5-10k is stably attainable. As ePIC builds up its own computing  
 9264 resources we expect opportunistic resources like the OSG to continue to play a role, in particular for  
 9265 simulation production (detector and physics simulation). Simulation is a relatively simple work-  
 9266 flow that puts moderate demands on resources (storage needs, I/O intensity, memory), steady  
 9267 state processing, and a relatively relaxed time to complete requirement. While ePIC’s essential  
 9268 simulation requirements should be accommodated by planned and assuredly available resources,  
 9269 anticipating that ePIC science will be compute limited the exploitation of opportunistic resources  
 9270 should be foreseen. OSG has its origins as the US component of the Worldwide LHC Computing

9271 Grid (WLCG). The WLCG is evolving to also support non-LHC experiments (e.g. DUNE, SKA)  
 9272 and we can anticipate that opportunistic resources will be available to ePIC internationally as well.

9273 Commercial clouds are being actively used by science communities (Rubin Observatory and AT-  
 9274 LAS are examples) with their capabilities and cost models under study. Opportunistic (pre-  
 9275 emptible) usage modes together with workflows that elastically spike into the resource to support  
 9276 fast-turnaround use cases such as analysis are the most promising in terms of cost effectiveness. In  
 9277 ePIC we will monitor such developments and participate as we are able, and will decide at a later  
 9278 date whether such resources will have a role in our computing model.

9279 Special resources include non-x86 processor architectures such as ARM, accelerators such as GPUs  
 9280 and TPUs, and no doubt others yet to emerge over the next decade. A requirement on ePIC S&C  
 9281 infrastructure is to have the flexibility and extensibility in the software and CI to add support  
 9282 for architectures of interest as they appear. The ARM architecture is already supported, and we  
 9283 anticipate it will have an important role in coming years given its cost effectiveness per dollar and  
 9284 per watt, and the relative ease of the port. FPGAs are used in the Streaming DAQ for low-level data  
 9285 processing and reduction. GPUs are highly likely to play a role online; whether the same is true  
 9286 offline is unclear. Nonetheless support for high concurrency in the software will be needed, with  
 9287 requirements such as multithreading support, and advantages such as efficient memory utilization.  
 9288 The rise of AI/ML and accompanying proliferation of specialized accelerators such as TPUs makes  
 9289 it probable we will exploit them, perhaps largely transparently behind software APIs. We will track  
 9290 the technologies as we pursue our own AI/ML R&D and applications.

9291 Large supercomputers such as the leadership class facilities (LCFs) developed by the DOE and  
 9292 NSF are most often constituted by what we've called special resources. Whether such machines  
 9293 are effective for ePIC use will be a case by case evaluation. Today's GPU based machines offer  
 9294 limited potential given the dearth of GPU-capable workloads in ePIC (a common situation in NP  
 9295 and HEP), though we are doing R&D in GPU-amenable areas such as Cherenkov detector simula-  
 9296 tion. The US will have its first leadership class ARM machine in 2026, at the NSF's TACC facility,  
 9297 with Japan and Europe hosting others; such machines we would already be able to use effectively.  
 9298 LCFs are increasingly being designed as AI/ML factories; such machines we will assuredly be able  
 9299 to use for at least training and optimization. We have since Sep 2023 an R&D project underway  
 9300 to leverage large scale resources for the processing-intensive AI application of EIC detector design  
 9301 optimization.

9302 **Authorization and Access** Authorization and access mechanisms are evolving both in their  
 9303 technical aspects and the institutional policies that govern their use, thereby impacting the accessi-  
 9304 bility for users. The foremost priority of the ePIC Collaboration is to ensure that every collaborator  
 9305 has access to the resources of the collaboration, including data, websites, collaborative tools, infor-  
 9306 mation systems, document repositories and so on, today and reliably in the future. This consider-  
 9307 ation can be a leading or determining factor in the tools and services we use, and where they are  
 9308 hosted. It has been a factor in choosing GitHub as code repository and a cloud-based Mattermost  
 9309 instance, for example. We will continue to make this a requirement.

9310 **Distributed Computing** The ePIC collaboration consists of a globally distributed community  
 9311 of scientists engaged in the experiment's data and compute intensive scientific program. Section  
 9312 8.3.11 described the use cases and workflows that the ePIC computing infrastructure must support.  
 9313 Section 8.3.11 described the computing resources of ePIC from the detector to the host labs and on  
 9314 to the globally distributed data and processing centers providing the collaboration with resources,  
 9315 and finally to the local resources used by analysts at their institution or from their laptop. This

9316 Section describes the distributed computing software and services that will be needed in order to  
9317 knit these resources into a coherent computing fabric for ePIC that serves the full spectrum of use  
9318 cases.

9319 The ePIC experiment follows a lineage of “big science” collaborations using computing resources  
9320 on a global scale, the most prominent example to date being CERN’s LHC experiments, which  
9321 in their development towards the High Luminosity LHC (HL-LHC) are also preparing for a rich  
9322 and data intensive physics program in the 2030s. The LHC’s ALICE and LHCb experiments have  
9323 further commonality with ePIC in having introduced streaming computing models for the LHC’s  
9324 present Run-3. The LHC experiments and their collaborators in the WLCG community have built  
9325 and continue to develop expertise, tools and global infrastructure that the proliferating big science  
9326 community can draw on. The ePIC approach to distributed computing described here is built  
9327 on leveraging and collaborating with this community, bootstrapping our distributed computing  
9328 infrastructure from existing components and approaches where possible so our own efforts can  
9329 focus on the extensions and tailoring needed to support the unique aspects of ePIC’s streaming  
9330 computing model and global collaboration.

9331 **Processing Requirements for ePIC Streaming Data** The processing of ePIC streaming data  
9332 has characteristics that are markedly different from the workflows commonly found in NP and  
9333 HEP experiments to date. Current convention is that data is acquired in online workflows that  
9334 deliver the data to hierarchical storage as large files, and then processed by offline workflows with  
9335 a typically substantial latency period after acquisition (apart from promptly processed subsets for  
9336 monitoring, data quality and possibly calibration purposes). In this scenario the offline processing  
9337 maps readily onto the batch queue based resource provisioning mechanisms of computing centers.  
9338 Offline processing payloads are sent to batch queues and consume input files distributed appro-  
9339 priately for resource locality. Keys to the applicability of this straightforward approach are the  
9340 discrete, coarse grained processing units in the form of files and collections of files (datasets), and  
9341 the decoupling of processing with respect to real time data acquisition. The case of ePIC streaming  
9342 data processing, however, has neither of these characteristics.

9343 In ePIC streaming data processing, a quasi-continuous flow of fine-grained data must be processed  
9344 promptly with the dynamic flexibility to match in near real time the inflow of acquired data to  
9345 processing resources that stand ready to consume it. Prompt processing is necessary to ensure data  
9346 quality and detector integrity during data taking, and while processing of a subset could achieve  
9347 those aims, processing the full dataset quickly is necessary to minimize the time required for cali-  
9348 brating the detector and delivering analysis-ready reconstructed data promptly, a primary goal of  
9349 ePIC. For ePIC data processing, with the two host labs symmetrically serving as Echelon 1 process-  
9350 ing centers, the processing resources used at any given time must be transparent to the workflow  
9351 engine, effectively a requirement that a distributed processing capability be an integral part of the  
9352 system. The data sources are distributed as well; in a streaming computing model that dissolves  
9353 much of the distinction between online and offline, the system must be flexible towards decisions  
9354 as to the parallelism of data delivery received from the DAQ, i.e. where the event builder function  
9355 occurs. The system must support processing parallel streams of data from subdetector, accelera-  
9356 tor, beamline and other sources, augmented by sufficient metadata to make their association and  
9357 merging fault-proof. The minimized latency and high system complexity require that a high level  
9358 of automation and resilience to changing conditions be built into the streaming processing system,  
9359 necessary also to keep the operations effort at a manageable level.

9360 Summarizing the driving characteristics of ePIC streaming data processing, it is time critical, pro-  
9361 ceeding in near real time; it is data driven, consuming a fine-grained and quasi-continuous data  
9362 flow across parallel streams; it is adaptive and highly automated, in being flexible and robust



against dynamic changes in datataking patterns, resource availability and faults; and it is inherently distributed in its data sources and its processing resources. This model presents challenges for an infrastructure based on batch jobs and coarse grained files. However, the safe assumption for the infrastructure of the 2030s is that batch-style processing and coarse grained files – particularly as they map onto archival storage – will remain. A robust approach to building the ePIC streaming computing model and system will be to accommodate, but effectively hide, those underlying characteristics of the infrastructure. We may ultimately not need to accommodate them, for example Kubernetes or similar mechanisms of dynamic processing resource provisioning may displace the batch model. We should accommodate both and be resilient against technology evolution.

**Workflow Management** As described, the requirements of ePIC’s streaming based prompt reconstruction are distinct from the typical workflow management practices of contemporary experiments. Streaming is however a fertile and rapidly evolving field, in our community and well beyond. Many streaming data processing frameworks and tools exist and evolution is rapid. ePIC should be ready both to take judicious advantage, and avoid technology lock-in. The tools generally share a fundamentally similar distributed parallel model, and have common features that do not risk lock-in such as the use of standard workflow descriptions (e.g. DAG, CWL). Some systems directly manage the processing resources, such as Apache Storm and Spark, others can overlay on conventional batch or dynamic resources (such as Kubernetes); HEP/NP’s own PanDA is such a system. The underlying facilities must support high availability and service quality, though a distributed system mitigates against very stringent requirements on a single facility. The facility and the streaming workflow management system in tandem must support data flow optimization in real time.

Resources should be flexible across use cases and workflows, readily usable for other purposes when datataking is not active. For example, applications should be able to scale elastically and exploit heterogeneous hardware such as an AI/ML application spiking into an accelerated resource for low-latency turnaround. Some workflows such as simulation and reprocessing are served well by conventional batch processing, lending advantage to all ePIC’s major resources supporting batch.

The international nature of the ePIC Collaboration and its computing makes it essential that workflow management tools support the use of computing resources around the world, for essentially all managed workflows apart from prompt reconstruction, and for physics analysis.

**Data Management and Access** Prompt processing of data streaming from the detector will yield file based data suitable for consumption by hierarchical storage and by file-based data management tools. Raw data copies will be written to archival storage at the two host labs, with the expectation that retrieval is rare. (Under normal operation, no production workflow involves archival data retrieval.) Data management tools must support the distribution and use of data around the world, serving ePIC’s global processing resources and community of analysts. Disk resident replicas at Echelon 1 and 2 sites will be managed by the data management system. Client tools for accessing and storing data at managed data stores will be usable at all Echelons including local/personal computers with appropriate authentication. Authentication and authorization (AA) mechanisms must support access for all ePIC collaborators globally.

The broad acceptance of the Rucio data management system as a standard, within HEP and increasingly within NP, makes it the likely system for ePIC datataking use, in its evolved 2030s form. Rucio is being integrated and tested in ePIC now, and ePIC will engage with and contribute to the (very open) Rucio community. Rucio and the distributed computing community is migrating

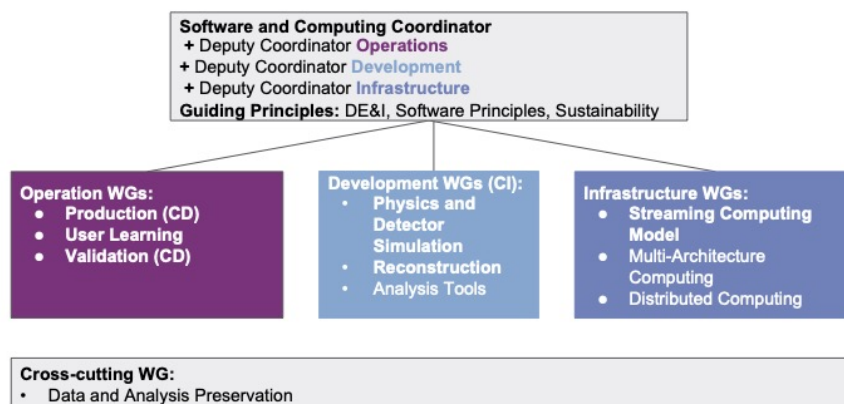


**Figure 8.288:** Organizational chart of the Software and Computing Effort in ePIC. The Streaming Computing Working Group is joint with Electronics and DAQ Working Group in the Technical Effort to ensure that DAQ and Computing are developed together.

to SciToken based AA mechanisms which enable a federated ecosystem for uniform authorization across distributed scientific computing infrastructures, and should be capable of meeting the collaborator access requirement.

Data movement tools are in a state of flux. The long-used third party copy tool gridftp was recently retired, with http chosen as the basis for replacing it. XRootD is a powerful community-standard tool with data movement functionality tuned to the needs of HEP/NP (e.g. efficient handling of ROOT based data, in terms of both movement and caching). FTS is the data mover underpinning Rucio as used by the LHC experiments. Object store based data storage and movement (supporting the S3 API) are increasingly common. Some DOE computing facilities require the use of Globus data mover tools. Fortunately Rucio can hide much of this fragmentation (Rucio is not in itself a data mover, it interfaces with them). ePIC will leverage this encapsulation and avoid lock-in.

## Project Organization and Collaboration

**Organization of DAQ and Computing in ePIC** The scientific management of the ePIC collaboration is organized in three efforts that report to the spokesperson and deputy spokesperson: an analysis effort with currently two Analysis Coordinators, a technical effort with a Technical Coordinator, and a software and computing effort with a Software & Computing coordinator (SCC). The SCC oversees all aspects of software and computing in ePIC and has three deputies sharing the responsibilities for development, operations, and infrastructure.

Development currently has two active working groups: Physics and Detector Simulations as well as Reconstruction. Another working group on Analysis Tools is being planned. Operations comprises three active working groups: Production, User Learning, and Validation. Among the Infrastructure working groups, which consist of Streaming Computing Model, Multi-Architecture Computing, and Distributed Computing, only the Streaming Computing Model group is active at present, the others not being an immediate priority. Moreover, there is a planned cross-cutting working group on data and analysis preservation. The activation of the working groups will depend on the number of people actively participating in software and computing.

Two of the three conveners of the Streaming Computing Model WG are also conveners of the Elec-

tronics and DAQ WG that is part of the technical effort. Both working groups have regular meetings, and a significant fraction of the attendees of these meetings are the same. This ensures that the DAQ and Computing are developed together with well-defined and well-understood interfaces, and ePIC builds a group of experts familiar with data processing from the DAQ to the analysis.

### Long Term Software and Computing Plan

**Timeline and High Level Milestones** ePIC Software & Computing has developed closely with the collaboration and with input from the EIC project a timeline of high level milestones, including the long-term. The milestones are grouped by the anticipated date for CD-2 approval, the detector construction phase, and the commissioning and operations phase. Priority is always given to meeting near-term needs, with the longer range timeline progressively exercising the streaming computing model to deliver for the needs of the CD process, for specific applications (e.g. test beams), for scaling and capability challenges, and ultimately for the phases of datataking. The series of milestones ensures that the agile development process is continuously confronted with real world exercising of the software and the developing realization of the computing model.

**Preparations for CD-2 and the Technical Design Report** ePIC is providing support to the EIC Project in the preparations for CD-2 decision process and the Technical Design Report for the detector, both of which are due in November 2024:

- Software and simulation readiness for TDR preparation (and subsequent phases of the CD process).
- Provide for each use case Sec. 8.3.11 detailed estimates on the compute resources; update the networking and storage estimates according to format of streaming data format that is currently being defined.

**Detector Construction Phase** The subsystems of the ePIC Detector must be constructed by 2030. During the construction, the detector designs will be further optimized, considering changes in costing and the availability of materials. Additionally, prototypes of the various detector systems will undergo testing. This will facilitate software testing and provide an opportunity for validation of the simulations based on the results from the test-beam measurements. The relatively extended duration of the construction phase presents an ideal timescale for the further development and implementation of the ePIC Streaming Computing Model:

- Provisioning DAQ and software sufficient for test beams, which can serve as small scale real-world testbeds for the developing DAQ and software.
- Streaming challenges exercising the streaming workflows from DAQ through offline reconstruction, and the Echelon 0 and Echelon 1 computing and connectivity.
- Data challenges exercising scaling and capability tests as distributed ePIC computing resources at substantial scale reach the floor, including exercising the functional roles of the Echelon tiers, particularly Echelon 2, the globally distributed resources essential to meeting ePIC's computing requirements.
- Analysis challenges exercising autonomous alignment and calibrations.
- Analysis challenges exercising end-to-end workflows from (simulated) raw data to exercising the analysis model.

**Detector Commissioning and Early Datataking Phase** In approximately a decade, when the ePIC Detector is completed, the experiment’s commissioning phase will commence. This phase will come with distinct expectations and requirements in comparison to steady-state operation. For instance, it will involve the utilization of semi-triggered data-taking modes, initial calibrations, introduction of zero suppression, and the gradual extension of near real-time processing from Echelon 1 to Echelon 2, among other tasks. Successful software and computing efforts during the commissioning phase will necessitate careful planning, drawing from the experience gained in the data and analysis challenges during the detector construction phase.

During the initial data-taking phase, immediately following the commissioning phase, simpler and more conservative approaches will be adopted as the ePIC Streaming Computing Model is gradually being deployed and validated.

**Data and Analysis Preservation** A guiding principle [?] of ePIC S&C is that data and analysis preservation (DAP) will be an integral part of EIC software and workflows, aiming for analyses that are fully reproducible, re-usable, and re-interpretable, based on reusable software and amenable to adjustments and new interpretations.

The ePIC Collaboration is planning to incorporate DAP into its software and computing from an early stage. A cross-cutting working group is foreseen in the org chart and will be activated during the next year. It will address DAP requirements and a timeline for DAP developments, prioritizing those with value for ePIC computing and analysis in the near as well as the long term, such as a robust and user friendly infrastructure for containerization in analysis, which is already well advanced in ePIC.

The S&C infrastructure that ePIC is establishing now will facilitate DAP, including containerization of the ePIC software stack, automation of well defined workflows using workflow definition languages (currently used in GitLab based CI), centralized workflow and metadata management (supporting distributed production on OSG), a curated and sustainable code repository and web presence (GitHub and its website publishing tools), and data management supporting the full data life cycle and provenance (Rucio integration is in progress). A prominent missing component at present is document management, being addressed at the Collaboration level.

## 8.4 Detector Integration

Add text here.

### 8.4.1 Installation and Maintenance

Add text here.

## 8.5 Detector Commissioning and Pre-Operations

Add text here.

# References

- [1] A. Bacchetta, V. Bertone, C. Bissolotti, G. Bozzi, M. Cerutti, F. Delcarro, M. Radici, L. Rossi, and A. Signori, "Flavor dependence of unpolarized quark transverse momentum distributions from a global fit," *JHEP*, vol. 08, p. 232, 2024.
- [2] Irene Dutta and Christopher Madrid and Ryan Heller and Shirsendu Nanda and Danush Shekar and Claudio San Martín and Matías Barria and Artur Apresyan and Zhenyu Ye and William K. Brooks and Wei Chen and Gabriele D'Amen and Gabriele Giacomini and Alessandro Tricoli and Aram Hayrapetyan and Hakseong Lee and Ohannes Kamer Köseyan and Sergey Los and Koji Nakamura and Sayuka Kita and Tomoka Imamura and Cristian Peña and Si Xie, "Results for pixel and strip centimeter-scale AC-LGAD sensors with a 120 GeV proton beam," 7 2024.
- [3] F. T. Acosta, B. Karki, P. Karande, A. Angerami, M. Arratia, K. Barish, R. Milton, S. Morán, B. Nachman, and A. Sinha, "The optimal use of segmentation for sampling calorimeters," *JINST*, vol. 19, no. 06, p. P06002, 2024.
- [4] M. M. David Ruth, Alex Jentsch, "Advanced methods for roman pots reconstruction at the eic." [https://indico.cern.ch/event/1199314/contributions/5193191/attachments/2619028/4527696/DIS\\_RNDtalk\\_DRuth.pdf](https://indico.cern.ch/event/1199314/contributions/5193191/attachments/2619028/4527696/DIS_RNDtalk_DRuth.pdf), 2023.
- [5] S. Lai *et al.*, "Software Compensation for Highly Granular Calorimeters using Machine Learning," *JINST*, vol. 19, p. P04037, 2024.
- [6] S. J. Paul, R. Milton, S. Morán, B. Schmookler, and M. Arratia, "Feasibility study of measuring  $\Lambda 0 \rightarrow n \pi 0$  using a high-granularity zero-degree calorimeter at the future electron-ion collider," *Phys. Rev. D*, vol. 111, no. 9, p. 092013, 2025.
- [7] R. Milton, S. J. Paul, B. Schmookler, M. Arratia, P. Karande, A. Angerami, F. T. Acosta, and B. Nachman, "Design and simulation of a SiPM-on-tile ZDC for the future EIC, and its performance with graph neural networks," *Nucl. Instrum. Meth. A*, vol. 1079, p. 170613, 2025.
- [8] R. Abdul Khalek *et al.*, "Science Requirements and Detector Concepts for the Electron-Ion Collider: EIC Yellow Report," *Nucl. Phys. A*, vol. 1026, p. 122447, 2022.
- [9] A. Accardi *et al.*, "Electron Ion Collider: The Next QCD Frontier: Understanding the glue that binds us all," *Eur. Phys. J. A*, vol. 52, no. 9, p. 268, 2016.
- [10] A. Accardi *et al.*, "Electron Ion Collider: The Next QCD Frontier: Understanding the glue that binds us all," *Eur. Phys. J. A*, vol. 52, no. 9, p. 268, 2016.
- [11] "National Academies of Sciences, Engineering, and Medicine, An Assessment of U.S.-Based Electron-Ion Collider Science," *The National Academies Press, Washington, DC*, 2018.
- [12] J. K. Adkins *et al.*, "Design of the ECCE Detector for the Electron Ion Collider," 9 2022.

- [13] J. Adam *et al.*, “ATHENA detector proposal — a totally hermetic electron nucleus apparatus proposed for IP6 at the Electron-Ion Collider,” *JINST*, vol. 17, no. 10, p. P10019, 2022.
- [14] M. Arratia, D. Britzger, O. Long, and B. Nachman, “Reconstructing the kinematics of deep inelastic scattering with deep learning,” *Nucl. Instrum. Meth. A*, vol. 1025, p. 166164, 2022.
- [15] A. MetZhao:2016rfuz and A. Vossen, “Parton Fragmentation Functions,” *Prog. Part. Nucl. Phys.*, vol. 91, pp. 136–202, 2016.
- [16] P. J. Mulders and R. D. Tangerman, “The Complete tree level result up to order  $1/Q$  for polarized deep inelastic lepton production,” *Nucl. Phys. B*, vol. 461, pp. 197–237, 1996. [Erratum: *Nucl. Phys. B* 484, 538–540 (1997)].
- [17] A. Bacchetta, M. Diehl, K. Goeke, A. Metz, P. J. Mulders, and M. Schlegel, “Semi-inclusive deep inelastic scattering at small transverse momentum,” *JHEP*, vol. 02, p. 093, 2007.
- [18] D. W. Sivers, “Single Spin Production Asymmetries from the Hard Scattering of Point-Like Constituents,” *Phys. Rev. D*, vol. 41, p. 83, 1990.
- [19] D. W. Sivers, “Hard scattering scaling laws for single spin production asymmetries,” *Phys. Rev. D*, vol. 43, pp. 261–263, 1991.
- [20] E. C. Aschenauer, V. Batozskaya, S. Fazio, K. Gates, H. Moutarde, D. Sokhan, H. Spiesberger, P. Sznajder, and K. Tezgin, “EpIC: novel Monte Carlo generator for exclusive processes,” *Eur. Phys. J. C*, vol. 82, no. 9, p. 819, 2022.
- [21] D. Boer *et al.*, “Physics case for quarkonium studies at the Electron Ion Collider,” 9 2024.
- [22] L. Frankfurt, M. Strikman, and M. Zhalov, “Elastic and large  $t$  rapidity gap vector meson production in ultraperipheral proton–ion collisions,” *Physics Letters B*, vol. 640, no. 4, pp. 162–169, 2006.
- [23] A. Tumasyan, W. Adam, and Others, “Probing small bjorken- $x$  nuclear gluonic structure via coherent  $j/\psi$  photoproduction in ultraperipheral pb-pb collisions at  $\sqrt{s_{NN}} = 5.02$  TeV,” *Phys. Rev. Lett.*, vol. 131, p. 262301, Dec 2023.
- [24] A. Baltz, G. Baur, D. d’Enterria, L. Frankfurt, F. Gelis, V. Guzey, K. Hencken, Y. Kharlov, M. Klasen, S. Klein, V. Nikulin, J. Nystrand, I. Pshenichnov, S. Sadovsky, E. Scapparone, J. Seger, M. Strikman, M. Tverskoy, R. Vogt, S. White, U. Wiedemann, P. Yepes, and M. Zhalov, “The physics of ultraperipheral collisions at the LHC,” *Physics Reports*, vol. 458, no. 1, pp. 1–171, 2008.
- [25] J.-P. Lansberg, K. Lynch, C. Van Hulse, and R. McNulty, “Inclusive photoproduction of vector quarkonium in ultra-peripheral collisions at the LHC,” 9 2024.
- [26] S. R. Klein and H. Mäntysaari, “Imaging the nucleus with high-energy photons,” *Nature Rev. Phys.*, vol. 1, no. 11, pp. 662–674, 2019.
- [27] K. J. Eskola, C. A. Flett, V. Guzey, T. Löytäinen, and H. Paukkunen, “Exclusive quarkonium photoproduction in  $A+A$  UPCs at the LHC in NLO pQCD,” *PoS*, vol. HardProbes2023, p. 107, 2024.
- [28] C. A. Flett, J. P. Lansberg, S. Nabeebaccus, M. Nefedov, P. Sznajder, and J. Wagner, “Exclusive vector-quarkonium photoproduction at NLO in  $\alpha_s$  in collinear factorisation with evolution of the generalised parton distributions and high-energy resummation,” 9 2024.
- [29] S. R. Klein, J. Nystrand, J. Seger, Y. Gorbunov, and J. Butterworth, “Starlight: A monte carlo simulation program for ultra-peripheral collisions of relativistic ions,” *Computer Physics Communications*, vol. 212, pp. 258–268, 2017.

- [30] Y. X. Zhao, A. Deshpande, J. Huang, K. S. Kumar, and S. Riordan, "Neutral-Current Weak Interactions at an EIC," *Eur. Phys. J. A*, vol. 53, no. 3, p. 55, 2017.
- [31] "Radiation Doses." [https://wiki.bnl.gov/EPIC/index.php?title=Radiation\\_Doses](https://wiki.bnl.gov/EPIC/index.php?title=Radiation_Doses).
- [32] S. Agostinelli *et al.*, "GEANT4—a simulation toolkit," *Nucl. Instrum. Meth. A*, vol. 506, p. 250, 2003.
- [33] "The electron-ion collider user group."
- [34] R. A. Khalek *et al.*, "Science Requirements and Detector Concepts for the Electron-Ion Collider: EIC Yellow Report," *Nucl. Instr. and Meth. A*, vol. 1026, p. 122447, 2022.
- [35] "The epic collaboration website."
- [36] A. Collaboration, "Technical Design report for the ALICE Inner Tracking System 3 - ITS3 ; A bent wafer-scale monolithic pixel detector," tech. rep., CERN, Geneva, 2024.
- [37] M. Karagounis, D. Arutinov, M. Barbero, F. Huegging, H. Krueger, and N. Wermes, "An integrated shunt-ldo regulator for serial powered systems," in *2009 Proceedings of ESSCIRC*, pp. 276–279, 2009.
- [38] A. Paramonov, "FELIX: the Detector Interface for the ATLAS Experiment at CERN," *EPJ Web Conf.*, vol. 251, p. 04006, 2021.
- [39] lpGBT Design Team, "lpGBT documentation – release," 2024.
- [40] J. Troska *et al.*, "The VTRx+, an optical link module for data transmission at HL-LHC," 2017.
- [41] D. Higinbotham and *et al.*, "Science requirements and detector concepts for the electron-ion collider: Eic yellow report," *Nuclear Physics A*, vol. 1026, p. 122447, 2022.
- [42] F. Willeke and J. Beebe-Wang, "Electron ion collider conceptual design report 2021," 2 2021.
- [43] ePIC, "Summary of epic background rates," 2024.
- [44] EIC, "Eic detector geometry," 2024.
- [45] D. Neyret, P. Abbon, M. Anfreville, V. Andrieux, Y. Bedfer, D. Durand, S. Herlant, N. d'Hose, F. Kunne, S. Platchkov, F. Thibaud, M. Usseglio, and M. Vandenbroucke, "Aging effects in the compass hybrid gem-micromegas pixelized detectors," *Nuclear Instruments and Methods in Physics Research Section A: Accelerators, Spectrometers, Detectors and Associated Equipment*, vol. 1065, p. 169511, 2024.
- [46] C. Altunbas, M. Capeans, K. Dehmelt, J. Ehlers, J. Friedrich, I. Konorov, A. Gandi, S. Kappler, B. Ketzer, R. De Oliveira, S. Paul, A. Placci, L. Ropelewski, F. Sauli, F. Simon, and M. van Steenis, "Construction, test and commissioning of the triple-gem tracking detector for compass," *Nuclear Instruments and Methods in Physics Research Section A: Accelerators, Spectrometers, Detectors and Associated Equipment*, vol. 490, no. 1, pp. 177–203, 2002.
- [47] T. Kawamoto *et al.*, "New Small Wheel Technical Design Report," *CERN-LHCC-2013-006, ATLAS-TDR-020, CERN-LHCC-2013-006, ATLAS-TDR-020*, 6 2013.
- [48] M. Poli Lener, G. Bencivenni, R. de Olivera, G. Felici, S. Franchino, M. Gatta, M. Maggi, G. Morello, and A. Sharma, "The  $\mu$ -rwell: A compact, spark protected, single amplification-stage mpgd," *Nuclear Instruments and Methods in Physics Research Section A: Accelerators, Spectrometers, Detectors and Associated Equipment*, vol. 824, pp. 565–568, 2016. Frontier Detectors for Frontier Physics: Proceedings of the 13th Pisa Meeting on Advanced Detectors.



- [49] E. Farina, B. A. Gonzalez, P. Iengo, L. Longo, J. Samarati, G. Sekhniaidze, O. Sidiropoulou, and J. Wotschack, "Resistive micromegas high-rate and long-term ageing studies at the cern gamma irradiation facility," *Nuclear Instruments and Methods in Physics Research Section A: Accelerators, Spectrometers, Detectors and Associated Equipment*, vol. 1042, p. 167423, 2022.
- [50] M. Chefdeville and et al., "Development of micromegas detectors with resistive anode pads," *Nuclear Instruments and Methods in Physics Research Section A: Accelerators, Spectrometers, Detectors and Associated Equipment*, vol. 1003, p. 165268, 2021.
- [51] L. Shekhtman, G. Fedotovitch, A. Kozyrev, V. Kudryavtsev, T. Maltsev, and A. Ruban, "Development of  $\mu$ rwell detectors for the upgrade of the tracking system of cmd-3 detector," *Nuclear Instruments and Methods in Physics Research Section A: Accelerators, Spectrometers, Detectors and Associated Equipment*, vol. 936, pp. 401–404, 2019.
- [52] A. Acker, D. Attié, S. Aune, J. Ball, P. Baron, Q. Bertrand, D. Besin, T. Bey, F. Bossù, R. Boudouin, M. Boyer, G. Christiaens, P. Contrepois, M. Defurne, E. Delagnes, M. Garçon, F. Georges, J. Giraud, R. Granelli, N. Grouas, C. Lahonde-Hamdoun, T. Lerch, I. Mandjavidze, O. Meunier, Y. Moudde, S. Procureur, M. Riallot, F. Sabatié, M. Vandenbroucke, and E. Virique, "The clas12 micromegas vertex tracker," *Nuclear Instruments and Methods in Physics Research Section A: Accelerators, Spectrometers, Detectors and Associated Equipment*, vol. 957, p. 163423, 2020.
- [53] I. Giomataris, R. De Oliveira, S. Andriamonje, S. Aune, G. Charpak, P. Colas, A. Giganon, P. Rebougeard, and P. Salin, "Micromegas in a bulk," *Nucl. Instrum. Meth. A*, vol. 560, pp. 405–408, 2006.
- [54] H. Schindler and R. Veenhof, "Garfield++," 2024.
- [55] K. Gnanvo and et al., "Development of double-sided thin-gap gem- $\mu$ rwell for tracking at the eic." [https://www.jlab.org/sites/default/files/eic\\_rd\\_prm/files/2023\\_Proposals/20230714\\_eRD\\_tgMPGD\\_Proposal\\_FY23\\_Final\\_EICGENRandD2023\\_16.pdf](https://www.jlab.org/sites/default/files/eic_rd_prm/files/2023_Proposals/20230714_eRD_tgMPGD_Proposal_FY23_Final_EICGENRandD2023_16.pdf), 2023.
- [56] K. Gnanvo, N. Liyanage, B. Mehl, and R. de Oliveira, "Performance of a resistive micro-well detector with capacitive-sharing strip anode readout," *Nuclear Instruments and Methods in Physics Research Section A: Accelerators, Spectrometers, Detectors and Associated Equipment*, vol. 1047, p. 167782, 2023.
- [57] M. Calvi, P. Carniti, C. Gotti, C. Matteuzzi, and G. Pessina, "Single photon detection with SiPMs irradiated up to  $10^{14} \text{ cm}^{-2}$  1-MeV-equivalent neutron fluence," *Nucl. Instrum. Meth. A*, vol. 922, pp. 243–249, 2019.
- [58] "Technical Design Report: A High-Granularity Timing Detector for the ATLAS Phase-II Upgrade," tech. rep., CERN, Geneva, 2020.
- [59] C. Madrid, R. Heller, C. San Martín, S. Nanda, A. Apresyan, W. Brooks, W. Chen, G. Giacomini, O. Kamer Köseyan, S. Los, C. Peña, R. Rios, A. Tricoli, S. Xie, and Z. Ye, "First survey of centimeter-scale ac-lgad strip sensors with a 120 gev proton beam," *Journal of Instrumentation*, vol. 18, p. P06013, June 2023.
- [60] C. Bishop, A. Das, J. Ding, M. Gignac, F. Martinez-McKinney, S. Mazza, A. Molnar, N. Nagel, M. Nizam, J. Ott, H.-W. Sadrozinski, B. Schumm, A. Seiden, T. Shin, A. Summerell, M. Wilder, and Y. Zhao, "Long-distance signal propagation in ac-lgad," *Nuclear Instruments and Methods in Physics Research Section A: Accelerators, Spectrometers, Detectors and Associated Equipment*, vol. 1064, p. 169478, 2024.
- [61] L. Menzio et al., "First test beam measurement of the 4D resolution of an RSD pixel matrix connected to a FAST2 ASIC," *Nucl. Instrum. Meth. A*, vol. 1065, p. 169526, 2024.

- [62] S. Xie, A. Apresyan, R. Heller, C. Madrid, I. Dutta, A. Hayrapetyan, S. Los, C. Peña, and T. Zimmerman, "Design and performance of the fermilab constant fraction discriminator ASIC," *Nuclear Instruments and Methods in Physics Research Section A: Accelerators, Spectrometers, Detectors and Associated Equipment*, vol. 1056, p. 168655, 2023.
- [63] J. D. Brandenburg *et al.*, "The STAR Forward Silicon Tracker," 7 2024.
- [64] C. Chock, K. Flood, L. Macchiarulo, F. Martinez-Mckinney, A. Martinez-Rojas, S. Mazza, I. Mostafanezhad, M. Nizam, J. Ott, R. Perron, E. Ryan, H.-W. Sadrozinski, B. Schumm, A. Seiden, K. Shin, M. Tarka, D. Uehara, M. Wilder, and Y. Zhao, "First test results of the trans-impedance amplifier stage of the ultra-fast hpsoc ASIC," *Journal of Instrumentation*, vol. 18, p. C02016, feb 2023.
- [65] O. H. W. Siegmund *et al.*, "Advances in microchannel plates and photocathodes for ultraviolet photon counting detectors," *Society of Photo-Optical Instrumentation Engineers Proceedings*, vol. 81450J.
- [66] C. J. Hamel *et al.*, "LAPPD and HRPPD: Upcoming Upgrades to Incom's Fast Photosensors,"
- [67] "Popecki." <https://indico.cfnsbu.physics.sunysb.edu/event/265/contributions/922/attachments/261/411/LAPPD%20and%20HRPPD%20update%20EIC%20Workshop%2005-08-2024.pptx>.
- [68] J. A. et al, "Performance of an LAPPD in magnetic fields," *Nucl.Instrum.Meth. A*, no. 1072, p. 170122, 2025.
- [69] "EICROC ASIC." [https://indico.bnl.gov/event/18539/contributions/73731/attachments/46348/78403/CdLT\\_EICROC\\_6mar23.pdf](https://indico.bnl.gov/event/18539/contributions/73731/attachments/46348/78403/CdLT_EICROC_6mar23.pdf).
- [70] "Organization for Micro-Electronics desiGn and Applications." <https://portail.polytechnique.edu/omega/>.
- [71] J. Anderson *et al.*, "FELIX: a PCIe based high-throughput approach for interfacing front-end and trigger electronics in the ATLAS Upgrade framework," *JINST*, vol. 11, no. 12, p. C12023, 2016.
- [72] "Chiba Aerogel Factory Co., Ltd.." <https://www.aerogel-factory.jp/>.
- [73] M. Yonenaga *et al.*, "Performance evaluation of the aerogel RICH counter for the Belle II spectrometer using early beam collision data," *Prog. Theor. Exp. Phys.*, no. 093H01, 2020.
- [74] "ePIC IRT Package." <https://github.com/eic/irt/tree/pfrich>.
- [75] R. Brun and F. Rademakers, "ROOT - An Object Oriented Data Analysis Framework, Proceedings AIHENP'96 Workshop, Lausanne," *Nucl. Inst. & Meth. in Phys. Res. A*, no. 389, pp. 81–86, 1997.
- [76] M. Tabata, I. Adachi, Y. Hatakeyama, H. Kawai, T. Morita, and T. Sumiyoshi, "Large-area silica aerogel for use as cherenkov radiators with high refractive index, developed by supercritical carbon dioxide drying," *The Journal of Supercritical Fluids*, vol. 110, pp. 183–192, 2016.
- [77] "CAEN A1515BV 16-channel floating ground High Voltage module." <https://www.caen.it/products/a1515b/>.
- [78] "CAEN SY4527 High Voltage mainframe." <https://www.caen.it/products/SY4527/>.
- [79] "Wiener Mpod Low Voltage system." <https://www.wiener-d.com/power-supplies/mpod-lv-hv/>.

- [80] A. Buzykaev, A. Danilyuk, S. Ganzhur, E. Kravchenko, and A. Onuchin, "Measurement of optical parameters of aerogel," *Nuclear Instruments and Methods in Physics Research Section A: Accelerators, Spectrometers, Detectors and Associated Equipment*, vol. 433, no. 1, pp. 396–400, 1999.
- [81] A. J. Hunt, "Light scattering for aerogel characterization," *Journal of Non-Crystalline Solids*, vol. 225, pp. 303–306, 1998.
- [82] S. K. Sahu *et al.*, "Measurement of Radiation Damage on Silica Aerogel Cherenkov Radiator," *Nucl. Instrum. Meth. A*, vol. 382, pp. 441–446, 1996.
- [83] M. Tabata *et al.*, "Silica aerogel radiator for use in the A-RICH system utilized in the Belle II experiment," *Nucl. Instrum. Meth. A*, vol. 766, pp. 212–216, 2014.
- [84] R. Abjean, A. Bideau-Mehu, and Y. Guern, "Refractive index of hexafluoroethane (C-2F-6) in the 300-nm to 150-nm wavelength range," *Nucl. Instrum. Meth. A*, vol. 354, pp. 417–418, 1995.
- [85] F. Cossio *et al.*, "ALCOR: A mixed-signal ASIC for the dRICH detector of the ePIC experiment at the EIC," *Nucl. Instrum. Meth. A*, vol. 1069, p. 169817, 2024.
- [86] C. Piemonte and A. Gola, "Overview on the main parameters and technology of modern Silicon Photomultipliers," *Nucl. Instrum. Meth. A*, vol. 926, pp. 2–15, 2019.
- [87] L. P. Rignanese, P. Antonioli, R. Preghenella, and E. Scapparone, "SiPMs and examples of applications for low light detection in particle and astroparticle physics," *Riv. Nuovo Cim.*, vol. 47, no. 5, pp. 299–349, 2024. [Erratum: Riv.Nuovo Cim. 47, (2024)].
- [88] R. Hawkes, G. Bombardi, *et al.*, "Silicon photomultiplier performance tests in magnetic resonance pulsed fields," vol. 5, pp. 3400–3403, 2007.
- [89] S. España, L. Fraile, J. Herraiz, J. Udías, M. Desco, and J. Vaquero, "Performance evaluation of sipm photodetectors for pet imaging in the presence of magnetic fields," *Nuclear Instruments and Methods in Physics Research Section A: Accelerators, Spectrometers, Detectors and Associated Equipment*, vol. 613, no. 2, pp. 308–316, 2010.
- [90] F. Acerbi *et al.*, "Cryogenic Characterization of FBK HD Near-UV Sensitive SiPMs," *IEEE Trans. Electron. Dev.*, vol. 64, pp. 521–526, 10 2016.
- [91] S. Merzi, F. Acerbi, C. Aicardi, D. Fiore, V. Goiffon, A. G. Gola, O. Marcelot, A. Materne, and O. Saint-Pe, "Radiation Damage on Silicon Photomultipliers from Ionizing and Non-Ionizing Radiation of Low-Earth Orbit Operations," *Sensors*, vol. 24, no. 15, p. 4990, 2024.
- [92] E. Garutti and Y. Musienko, "Radiation damage of SiPMs," *Nucl. Instrum. Meth. A*, vol. 926, pp. 69–84, 2019.
- [93] T. Tsang, T. Rao, S. Stoll, and C. Woody, "Neutron radiation damage and recovery studies of SiPMs," *JINST*, vol. 11, no. 12, p. P12002, 2016.
- [94] M. Cordelli, E. Diociaiuti, A. Ferrari, S. Miscetti, S. Müller, G. Pezzullo, and I. Sarra, "An induced annealing technique for SiPMs neutron radiation damage," *JINST*, vol. 16, no. 12, p. T12012, 2021.
- [95] "R-116 Safety data sheet." <https://refrigerants.com/wp-content/uploads/2020/01/SDS-R116.pdf>.
- [96] EU, "Regulation (EU) 2024/573 of the European Parliament and of the Council on fluorinate greenhouse gases," <https://eur-lex.europa.eu/eli/reg/2024/573/oj>, 2024.
- [97] M. Kubantsev, I. Larin, and A. Gasparian, "Performance of the PrimEx electromagnetic calorimeter," *AIP Conf. Proc.*, vol. 867, no. 1, pp. 51–58, 2006.

- [98] T. Horn *et al.*, “Scintillating crystals for the Neutral Particle Spectrometer in Hall C at JLab,” *Nucl. Instrum. Meth. A*, vol. 956, p. 163375, 2020.
- [99] A. Asaturyan *et al.*, “Electromagnetic calorimeters based on scintillating lead tungstate crystals for experiments at Jefferson Lab,” *Nucl. Instrum. Meth. A*, vol. 1013, p. 165683, 2021.
- [100] F. Ameli *et al.*, “Streaming readout for next generation electron scattering experiments,” *Eur. Phys. J. Plus*, vol. 137, no. 8, p. 958, 2022.
- [101] T. D. Beattie *et al.*, “Construction and Performance of the Barrel Electromagnetic Calorimeter for the GlueX Experiment,” *Nucl. Instrum. Meth. A*, vol. 896, pp. 24–42, 2018.
- [102] I. Brewer, M. Negro, N. Striebig, C. Kierans, R. Caputo, R. Leys, I. Peric, H. Fleischhack, J. Metcalfe, and J. Perkins, “Developing the future of gamma-ray astrophysics with monolithic silicon pixels,” *Nucl. Instrum. Meth. A*, vol. 1019, p. 165795, 2021.
- [103] Y. Suda *et al.*, “Performance evaluation of the high-voltage CMOS active pixel sensor AstroPix for gamma-ray space telescopes,” *Nucl. Instrum. Meth. A*, vol. 1068, p. 169762, 2024.
- [104] K. Simonyan and A. Zisserman, “Very deep convolutional networks for large-scale image recognition,” *arXiv preprint arXiv:1409.1556*, 2014.
- [105] J. Shlomi, P. Battaglia, and J.-R. Vlimant, “Graph neural networks in particle physics,” *Machine Learning: Science and Technology*, vol. 2, no. 2, p. 021001, 2020.
- [106] C. R. Qi, H. Su, K. Mo, and L. J. Guibas, “Pointnet: Deep learning on point sets for 3d classification and segmentation,” in *Proceedings of the IEEE conference on computer vision and pattern recognition*, pp. 652–660, 2017.
- [107] H. Klest, M. Žurek, T. D. Beattie, M. Jadhav, S. Joosten, B. Kim, M. Kim, J. Metcalfe, Z. Papan-dreou, and J. Richards, “Evaluation of the Response to Electrons and Pions in the Scintillating Fiber and Lead Calorimeter for the Future Electron-Ion Collider,” 4 2025.
- [108] ePIC Collaboration, “Background studies - epic.” <https://wiki.bnl.gov/EPIC/index.php?title=Background>, 2023. Accessed: 2024-09-28.
- [109] O. D. Tsai *et al.*, “Results of \& on a new construction technique for W/ScFi Calorimeters,” *J. Phys. Conf. Ser.*, vol. 404, p. 012023, 2012.
- [110] C. A. Aidala *et al.*, “Design and Beam Test Results for the sPHENIX Electromagnetic and Hadronic Calorimeter Prototypes,” *IEEE Trans. Nucl. Sci.*, vol. 65, no. 12, pp. 2901–2919, 2018.
- [111] T. Nicholls *et al.*, “Performance of an electromagnetic lead / scintillating fiber calorimeter for the H1 detector,” *Nucl. Instrum. Meth. A*, vol. 374, pp. 149–156, 1996.
- [112] O. D. Tsai *et al.*, “Development of a forward calorimeter system for the STAR experiment,” *J. Phys. Conf. Ser.*, vol. 587, no. 1, p. 012053, 2015.
- [113] F. Aaron *et al.*, “Measurement of the proton structure function  $f_1(x, q^2)$  at low  $x$ ,” *Physics Letters B*, vol. 665, no. 4, pp. 139–146, 2008.
- [114] R.-D. Appuhn *et al.*, “The h1 lead/scintillating-fibre calorimeter,” *Nuclear Instruments and Methods in Physics Research Section A: Accelerators, Spectrometers, Detectors and Associated Equipment*, vol. 386, no. 2, pp. 397–408, 1997.
- [115] “SiPM radiation hardness study.” <https://indico.bnl.gov/event/24087/#17-further-rad-hard-studies-an>.
- [116] A. White *et al.*, “Design, construction and commissioning of a technological prototype of a highly granular sipm-on-tile scintillator-steel hadronic calorimeter,” *Journal of Instrumentation*, vol. 18, p. P11018, nov 2023.

- [117] V. Andrieux, R. Nothnagel, C. Riedl, and D. Sharma, “Vector-meson reconstruction in the epic backward hcal,” tech. rep., UIUC, nov 2024. <https://doi.org/10.5281/zenodo.14200156>.
- [118] M. Salajegheh, H. Khanpour, U.-G. Meißner, H. Hashamipour, and M. Soleymaninia, “Determination of diffractive PDFs from a global QCD analysis of inclusive diffractive DIS and dijet cross-section measurements at HERA,” *Phys. Rev. D*, vol. 107, no. 9, p. 094038, 2023.
- [119] E. Meschi, T. Monteiro, C. Seez, and P. Vikas, “Electron Reconstruction in the CMS Electromagnetic Calorimeter,” tech. rep., CERN, Geneva, 2001.
- [120] “The algorithm for the PWO calorimeter.” [https://www.jlab.org/primex/weekly\\_meetings/primexII/slides\\_2012\\_01\\_20/island\\_algorithm.pdf](https://www.jlab.org/primex/weekly_meetings/primexII/slides_2012_01_20/island_algorithm.pdf).
- [121] A. Laudrain and on behalf of the CALICE Collaboration, “The calice ahcal: a highly granular sipm-on-tile hadron calorimeter prototype,” *Journal of Physics: Conference Series*, vol. 2374, p. 012017, nov 2022.
- [122] “The Phase-2 Upgrade of the CMS Endcap Calorimeter,” tech. rep., CERN, Geneva, 2017.
- [123] M. Arratia *et al.*, “A high-granularity calorimeter insert based on SiPM-on-tile technology at the future Electron-Ion Collider,” *Nucl. Instrum. Meth. A*, vol. 1047, p. 167866, 2023.
- [124] M. Arratia, B. Bagby, P. Carney, J. Huang, R. Milton, S. J. Paul, S. Preins, M. Rodriguez, and W. Zhang, “Beam Test of the First Prototype of SiPM-on-Tile Calorimeter Insert for the EIC Using 4 GeV Positrons at Jefferson Laboratory,” *Instruments*, vol. 7, no. 4, p. 43, 2023.
- [125] S. J. Paul and M. Arratia, “Leveraging staggered tessellation for enhanced spatial resolution in high-granularity calorimeters,” *Nucl. Instrum. Meth. A*, vol. 1060, p. 169044, 2024.
- [126] M. Arratia, L. Garabito Ruiz, J. Huang, S. J. Paul, S. Preins, and M. Rodriguez, “Studies of time resolution, light yield, and crosstalk using SiPM-on-tile calorimetry for the future Electron-Ion Collider,” *JINST*, vol. 18, no. 05, p. P05045, 2023.
- [127] “Point Cloud Deep Learning Methods for Pion Reconstruction in the ATLAS Experiment,” tech. rep., CERN, Geneva, 2022. All figures including auxiliary figures are available at <https://atlas.web.cern.ch/Atlas/GROUPS/PHYSICS/PUBNOTES/ATL-PHYS-PUB-2022-040>.
- [128] ePIC Collaboration, “Far-forward detectors - epic.” <https://wiki.bnl.gov/EPIC/index.php?title=FarForward>, 2024. Accessed: 2024-12-06.
- [129] E. C. Aschenauer, S. Fazio, G. Giacomini, A. Jentsch, A. Kiselev, and A. Tricoli, “Sensors for roman pots at the eic.” [https://indico.bnl.gov/event/7449/contributions/35871/attachments/27124/41452/Tricoli\\_Roman\\_Pots\\_EIC\\_TempleMgt\\_ACLGAD\\_march2020.pdf](https://indico.bnl.gov/event/7449/contributions/35871/attachments/27124/41452/Tricoli_Roman_Pots_EIC_TempleMgt_ACLGAD_march2020.pdf), 2020.
- [130] R. Abdul Khalek *et al.*, “Science Requirements and Detector Concepts for the Electron-Ion Collider: EIC Yellow Report,” *Nucl. Phys. A*, vol. 1026, p. 122447, 2022.
- [131] D. Cebra, Z. Sweger, X. Dong, Y. Ji, and S. R. Klein, “Backward-angle ( $u$ -channel) production at an electron-ion collider,” *Phys. Rev. C*, vol. 106, p. 015204, Jul 2022.
- [132] Z. Sweger, S. Yoo, Z. Zeng, D. Cebra, S. R. Klein, Y. Ji, X. Dong, and M. Kim, “Modeling backward-angle ( $u$ -channel) virtual compton scattering at the future electron-ion collider,” *Phys. Rev. C*, vol. 108, p. 055205, Nov 2023.
- [133] S. Chekanov *et al.*, “Leading neutron production in  $e^+ p$  collisions at HERA,” *Nucl. Phys. B*, vol. 637, pp. 3–56, 2002.

- [134] C. Adloff *et al.*, “Measurement of leading proton and neutron production in deep inelastic scattering at HERA,” *Eur. Phys. J. C*, vol. 6, pp. 587–602, 1999.
- [135] F. D. Aaron *et al.*, “Measurement of Leading Neutron Production in Deep-Inelastic Scattering at HERA,” *Eur. Phys. J. C*, vol. 68, pp. 381–399, 2010.
- [136] V. Andreev *et al.*, “Measurement of Feynman- $x$  Spectra of Photons and Neutrons in the Very Forward Direction in Deep-Inelastic Scattering at HERA,” *Eur. Phys. J. C*, vol. 74, no. 6, p. 2915, 2014.
- [137] F. Carvalho, K. P. Khemchandani, V. P. Gonçalves, F. S. Navarra, D. S. Spiering, and A. Martínez Torres, “Leading  $\Lambda$  production in future electron-proton colliders,” *Phys. Rev. D*, vol. 108, no. 9, p. 094034, 2023.
- [138] J. Arrington *et al.*, “Revealing the structure of light pseudoscalar mesons at the electron-ion collider,” *J. Phys. G*, vol. 48, no. 7, p. 075106, 2021.
- [139] V. P. Goncalves, F. S. Navarra, and D. Spiering, “Exclusive processes with a leading neutron in  $ep$  collisions,” *Phys. Rev. D*, vol. 93, no. 5, p. 054025, 2016.
- [140] V. Andreev *et al.*, “Exclusive  $\rho^0$  meson photoproduction with a leading neutron at HERA,” *Eur. Phys. J. C*, vol. 76, no. 1, p. 41, 2016.
- [141] Y. Hatta and J. Schoenleber, “Sullivan process near threshold and the pion gravitational form factors,” 6 2025.
- [142] A. Aktas *et al.*, “Measurement of dijet cross sections in  $ep$  interactions with a leading neutron at HERA,” *Eur. Phys. J. C*, vol. 41, pp. 273–286, 2005.
- [143] S. Chekanov *et al.*, “Measurement of dijet photoproduction for events with a leading neutron at HERA,” *Nucl. Phys. B*, vol. 827, pp. 1–33, 2010.
- [144] M. Siddikov and I. Schmidt, “Generalized parton distributions from charged current meson production in  $ep$  experiments,” *Phys. Rev. D*, vol. 96, no. 9, p. 096006, 2017.
- [145] A. Jentsch, Z. Tu, and C. Weiss, “Deep-inelastic electron-deuteron scattering with spectator nucleon tagging at the future Electron Ion Collider: Extracting free nucleon structure,” *Phys. Rev. C*, vol. 104, no. 6, p. 065205, 2021.
- [146] Z. Tu, A. Jentsch, M. Baker, L. Zheng, J.-H. Lee, R. Venugopalan, O. Hen, D. Higinbotham, E.-C. Aschenauer, and T. Ullrich, “Probing short-range correlations in the deuteron via incoherent diffractive  $J/\psi$  production with spectator tagging at the EIC,” *Phys. Lett. B*, vol. 811, p. 135877, 2020.
- [147] W. Brooks, I. Schmidt, and M. Siddikov, “Deeply virtual meson production on neutrons,” *Phys. Rev. D*, vol. 98, no. 11, p. 116006, 2018.
- [148] S. R. Klein, “Challenges to the Good-Walker paradigm in coherent and incoherent photoproduction,” *Phys. Rev. C*, vol. 107, no. 5, p. 055203, 2023.
- [149] A. Hobart *et al.*, “First Measurement of Deeply Virtual Compton Scattering on the Neutron with Detection of the Active Neutron,” *Phys. Rev. Lett.*, vol. 133, no. 21, p. 211903, 2024.
- [150] J. Huang, S. Preins, R. Tsiao, M. Rodriguez, B. Schmookler, and M. Arratia, “Measurement of SiPM Dark Currents and Annealing Recovery for Fluences Expected in ePIC Calorimeters at the Electron-Ion Collider,” 3 2025.
- [151] “lpGBT Documentation.”



- 9882 [152] G. B. et al., "HGCROC-Si and HGCROC-SiPM: the front-end readout ASICs for the CMS HG-  
9883 CAL," in *IEEE Nuclear Science Symposium and Medical Imaging Conference (NSS/MIC)*, pp. 1–4,  
9884 2020.
- 9885 [153] X. H. et al., "The testing and performance of the ETROC2 for CMS MTD Endcap Timing Layer  
9886 (ETL) upgrade," in *2024 IEEE Nuclear Science Symposium (NSS), Medical Imaging Conference  
9887 (MIC) and Room Temperature Semiconductor Detector Conference (RTSD)*, pp. 1–2, 2024.
- 9888 [154] S. B. et al., "SAMPa chip: a new ASIC for the ALICE TPC and MCH upgrades.," *Journal of  
9889 Instrumentation*, February 2016.
- 9890 [155] A. Pilyar, "The 32-channel Readout Front end Card FEC32S based on SAMPa ASIC for the  
9891 Dubna NICA TPC," in *2018 IEEE XXVII International Scientific Conference Electronics – ET*,  
9892 pp. 1–3, 2018.
- 9893 [156] J. Troska, A. Brandon-Bravo, S. Detraz, A. Kraxner, L. Olanterä, C. Scarcella, C. Sigaud,  
9894 C. Soos, and F. Vasey, "The VTRx+, an optical link module for data transmission at HL-LHC,"  
9895 *PoS*, vol. TWEPP-17, p. 048, 2017.
- 9896 [157] J. Anderson *et al.*, "FELIX: a PCIe based high-throughput approach for interfacing front-end  
9897 and trigger electronics in the ATLAS Upgrade framework," *JINST*, vol. 11, no. 12, p. C12023,  
9898 2016.
- 9899 [158] R. A. et al., "APEIRON: A framework for high level programming of dataflow applications  
9900 on Multi-FPGA systems," *EPJ Web of Conferences*, no. 11002, 2024.